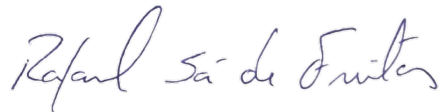


Universidade de São Paulo
Instituto de Física

Síntese, estrutura e propriedades magnéticas da série
de compostos $\text{Yb}_2\text{Zr}_x\text{Ti}_{2-x}\text{O}_7$

Francisco Lieberich



Orientador: Prof. Dr. Rafael Sá de Freitas

Dissertação apresentada ao Instituto de Física da Universidade de São Paulo, como requisito parcial para a obtenção do título de Mestre em Ciências.

Banca Examinadora:

Prof. Dr. Rafael Sá de Freitas (IF-USP)

Prof. Dr. Rômulo Augusto Ando (IQ-USP)

Prof. Dr. Cristiane Barbieri Rodella (LNLS-CNPEM)

São Paulo
2023

FICHA CATALOGRÁFICA
Preparada pelo Serviço de Biblioteca e Informação
do Instituto de Física da Universidade de São Paulo

Lieberich, Francisco

Síntese, estrutura e propriedades magnéticas da série de compostos $\text{Yb}_2\text{Zr}_x\text{Ti}_{2-x}\text{O}_7$ / Synthesis, structure and magnetic properties of the series of compounds $\text{Yb}_2\text{Zr}_x\text{Ti}_{2-x}\text{O}_7$. São Paulo, 2023.

Dissertação (Mestrado) - Universidade de São Paulo. Instituto de Física. Depto. de Física de Materiais e Mecânica.

Orientador(a): Prof. Dr. Rafael Sá de Freitas

Área de Concentração: Fenômenos Magnéticos

Unitermos: 1. Pirocloro; 2. Fluorita; 3. Desordem estrutural; 4. Magnetismo frustrado; 5. Magnetismo a baixa temperatura.

USP/IF/SBI-011/2023

University of São Paulo
Physics Institute

Synthesis, structure and magnetic properties of the
series of compounds $\text{Yb}_2\text{Zr}_x\text{Ti}_{2-x}\text{O}_7$

Francisco Lieberich

Supervisor: Prof. Dr. Rafael Sá de Freitas

Dissertation submitted to the Physics Institute of the
University of São Paulo in partial fulfillment of the
requirements for the degree of Master of Science.

Examining Committee:

Prof. Dr. Rafael Sá de Freitas (IF-USP)

Prof. Dr. Rômulo Augusto Ando (IQ-USP)

Prof. Dr. Cristiane Barbieri Rodella (LNLS-CNPEM)

São Paulo
2023

Acknowledgements

I want to acknowledge all the incredible people surrounding me, that helped me, directly or indirectly, to become the person and scientist that I am. This thesis could not have been written without them. In particular, I wish to thank

- my advisor Rafael, for his constant guidance, support, patience, and for showing me how to become a researcher
- undergraduate student Pedro, for introducing me to the laboratory, all the work we did together, and many interesting conversations
- Dimy, for performing many of the measurements in this thesis and also for many stimulating conversations
- technician Luciano, for helping me with various problems in the lab
- former PhD students Henrique and Gustavo
- undergraduate students Rafael, Wilson and Leonardo
- Prof. Fernando Garcia, for introducing me to the EXAFS technique and helping to write the synchrotron proposal that we submitted
- technician Antonio Carlos, for assisting me with many of the x-ray diffraction measurements
- Marcos, Paulo and Alan, from the mechanics workshop
- the Physics Institute and Materials Physics Department, for their facilities and staff
- Prof. Gabriel Pasca, Dr. Anastasia Burimova and their graduate students, from IPEN, for the use of their x-ray diffractometer while the crystallography department of IFUSP was still closed due to COVID
- all the teachers of the classes and courses I took, at IFUSP and elsewhere
- the developers of all the free, open source or freely available software I used at some point during my masters, including GSAS-II, FullProf, Mag2Pol, Jana, QualX, Vesta, SpinW, Spectre, PyCrystalField, and many tools of the Bilbao Crystallographic Server
- my family, especially my mother and my sister, for their constant support and love

- everyone that helped me in some way but I forgot to mention explicitly

This study was financed in part by the Coordenação de Aperfeiçoamento de Pessoal de Nível Superior - Brasil (CAPES) - Finance Code 001.

Abstract

The series of novel compounds $\text{Yb}_2\text{Zr}_x\text{Ti}_{2-x}\text{O}_7$, with composition ranging from $x = 0.0$ to $x = 2.0$, were synthesized by the solid-state reaction and by the sol-gel method. The structures of the compounds were investigated using x-ray diffraction, Raman spectroscopy and electron microscopy. Pure phase samples could not be synthesized by the solid-state reaction, except for $\text{Yb}_2\text{Ti}_2\text{O}_7$. The sol-gel samples did form pure phases, although with an increased degree of structural disorder. Along the $\text{Yb}_2\text{Zr}_x\text{Ti}_{2-x}\text{O}_7$ series the structure ranges from an ordered pyrochlore, for $x \leq 0.5$, to a disordered fluorite, for $x = 1.0, 1.5$, and finally to the rhombohedral δ -phase, for $x = 2.0$. The morphotropic transition from pyrochlore to fluorite occurs in the range $0.5 < x < 1.0$, somewhat less than the value predicted by the structural tolerance factor, $x = 1.21$. The intermediate compositions, close to the morphotropic phase boundary, exhibit either structural distortions or short-range local order that does not extend to the long-range crystal structure. Low temperature magnetization and AC magnetic susceptibility measurements were used to characterize the magnetic ground state of these magnetically frustrated compounds. The transition to long range magnetic order is suppressed with increasing structural disorder, suggesting an increase in magnetic frustration and possible stabilization of a spin liquid ground state for $\text{Yb}_2\text{Zr}_2\text{O}_7$.

Keywords: Pyrochlore; Fluorite; Structural disorder; Frustrated magnetism; Low-temperature magnetism.

Resumo

A série de novos compostos $\text{Yb}_2\text{Zr}_x\text{Ti}_{2-x}\text{O}_7$, com composição variando de $x = 0.0$ a $x = 2.0$, foi sintetizada pela reação no estado sólido e pelo método sol-gel. As estruturas dos compostos foram investigadas por difração de raios-x, espectroscopia Raman e microscopia eletrônica. Amostras de fase pura não puderam ser sintetizadas pela reação de estado sólido, exceto para $\text{Yb}_2\text{Ti}_2\text{O}_7$. As amostras sol-gel formaram fases puras, embora com maior grau de desordem estrutural. Ao longo da série $\text{Yb}_2\text{Zr}_x\text{Ti}_{2-x}\text{O}_7$ a estrutura varia de um pirocloro ordenado, para $x \leq 0.5$, a uma fluorita desordenada, para $x = 1.0, 1.5$, e finalmente à fase δ , para $x = 2.0$. A transição morfotrópica de pirocloro para fluorita ocorre na faixa $0.5 < x < 1.0$, um pouco menor que o valor previsto pelo fator de tolerância estrutural, $x = 1.21$. As composições intermediárias, próximas à fronteira morfotrópica, exibem distorções estruturais ou ordem local de curto alcance que não se estende à estrutura cristalina de longo alcance. Medições de magnetização de baixa temperatura e suscetibilidade magnética AC foram usadas para caracterizar o estado fundamental magnético desses compostos magnéticos frustrados. A transição para ordem magnética de longo alcance é suprimida com o aumento da desordem estrutural, sugerindo um aumento na frustração magnética e possível estabilização de um estado fundamental líquido de spin para $\text{Yb}_2\text{Zr}_2\text{O}_7$.

Palavras-chave: Pirocloro; Fluorita; Desordem estrutural; Magnetismo frustrado; Magnetismo a baixa temperatura.

Contents

Acknowledgements	i
Abstract	iii
Resumo	v
Contents	vii
List of Figures	xi
List of Tables	xix
Listings	xxi
1 Introduction	1
1.1 Pyrochlore Oxides	1
1.2 Motivation For this Thesis	3
2 Crystal Structure	5
2.1 Introduction to Crystallography	5
2.2 Structures	9
2.2.1 Fluorite	10
2.2.2 Defect Fluorite	10
2.2.3 Pyrochlore	12
2.2.4 δ -phase	18
2.2.5 Other Structures	20
2.3 Structure Prediction	22
2.3.1 Tolerance factors	22
2.3.2 Phase Maps	32
2.3.3 Phase Diagrams	35
3 Frustrated Magnetism	41
3.1 Magnetization of a Paramagnet	41
3.2 Magnetic Susceptibility	43
3.3 Contributions to the Susceptibility	44
3.4 Curie-Weiss Paramagnetism	45
3.5 Magnetic Interactions	47
3.6 Magnetic Order	51

3.7	Lanthanides	53
3.8	Magnetic Frustration	56
3.9	Frustrated Lattices	58
3.10	Complex Spin States	59
3.11	Pyrochlore Magnetism	64
3.12	$\text{Yb}_2\text{Ti}_2\text{O}_7$	69
4	Synthesis	77
4.1	Solid-state reaction	77
4.1.1	Procedure	79
4.2	Sol-gel synthesis	82
4.2.1	Procedure	83
4.3	$\text{Yb}_2\text{Zr}_x\text{Ti}_{2-x}\text{O}_7$ Samples	86
4.4	Microscopy	88
4.4.1	Energy-Dispersive Spectroscopy	93
5	X-Ray Diffraction	97
5.1	Introduction	97
5.2	Pyrochlore vs Fluorite: Local Order	105
5.3	Qualitative Phase Analysis	114
5.4	Instrumental Parameters	119
5.5	Rietveld Refinement	126
5.6	Results for $\text{Yb}_2\text{Zr}_x\text{Ti}_{2-x}\text{O}_7$	136
5.6.1	Phase Analysis	141
5.6.2	Qualitative Results	142
5.6.3	Refinement Results	150
5.6.4	$\text{Yb}_2\text{Zr}_x\text{Ti}_{2-x}\text{O}_7$ Phase Diagram	162
6	Raman Spectroscopy	163
6.1	Introduction	163
6.2	Pyrochlore Raman Modes	169
6.3	Experimental Results	173
7	Magnetic Properties	191
7.1	Experimental Setup	191
7.1.1	Lock-in amplifier	191
7.1.2	Susceptometer	194
7.1.3	Vibrating Sample Magnetometer	199
7.1.4	Adiabatic Demagnetization	201
7.2	Magnetization of $\text{Yb}_2\text{Zr}_x\text{Ti}_{2-x}\text{O}_7$	208
7.3	Susceptibility of $\text{Yb}_2\text{Zr}_x\text{Ti}_{2-x}\text{O}_7$	211
8	Conclusion	221
8.1	Summary	221
8.2	Future Work	224
8.2.1	EXAFS Proposal	226
8.2.2	PDF Proposal	228
A	EXAFS Proposal	231

B PDF Proposal	241
Bibliography	249

List of Figures

1.1	Sublattices formed by A and B elements in the pyrochlore structure.	2
1.2	Periodic table in which highlighted elements show possible A ³⁺ and B ⁴⁺ cations in the A ₂ B ₂ O ₇ pyrochlore structure.	2
2.1	A depiction of a two-dimensional lattice (left), with a highlighted unit cell (middle) and the tiling of space generated by translating the unit cell (right).	6
2.2	Possible two-dimensional lattices, distinguished by their symmetry [52].	6
2.3	An example of a unit cell for the two-dimensional lattice of Figure 2.1 and a table listing the coordinates of the atoms in the basis.	7
2.4	The crystal structure, created by acting on the unit cell and its basis with the translations that define the lattice.	7
2.5	The 14 possible 3d Bravais lattices, distinguished by their symmetry [53].	7
2.6	Conventional unit cell of the general AX ₂ fluorite structure.	10
2.7	Asymmetric unit (middle) for the AX ₂ fluorite structure and the full unit cell (right), generated by applying Fm $\bar{3}$ m symmetries to the asymmetric unit.	11
2.8	Unit cells for each of the sublattices that make up the A ₂ B ₂ O ₇ pyrochlore structure. O _{8b} are colored orange to distinguish them from the green O _{48f}	14
2.9	Lattices of corner-sharing tetrahedra, formed by A ³⁺ and B ⁴⁺ cations in the pyrochlore structure.	15
2.10	Two consecutive 111 slices of the pyrochlore structure, perpendicular to the $\langle 111 \rangle$ body diagonal of the unit cell.	16
2.11	Two consecutive 110 slices of the pyrochlore structure, perpendicular to the $\langle 110 \rangle$ face diagonal of the unit cell.	16
2.12	Coordination polyhedra formed by the nearest neighbors of each atom in the pyrochlore structure, including the usually vacant 8a site.	17
2.13	Oxygen ions in pyrochlore unit cell, with $x_{48f} = 0.30, 0.33, 0.35, 0.375$	17
2.14	The coordination polyhedra centered on the A ³⁺ and B ⁴⁺ cations for $x_{48f} = 0.3125, 0.33, 0.35, 0.375$	18
2.15	A ₄ B ₃ O ₁₂ δ -phase asymmetric unit (left) and a full unit cell (right).	19
2.16	Cation coordination polyhedra in the δ -phase structure.	19
2.17	Relation between the pyrochlore, weberite and fluorite structures.	21
2.18	Correlation between tolerance factor t_5 and $t_1 = \frac{r_A}{r_B}$, from [75].	27
2.19	Calculated tolerance factor t_6 (2.15) for 180 pyrochlore compounds, from [66].	27
2.20	Expected and observed structures along with the nominal t_1 (empty squares) and actual t'_1 (filled circles)[76].	29
2.21	Expected and observed structures along with the nominal t_2 (t -Isupov) and actual t'_2 [76].	29

2.22	Nominal t_3 and actual t'_3 values for the synthesized compounds [76].	30
2.23	Nominal t_4 and actual t'_4 values for the synthesized compounds [76].	30
2.24	Expected and observed structures along with the nominal t_5 (t_{new}) and actual t'_5 [76].	31
2.25	Phase map constructed from literature studies [58]. Each phase is associated to a color: monoclinic (black), pyrochlore (red, yellow), fluorite (grey), δ -phase (cyan). Color combinations indicate a compound that has been found in more than one phase and an empty box indicates that it has been found as both pyrochlore and fluorite.	32
2.26	Phase map constructed from simulations [58]. Each phase is associated to a color: non-cubic (dark blue), pyrochlore (yellow, orange), δ -phase (black, cyan), fluorite (red). Yellow/red squares represent pyrochlore phases formed under high pressure [77].	33
2.27	High-temperature (2000K) phase map constructed from simulations [58]. Each phase is associated to a color: non-cubic (blue), pyrochlore (yellow), δ -phase (black), fluorite (red). Yellow/red squares represent pyrochlore phases formed under high pressure [77].	33
2.28	Phase map from structures reported in the literature [59]. Each phase is associated to a color: monoclinic (grey), pyrochlore (blue), δ -phase (orange), fluorite (black). Hollow symbols represent a single phase, while solid symbols indicate that both the ordered structure and disordered fluorite have been observed.	34
2.29	Phase diagram for the $\text{Yb}_2\text{O}_3\text{--ZrO}_2$ binary system, from [82]. Each region represents a structure or solid solution within a certain symmetry class: M = monoclinic, Flu = fluorite, Tet = tetragonal, C = cubic, δ = rhombohedral δ -phase, H = hexagonal, L = liquid.	36
2.30	Phase diagram for the $\text{Yb}_2\text{O}_3\text{--ZrO}_2$ binary system, from [83]. Each region represents a structure or solid solution within a certain symmetry class: M = monoclinic, T = tetragonal, F = fluorite, C = cubic, δ = rhombohedral δ -phase, H = hexagonal, L = liquid.	36
2.31	Phase diagram for the $\text{Yb}_2\text{O}_3\text{--ZrO}_2$ binary system, from [78], original source is [84]. Each region represents a structure or solid solution (ss) within a certain symmetry class: C = cubic, H = hexagonal, H_1 = δ -phase (blue), C_1 = fluorite solid solution (light shade).	37
2.32	Phase diagram for the $\text{Yb}_2\text{O}_3\text{--HfO}_2$ system, from [85]. Each region represents a structure or solid solution (SS) within a certain symmetry class: M = monoclinic, T = tetragonal, F = fluorite, C = cubic, H = hexagonal, δ = δ -phase, H_3 = $\text{Yb}_6\text{HfO}_{11}$ phase.	37
2.33	Phase diagram for the $\text{Yb}_2\text{O}_3\text{--TiO}_2$ system, from [86]. Vertical axis units are $^\circ\text{C}$. Each region represents a structure or solid solution within a certain symmetry class: F = fluorite, C = cubic, H = hexagonal, L = liquid, H = hexagonal.	38
2.34	Phase diagram for the $\text{Yb}_2\text{O}_3\text{--TiO}_2$ system, from [87], adapted from [88]. Each region represents a structure or solid solution within a certain symmetry class: DF = defect fluorite, P = pyrochlore, C = cubic Yb_2O_3 , T = TiO_2	38
2.35	Ternary phase diagram for the $\text{Yb}_2\text{O}_3\text{--La}_2\text{O}_3\text{--ZrO}_2$ system [82] at 1523K.	39
3.1	Ferromagnetic (FM) and antiferromagnetic (AFM) interactions between two spins, represented as arrows.	48

3.2	Nearest neighbor (NN) and next nearest neighbor (NNN) interactions between spins on a lattice, with interaction strengths J_1 and J_2 , respectively.	49
3.3	Canting of FM spins as a result of the antisymmetric Dzyaloshinskii-Moriya exchange interaction (not to scale).	49
3.4	Lowest energy configuration for two spins coupled by the dipolar interaction.	50
3.5	Transition from long-range ordered phase at low temperature to disordered paramagnetic phase at high temperature.	51
3.6	Inverse magnetic susceptibility behavior for an antiferromagnet, a paramagnet and a ferromagnet.	51
3.7	The magnetic family tree, a portrait of how the different types of magnetism are related. Adapted from [98].	52
3.8	Magnetic properties of lanthanide ions, using Hund's rules to determine the ground state. Experimental values for μ_{eff} from [93, 100].	54
3.9	Spin (S), orbital (L) and total (J) angular momentum of the Ln^{3+} trivalent lanthanide ions, in units of μ_B . The experimental values are from [93, 100].	55
3.10	Calculated and experimentally measured magnetic moments of the 3+ lanthanide ions.	55
3.11	AFM Ising spins on a square are not frustrated (left) but are frustrated on a triangle (middle). A NNN interaction could make the square frustrated too (right).	56
3.12	Inverse magnetic susceptibility behavior for a conventional and a frustrated antiferromagnet.	57
3.13	Triangular lattice (left) and kagomé lattice (right) are both composed of the basic frustrated unit in two dimensions, the triangle (middle).	58
3.14	The face-centered cubic lattice (left) and the pyrochlore lattice (right) are both composed of the basic frustrated unit in three dimensions, the tetrahedron (middle).	58
3.15	Degenerate ground states for AFM Ising spins on an equilateral triangle. Red color is assigned to the energetically unfavorable interaction.	59
3.16	Model of a spin liquid as a superposition of all possible singlet partitions of the spins on a triangular lattice [112].	60
3.17	Model of a spin glass as a collection of spins placed at random sites on a lattice.	60
3.18	Possible states of a tetrahedron in the spin ice structure.	61
3.19	Residual magnetic entropy of the classical spin ice $\text{Ho}_2\text{Ti}_2\text{O}_7$	63
3.20	Effective magnetic monopoles that arise when the spin ice rule is violated [125].	63
3.21	Surroundings of the A cation in the $\text{A}_2\text{B}_2\text{O}_7$ pyrochlore structure.	64
3.22	Spin configurations for each type of order [137].	68
3.23	Heat capacity of $\text{Yb}_2\text{Ti}_2\text{O}_7$, adapted from [144].	69
3.24	Splayed ferromagnetic ground state of $\text{Yb}_2\text{Ti}_2\text{O}_7$, showing a unit cell and one tetrahedron, with the splay angle θ indicated (not to scale).	71
3.25	Classical phase diagram for the anisotropic nearest-neighbor exchange hamiltonian (3.54) with $J_3 < 0$ and $J_4 = 0$ [140].	73
3.26	Quantum phase diagram for the anisotropic nearest-neighbor exchange hamiltonian (3.54) with $J_3 < 0$ and $J_4 = 0$ [140].	73
3.27	Linear spin wave prediction and the experimental spectrum for $\text{Yb}_2\text{Ti}_2\text{O}_7$ at $T = 150\text{mK}$ [176].	74
3.28	Measured neutron scattering data (left) and calculated cross-sections (right), for various applied magnetic field values [175].	74

3.29	Differently oriented FM domains connected by domain walls with AFM character [175].	75
4.1	Schematic representation of the solid-state reaction method, adapted from [185].	77
4.2	Schematic depiction of the sintering process [182].	78
4.3	ZrO ₂ before (left) and after (right) being dried in an oven at 700°C for 12h.	79
4.4	Paste formed by mixing precursor oxides with ethanol.	80
4.5	Pellet formed by pressing powder sample (left) and alumina crucible used as container during calcination (right).	81
4.6	Hydraulic bench press (left) and metal dye set (right).	81
4.7	Mufla SP-1200 oven, used to calcine the Yb ₂ Zr _x Ti _{2-x} O ₇ samples.	81
4.8	Schematic representation of the sol-gel reaction method, adapted from [192].	82
4.9	Beaker with solution set inside an oil container that functions as a heat bath.	84
4.10	Solution in the oil bath, before (left), during profuse bubbling (middle) and after release of the gas (right).	85
4.11	Yellowish-green gel formed after drying the solution, viewed from above (left) and below (right).	85
4.12	White crust formed after firing the gel at 700°C.	85
4.13	JEOL JSM-6010LA SEM (left) and stubs used to mount the samples (right).	89
4.14	SEM images of the SG sample Yb ₂ Zr _x Ti _{2-x} O ₇ , $x = 1.5$, sintered at 1500°C for 3h.	90
4.15	SEM images of the SG sample Yb ₂ Zr _x Ti _{2-x} O ₇ , $x = 2.0$, sintered at 900°C for 24h.	91
4.16	SEM images of the SG sample Yb ₂ Zr _x Ti _{2-x} O ₇ , $x = 2.0$, sintered at 1500°C for 3h.	92
4.17	EDS spectrum for the sample Yb ₂ Zr _x Ti _{2-x} O ₇ , $x = 1.5$, sintered at 1500°C for 3h.	93
4.18	EDS spectrum for the sample Yb ₂ Zr _x Ti _{2-x} O ₇ , $x = 2.0$, sintered at 900°C for 24h.	94
4.19	EDS spectrum for the sample Yb ₂ Zr _x Ti _{2-x} O ₇ , $x = 2.0$, sintered at 1500°C for 3h.	94
5.1	Bragg-Brentano diffraction geometry, adapted from [205].	98
5.2	Schematic depiction of an x-ray diffractogram.	98
5.3	A family of lattice planes intersecting atoms in the crystal structures. Only two planes are shown but there are infinitely many parallel planes with a constant spacing d	99
5.4	X-rays diffracted from parallel lattice planes interfere constructively when (5.1) holds [207].	99
5.5	Rule of thumb for determining the $\Delta(2\theta)$ step size: to resolve a peak it should contain at least ~ 5 measured points on each side of the maximum.	101
5.6	Distinction between powder particles and crystallites, from [209].	104
5.7	Full width at half of the maximum intensity I_M (FWHM) for a peak centered at θ_B	104
5.8	Simulated diffractogram for a pyrochlore with $a = 10\text{\AA}$ and a defect fluorite with $a = 5\text{\AA}$, with CuK α radiation. Some peaks are labeled by their Miller indices.	105
5.9	Calculated energy difference between the pyrochlore and various partially ordered quasi-weberite structures for the lanthanide zirconates Ln ₂ Zr ₂ O ₇ [227].	111
5.10	Collective tilting of the A ₄ O _{8b} tetrahedra in the pyrochlore structure (left), analogous to that in β -cristoballite SiO ₂ (right) [230].	112

5.11	Alternating large and small tetrahedra in the breathing pyrochlore lattice, with increasing ratio between the edge lengths of the large and small tetrahedra. . .	113
5.12	QualX window, showing the phase analysis for the SS sample $\text{Yb}_2\text{Zr}_x\text{Ti}_{2-x}\text{O}_7$	114
5.13	Restraints imposed on results of the Search-Match algorithm.	116
5.14	List of possible phases returned by the Search-Match algorithm. Highlighted phases at the top of the list are accepted phases.	116
5.15	Experimental powder diffractogram and tick marks for the accepted phases, indicating peak positions.	117
5.16	List of peak positions and intensities in experimental data and accepted phases.	117
5.17	Gaussian and Lorentzian functions with the same FWHM and total area. . . .	121
5.18	Peak fitting of Al_2O_3 reference material in GSAS-II (logarithmic intensity scale).	123
5.19	List of peak positions, intensities and widths, used in the fitting procedure, . .	124
5.20	Instrumental parameters calculated by GSAS-II to best fit the experimental peak profile.	124
5.21	Instrumental peak profile curves calculated from the instrumental parameters. .	125
5.22	Close-up view of fitted peaks in GSAS-II (logarithmic intensity scale).	125
5.23	GSAS-II window displaying the atomic coordinates and other information, imported from the CIF file.	127
5.24	Fixed points that were added manually to guide the fitting of the background polynomial (logarithmic intensity scale).	129
5.25	Example of the initial steps of a Rietveld refinement. The difference curve clearly shows some problems with the fit.	130
5.26	Limits imposed on the range of the ADP variables.	131
5.27	Constraints generated by making the Zr and Ti atoms equivalent.	132
5.28	Example of a warning dialog in GSAS-II.	133
5.29	The variance-covariance matrix for the refined variables.	134
5.30	Shifts that the refined parameters underwent in the last refinement cycle, normalized by their standard uncertainties (esd).	134
5.31	XRD patterns for the SS $\text{Yb}_2\text{Zr}_x\text{Ti}_{2-x}\text{O}_7$ samples, sintered at 1500°C (square root intensity scale).	137
5.32	XRD patterns for the SG $\text{Yb}_2\text{Zr}_x\text{Ti}_{2-x}\text{O}_7$ samples, sintered at 1500°C (square root intensity scale).	138
5.33	XRD patterns for the SG $\text{Yb}_2\text{Zr}_x\text{Ti}_{2-x}\text{O}_7$ samples, sintered at 1200°C (square root intensity scale).	139
5.34	XRD patterns for the SG $\text{Yb}_2\text{Zr}_x\text{Ti}_{2-x}\text{O}_7$ samples, sintered at 900°C (square root intensity scale).	140
5.35	Comparison of the XRD pattern of ZrO_2 before and after being heated at 700°C .	141
5.36	The 111 and 200 fluorite peaks show an approximately linear shift in position with increasing x for SS $\text{Yb}_2\text{Zr}_x\text{Ti}_{2-x}\text{O}_7$ samples.	143
5.37	Experimental lattice parameter values for both SG and SS samples and calculated lattice parameters from Table 2.11.	144
5.38	The 622 pyrochlore peak for the SG and SS $\text{Yb}_2\text{Ti}_2\text{O}_7$ samples, clearly indicating their distinct lattice parameters.	145
5.39	The 111 fluorite peak for SG $\text{Yb}_2\text{Zr}_x\text{Ti}_{2-x}\text{O}_7$ samples with $x = 0.0, 0.15, 0.3$, sintered at various temperatures	146
5.40	Weak pyrochlore superstructure peaks in the XRD pattern of $\text{Yb}_2\text{Zr}_x\text{Ti}_{2-x}\text{O}_7$ with $x = 1.0$	147

5.41	Weak pyrochlore superstructure peaks in the XRD pattern of $\text{Yb}_2\text{Zr}_x\text{Ti}_{2-x}\text{O}_7$ with $x = 1.0$, visualized on a logarithmic scale.	147
5.42	Diffractogram of $\text{Yb}_2\text{Zr}_x\text{Ti}_{2-x}\text{O}_7$ with $x = 1.0$ (1200°C), deconvoluted as a superposition of pseudo-Voigt functions.	149
5.43	Normalized intensity of the diffuse 111, 331 and 442 superstructure peaks for the $x = 1.0, 1.5$ samples.	149
5.44	A refinement of the SS $\text{Yb}_2\text{Ti}_2\text{O}_7$ sample (linear intensity scale).	152
5.45	A refinement of the SS $\text{Yb}_2\text{Ti}_2\text{O}_7$ sample (logarithmic intensity scale).	152
5.46	A refinement of the SG $\text{Yb}_2\text{Ti}_2\text{O}_7$ sample (linear intensity scale).	153
5.47	A refinement of the SG $\text{Yb}_2\text{Ti}_2\text{O}_7$ sample (logarithmic intensity scale).	153
5.48	A refinement of $\text{Yb}_2\text{Zr}_x\text{Ti}_{2-x}\text{O}_7$ with $x = 0.15$, sintered at 1500°C (linear intensity scale).	156
5.49	A refinement of $\text{Yb}_2\text{Zr}_x\text{Ti}_{2-x}\text{O}_7$ with $x = 0.15$, sintered at 1500°C (logarithmic intensity scale).	156
5.50	Secondary peaks adjacent to the pyrochlore peaks for $\text{Yb}_2\text{Zr}_x\text{Ti}_{2-x}\text{O}_7$ with $x = 0.3$, sintered at 1500°C	157
5.51	A refinement of the SG $\text{Yb}_2\text{Ti}_2\text{O}_7$ sample (linear intensity scale).	160
5.52	A refinement of the SG $\text{Yb}_2\text{Ti}_2\text{O}_7$ sample (logarithmic intensity scale).	160
5.53	Approximate temperature-composition phase diagram for the $\text{Yb}_2\text{Zr}_x\text{Ti}_{2-x}\text{O}_7$ compounds. Colors represent the structure: blue = pyrochlore, red = fluorite, green = δ -phase.	162
6.1	Molecule excited by monochromatic light scattering both elastically and inelastically [267].	164
6.2	Scattering processes visualized on an energy level diagram and the resulting spectrum [267].	164
6.3	Schematic representation of a Raman spectroscopy setup [268].	166
6.4	Symmetries of H_2O molecule.	167
6.5	Vibrational modes of H_2O molecule.	168
6.6	Peak in Raman spectrum of polycrystalline silicon.	174
6.7	Raman spectra of the precursor oxide Yb_2O_3 , compared with data from the literature.	174
6.8	Raman spectra of the SS and SG $\text{Yb}_2\text{Zr}_x\text{Ti}_{2-x}\text{O}_7$ samples with $x = 1.5$	175
6.9	Raman spectra of the SS and SG $\text{Yb}_2\text{Ti}_2\text{O}_7$ samples.	175
6.10	Raman spectra for the SS and SG $\text{Yb}_2\text{Ti}_2\text{O}_7$ samples compared with data from the literature [278, 282, 294].	177
6.11	Raman spectra of the $\text{Yb}_2\text{Zr}_x\text{Ti}_{2-x}\text{O}_7$ samples with $x = 0.5$	178
6.12	Raman spectra of the $\text{Yb}_2\text{Zr}_x\text{Ti}_{2-x}\text{O}_7$ samples with $x = 1.5$	178
6.13	Raman spectra of the $\text{Yb}_2\text{Zr}_2\text{O}_7$ samples, sintered at 900°C and 1500°C	179
6.14	Raman spectrum for the $\text{Yb}_2\text{Zr}_2\text{O}_7$ sample compared with data for $\text{Yb}_4\text{Zr}_3\text{O}_{12}$ from the literature [281].	179
6.15	Deconvolution of the Raman spectrum for the SG $\text{Yb}_2\text{Ti}_2\text{O}_7$ sample sintered at 1200°C	181
6.16	Examples of two highly overlapping peaks. The positions and widths of the peaks are fixed while the intensity of the leftmost peak increases from panel a to panel d.	182
6.17	Examples of two highly overlapping peaks. The leftmost peak remains fixed while the width of the large peak increases from panel a to panel d.	183

6.18	Raman spectra of the $\text{Yb}_2\text{Zr}_x\text{Ti}_{2-x}\text{O}_7$ samples sintered at 1200°C	185
6.19	Raman spectra of the $\text{Yb}_2\text{Zr}_x\text{Ti}_{2-x}\text{O}_7$ samples and the SS $\text{Yb}_2\text{Ti}_2\text{O}_7$ sample, sintered at 1500°C	186
6.20	Frequencies of the strongest modes as a function of composition x for $\text{Yb}_2\text{Zr}_x\text{Ti}_{2-x}\text{O}_7$ samples, sintered at 1500°C	187
6.21	Frequencies of the strongest modes as a function of the lattice parameter a for $\text{Yb}_2\text{Zr}_x\text{Ti}_{2-x}\text{O}_7$ samples, sintered at 1500°C	187
7.1	Schematic representation of a LIA [314].	192
7.2	Front panel of an SR830 LIA.	193
7.3	Block diagram of the components inside an SR830 LIA [315].	193
7.4	Susceptometer, composed of a primary coil and a pair of counterwound secondary coils.	195
7.5	Two cryostats in our laboratory, containing the susceptometer (left) and VSM (right).	195
7.6	Linear fit of the inverse of the susceptometer's background subtracted output signal $(V - V_0)^{-1}$	198
7.7	Comparison of susceptibility data of ferric ammonium sulfate for the susceptometer and a Quantum Design SQUID.	198
7.8	Schematics of a vibrating sample magnetometer.	199
7.9	Magnetic moment of ferric ammonium sulfate crystal and fitted Brillouin function.	200
7.10	Magnetic moment per magnetic ion of ferric ammonium sulfate and the expected saturation level for Fe^{3+} ions.	201
7.11	Cooling cycle of an adiabatic demagnetization refrigerator [328].	202
7.12	Sample holder with heat-sinking post on top (left), cross-sectional view showing the bore hole that contains the susceptometer coils (middle) and capsule containing the sample (right).	204
7.13	Cross-sectional view of the cryostat containing the ADR system (left) and the insert with the sample holder and paramagnetic salt (right). Adapted from [330].	205
7.14	Raw susceptibility data for a sample measured with the ADR's susceptometer and a smooth interpolation.	206
7.15	Susceptibility data from the ADR's susceptometer, calibrated to fit the data from the helium bath susceptometer (Section 7.1.2) in the region where these overlap, $\sim 0.6\text{K} - 1.5\text{K}$	207
7.16	Magnetic moment per Yb^{3+} ion in $\text{Yb}_2\text{Zr}_x\text{Ti}_{2-x}\text{O}_7$ for magnetic fields up to 14.5T	208
7.17	Saturation level, measured at $\mu_0 H = 14.5\text{T}$, of magnetic moments for $\text{Yb}_2\text{Zr}_x\text{Ti}_{2-x}\text{O}_7$ with varying composition x . Lines are only a guide to the eyes, suggesting a systematic variation.	209
7.18	Correlation between the saturation moment m_{sat} and susceptibility. Points on the dashed line have a constant ratio $m_{\text{sat}}/\chi_{\text{AC}}$	209
7.19	Comparison of magnetization for SG $\text{Yb}_2\text{Ti}_2\text{O}_7$ (1200°C) with digitized data from the literature [332, 153, 333].	210
7.20	Molar susceptibilities of $\text{Yb}_2\text{Zr}_x\text{Ti}_{2-x}\text{O}_7$, in the temperature range $T = 4\text{K}$ to $T = 0.5\text{K}$	212
7.21	Inverse molar susceptibilities of $\text{Yb}_2\text{Zr}_x\text{Ti}_{2-x}\text{O}_7$, in the temperature range $T = 4\text{K}$ to $T = 0.5\text{K}$	212

7.22	Susceptibility of $\text{Yb}_2\text{Ti}_2\text{O}_7$, measured with the helium bath susceptometer, in two temperature ranges: from $T = 4\text{K}$ to $T = 1.2\text{K}$, while pumping ^4He , and from $T = 1.2\text{K}$ to $T = 0.5\text{K}$, while pumping ^3He	213
7.23	Linear fit to the paramagnetic region, from 1.2K to 4K, of the inverse susceptibility of $\text{Yb}_2\text{Ti}_2\text{O}_7$. The inset shows a magnified view of the deviation from linear Curie-Weiss behavior below $T = 1.1\text{K}$	213
7.24	Curie-Weiss temperature θ_{CW} for the $\text{Yb}_2\text{Zr}_x\text{Ti}_{2-x}\text{O}_7$ samples, extracted from the Curie-Weiss fit.	215
7.25	Effective moments μ_{eff} for the $\text{Yb}_2\text{Zr}_x\text{Ti}_{2-x}\text{O}_7$ samples, extracted from the Curie-Weiss fit, and for a free Yb^{3+} ion, $\mu_{\text{eff}} = 4.5356 \mu_B$	215
7.26	AC susceptibility for the SG and SS $\text{Yb}_2\text{Ti}_2\text{O}_7$ samples, compared to digitized data from the literature [334, 153].	216
7.27	AC susceptibility for all of the SG $\text{Yb}_2\text{Zr}_x\text{Ti}_{2-x}\text{O}_7$ samples, measured with the ADR's susceptometer.	216
7.28	AC susceptibility, measured with the ADR's susceptometer, of the $\text{Yb}_2\text{Zr}_x\text{Ti}_{2-x}\text{O}_7$ samples with $x = 0.5$	217
7.29	AC susceptibility, measured with the ADR's susceptometer, of the $\text{Yb}_2\text{Zr}_2\text{O}_7$ samples.	217
7.30	Susceptibility peak temperature T_C as a function of composition x in $\text{Yb}_2\text{Zr}_x\text{Ti}_{2-x}\text{O}_7$. All samples are SG except for the one indicated as SS ($x = 0.0$).	220
7.31	Frustration index f as a function of composition x in $\text{Yb}_2\text{Zr}_x\text{Ti}_{2-x}\text{O}_7$	220
A.1	Graphical abstract submitted as part of the research proposal.	231

List of Tables

2.1	Wyckoff positions for the space group $Fd\bar{3}m$ (origin choice 2).	9
2.2	Unit cell coordinates, Wyckoff positions and site occupancies for the asymmetric unit of the fluorite structure AX_2	10
2.3	Unit cell coordinates, Wyckoff positions and site occupancies for the asymmetric unit of the fluorite structure ABX_4	11
2.4	Unit cell coordinates, Wyckoff positions and site occupancies for each atom in the asymmetric unit of the defect fluorite structure $A_2B_2O_7$	11
2.5	Unit cell coordinates, Wyckoff positions and site occupancies for the asymmetric unit of the defect fluorite structure $Yb_2Zr_xTi_{2-x}O_7$ with $x = 1.5$	12
2.6	Unit cell coordinates, Wyckoff positions and site occupancies for the pyrochlore structure $A_2B_2O_7$	13
2.7	Unit cell coordinates, Wyckoff positions and site occupancies for the asymmetric unit of the pyrochlore structure $Yb_2Zr_xTi_{2-x}O_7$ with $x = 0.5$	13
2.8	Unit cell coordinates, Wyckoff positions and site occupancies for the asymmetric unit of the δ -phase structure $A_4B_3O_{12}$	19
2.9	Some common phases in the pyrochlore family, ranked according to the ratio between the number of anions and the number of cations in their composition.	22
2.10	Ionic radii and coordination of the ions that compose the $Yb_2Zr_xTi_{2-x}O_7$ structure [68].	23
2.11	Calculated lattice parameters $a(r_i)$, $a(r_i, \chi_i)$ and a' for $Yb_2Zr_xTi_{2-x}O_7$ according to (2.11), (2.12) and (2.13), respectively.	26
2.12	Unit cell occupancies for the cations in the pyrochlore structure, with inversion ratio s (see Table 2.6).	28
2.13	Average r_B , tolerance factors t_i and predicted x value for the pyrochlore/fluorite transition in the $Yb_2Zr_xTi_{2-x}O_7$ series.	31
2.14	Molar percentage of A_2O_3 for some stoichiometries in the A_2O_3 – BO_2 binary system.	35
3.1	Diamagnetic contributions to the susceptibility due to single ions in the compounds $Yb_2Zr_xTi_{2-x}O_7$ and $(NH_4)Fe(SO_4)_2(H_2O)_{12}$ [96].	44
4.1	Sintering time and temperature for all samples of $Yb_2Zr_xTi_{2-x}O_7$ produced in this work (SG = sol-gel, SS = solid-state). In each section the sintering steps are listed in chronological order.	87
4.2	Measured and nominal composition values and their ratio, for the sample $Yb_2Zr_xTi_{2-x}O_7$, $x = 1.5$, sintered at 1500°C for 3h.	95
4.3	Measured and nominal composition values and their ratio, for the sample $Yb_2Zr_xTi_{2-x}O_7$, $x = 2.0$, sintered at 900°C for 24h.	95

4.4	Measured and nominal composition values and their ratio, for the sample $\text{Yb}_2\text{Zr}_x\text{Ti}_{2-x}\text{O}_7$, $x = 2.0$, sintered at 1500°C for 3h.	95
5.1	The main structural parameters that can be deduced from the positions, intensities and shapes of the peaks in a powder diffractogram.	101
5.2	List of Miller indices hkl , lattice spacings d (in \AA), 2θ positions (in degrees) and multiplicities $mult$ for the diffraction peaks of the pyrochlore and fluorite structures, assuming lattice parameters of 10\AA and 5\AA , respectively, and $\text{CuK}\alpha$ radiation.	107
5.3	Instruments used to collect powder diffractograms of samples in this work.	136
5.4	Phases present in $\text{Yb}_2\text{Zr}_2\text{O}_7$ samples after each step in the solid-state synthesis.	141
5.5	Peak maximum positions $2\theta_B$ for SS and SG $\text{Yb}_2\text{Zr}_x\text{Ti}_{2-x}\text{O}_7$ samples and the equivalent pyrochlore lattice parameter a deduced from Bragg's law.	144
5.6	Crystallite size μ for the SG $\text{Yb}_2\text{Ti}_2\text{O}_7$ samples, determined by the Scherrer method.	146
5.7	Ratio between the 111 and 222 pyrochlore peak intensities, I_{111}/I_{222} , for the $\text{Yb}_2\text{Zr}_x\text{Ti}_{2-x}\text{O}_7$ samples $x = 1.0, 1.5$	150
5.8	Ratio between the combined intensity of the pyrochlore superstructure peaks, I_p , to the combined intensity of the fluorite peaks, I_f	150
5.9	Results of the refinement of SS $\text{Yb}_2\text{Ti}_2\text{O}_7$, sintered at 1500°C	154
5.10	Results of the refinement of SG $\text{Yb}_2\text{Ti}_2\text{O}_7$, sintered at 1500°C	154
5.11	Results of the refinement of $\text{Yb}_2\text{Zr}_x\text{Ti}_{2-x}\text{O}_7$ with $x = 0.15$, sintered at 1500°C	155
5.12	Miller indices and positions of the main pyrochlore $2\theta_{main}$ and secondary $2\theta_{sec}$ peaks for the $\text{Yb}_2\text{Zr}_x\text{Ti}_{2-x}\text{O}_7$ samples with $x = 0.3, 0.5$, sintered at 1500°C	157
5.13	Results of the refinement of $\text{Yb}_2\text{Zr}_x\text{Ti}_{2-x}\text{O}_7$ with $x = 2.0$, sintered at 1500°C	161
6.1	Multiplication table for the group C_{2v}	167
6.2	Character table for the group C_{2v}	168
6.3	Symmetry properties for each vibrational mode of the H_2O molecule.	168
6.4	Force constants for the $\text{Yb}_2\text{Ti}_2\text{O}_7$ pyrochlore structure [277].	172
6.5	Calculated $\tilde{\nu}_{cal}$ and experimental $\tilde{\nu}_{exp}$ frequencies for the vibrational modes of the $\text{Yb}_2\text{Ti}_2\text{O}_7$ pyrochlore structure [277].	172
6.6	IR modes for the $\text{Yb}_2\text{Ti}_2\text{O}_7$ pyrochlore structure, according to [299].	173
6.7	Modes assigned to each of the five clearly visible peaks in the spectrum of the SG $\text{Yb}_2\text{Ti}_2\text{O}_7$ sample, along with the dominant bond stretch or bend contributing to that mode.	176
6.8	Position, FWHM and percentual area of the Lorentzian peaks fitted to the Raman spectrum of the SG $\text{Yb}_2\text{Ti}_2\text{O}_7$ sample, sintered at 1200°C	181
6.9	Bond distances and angles extracted from Rietveld refinement for the SG $\text{Yb}_2\text{Ti}_2\text{O}_7$ sample.	189
7.1	Curie-Weiss temperature θ_{CW} , molar Curie constant C_m and effective moment μ_{eff} , extracted from the Curie-Weiss fit, for the $\text{Yb}_2\text{Zr}_x\text{Ti}_{2-x}\text{O}_7$ samples.	214
7.2	Peak temperature T_C , Curie-Weiss temperature θ_{CW} and frustration index f for $\text{Yb}_2\text{Zr}_x\text{Ti}_{2-x}\text{O}_7$. All samples are SG except for SS $x = 0.0$	219

Listings

- 5.1 Default CuK α lab instrument parameters provided by GSAS-II. 122
- 5.2 Fitted instrument parameters for Al₂O₃ reference material measured by the Bruker D8 Focus diffractometer. 126
- 5.3 Section of a CIF file for Yb₂Ti₂O₇ displaying the relevant information for Rietveld refinement. 126

Introduction

In this chapter we introduce the pyrochlore oxides, offer some motivation for studying the $\text{Yb}_2\text{Zr}_x\text{Ti}_{2-x}\text{O}_7$ compounds that are the subject of this thesis and give a brief outline of the remaining chapters.

1.1 Pyrochlore Oxides

The pyrochlore oxide family of materials contains more than 200 compounds with the structural formula $\text{A}_2\text{B}_2\text{O}_7$, where often A is a rare-earth element (see Section 3.7) and B is a transition metal or semimetal, but other combinations including alkaline earth elements and nonmetals are also common. The mineral pyrochlore, $(\text{Na,Ca})_2\text{Nb}_2\text{O}_6(\text{OH,F})$, first described in 1826, is isostructural to the $\text{A}_2\text{B}_2\text{O}_7$ pyrochlore oxides and gives the family its name. The term 'pyrochlore' derives from the Greek $\pi\upsilon\rho$ (fire) and $\chi\lambda\omega\rho\acute{o}\varsigma$ (green), since this mineral typically turns green on ignition [1].

The pyrochlore materials exhibit a wide array of physicochemical properties, having been studied for uses as diverse as thermal barrier coatings [2], adiabatic cooling [3], oxygen ion conductors [4], proton conductors [5], nuclear waste disposal matrices [6], high dielectric constant capacitors [7], negative temperature coefficient thermistors [8], hot corrosion ceramics [9], photocatalysts [10], oxygen catalysts [11], methane catalysts [12], gas sensors [13], solid oxide fuel cells [14] and environmentally friendly pigments [15].

In addition to these technological applications, pyrochlores have sparked intense interest of the physics community due to numerous interesting phenomena such as frustrated magnetism [16], giant magnetoresistance [17], topological Hall effect [18], metal-insulator transitions [19], magnetocaloric effect [20], quantum paraelectric behavior [21], magnetic monopoles [22] and Dirac strings [23], superconductivity [24], metallic ferroelectricity [25], multiferroicity [26], magnon Hall effect [27], the spin liquid [28], spin glass [29] and spin ice [30] states, among others.

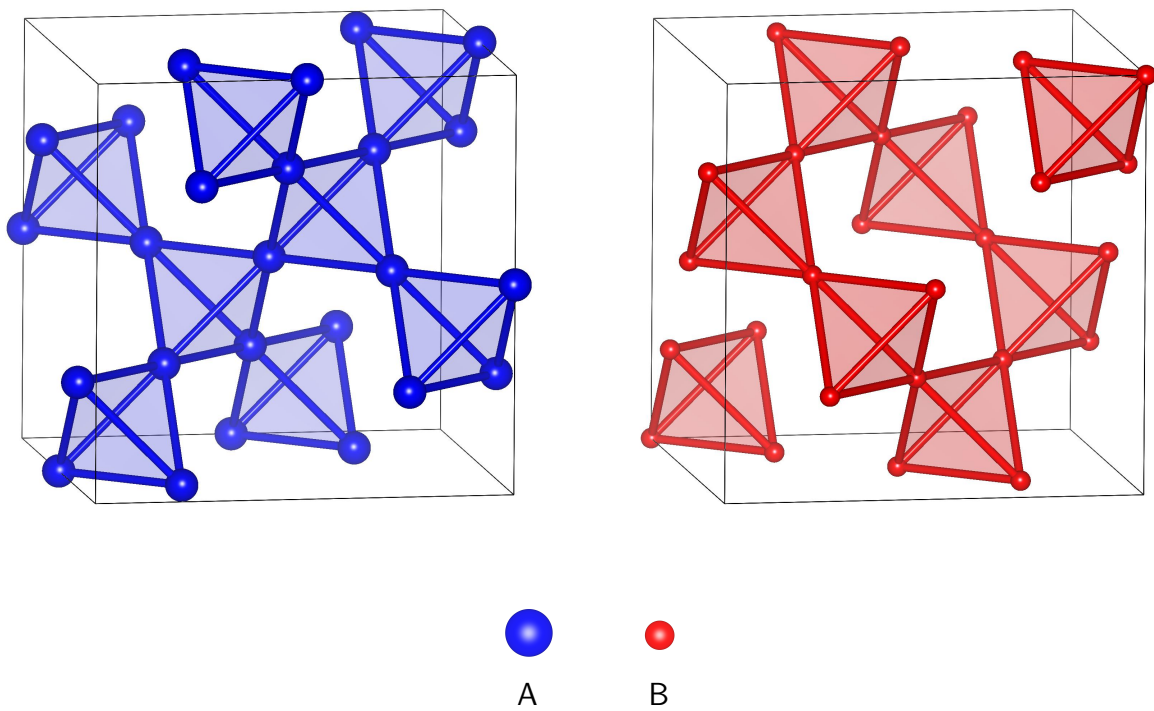


Figure 1.1 Sublattices formed by A and B elements in the pyrochlore structure.

$A_2B_2O_7$

H																			He
Li	Be											B	C	N	O	F			Ne
Na	Mg											Al	Si	P	S	Cl			Ar
K	Ca	Sc	Ti	V	Cr	Mn	Fe	Co	Ni	Cu	Zn	Ga	Ge	As	Se	Br			Kr
Rb	Sr	Y	Zr	Nb	Mo	Tc	Ru	Rh	Pd	Ag	Cd	In	Sn	Sb	Te	I			Xe
Cs	Ba		Hf	Ta	W	Re	Os	Ir	Pt	Au	Hg	Tl	Pb	Bi	Po	At			Rn
Fr	Ra		Rf	Db	Sg	Bh	Hs	Mt	Ds	Rg	Cn	Nh	Fl	Mc	Lv	Ts			Og

La	Ce	Pr	Nd	Pm	Sm	Eu	Gd	Tb	Dy	Ho	Er	Tm	Yb	Lu
Ac	Th	Pa	U	Np	Pu	Am	Cm	Bk	Cf	Es	Fm	Md	No	Lr

Figure 1.2 Periodic table in which highlighted elements show possible A^{3+} and B^{4+} cations in the $A_2B_2O_7$ pyrochlore structure.

In the $A_2B_2O_7$ pyrochlore structure both A and B elements form separate but identical sublattices of corner-sharing tetrahedra, illustrated in Figure 1.1. These two sublattices interpenetrate, so that when combined they form a face-centered cubic lattice. The lattice composed of corner-sharing tetrahedra is one of the canonical frustrated lattices (Section 3.8).

The most common oxidation state for the cations (positively charged ions) in the pyrochlore structure is trivalent A^{3+} and tetravalent B^{4+} , although there are also divalent A^{2+} , pentavalent B^{5+} and even some monovalent A^{1+} , hexavalent B^{6+} compounds. Figure 1.2 shows a periodic table with possible A^{3+} and B^{4+} elements highlighted [31, 16]. The A and B ions belong to distinct crystallographic sites, therefore it is possible for multiple elements to occupy the A or B site (or both). There also exist pyrochlore compounds in which the anion (negatively charged ion) is not O^{2-} but instead F^- , although these fluorides have been studied much less than the oxide pyrochlores [32].

For most magnetic pyrochlores the A^{3+} ion is magnetic, while B^{4+} is non-magnetic. Some materials contain a 'pyrochlore' sublattice, consisting of corner-sharing tetrahedra, although they don't have the same structure as the $A_2B_2O_7$ pyrochlores. An example of this are the AB_2O_4 spinel compounds, where the B sublattice is formed by corner-sharing tetrahedra, but the spinel A sublattice has a different structure from that of the pyrochlore A lattice. Thus the term pyrochlore, somewhat confusingly, can apply to the actual pyrochlore structure (Chapter 2), the $A_2B_2O_7$ stoichiometry, or the lattice of corner-sharing tetrahedra.

1.2 Motivation For this Thesis

The compounds in the series $Yb_2Zr_xTi_{2-x}O_7$, with x varying between $x = 0.0$ and $x = 2.0$, have not been previously synthesized, to the best of our knowledge. The $x = 0.0$ endpoint of this series, $Yb_2Ti_2O_7$, has been the focus of much attention due to its unusual magnetic dynamics and a ground state marked by competition between ferromagnetic and antiferromagnetic phases. To date there are over 50 publications concerned with the magnetic properties of $Yb_2Ti_2O_7$ and some of the existing literature on this compound is reviewed in Section 3.12. On the other hand, we found no publications on the magnetic properties of the opposite endpoint, $x = 2.0$, of the $Yb_2Zr_xTi_{2-x}O_7$ series, $Yb_2Zr_2O_7$. Several studies on $Yb_2Zr_2O_7$ exist, but they are mostly concerned with non-magnetic physical properties and technological applications [33, 34, 35, 9, 36, 37, 38, 39, 40].

Numerous publications have investigated the effects of element substitution in pyrochlore compounds. Of these studies we may distinguish between those in which the magnetic ion is diluted with another ion (which could also be magnetic), typically $A_xA'_{2-x}B_2O_7$ where A is magnetic, and those in which the proportions of the non-magnetic ions are varied, typically $A_2B_xB'_{2-x}O_7$ where B and B' are non-magnetic. In the former case the magnetic properties are directly affected by the substitution, while in the latter case they vary only indirectly through changes in the crystalline environment or structure of the compounds. The substitutional series $Yb_2Zr_xTi_{2-x}O_7$ fits into the latter category, since Yb^{3+} is magnetic, while Ti^{4+} and Zr^{4+} are not.

Such variations in the elemental composition allow the properties of the compounds to be tuned to certain critical values, where interesting phenomena manifest that might not occur for the pure $A_2B_2O_7$ compounds. Much of the effort of condensed matter physicists has

been dedicated to explore quantum critical points and other interesting regions in the phase diagrams of various compounds. A technique often employed to explore usually inaccessible regions of a compound's phase diagram is hydrostatic pressure or, less commonly, uniaxial strain. The chemical substitution of one element by another changes the chemical potential, which is analogous to physical pressure, according to the principles of thermodynamics [41]. Therefore a variation in chemical composition can have similar effects to the application of physical pressure, although it cannot be independently controlled as easily.

A change in composition of the type $A_xA'_{2-x}B_2O_7$ or $A_2B_xB'_{2-x}O_7$, with varying proportions of A/A' or B/B' , can also change the structure of the compounds, depending mainly on the ionic radii of the ions that compose the crystal structure. This possibility is extensively discussed in Section 2.3, and in fact the tolerance factor (Section 2.3.1) predicts a morphotropic transition (relating to a change in chemical composition) between pyrochlore and defect fluorite structures somewhere along the middle of the series $Yb_2Zr_xTi_{2-x}O_7$. The structural transformation complicates the investigation of magnetic properties in $Yb_2Zr_xTi_{2-x}O_7$, therefore the larger part of this thesis is actually concerned with the structural properties of these compounds.

The remainder of this thesis is structured as follows:

Chapter 2 introduces the basic concepts of crystallography, describes the fluorite, pyrochlore and related structures and reviews some approaches to structure prediction.

Chapter 3 introduces the fundamental concepts of magnetism, frustrated magnetism and how these apply to the magnetic pyrochlore oxides, specifically $Yb_2Ti_2O_7$.

Chapter 4 describes the solid-state and sol-gel methods, the synthesis of the $Yb_2Zr_xTi_{2-x}O_7$ compounds through both of these routes, and results of scanning electron microscopy for a few of the samples.

Chapter 5 introduces the basics of x-ray diffraction and explains how diffraction data was interpreted to yield information on structural properties.

Chapter 6 introduces the basics of spectroscopy, describes how the Raman spectra were analyzed and the implications for the structural properties.

Chapter 7 describes the experimental setup used to measure low-temperature magnetic properties, how the data was analyzed and interpreted.

Chapter 8 summarizes the main findings of the previous chapters and mentions some possibilities to extend the work in this thesis.

Appendix A and **Appendix B** contain synchrotron proposals related to future work on the $Yb_2Zr_xTi_{2-x}O_7$ compounds.

Crystal Structure

This chapter introduces the basic concepts of crystallography and the structures of the compounds in the $A_2B_2O_7$ pyrochlore family. We also discuss ways of predicting the structure of the compounds in this family, including tolerance factors and stability maps generated by computer simulations. All figures of crystal structures in this chapter were generated using the crystallographic visualization software Vesta 3 [42].

2.1 Introduction to Crystallography

Crystallography is fundamental to much of solid-state physics because most solid materials have a periodic structure, at least to a good approximation. It is relevant even to more general condensed matter physics, since often properties of fluids, amorphous materials and complex systems rely on concepts from crystallography. In practice, we need some understanding of crystallography to interpret results from x-ray diffraction (Chapter 5) and Raman scattering (Chapter 6). For a more comprehensive introduction to the concepts of crystallography the reader is advised to consult [43, 44, 45, 46, 47].

A crystal structure is, by definition, a periodic arrangement of elements (either atoms, ions or molecules) in space. Thus the defining feature of a crystal is its translational symmetry, which we describe by means of a lattice. A lattice is an infinite set of points possessing translational symmetry. The set of all translational symmetries has the structure of a group generated by d vectors, where d is the dimension of the lattice. For the three-dimensional lattices ($d = 3$) used to describe real crystal structures this means that, assuming that the origin is a lattice point, all lattice points R are of the form

$$R = n_1\mathbf{a}_1 + n_2\mathbf{a}_2 + n_3\mathbf{a}_3 \quad (2.1)$$

where n_i are integers and \mathbf{a}_i are linearly independent vectors. The set of primitive translation

vectors \mathbf{a}_i form the a polyhedron known as the primitive unit cell. Translating the unit cell by multiples of the primitive translation vectors \mathbf{a}_i we can fill up the whole space with copies of the unit cell. As an example, the left panel in Figure 2.1 depicts a two-dimensional lattice, keeping in mind that the actual lattice is infinite in both plane directions. Choosing two primitive translation vectors we get a unit cell, which is the highlighted parallelogram (middle), and the tiling of space generated by translating the unit cell (right).

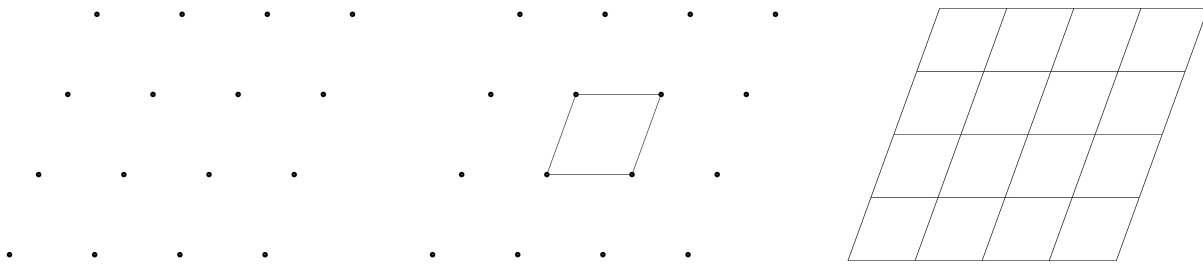


Figure 2.1 A depiction of a two-dimensional lattice (left), with a highlighted unit cell (middle) and the tiling of space generated by translating the unit cell (right).

In two-dimensional space all the possible lattices fall into five categories, the so called two-dimensional Bravais lattices, depicted in Figure 2.2. Each of these categories has a unique type of symmetry, so two distinct lattices which possess the same symmetries nevertheless fit into the same Bravais lattice class. The set of symmetries of an object has the structure of a group, a crucial concept in crystallography. The usual abstract definition of a group [48, 49] as a set of elements satisfying certain conditions is in fact equivalent to the statement that a group is the set of symmetries of an object [50, 51].

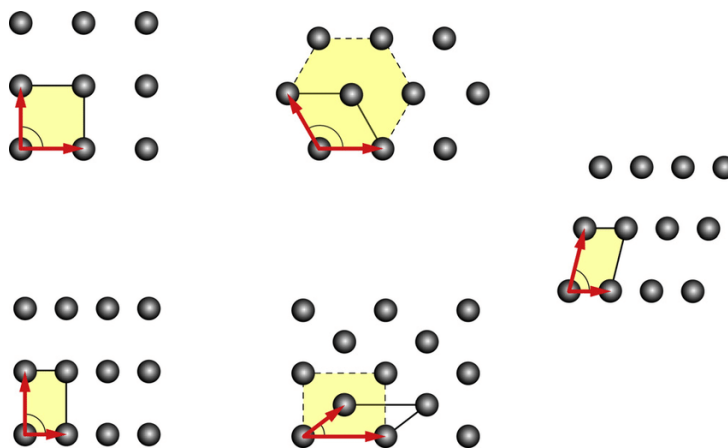


Figure 2.2 Possible two-dimensional lattices, distinguished by their symmetry [52].

The contents of a unit cell are described by a basis, which is a list of atoms and the coordinates of their positions in the unit cell. The coordinates are given as fractions of the unit cell dimensions $a_i = |\mathbf{a}_i|$, commonly known as lattice parameters, so all coordinates should be in the interval $[0, 1)$, although sometimes negative coordinates in the range $(-1, 0]$ are also allowed. Figure 2.3 shows an example of a unit cell for the two-dimensional lattice of Figure 2.1 and a table listing the coordinates of the atoms in the basis.

Acting on the unit cell and its basis with the translations that define the lattice we obtain

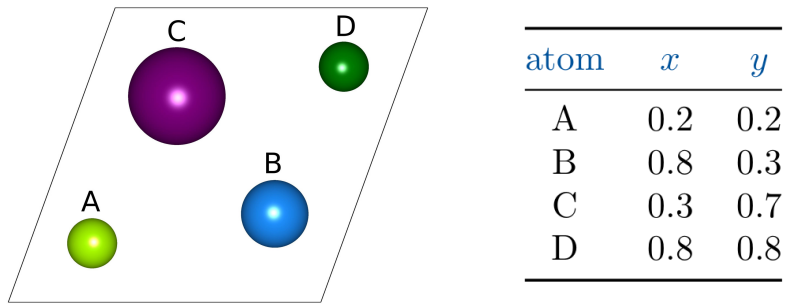


Figure 2.3 An example of a unit cell for the two-dimensional lattice of Figure 2.1 and a table listing the coordinates of the atoms in the basis.

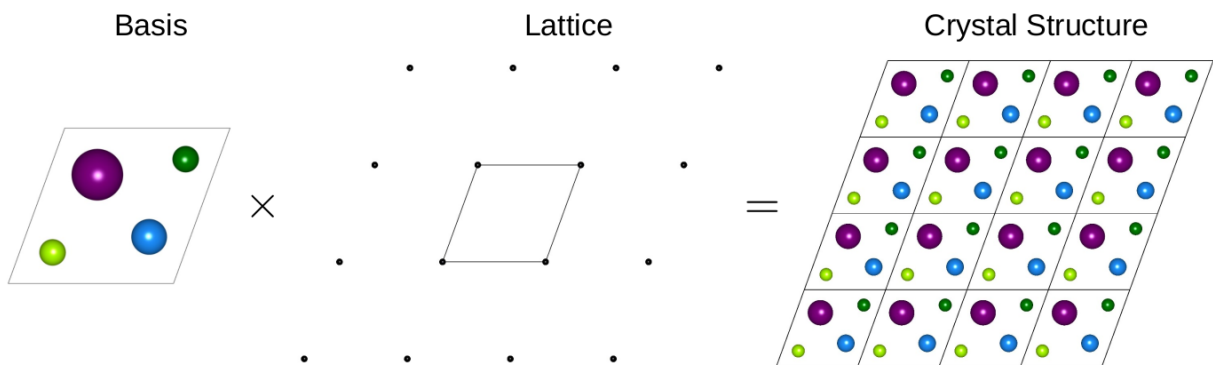


Figure 2.4 The crystal structure, created by acting on the unit cell and its basis with the translations that define the lattice.

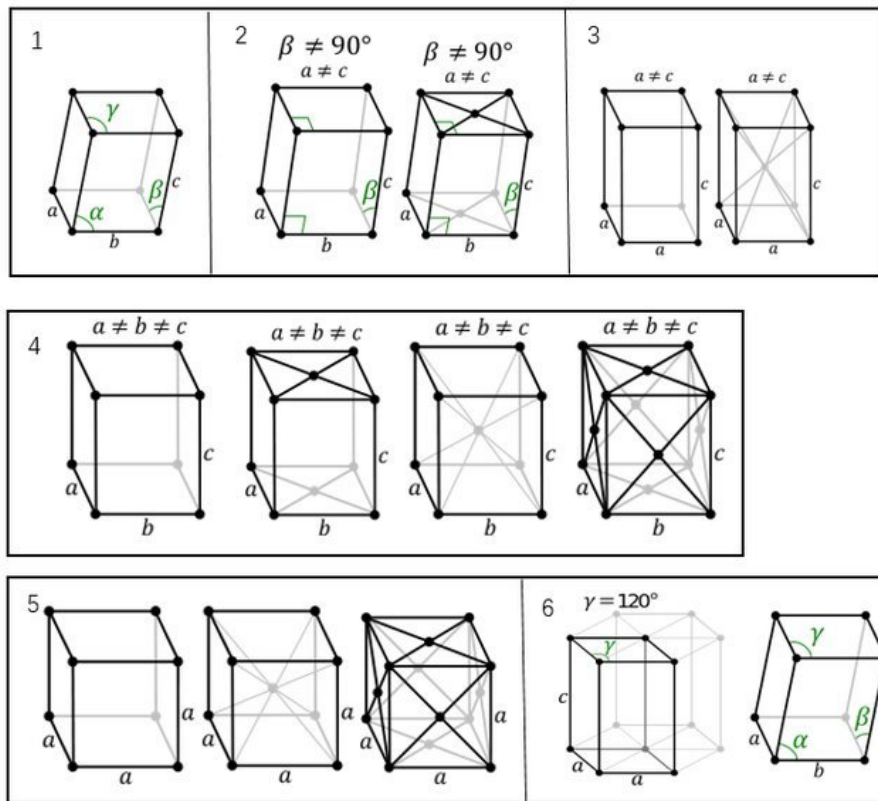


Figure 2.5 The 14 possible 3d Bravais lattices, distinguished by their symmetry [53].

the full crystal structure, depicted in Figure 2.4, also infinite in both directions. The three-dimensional case is exactly analogous: a lattice is composed with a unit cell, containing a basis of atoms, to form the crystal structure. In three dimensions there are fourteen possible Bravais lattices, shown in Figure 2.5.

A primitive unit cell always contains exactly one lattice point, but in many cases it is convenient to use a unit cell that is not primitive, containing more than one lattice point. These are termed conventional unit cells and usually are chosen to reflect the symmetry of the underlying Bravais lattice. In this way we get the body-centered and side-centered lattices, with two lattice points per conventional unit cell, and face-centered lattices, with four lattice points per conventional unit cell. The unit cell is usually specified by its dimensions (the lattice parameters a, b, c), and the angles between adjacent faces (α, β, γ). Most structures referred to in this thesis are cubic, so $a = b = c$, $\alpha = \beta = \gamma = 90^\circ$ and it is sufficient to specify the unique lattice parameter a .

Any crystal structure possesses certain symmetries, such as translations, rotations, reflections, inversion, etc. As stated previously this set of symmetries forms a group, the so called space group. In two dimensions they are known as wallpaper groups, and there are 17 distinct possibilities [54]. In three dimensions there are 230 possible space groups, which are commonly divided into the 7 crystal systems (triclinic, monoclinic, orthorhombic, tetragonal, trigonal, hexagonal, cubic), corresponding to the symmetry properties of their underlying Bravais lattices [55]. In order to represent magnetic structures (or other phenomena with inherent polarization) it is necessary to consider the 1651 magnetic space groups, also known as Shubnikov groups [56].

Each of the 230 space groups is assigned a symbol that describes the symmetry operations it contains. The most common naming convention for space groups is Hermann-Mauguin notation, consisting of two to four symbols for each space group. Each of the symbols in the name represents certain symmetries in a way that allows unique reconstruction of the space group from its name. As an example, the space group of the pyrochlore structure is $Fd\bar{3}m$, numbered 227 in the International Tables for Crystallography Volume A, the standard reference for crystallographic information [55]. Since $Fd\bar{3}m$ belongs to the cubic crystal system (the underlying Bravais lattice has cubic symmetry) it is easiest to visualize the symmetry operations contained in the space group through their action on a cube, the conventional unit cell. The meaning assigned to each symbol in $Fd\bar{3}m$ is as follows:

- F** Face-centered lattice. Other possibilities are primitive (P), I (body-centered), R (rhombohedral) and A, B or C (side-centered).
- d** Glide plane (a combination of reflection and translation) with the translation along a quarter of a face diagonal of the cube.
- $\bar{3}$** Threefold rotational symmetry (3) around the cube's body diagonal, along with a reflection through a plane perpendicular to the rotational axis (represented by the bar on top of the 3).
- m** Mirror (reflection) through a plane perpendicular to the face diagonal

When defining a crystal structure it is redundant to list all of the atoms contained in the unit cell because there are symmetries relating atoms in different positions. It is convenient to

absorb this redundancy by listing only the atoms inhabiting symmetry-inequivalent positions in the unit cell. These inequivalent positions are not related by symmetry operations in the space group of the structure and are termed Wyckoff positions. Each Wyckoff position is given a number and a letter, such that the number represents how many equivalent positions there are and the letters are given sequentially (from a to z), starting at the most special position (with the highest symmetry) to the most general position (with the least amount of symmetry).

Table 2.1 shows the Wyckoff positions for the space group $Fd\bar{3}m$. Only one of the coordinates associated with the Wyckoff positions is given, it being understood that applying the $Fd\bar{3}m$ symmetries to that set of coordinates will yield the full set of equivalent coordinates in the unit cell, equal in number to the multiplicity. The site symmetry describes symmetries which keep that point fixed, so that the most general position (192i) has only trivial symmetry and the number of symmetries increases going down the list.

Multiplicity	Letter	Site Symmetry	Coordinates
192	i	1	(x, y, z)
96	h	. . 2	$(0, y, -y)$
96	g	. . m	(x, x, z)
48	f	2 . m m	$(x, \frac{1}{8}, \frac{1}{8})$
32	e	. 3 m	(x, x, x)
16	d	. -3 m	$(\frac{1}{2}, \frac{1}{2}, \frac{1}{2})$
16	c	. -3 m	$(0, 0, 0)$
8	b	-4 3 m	$(\frac{3}{8}, \frac{3}{8}, \frac{3}{8})$
8	a	-4 3 m	$(\frac{1}{8}, \frac{1}{8}, \frac{1}{8})$

Table 2.1 Wyckoff positions for the space group $Fd\bar{3}m$ (origin choice 2).

Some space groups have two choices for the origin, depending on whether the point of highest symmetry or a point with inversion symmetry is chosen as the origin. For software that deals with diffraction it is most convenient to have inversion symmetry through the origin. That is why in this work we always use the second origin choice for $Fd\bar{3}m$.

The list of atoms inhabiting symmetry-inequivalent positions in the unit cell is known as the asymmetric unit. It is the minimal set of atoms that can generate the whole crystal structure when acted upon by the symmetry operations in the corresponding space group. Section 2.2 contains a few examples of structures and their asymmetric units.

2.2 Structures

In this section we explore in detail the structure of the fluorite, pyrochlore and δ -phases, which were found to be present in our $Yb_2Zr_xTi_{2-x}O_7$ samples using x-ray diffraction (Chapter 5).

2.2.1 Fluorite

Many AX_2 compounds crystallize with the same structure as the mineral fluorite, CaF_2 , in which Ca^{2+} cations form an fcc lattice and F^- anions occupy the interior of the conventional unit cell, depicted in Figure 2.6. Each conventional unit cell contains four formula units $4 \times AX_2 = A_4X_8$ (i.e. $Z = 4$ [57]). The space group associated to the fluorite structure is $Fm\bar{3}m$ (No. 225 [55]).

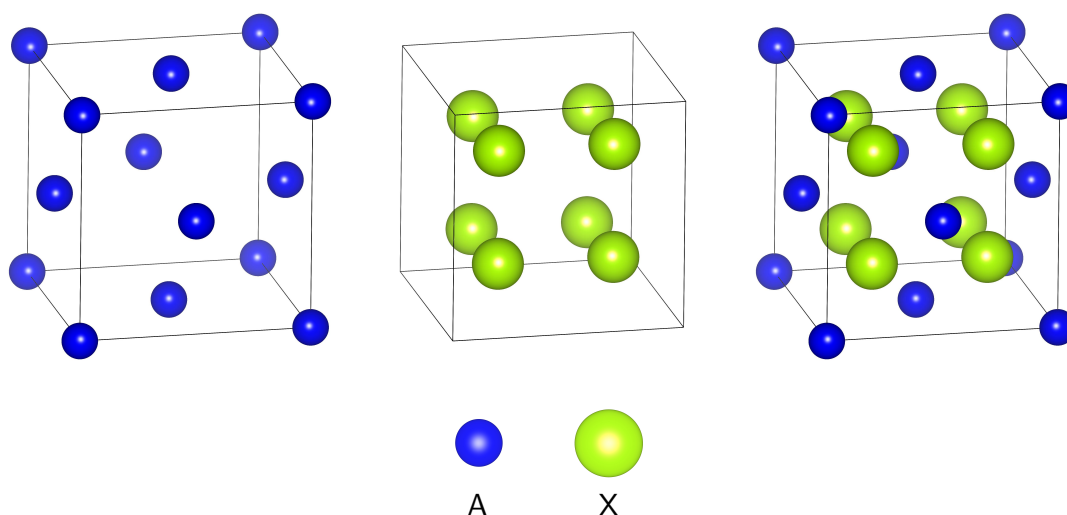


Figure 2.6 Conventional unit cell of the general AX_2 fluorite structure.

The structure is most conveniently specified by its asymmetric unit, listed in Table 2.2.

ion	position	x	y	z	occ
A	4a	0	0	0	1
X	8c	0.25	0.25	0.25	1

Table 2.2 Unit cell coordinates, Wyckoff positions and site occupancies for the asymmetric unit of the fluorite structure AX_2 .

Applying the $Fm\bar{3}m$ symmetries to the asymmetric unit yields the full structure, as depicted in Figure 2.7. Each A ion has eight nearest neighbor X ions, while each X ion has four nearest neighbor A sites.

In general the AX_2 structure could be composed of either A^{2+} and X^- ions or A^{4+} and X^{2-} ions. Another possibility is that instead of one element, A, at the 4a Wyckoff position there could be a mixture of two elements, A and B, with stoichiometry $A_yB_{1-y}X_2$. For example, if the mixture is even ($y = 0.5$) the stoichiometry would be $A_{0.5}B_{0.5}X_2 = ABX_4$ and the asymmetric unit would contain a random mixture of A and B at the 4a site, indicated by a site occupation $occ = 0.5$ in Table 2.3.

2.2.2 Defect Fluorite

The defect fluorite structure is an anion-deficient variant of the fluorite structure, containing vacant anion positions (defects). Using the example in Table 2.3 with $X = O^{2-}$, if the cations

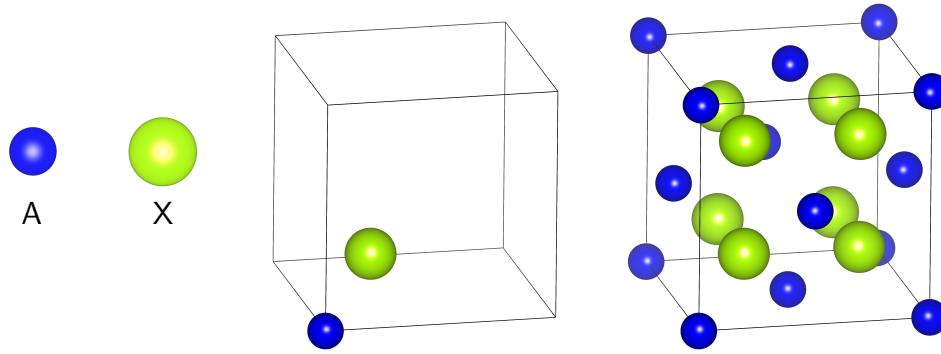


Figure 2.7 Asymmetric unit (middle) for the AX_2 fluorite structure and the full unit cell (right), generated by applying $Fm\bar{3}m$ symmetries to the asymmetric unit.

ion	position	x	y	z	occ
A	4a	0	0	0	0.5
B	4a	0	0	0	0.5
X	8c	0.25	0.25	0.25	1

Table 2.3 Unit cell coordinates, Wyckoff positions and site occupancies for the asymmetric unit of the fluorite structure ABX_4 .

were A^{3+} and B^{4+} instead of A^{4+} and B^{4+} then $\frac{1}{8}$ of the anion positions O^{2-} would need to be vacant in order to ensure electric charge neutrality. In that case $ABO_4 = A_2B_2O_8$ would become $A_2B_2O_7$ and the asymmetric unit would be defined by Table 2.4. Each conventional unit cell contains one formula unit $A_2B_2O_7$ (i.e. $Z = 1$ [57]).

ion	position	x	y	z	occ
A^{3+}	4a	0	0	0	0.5
B^{4+}	4a	0	0	0	0.5
O^{2-}	8c	0.25	0.25	0.25	0.875

Table 2.4 Unit cell coordinates, Wyckoff positions and site occupancies for each atom in the asymmetric unit of the defect fluorite structure $A_2B_2O_7$.

We assume that the distribution of both cations and anion vacancies are random, so the structure is no longer perfectly ordered but on average will assume the fluorite structure. Throughout this work we use the terms fluorite and defect fluorite interchangeably for the sake of convenience, but it should be understood that in most cases we are in fact referring to the defect fluorite structure.

Sometimes the $A_2B_2O_7$ defect fluorite formula unit is written as $[A,B]_4O_7$ or $[AB]_2O_7$ to emphasize that the cations are disordered, both A^{3+} and B^{4+} randomly occupying a single crystallographic site (the 4a Wyckoff position). In the $A_2B_2O_7$ pyrochlore structure (Section 2.2.3) the cations are not mixed and inhabit distinct sites, so it makes sense to distinguish the A and B positions in the $A_2B_2O_7$ formula unit, though they are equivalent in the fluorite structure.

While in the ideal fluorite every cation is eightfold coordinated and every anion is fourfold coordinated, the oxygen vacancies in the defect fluorite cause the average coordination of a cation to decrease to seven. Since the structure is in principle random, this does not imply that every cation has precisely seven nearest neighbors, rather some of them might have eight or less than seven neighbors.

In the case of $\text{Yb}_2\text{Zr}_x\text{Ti}_{2-x}\text{O}_7$ compounds which assume the defect fluorite structure the site occupation parameters vary with composition x such that the total occupation of Ti and Zr atoms remains constant and reflects the proportions of each element, e.g. for $\text{Yb}_2\text{Zr}_x\text{Ti}_{2-x}\text{O}_7$ with $x = 1.5$ we have

$$occ_{4a}(\text{Ti}) + occ_{4a}(\text{Zr}) = 0.5 \quad (2.2)$$

and

$$\frac{occ_{4a}(\text{Zr})}{occ_{4a}(\text{Ti})} = \frac{x}{2-x} = \frac{1.5}{0.5} \quad (2.3)$$

so

$$occ_{4a}(\text{Ti}) = 0.125 \quad occ_{4a}(\text{Zr}) = 0.375 \quad (2.4)$$

as shown in Table 2.5.

ion	position	x	y	z	occ
Yb^{3+}	4a	0	0	0	0.5
Ti^{4+}	4a	0	0	0	0.125
Zr^{4+}	4a	0	0	0	0.375
O^{2-}	8c	0.25	0.25	0.25	0.875

Table 2.5 Unit cell coordinates, Wyckoff positions and site occupancies for the asymmetric unit of the defect fluorite structure $\text{Yb}_2\text{Zr}_x\text{Ti}_{2-x}\text{O}_7$ with $x = 1.5$.

2.2.3 Pyrochlore

The $\text{A}_2\text{B}_2\text{O}_7$ pyrochlore structure is a superstructure of the defect fluorite in which the cations and oxygen vacancies are ordered. Its space group is $\text{Fd}\bar{3}\text{m}$ (No. 227 [55]). Due to the increased order the lattice parameters of the pyrochlore structure are doubled in relation to the corresponding defect fluorite structure, usually being close to 10\AA , while the fluorites have a lattice parameter of approximately 5\AA [31]. The pyrochlore structure is said to be a superstructure of the fluorite structure since the fluorite symmetries are a superset of the pyrochlore symmetries. This is not apparent if we simply consider the number of symmetry operations in $\text{Fd}\bar{3}\text{m}$ and $\text{Fm}\bar{3}\text{m}$ because of the doubling of the unit cell, but a $2 \times 2 \times 2$ fluorite supercell has a larger set of symmetries than that of a single pyrochlore unit cell. Therefore

the pyrochlore structure is more ordered but less symmetric than the fluorite structure. This is analogous to the distinction, rooted in symmetry, between a liquid and a solid: the solid is more ordered but less symmetric since it does not possess the liquid's isotropic rotational symmetry. Table 2.6 lists the atoms in the asymmetric unit of the pyrochlore structure. Each conventional unit cell contains eight formula units $A_2B_2O_7$ (i.e. $Z = 8$ [57]).

ion	position	x	y	z	occ
A^{3+}	16d	0.5	0.5	0.5	1
B^{4+}	16c	0	0	0	1
O^{2-}	8b	0.375	0.375	0.375	1
O^{2-}	48f	x_{48f}	0.125	0.125	1

Table 2.6 Unit cell coordinates, Wyckoff positions and site occupancies for the pyrochlore structure $A_2B_2O_7$.

In this case, unlike with the defect fluorite, there is no positional disorder, evidenced by all site occupations equaling one in Table 2.6. From the table we also see that there is a free parameter, x_{48f} , that is not constrained by symmetry to have a specific value. All of the other coordinates are fixed by the symmetry of the corresponding Wyckoff position, so that e.g. $0.375 = \frac{3}{8}$ exactly. The A and B cations occupy the 16d and 16c Wyckoff positions, respectively (Table 2.1), which have the same site symmetry ($\bar{3}m = D_{3d}$) but different surroundings, since the anions occupy the 8b site but the 8a site remains vacant.

Occasionally the $A_2B_2O_7$ pyrochlore formula unit is written as $A_2B_2O_6O'$ to distinguish the distinct oxygen positions $O = O_{48f}$ and $O' = O_{8b}$. Figure 2.8 shows the unit cells for each of the sublattices that make up the $A_2B_2O_7$ pyrochlore structure. The O_{8b} anions are colored orange to distinguish them from the green O_{48f} anions.

In the case of $Yb_2Zr_xTi_{2-x}O_7$ compounds that assume the pyrochlore structure the site occupancies vary with composition x in a way analogous to the explanation preceding Table 2.5. For example, if $x = 0.5$ then the structure would be as listed in Table 2.7.

ion	position	x	y	z	occ
Yb^{3+}	16d	0.5	0.5	0.5	1
Zr^{4+}	16c	0	0	0	0.25
Ti^{4+}	16c	0	0	0	0.75
O^{2-}	8b	0.375	0.375	0.375	1
O^{2-}	48f	x_{48f}	0.125	0.125	1

Table 2.7 Unit cell coordinates, Wyckoff positions and site occupancies for the asymmetric unit of the pyrochlore structure $Yb_2Zr_xTi_{2-x}O_7$ with $x = 0.5$.

As already noted in Section 1.1, both A^{3+} and B^{4+} cations form lattices of corner-sharing tetrahedra, depicted in Figure 2.9. These identical lattices are displaced with respect to one another by half of the unit cell body diagonal. The edge length of the tetrahedra is

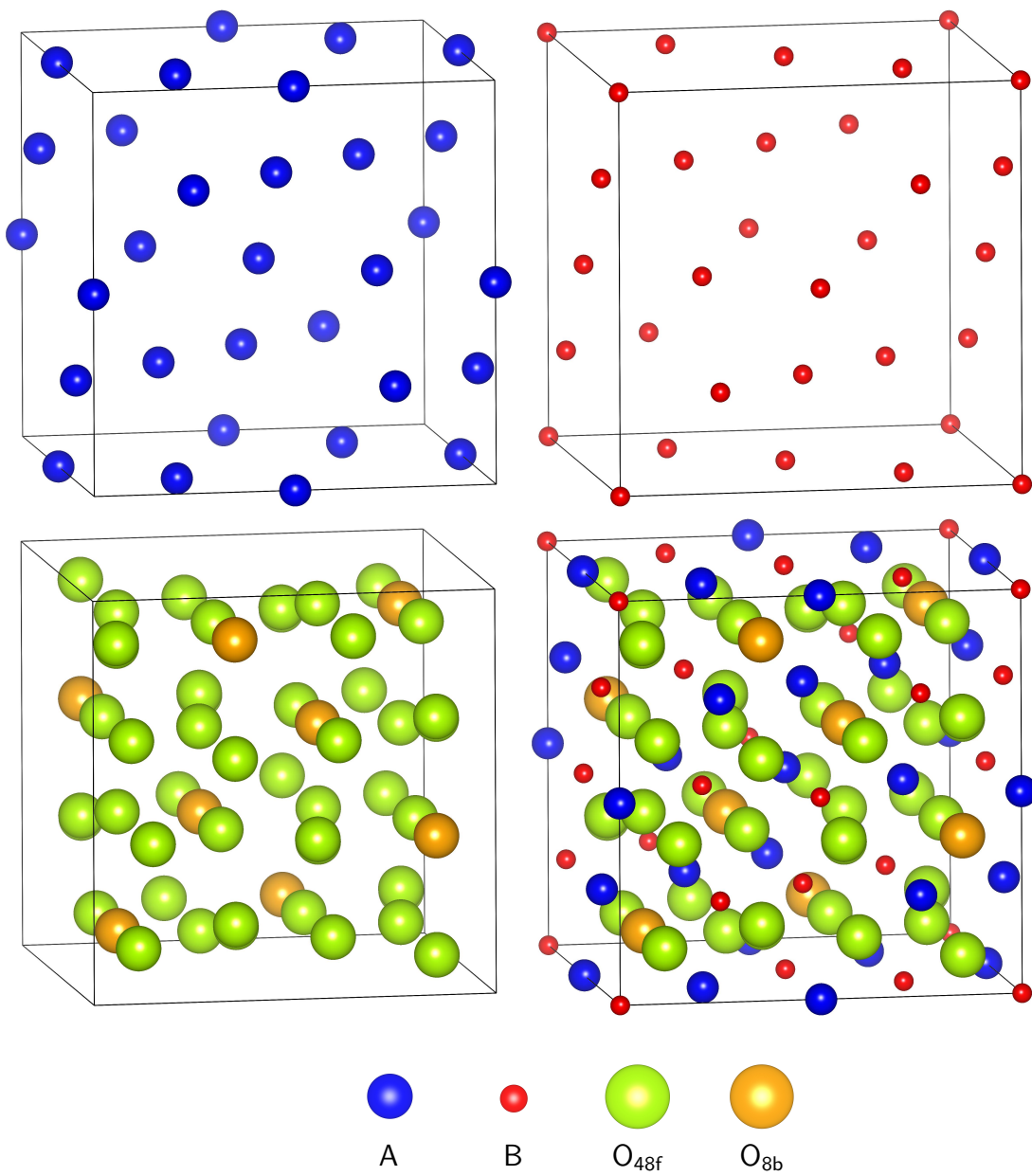


Figure 2.8 Unit cells for each of the sublattices that make up the $A_2B_2O_7$ pyrochlore structure. O_{8b} are colored orange to distinguish them from the green O_{48f} .

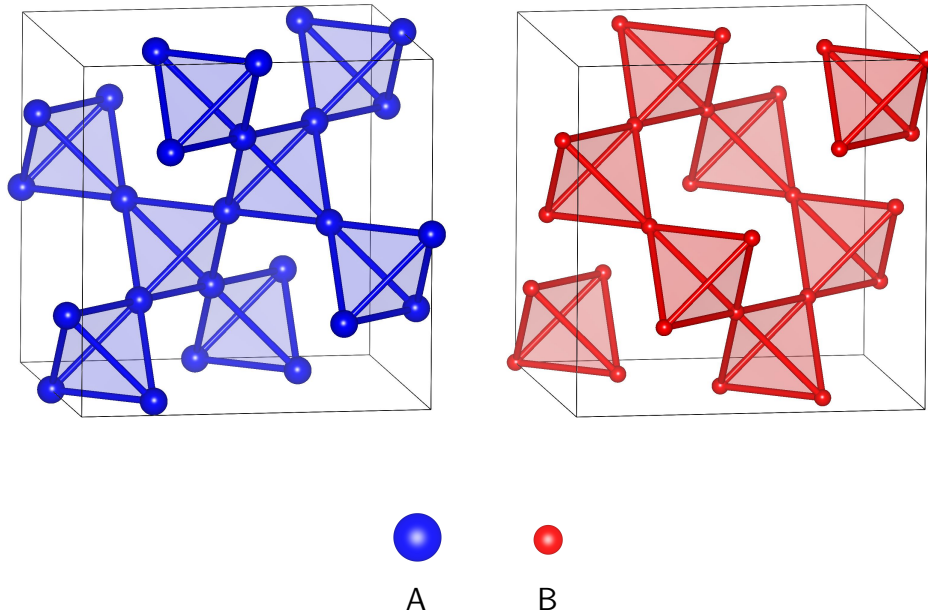


Figure 2.9 Lattices of corner-sharing tetrahedra, formed by A^{3+} and B^{4+} cations in the pyrochlore structure.

$\frac{a}{2\sqrt{2}} = 3.54\text{\AA}$ assuming $a = 10\text{\AA}$. The O^{2-} anions occupy the spaces within and between these cation lattices.

The 111 planes, perpendicular to the $\langle 111 \rangle$ body diagonal of the unit cell, consist of alternating A_3B and AB_3 layers, depicted in Figure 2.10. In the A_3B layers the A ions form a kagome lattice (Section 3.9) with the interior of the hexagons occupied by B ions, while in the AB_3 layers the roles of A and B are reversed. The 110 planes, perpendicular to the $\langle 110 \rangle$ face diagonal of the unit cell, consist of alternating planes with A^{3+} and B^{4+} cations ordered in stripes and in a checkerboard pattern, as can be seen in Figure 2.11.

The nearest neighbors of the ions in each Wyckoff position, including the usually vacant 8a site, are

- A^{3+} eight O^{2-} neighbors, two O_{8b} and six O_{48f} , forming an AO_8 polyhedron, a distorted cube
- B^{4+} six O^{2-} neighbors, all O_{48f} , forming a BO_6 polyhedron, a somewhat distorted octahedron
- O_{48f}^{2-} four cation neighbors, two A^{3+} and two B^{4+} , forming an OA_2B_2 tetrahedron
- O_{8b}^{2-} four cation neighbors, all A^{3+} , forming an OA_4 tetrahedron
- O_{8a}^{2-} four cation neighbors, all B^{4+} , forming an OB_4 tetrahedron

The coordination polyhedra, formed by the nearest neighbors of each atom are depicted in Figure 2.12.

Considering a $2 \times 2 \times 2$ fluorite supercell we see that it maps to a single pyrochlore unit cell with oxygen coordinate $x_{48f} = \frac{3}{8} = 0.375$. In the pyrochlore structure x_{48f} relaxes from this value

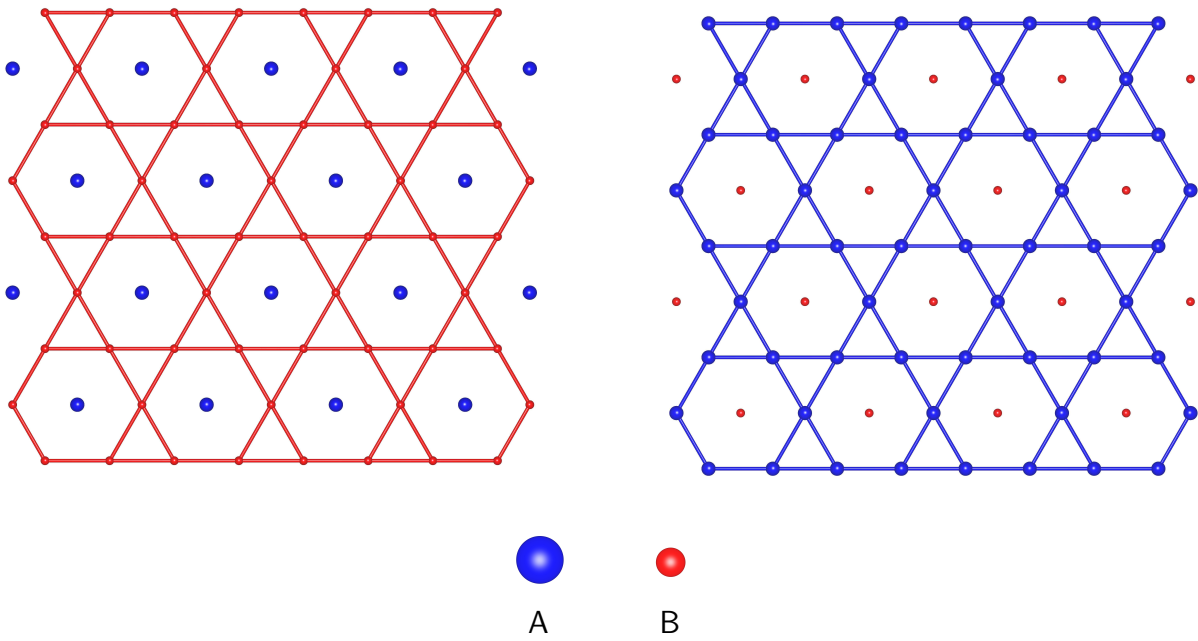


Figure 2.10 Two consecutive 111 slices of the pyrochlore structure, perpendicular to the $\langle 111 \rangle$ body diagonal of the unit cell.

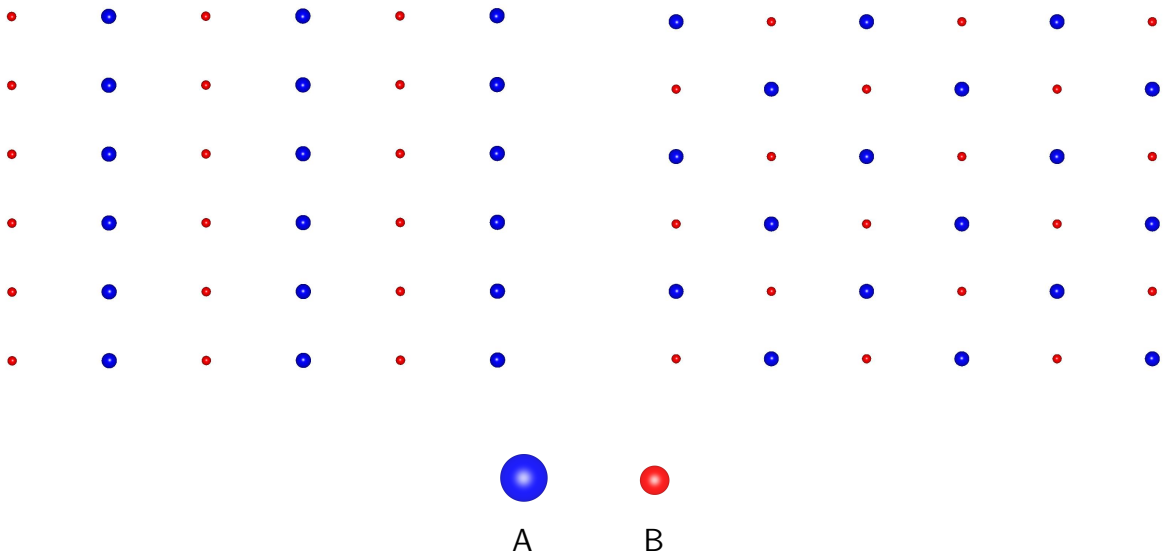


Figure 2.11 Two consecutive 110 slices of the pyrochlore structure, perpendicular to the $\langle 110 \rangle$ face diagonal of the unit cell.

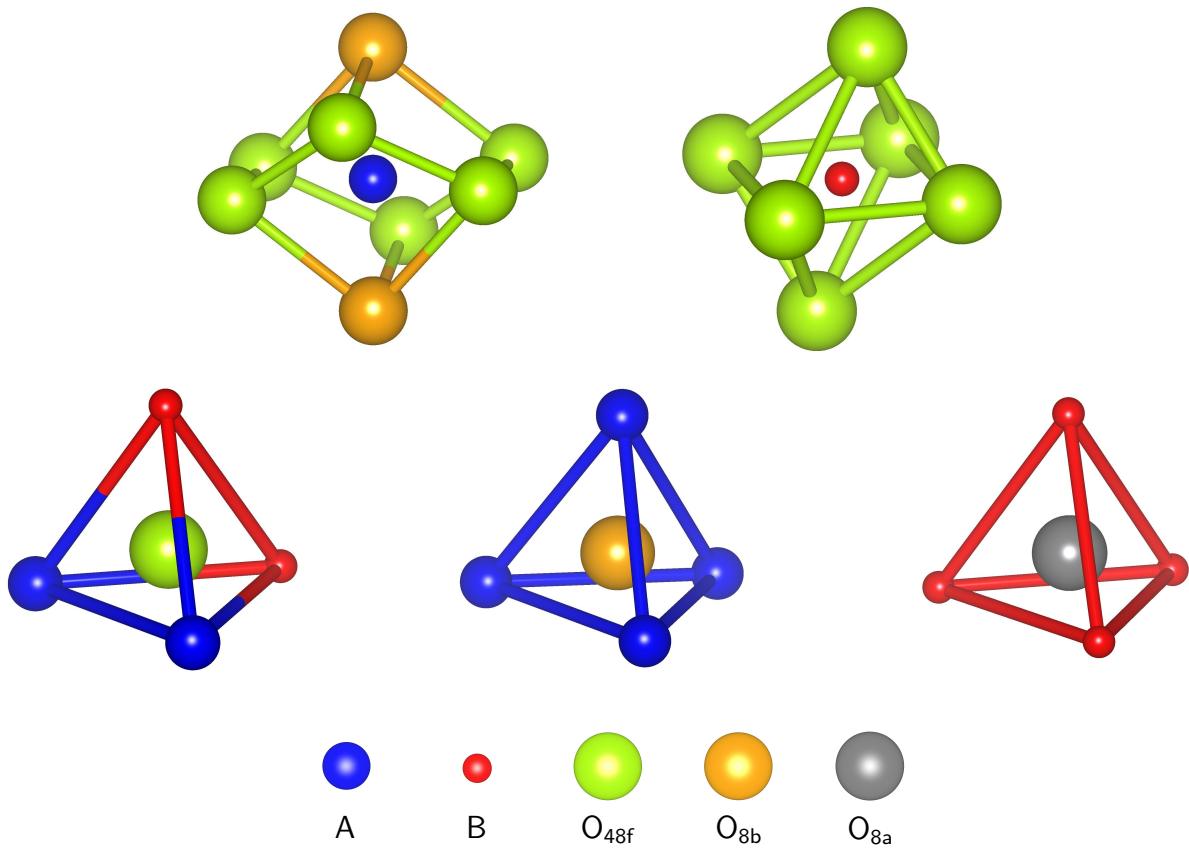


Figure 2.12 Coordination polyhedra formed by the nearest neighbors of each atom in the pyrochlore structure, including the usually vacant 8a site.

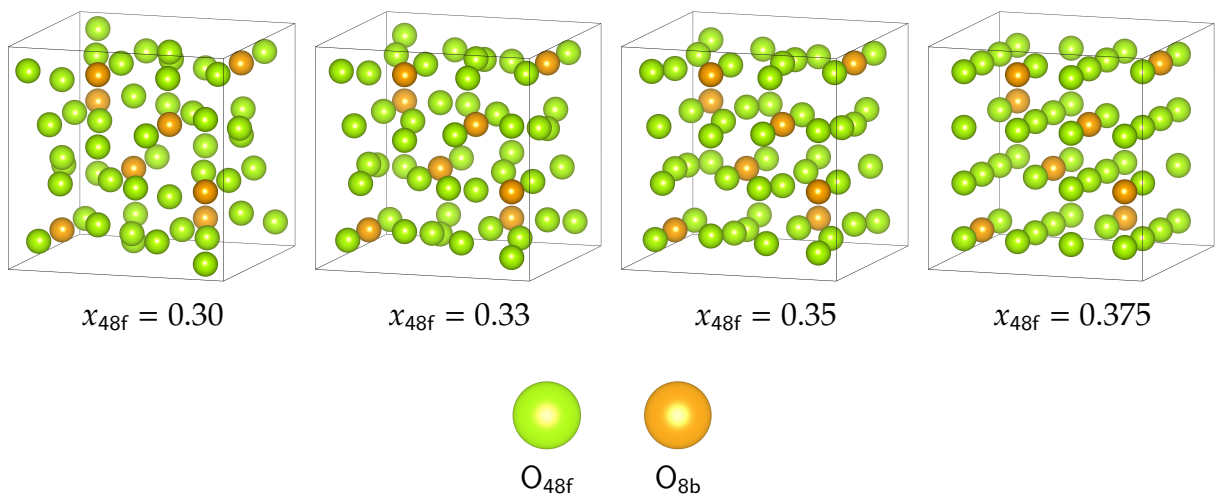


Figure 2.13 Oxygen ions in pyrochlore unit cell, with $x_{48f} = 0.30, 0.33, 0.35, 0.375$.

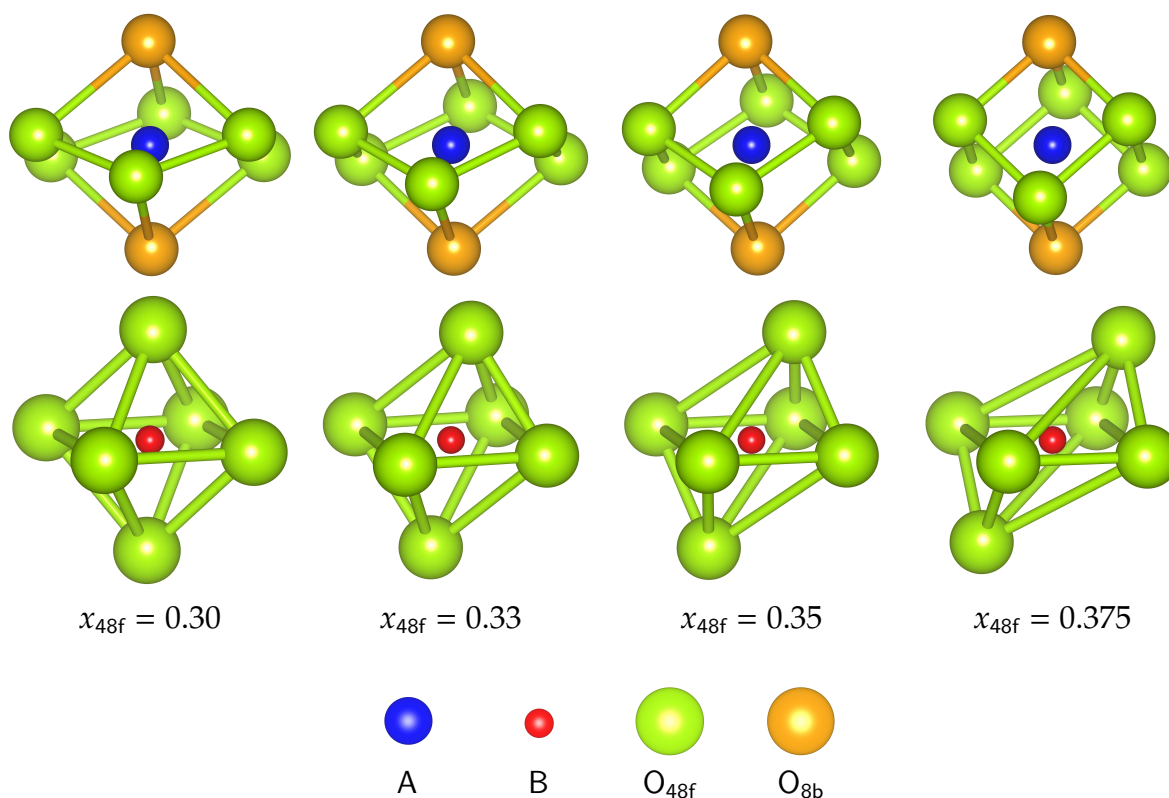


Figure 2.14 The coordination polyhedra centered on the A^{3+} and B^{4+} cations for $x_{48f} = 0.3125, 0.33, 0.35, 0.375$.

because the oxygen ions accommodate to partially fill the vacancies that would be present in the corresponding defect fluorite structure. In the pyrochlore structure these vacancies correspond to the unfilled 8a sites, with unit cell coordinates $\left(\frac{3}{8}, \frac{3}{8}, \frac{3}{8}\right)$ (see Table 2.1). The actual value of x_{48f} usually lies in the range $0.30 \leq x_{48f} \leq 0.35$ for most pyrochlores. Figure 2.13 shows how the O^{2-} anions are arranged in the conventional unit cell for some values of x_{48f} .

The value of x_{48f} also controls the geometry of the coordination polyhedra surrounding the cations. For $x_{48f} = \frac{3}{8} = 0.375$ we get perfect AO_8 cubes and distorted BO_6 , while for $x_{48f} = \frac{5}{16} = 0.3125$ we get perfect BO_6 octahedra and distorted AO_8 cubes. Figure 2.14 shows the coordination polyhedra centered on the A^{3+} and B^{4+} cations for some values of x_{48f} in between these two extremes. There is a kind of competition between the elastic tension caused by deformation of these two polyhedra. Since the B-O bonds are usually more rigid (stronger, more ionic in nature) than the A-O bonds (weaker, more covalent) the actual values of x_{48f} are often closer to the lower limit $x_{48f} = 0.3125$ than the upper limit $x_{48f} = 0.375$, with AO_8 cubes significantly more distorted than the BO_6 octahedra.

2.2.4 δ -phase

The δ -phase structure has stoichiometry $A_4B_3O_{12}$, which is equivalent to a stuffed pyrochlore, $A_{2+x}B_{2-x}O_{7-x/2}$, with $x = \frac{2}{7} = 0.2857$, i.e. $A_{2.29}B_{1.71}O_{6.86}$. This rhombohedral structure is much less studied than the pyrochlore and fluorite structures since it has a more narrow range of stability and more limited options for A^{3+} and B^{4+} elements. It is stable only for compounds containing smaller rare-earth ions and does not tolerate oxygen nonstoichiometry as much as the pyrochlore/fluorite structures [58, 59, 60].

ion	position	x	y	z	occ
A ³⁺	3a	0	0	0	f
B ⁴⁺	3a	0	0	0	$1 - f$
A ³⁺	18f	x_1	y_1	z_1	g
B ⁴⁺	18f	x_1	y_1	z_1	$1 - g$
O ²⁻	18f	x_2	y_2	z_2	1
O ²⁻	18f	x_3	y_3	z_3	1

Table 2.8 Unit cell coordinates, Wyckoff positions and site occupancies for the asymmetric unit of the δ -phase structure $A_4B_3O_{12}$.

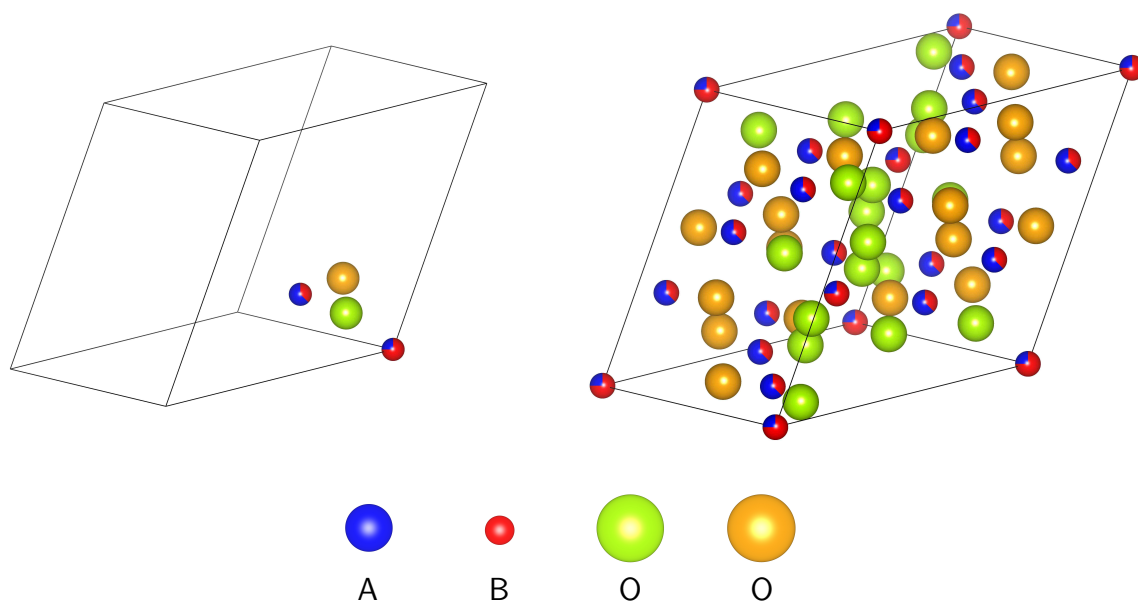


Figure 2.15 $A_4B_3O_{12}$ δ -phase asymmetric unit (left) and a full unit cell (right).

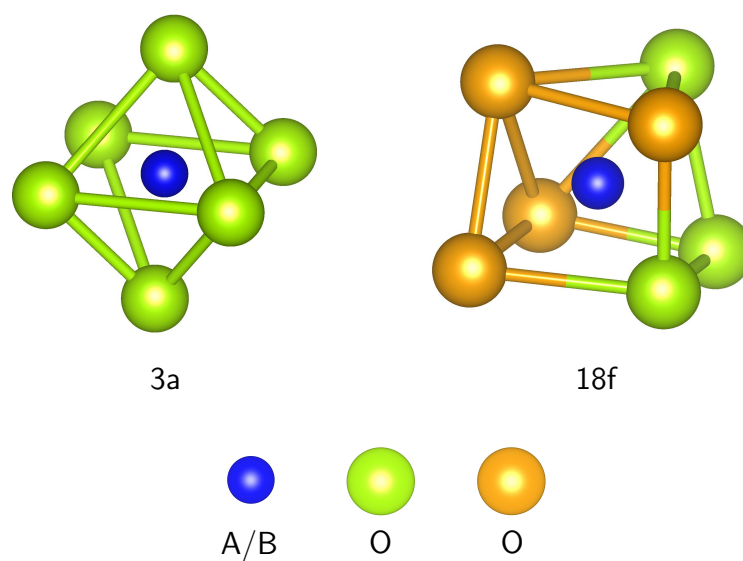


Figure 2.16 Cation coordination polyhedra in the δ -phase structure.

The space group of the δ -phase is $R\bar{3}$ (No. 148 [55]) and its structural parameters are $\alpha = \beta = 90^\circ$, $\gamma = 120^\circ$, $a = b \approx 9.6\text{\AA}$ and $c \approx 8.9\text{\AA}$. This structure breaks the cubic symmetry of the parent fluorite phase and is not a fluorite superstructure, although there is some lattice plane continuity when deforming a fluorite into the δ -phase, as is evident from their diffraction patterns (Chapter 5). The oxygen vacancies in the δ -phase are ordered in chains oriented approximately along the $\langle 111 \rangle$ direction of the parent fluorite unit cell. Therefore the δ -phase can be considered as a rhombohedral distortion of the fluorite with anionic vacancies along one of the threefold axes.

The unit cell coordinates, Wyckoff positions and site occupancies for the asymmetric unit of the $A_4B_3O_{12}$ δ -phase structure are listed in Table 2.8. The site occupation parameters f and g are not independent and have to satisfy $f + 6g = 4$ to ensure the proper 4:3:12 stoichiometry. The structure is less symmetric than the fluorite and pyrochlore phases, as is clear from the large number of free parameters in Table 2.8.

Figure 2.15 shows the $A_4B_3O_{12}$ δ -phase asymmetric unit and a full unit cell. The A^{3+} and B^{4+} cations are randomly mixed on two sites and the O^{2-} anions occupy two distinct sites. In this sense the structure is intermediate between the disordered fluorite, with mixed cations and one anion site, and the ordered pyrochlore, with no cation mixing and separate anion sites.

There are two distinct symmetry cation positions in the δ -phase structure, the 3a (0,0,0) and 18f (x, y, z) Wyckoff positions. Both of these sites are randomly occupied by a mixture of the A^{3+} and B^{4+} cations but their surroundings are different, as illustrated in Figure 2.16. The 3a position is surrounded by six O^{2-} forming a distorted octahedron, while the 18f cation position is surrounded by seven O^{2-} forming a distorted, truncated cube shape. The oxygen ions occupying the two distinct sites in Table 2.8 are colored differently in Figure 2.16 to distinguish them.

2.2.5 Other Structures

The monoclinic $A_2B_2O_7$ phase is stable for larger A^{3+} and smaller B^{4+} ions than for those found in the pyrochlore phase, for instance for the titanates $A_2Ti_2O_7$ the stability condition is $r_{Ln} \geq r_{Nd}$, i.e. Ln = La–Nd. This structure is much less symmetric than the pyrochlore, with space group $P2_1$ (No.4 [55]), $a \approx 25\text{\AA}$, $b \approx 8\text{\AA}$ and $c \approx 6\text{\AA}$. It is related to the layered perovskite structure [61].

The $A_2B_2O_7$ weberite structure is isomorphous to the mineral weberite, Na_2MgAlF_7 . It can be thought of as an intermediate between pyrochlore and fluorite, in the sense that the cations are partially ordered, with some crystallographic sites containing only A or B cations and other sites containing a random mixture of A and B, as illustrated in Figure 2.17.

The traditional weberite structure is orthorhombic, with space group $Imma$ (No. 74 [55]), which is a subgroup of $Fd\bar{3}m$. It is a fluorite superstructure and a pyrochlore substructure, with lattice parameters a_w, b_w, c_w related to the corresponding fluorite and pyrochlore lattice parameters a_f and a_p by $a_w = c_w = \sqrt{2}a_f = a_p/\sqrt{2}$ and $b_w = 2a_f = a_p$ [62].

The weberite is similar to a pyrochlore in which the ordering of cations in the AB_3 and A_3B layers (011 layers in the weberite, corresponding to the 111 layers in pyrochlore, Figure 2.10) is different. There is a wide variety of weberite variants with slightly different symmetry [62].

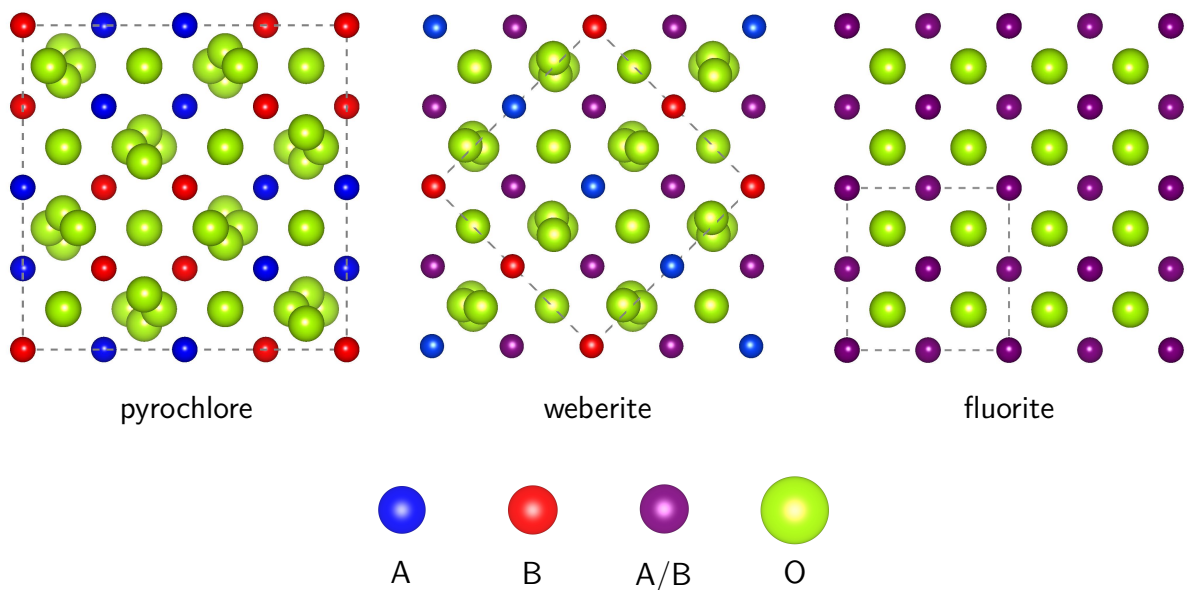


Figure 2.17 Relation between the pyrochlore, weberite and fluorite structures.

Another common fluorite superstructure is the orthorhombic β -phase structure of A_2BO_5 compounds. As for the δ -phase, this stoichiometry can be thought of as a stuffed pyrochlore, $A_{2+x}B_{2-x}O_{7-x/2}$, with $x = \frac{2}{3}$. This structure contains edge-sharing tetrahedra as in the fluorite (fcc) structure but is more complex, with interwoven triangular layers that form the caps of the tetrahedral network [63].

There are many other potentially relevant structures, too numerous to list here. Most of these phases are superstructures of the basic fluorite structure in a similar fashion to the superstructure relation between pyrochlore and fluorite. Their stoichiometries and symmetries (space groups) range widely, from phases with mixed cations on the same crystallographic sites and oxygen vacancies, to phases with ordered cations on multiple distinct sites. Some of these phases could be present as minority fractions in the $Yb_2Zr_xTi_{2-x}O_7$ compounds we synthesized (see discussion in Section 5.3).

One way to categorize the various phases in the pyrochlore family is by ranking them according to the ratio between the number of anions and the number of cations in their composition. Table 2.9 lists some of the most common phases according to this criterion. All of these stoichiometries can be expressed as a general fluorite derivative $A^{3+}_m B^{4+}_n O_{2n+3m/2}$ with various values of m and n . For $m + n = 4$ these can be written as $A_{2+x}B_{2-x}O_{7-x/2}$ where $x > 0$ for a stuffed pyrochlore and $x < 0$ for a diluted pyrochlore, one example of each being listed in Table 2.9. Note that a certain stoichiometry can be associated with various distinct structures and in some cases even a single compound can crystallize with multiple structures. On the other hand, in some cases a specific structure can accommodate a range of slightly varying stoichiometries.

structure	stoichiometry	anion/cation ratio
fluorite	BO_2 AB_2O_6	2.0000
diluted pyrochlore	$\text{A}_{1.9}\text{B}_{2.1}\text{O}_{7.05}$	1.7625
pyrochlore defect fluorite monoclinic phase weberite	$\text{A}_2\text{B}_2\text{O}_7$	1.7500
stuffed pyrochlore	$\text{A}_{2.1}\text{B}_{1.9}\text{O}_{6.95}$	1.7375
δ -phase	$\text{A}_4\text{B}_3\text{O}_{12}$ A_6BO_{12}	1.7143
β -phase	A_2BO_5	1.6667
–	A_6BO_{11}	1.5714
bixbyite	A_2O_3 $\text{A}_2\text{B}_2\text{O}_6$	1.5000

Table 2.9 Some common phases in the pyrochlore family, ranked according to the ratio between the number of anions and the number of cations in their composition.

2.3 Structure Prediction

Materials with chemical formula $\text{A}_2\text{B}_2\text{O}_7$ may assume several different structures, including the pyrochlore, fluorite, weberite, layered perovskite phases and various other phases with the same or similar stoichiometry, some of which were introduced in Section 2.2. Predicting which structure a given material will assume is an interesting challenge, given the large number of possibilities for both the A and B elements. The most reliable results come from computer simulations (Section 2.3.2), but we also introduce a simpler approach (Section 2.3.1) which provides a useful heuristic for predicting structures and can be quite accurate except close to phase boundaries on structure-composition phase diagrams.

2.3.1 Tolerance factors

A tolerance factor is a single constant that combines the ionic radii of the ions in the material and possibly other parameters, such as lattice parameters, atomic coordinates and electronegativities. Different ranges of values for this constant correspond to different predicted structures. The interatomic separations, and by extension the lattice parameters, are determined mainly

by the oxidation states and ionic radii of the ions composing the structure. Therefore it is expected that some structural properties can be predicted considering simply the ionic radii (and possibly other parameters) of the ions in the material.

The concept of tolerance factor was first introduced by Goldschmidt [64] to describe the structure of ABO_3 perovskites, but similar tolerance factors have been proposed for other materials, such as spinels [65], garnets [66] and ilmenite [67]. The Goldschmidt tolerance factor t_0 is a dimensionless number defined as

$$t_0 = \frac{1}{\sqrt{2}} \frac{r_A + r_O}{r_B + r_O} \quad (2.5)$$

where r_i are the ionic radii of the corresponding ions in the ABO_3 structure. The factor $\sqrt{2}$ is included as a convenience, it represents the ratio between the B–O bond length ($r_B + r_O$, half of the cubic lattice parameter) and the A–O bond length ($r_A + r_O$, half of the cube's face diagonal). According to the value of t_0 the structure will be hexagonal/tetragonal ($t_0 > 1$), cubic ($1 > t_0 > 0.9$) or orthorhombic/rhombohedral ($0.9 > t_0 > 0.71 = 1/\sqrt{2}$). The tolerance factor is also correlated to various other physical properties, hence its usefulness.

Several different tolerance factors have been proposed for the pyrochlore structure. The simplest one, introduced in [31], is just a ratio between the ionic radii of the A and B ions,

$$t_1 = \frac{r_A}{r_B} \quad (2.6)$$

According to [31] the stability region for the pyrochlore structure is $1.46 \leq t_1 \leq 1.72$. If $t_1 < 1.46$ the ionic radii are too similar to assume the ordered pyrochlore structure and the disordered defect fluorite structure results. If $t_1 > 1.72$ then the stable structure is the monoclinic structure mentioned in Section 2.2.5.

As will be discussed in Section 3.7, the ionic radii of lanthanide ions decrease with increasing atomic number, from 1.16\AA in La^{3+} to 0.977\AA in Lu^{3+} . There are several slightly different definitions for the ionic radius, the values quoted here are derived from r^3 vs V plots [68]. The ionic radius also slightly depends on the ion's coordination (number of nearest neighbors). To be consistent we always consider eightfold coordinated A^{3+} cations, sixfold coordinated B^{4+} cations and fourfold coordinated O^{2-} anions, as they would be in the pyrochlore structure, even though in the more disordered structures there may also be, for instance, seven or sixfold coordinated A^{3+} ions.

ion	coordination	radius (\AA)
Yb^{3+}	8	0.985
Ti^{4+}	6	0.605
Zr^{4+}	6	0.72
O^{2-}	4	1.38

Table 2.10 Ionic radii and coordination of the ions that compose the $\text{Yb}_2\text{Zr}_x\text{Ti}_{2-x}\text{O}_7$ structure [68].

If the A and/or B sites contain a mixture of elements, as in $\text{Yb}_2\text{Zr}_x\text{Ti}_{2-x}\text{O}_7$, the ionic radius of that site is assumed to be an average of the ionic radii of the elements, weighted by their molar fractions. The ionic radii for the elements in $\text{Yb}_2\text{Zr}_x\text{Ti}_{2-x}\text{O}_7$ are listed in Table 2.10.

Another tolerance factor t_2 , introduced by Isupov [69], is defined as

$$t_2 = \frac{\sqrt{3}}{2} \frac{r_A + r_O}{r_B + r_O} \quad (2.7)$$

As with t_0 , the constant $\frac{\sqrt{3}}{2} = 0.866$ is a geometric factor included so that $t_2 = 1$ when the pyrochlore BO_6 octahedra are ideal, i.e. $x_{48f} = 0.3125 = \frac{5}{16}$, although for real pyrochlores x_{48f} can assume different values (Section 2.2.3). Assuming ideal BO_6 octahedra the constant prefactor in (2.7) is a ratio of distances between the ions,

$$\frac{A - \text{O}_{48f}}{A - \text{O}_{8b}} = \frac{\sqrt{3}}{2} \quad (2.8)$$

Other tolerance factors have been proposed that take into account additional parameters, such as the value of the oxygen coordinate x_{48f} and the lattice parameter a , increasing their predictive power at the expense of becoming more complicated. In [70] the authors propose two tolerance factors, t_3 and t_4 ,

$$t_3 = \sqrt{\frac{(x_{48f} - \frac{1}{4})^2 + \frac{1}{32}}{(x_{48f} - \frac{1}{2})^2 + \frac{1}{32}}} \frac{r_A + r_O}{r_B + r_O} \quad (2.9)$$

$$t_4 = \frac{3\sqrt{3}}{8} \frac{a}{r_B + r_O} \quad (2.10)$$

t_3 considers only the geometry of the A_2B_2 tetrahedra, which contain an O_{48f} ion, while t_4 is derived from the geometry of the A_4 tetrahedra, which contain an O_{8b} ion. These parameters offer more precise predictions than those that rely solely on the ionic radii, but their disadvantage is that they require knowing either the oxygen coordinate x_{48f} or the lattice parameter a . Usually these are not known prior to synthesizing the compounds and have to be measured experimentally or calculated by computationally expensive and time consuming ab initio approaches, although they can be approximately predicted empirically. In [70] two of these methods, based on BVS (bond valence sum) calculations and Nikiforov's work, are used to predict the normalized dielectric difference in several pyrochlore compounds.

It should be noted that, while a can be reliably extracted from x-ray diffraction experiments (Chapter 5), neutron diffraction is required to obtain accurate values of x_{48f} , since x-rays are not very sensitive to light elements such as oxygen. This means that the value of x_{48f} determined through x-ray-diffraction is quite sensitive to subtle errors in the data analysis in addition to being sensitive to synthesis conditions and structural disorder. Therefore tolerance factors based solely on the ionic radii and a , such as t_4 , are expected to be more robust than those that take into account x_{48f} , such as t_3 . In [71] it is shown that x_{48f} can be expressed as a

function the mean cubic and octahedral bond lengths, however this approach also has poor predictive character since it requires knowledge of those structural parameters, which is not available prior to synthesis and characterization.

In addition to the oxidation states and ionic radii, another factor that could help predict structural properties is the electronegativity of the ions composing the material. It has been found in [72], by analyzing data for 92 pyrochlore compounds from 168 literature sources, that taking into account electronegativity values yields better predictions of the pyrochlore lattice parameter for compositions with mixed cations or anions. In this study the best fit to the data was calculated using only the ionic radii r_i (2.11) and both ionic radii r_i and electronegativities χ_i (2.12),

$$a(r_i) [A_2B_2X_2] = 1.91712 (r_A + r_X) + 2.76428 (r_B + r_X) + 0.04008 \quad (2.11)$$

$$a(r_i, \chi_i) [A_2B_2X_2] = 1.99818 (r_A + r_X) + 2.64754 (r_B + r_X) + 0.02238 (\chi_X - \chi_A) + 0.06215 (\chi_X - \chi_B) - 0.07432 \quad (2.12)$$

where the lattice parameter and ionic radii are in Å and χ is dimensionless. Equation eq. (2.11) is sufficient to account for the lattice parameters of $A_2B_2X_7$ compounds with only three species (A, B, X), but (2.12) significantly improves the fitting of experimental data for compositions with more than three species (mixed cations or anions, as in $AA'B_2X_7$). When there are mixed species on one of the sites the ionic radius and electronegativity are averaged values, weighted by the molar fraction of each species. Note that the coefficients of the electronegativities in (2.12) are small compared to the coefficients of the ionic radii, so that most of the variability in lattice parameters is due to differences in ionic radii.

For $Yb_2Ti_2O_7$ the calculated lattice parameters are $a(r_i) = 10.0612\text{Å}$ according to eq. (2.11) and $a(r_i, \chi_i) = 10.761\text{Å}$ according to eq. (2.12), which agree with the experimentally determined values ranging from 10.02Å (ICSD 154077 [73]) to 10.09Å (ICSD 173750 [73]). Using $\chi_{Yb} \approx 1.15$, $\chi_{Zr} = 1.33$, $\chi_{Ti} = 1.54$ and $\chi_O = 3.44$ [74] we calculated the predicted lattice parameters for $Yb_2Zr_xTi_{2-x}O_7$ according to (2.11) and (2.12), listed in Table 2.11. Clearly the trend is for the lattice parameter to increase with x , which is proportional to the amount of Zr in the composition.

In [75] the authors propose a different expression for the lattice parameter, based on 110 experimental values for 79 pyrochlore compounds,

$$a' = \frac{8}{\sqrt{3}} \left[1.43373 (r_A + r_O) - 0.42931 \frac{(r_A + r_O)^2}{r_B + r_O} \right] \quad (2.13)$$

which depends only on the ionic radii r_i but allows a nonlinear dependence on those, in contrast to the linear dependence on r_i in the previously defined tolerance factors. The predicted lattice

x	$a(r_i)$	$a(r_i, \chi_i)$	a'
0.0	10.0612	10.0761	10.0740
0.15	10.0850	10.0999	10.0982
0.3	10.1088	10.1237	10.1221
0.5	10.1406	8.4763	10.1538
1.0	10.2201	10.2348	10.2313
1.5	10.2996	10.3142	10.3067
2.0	10.3791	10.3936	10.3800

Table 2.11 Calculated lattice parameters $a(r_i)$, $a(r_i, \chi_i)$ and a' for $\text{Yb}_2\text{Zr}_x\text{Ti}_{2-x}\text{O}_7$ according to (2.11), (2.12) and (2.13), respectively.

parameter values a' for $\text{Yb}_2\text{Zr}_x\text{Ti}_{2-x}\text{O}_7$ according to (2.13) are also listed in Table 2.11. Using a' in the definition of tolerance factor t_4 (2.10) we get the tolerance factor t_5 ,

$$t_5 = 1.43373 - 0.42931 \frac{r_A + r_O}{r_B + r_O} \quad (2.14)$$

Considering all the compounds fitted in [75], those that assume the pyrochlore structure are centered around $t_5 = 0.913$, and $t_5 = 0.894$ marks the cutoff value between pyrochlore and weberite structures. The simpler tolerance factor t_1 also allows one to distinguish the pyrochlore and weberite structure (the weberite structure is assumed for $t_1 > 1.84$) but misclassifies several pyrochlore structures formed through high-pressure synthesis, encircled in Figure 2.18. t_5 could be used to distinguish these high-pressure synthesis compounds, since the data points associated to them are somewhat separated from those representing common weberite structures in Figure 2.18. Pyrochlore compounds that contain ions with stereochemically active non-binding lone electron pairs, such as Bi^{3+} , Pb^{2+} and Te^{4+} , do not agree as well with the tolerance factor predictions since the lone electron pair violates the assumption of approximately spherical ions, upon which the whole tolerance factor approach is based (close-packing of spheres).

In [66], based on geometric considerations, another tolerance factor t_6 is proposed,

$$t_6 = \frac{3}{\sqrt{17}} \frac{r_A + r_O}{r_B + r_O} \quad (2.15)$$

This only differs from t_2 (2.7) by the multiplicative constant $\frac{3}{\sqrt{17}} = 0.72761$ instead of $\frac{\sqrt{3}}{2} = 0.866$. The authors argue that the ideal pyrochlore structure should have $t_6 = 1$ but acknowledge that in practice the values are clustered around $t_6 \approx 0.88$. Figure 2.19 [66] shows the calculated tolerance factor t_6 for 180 pyrochlore compounds and the cutoff values that define the stability fields for the pyrochlore structure, $0.826 \leq t_6 \leq 0.943$.

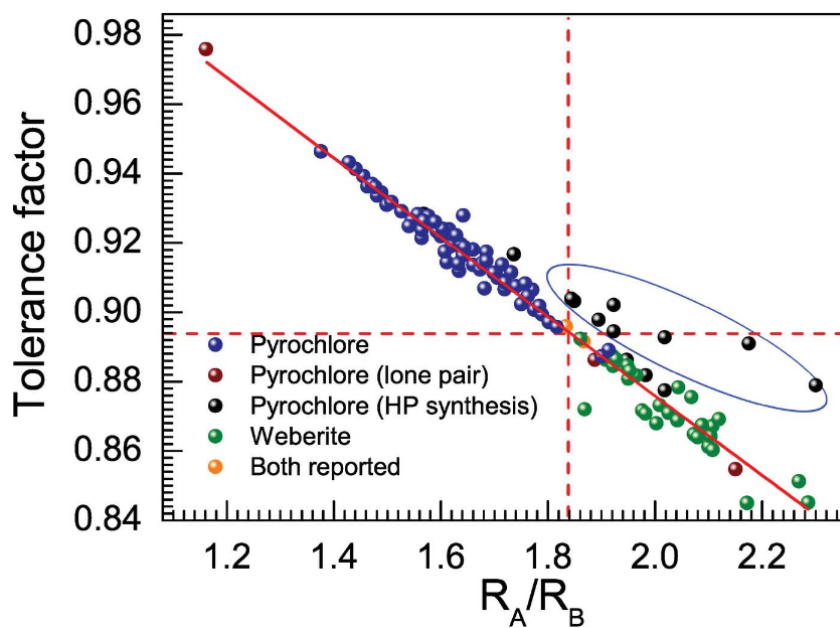


Figure 2.18 Correlation between tolerance factor t_5 and $t_1 = \frac{r_A}{r_B}$, from [75].

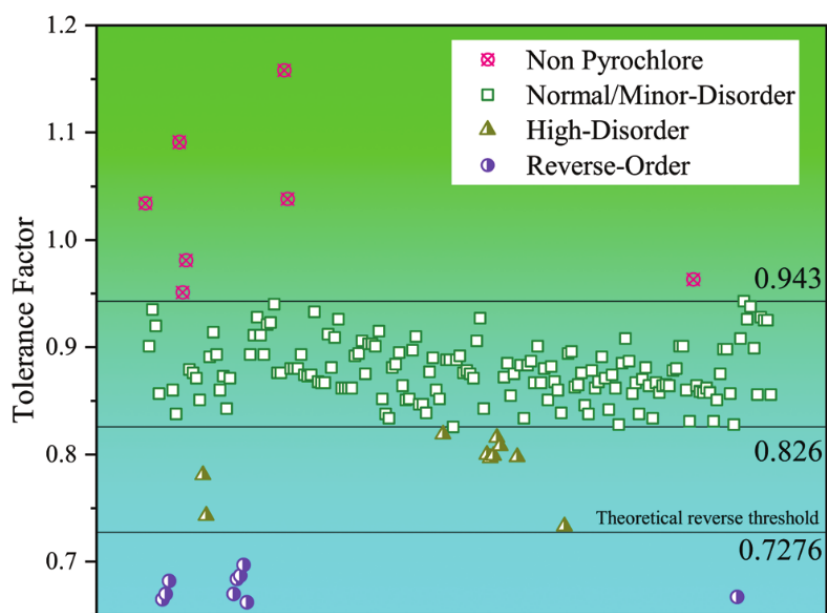


Figure 2.19 Calculated tolerance factor t_6 (2.15) for 180 pyrochlore compounds, from [66].

A critical review of the tolerance factors t_1 to t_5 is performed in [76]. In this study compounds of the type $\text{Gd}_{2-x}\text{Ln}_x\text{Zr}_2\text{O}_7$ were synthesized with various substituting lanthanides $\text{Ln} = \text{Nd}, \text{Sm}, \text{Dy}, \text{Ho}, \text{Y}, \text{Er}$, two doping levels $x = 0.2, 0.8$, and the experimentally determined structures of these compounds were used to test the accuracy of the predictions offered by the different tolerance factors. $\text{Gd}_2\text{Zr}_2\text{O}_7$ was chosen as the base compound since $t_1[\text{Gd}_2\text{Zr}_2\text{O}_7] = 1.462$, lying almost exactly at the stability boundary between fluorite and pyrochlore structures at $t_1 = 1.46$, so by doping it with other lanthanides various t_1 values on both sides of the boundary could be explored.

Before discussing their results we need to distinguish between the nominal $t_1 = r_A/r_B$ ratio and the actual cation radius ratio t'_1 when taking into account the real site occupations determined by x-ray diffraction (Chapter 5). In this context it is useful to introduce r_{16d} and r_{16c} , the average radius of the cations at the 16d and 16c Wyckoff sites, respectively, and define

$$t'_1 = \frac{r_{16d}}{r_{16c}} = \frac{s r_A + (1-s) r_B}{s r_B + (1-s) r_A} \quad (2.16)$$

where s is the degree of inversion, defined as the fraction of A^{3+} at the 16c (B) site or equivalently as the fraction of B^{4+} at the 16d (A) site (see Table 2.12). The defects caused by exchange of cations between the A and B lattices are called antisite defects, since the cation migrates from its proper site to an antisite on the opposite sublattice. In the ideal pyrochlore structure $s = 0$ and the actual and nominal cation radius ratios coincide, $t'_1 = t_1$. For the completely disordered fluorite structure $s = 0.5$ (the 16d and 16c pyrochlore positions coalesce into a single 4a fluorite position) so that $t'_1 = 1$ regardless of the nominal value t_1 .

ion	position	x	y	z	occ
A^{3+}	16d	0.5	0.5	0.5	1-s
B^{4+}	16d	0.5	0.5	0.5	s
A^{3+}	16c	0	0	0	s
B^{4+}	16c	0	0	0	1-s

Table 2.12 Unit cell occupancies for the cations in the pyrochlore structure, with inversion ratio s (see Table 2.6).

We may define actual values t'_i for the other tolerance factors analogously to the definition of t'_1 (2.16), substituting the r_A and r_B values in the definition of the t_i by r_{16d} and r_{16c} .

Figure 2.20 shows the expected and observed structures of the compounds synthesized in [76] along with the nominal t_1 (empty squares) and actual t'_1 (filled circles). The experimentally determined boundary between pyrochlore and fluorite lies at $t_1 = 1.457$, slightly lower than the expected $t_1 = 1.46$. Note that the degree of inversion s , indicated as a percentage on the right axis label, is nonzero ($\approx 7\%$ or $s \approx 0.07$) even for the pyrochlores far away from the boundary, causing a significant difference between the nominal and actual values for the tolerance factor. It is speculated that the heat treatment for 12h at 1400°C might not have been sufficient to fully equilibrate the structure and some defects induced by the mechanochemical synthesis remain in the annealed samples.

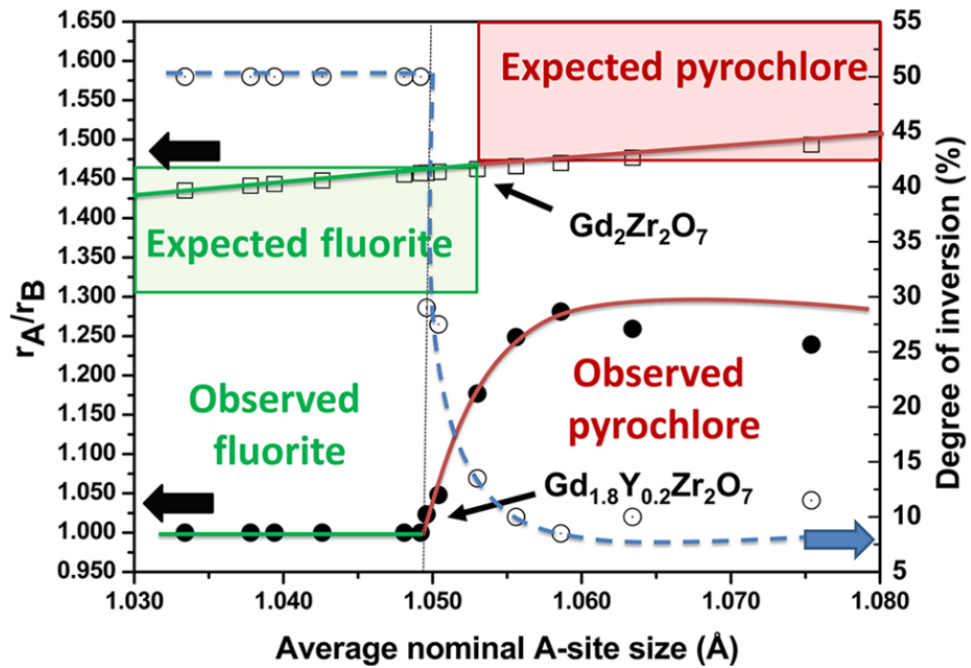


Figure 2.20 Expected and observed structures along with the nominal t_1 (empty squares) and actual t_1 (filled circles)[76].

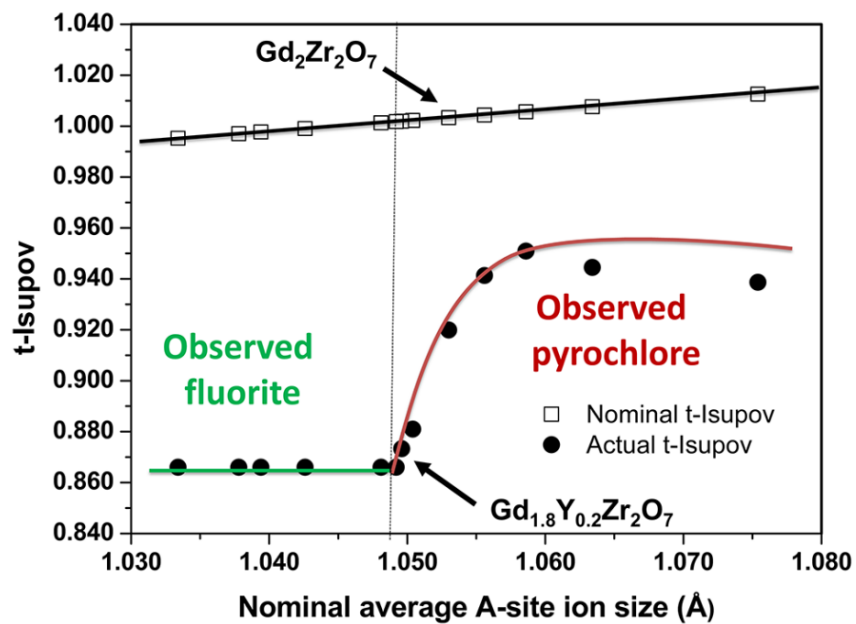


Figure 2.21 Expected and observed structures along with the nominal t_2 (t -Isupov) and actual t_2 [76].

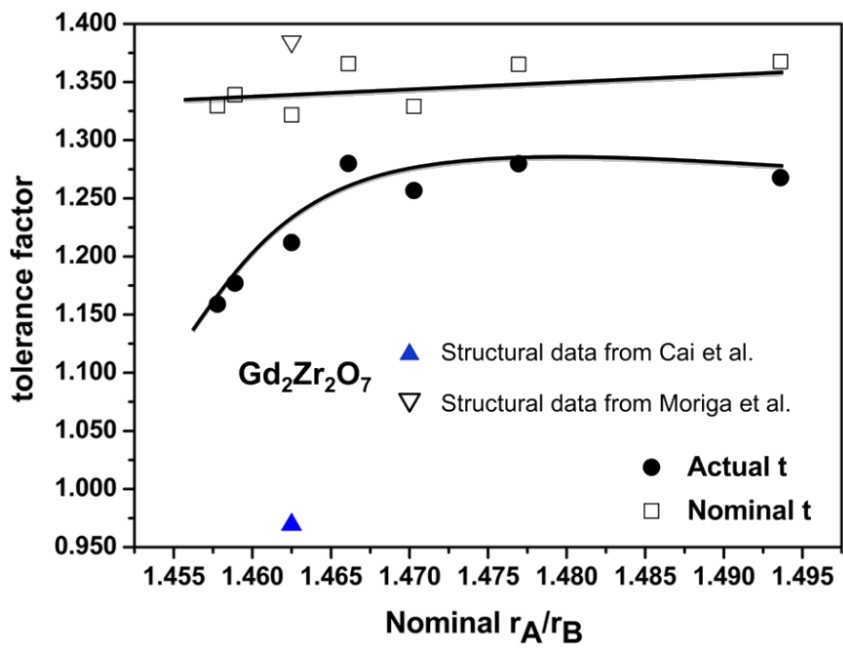


Figure 2.22 Nominal t_3 and actual t'_3 values for the synthesized compounds [76].

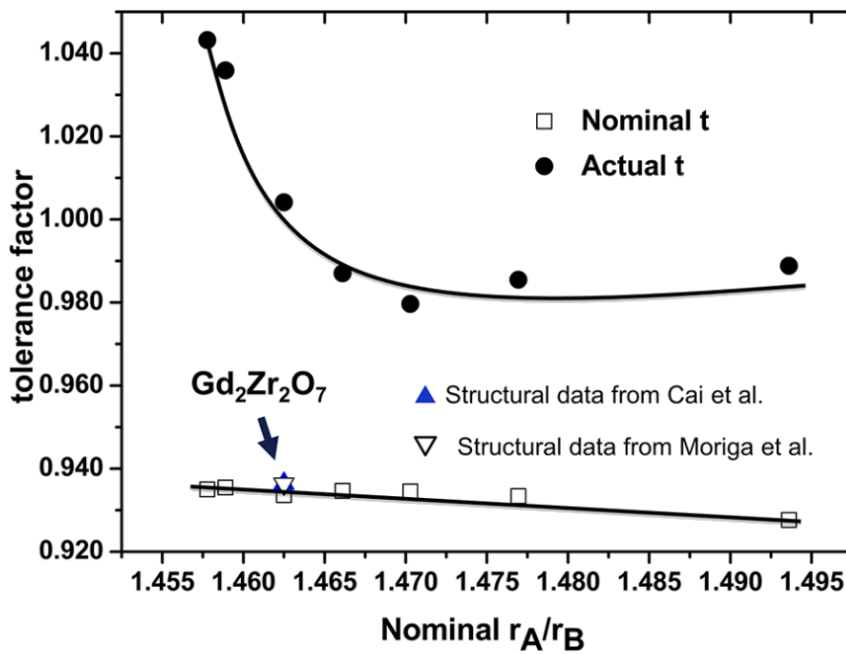


Figure 2.23 Nominal t_4 and actual t'_4 values for the synthesized compounds [76].

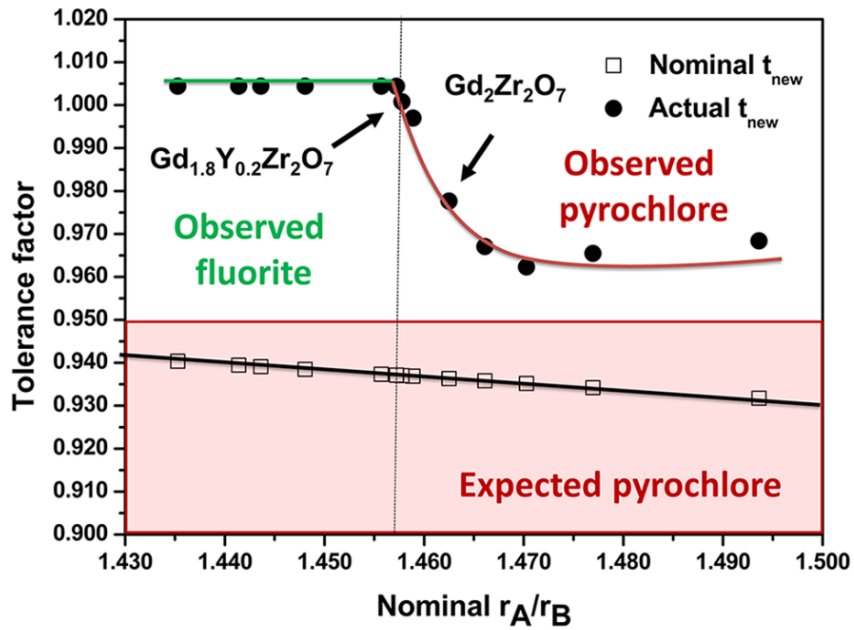


Figure 2.24 Expected and observed structures along with the nominal t_5 (t_{new}) and actual t'_5 [76].

x	$r_B(\text{\AA})$	t_1	t_5	t_6
0.0	0.605	1.628	0.922	0.867
0.15	0.613	1.605	0.924	0.863
0.3	0.622	1.583	0.927	0.859
0.5	0.634	1.554	0.930	0.855
1.0	0.663	1.487	0.937	0.842
1.5	0.691	1.425	0.944	0.831
2.0	0.720	1.368	0.950	0.819
transition		1.21	1.92	1.71

Table 2.13 Average r_B , tolerance factors t_i and predicted x value for the pyrochlore/fluorite transition in the $\text{Yb}_2\text{Zr}_x\text{Ti}_{2-x}\text{O}_7$ series.

Figure 2.21 shows the nominal and actual values of t_2 for the same compounds. The nominal values vary smoothly in a very narrow range, so it has no advantage over the simpler t_1 , while the actual values show a more pronounced transition but have no predictive value since they require knowledge of the experimentally determined degree of inversion s .

Figures 2.22 and 2.23 show the nominal and actual values for t_3 and t_4 , respectively. The same remarks as for t_2 apply here as well. The nominal values show little (t_4) or erratic (t_3) variation, while the actual values more clearly detect the structural transition but are not useful as a predictive tool.

According to t_5 the predicted structure of all compounds is a pyrochlore, which does not match

experimental observation (Figure 2.24). It should be noted that Raman spectroscopy on the same compounds did reveal signs of short-range ordering so that it cannot be ruled out that extended annealing at higher temperature than 1400°C could produce different structures.

In summary, according to [76] none of the tolerance factors t_1-t_5 (and $t_6 \propto t_2$ also) is a reliable and robust criterion to predict the structures and perhaps the most useful is the simplest one, t_1 . Table 2.13 lists the calculated values for the average r_B , tolerance factors t_i and predicted x value for the pyrochlore to fluorite transition in the $\text{Yb}_2\text{Zr}_x\text{Ti}_{2-x}\text{O}_7$ series according to each tolerance factor. Given the results in Chapter 5, the predicted value according to the t_1 criterion, $x = 1.21$, is closest to the experimental value for the transition, which is between $x = 0.5$ and $x = 1.0$.

2.3.2 Phase Maps

Phase stability diagrams (also called structure composition diagrams, phase maps, etc.) represent the stable phases for $\text{A}_2\text{B}_2\text{O}_7$ compounds with various combinations of A and B elements. A natural way of ordering the different elements is by their ionic radius, thus most of these diagrams have the ionic radius r_A of the A element on one axis and the ionic radius r_B of the B element on the other axis. Not all combinations of A and B elements are possible to synthesize since some are not thermodynamically stable. Some combinations are stable but require high pressures during the synthesis.

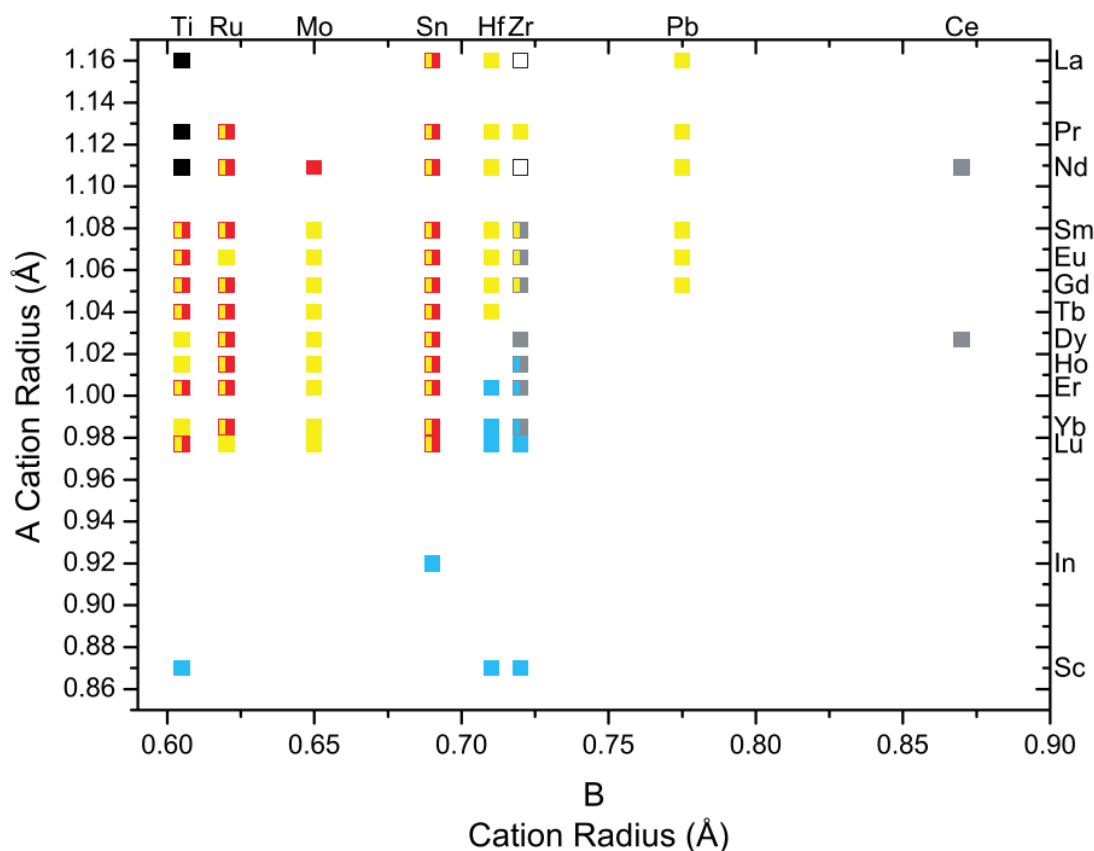


Figure 2.25 Phase map constructed from literature studies [58]. Each phase is associated to a color: monoclinic (black), pyrochlore (red, yellow), fluorite (grey), δ -phase (cyan). Color combinations indicate a compound that has been found in more than one phase and an empty box indicates that it has been found as both pyrochlore and fluorite.

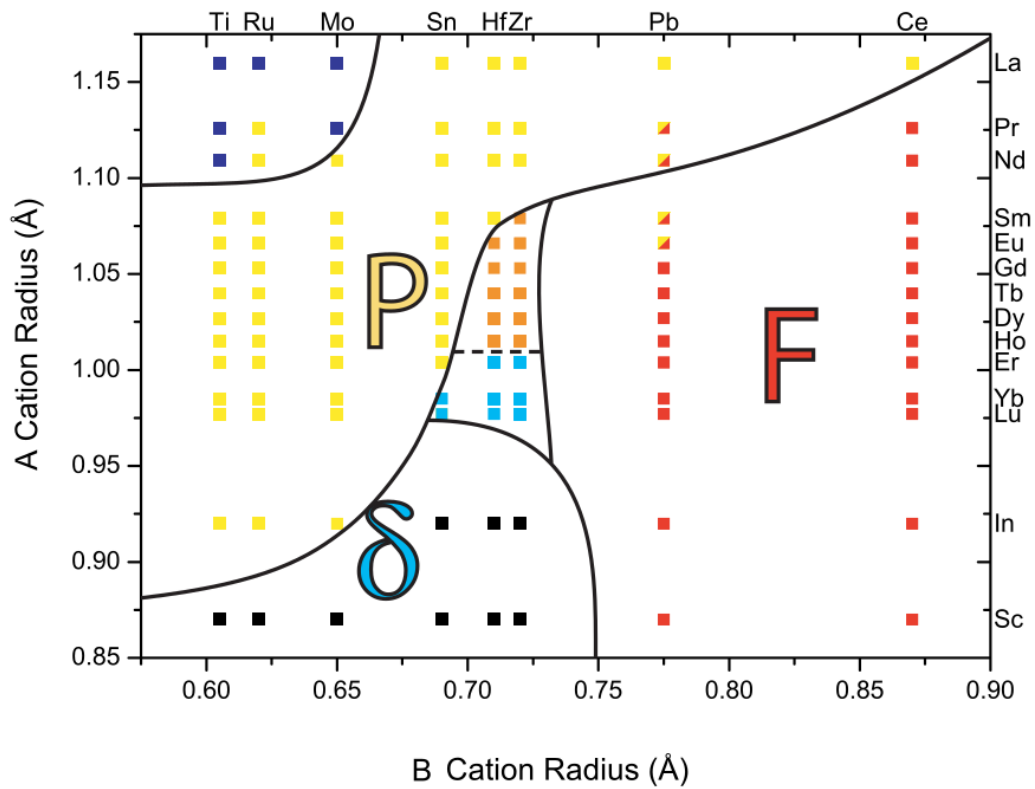


Figure 2.26 Phase map constructed from simulations [58]. Each phase is associated to a color: non-cubic (dark blue), pyrochlore (yellow, orange), δ -phase (black, cyan), fluorite (red). Yellow/red squares represent pyrochlore phases formed under high pressure [77].

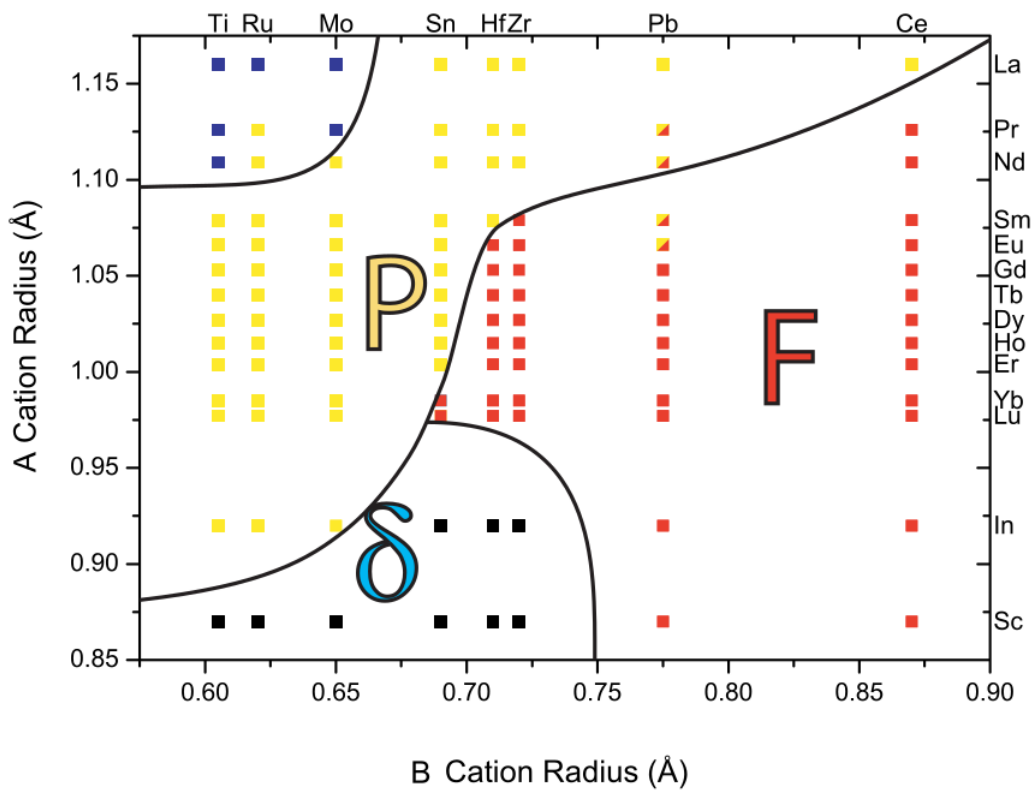


Figure 2.27 High-temperature (2000K) phase map constructed from simulations [58]. Each phase is associated to a color: non-cubic (blue), pyrochlore (yellow), δ -phase (black), fluorite (red). Yellow/red squares represent pyrochlore phases formed under high pressure [77].

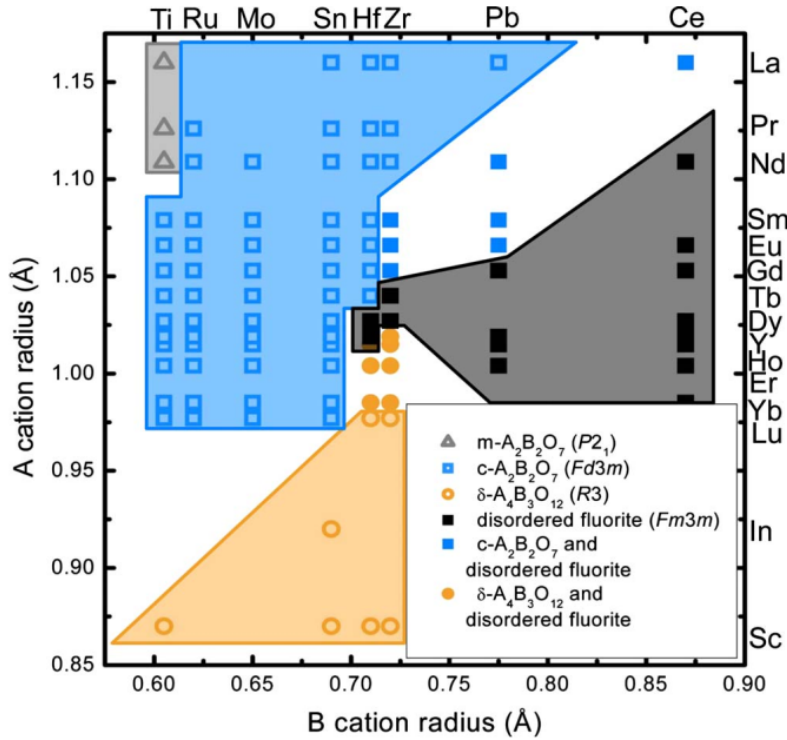


Figure 2.28 Phase map from structures reported in the literature [59]. Each phase is associated to a color: monoclinic (grey), pyrochlore (blue), δ -phase (orange), fluorite (black). Hollow symbols represent a single phase, while solid symbols indicate that both the ordered structure and disordered fluorite have been observed.

Several of these stability diagrams can be found in [58], where the structural stability of these compounds is studied, since it correlates with their radiation durability and performance as nuclear wastefrom disposal materials [78]. Figure 2.25 shows a phase map constructed from experimentally determined structures. Two colors were assigned to the pyrochlore structure to distinguish the sources of the information, the red data points being based on experimental studies (see [58] for references to all publications), while yellow data points are based on the review [31].

Structure simulations using a method based on pair charge potentials [58] were used to construct the diagram in Figure 2.26. The regions labeled with P, F and δ contain compounds that assume the pyrochlore, fluorite and δ -phase structures, respectively. The upper-left region contain a non-cubic phase, likely the $P2_1$ monoclinic structure (Section 2.2.5).

The two central regions are more uncertain, with tentatively drawn boundaries. These regions contain compounds that assume different structures depending on the conditions imposed during synthesis. The pyrochlore structure should be stable in the FP (orange) region, while the δ -phase should be stable in the $F\delta$ (cyan) region, but both phases form through an order-disorder transformation upon cooling below a critical temperature on the order of 1900K. The critical temperature increases with increasing ionic radius r_A of the A element in the FP region while it decreases with increasing r_A in the $F\delta$ region. A low critical temperature is usually a sign of less stability, so the precise location for the right boundary of the $F\delta$ region and the left boundary of the FP region might be harder to predict accurately.

In complex oxides all sublattices disorder in an order-disorder transformation. For fluorite

derivatives such as the pyrochlores only two types of reaction are significant, cation antisite defects and anion Frenkel defects [78]. The pyrochlore oxides are somewhat unusual since both of these effects seem to be equally important in determining the order-disorder transformation temperature, unlike most other complex oxides where one of the disordering effects is dominant [79, 80, 81].

Figure 2.27 is similar to Figure 2.26, but while Figure 2.26 indicates the quenched structures at room temperature, Figure 2.27 shows the high-temperature structures assumed by these compounds at approximately 2000K, above the order-disorder transformation temperature. The central region in Figure 2.26, containing the FP and F δ compounds, is now subsumed by the fluorite structure. Extensive radiation damage can cause disordering of the structure similar to the effect of high temperature [58].

Figure 2.28 shows a similar stability diagram, with slightly different boundaries for the regions associated to each phase.

2.3.3 Phase Diagrams

Another kind of phase diagram commonly used to predict the structures of compounds is the binary A_2O_3 – BO_2 composition-temperature phase diagram. In this type of diagram the structure is plotted as a function of temperature and stoichiometry, which varies between 0% A_2O_3 and 100% BO_2 to 100% A_2O_3 and 0% BO_2 . The molar percentage of A_2O_3 is similar in spirit to the anion/cation ratio of Table 2.9, and both quantities are actually directly proportional to one another. Table 2.14 lists the molar percentage of A_2O_3 for some stoichiometries in the A_2O_3 – BO_2 binary system.

stoichiometry	mol % A_2O_3
$A_2B_2O_7$	33
$A_4B_3O_{12}$	40
A_6BO_{11}	75

Table 2.14 Molar percentage of A_2O_3 for some stoichiometries in the A_2O_3 – BO_2 binary system.

Figures 2.29 to 2.31 show three Yb_2O_3 – ZrO_2 binary phase composition diagrams, though Figure 2.31 only contains the high-temperature region $T \geq 1000^\circ\text{C}$, and Figure 2.32 shows an Yb_2O_3 – HfO_2 phase diagram. Since the ionic radii of Hf and Zr are very similar, $r_{\text{Hf}} = 0.71\text{\AA} \approx r_{\text{Zr}} = 0.72\text{\AA}$ [68] the Yb_2O_3 – HfO_2 phase diagram should also be approximately valid for the Yb_2O_3 – ZrO_2 binary system.

Comparing these phase diagrams we see slight differences due to variations in experimental methods and simulation methodologies. At room temperature $Yb_2Zr_2O_7$ (33 mol% of Yb_2O_3) is predicted to assume a solid solution of the δ -phase with monoclinic ZrO_2 , but slightly above room temperature a solid solution of the δ -phase with a fluorite phase is predicted to be stable. Other studies that have explored the chemistry and physics of the Yb_2O_3 – ZrO_2 binary system are [33, 34, 35].

Figures 2.33 and 2.34 show phase diagrams for the Yb_2O_3 – TiO_2 system, although only the high-temperature regions, for $T \geq 900^\circ\text{C}$ and $T \geq 1200^\circ\text{C}$, respectively.

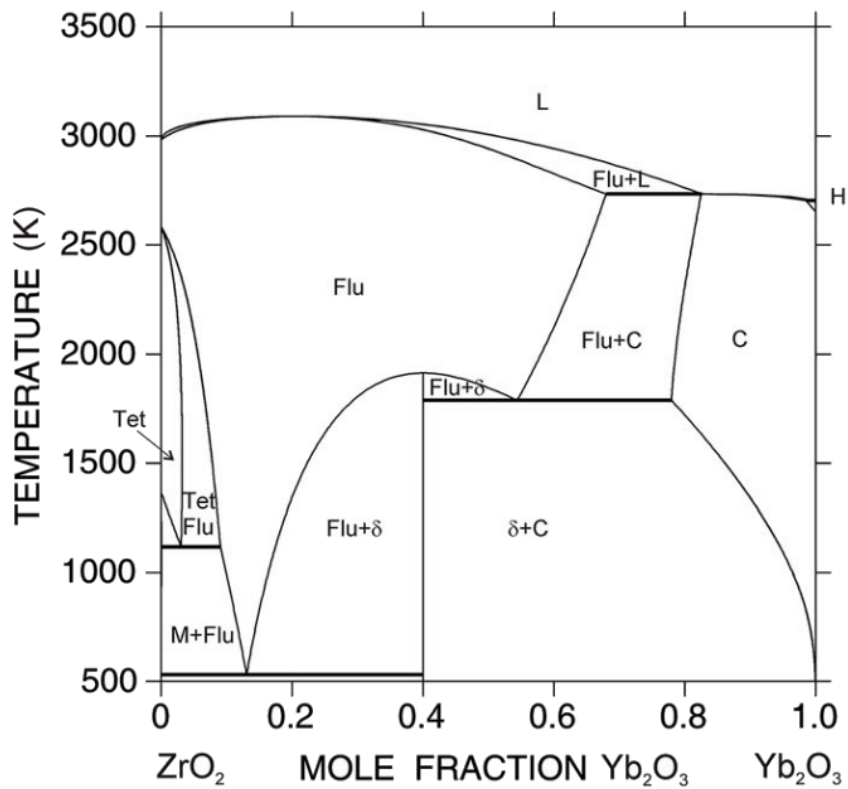


Figure 2.29 Phase diagram for the $\text{Yb}_2\text{O}_3\text{--ZrO}_2$ binary system, from [82]. Each region represents a structure or solid solution within a certain symmetry class: M = monoclinic, Flu = fluorite, Tet = tetragonal, C = cubic, δ = rhombohedral δ -phase, H = hexagonal, L = liquid.

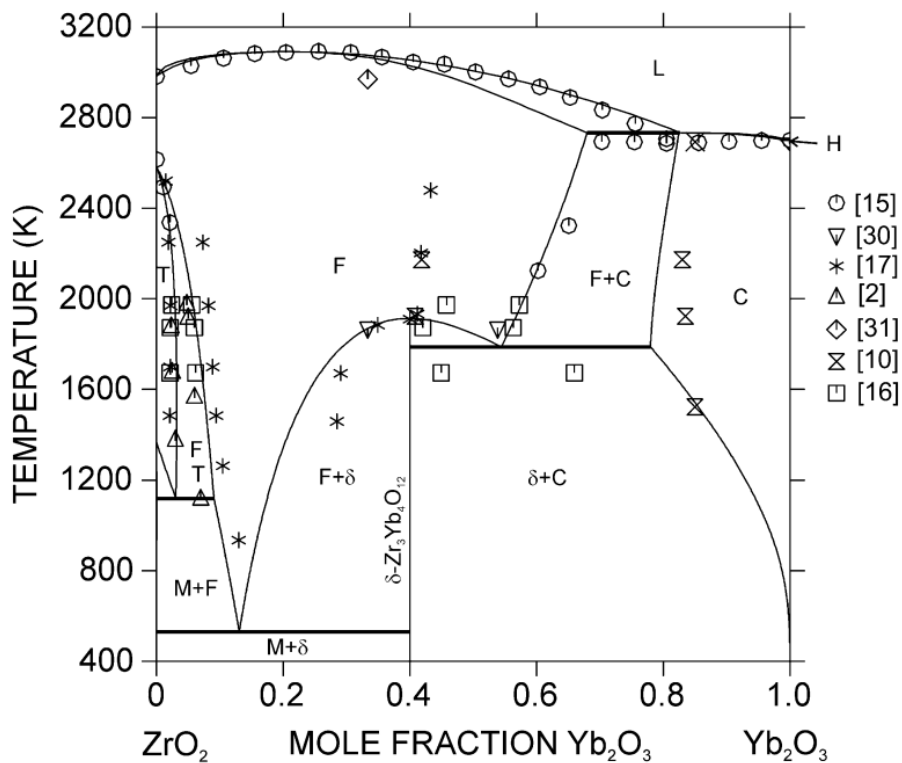


Figure 2.30 Phase diagram for the $\text{Yb}_2\text{O}_3\text{--ZrO}_2$ binary system, from [83]. Each region represents a structure or solid solution within a certain symmetry class: M = monoclinic, T = tetragonal, F = fluorite, C = cubic, δ = rhombohedral δ -phase, H = hexagonal, L = liquid.

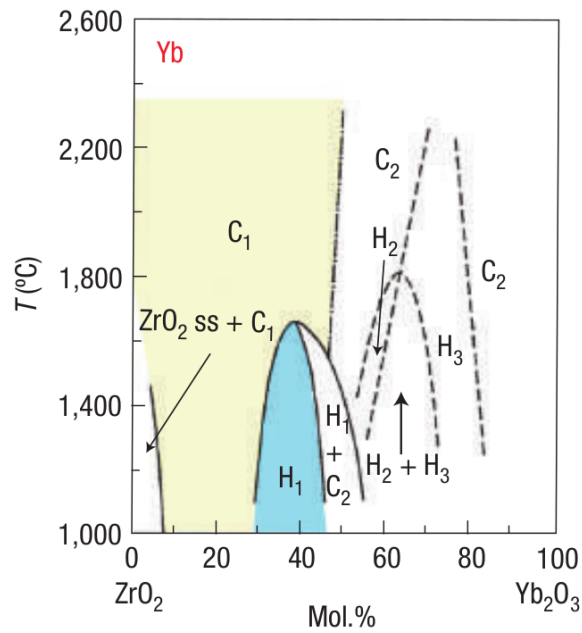


Figure 2.31 Phase diagram for the $\text{Yb}_2\text{O}_3\text{-ZrO}_2$ binary system, from [78], original source is [84]. Each region represents a structure or solid solution (ss) within a certain symmetry class: C = cubic, H = hexagonal, H_1 = δ -phase (blue), C_1 = fluorite solid solution (light shade).

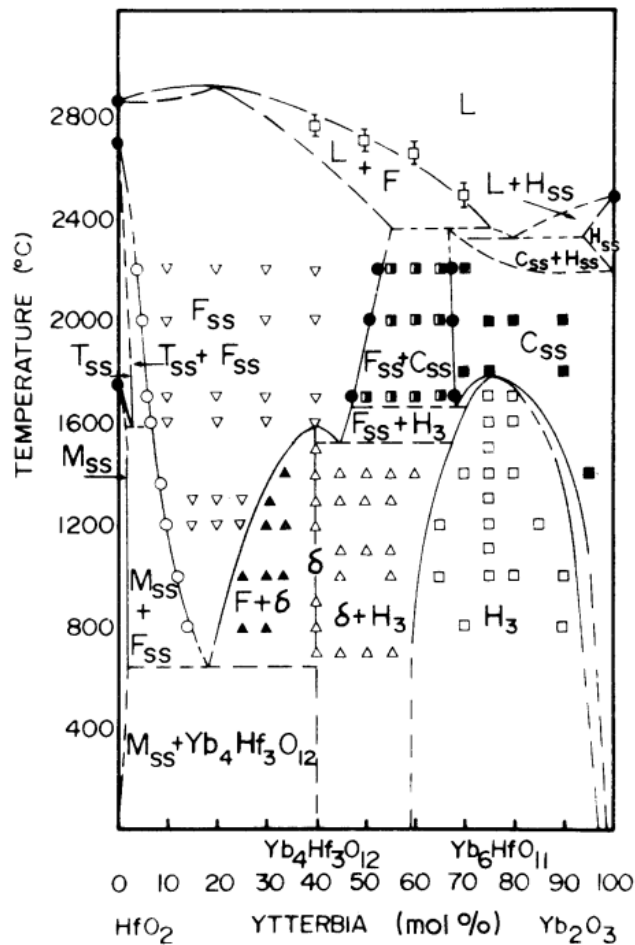


Figure 2.32 Phase diagram for the $\text{Yb}_2\text{O}_3\text{-HfO}_2$ system, from [85]. Each region represents a structure or solid solution (SS) within a certain symmetry class: M = monoclinic, T = tetragonal, F = fluorite, C = cubic, H = hexagonal, δ = δ -phase, H_3 = $\text{Yb}_6\text{HfO}_{11}$ phase.

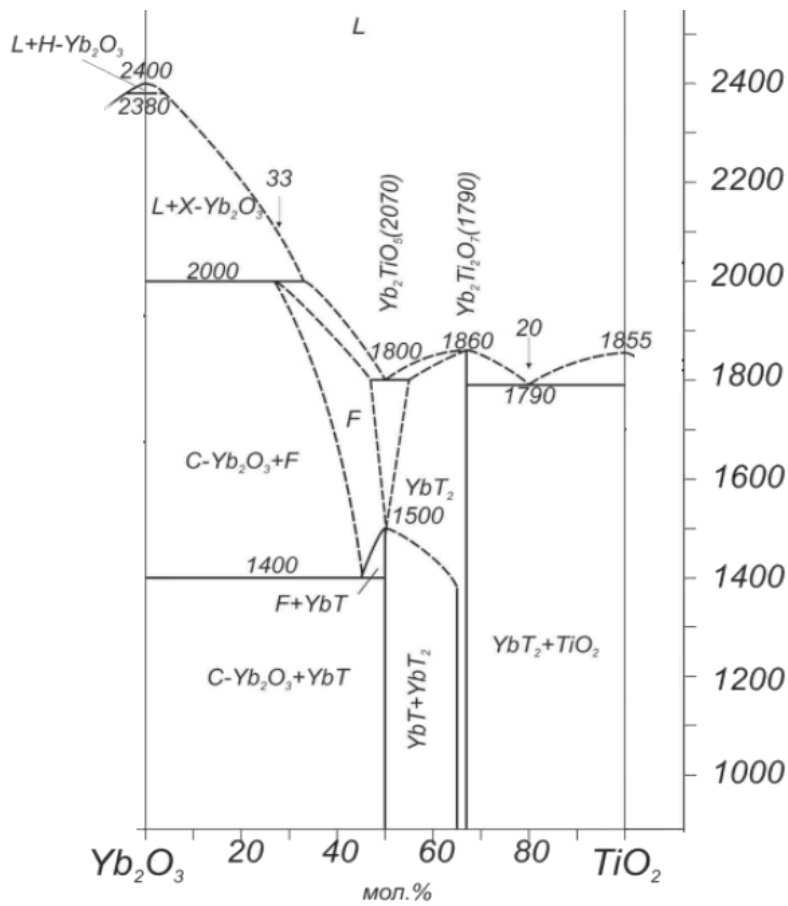


Figure 2.33 Phase diagram for the Yb_2O_3 - TiO_2 system, from [86]. Vertical axis units are $^{\circ}\text{C}$. Each region represents a structure or solid solution within a certain symmetry class: F = fluorite, C = cubic, H = hexagonal, L = liquid, H = hexagonal.

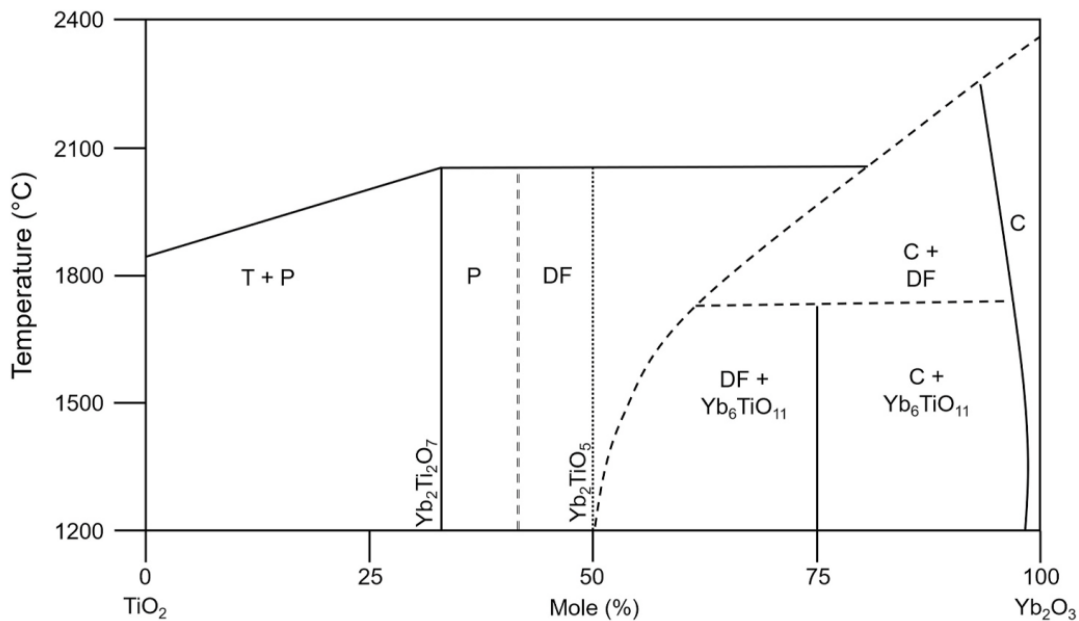


Figure 2.34 Phase diagram for the Yb_2O_3 - TiO_2 system, from [87], adapted from [88]. Each region represents a structure or solid solution within a certain symmetry class: DF = defect fluorite, P = pyrochlore, C = cubic Yb_2O_3 , T = TiO_2 .

There are also ternary composition diagrams for systems of the form $A_2O_3-A'_2O_3-BO_2$ or $A_2O_3-BO_2-B'O_2$. Since the two plane axes are known used to express the composition, these are isothermal sections of the phase diagram, representing the structures at a specific temperature. Figure 2.35 shows an example of a ternary phase diagram for the $Yb_2O_3-La_2O_3-ZrO_2$ system at 1523K [82]. We found no ternary phase diagram for the $Yb_2O_3-ZrO_2-TiO_2$ system in the literature.

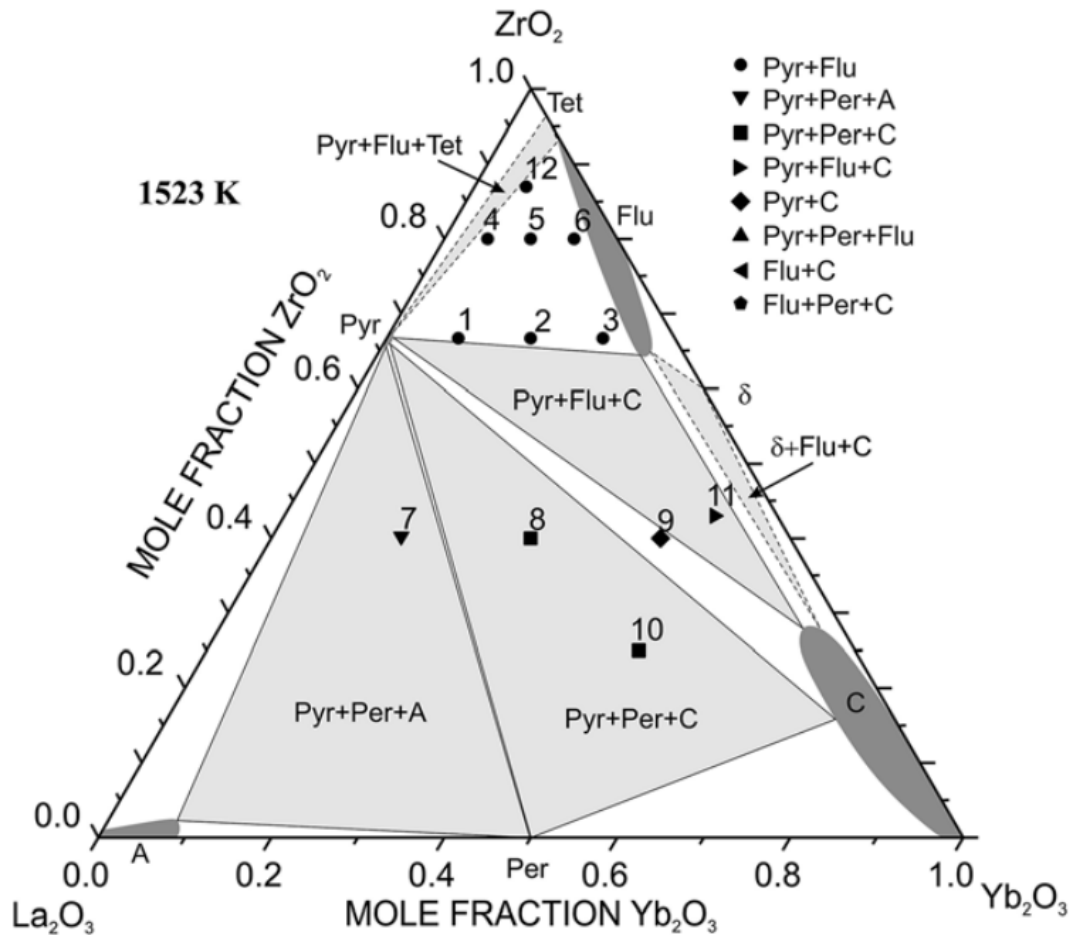


Figure 2.35 Ternary phase diagram for the $Yb_2O_3-La_2O_3-ZrO_2$ system [82] at 1523K.

Frustrated Magnetism

This chapter introduces the basic concepts of magnetism required to interpret the experimental data in Chapter 7, frustrated magnetism and how these concepts apply to the lanthanides and pyrochlore compounds. At the end we review some of the literature on $\text{Yb}_2\text{Ti}_2\text{O}_7$ in a framework that also is applicable to other pyrochlore magnets.

3.1 Magnetization of a Paramagnet

Consider an ideal paramagnet, containing atoms with localized and non-interacting magnetic moments. The magnetic moment μ of an atom is related to its total angular momentum J , in units of \hbar , by

$$\mu = gJ\mu_B \quad (3.1)$$

where $\mu_B = \frac{e\hbar}{2m_e} = 9.2740100783(28)10^{-24} \text{ J T}^{-1}$ is the Bohr magneton [89] and

$$g = \frac{3}{2} + \frac{S(S+1) - L(L+1)}{2J(J+1)} \quad (3.2)$$

is the Landé g-factor for an atom with orbital angular momentum L and spin S [90, 91]. For example, the ground state of an Yb^{3+} ion has $J = \frac{7}{2}$, $S = \frac{1}{2}$ and $L = 3$, according to Hund's rules applied to the $4f^{13}$ electron shell configuration, thus $g = \frac{8}{7}$.

The energy of a magnetic moment μ in a magnetic field B is $E = -\mu \cdot B$ [92], so the partition

function for a single magnetic moment is

$$Z = \sum \exp\left(\frac{\mu \cdot B}{k_B T}\right) = \sum_{m_j=-J}^J \exp\left(m_j \frac{g\mu_B B}{k_B T}\right) = \sum_{m_j=-J}^J \exp(m_j x) \quad (3.3)$$

where

$$x = \frac{g\mu_B B}{k_B T} \quad (3.4)$$

Summing up the geometric series eq. (3.3) we get

$$Z = \frac{\sinh\left[(2J+1)\frac{x}{2}\right]}{\sinh\left[\frac{x}{2}\right]} \quad (3.5)$$

The expected value of m_j is

$$\langle m_j \rangle = \frac{\sum_{m_j=-J}^{m_j=+J} m_j \exp(m_j x)}{\sum_{m_j=-J}^{m_j=+J} \exp(m_j x)} = \frac{1}{Z} \frac{\partial Z}{\partial x} \quad (3.6)$$

so that the magnetization is

$$M = Ng\mu_B \langle m_j \rangle = \frac{ng\mu_B}{Z} \frac{\partial Z}{\partial B} \frac{\partial B}{\partial x} = nk_B T \frac{\partial \ln Z}{\partial B} \quad (3.7)$$

where N is the number of magnetic moments per unit volume. Differentiating (3.5) leads to

$$M = M_{\text{sat}} B_J(y) \quad (3.8)$$

where

$$M_{\text{sat}} = NgJ\mu_B \quad (3.9)$$

is the saturation magnetization,

$$y = Jx = \frac{gJ\mu_B B}{k_B T} \quad (3.10)$$

and

$$B_J(y) = \frac{2J+1}{2J} \coth\left(\frac{2J+1}{2J}y\right) - \frac{1}{2J} \coth\left(\frac{1}{2J}y\right) \quad (3.11)$$

is the Brillouin function for angular momentum J [90, 91].

In most of this work we use molar quantities instead of volumetric quantities, since we do not know the density of the powder samples. The saturation moment m_{sat} is defined analogously to (3.9),

$$m_{\text{sat}} = n g J \mu_B \quad (3.12)$$

where now n is the absolute number of magnetic moments. Setting $n = N_A = 6.02214076 \cdot 10^{23}$, the Avogadro constant [89], we get the molar saturation moment. The saturation moment for a single Yb^{3+} ion, $n = 1$, is

$$m_{\text{sat}} = g J \mu_B = \frac{8}{7} \frac{7}{2} \mu_B = 4 \mu_B \quad (3.13)$$

3.2 Magnetic Susceptibility

When investigating magnetic materials the magnetic susceptibility is an indispensable characterization technique that is very widely used. The defining relation for magnetic susceptibility χ is

$$M = \chi H \quad (3.14)$$

where M is the magnetization (magnetic moment per unit volume) and H is the applied magnetic field. Definition (3.14) assumes that M and H are linearly related, which is usually valid at high temperature and low magnetic field [92]. We also define χ_m , the molar susceptibility, which is the magnetic moment per mole of magnetic ions, related to χ by the volume v_{mol} of one mole of magnetic ions,

$$\chi_m = v_{\text{mol}} \chi \quad (3.15)$$

When H is a constant DC field the susceptibility is proportional to the magnetization, although typically magnetization is measured at a fixed temperature and varying field, while susceptibility is measured using a constant field and varying the temperature [93]. AC susceptibility measurements, where H varies sinusoidally, offers additional information on magnetic dynamics [94, 95]. In the limit where the sample has no low-energy excitations the AC susceptibility is in principle frequency-independent and equivalent to the DC susceptibility.

3.3 Contributions to the Susceptibility

Materials can have both positive and negative contributions to their magnetic susceptibility. For insulating materials the main contributions are the orbital diamagnetism, van Vleck paramagnetism and Curie-Weiss paramagnetism. For conductive materials we also have to consider Pauli paramagnetism, Landau diamagnetism and itinerant moment paramagnetism [90, 91].

Orbital diamagnetism is a temperature-independent negative contribution to χ that is present in all materials. It arises due to the reaction of the electrons' orbital motion to an external field, similar in spirit to Lenz's law [92]. It is a rather small contribution to χ , usually on the order of $10^{-5} - 10^{-6}$ emu mol⁻¹, that is easily overshadowed by other contributions, when present. The diamagnetic contribution is temperature independent and can be accurately estimated by summing the contributions of all constituent atoms or ions in a material [96]. Table 3.1 lists the diamagnetic contributions to the susceptibility due to single ions in the compounds Yb₂Zr_xTi_{2-x}O₇ and (NH₄)Fe(SO₄)₂(H₂O)₁₂ (used for calibration, see Section 7.1.3).

ion	χ_d (10 ⁻⁶ emu mol ⁻¹)
Yb ³⁺	-18
Ti ⁴⁺	-5
Zr ⁴⁺	-10
O ²⁻	-12
Fe ³⁺	-40.1
NH ₄ ⁺	-13.3
SO ₄ ²⁻	-40.1
H ₂ O	-13

Table 3.1 Diamagnetic contributions to the susceptibility due to single ions in the compounds Yb₂Zr_xTi_{2-x}O₇ and (NH₄)Fe(SO₄)₂(H₂O)₁₂ [96].

Adding the contributions for single ions yields an approximate value for the diamagnetic susceptibility, for example

$$\chi_d [\text{Yb}_2\text{Ti}_2\text{O}_7] \approx 2\chi_d [\text{Yb}^{3+}] + 2\chi_d [\text{Ti}^{4+}] + 7\chi_d [\text{O}^{2-}] = -1.3 \cdot 10^{-4} \text{ emu mol}^{-1} \quad (3.16)$$

Similar calculations give

$$\chi_d [\text{Yb}_2\text{Zr}_2\text{O}_7] \approx -1.4 \cdot 10^{-4} \text{ emu mol}^{-1} \quad (3.17)$$

$$\chi_d [\text{NH}_4\text{Fe}(\text{SO}_4)_2(\text{H}_2\text{O})_{12}] \approx -2.4 \cdot 10^{-4} \text{ emu mol}^{-1} \quad (3.18)$$

In Section 7.1.3 we show that for $(\text{NH}_4)\text{Fe}(\text{SO}_4)_2(\text{H}_2\text{O})_{12}$ the paramagnetic contribution to χ is 5 orders of magnitude larger than χ_d , and similar remarks hold for $\text{Yb}_2\text{Zr}_x\text{Ti}_{2-x}\text{O}_7$. Therefore we can neglect orbital diamagnetism for the compounds studied in this work and will not further concern ourselves with this effect.

Another contribution to the susceptibility is van Vleck paramagnetism, which arises due to low-lying excited states of an atom or ion. Such states can contribute to the susceptibility by being thermally populated, as usual, but there is also a temperature-independent contribution. This second-order effect vanishes for elements with closed shells and is most significant when the total angular momentum $J = 0$ but $L, S \neq 0$, which occurs when an electronic shell is one electron short of being half filled. In that case there is no paramagnetic contribution according to first-order perturbation theory (since $J = 0$), but the second-order perturbative correction to the Zeeman interaction is nonzero.

For the lanthanides this means that europium (Eu) compounds are the most affected, since Eu has 6 out of a total of 14 electrons in its 4f shell. The first excited multiplet of Eu^{3+} , with $J = 1$, has an energy gap of only 330K to the ground state multiplet [91]. The next lanthanide ion most significantly affected by the van Vleck contribution is Sm^{3+} , which has an energy gap of 1225K between the $J = \frac{5}{2}$ ground state and the first excited state with $J = \frac{7}{2}$. In contrast, Yb^{3+} has a large energy gap of 14490K to its first excited state. Since the size of the contribution is inversely proportional to the energy gap, we can safely ignore van Vleck paramagnetism for the series of compounds $\text{Yb}_2\text{Zr}_x\text{Ti}_{2-x}\text{O}_7$.

Curie-Weiss paramagnetism is the dominant contribution to magnetic susceptibility for our samples and is described in the following section.

3.4 Curie-Weiss Paramagnetism

The starting point for the Curie-Weiss mean-field theory of localized moment magnets is Weiss' accounting for the molecular mean field in the expression for the internal magnetic field,

$$H_i = H + \alpha M \quad (3.19)$$

so the internal field H_i felt by the magnetic moments is the sum of an externally applied field H and a field generated by the magnetization of the moments themselves. Using this phenomenological approach we can calculate the susceptibility for a localized moment magnet.

Since the definition of the susceptibility (3.14) assumes a low field, where χ is linear, and for small y we can expand the Brillouin function (3.11) as

$$B_J(y) = \frac{J+1}{3J}y + O(y^2) \quad (3.20)$$

we can approximate the relative magnitude of the magnetization, given by the Brillouin func-

tion, as

$$\frac{M}{M_s} = B_J(y) \approx \frac{J+1}{3J} y \quad (3.21)$$

where now the variable y (3.10) incorporates the molecular mean field $B_i = \mu_0 H_i$:

$$y = \frac{gJ\mu_B}{k_B T} \mu_0 (H + \alpha M) \quad (3.22)$$

Recalling that $M_s = NgJ\mu_B$ (3.9) we get

$$M \approx \frac{N\mu_0 g^2 J(J+1)\mu_B^2}{3k_B T} (H + \alpha M) = \frac{C}{T} (H + \alpha M) \quad (3.23)$$

where

$$C = \frac{N\mu_0 g^2 J(J+1)\mu_B^2}{3k_B} \quad (3.24)$$

is the Curie constant. Setting $N = N_A = 6.02214 \cdot 10^{23}$ in (3.24) we obtain C_m , the molar Curie constant. Rearranging (3.23),

$$M = \frac{C}{T - \alpha C} H = \frac{C}{T - \theta_{CW}} H \quad (3.25)$$

where $\theta_{CW} = \alpha C$ is the so-called Curie-Weiss temperature. This gives us an approximation for the susceptibility χ , the Curie-Weiss law

$$\chi = \frac{C}{T - \theta_{CW}} \quad (3.26)$$

This approximation is expected to fail when T is close to the critical temperature T_C associated to a phase transition, where χ obeys a power law

$$\chi \propto (T - T_C)^{-\gamma} \quad (3.27)$$

for some critical exponent γ that depends on the universality class of the transition [41]. We can fit the linear region of the inverse susceptibility χ^{-1} (not too close to T_C) to a line. In the Curie-Weiss approximation

$$\chi^{-1} = C^{-1}(T - \theta_{CW}) \quad (3.28)$$

so the slope of the line provides C and the x-intercept is θ_{CW} . The Curie constant can be used to calculate the effective value of magnetic moments in the sample, while θ_{CW} tells us how these moments are correlated, on average. The effective moment μ_{eff} is defined as

$$\mu_{\text{eff}} = g \sqrt{J(J+1)} \mu_B \quad (3.29)$$

so that (3.24) can be written as

$$C = \frac{N \mu_0 \mu_{\text{eff}}^2}{3k_B} \quad (3.30)$$

From the measured values of the molar Curie constant C_m ($N = N_A$) we can calculate the effective moment

$$\mu_{\text{eff}} = \sqrt{\frac{3k_B}{N_A \mu_0} C_m} \quad (3.31)$$

and compare this with the theoretically predicted value. Letting C_m denote the unit-less value of the molar Curie constant we can express the effective moment μ_{eff} in SI or CGS (emu) units,

$$\begin{aligned} \mu_{\text{eff}} &= 797.727 \sqrt{C_m} \mu_B \quad (\text{SI}) \\ &= 2.82787 \sqrt{C_m} \mu_B \quad (\text{CGS emu}) \end{aligned} \quad (3.32)$$

For Yb^{3+} the ground state has $J = \frac{7}{2}$, $S = \frac{1}{2}$ and $L = 3$, so the g-factor (3.2) is $g = \frac{8}{7}$. Thus the theoretically predicted value of μ_{eff} for Yb^{3+} is

$$\mu_{\text{eff}} = 4.5356 \mu_B \quad (3.33)$$

It should be noted that the derivation of the Curie-Weiss law assumes a degenerate angular momentum ground state manifold. If the crystal field splitting is comparable to or greater than the temperature, some of the states in this manifold will be preferentially populated, which can lead to a skewed moment and a reduction of the effective moment from the value predicted by (3.32).

3.5 Magnetic Interactions

In an insulating solid the magnetic properties usually derive from localized magnetic moments, as opposed to the delocalized itinerant band magnetism in conductive materials. Our model of a magnetic insulator thus consists of a crystalline lattice with magnetic moments embedded

in it, and the interactions between these localized moments generate the magnetic phenomena we are concerned with. In the case of pyrochlores the magnetic moments are usually associated to lanthanide ions, which have a non-zero moment due to unpaired electrons in their outermost electronic shells (Section 3.7).

We will now describe the most relevant types of interaction between magnetic moments. In this discussion we use the terms magnetic moment and angular momentum (or spin) interchangeably, since they are proportional to one another according to (3.1).

The exchange interaction is quantum-mechanical in origin and depends on the overlap of the wavefunctions describing neighboring electron orbitals. The antisymmetrization requirements for multielectron wavefunctions give rise to an effective coupling when two electron orbitals spatially overlap. This effective coupling is called an exchange interaction and is represented by the hamiltonian H ,

$$H = -J \mathbf{S}_i \cdot \mathbf{S}_j \quad (3.34)$$

where \mathbf{S}_i and \mathbf{S}_j are the spin operators for each electron and J is a constant. The exchange constant J can be expressed in terms of integrals involving the wavefunctions of the two electrons [90, 91]. When $J > 0$ parallel spins are energetically favored, while for $J < 0$ antiparallel spins have the lowest energy. These two conditions are commonly described as ferromagnetic (FM) and antiferromagnetic (AFM) interactions, respectively (see Figure 3.1).

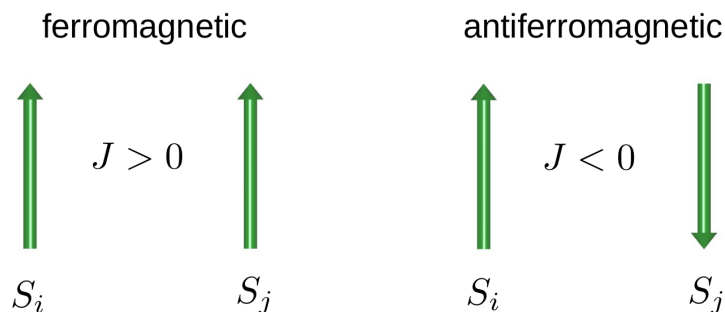


Figure 3.1 Ferromagnetic (FM) and antiferromagnetic (AFM) interactions between two spins, represented as arrows.

The interaction that arises when two electronic orbitals directly overlap is called direct exchange and is very short ranged, being limited to neighboring atoms or ions. Another form of exchange interaction, indirect exchange or superexchange, occurs when two electronic orbitals do not overlap directly to any significant extent. The most common situation is that the exchange interaction between two cations is mediated by an intermediary anion and can be understood by considering virtual states of the intermediary ion. The coupling of the two cations is usually antiferromagnetic and the effective interaction is described by the same hamiltonian (3.34) as for direct exchange but with a different interaction energy J , that can be calculated using second-order perturbation theory [90, 91].

To model a lattice of magnetic atoms we need to consider the interactions between pairs of atoms. Usually only the few closest neighbors of a given atom need to be considered, since the interaction strength quickly decays with distance. Thus we may consider interactions

between nearest neighbors (NN), next nearest neighbors (NNN) and so on. Each of these has an interaction strength J_i , as illustrated in Figure 3.2.

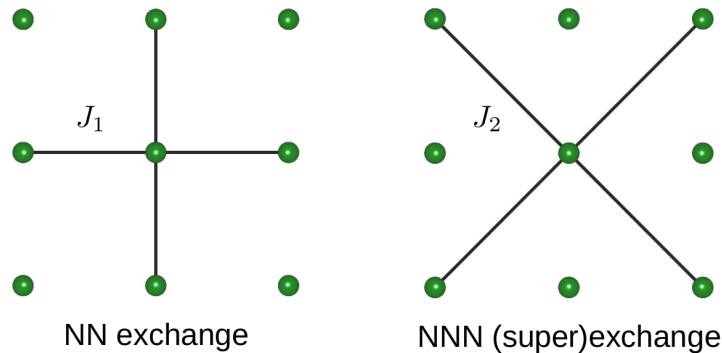


Figure 3.2 Nearest neighbor (NN) and next nearest neighbor (NNN) interactions between spins on a lattice, with interaction strengths J_1 and J_2 , respectively.

For spins on a lattice the hamiltonian can be expressed as

$$H = \frac{1}{2} \sum_{ij} J_{ij} \mathbf{S}_i \cdot \mathbf{S}_j \quad (3.35)$$

where the sum runs over all possible atoms, indexed by i, j and J_{ij} is the interaction strength between the spin \mathbf{S}_i and the spin \mathbf{S}_j . The prefactor $\frac{1}{2}$ is included to account for the double counting of the bond between each pair of atoms (once as ij and once as ji). The hamiltonian could also be expressed as

$$H = \sum_{(ij)} J_{ij} \mathbf{S}_i \cdot \mathbf{S}_j \quad (3.36)$$

where now the sum runs over all pairs (ij) of atoms, so there is no double counting of bonds.

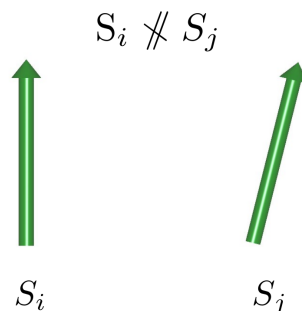


Figure 3.3 Canting of FM spins as a result of the antisymmetric Dzyaloshinskii-Moriya exchange interaction (not to scale).

Another potentially relevant interaction is the antisymmetric exchange, also known as Dzyaloshinskii-Moriya interaction. Similarly to superexchange it also depends on virtual states but is mediated by the spin-orbit interaction instead of an intermediary ion. Acting between spins \mathbf{S}_i and \mathbf{S}_j

its hamiltonian is

$$H = \mathbf{D} \cdot \mathbf{S}_i \times \mathbf{S}_j \quad (3.37)$$

where \mathbf{D} is a vector which is usually restricted by the local symmetry to lie in a certain direction or plane. Combined with the dominant FM or AFM interactions this often leads to a slight canting of neighboring spins, such that they are no longer exactly aligned (Figure 3.3).

Lastly, we need to consider the dipolar interaction that exists between any magnetic dipoles. This effect is usually weak but can be significant when other interactions are competing or closely balanced, as is common in frustrated systems (Section 3.8). The hamiltonian that describes the dipolar interaction is

$$H_{ij} = \frac{\gamma_i \gamma_j \hbar^2 \mu_0}{4\pi} \frac{\mathbf{S}_i \cdot \mathbf{S}_j - 3 \mathbf{S}_i \cdot \hat{\mathbf{r}}_{ij} \mathbf{S}_j \cdot \hat{\mathbf{r}}_{ij}}{r_{ij}^3} \quad (3.38)$$

where γ_i, γ_j are the gyromagnetic ratios for the spins $\mathbf{S}_i, \mathbf{S}_j$, which are separated by a distance r_{ij} in the direction of the unit vector $\hat{\mathbf{r}}_{ij}$. Notably, the dipolar interaction decays as r_{ij}^{-3} , making it relatively long-range compared to the exponentially decaying exchange interaction. The lowest energy state is for both spins, \mathbf{S}_i and \mathbf{S}_j , to align with their mutual separation vector \mathbf{r}_{ij} , as illustrated in Figure 3.4. Except for a one-dimensional chain this is impossible to satisfy for all interacting spins, thus the dipolar interaction is in a sense intrinsically frustrated.

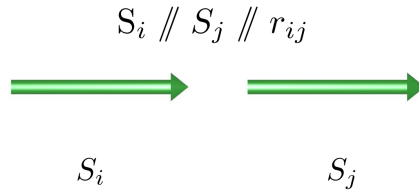


Figure 3.4 Lowest energy configuration for two spins coupled by the dipolar interaction.

The sign of the Curie-Weiss constant θ_{CW} (3.26) indicates the dominant type of magnetic correlations between magnetic moments. A positive sign corresponds to ferromagnetic correlations and a negative sign corresponds to antiferromagnetic correlations, while $\theta_{CW} = 0$ for an ideal paramagnet. In dilute magnetic materials the magnetic moments barely interact due to being widely separated and $\theta_{CW} \approx 0$.

Considering the hamiltonian (3.36) for exchange-interacting spins on a lattice we can express θ_{CW} in terms of the interaction strengths J_i . Assuming that at each level n there are z_n neighbors interacting with energy J_n (i.e. z_1 nearest neighbors, z_2 next nearest neighbors, etc.) then it can be derived from mean-field theory [97] that

$$\theta_{CW} = \frac{2S(S+1)}{3k_B} \sum_{n=1}^{\infty} z_n J_n \quad (3.39)$$

The significance of this formula is that it relates the macroscopic parameter θ_{CW} , which can

be determined experimentally, to the microscopic parameters of the model, which are not immediately accessible to experiment.

3.6 Magnetic Order

The effect of the interactions described in Section 3.5 is that when the thermal disorder is reduced the magnetic moments in a system undergo a phase transition to an ordered or frozen state, which is an inherently collective phenomenon. For common (non-frustrated) magnetic materials a phase transition occurs at a temperature T^* that is close to the Curie-Weiss constant, $T^* \approx \theta_{CW}$. At low temperature, $T < T^*$, the system possesses long-range order, so that the correlation between magnetic moments extends over distances far greater than the distance separating neighboring spins. When the temperature is raised to $T \approx T^*$, close to the phase transition, the correlation length is reduced, so the system has some amount of short-range order but far away regions are uncorrelated. At high temperature, $T > T^*$, the phase is paramagnetic, so the spins are uncorrelated and their orientations are essentially random (Figure 3.5).

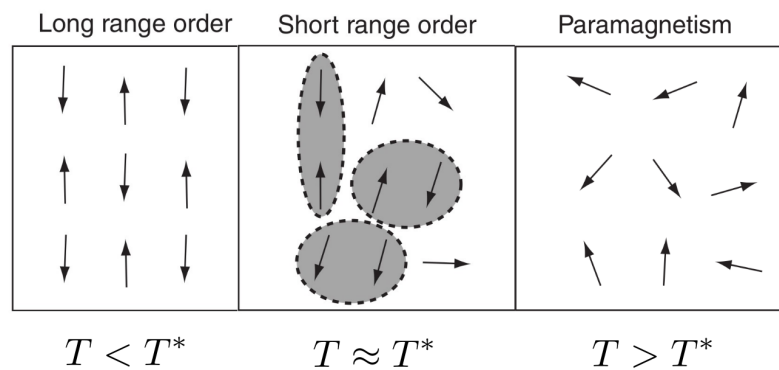


Figure 3.5 Transition from long-range ordered phase at low temperature to disordered paramagnetic phase at high temperature.

The phase transition manifests itself experimentally as a peak in magnetic or thermodynamic bulk quantities, such as the specific heat and magnetic susceptibility. Figure 3.6 illustrates how the inverse magnetic susceptibility behaves depending on the dominant type of correlation, ferromagnetic ($\theta_{CW} > 0$), paramagnetic ($\theta_{CW} = 0$) and antiferromagnetic ($\theta_{CW} < 0$).

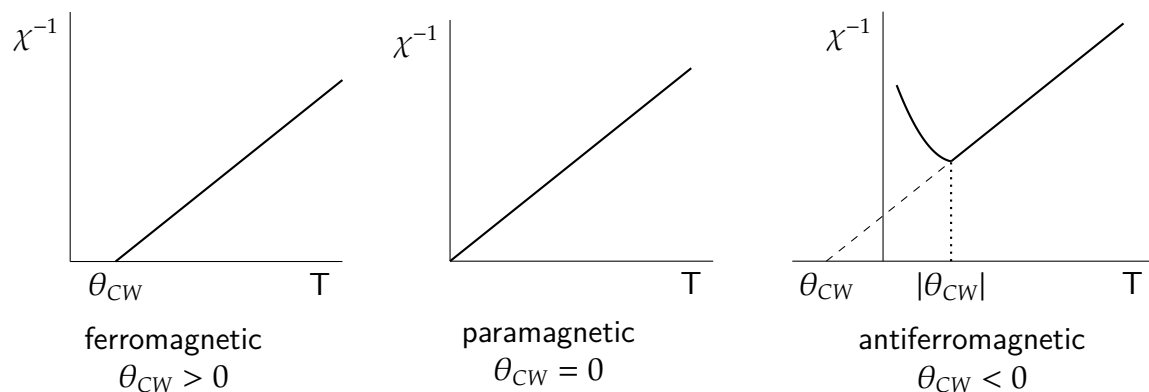


Figure 3.6 Inverse magnetic susceptibility behavior for an antiferromagnet, a paramagnet and a ferromagnet.

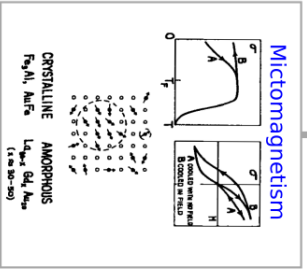
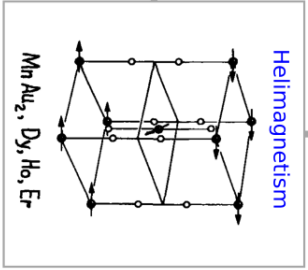
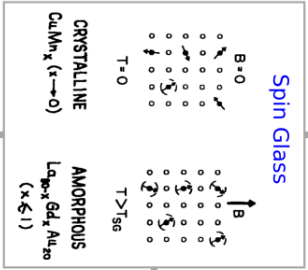
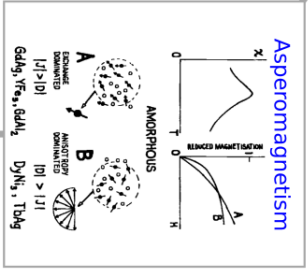
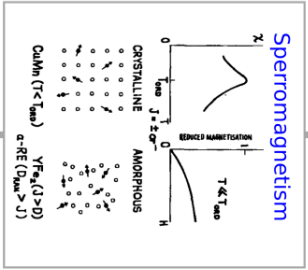
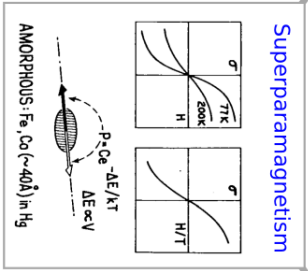
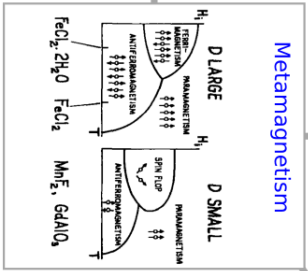
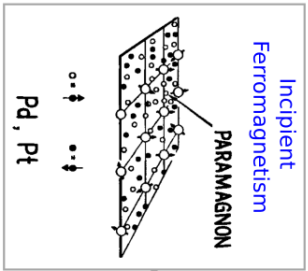
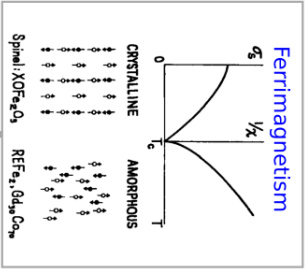
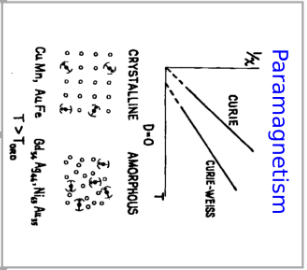
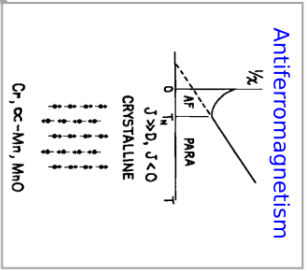
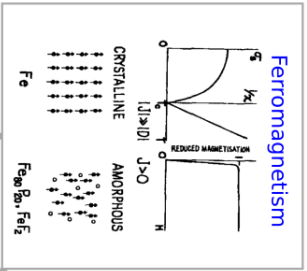
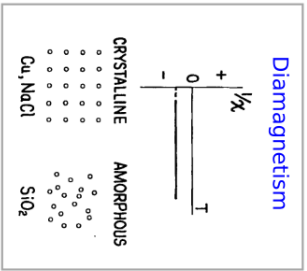


Figure 3.7 The magnetic family tree, a portrait of how the different types of magnetism are related. Adapted from [98].

The order that exists at low temperature can assume many forms, some of which will be described in Section 3.10. They range from relatively simple structures such as the conventional ferromagnetic, antiferromagnetic and ferrimagnetic states to complex magnetic structures that may have multiple propagation vectors, be incommensurate with the underlying lattice etc. Some classifications of the kinds of magnetic ordering have been proposed, for example the magnetic family tree in Figure 3.7, that portrays how the various types of magnetism are related. It is arguable whether some of these types of order warrant their own separate categories and several new types of order have been proposed, recently including altermagnetism [99].

3.7 Lanthanides

The lanthanides are chemical elements with atomic numbers 57 to 71, from lanthanum (La) to lutetium (Lu). These elements, along with the chemically similar scandium (Sc) and yttrium (Y), are known as rare-earth elements. Lanthanides are rather heavy, with large atomic number Z , so that spin-orbit coupling, which scales approximately as Z^4 , sets the dominant energy scale [91]. The crystal field and Zeeman effects are treated perturbatively over the dominant spin-orbit interaction.

The lanthanides have partially filled 4f electron shells, from $4f^0$ in La to $4f^{14}$ in Lu. These partially filled 4f orbitals are highly localized and shielded from the crystalline electric field by the more spatially extended 5s, 5p and 6s orbitals (for the Ln^{2+} , Ln^{3+} and Ln^{4+} lanthanide cations the 6s orbital is empty). Thus in insulating rare-earth compounds the 4f orbitals have negligible direct or indirect overlap, leading to very weak exchange interactions, with magnetic ordering temperatures typically on the order of 1K or less.

The relative strength of spin-orbit coupling means that 4f elements' ground state is accurately described by Hund's rules, with a well-defined total angular momentum J . The $(2J + 1)$ -fold degenerate ground state manifold is separated from the first excited spin-orbit manifold by an energy gap of order 1eV ($\sim 10^4\text{K}$) (except for Eu^{3+} and Sm^{3+} , as mentioned in our discussion on van Vleck paramagnetism in Section 3.3).

Figure 3.8 shows some magnetic properties of lanthanide ions. The ions La^{3+} , Ce^{4+} , Yb^{2+} and Lu^{3+} have filled shell electron configurations (either $4f^0 5p^2 5d^0 6s^0$ or $4f^{14} 5p^2 5d^0 6s^0$) and therefore are non-magnetic. Promethium (Pm) is extremely rare and radioactive, the most stable isotopes having half-lives of only a few years. Experimental values for μ_{eff} are from [93, 100] and agree quite well with theoretical values using Hund's rules, except for Eu^{3+} and Sm^{3+} , which is mostly due to the van Vleck contribution.

Figures 3.9 and 3.10 show the spin (S), orbital (L) and total (J) angular momenta and the calculated and experimentally measured magnetic moments of the Ln^{3+} trivalent lanthanide ions.

The crystalline electric field lifts the $(2J + 1)$ -fold degeneracy of the ground state, inducing splittings on the order of 10meV to 100meV (10^2K to 10^3K). Ions that have an odd number of electrons have half-integer spin and are forced by time-reversal symmetry to have doubly-degenerate states, according to Kramers' theorem [101], while the quantum states of ions with an even number of electrons are not necessarily degenerate. In Figure 3.8 the odd-electron Kramers ions are shaded differently from the non-Kramers ions that have an even number of

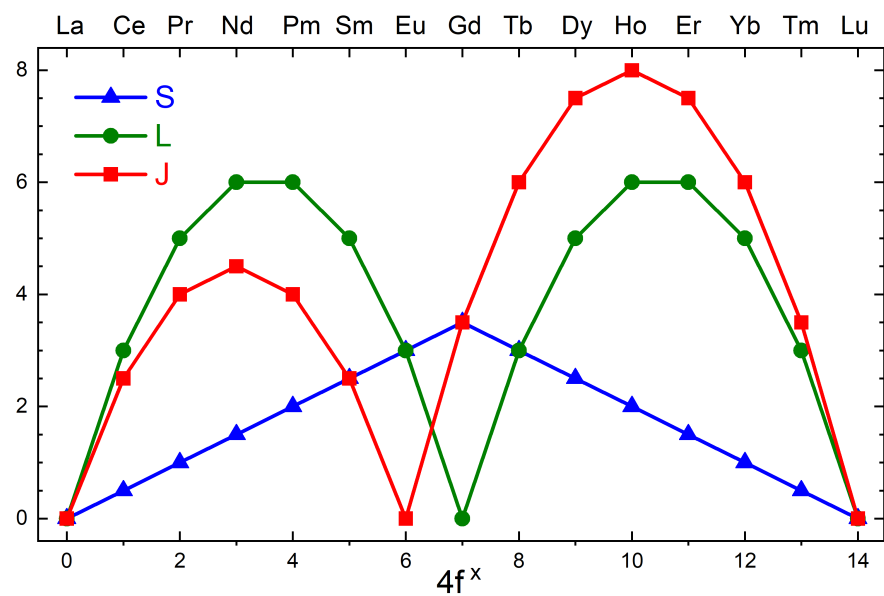


Figure 3.9 Spin (S), orbital (L) and total (J) angular momentum of the Ln³⁺ trivalent lanthanide ions, in units of μ_B . The experimental values are from [93, 100].

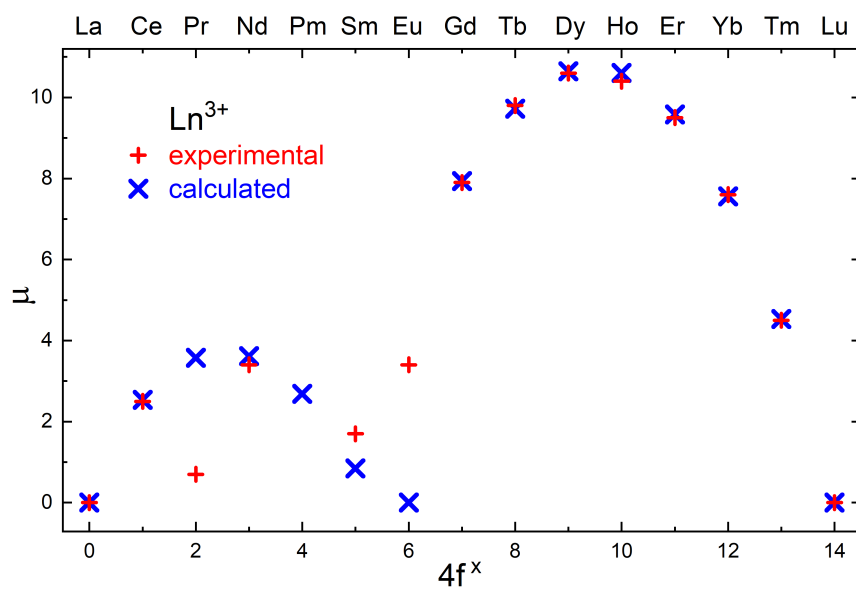


Figure 3.10 Calculated and experimentally measured magnetic moments of the 3+ lanthanide ions.

electrons.

3.8 Magnetic Frustration

The concept of frustration, a central theme in areas such as statistical and condensed matter physics, was first introduced in 1977 by Philip Anderson [102, 103] and Gerard Toulouse [104, 105], although frustrated systems had been studied before. The term applies to situations in which conflicting interactions between microscopic elements in a system render them 'frustrated' because any configuration they might assume cannot satisfy all of the constraints imposed by the interactions. Thus a system of spins is magnetically frustrated if it cannot simultaneously minimize the energy of each pair or set of interacting magnetic moments. The system will assume a state that is a compromise between the conflicting constraints set by the competing interactions. This often leads to complex structures, unlike the simple structures that would be favored by a subset of the interactions.

The simplest example of magnetic frustration occurs when three spins are arranged in an equilateral triangle with Ising anisotropy (easy-axis anisotropy) that forces them to align with the axis normal to the plane of the triangle. If these spins interact antiferromagnetically with their nearest neighbors then the interactions are frustrated, since in any configuration of the spins at least one of the interactions is not in its preferred minimal energy state.

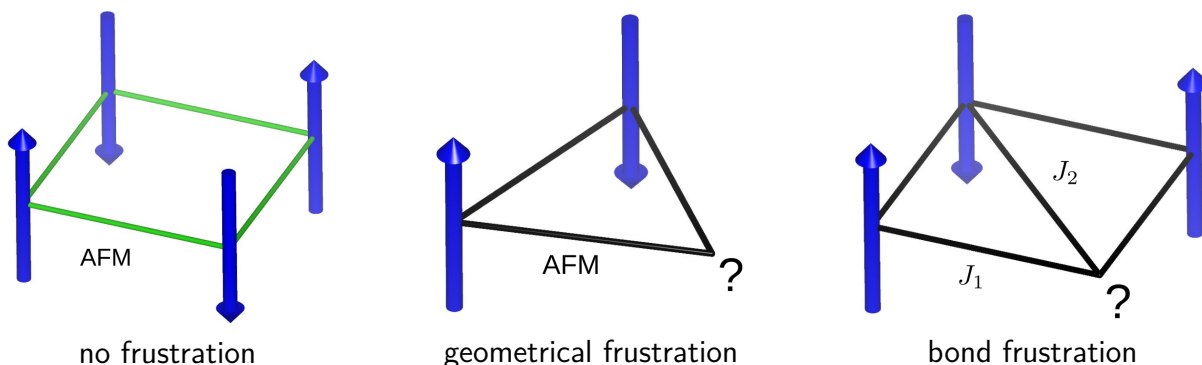


Figure 3.11 AFM Ising spins on a square are not frustrated (left) but are frustrated on a triangle (middle). A NNN interaction could make the square frustrated too (right).

This kind of frustration is geometrical since it arises due to the geometry of the lattice on which the spins are arranged. If the same spins were arranged on a square there would be no frustration, unless we also consider interactions with further neighbors. This could give rise to a distinct type of frustration, bond frustration, if the interactions J_1 between nearest neighbors and J_2 between next-nearest neighbors are balanced so that the spin on any one vertex is ambivalent as to pointing up or down.

Models of lattices with bond frustration have a very rich theory but are hard to realize experimentally since the interaction strengths (J_1 and J_2 in the above example) have to be tuned to a value close to the critical value where the interactions are perfectly frustrated. Geometrical frustration is relatively easier to come by since lattices with geometric patterns such as those illustrated in Figures 3.13 and 3.14 are quite common in the crystal structures of solid-state compounds. In practice there are situations intermediate between geometric and bond frustration, particularly for systems that display some degree of randomness in the geometric structure and/or interaction strengths.

Another kind of non-geometric frustration occurs for materials with highly anisotropic interactions induced by strong spin-orbit coupling. An example of anisotropically frustrated compounds are the Kitaev materials [106, 107], featuring a honeycomb lattice which is bipartite and therefore not geometrically frustrated. Their low-energy physics is well described by Kitaev's model [108], where the interactions along the three honeycomb directions are different, generating the anisotropy.

As mentioned in Section 3.6, for common magnetic materials a phase transition occurs at a temperature $T^* \approx |\theta_{CW}|$. For frustrated compounds this is no longer the case, the phase transition temperature T^* is considerably smaller than $|\theta_{CW}|$. The frustration index f , defined as

$$f = \frac{|\theta_{CW}|}{T^*} \quad (3.40)$$

has become a common semi-quantitative indicator of the degree of frustration in materials [109, 16]. An unfrustrated material is expected to order at $T \approx |\theta_{CW}|$ ($f \approx 1$), since $|\theta_{CW}|$ represents the scale at which interactions between magnetic moments become significant. In reality unfrustrated materials can have $f \lesssim 3$ due to effects not considered in deriving the Curie-Weiss law (3.26). Frustrated materials have $f > 3$, typically f is on the order of 10 or even 100.

Experimentally frustration manifests as an inverse magnetic susceptibility that remains linear even below the Curie-Weiss scale, only deviating from linear behavior at a temperature T^* that is well below $|\theta_{CW}|$, as illustrated in Figure 3.12 (compare with Figure 3.6). The state of the system in the intermediate regime, $T^* < T < |\theta_{CW}|$ is sometimes called a cooperative paramagnet, since it still behaves as a paramagnet although the interactions (cooperation) between spins are significant.

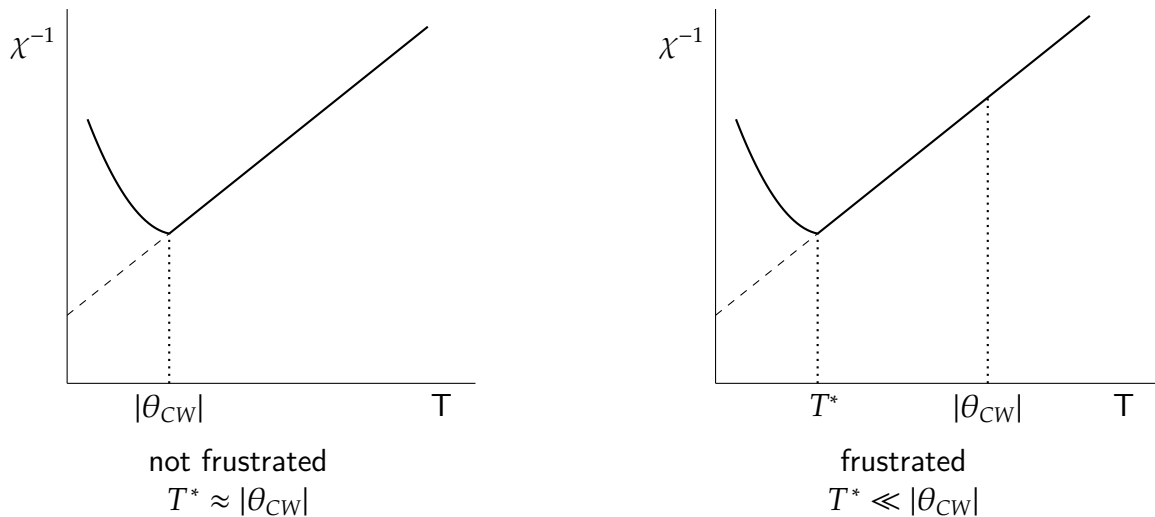


Figure 3.12 Inverse magnetic susceptibility behavior for a conventional and a frustrated antiferromagnet.

3.9 Frustrated Lattices

Most geometrically frustrated lattices are composed of either triangles or tetrahedra, which can be thought of as the basic frustrated units in two and three dimensions, respectively. These frustrated units can be composed into a lattice by joining them through their edges or vertices, giving rise to the triangular, kagome, fcc (face-centered cubic) and pyrochlore lattices, illustrated in Figures 3.13 and 3.14. Some other frustrated lattices worth mentioning are the garnet and hyper-kagome lattices, both of them composed of triangles arranged in a more complex three-dimensional pattern.

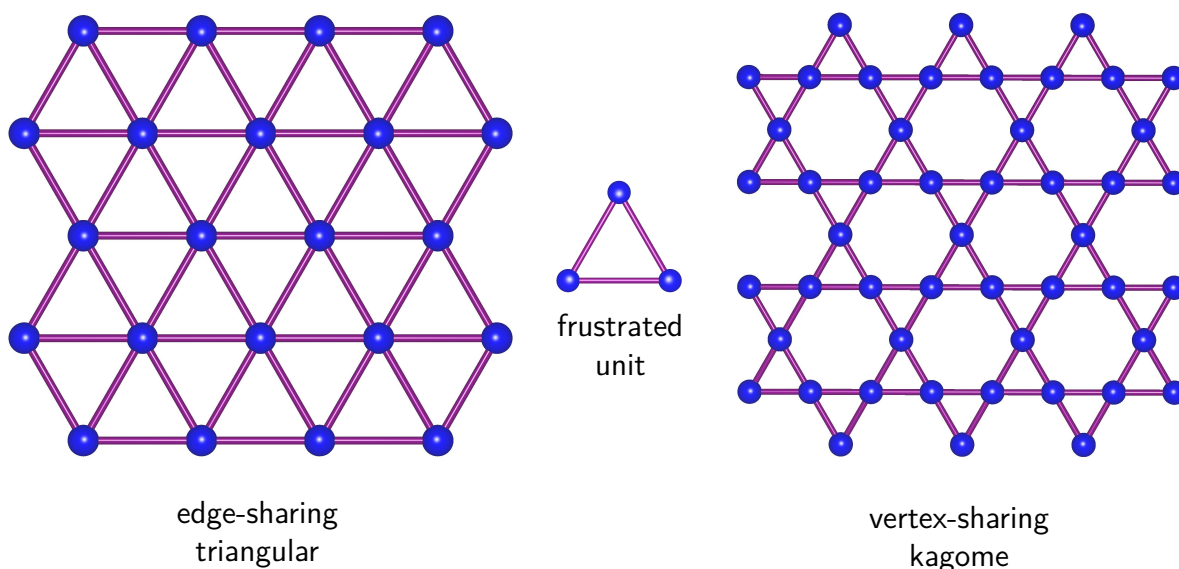


Figure 3.13 Triangular lattice (left) and kagomé lattice (right) are both composed of the basic frustrated unit in two dimensions, the triangle (middle).

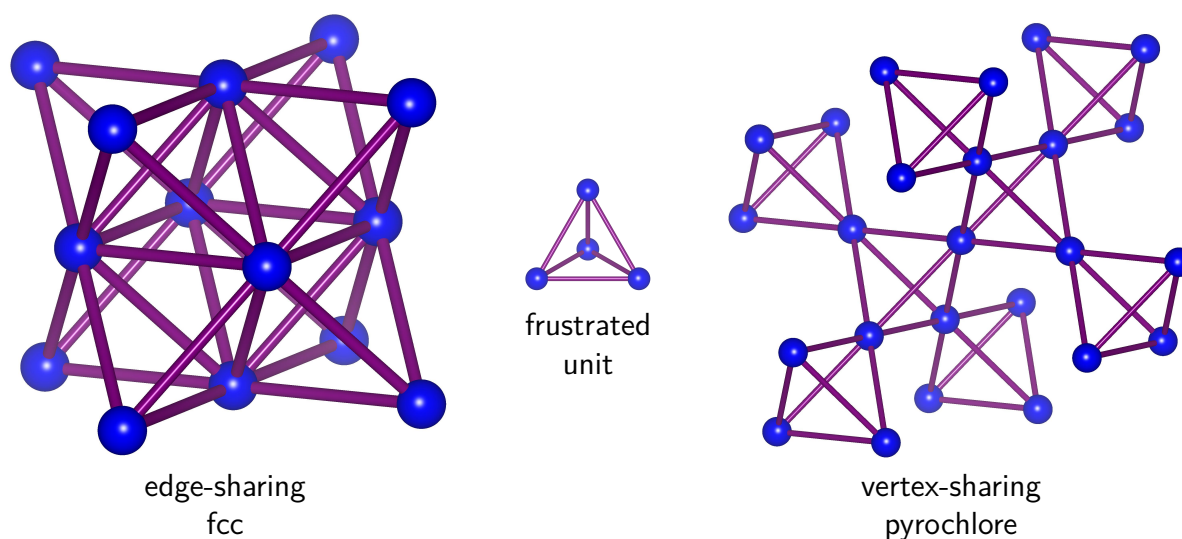


Figure 3.14 The face-centered cubic lattice (left) and the pyrochlore lattice (right) are both composed of the basic frustrated unit in three dimensions, the tetrahedron (middle).

3.10 Complex Spin States

The ground state of the AFM Ising spins on an equilateral triangle is degenerate since all six configurations in Figure 3.15 have the same energy, with one frustrated interaction that is colored in red. This is a common theme for frustrated systems, which often have a large number of degenerate or nearly-degenerate states which are close to or coincide with the ground state.

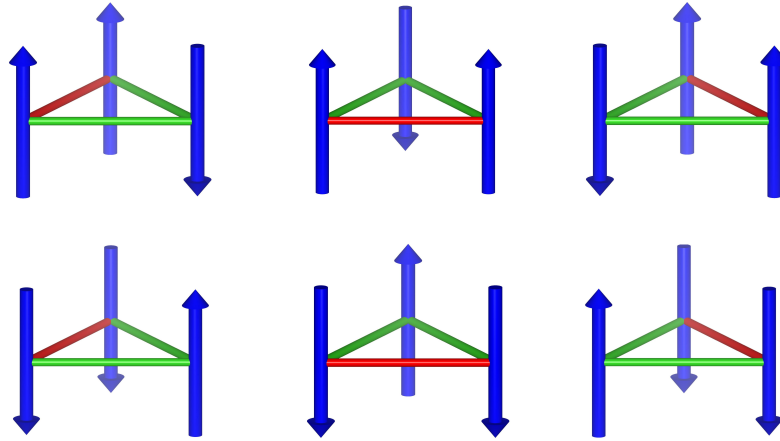


Figure 3.15 Degenerate ground states for AFM Ising spins on an equilateral triangle. Red color is assigned to the energetically unfavorable interaction.

Considering the simple units of frustrated lattices, such as the triangle and tetrahedron, often there is no unique way of extending the configuration of spins in one of these units to the adjacent units in order to minimize the system's energy. In those cases the number of equivalent configurations is proportional to the number of frustrated units or spins, so that the degeneracy is macroscopic, scaling with the size of the system. In thermodynamic terms this means that the entropy of the ground state is not zero, as the third law of thermodynamics states, but rather a nonzero residual entropy exists that is extensive, proportional to the systems volume.

In systems with some local constraints that can be implemented in many ways to form a global state, the spins might be able to fluctuate, changing their orientations similarly to the fluctuations in position of the atoms in a liquid. Such a state is called a spin liquid, and some pyrochlore compounds display spin liquid behavior, for instance the spin liquid candidate $Tb_2Ti_2O_7$ [110, 111].

A quantum spin liquid is a state in which the spins continue to fluctuate even at zero temperature, driven by quantum fluctuations rather than thermal ones. The resonating valence bond model is often used to describe a quantum spin liquid state. The principle is that neighboring spins combine into a spin singlet,

$$|\psi\rangle = \frac{1}{\sqrt{2}} (|\uparrow\downarrow\rangle - |\downarrow\uparrow\rangle) \tag{3.41}$$

and the spin liquid is formed by a superposition of all possible configurations of singlets. The effect of this resonating quantum state is that the entanglement spreads not only to neighboring spins but also to far away ones, as illustrated in Figure 3.16. To date no compound has been

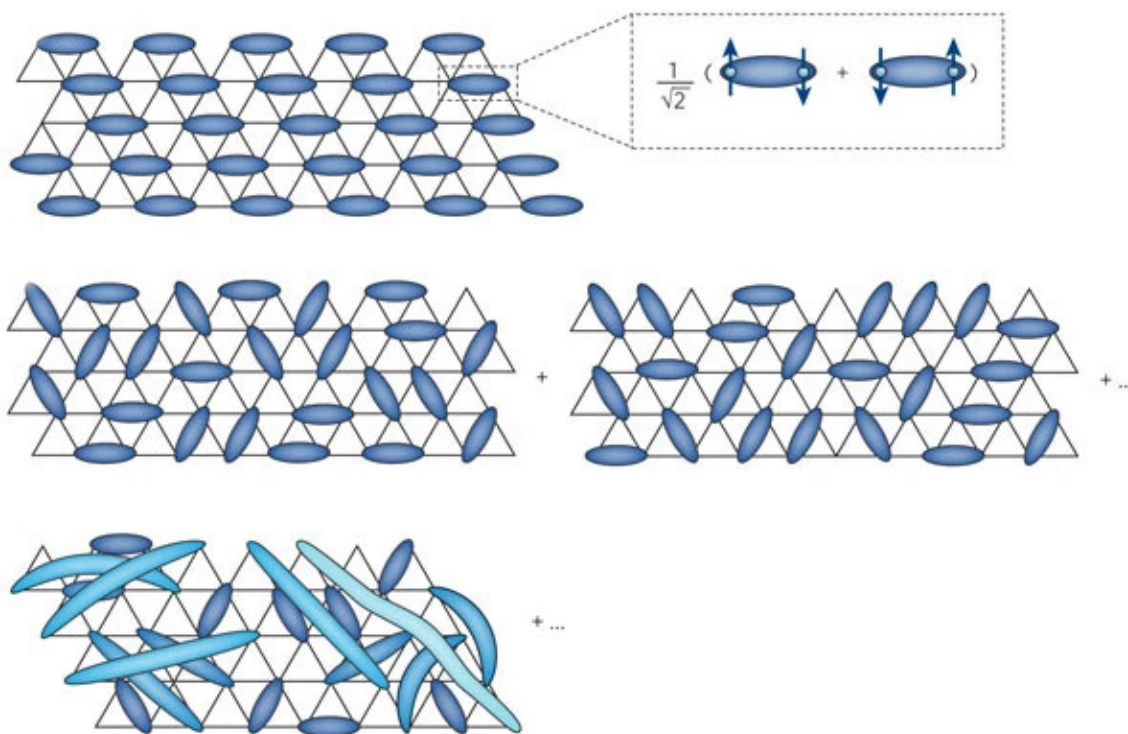


Figure 3.16 Model of a spin liquid as a superposition of all possible singlet partitions of the spins on a triangular lattice [112].

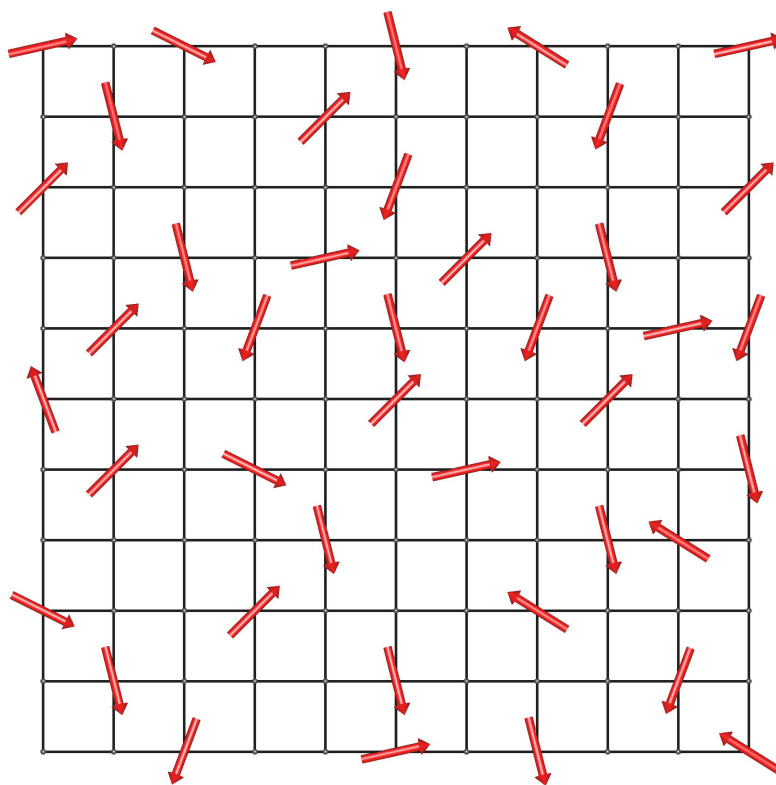


Figure 3.17 Model of a spin glass as a collection of spins placed at random sites on a lattice.

definitively identified as a quantum spin liquid, although many candidates have been proposed [112, 113, 114, 115, 116, 117, 118].

When magnetic frustration and disorder coexist a spin glass state can be formed, where the spins are disordered but highly correlated below the glass phase transition temperature. The low-temperature state is not ordered in the conventional sense, rather it exhibits a frozen order similar to the frozen positional disorder in glasses, which are amorphous forms of solid matter often formed by quenching (rapidly cooling) a liquid so that a crystalline phase does not form. Figure 3.17 shows a common model to describe spin glass phases, where magnetic moments are distributed randomly on a lattice, such that the sign and/or magnitude of the interaction depends on their distances and geometric arrangement. Some pyrochlore oxides exhibit spin glass behavior, for instance $\text{Tb}_2\text{Mo}_2\text{O}_7$ [119] and $\text{Y}_2\text{Mo}_2\text{O}_7$ [29]. More information on spin glasses can be found in the experimental reviews [120, 121, 122, 123].

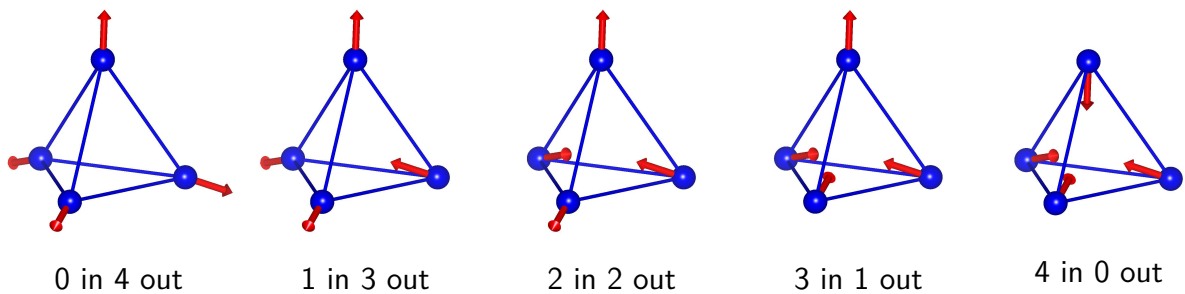


Figure 3.18 Possible states of a tetrahedron in the spin ice structure.

Another intriguing state is the spin ice state that exists when spins on the pyrochlore lattice interact ferromagnetically and have strong uniaxial (Ising) anisotropy in the local $\langle 111 \rangle$ direction. These conditions are satisfied for the pyrochlores $\text{Dy}_2\text{Ti}_2\text{O}_7$ and $\text{Ho}_2\text{Ti}_2\text{O}_7$, the so called classical spin ices. Considering only one of the pyrochlore tetrahedra, the spins on each vertex are forced to point either towards the center of the tetrahedron or in the opposite direction, giving rise to $2^4 = 16$ possible configurations. These can be divided into the categories shown in Figure 3.18 according to how many spins point into the tetrahedron.

The ferromagnetic interaction favors the states that have two spins pointing inwards and two spins pointing outwards, so that the sum of the spins on the tetrahedron is as large as possible. To see why this condition minimizes the energy we can rewrite the exchange hamiltonian (3.36) restricted to the spins on one tetrahedron as

$$H = -J \sum_{(ij)} \mathbf{S}_i \cdot \mathbf{S}_j = -\frac{1}{2} J \left[\left(\sum_i \mathbf{S}_i \right)^2 - \sum_i S_i^2 \right] \quad (3.42)$$

where the sums run over the spins i or pairs of spins (ij) in a tetrahedron. Since the magnitude $S_i = |\mathbf{S}_i|$ of the spins is fixed, the minimal energy is attained when the sum of the spins is maximal. The two-in two-out minimal energy configurations are said to satisfy the ice rule, due to an analogy with the proton structure of ordinary water ice that lead to the adoption of the term 'spin ice' to describe the spin system.

In the most common hexagonal phase of H_2O ice the O^{2-} oxygen ions are ordered but the H^+

hydrogen ions (protons) are disordered, although they satisfy a local constraint. Every proton is located on the line that connects two O^{2-} ions and the constraint is that every O^{2-} has two protons close to it (as in the H_2O molecule) and two protons far away. This model was used by Linus Pauling to calculate the residual low-temperature entropy of ice due to the proton disorder [124]. The residual entropy value predicted by Pauling agrees with experimental data remarkably well for such a simple argument, and it applies equally well to the spin ice state, as we will now describe.

Out of the 16 possible configurations only $\binom{4}{2} = 6$ satisfy the ice rule, so that the fraction of favorable states is $\frac{6}{16} = \frac{3}{8}$. To simplify the problem we assume that the spin configurations of each tetrahedron are independent, while in reality they are not. It is not obvious why this simplification leads to good predictions. This matter has been discussed extensively in the literature and requires considering the long-range nature of the dipolar interaction (3.38), which the simple FM Ising spin ice model neglects. If our system contains N spins in total, then there are $\frac{N}{2}$ tetrahedra and assuming their independence a fraction $(\frac{3}{8})^{N/2}$ of all the 2^N possible states are favorable, so the ground-state entropy is

$$S = k_B \ln \left[\left(\frac{3}{8} \right)^{\frac{N}{2}} 2^N \right] = \frac{1}{2} \ln \frac{3}{2} k_B N \quad (3.43)$$

and the molar entropy residual entropy ΔS is

$$\frac{\Delta S}{R} = \frac{1}{2} \ln \frac{3}{2} = 0.202732554 \quad (3.44)$$

where $R = k_B N_A = 8.314462618 \text{ JK}^{-1} \text{ mol}^{-1}$ is the universal gas constant [89]. Note that the entropy is extensive, scaling with the system size N . Experimentally the residual magnetic entropy can be determined by integrating the magnetic specific heat, although it can be challenging to distinguish the contributions to the specific heat arising due to the various degrees of freedom in a solid, including the electronic, lattice and nuclear magnetic contributions. The specific heat C is related to the entropy S by

$$S(T_2) - S(T_1) = \int_{T_1}^{T_2} \frac{C(T)}{T} dT \quad (3.45)$$

so that by subtracting the magnetic contribution to the entropy integral in (3.45) from the high-temperature entropy we obtain the residual low-temperature entropy. Figure 3.19 shows the residual entropy calculated from the electronic magnetic contribution to the specific heat of $\text{Ho}_2\text{Ti}_2\text{O}_7$, previously measured in our laboratory. The experimental value agrees well with the predicted one in (3.44).

Very interesting physics results when the spin ice ground state is excited by the flipping of a spin, thereby violating the two-in two-out ice rule in both of the tetrahedra it belongs to. The magnetic flux entering and exiting the excited tetrahedron are no longer balanced, so it acts as a magnetic monopole, a bare magnetic charge, depicted in Figure 3.20. One of Maxwell's equations states that there are no sources of magnetic charge, $\nabla \cdot B = 0$, and to date there

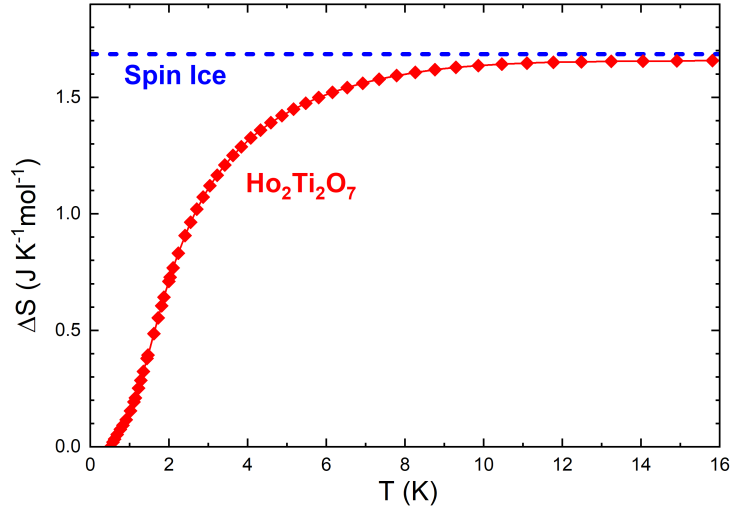


Figure 3.19 Residual magnetic entropy of the classical spin ice $\text{Ho}_2\text{Ti}_2\text{O}_7$.

is no evidence for fundamental particles that carry a magnetic charge. In the continuum approximation to the spin ice the average magnetic field H is no longer divergenceless at the location of the excitation, $\nabla \cdot H \neq 0$, so the excitation effectively behaves as a magnetic monopole.

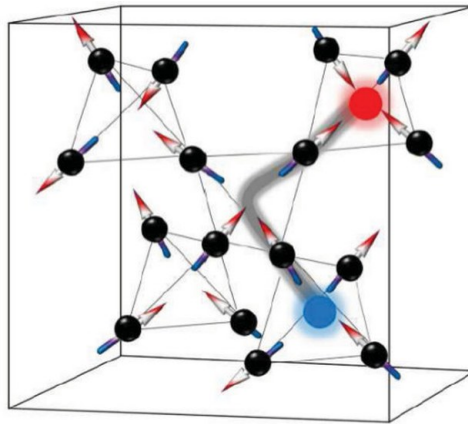


Figure 3.20 Effective magnetic monopoles that arise when the spin ice rule is violated [125].

By flipping further spins in neighboring tetrahedra the excitation can traverse the medium and thus constitutes an emergent, deconfined particle. Since a spin flip creates a pair of opposite monopoles, a string of flipped spins joins them when they separate, a so called Dirac string, also represented in Figure 3.20. The effective interactions between magnetic monopoles are described by a potential $V(r)$ analogous to the Coulomb potential for electric charges,

$$V(r_{\alpha\beta}) = \frac{\mu_0}{4\pi} \frac{Q_\alpha Q_\beta}{r_{\alpha\beta}} \quad (3.46)$$

where Q_α , Q_β are the charges of two monopoles separated by a distance $r_{\alpha\beta}$. That is why the monopole phase is called a Coulomb phase, which exhibits emergent gauge dynamics exactly analogous to conventional electrodynamics. More information on the spin ice state and its monopole excitations can be found in [126, 30, 127, 128, 129, 22, 130, 131, 23, 132, 133, 134].

3.11 Pyrochlore Magnetism

For most of the magnetic $A_2B_2O_7$ pyrochlores the magnetism is due to a lanthanide cation at the A site of the crystal structure. For these rare-earth magnetic pyrochlores the single-ion physics dominates over the two-ion interactions, so that the single-ion physics must be dealt with first. The hierarchy of energy scales is: Coulomb interactions \gg spin-orbit coupling \gg crystalline environment \gg two-ion interactions, so that each effect can be considered perturbatively with respect to the previous ones.

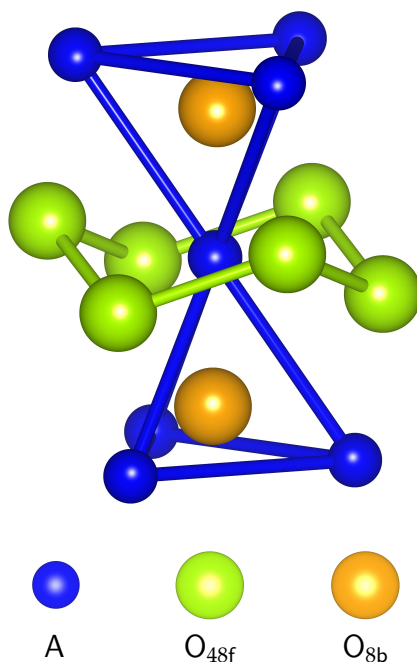


Figure 3.21 Surroundings of the A cation in the $A_2B_2O_7$ pyrochlore structure.

The environment of the magnetic ion creates an electric charge distribution, known as the crystalline electric field. As already mention in Section 3.7, this crystalline field splits the degeneracy of the states with total angular momentum J . The surroundings of the magnetic A^{3+} cation in the pyrochlore structure are depicted in Figure 3.21. Centered in the horizontal plane there is a puckered ring of six O_{48f} oxygen ions, similar to the chair conformation of cyclic organic molecules. Vertically above and below the central A^{3+} cation there are two O_{8b} oxygen ions, in the center of the A_4 tetrahedra.

The two O_{8b} ions are closer to the central ions than the six O_{48f} ions, in fact the $A-O_{8b}$ bond is unusually short when compared to most other cation-oxygen bonds in other oxides [31]. The strong $A-O_{8b}$ bond defines the local anisotropy axis of the A^{3+} cation, thereby influencing its magnetic properties. This local anisotropy axis is in the $[111]$ direction (the vertical axis in Figure 3.21) or one of the eight equivalent directions denoted by $\langle 111 \rangle$, all parallel to a body diagonal of the conventional unit cell. This axis is also known as the C_3 axis, since the crystal structure possesses a threefold rotational symmetry around it, while there are two twofold C_2 symmetry axes perpendicular to the C_3 axis.

Different lanthanide ions have different types of anisotropy in the pyrochlore structure. Gd^{3+} has no orbital angular momentum, $L = 0$, so that the crystal field splitting is to first approximation nonexistent, since it is mediated by the spin-orbit interaction, proportional to $\mathbf{S} \cdot \mathbf{L}$.

Thus Gd^{3+} has an approximately isotropic spin, also known as a Heisenberg spin, which can point freely in any direction (though in some pyrochlores, such as $\text{Gd}_2\text{Ti}_2\text{O}_7$ and $\text{Gd}_2\text{Sn}_2\text{O}_7$, the Gd^{3+} can exhibit significant anisotropy effects [135, 136]). Some ions such as Tb^{3+} , Ho^{3+} and Dy^{3+} have an easy-axis anisotropy, also called uniaxial or Ising anisotropy, causing them to preferentially align parallel to the local $\langle 111 \rangle$ axis. Other ions such as Er^{3+} and Yb^{3+} have an easy-plane anisotropy, also known as planar or xy anisotropy, and preferentially lie in the plane perpendicular to the local $\langle 111 \rangle$ axis.

The energy of the spin state depends on its alignment with the local $\langle 111 \rangle$ axis, given by quantum number m_J , the projection of J onto that axis. The ground state $|\psi\rangle$ will be a superposition of the different m_J states,

$$|\psi\rangle = \sum_{m=-J}^{m=+J} c_m |m\rangle \quad (3.47)$$

where the coefficients c_m depend on the ion under consideration and the crystalline environment. In many cases the lowest energy state is a doublet, whose degeneracy is enforced either by Kramers' theorem (Section 3.7) or by the symmetry of the crystalline environment for the non-Kramers ions. Denoting the states in this doublet as $|+\rangle$ and $|-\rangle$ we can define pseudospin operators

$$\begin{aligned} S^+ &= |+\rangle\langle -| \\ S^- &= |-\rangle\langle +| \\ S^z &= \frac{1}{2} (|+\rangle\langle +| - |-\rangle\langle -|) \end{aligned} \quad (3.48)$$

The doublet can be classified by the irreducible representation of the site symmetry group $D_{3d} (\bar{3}m)$. There are three distinct cases, one non-Kramers and two Kramers doublets, that transform differently under the C_2 , C_3 site symmetries and time reversal [137]. Yb^{3+} in $\text{Yb}_2\text{Ti}_2\text{O}_7$ belongs to the Kramers effective spin-1/2 case since it behaves exactly like an $S = 1/2$ spin under the symmetry operations. At low temperature the higher energy states are not accessible so the effective spin-1/2 model provides a useful model to study the ground state and low-temperature properties of $\text{Yb}_2\text{Ti}_2\text{O}_7$ and similar compounds.

Using a local coordinate frame where $\hat{\mathbf{z}}$ lies on the C_3 axis and $\hat{\mathbf{y}}$ along one of the C_2 axes, the magnetic anisotropy can be quantified in terms of the \mathbf{g} -tensor, with two independent components, g_z and g_{\pm} , that are related to the magnetic moment $\boldsymbol{\mu}$ by

$$\boldsymbol{\mu} = -\mu_B [g_{\pm}(S^x\hat{\mathbf{x}} + S^y\hat{\mathbf{y}}) + g_z S^z\hat{\mathbf{z}}] \quad (3.49)$$

where

$$\begin{aligned} S^x &= \frac{1}{2} (S^+ + S^-) \\ S^y &= \frac{1}{2i} (S^+ - S^-) \end{aligned} \quad (3.50)$$

are linear combinations of the pseudospin operators defined in (3.48). The operators S^x , S^y , S^z satisfy the usual commutation relations,

$$[S^\mu, S^\nu] = i \epsilon_{\mu\nu\rho} S^\rho \quad (3.51)$$

which justifies naming them pseudospin operators. The symmetry-allowed interactions between the lanthanide ions on the pyrochlore lattice are quite complex, involving multipole operators in the angular momentum \mathbf{J} and the crystal field potential operators [137]. However if we consider only the low-energy effective description in terms of the ground state doublets then the situation simplifies significantly. Projecting the full hamiltonian onto the subspace spanned by the ground state doublets yields the effective hamiltonian

$$H = \sum_{(ij)} \left[J_{zz} S_i^z S_j^z - J_{\pm} S_i^+ S_j^- + J_{\pm\pm} \gamma_{ij} S_i^+ S_j^+ + J_{z\pm} \zeta_{ij} (S_i^z S_j^+ + S_i^+ S_j^z) \right] + h.c. \quad (3.52)$$

with interaction parameters J_{zz} , J_{\pm} , $J_{\pm\pm}$, $J_{z\pm}$, where the sum runs over all pairs of neighbors (ij) , the S_i are the pseudospin operators for spin i , defined in (3.48) and (3.50), $h.c.$ means the hermitian conjugate of the whole expression and

$$\zeta = -\gamma^* = \begin{bmatrix} 0 & -1 & \xi & \xi^{-1} \\ -1 & 0 & \xi^{-1} & \xi \\ \xi & \xi^{-1} & 0 & -1 \\ \xi^{-1} & \xi & -1 & 0 \end{bmatrix} \quad (3.53)$$

where $\xi = \exp(i\pi/3)$. The form (3.52) is the most general anisotropic nearest-neighbor exchange hamiltonian that respects the symmetries of the pyrochlore lattice. This expression, in terms of the local coordinates of each spin, can be recast in a global coordinate frame where the interaction constants are easier to interpret,

$$H = \sum_{(ij)} \mathbf{S}_i^T \mathbf{J}_{ij} \mathbf{S}_j \quad (3.54)$$

where now the pseudospin operators \mathbf{S}_i are expressed in the global coordinate frame and the effective exchange matrix \mathbf{J}_{ij} between nearest neighbors is

$$\mathbf{J}_{ij} = \begin{bmatrix} J_2 & J_4 & J_4 \\ -J_4 & J_1 & J_3 \\ -J_4 & J_3 & J_1 \end{bmatrix} \quad (3.55)$$

or one of five equivalent permutations thereof, depending on which of the six edges of the tetrahedron is considered. The form of this exchange matrix is dictated by symmetry, such that the parameters $J_1 - J_4$ encode both the interactions and their anisotropy. The exchange parameters can be interpreted as planar J_1 , uniaxial J_2 , symmetric off-diagonal J_3 and antisymmetric Dzyaloshinskii-Moriya J_4 terms, or equivalently combinations of $J_1 - J_4$ can be interpreted as Heisenberg, Kitaev, pseudodipolar and Dzyaloshinskii-Moriya terms.

Some limits and special cases of these parameters have been studied extensively, for instance the spin ice model corresponds to $J_1 = -J_2 = J_3 = J_4 < 0$ and the Heisenberg limit is $J_1 = J_2, J_3 = J_4 = 0$. The local parameters are related to the global ones by

$$\begin{aligned} J_{zz} &= -\frac{1}{3}(2J_1 - J_2 + 2J_3 + 4J_4) \\ J_{\pm} &= \frac{1}{6}(2J_1 - J_2 - J_3 - 2J_4) \\ J_{\pm\pm} &= \frac{1}{6}(J_1 + J_2 - 2J_3 + 2J_4) \\ J_{z\pm} &= \frac{1}{3\sqrt{2}}(J_1 + J_2 + J_3 - J_4) \end{aligned} \quad (3.56)$$

There are six types of ordered states that have distinct symmetry and in the effective spin-1/2 case correspond to dipolar magnetic order. Figure 3.22 shows examples of the spin configurations for each type of order. The possible states include the ψ_4 Palmer-Chalker (PC) state [138], the ψ_3 coplanar antiferromagnet, the ψ_2 non-coplanar antiferromagnet, the all-in all-out (AIAO) state, the two-in two-out spin ice (SI) and the splayed ferromagnet (SFM).

The T_{1g} and T'_{1g} orders transform identically under spatial symmetry (but oppositely under time reversal) so for the effective spin-1/2 case they can be mixed freely to form a splayed ferromagnet. In this state the pseudospins are mostly aligned, forming a small angle θ with one of the cubic [100] axes. The splay angle θ determines the mixing between the T_{1g} and T'_{1g} order.

For classical spins the problem of finding the magnetic ground state for the whole system can be neatly separated into two parts: finding the ground state for a single tetrahedron, and then composing the minimal energy configurations for single tetrahedra to tile the pyrochlore lattice, using the so called 'Lego-brick rules'. The states obtained in this way have four sublattices, with vanishing crystal momentum ($\mathbf{k} = 0$ propagation vector), and are sufficient to describe many of the magnetic pyrochlore ground states (with important exceptions, for

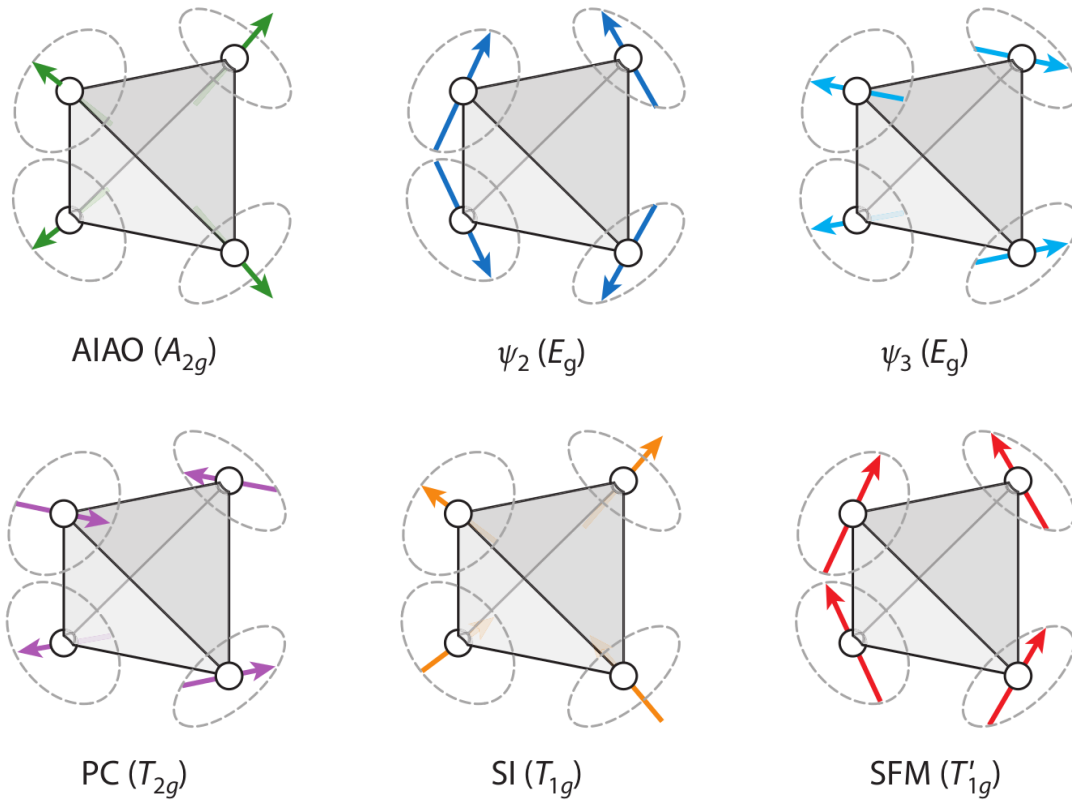


Figure 3.22 Spin configurations for each type of order [137].

instance, $\text{Gd}_2\text{Ti}_2\text{O}_7$ requires two propagation vectors [139]). It can be proven that for any set of exchange constants $J_1 - J_4$ there exists a classical $\mathbf{k} = 0$ ground state of the hamiltonian (3.54) with four-sublattice long-range magnetic order [140].

All of the configurations in Figure 3.22 can be obtained within a narrow range of exchange parameters so that in certain regions of the phase diagram the structures are almost degenerate. At the boundaries between different phases the configurations are exactly degenerate, at least on a classical level, and the ground state manifold is expanded. This type of degeneracy is not enforced by symmetry but rather accidental, so that phase competition can arise. Quantum fluctuations can select a ground state from the classically degenerate states by a mechanism known as order-by-disorder, which plays an important role in the physics of some pyrochlore compounds, such as $\text{Er}_2\text{Ti}_2\text{O}_7$ [137, 141, 142].

Accidental symmetries are of enormous fundamental interest for the unusual physics they give rise to, since physical properties that cannot be traced back to broken symmetries transcend the Landau paradigm of phase transitions [143]. As prominent examples, spin liquids and other magnetically frustrated systems can display fractionalized excitations and topological properties, two topics that have driven much theoretical and experimental research in the last decades.

3.12 $\text{Yb}_2\text{Ti}_2\text{O}_7$

The first literature report on the low-temperature properties of $\text{Yb}_2\text{Ti}_2\text{O}_7$ dates from 1969 [144], which describes a heat capacity singularity at $T_C = 214\text{mK}$ and a broad feature at $T \approx 2\text{K}$, as shown in Figure 3.23. Integrating the heat capacity a residual entropy of $\Delta S/R = 0.671$ was obtained, which is close to $\Delta S/R = \ln 2 = 0.693$, suggesting a twofold degeneracy of the ground state for each spin.

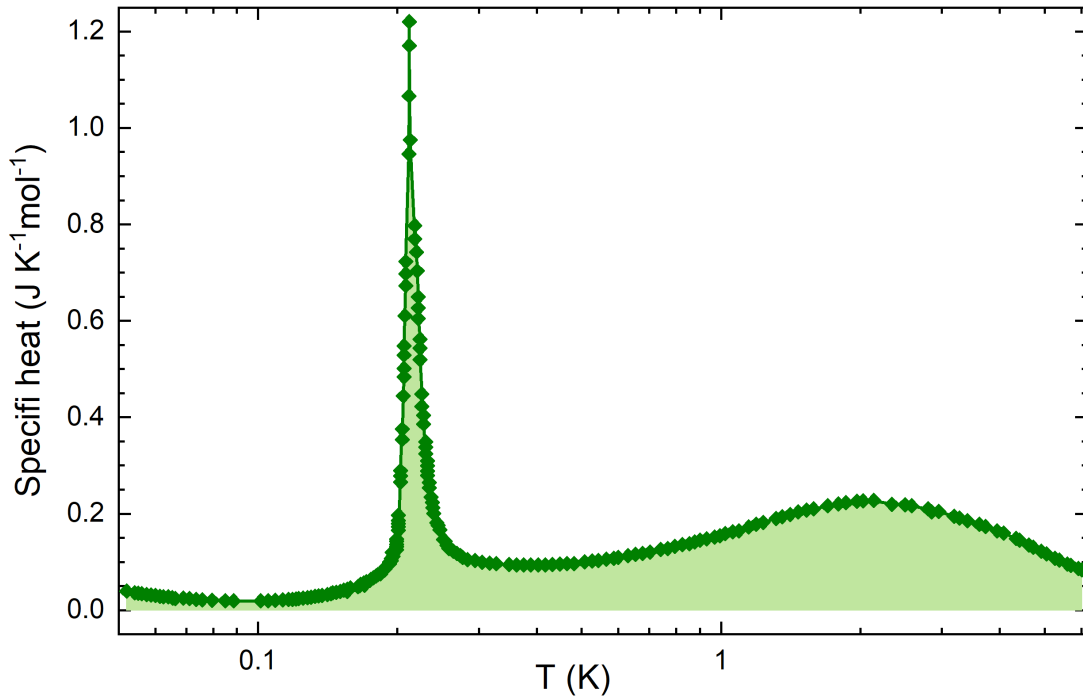


Figure 3.23 Heat capacity of $\text{Yb}_2\text{Ti}_2\text{O}_7$, adapted from [144].

In the following decades there were only very few publications on $\text{Yb}_2\text{Ti}_2\text{O}_7$ until a resurgence of interest in the early 2000s. The classical spin ices $\text{Ho}_2\text{Ti}_2\text{O}_7$ and $\text{Dy}_2\text{Ti}_2\text{O}_7$, described in Section 3.10, have large spins and strong Ising anisotropy, so that their behavior is well described by a classical model. Spin liquids and similar states with strong quantum effects can be obtained by enhancing the conditions that suppress magnetic order, using the effects of small spins, low dimensionality and frustration. Pyrochlores that contain smaller spins with XY anisotropy, as is the case with Yb^{3+} in $\text{Yb}_2\text{Ti}_2\text{O}_7$, are effectively spin- $\frac{1}{2}$ and therefore expected to exhibit significant quantum effects. The search for a quantum analog of the classical spin ices, a quantum spin ice, was one of the motivations that lead to renewed interest in $\text{Yb}_2\text{Ti}_2\text{O}_7$ [145].

One of the first newer studies on $\text{Yb}_2\text{Ti}_2\text{O}_7$ [146] demonstrated, using ^{170}Yb Mössbauer spectroscopy and muon spin relaxation, that the spin fluctuation rate reduces by a few orders of magnitude at $T_C \approx 0.24\text{K}$ and remains constant below T_C . Neutron scattering measurements did not reveal magnetic Bragg peaks, which are a signature of long-range order, so their interpretation was that at T_C there is a first-order transition that is not associated with long-range order, rather with the spin dynamics in the time domain. The absence of long-range order is consistent with a quantum spin ice or spin liquid model, where spin fluctuations persist to extremely low temperature.

With the resurgence in interest sparked by these initial papers, many investigations on $\text{Yb}_2\text{Ti}_2\text{O}_7$ were performed, often leading to contradictory results. Some neutron diffraction studies revealed weak magnetic Bragg peaks below $T \approx 0.24\text{K}$ [147, 148, 149, 150, 151, 152, 153, 154], while others did not [155, 156, 157, 146, 158, 159, 160, 161, 155, 162]. Muon spin relaxation studies yielded equally ambiguous results [154, 162, 156, 146, 163]. The dynamic properties were also disputed, with some reporting static spins [154, 150] while others reported slowly fluctuating spins down to the lowest temperature [159, 158, 146, 162, 164, 165, 153].

The properties of powder and single crystal samples differed significantly, for instance most powders exhibited a sharp specific heat transition at $T_C \approx 260\text{mK}$ [144, 166, 164, 162, 154], whereas for single crystals the transition was broadened, up to ten times less intense, and shifted to lower temperature, in the $T \approx 150\text{mK}$ – 200mK range [167, 164, 148, 162, 154]. Similarly, the magnetic susceptibility transition appeared at $T_C \approx 245\text{mK}$ for powder samples and at $T_C \approx 150\text{mK}$ for crystals [153].

This confusing state of affairs has been in large part resolved, with discrepancies among different studies attributed mostly to differences in sample quality. Studies that carefully controlled the synthesis technique showed that the specific heat anomaly and other properties are highly sensitive to variations in stoichiometry on the level of 1% [168, 167, 169, 170]. The small amount of structural disorder in non-pristine samples probably explains most of the discrepancies between different studies.

Many of the crystals in earlier publications, grown by the floating-zone technique, were found to be non-stoichiometric even though they were grown from powders with the proper stoichiometry. These crystals also displayed various colors, ranging from a deep red to yellow-grayish and brown-greenish. The color of the crystals can be used as an indicator for off-stoichiometry, so that, for instance, crystals with an Yb excess in the composition usually are some shade of red. Ideal stoichiometric $\text{Yb}_2\text{Ti}_2\text{O}_7$ crystals should be translucent and colorless, due to the 3.34eV optical bandgap calculated using density functional theory [171].

It is now known that the crystal growth process itself can unbalance the stoichiometry, so that off-stoichiometric crystals can be produced even if the powder is stoichiometric. To combat these problems, in [168] the authors used the travelling solvent floating-zone method, where a flux of 30% TiO_2 and 70% $\text{Yb}_2\text{Ti}_2\text{O}_7$ is used to lower the temperature of the molten zone and help precipitate out a pure $\text{Yb}_2\text{Ti}_2\text{O}_7$ crystal [172, 173]. The resulting single crystal was clear and colorless, apparently of very high quality.

A systematic study of the effects of non-stoichiometry was performed on the stuffed/diluted pyrochlore compounds $\text{Yb}_{2+x}\text{Ti}_{2-x}\text{O}_{7-x/2}$ for $x = -0.02, -0.01, 0.00, 0.01, 0.02, 0.08$ [168]. It was found that any deviation from ideal stoichiometry ($x = 0.00$) resulted in a decrease of the sharp first-order specific heat transition temperature, which is $T_C = 268(4)\text{mK}$ for the undoped $\text{Yb}_2\text{Ti}_2\text{O}_7$ sample. It was found that the Yb/Ti site inversion ratio (see Table 2.12) was on the order of 1% even for the highest quality $\text{Yb}_2\text{Ti}_2\text{O}_7$ powder samples, while the corresponding crystal did not display any detectable site inversion.

In [174] ultrapure $\text{Yb}_2\text{Ti}_2\text{O}_7$ samples grown in an oxygen-depleted atmosphere were compared to those grown in a standard atmosphere and annealed in oxygen. The color of the crystals differed, for instance the as-grown crystal was brown while the one annealed in oxygen was transparent. Diffuse neutron scattering was used as an extremely sensitive probe for structural

defects and compared to Monte Carlo simulations. The results confirm that oxygen vacancies are filled during the annealing process and that vacancies seem to stabilize a spin liquid state, with no long-range order, while the annealed sample possessed an ordered ferromagnetic ground state.

Although the Yb^{3+} ion is protected by Kramers degeneracy, its ground state is still very sensitive to deviations from perfect crystallinity. A splayed ferromagnetic (SFM) ground state can be stabilized by modest hydrostatic pressure, suggesting that most samples have a residual strain distribution that affects the low-energy physics [163]. The effects of chemical pressure, induced by stuffing $\text{Yb}_2\text{Ti}_2\text{O}_7$ with Yb^{3+} ions, result in the opposite effect, washing out the characteristic spin correlations and stabilizing a spin liquid phase [174].

In the most recent studies great care has been taken to assure ultrapure stoichiometric $\text{Yb}_2\text{Ti}_2\text{O}_7$ samples. Since many of the previously published findings have validity partially limited to specific samples, we will not further discuss those conflicting reports and focus on the most recent publications, which used very high quality samples, such as [175]. It is now well established that $\text{Yb}_2\text{Ti}_2\text{O}_7$ undergoes a first-order transition into a splayed ferromagnetic ground state at $T_C = 0.27\text{K}$. The ground state is a splayed ferromagnet, with a splay angle of about $\theta = 5.3(8)^\circ$, as illustrated in Figure 3.24. The ground state has no residual classical degeneracy but exhibits highly unusual dynamic behavior.

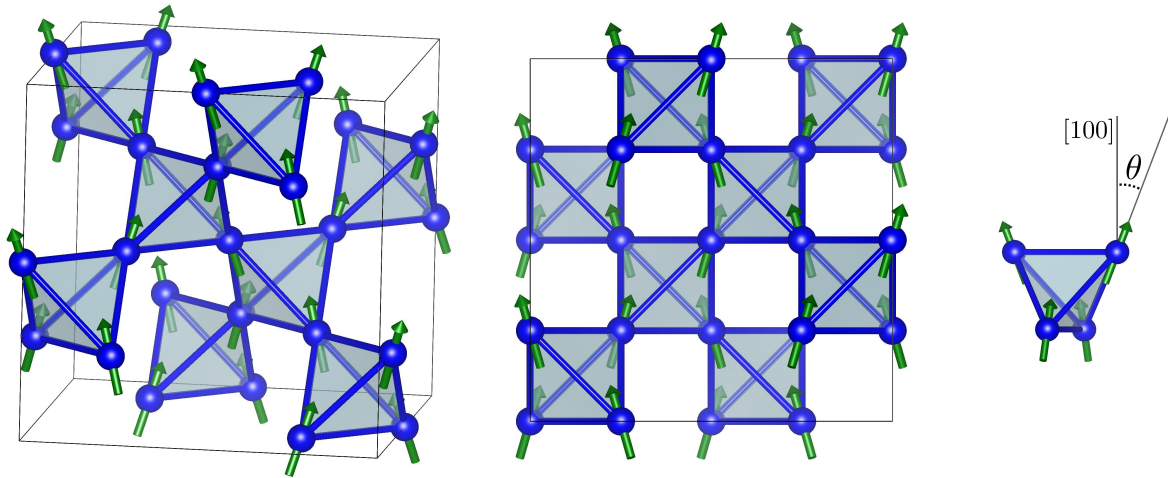


Figure 3.24 Splayed ferromagnetic ground state of $\text{Yb}_2\text{Ti}_2\text{O}_7$, showing a unit cell and one tetrahedron, with the splay angle θ indicated (not to scale).

For Yb^{3+} in $\text{Yb}_2\text{Ti}_2\text{O}_7$ the axial component, in the local $\langle 111 \rangle = \hat{z}$ direction, is $g_z = 2.14(3)$ and the planar component is $g_{\pm} = 4.17(2)$, so that planar anisotropy dominates [176]. This also means that the effective moment's magnitude is modified from its free ion value to $\mu_{\text{eff}} \approx 1.3(1)\mu_B$.

The energy gap to the first excited state is $76.7\text{meV} \sim 890\text{K}$, therefore at low temperature the effective spin-1/2 model with hamiltonian (3.52) or (3.54) is an excellent approximation to the low-temperature physics [177]. According to [175] for the exchange parameters in (3.55)

are

$$\begin{aligned}
J_1 &= -0.026(2)\text{meV} \\
J_2 &= -0.307(3)\text{meV} \\
J_3 &= -0.323(3)\text{meV} \\
J_4 &= +0.028(2)\text{meV}
\end{aligned}
\tag{3.57}$$

Using (3.56) we obtain the exchange parameters in the local coordinate frame,

$$\begin{aligned}
J_{zz} &= +0.094(4)\text{meV} \\
J_{\pm} &= +0.087(1)\text{meV} \\
J_{\pm\pm} &= -0.061(1)\text{meV} \\
J_{z\pm} &= -0.161(1)\text{meV}
\end{aligned}
\tag{3.58}$$

where we assumed that $J_1 - J_4$ are uncorrelated to calculate the uncertainties. Clearly the $J_{z\pm}$ transverse exchange is dominant and the other parameters are comparable in magnitude, a case far from the originally proposed quantum spin ice scenario, with $J_{zz} > 0$ and $J_{\pm} = J_{\pm\pm} = J_{z\pm} = 0$.

Phase competition has emerged as a useful model to explain many of the unusual properties of pyrochlores such as $\text{Yb}_2\text{Ti}_2\text{O}_7$, $\text{Er}_2\text{Ti}_2\text{O}_7$ and $\text{Er}_2\text{Sn}_2\text{O}_7$, which all belong to the Kramers effective spin-1/2 case. For these three compounds, as for various other pyrochlores, the parameters in (3.55) satisfy $J_3 < 0$ and $J_4 \approx 0$, so that we may construct a phase diagram by setting $J_4 = 0$ and choosing as axes J_1 and J_2 normalized by $|J_3|$. Figure 3.25 shows such a classical phase diagram for the anisotropic nearest-neighbor exchange hamiltonian (3.54). The labeled points are the best estimates from the values obtained by inelastic neutron scattering for $\text{Yb}_2\text{Ti}_2\text{O}_7$ [156], $\text{Er}_2\text{Ti}_2\text{O}_7$ [178] and $\text{Er}_2\text{Sn}_2\text{O}_7$ [179].

Figure 3.26 shows the phase diagram for the classical model with the quantum corrections produced by linear spin wave theory [140]. The white regions (not including the white circle) are those in which the quantum fluctuations destroy the classically ordered ground state. The effect is strongest close to the Heisenberg limit, $J_1/|J_3| = J_2/|J_3| \rightarrow \infty$ and close to the central region $J_1/|J_3| = J_2/|J_3| \rightarrow 0$, where classically a spin liquid state is expected. These predictions suggest that those regions might contain quantum spin liquid (QSL) phases, although the linear spin wave approximation cannot fully account for quantum fluctuations.

Even though $\text{Yb}_2\text{Ti}_2\text{O}_7$ is still predicted to lie in the ordered SFM phase, the effects of classical phase competition could significantly affect the quantum fluctuations of the ground state, due to the proximity to the boundaries with the AFM and QSL phases. The most recent and reliable values for the parameters $J_1 - J_4$, listed in (3.57), place the point corresponding to $\text{Yb}_2\text{Ti}_2\text{O}_7$ even closer to the AFM/FM boundary. It should be noted that in reality J_4 is not that close to zero, as was assumed when constructing the phase diagrams of Figures 3.25 and 3.26, and the nonzero J_4 slightly shifts the location of the boundary.

A signature feature of $\text{Yb}_2\text{Ti}_2\text{O}_7$ in its paramagnetic state are the rods that appear in the (111) directions of reciprocal space in neutron scattering experiments. The origin of these

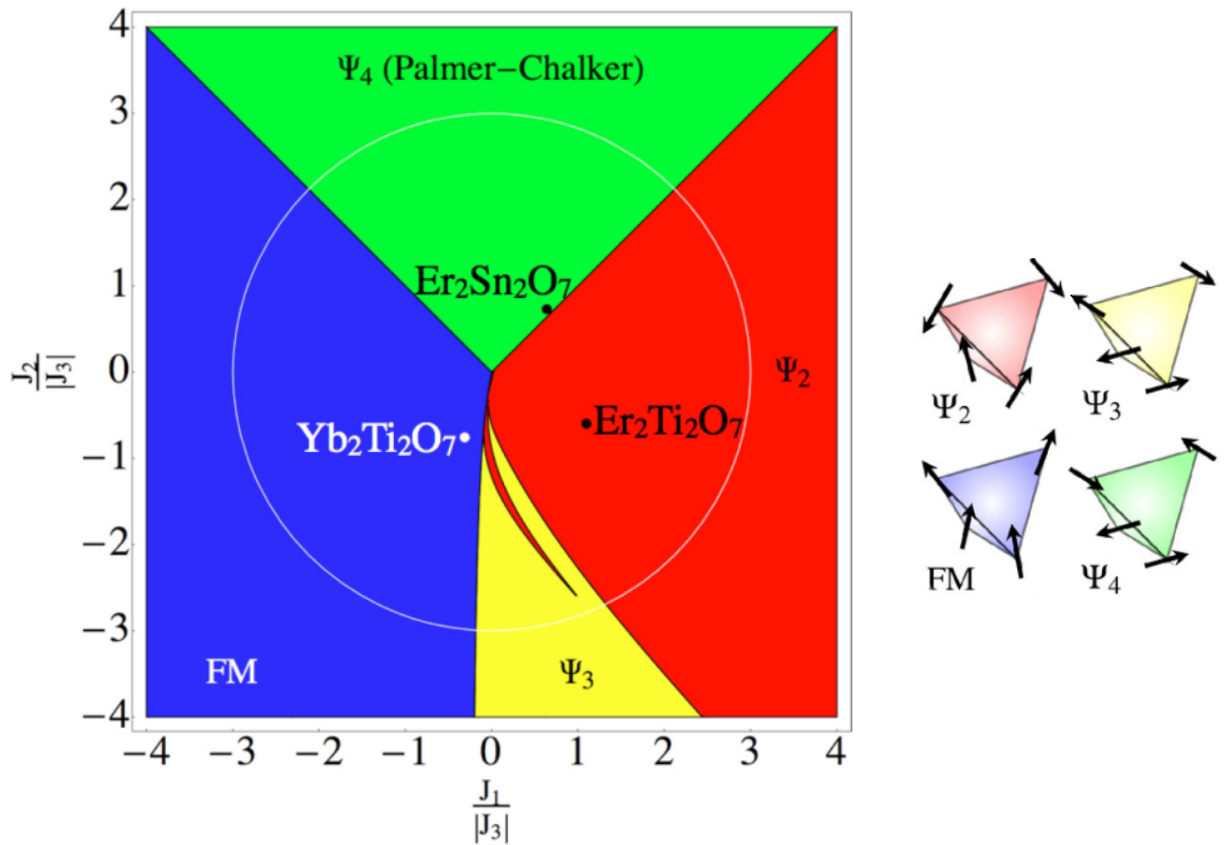


Figure 3.25 Classical phase diagram for the anisotropic nearest-neighbor exchange Hamiltonian (3.54) with $J_3 < 0$ and $J_4 = 0$ [140].

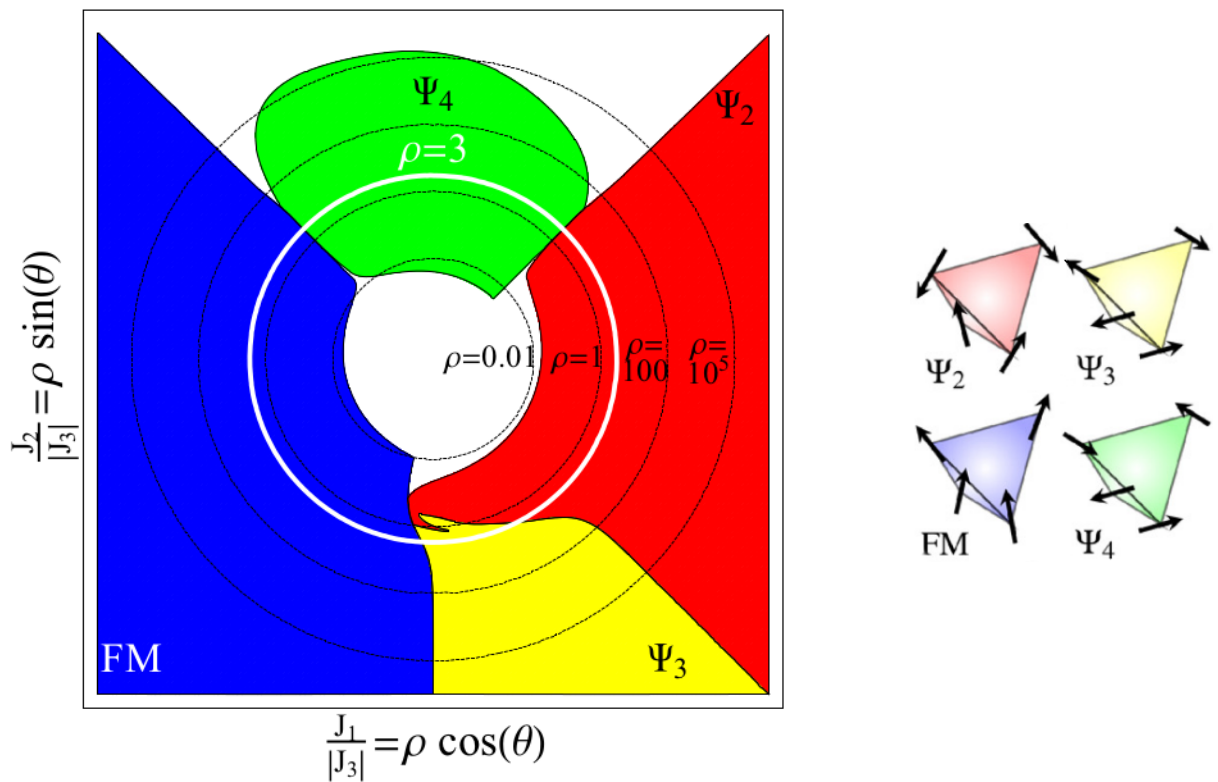


Figure 3.26 Quantum phase diagram for the anisotropic nearest-neighbor exchange Hamiltonian (3.54) with $J_3 < 0$ and $J_4 = 0$ [140].

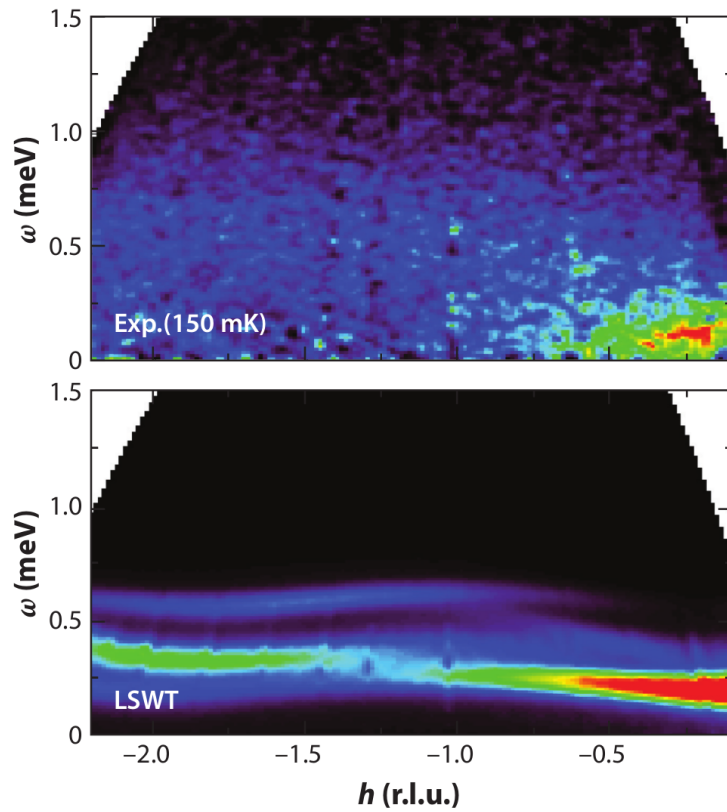


Figure 3.27 Linear spin wave prediction and the experimental spectrum for $\text{Yb}_2\text{Ti}_2\text{O}_7$ at $T = 150\text{mK}$ [176].

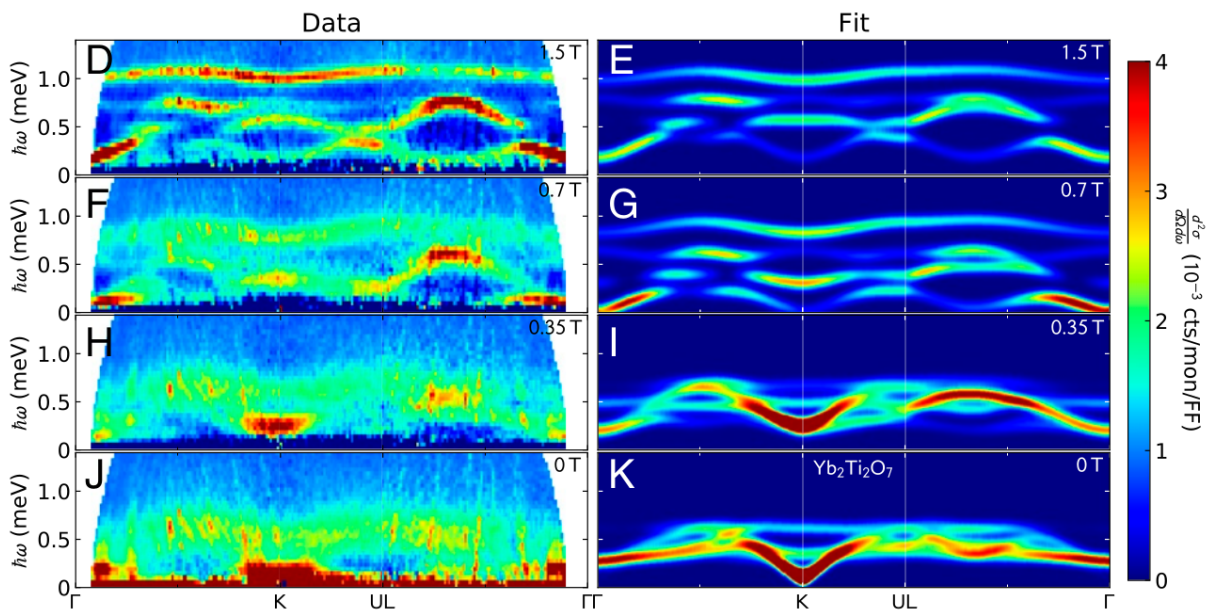


Figure 3.28 Measured neutron scattering data (left) and calculated cross-sections (right), for various applied magnetic field values [175].

striking rodlike features was considered somewhat mysterious for some time, but they are now understood to arise from the proximity to the ψ_2 , ψ_3 antiferromagnetic phases, representing a clear manifestation of the effects of multiphase competition [140, 180].

In [174] it is proposed that the magnetic scattering intensity at (220) in reciprocal space could serve as a 'smoking gun' for quantum mechanical effects in $\text{Yb}_2\text{Ti}_2\text{O}_7$, since it is perhaps the most distinguishing feature from the classical models to the experimental data. The spin wave gap at (220) goes to zero at the AFM/FM phase boundary, so that the size of the gap can be used to quantify the distance from the boundary.

The real mystery of $\text{Yb}_2\text{Ti}_2\text{O}_7$ lies in its spin dynamics. Due to the relatively large anisotropy in the exchange interactions there should be no gapless or nearly gapless excitations. One would expect a gapped magnon (a spin wave excitation) at about 0.2meV with a minimum near $\mathbf{k} = 0$, which is the ordering vector of the magnetic structure [176]. However actual measurements show a nearly gapless continuum of excitations, with no well-defined spin-wave modes. Figure 3.27 shows the clear difference between the linear spin wave prediction and the experimental spectrum for $\text{Yb}_2\text{Ti}_2\text{O}_7$ at $T = 150\text{mK}$.

The evolution of the excitation spectrum with magnetic field also poses an interesting puzzle. An applied field in the [100] cubic direction should preserve the symmetry of the SFM state but the excitation continuum evolves smoothly into the expected sharp spin-wave modes with increasing field, without any apparent phase transition.

A very thorough investigation is performed in [175], using elastic, inelastic and small angle neutron scattering and Monte Carlo simulations to bring light to these enigmatic properties of $\text{Yb}_2\text{Ti}_2\text{O}_7$. They find that indeed ferromagnetism and antiferromagnetism coexist in the ground state and that linear spin wave theory is able to represent most features of the experimental spectrum but not the significant broadening of excitations at low fields, as shown in Figure 3.28.

Based on the (220) Bragg intensity the volume fraction of the AFM phase is $< 10\%$, though other data indicate that AFM regions make up on the order of 43% of the sample. These are not inconsistent, since the AFM correlations could be highly localized in space or time, but the constraint set by elastic scattering rules out extended pockets of the AFM phase.

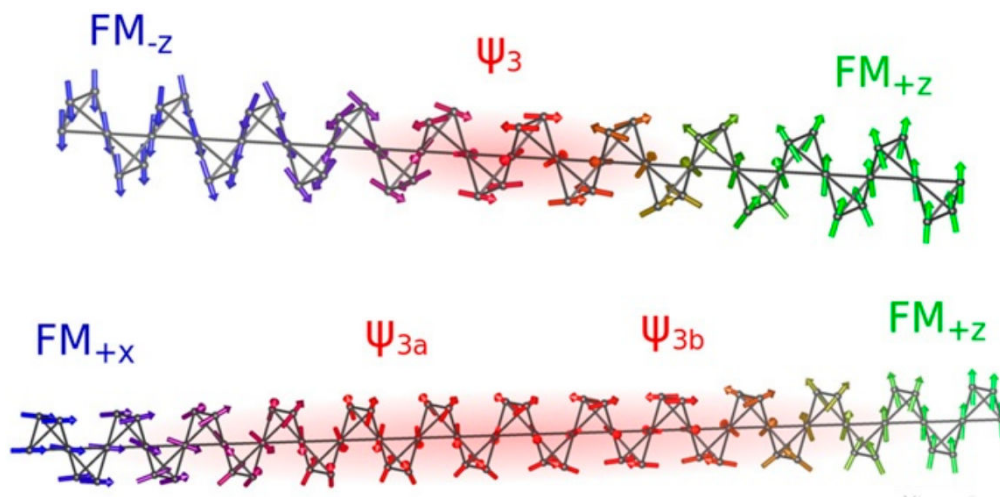


Figure 3.29 Differently oriented FM domains connected by domain walls with AFM character [175].

Small angle scattering was used to study the mesoscale spin correlations and indicates the existence of lamellar domains perpendicular to the [111] direction, with a correlation length of 62(6)nm. The onset of these correlations occurs at $T \approx 270\text{mK}$, so they are clearly associated to the magnetic ordering, but no periodic structures in the 10nm – 100nm range exist. The authors propose that domain walls between differently oriented FM domains could have AFM character, as illustrated in Figure 3.29, which would be consistent with the short-range nature of the AFM correlations. It is speculated that these domain walls are stabilized by the influence of dipolar interactions, which were neglected in the Monte Carlo simulations.

Currently there are still some poorly understood properties of $\text{Yb}_2\text{Ti}_2\text{O}_7$, such as the dynamics in the temperature range $0.27\text{K} < T < 2\text{K}$, where a short-range correlated magnetic phase exists. The broad anomaly in the heat capacity at $T \approx 2\text{K}$ (Figure 3.23) is associated with the transition from the high-temperature paramagnetic phase to the intermediary short-range correlated phase. This broad transition is not a Schottky-type anomaly associated to crystalline electric field levels, since the first excited state is at $\approx 890\text{K}$, but rather associated to FM/AFM phase competition, although a microscopic explanation for its exact shape has yet to be proposed.

In [181] it was found that in the intermediate-temperature correlated phase the spin correlations obey a dynamical scaling law reminiscent of those observed in quantum critical systems. The diffuse rods of scattering in the (111) directions of reciprocal space signal the existence of structured spin correlations that arise due to the proximity to the AFM phase, however their energy dependence is still an open issue. The authors used inelastic neutron scattering, with exceptionally high energy resolution, to explore the dependence of (111) scattering intensity S_{111} on the energy transfer $\hbar\omega$ and found that a scaling law was obeyed, similar to those observed for states near to a quantum critical point of a material's phase diagram,

$$k_B T S_{111}(\hbar\omega) = f\left(\frac{\hbar\omega}{k_B T}\right) \quad (3.59)$$

where f is a scaling function. The authors speculate that multiphase competition has universal consequences on the finite-temperature dynamics that are independent of the specific system's microscopic hamiltonian. Perhaps there is a mechanism, such as quantum fluctuations preferring entropic states, that drives the $\text{Yb}_2\text{Ti}_2\text{O}_7$ system to the AFM/FM phase boundary or QSL critical point [180, 175]. Thus both the static and dynamical properties of $\text{Yb}_2\text{Ti}_2\text{O}_7$ yield insights that might be more generally applicable to a variety of systems that exhibit multiphase competition.

Synthesis

In this chapter we describe the $\text{Yb}_2\text{Zr}_x\text{Ti}_{2-x}\text{O}_7$ sample preparation using two synthesis methods, the solid-state reaction and the sol-gel method, and discuss the advantages and shortcomings of each method. We also present and discuss the results of scanning electron microscopy performed on a few of the $\text{Yb}_2\text{Zr}_x\text{Ti}_{2-x}\text{O}_7$ samples.

4.1 Solid-state reaction

The solid-state reaction is a common synthesis method for many ceramic and oxide materials [182, 183, 184]. It is based on the simple idea of mixing powder reactants, compressing this mixture and firing at high temperature to yield the desired product, as represented schematically in Figure 4.1.

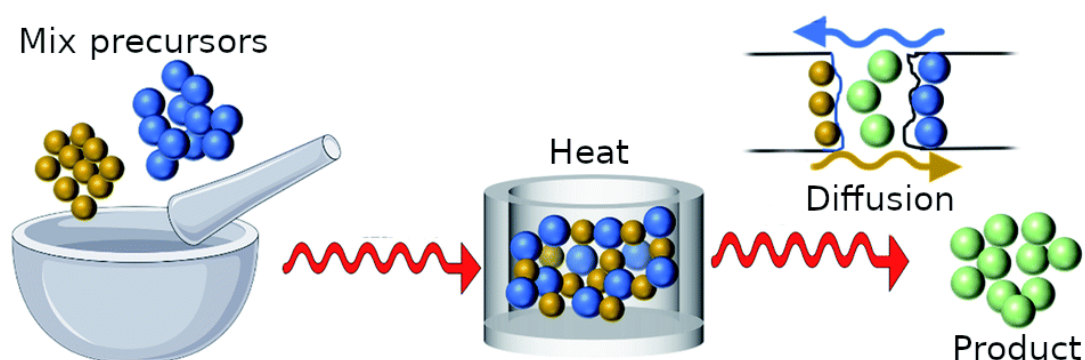


Figure 4.1 Schematic representation of the solid-state reaction method, adapted from [185].

While compared to other methods the reaction conditions for the solid-state synthesis are simpler to implement, it also has some drawbacks that can lead to phase separation or stoichiometric heterogeneity. Contrary to chemical reactions in fluid phases, which proceed homogeneously, solid-state reactions only occur at the contact interface between powder particles and progress

by mass diffusion over these boundaries, so that overall reaction rates are determined by the mobility and permeability of the boundaries between the powder grains.

When mixing two or more powders it can be difficult to achieve a sufficiently homogeneous mixture and atomic-level mixing is impossible. Since the reaction takes place at contact points between adjacent particles and conversion of the precursors to the intended product is limited by mass transport, if diffusion is hindered there can be areas of unreacted starting material.

Some of these issues can be overcome by mechanical milling, which mixes the precursors more uniformly and reduces their particle size, thus increasing the surface area for the reaction. However such processes are impractical for producing small amounts of material and extended sintering with intermittent grinding steps may still be required to achieve a satisfactory result. As far from equilibrium techniques mechanochemical methods frequently lead to highly defective phases, which may be uncommon or inaccessible through more conventional processing methods. They have become very popular in many areas of materials science [186, 187, 188].

The ways by which atoms or ions are transferred in a solid-state reaction can be classified as vaporization-condensation, surface diffusion, bulk diffusion, grain boundary diffusion, viscous flow and creep flow. Intrinsic factors that significantly affect reaction rates are particle sizes, morphologies, surface and point defects, crystal lattice irregularities and the crystallinity index. Extrinsic parameters such as pressure, mechano-acoustic vibration, atmosphere composition, electric fields, magnetic fields and irradiation can also be leveraged to control the reaction. Due to this variety of possible intrinsic and extrinsic factors actual solid state reaction processes are very complicated, but their equilibria can be modeled using simple principles of chemical thermodynamics. This leads to expressions for reaction rates as functions of activation energies, free energy differences, diffusion constants and the surface contact area between powder particles [182, 183, 184].

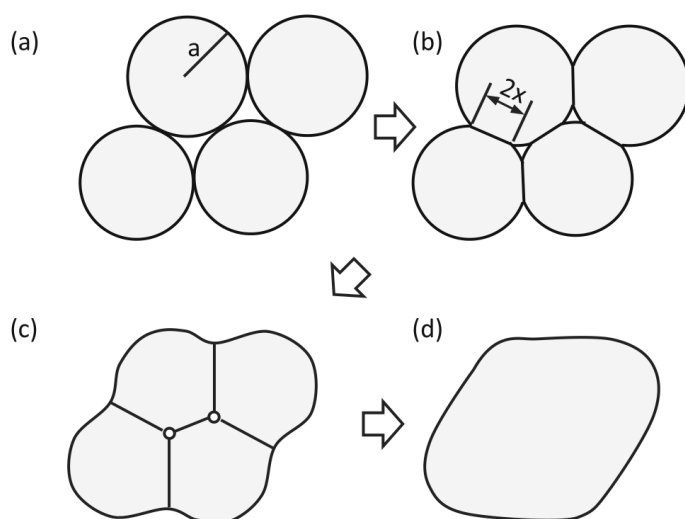


Figure 4.2 Schematic depiction of the sintering process [182].

The sintering at high temperature may involve a change in chemical composition or a structural phase transformation, which often is not reversible when subsequently lowering the temperature. The final polycrystalline material is composed of agglomerated crystalline grains with different crystal orientations and a wide range of sizes. The grain size distribution often has

an upper limit, with a long tail of smaller grains and can even be bimodal. If sintering is not complete then microscopic pores will be present in the resulting material, shown schematically in Figure 4.2 [182]. The packing fraction is the ratio between the measured density of a powder sample and the theoretical maximal density based on the unit cell parameters measured by x-ray diffraction (Chapter 5). When unknown, the packing fraction for a powder is often assumed to be on the order of 0.6 [189].

4.1.1 Procedure

The chemical reaction in the solid-state synthesis of $\text{Yb}_2\text{Zr}_x\text{Ti}_{2-x}\text{O}_7$ is described by



The required materials are

- Ytterbium oxide: Yb_2O_3
- Titanium oxide: TiO_2
- Zirconium oxide: ZrO_2
- Ethanol (99%): $\text{C}_2\text{H}_6\text{O}$

Lanthanide sesquioxides (Ln_2O_3) are often highly reactive with atmospheric CO_2 and H_2O , therefore it is recommended to fire the precursor oxides at a temperature of 600°C – 900°C to decompose any carbonates, oxycarbonates or hydroxides that may have formed and evaporate moisture absorbed by the powders from the atmosphere. The presence of these functional groups would not be a problem in itself because the high temperatures employed during synthesis will drive them off, but the proper stoichiometry of the synthesized compounds could be affected if the contamination is significant enough to alter the weighed masses of the precursors.



Figure 4.3 ZrO_2 before (left) and after (right) being dried in an oven at 700°C for 12h.

In our laboratory all precursors are kept tightly sealed to minimize moisture absorption and the precursors were fired at 700°C prior to the synthesis of the $\text{Yb}_2\text{Zr}_x\text{Ti}_{2-x}\text{O}_7$ samples. The

ZrO₂ powder suffered a dramatic color change after this heat treatment, changing from a dark brown color to a light beige, as shown in Figure 4.3. We do not know what caused this color change, probably reaction products of ZrO₂ with atmospheric gases that were present in the initially dark powder. We used x-ray diffraction and Raman spectroscopy to confirm the purity of the precursors (Sections 5.3 and 6.3).

Stoichiometric quantities of these precursors were weighed using an analytical balance and thoroughly mixed in an agate mortar with a small amount of ethanol (Figure 4.4). The ethanol facilitates the mixing of the powders as a paste, leading to a more homogeneous mixture. After grinding this paste for 5 minutes we waited for about 30 minutes until the ethanol had evaporated, ground the dried crust into a powder once more and carefully scraped all the powder from the mortar and pestle.

The powder samples were compressed using a hydraulic bench press to form cylindrical pellets (Figures 4.5 and 4.6). These pellets were sintered at a temperature of 1200°C or 1500°C with hold times ranging from 3h to 96h. The heat treatments were done in standard atmosphere by an oven with a heating rate of 10°C/min and cooling rate of 3°C/min (Figure 4.7). After each sintering step the pelletized samples were ground in a mortar and the final powdered samples were conserved in sealed Eppendorf tubes inside a desiccator.



Figure 4.4 Paste formed by mixing precursor oxides with ethanol.



Figure 4.5 Pellet formed by pressing powder sample (left) and alumina crucible used as container during calcination (right).



Figure 4.6 Hydraulic bench press (left) and metal die set (right).

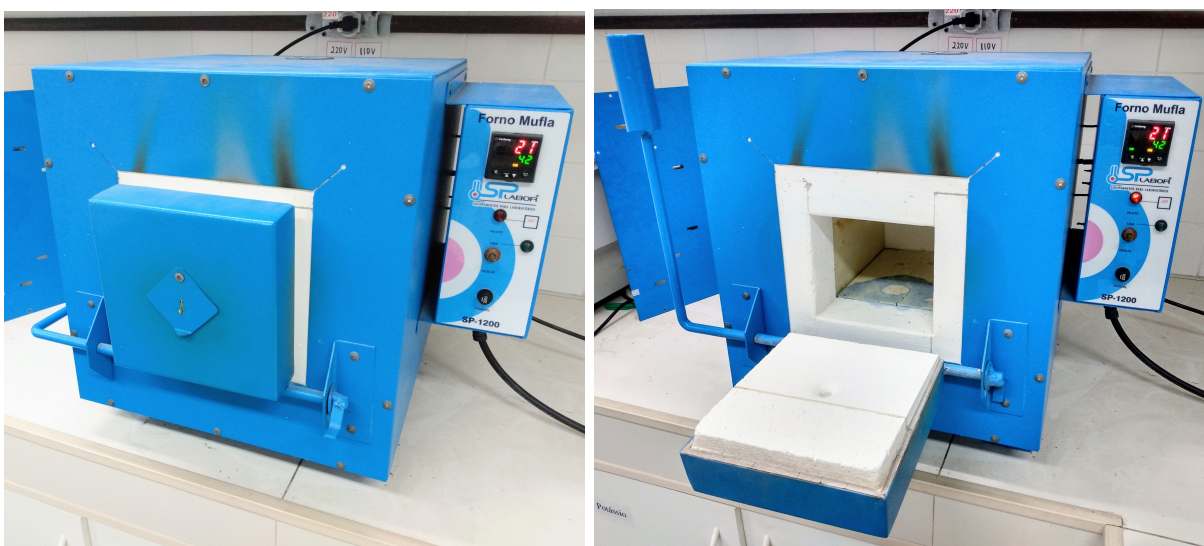


Figure 4.7 Muffa SP-1200 oven, used to calcine the $\text{Yb}_2\text{Zr}_x\text{Ti}_{2-x}\text{O}_7$ samples.

4.2 Sol-gel synthesis

To address some of the challenges of the solid-state method, many solution-based wet-chemical synthesis methods have evolved, such as coprecipitation, hydrothermal processing, solvothermal methods and sol-gel chemistry. Among these somewhat overlapping categories we focus on sol-gel chemistry, which can be broadly defined as the synthesis of solid materials such as metal oxides from solution-state precursors. This includes a diverse range of chemical reactions such as crosslinking metal alkoxides to form metal-oxane gels, metal ion-chelate complexes and organic polymer gels containing metal species [190, 191].

The sol-gel method consists in the preparation of inorganic polymers or ceramics from a liquid solution (sol) into a viscous networked structure (gel), which is then heated or otherwise processed to obtain the solid product, as represented schematically in Figure 4.8. The choice of precursors and reaction method is important since they may affect the chemical composition and physical structure of the resulting materials.

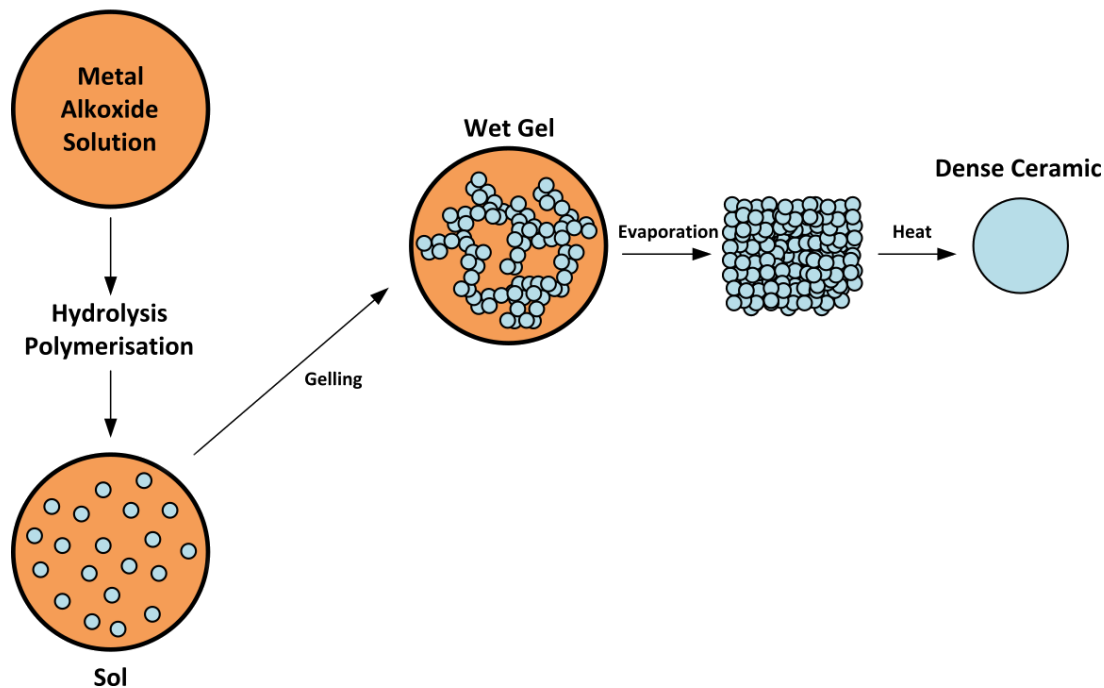


Figure 4.8 Schematic representation of the sol-gel reaction method, adapted from [192].

According to [190] the sol-gel process can be summarized in the following steps:

1. Synthesis of the sol from hydrolysis and partial condensation of alkoxides.
2. Formation of the gel via polycondensation to form metal-oxo-metal or metal-hydroxy-metal bonds.
3. Syneresis or aging, where condensation continues within the gel network with the expulsion of solvent.
4. Drying of the gel to form a dense xerogel or aerogel.
5. Removal of surface M-OH groups through calcination at temperatures up to 800°C.

By trapping the molecular randomness of the liquid solution state into a gel, atomic level mixing of the reagents is ensured and the resulting samples usually are more homogeneous than those produced by the solid-state reaction. The improved atomic-level mixing also means that the sol-gel method requires lower temperatures and shorter processing times than the solid-state method. Furthermore, this type of chemistry enables greater control over particle morphology and size. A homogeneous precursor solution does not necessarily ensure homogeneity of the resulting gel, therefore many of the proposed reaction routes have been designed to combat or control phase segregation during the synthesis [190].

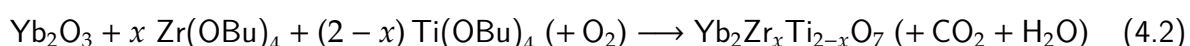
Conversion of the gel into a metal oxide is achieved by pyrolysis at a system-dependent temperature, most commonly under an air atmosphere. Typically the organic components of the gel undergo combustion at temperatures between 300°C and 400°C. This procedure can be used to produce crystalline and amorphous forms of metal oxides. When a crystalline form is produced the presence of the organic matrix ensures an even distribution of the nucleation sites, usually leading to small crystallites. Even when the system only crystallizes at higher temperatures (700°C or more) the homogeneity of the precursor gel ensures a good mixture of the metal oxides in the intermediary amorphous phase, after combustion of the organic components. This is one of the key advantages of the sol-gel method, especially important when synthesizing compounds with three or more metal oxides, in which small impurities or structural irregularities can significantly affect the properties of the end product [191].

Some factors that can affect the structural properties of the metal oxide end product are the mechanical mixing of the solution and gel, the rate of solvent evaporation during gelation and the temperature and timing of the heat treatments. The latter is important for drying the gel, removing surface hydroxyl groups and densifying the structure to become a polycrystalline ceramic or crystalline material. In many sol-gel reactions the outgassing due to thermal decomposition of organic precursors leads to porous solids with a foam-like microstructure.

One of the most common sol-gel synthesis routes uses citric acid, which is readily available, cheap and effective as a chelating agent. The citric acid sol-gel method, also known as citrate sol-gel method, is the one used in this work. In a typical synthesis aqueous metal salts, usually nitrates, are mixed with citric acid and the resulting solution heated to form a viscous gel. The metal nitrates serve as oxidizers for the organic citric acid fuel in the pyrolysis step. The procedural details of our method were based on the synthesis of $Y_2Ti_2O_7$ in [193], as described in Section 4.2.1.

4.2.1 Procedure

In the sol-gel synthesis of $Yb_2Zr_xTi_{2-x}O_7$ the chemical reaction is described by



where Bu stands for butyl, an organic group with chemical formula C_4H_9 . The required materials are

- Ytterbium oxide: Yb_2O_3
- Titanium n-butoxide: $Ti(OBu)_4$

- Zirconium n-butoxide: $\text{Zr}(\text{OBu})_4$
- Nitric acid (concentrated, 65%): HNO_3
- Citric acid (monohydrate, 99%): $\text{C}_6\text{H}_8\text{O}_7$
- Ethanol (99%): $\text{C}_2\text{H}_6\text{O}$
- Water (deionized): H_2O

Ytterbium oxide was dispersed in few drops of water and then concentrated nitric acid was added dropwise to dissolve the oxide, under magnetic agitation. The reaction of the oxide with the nitric acid creates the corresponding nitrate, $\text{Yb}(\text{NO}_3)_3$, which is commonly used as the Yb precursor in this type of reaction. The solution was gently heated to about 70°C in order to assist the reaction of the oxide with the nitric acid. An excess of approximately 20ml of concentrated nitric acid per gram of oxide was used, given that the nitric acid excess readily evaporates.

In parallel, a solution of citric acid in ethanol was prepared, with approximately 5ml of ethanol per gram of citric acid. The molar amounts n_{CA} , n_{Ti} and n_{Zr} of citric acid, titanium and zirconium precursors should satisfy $n_{\text{CA}} = 2.5(n_{\text{Ti}} + n_{\text{Zr}})$. This solution was also stirred for about 1h, until all the citric acid had dissolved in the ethanol. Then the appropriate amounts of titanium and/or zirconium butoxides were slowly added using a pipette, while still under vigorous magnetic agitation. The butoxides, especially the zirconium one, tend to form a precipitate when mixed into the solution, which can stick to the sides of the container. After mixing in the butoxides the solution was stirred for about 30m, until most of the precipitate had dissolved.

The two solutions, one containing the Yb precursor and the other one containing the Zr/Ti precursors, were combined in a beaker that was placed in an oil bath on top of a hot plate. The combined solution was heated and kept at 80°C by the oil bath, under constant magnetic stirring and inside a fume hood (Figure 4.9).



Figure 4.9 Beaker with solution set inside an oil container that functions as a heat bath.



Figure 4.10 Solution in the oil bath, before (left), during profuse bubbling (middle) and after release of the gas (right).

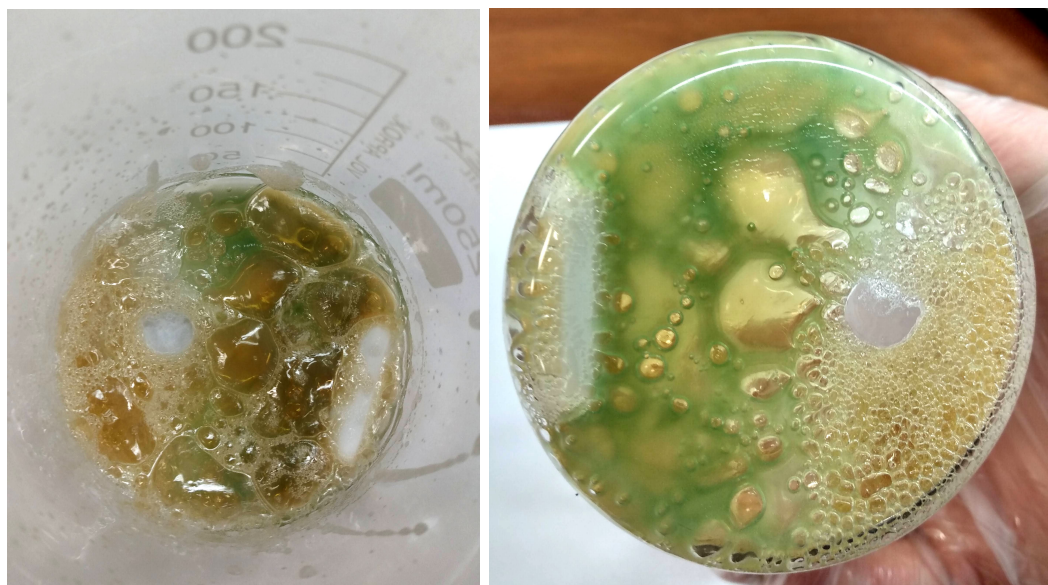


Figure 4.11 Yellowish-green gel formed after drying the solution, viewed from above (left) and below (right).

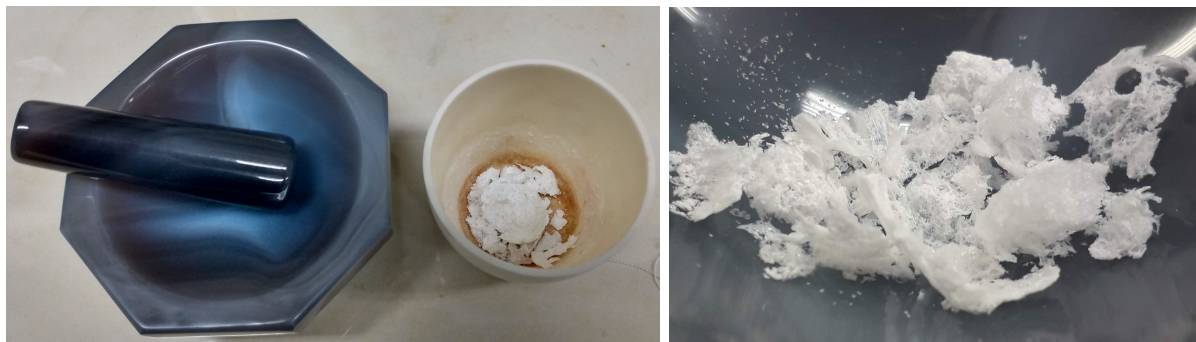


Figure 4.12 White crust formed after firing the gel at 700°C.

While reacting at 80°C the solution slowly releases excess solvents and after some time increases in temperature due to the exothermic nature of the reaction. At a certain point the temperature spikes and a noxious dark red gas is released, mostly NO₂. At this point the solution can bubble profusely (Figure 4.10) and it is advisable to remove the container from the heat bath until bubbling subsides.

After about 12h in the heat bath at 80°C the solution dried to form a xerogel, with the appearance of a yellowish-green glassy resin (Figure 4.11). This gel was scraped from the beaker into an alumina crucible and fired at 700°C for 3h. This resulted in a white crust (Figure 4.12), which was then ground into a powder using an agate mortar.

The powder samples were compressed using a hydraulic bench press to form cylindrical pellets (Figures 4.5 and 4.6). These pellets were placed in alumina crucibles and sintered at temperatures ranging from 900°C to 1500°C, with hold times ranging from 24h to 60h. The heat treatments were done in standard atmosphere by an oven with a heating rate of 10°C/min and cooling rate of 3°C/min. After sintering the pelletized samples were ground in an agate mortar and the resulting powdered samples were conserved in sealed Eppendorf containers inside a desiccator.

4.3 Yb₂Zr_xTi_{2-x}O₇ Samples

Table 4.1 shows the sintering time and temperature for all samples of Yb₂Zr_xTi_{2-x}O₇ we produced, through sol-gel (SG) and solid-state (SS) routes. The SG samples were sintered at successively higher temperatures, while SS samples were mostly sintered at only one temperature (1500°C). In each section of Table 4.1 the sintering steps are listed in chronological order. In between each sintering step x-ray diffraction was used to determine the structure of the samples.

	700°C	900°C	1000°C	1100°C	1200°C	1500°C
SG $x = 0.0, 0.15, 0.3$	3h					
		48h				
			48h			
				48h		
					60h	
						40h
SG $x = 0.5, 1.0$	24h					
		24h				
					60h	
						40h
SG $x = 1.5, 2.0$	24h					
		24h				
					60h	
						3h
						40h
SS $x = 0.0$						10h
						40h
SS $x = 0.5, 1.0, 1.5, 2.0$						10h
						40h
						35h
					36h	

Table 4.1 Sintering time and temperature for all samples of $\text{Yb}_2\text{Zr}_x\text{Ti}_{2-x}\text{O}_7$ produced in this work (SG = sol-gel, SS = solid-state). In each section the sintering steps are listed in chronological order.

4.4 Microscopy

A scanning electron microscope (SEM) is a type of electron microscope that uses a focused electron beam to produce images of a sample. The beam is scanned over the surface of the sample and the electrons scattered by the material are detected and used to produce an image, where the shade of each pixel represents the intensity of scattered electrons while the beam was focused on the corresponding position of the sample's surface. The maximal resolution of the SEM can be as small as a few nanometers, depending on the focusing characteristics of the electron beam and other variables, but the magnification range is usually very wide. Due to the narrow electron beam SEM micrographs have a large depth of field, making them very useful to analyze surface topography of many kinds of specimens [194].

The sample must be able to withstand high vacuum conditions, since in conventional SEMs the sample stage is evacuated to avoid scattering of the electrons by the atmosphere surrounding the sample. The samples should also be somewhat conductive to allow an outflow of the impinging electrons, otherwise charge may accumulate at the imaged spot and affect the focusing of the beam. Samples are generally mounted using some type of conductive adhesive to provide electric grounding and non-conductive specimens are often covered with a very thin layer of conductive material by sputter coating or high-vacuum evaporation.

We used a JEOL JSM-6010LA SEM (Figure 4.13), located at the Nuclear and Energy Research Institute (IPEN). The measurements were performed by Dr. Dimy Nanclares Fernandes Sanches, a researcher at the Federal University of ABC (UFABC). The accelerating voltage was varied between 5keV and 20keV. A small amount of powder was deposited on a piece of double sided carbon tape that was glued onto one of the stubs shown in Figure 4.13.

Unfortunately we could not image all of the samples that were synthesized, since we only were granted access to the SEM instrument for one day. Figures 4.14 to 4.16 show some representative images of the $\text{Yb}_2\text{Zr}_x\text{Ti}_{2-x}\text{O}_7$ samples with $x = 1.5$, sintered at 1500°C , and with $x = 2.0$, sintered at 900°C , 1500°C .



Figure 4.13 JEOL JSM-6010LA SEM (left) and stubs used to mount the samples (right).

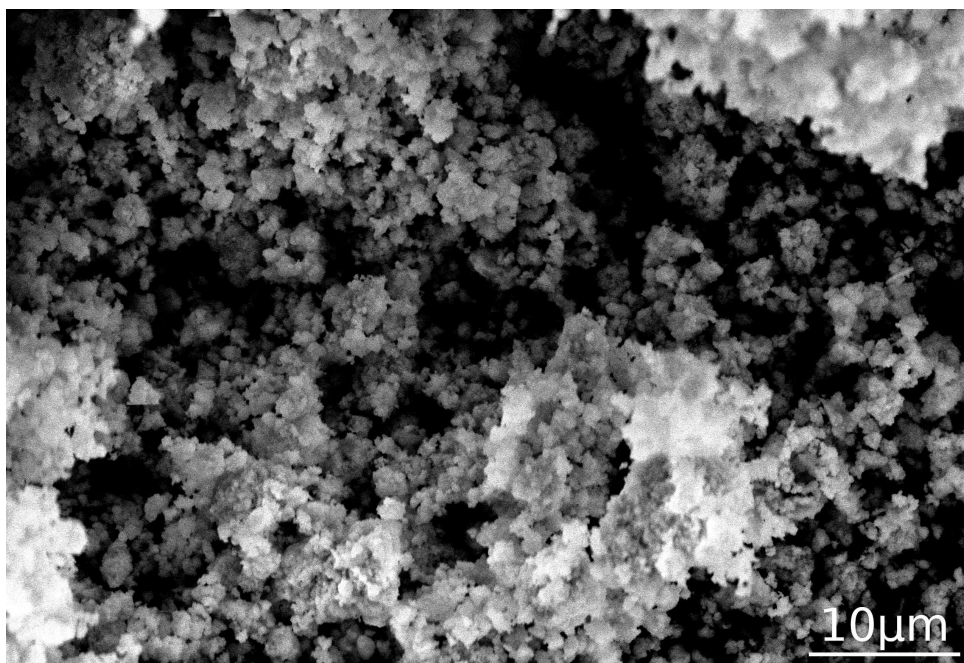
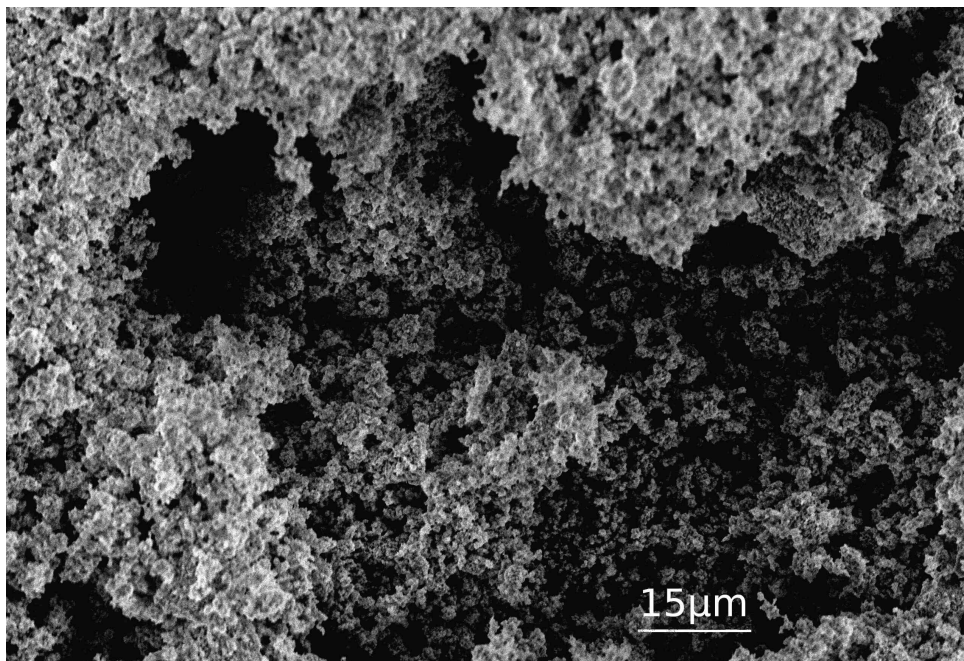


Figure 4.14 SEM images of the SG sample $\text{Yb}_2\text{Zr}_x\text{Ti}_{2-x}\text{O}_7$, $x = 1.5$, sintered at 1500°C for 3h.

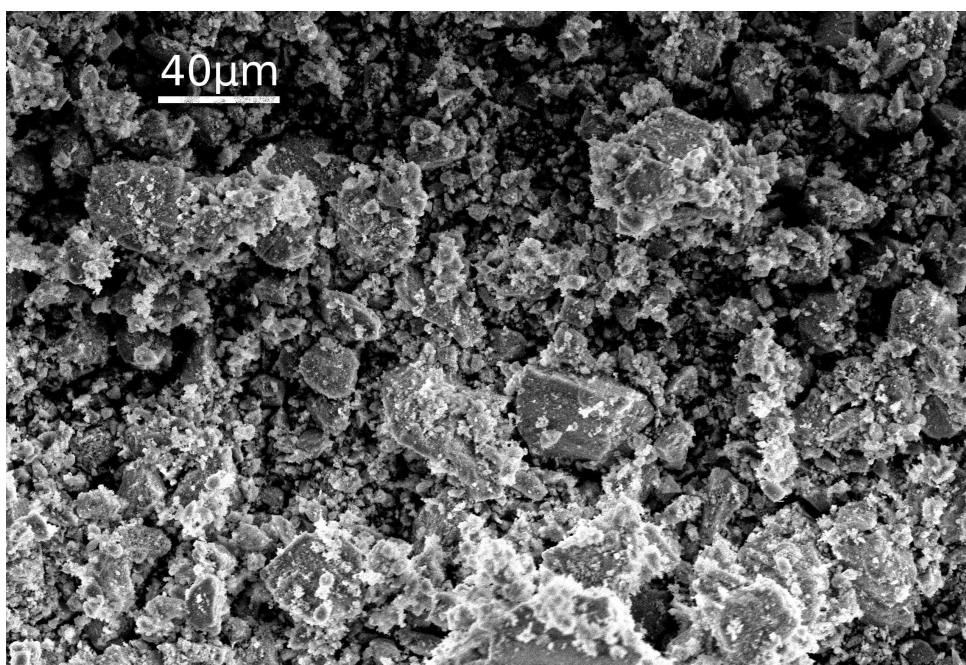
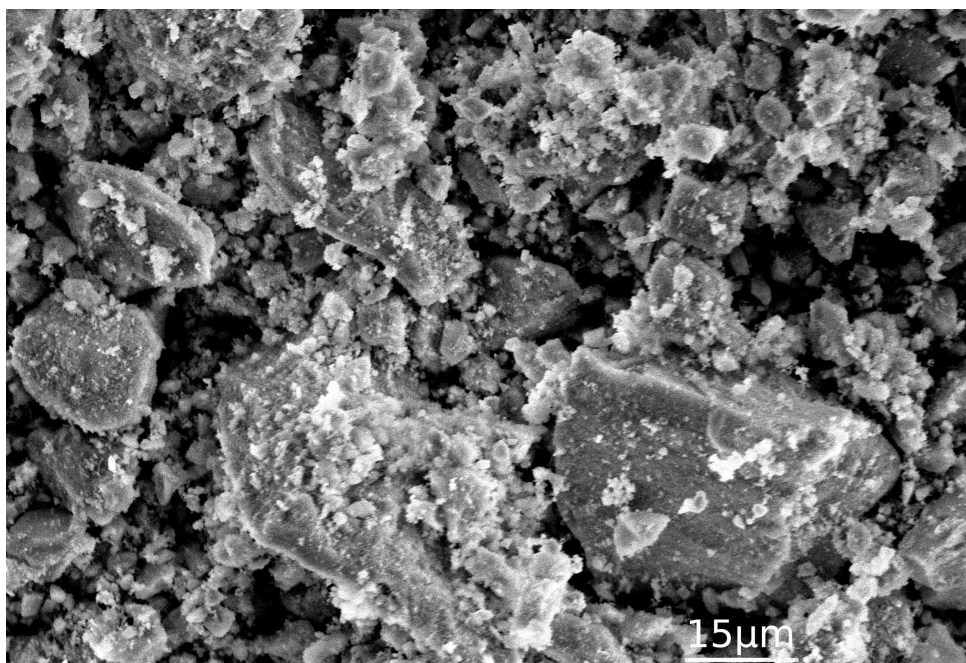


Figure 4.15 SEM images of the SG sample $\text{Yb}_2\text{Zr}_x\text{Ti}_{2-x}\text{O}_7$, $x = 2.0$, sintered at 900°C for 24h.

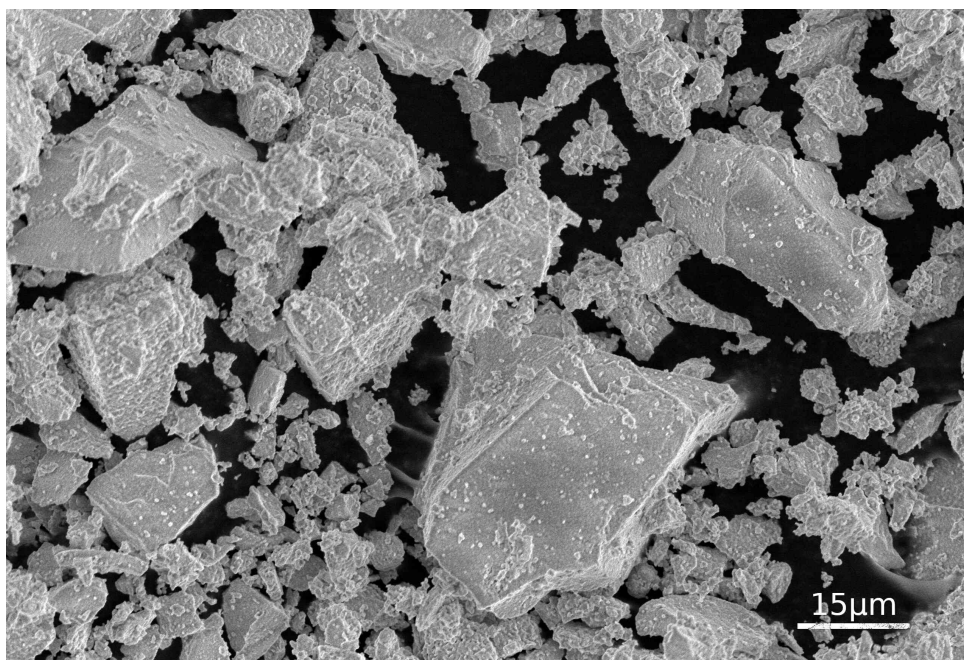
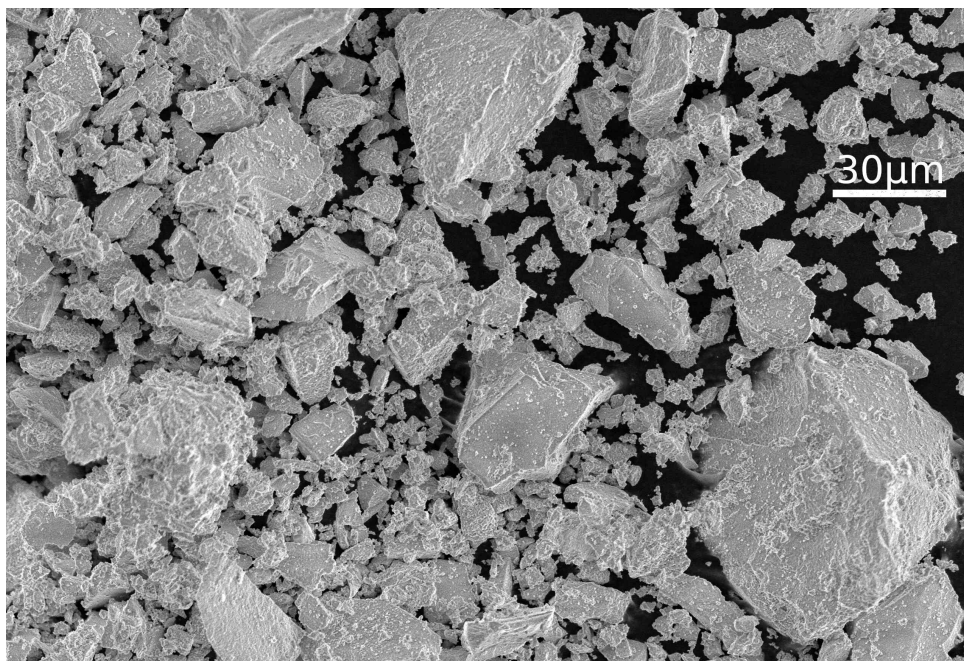


Figure 4.16 SEM images of the SG sample $\text{Yb}_2\text{Zr}_x\text{Ti}_{2-x}\text{O}_7$, $x = 2.0$, sintered at 1500°C for 3h.

The images above show clear morphological differences between the samples, both between samples with the same composition ($x = 2.0$) sintered at different temperature (900°C , 1500°C , in Figures 4.15 and 4.16) and between samples with the same sintering temperature (1500°C) and different compositions ($x = 1.5$, $x = 2.0$, in Figures 4.14 and 4.16). It is hard to draw any systematic conclusions about how composition and sintering temperature affect morphology due to the small number of samples that were imaged. It appears that the sample $\text{Yb}_2\text{Zr}_x\text{Ti}_{2-x}\text{O}_7$, $x = 1.5$, has a more regular foam-like morphology, with little structure at a scale of tens of micrometer or more. This could be related to the difficulty of accommodating the differently sized cations Ti^{4+} and Zr^{4+} in the crystal structure. The samples $\text{Yb}_2\text{Zr}_x\text{Ti}_{2-x}\text{O}_7$, $x = 2.0$, clearly have more structure at the tens of micrometer scale, with a few large grains on the order of $50\mu\text{m}$. Comparing the samples sintered at 900°C and 1500°C , it seems that the latter has a reduced amount of tiny foam-like grains than the former, possibly having been absorbed into the larger more uniform grains.

4.4.1 Energy-Dispersive Spectroscopy

Energy-dispersive x-ray spectroscopy (EDS) is a technique used to determine the elemental composition of a sample by analyzing the characteristic x-rays emitted by elements in the sample. This technique is often integrated into electron microscopes, since it only requires the addition of an energy-dispersive x-ray detector to the instrument. When the electron beam stimulates a specimen some atoms will lose their core electrons, leaving behind a hole in the core shell that contained the ejected electron. When a higher-energy electron from an outer shell fills the hole the energy difference between the outer and inner levels is given off as an x-ray photon. The energy of the x-ray is specific to the electronic structure of the element that emitted it and therefore can be used to determine the element.

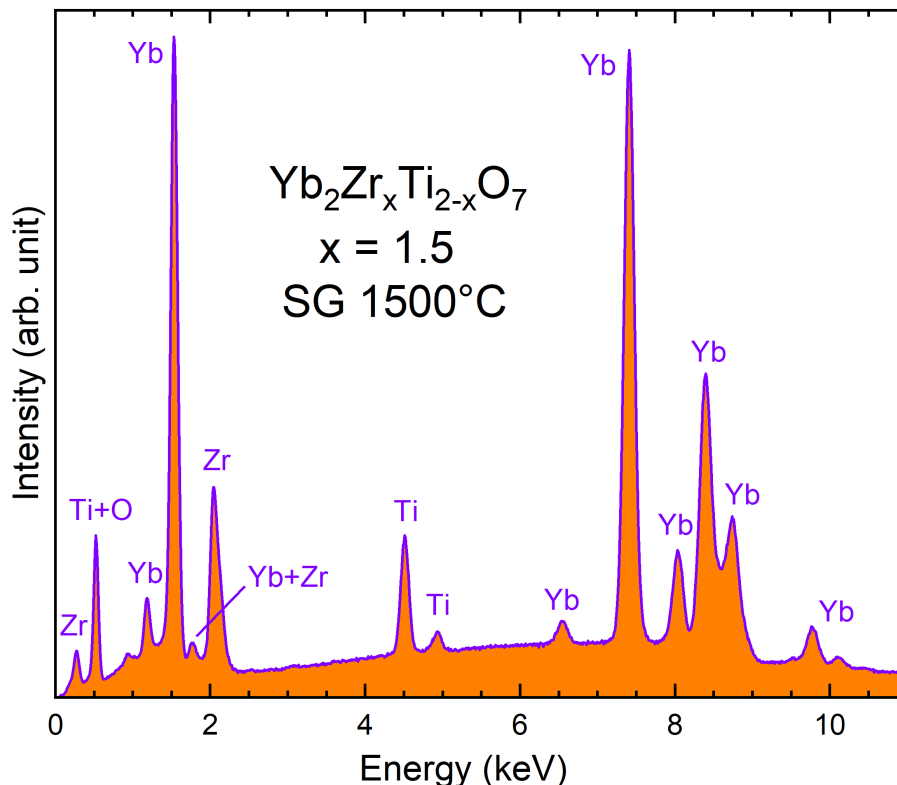


Figure 4.17 EDS spectrum for the sample $\text{Yb}_2\text{Zr}_x\text{Ti}_{2-x}\text{O}_7$, $x = 1.5$, sintered at 1500°C for 3h.

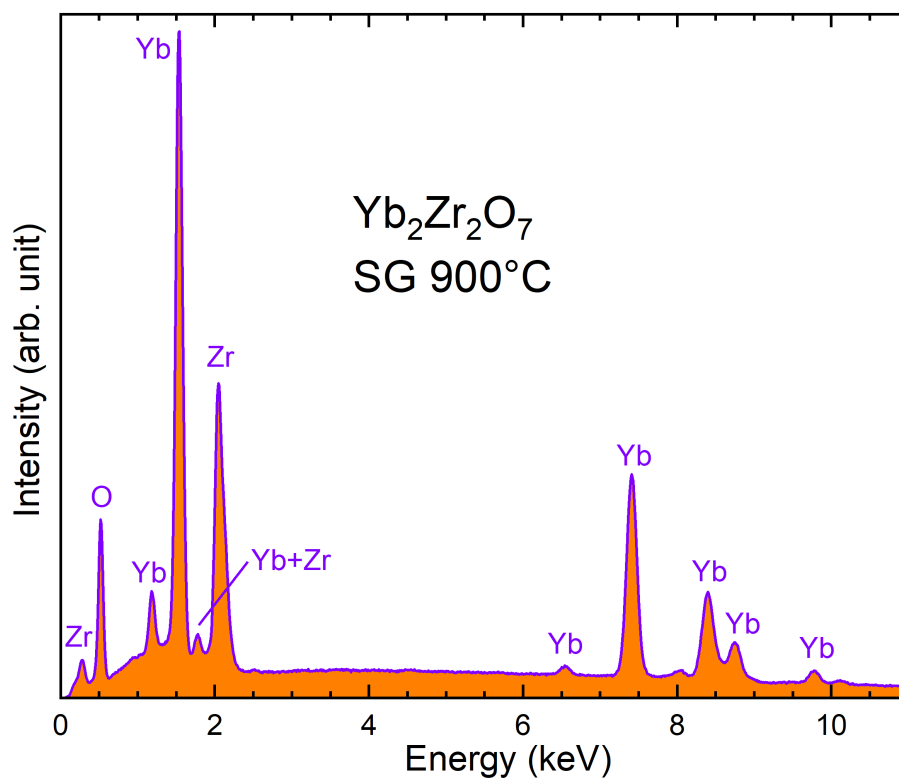


Figure 4.18 EDS spectrum for the sample $\text{Yb}_2\text{Zr}_x\text{Ti}_{2-x}\text{O}_7$, $x = 2.0$, sintered at 900°C for 24h.

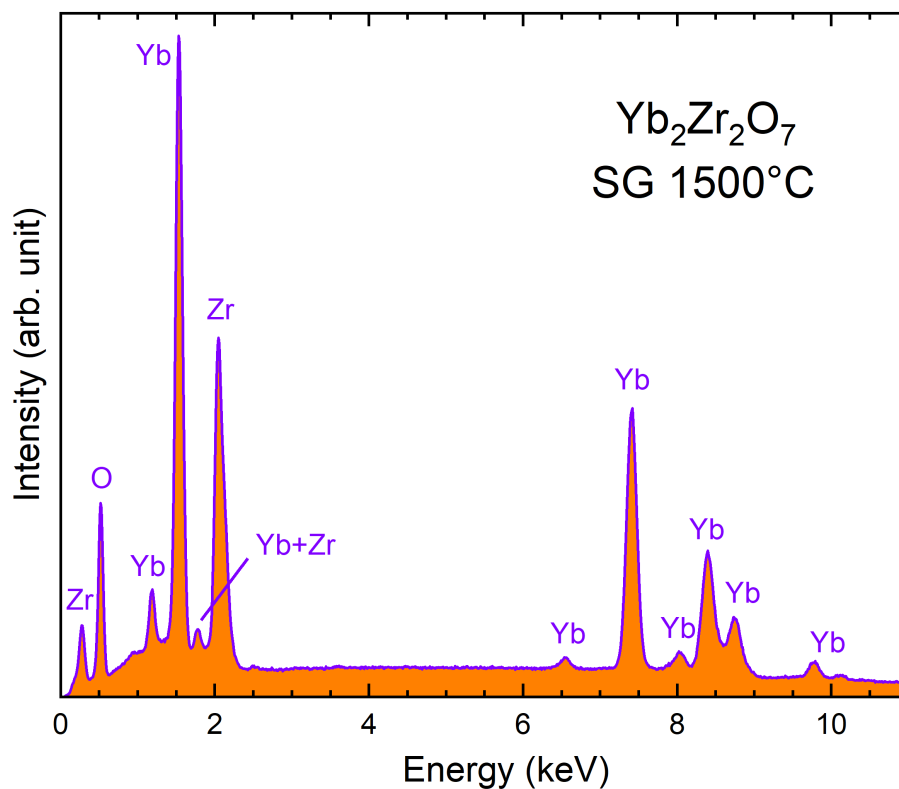


Figure 4.19 EDS spectrum for the sample $\text{Yb}_2\text{Zr}_x\text{Ti}_{2-x}\text{O}_7$, $x = 2.0$, sintered at 1500°C for 3h.

element	measured mol %	nominal mol %	ratio
Yb	17.08	18.18	0.94
Ti	7.55	4.55	1.66
Zr	9.17	13.64	0.67
O	66.2	63.64	1.04

Table 4.2 Measured and nominal composition values and their ratio, for the sample $\text{Yb}_2\text{Zr}_x\text{Ti}_{2-x}\text{O}_7$, $x = 1.5$, sintered at 1500°C for 3h.

element	measured mol %	nominal mol %	ratio
Yb	16.89	18.18	0.93
Zr	13.96	18.18	0.77
O	69.15	63.64	1.09

Table 4.3 Measured and nominal composition values and their ratio, for the sample $\text{Yb}_2\text{Zr}_x\text{Ti}_{2-x}\text{O}_7$, $x = 2.0$, sintered at 900°C for 24h.

element	measured mol %	nominal mol %	ratio
Yb	15.26	18.18	0.84
Zr	14.41	18.18	0.79
O	70.33	63.64	1.11

Table 4.4 Measured and nominal composition values and their ratio, for the sample $\text{Yb}_2\text{Zr}_x\text{Ti}_{2-x}\text{O}_7$, $x = 2.0$, sintered at 1500°C for 3h.

The EDS spectra obtained for the samples are shown in Figures 4.17 to 4.19, with each peak labeled by the element associated to its characteristic wavelength. The beam energy, equal to the accelerating voltage experienced by the electrons, was set at 20keV. This energy is sufficient to excite the O K transition ($K\alpha$ at 0.525keV), the Ti/Zr L, K transitions (Ti $L\alpha$ at 0.452keV, Ti $K\alpha$ at 4.508keV, Zr $L\alpha$ at 2.042keV, Ti $K\alpha$ at 15.744keV) and the Yb M, L transitions (Yb M at 1.521keV, Yb $L\alpha$ at 7.414keV) [195].

Integrating the area under the peaks in the spectrum and partitioning it according to the element we obtain an estimate for the composition of the sample. The software provided with the SEM instrument automatically performs this analysis, the results of which are shown in Tables 4.2 to 4.4 for the $Yb_2Zr_xTi_{2-x}O_7$ samples, including the measured and nominal composition values and the their ratio. The uncertainty values for the molar percentage provided by the software were below 1%, but it seems clear that these values are not reliable, since they deviate too much from the nominal composition to be considered reasonable. The values are also inconsistent in the sense that charge neutrality is not satisfied, assuming the standard oxidation states for the ions, Yb^{3+} , Ti^{4+} , Zr^{4+} and O^{2-} . It is possible that some ions with different oxidation states could be present but it would be necessary to postulate an unreasonable amount of those to account for the measured values in the tables above. These issues with quantitative accuracy of the elemental analysis by EDS are well-known [194].

X-Ray Diffraction

In this chapter we describe the basic theory underlying x-ray diffraction, explain how the experimental data was analyzed and discuss the results. The description of theoretical and experimental aspects of x-ray diffraction in this chapter is based on [196, 197, 198, 199]. Further details on the Rietveld Method can be found in [200, 201, 202, 203].

5.1 Introduction

Powder x-ray diffraction instruments, also known as diffractometers, usually use monochromatic x-ray radiation generated in a vacuum tube when electrons are accelerated and impact on a metal anode. The intense deceleration upon impact generates a continuous spectrum of x-rays (with a definite maximum energy related to the accelerating potential) and some characteristic x-ray wavelengths, depending on the anode material. Most common laboratory diffractometers possess a copper (Cu) target, thus generating the characteristic wavelengths for Cu, most notably $K\alpha_1$ (KL_3 transition, $\lambda = 1.54059290(50)\text{\AA}$ [204]), $K\alpha_2$ (KL_2 transition, $\lambda = 1.54442740(50)\text{\AA}$ [204]) and $K\beta$ ($KM_{2,3}$ transitions, $\lambda = 1.3922340(60)\text{\AA}$ [204]). The $K\alpha_1$ line is approximately twice as intense as the $K\alpha_2$ line. Since the $K\alpha_1$ and $K\alpha_2$ lines are so closely spaced it is common to consider a weighted average of both, a $K\alpha$ line with wavelength $\lambda(K\alpha) = \frac{2}{3}\lambda(K\alpha_1) + \frac{1}{3}\lambda(K\alpha_2) = 1.541871\text{\AA}$, as if it were monochromatic.

A nickel (Ni) filter can be used to filter out most of the undesirable $K\beta$ component from the x-rays generated by a copper source. Ni ($Z = 28$) is the element to the left of Cu ($Z = 29$) in the periodic table, so that the KM absorption edge of Ni falls in between the energies corresponding to the $K\alpha$ and $K\beta$ wavelengths of Cu and the more energetic Cu $K\beta$ x-rays are preferentially absorbed by Ni when compared to the longer wavelength $K\alpha$ rays. The filter is a very thin Ni foil, approximately $20\mu\text{m}$ in thickness. The thickness is a compromise between intensity reduction of the transmitted radiation and preferential attenuation of the $K\beta$ line. For a $20\mu\text{m}$ Ni foil the $K\alpha$ intensity is reduced by a factor of ≈ 2 but the $K\beta$ intensity reduces by ≈ 100 . Some modern semiconductor detectors do not require a $K\beta$ filter since they can

automatically discriminate $K\alpha$ and $K\beta$ photons by the statistics of the electron cascades they generate when impinging on the detector.

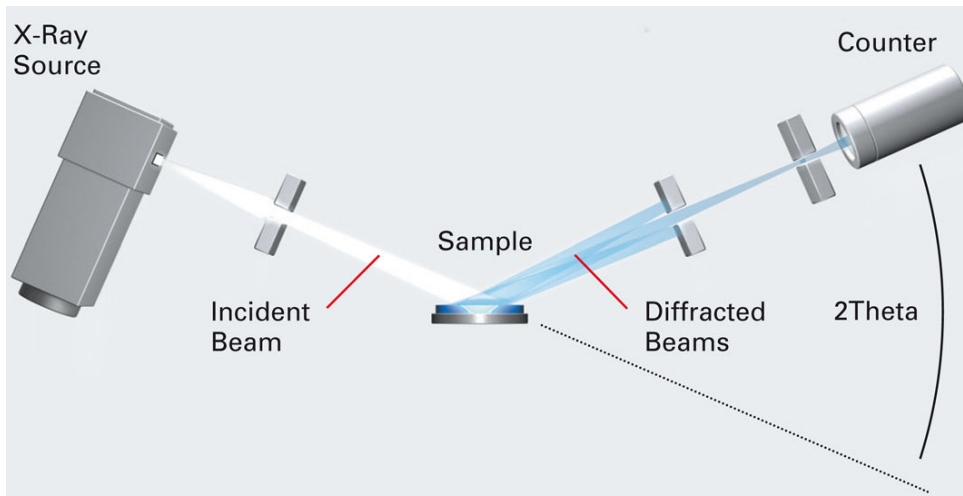


Figure 5.1 Bragg-Brentano diffraction geometry, adapted from [205].

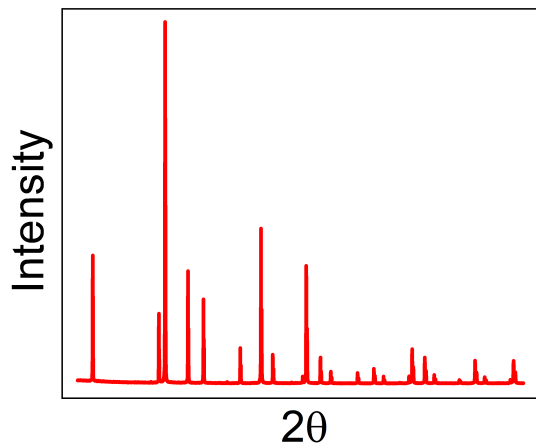


Figure 5.2 Schematic depiction of an x-ray diffractogram.

In the Bragg-Brentano diffraction geometry [206] the powder sample is placed horizontally, as depicted in Figure 5.1. The angle between the incoming beam and the position of the detector is 2θ , so the diffractogram is usually a graph of intensity as a function of the scattering angle 2θ , indicated schematically in Figure 5.2. The absolute intensity will vary depending on the conditions of the measurement and is essentially arbitrary as long as good photon counting statistics are obtained. If the number of absolute counts is too low the noise due to statistical fluctuations might significantly reduce the data quality. The units for the intensity axis are often given as counts (the absolute number of detected photons), counts per second (or other time unit) or just arbitrary units (a.u.). Sometimes the intensity is plotted on a logarithmic or square root scale to help highlight features that might not be visible when using a linear scale.

Maxima in the diffracted intensity are observed when θ satisfies Bragg's Law

$$2d\sin\theta = n\lambda \quad (5.1)$$

where d is the spacing of a lattice plane family in the sample's crystal structure, n is an

integer, and λ is the wavelength of the x-rays. A lattice plane family is a set of parallel planes, separated by a constant spacing d , that intersect atoms in the crystal structure, as represented in Figure 5.3, where only two of the infinitely many parallel planes are shown.

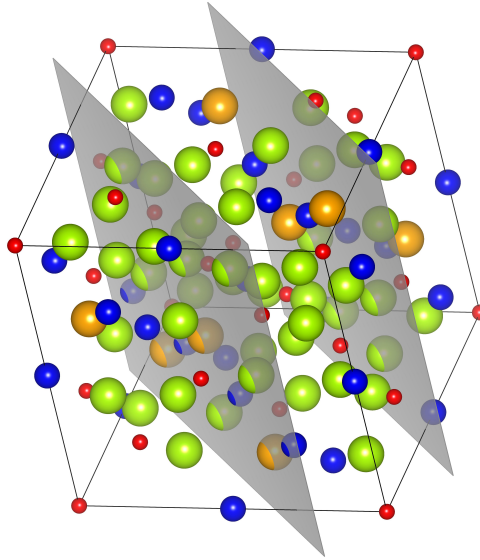


Figure 5.3 A family of lattice planes intersecting atoms in the crystal structures. Only two planes are shown but there are infinitely many parallel planes with a constant spacing d .

Bragg's Law (5.1) is easily derived as the geometrical condition for x-rays scattered elastically from parallel lattice planes to interfere constructively. The outgoing waves are in phase if their path length differs by an integer multiple of their wavelength and this condition leads to (5.1), as can be deduced from Figure 5.4.

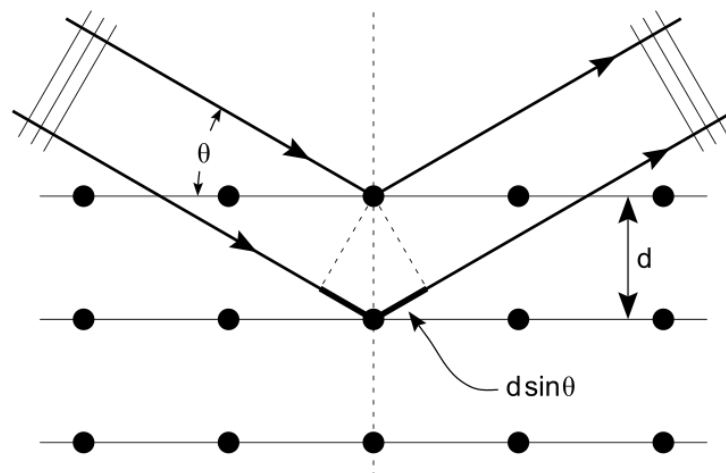


Figure 5.4 X-rays diffracted from parallel lattice planes interfere constructively when (5.1) holds [207].

Laue developed a description of diffraction that is entirely equivalent to Bragg's but stated in terms of the reciprocal lattice, a fundamental concept in solid-state physics. Considering all lattice points $\mathbf{R} = n_1\mathbf{a}_1 + n_2\mathbf{a}_2 + n_3\mathbf{a}_3$ (2.1), the reciprocal lattice is defined by set of vectors \mathbf{G} satisfying

$$\exp(i\mathbf{G} \cdot \mathbf{R}) = 1 \quad (5.2)$$

It can be proven that this set of vectors \mathbf{G} actually is a lattice, i.e. every reciprocal lattice point can be expressed as

$$\mathbf{G} = \mathbf{G}_{hkl} = h\mathbf{b}_1 + k\mathbf{b}_2 + l\mathbf{b}_3 \quad (5.3)$$

where h, k, l are integers and \mathbf{b}_i are linearly independent vectors, the reciprocal lattice basis vectors, which satisfy

$$\mathbf{a}_i \cdot \mathbf{b}_j = 2\pi \delta_{ij} \quad (5.4)$$

In the Laue formulation the momentum $\mathbf{p} = \hbar\mathbf{k}$ of an x-ray is most conveniently represented by its wave-vector \mathbf{k} and a peak in diffracted intensity is observed whenever the change in momentum $\Delta\mathbf{k} = \mathbf{k}_f - \mathbf{k}_i$ during the scattering event satisfies $\Delta\mathbf{k} = \mathbf{G}$, where i/f indicate the incoming/outgoing wave and \mathbf{G} is a reciprocal lattice vector. Each possible combination of the integer coefficients h, k, l in (5.3), known as Miller indices, is associated to a lattice plane family. The lattice planes associated to the Miller indices h, k, l are normal to \mathbf{G}_{hkl} and neighboring planes are separated by a distance d ,

$$d = \frac{2\pi}{|\mathbf{G}_{hkl}|} \quad (5.5)$$

For a cubic lattice with lattice parameter a this is equivalent to

$$d = \frac{a}{\sqrt{h^2 + k^2 + l^2}} \quad (5.6)$$

A rule of thumb for determining the $\Delta(2\theta)$ step size is that a peak should have at least ~ 5 measured points on each side of the maximum to be well resolved, as indicated in Figure 5.5. A larger step size will lead to inaccurate peak positions and shapes, while a smaller step size is often not practical in terms of measuring time.

In all cases the sample was rotated at 10rpm or 15rpm about the vertical axis, to improve the averaging of crystallite orientations. In this way any unevenness in the sample preparation and grain distribution gets smoothed out. Higher rotational speeds (20rpm or more) led to a spreading of the powder, which can reduce acquired data quality due to an uneven sample surface. Preferential orientation of powder grains or small crystallites can skew the relative peak intensities observed in a powder diffraction experiment. By spinning the powder around the axis normal to the sample surface the component of the preferential orientation vector parallel to the surface is averaged out and only the component normal to the surface could remain observable. Since most of the samples used in this work have cubic symmetry the effect of preferential orientation seems to be negligible.

Table 5.1 lists the main structural parameters that can be deduced from the positions, intensities and shapes of the peaks in a powder diffractogram. The position is the value of 2θ at which a maximum occurs, while the intensity is defined as the area under the peak (usually only the area above an interpolated curve that accounts for the background).

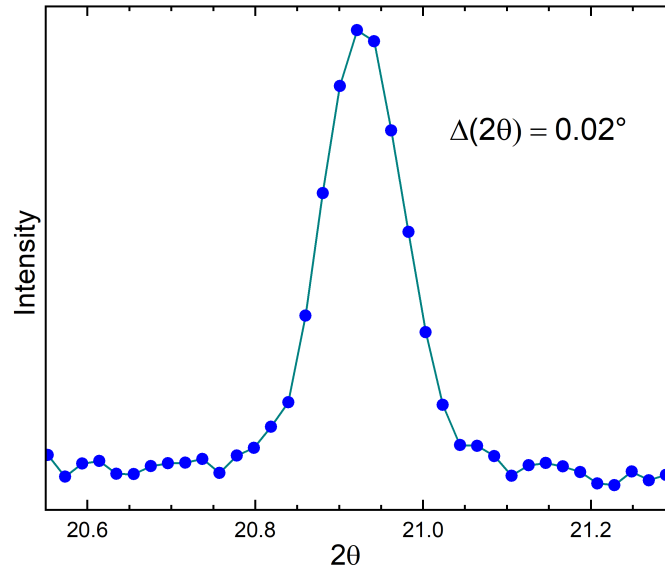


Figure 5.5 Rule of thumb for determining the $\Delta(2\theta)$ step size: to resolve a peak it should contain at least ~ 5 measured points on each side of the maximum.

Peak parameters	Structural parameters
Positions	Lattice, symmetry
Intensities	Unit cell composition, displacement
Shapes	Crystallite size, strain, disorder

Table 5.1 The main structural parameters that can be deduced from the positions, intensities and shapes of the peaks in a powder diffractogram.

The lattice and space group symmetry of the crystal structure determine possible positions for the peaks in a diffractogram, so that the peak positions provide information on the lattice and symmetry that is independent of the composition of the sample. There need not be an observable peak at every position allowed by symmetry because in some cases the diffracted intensity at a certain position is too low to be observable or the atoms in the structure might conspire to exactly cancel the scattering power for the corresponding reciprocal lattice vector. However usually at least some diffracted intensity will be observable at most of the positions that are allowed by symmetry. This is the principle that allows peak indexing of an unknown sample to be performed without knowledge of the sample composition or structure.

The unit cell contents determine the intensities of the peaks. Since x-rays are scattered almost exclusively by the electrons in a sample, there is a linear correlation between the scattering power of an atom or ion and the number of electrons it contains. The structure factor S is a function of the reciprocal lattice vector $\mathbf{G} = h\mathbf{b}_1 + k\mathbf{b}_2 + l\mathbf{b}_3$ that takes into account the positions of the atoms in the unit cell,

$$\begin{aligned} S(\mathbf{G}) &= \sum_j f_j(\mathbf{G}) \exp[i\mathbf{G} \cdot \mathbf{r}_j] \\ &= \sum_j f_j(\mathbf{G}) \exp[2\pi i (hx_j + ky_j + lz_j)] \end{aligned} \quad (5.7)$$

where the sum is over all atoms j in the unit cell, with coordinates $\mathbf{R}_j = x_j\mathbf{a}_1 + y_j\mathbf{a}_2 + z_j\mathbf{a}_3$. The diffracted intensity I_{hkl} at the 2θ value associated to the Miller indices hkl through Bragg's Law (5.1) is proportional to the modulus squared of S_{hkl} ,

$$I_{hkl} \propto |S_{hkl}|^2 = |S(h\mathbf{b}_1 + k\mathbf{b}_2 + l\mathbf{b}_3)|^2 \quad (5.8)$$

The atoms in a crystal structure are never truly stationary since even at zero temperature there remains some motion induced by quantum effects. At finite temperature the atoms also vibrate due to the thermal energy available to them. Assuming that for each atom j in the unit cell the displacement from its equilibrium position is \mathbf{u}_j , the structure factor will be modified by an exponential term [208],

$$\begin{aligned} S(\mathbf{G}) &= \sum_j f_j(\mathbf{G}) \exp[i\mathbf{G} \cdot \mathbf{r}_j] \exp[-2\pi^2 \langle (\mathbf{G} \cdot \mathbf{u}_j)^2 \rangle] \\ &= \sum_j f_j(\mathbf{G}) \exp[i\mathbf{G} \cdot \mathbf{r}_j] \exp[-2\pi^2 \mathbf{g}^T \mathbf{U}_j \mathbf{g}] \end{aligned} \quad (5.9)$$

where $\mathbf{g} = (h|\mathbf{b}_1|, k|\mathbf{b}_2|, l|\mathbf{b}_3|)$ are the coordinates of \mathbf{G} in a dimensionless reciprocal lattice basis, \mathbf{U}_j is the atomic displacement tensor for atom j and the average $\langle \dots \rangle$ can be understood as either a thermal or time average. The mean square displacement from atom's j equilibrium

position in the direction $\hat{\mathbf{n}}$ is

$$\langle (\mathbf{u}_j \cdot \hat{\mathbf{n}})^2 \rangle = \hat{\mathbf{n}}^T \mathbf{U}_j \hat{\mathbf{n}} \quad (5.10)$$

The atomic displacement tensor \mathbf{U}_j is symmetric, so in general it has six independent components. In many cases a further simplification is made and the mean square displacements of the atoms are assumed to be isotropic, so that the values of \mathbf{U}_j are combined into an average value, the isotropic displacement parameter,

$$U_{iso,j} = \frac{1}{3} \langle \mathbf{u}_j^2 \rangle \quad (5.11)$$

The effect of increasing the atomic displacement parameters (ADPs) is that the Bragg peak area gets redistributed into the diffuse background. This effect is more significant in the higher 2θ range, since the scattering amplitude S_j for a single atom j depends on the scattering vector \mathbf{G} exponentially,

$$\begin{aligned} S_j &= S_{j0} \exp \left[-\frac{1}{6} \mathbf{G}^2 \langle \mathbf{u}_j^2 \rangle \right] \\ &= S_{j0} \exp \left[-\frac{1}{2} \mathbf{G}^2 U_{iso,j} \right] \end{aligned} \quad (5.12)$$

where $S_{j0} = S_j(\mathbf{u}_j = 0)$ is the static scattering amplitude for a fixed atom, with $\mathbf{u}_j = 0$. Therefore the total scattered intensity is

$$I_{hkl} \propto |S_{hkl}|^2 \propto I_0 \exp \left[-U_{iso} \mathbf{G}^2 \right] \quad (5.13)$$

where I_0 is the static scattering intensity (with all $\mathbf{u}_j = 0$) and U_{iso} is a weighted average of $U_{iso,j}$ over all atoms in the unit cell.

We should be careful to distinguish a crystallite, which is a single crystalline domain, from the grains that form the visible particles in the powder. Figure 5.6 schematically depicts the distinction between a secondary particle, consisting of an aggregate of smaller grains or primary particles, which in turn may contain many crystallites. The terminology used here is by no means standard, and there might be no real distinction between these categories, e.g. in some cases every powder particle could actually be a single crystallite. Nevertheless, the crystallite is the relevant concept for powder diffraction, representing a coherent unit of crystallographic order. The crystallite size calculated by diffraction methods might be more appropriately termed the coherence length, which can be different from the crystallite size measured by direct imaging techniques, especially when the crystallites are significantly strained or display a high degree of structural disorder.

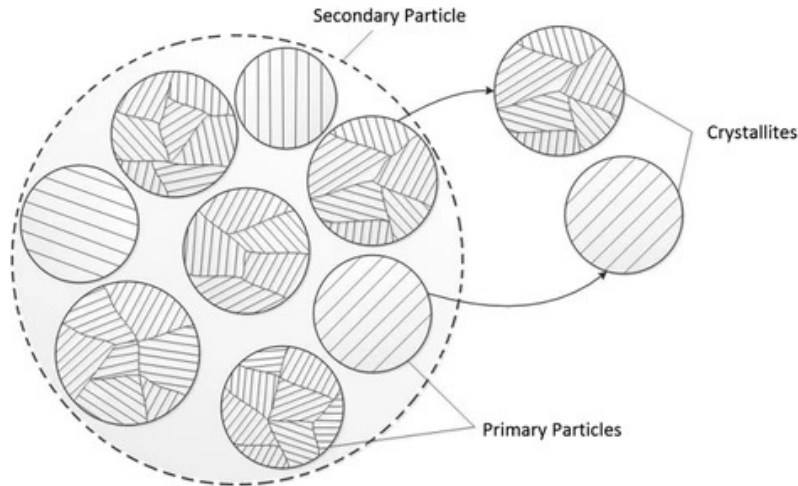


Figure 5.6 Distinction between powder particles and crystallites, from [209].

The crystallite size μ is commonly estimated by Scherrer's relation,

$$\mu = \frac{K\lambda}{\beta \cos \theta_B} \quad (5.14)$$

where K is a dimensionless geometric constant, λ is the x-ray wavelength and β is the sample contribution to the FWHM (full width at half maximum) of a diffraction peak centered at $2\theta_B$. Figure 5.7 shows a representation of the full width at half of the maximum intensity I_M , for a peak centered at θ_B . The curve in this example is a Gaussian curve (5.20) but the concept of FWHM holds more generally, even for asymmetric peaks. Note that when deriving (5.14) the symbol β usually represents the integral breadth, defined as the peak's area divided by its height, which is approximately equal to the FWHM, although more careful treatments do distinguish these quantities.

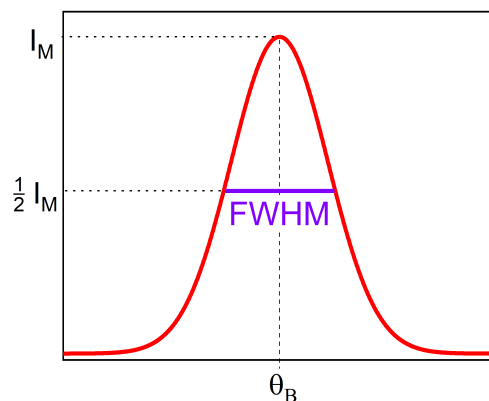


Figure 5.7 Full width at half of the maximum intensity I_M (FWHM) for a peak centered at θ_B .

The measured FWHM has contributions from both the instrument and the samples (see Section 5.4). The β value in (5.14) is just the contribution due to the sample, i.e. $\beta^2 = \text{FWHM}_{\text{measured}}^2 - \text{FWHM}_{\text{instrument}}^2$. The Scherrer constant K is of order unity, but can vary depending on the orientation of the scattering vector \mathbf{G} with respect to the crystallite shape and other factors [210]. We assume that the crystallites are spherical, since we have no informa-

tion concerning their actual shape. For spherical crystallites with cubic symmetry $K = 0.94$ if β represents the FWHM and $K = 0.89$ if β represents the integral breadth [211, 199].

There are more reliable methods to estimate crystallite size from diffraction peak shapes [212, 213, 214] but Scherrer's equation has the advantage of being simple and approximately accurate, although it often underestimates the crystallite size, especially for large crystallites with $\mu > 600nm$ [215, 216, 217].

5.2 Pyrochlore vs Fluorite: Local Order

Figure 5.8 shows a simulated diffractogram for a pyrochlore with $a = 10\text{\AA}$ and a defect fluorite with $a = 5\text{\AA}$, with some representative peaks labeled by their Miller indices. The relative intensities of the peaks for a pyrochlore will depend on the composition $A_2B_2O_7$, but the fluorite subcell peaks, evident at $2\theta \approx 31^\circ, 36^\circ, 52^\circ, 62^\circ$ are generally the most pronounced, along with a few superstructure peaks that are specific to the pyrochlore structure, such as the 111 peak at $2\theta \approx 15^\circ$.

Note that at every hkl fluorite peak position the pyrochlore structure has a corresponding peak with doubled Miller indices $2h, 2k, 2l$ due to the doubling of the lattice parameter. Note also that some peaks are labeled by multiple indices, such as the fluorite peak at $2\theta \approx 106^\circ$. This happens most frequently in high-symmetry crystal systems such as the cubic, due to a coincidence of lattice plane families with equal spacing. For the cubic system the spacing is controlled by (5.6), so that if the values of $h^2 + k^2 + l^2$ coincide (e.g. $3^2 + 3^2 + 3^2 = 5^2 + 1^2 + 1^2$) then those peaks are superimposed in the diffractogram.

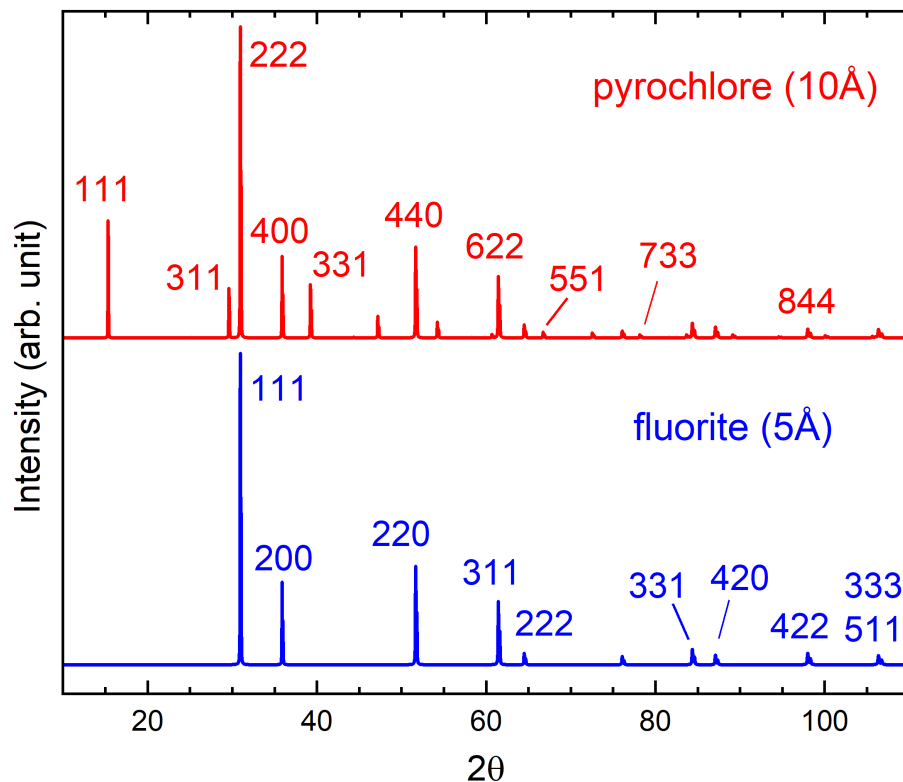


Figure 5.8 Simulated diffractogram for a pyrochlore with $a = 10\text{\AA}$ and a defect fluorite with $a = 5\text{\AA}$, with $\text{CuK}\alpha$ radiation. Some peaks are labeled by their Miller indices.

pyrochlore			fluorite			$d(\text{\AA})$	$2\theta(^{\circ})$	<i>mult</i>
<i>h</i>	<i>k</i>	<i>l</i>	<i>h</i>	<i>k</i>	<i>l</i>			
1	1	1				5.774	15.33	8
2	2	0				3.536	25.17	12
3	1	1				3.015	29.60	24
2	2	2	1	1	1	2.887	30.95	8
4	0	0	2	0	0	2.500	35.89	6
3	3	1				2.294	39.24	24
4	2	2				2.041	44.34	24
5	1	1				1.925	47.19	24
3	3	3				1.925	47.19	8
4	4	0	2	2	0	1.768	51.67	12
5	3	1				1.690	54.22	48
4	4	2				1.667	55.06	24
6	2	0				1.581	58.31	24
5	3	3				1.525	60.68	24
6	2	2	3	1	1	1.508	61.46	24
4	4	4	2	2	2	1.443	64.51	8
5	5	1				1.400	66.75	24
7	1	1				1.400	66.75	24
6	4	2				1.336	70.40	48
5	5	3				1.302	72.55	24
7	3	1				1.302	72.55	48
8	0	0	4	0	0	1.250	76.08	6
7	3	3				1.222	78.18	24
6	4	4				1.213	78.87	24
8	2	2				1.179	81.63	24
6	6	0				1.179	81.63	12
5	5	5				1.155	83.69	8
7	5	1				1.155	83.69	48
6	6	2	3	3	1	1.147	84.37	24
8	4	0	4	2	0	1.118	87.10	24
7	5	3				1.098	89.14	48
9	1	1				1.098	89.14	24
8	4	2				1.091	89.82	48
6	6	4				1.066	92.54	24
9	3	1				1.048	94.58	48
8	4	4	4	2	2	1.021	98.00	24
7	5	5				1.005	100.07	24
9	3	3				1.005	100.07	24
7	7	1				1.005	100.07	24
10	2	0				0.981	103.54	24
8	6	2				0.981	103.54	48
7	7	3				0.967	105.65	24
9	5	1				0.967	105.65	48
10	2	2	5	1	1	0.962	106.36	24
6	6	6	3	3	3	0.962	106.36	8

9	5	3				0.933	111.39	48
8	6	4				0.928	112.12	48
10	4	2				0.913	115.09	48
7	7	5				0.902	117.37	24
11	1	1				0.902	117.37	24
8	8	0	4	4	0	0.884	121.26	12
9	5	5				0.874	123.68	24
9	7	1				0.874	123.68	48
11	3	1				0.874	123.68	48
8	8	2				0.870	124.50	24
10	4	4				0.870	124.50	24
10	6	0				0.857	127.87	24
8	6	6				0.857	127.87	24

Table 5.2 List of Miller indices hkl , lattice spacings d (in Å), 2θ positions (in degrees) and multiplicities $mult$ for the diffraction peaks of the pyrochlore and fluorite structures, assuming lattice parameters of 10Å and 5Å, respectively, and CuK α radiation.

Table 5.2 lists the Miller indices, lattice spacings d , 2θ positions and multiplicities for the diffraction peaks of the pyrochlore and fluorite structures, assuming CuK α radiation and lattice parameters of 10Å and 5Å, respectively. The multiplicity of a reflection defines how many sets of equivalent lattice plane families correspond to a certain index hkl . For example, in a cubic system the multiplicity 100 is six, since there are six sets of equivalent planes: 100, $\bar{1}00$, 010, $0\bar{1}0$, 001, $00\bar{1}$, where the bar on top of a digit means that there is a negative sign applied to it.

In a two-dimensional single-crystal diffraction pattern these equivalent lattice plane families would appear as separate peaks, but due to the rotational averaging inherent to powder diffraction all of the equivalent reflections are superimposed at the same 2θ value in the one-dimensional diffractogram. Note also that the list contains only hkl combinations where all indices are odd or even. This is the result of a selection rule on allowable Miller indices imposed on any face-centered cubic (fcc) lattice [218], as is the case with both pyrochlore and fluorite structures.

The list in Table 5.2 arbitrarily terminates at $2\theta = 127.87^\circ$ ($d = 0.857\text{Å}$) but could continue on up to the limiting value of $2\theta = 180^\circ$ ($d = \lambda/2 = 0.771\text{Å}$ for CuK α x-rays). For most diffractometers the limiting 2θ value is $\approx 140^\circ$, due to the instrument design. The intensities in the high 2θ range are usually very weak and other factors also contribute to poor data quality in that region, so typically experiments will measure the diffraction pattern only up to $2\theta \approx 120^\circ$.

Complex oxides with aliovalent cations (cations with different valencies) often form superstructures of simpler compounds that contain only a single cation. In the simpler compound every cation position has the same coordination, while in the more complex superstructures the cations separate onto distinct sites to accommodate their innate tendencies to have different coordination. This principle directly applies to the $A_2B_2O_7$ compounds, which contain the aliovalent cations A^{3+} and B^{4+} (or A^{2+} and B^{5+}), and crystallize in the pyrochlore structure, a superstructure of the simple fluorite. In the AX_2 fluorite structure all cations are eightfold

coordinated, while in the $A_2B_2O_7$ pyrochlore structure there are both eightfold coordinated cation sites, occupied by the element A, and sixfold coordinated cation sites, occupied by the element B.

The $A_2B_2O_7$ defect fluorite structure is a compromise between these two, with cation sites that are on average sevenfold coordinated. The actual local structure in these defect fluorites will most likely have some pyrochlore-like correlations between ions in order to lower the energy of the local geometric configuration. This lowering of the energy by distortion of the local geometry away from the mean fluorite structure is what drives the ordering into the pyrochlore structure. Nevertheless, due to various factors both intrinsic and extrinsic this ordering may be only partially achieved, as seems to be the case with many of the $A_2B_2O_7$ defect fluorites.

The most relevant intrinsic factor that controls the ordering tendency is the ionic radii of the cations, which is why the tolerance factor approach (Section 2.3.1) works well as a heuristic to predict the structure. Thus it is possible to intrinsically control the structure through varying the chemical composition and changing the stoichiometry, by stuffing or dilution of one of the chemical species. Extrinsic factors that can influence the degree of order are irradiation (by ions or other high energy radiation), mechanical processing (milling), thermal processing (annealing or quenching from a high temperature state) and applied pressure (pressure quenching).

A comprehensive framework for explaining the role of local ordering in these structures also needs to take into account the role of metastable states, local minima in the energy landscape that are separated from the global minimum by an activation barrier. The structural energy landscape for these types of complex oxides is not yet well understood and is the subject of many current theoretical and computational investigations.

Intuitively we can understand that cation ordering leads to decreased energy and entropy of the configuration, so that competition between the energetic and entropic drives to minimize the free energy can lead to a structural transition when the temperature is raised sufficiently. However this intuitive picture is incomplete because it neglects the kinetic constraints that might not allow a system to reach the true equilibrium ground state on any reasonable time scale.

Diffuse scattering is often associated with local ordering that does not extend to the global structure. For instance in [63] diffuse scattering was observed in a fluorite-type XRD pattern of Yb_2TiO_5 at the positions where the pyrochlore superstructure peaks would appear. The diffuse scattering was dramatically increased in a neutron diffraction pattern of the same sample, suggesting that most of the local pyrochlore-type ordering is restricted to the oxygen sublattice, given that XRD is less sensitive to oxygen than to the heavier cation elements. As will be discussed in Section 5.6.2, some of the $Yb_2Zr_xTi_{2-x}O_7$ samples show this kind of diffuse scattering (see Figures 5.40 and 5.41).

We might distinguish between two conceptually distinct possible origins for this diffuse scattering effect. One option is that there is a matrix of a host structure that contains embedded in it domains of another phase and these are more or less well defined, spatially separated regions. In this case the broadness of the superstructure peaks would be indicative of highly stressed, very small pyrochlore domains embedded in a fluorite matrix.

The second option is that a certain kind of local order predominates, which is less symmetric

than the average structure. The unit cell corresponding to this local ordering could be repeated imprecisely in a not entirely periodic way, such that the local structural correlations are lost on the scale of only a few unit cells. In this scenario the unit cell suffers more or less random shifts when translated (as if the n_i in (2.1) were not always integers) the local structure is said to possess only pseudo-translational symmetry. In that case the average structure probed by XRD is a disordered fluorite but it is actually assembled by aperiodic modulation of local structural units of lesser symmetry.

These two options represent opposite sides of a continuum, since if in the first option the average domain size is small enough and the domain boundaries represent a significant volume fraction of the domains themselves, it may no longer make sense to consider domains at all, and we have arrived at the second option, with continuously shifting local order. Some of the suggestions for future work (Section 8.2) try to address the question of how we could distinguish the two options described above. Clearly we require some experimental technique that can probe the local order on the length scale of the purported domains.

Some studies reach the conclusion that these locally ordered fluorite derivative materials exhibit local, nanometric pockets of pyrochlore-type ordering and only appear disordered over larger length scales [219, 220, 221, 222]. Weberite structures have received increased attention in recent years since it was reported that the defect fluorite structure of $\text{Ho}_2\text{Zr}_2\text{O}_7$ is locally best described as a weberite-type structure [223]. The local order, probed through neutron total diffraction (Section 8.2.2), is of the weberite-type, with an orthorhombic unit cell (space group C_{2mm}), but there is no spatial coherence over length scales larger than about 15\AA , so that the average structure is a fluorite. Other studies have reached similar conclusions [224, 225, 226] and these might extend to many or all of the common $\text{A}_2\text{B}_2\text{O}_7$ defect fluorites.

In [80] $\text{La}_2\text{Zr}_2\text{O}_7$ samples sintered at various temperatures are analyzed using x-ray diffraction, Raman spectroscopy and electron energy-loss spectroscopy to characterize the local and long-range order. The structures of the samples range from a fully disordered fluorite to an ordered pyrochlore. Two characteristic length scales are assigned to each sample, μ_e and μ_o , which represent the coherence length of the crystal structure according to the even and odd pyrochlore reflections, extracted from Williamson-Hall plots of the XRD integral breadths. The crystallite sizes determined by transmission electron microscopy agree well with the μ_e values.

As explained previously with reference to Table 5.2, the odd reflections are specific to the pyrochlore superstructure, while the even reflections are also present for the fluorite substructure. When considering the samples sintered at successively lower temperatures it is observed that the width of the even reflections remains approximately constant whereas the odd reflections progressively broaden until they vanish completely. It is argued that when $\mu_o \approx \mu_e$ and both are large ($\approx 200\text{nm}$ or more), then the crystal structure is a well-ordered pyrochlore, whereas if $\mu_o \ll \mu_e$ then the structure is that of a small-grain pyrochlore composed of nanodomains, equivalent to the defect fluorite when viewed on larger length scales.

The authors propose a model for explaining the defect fluorite as an ensemble average of nanometric ordered pyrochlore domains randomly shifted from the pyrochlore origin setting by fractional translations of the unit cell, which is the second option we described above, to explain the origin of diffuse scattering. Specifically, they considered a model with eight types of domains, each consisting of pyrochlore unit cells but randomly shifted with respect to the

origin by one of the translation vectors

$$\begin{aligned}
 \mathbf{t}_1 &= (0, 0, 0) \\
 \mathbf{t}_2 &= (0, 1/4, 1/4) \\
 \mathbf{t}_3 &= (1/4, 0, 1/4) \\
 \mathbf{t}_4 &= (1/4, 1/4, 0)
 \end{aligned} \tag{5.15}$$

or the same vectors shifted by half of a unit cell diagonal,

$$\begin{aligned}
 \mathbf{t}_5 &= (1/2, 1/2, 1/2) \\
 \mathbf{t}_6 &= (1/2, 3/4, 3/4) \\
 \mathbf{t}_7 &= (3/4, 1/2, 3/4) \\
 \mathbf{t}_8 &= (3/4, 3/4, 1/2)
 \end{aligned} \tag{5.16}$$

Using this model the structure factor (5.7) becomes

$$S_f(hkl) = S_p(hkl) \sum_{i=1}^8 \exp \left[2\pi i (t_i^h h + t_i^k k + t_i^l l) \right] = S_p(hkl) Z(hkl) \tag{5.17}$$

where S_f and S_p are the fluorite/pyrochlore structure factors, Z is an interference function and $\mathbf{t}_i = (t_i^h, t_i^k, t_i^l)$ are the translation vectors listed above. Averaging over all domains, indexed by i in the sum that defines Z in (5.17), $Z(hkl) = 0$ for all the superstructure reflections and $Z(hkl) \neq 0$ for the fluorite substructure reflections. In this way the average defect fluorite results as the effect of interference of scattered waves from the shifted pyrochlore domains, while the local environment still reflects the pyrochlore structure.

The authors simulate such a multidomain pyrochlore crystal and confirm that the predictions from this model agree with the experimental diffraction and spectroscopy data. In particular, they compare the simulated pair distribution function (PDF) with the experimental one obtained from neutron total scattering. Each peak in one of these PDF plots represents a pair of atoms at a certain distance in the structure of a material. Since the local environment of the simulated nanodomain pyrochlore is the same as for the long-range ordered pyrochlore, there should be no broadening of the first few peaks that are associated to pair distances between closest neighbors of each of the atoms in the structure. These expectations agree well with experimental results reported, among others, by [223, 226] and the authors speculate that the principle of long-range disorder being generated by shifting short-range ordered domains could probably be extended to other complex oxides such as the spinels.

In [227] density functional theory calculations are used to study the local structure of the zirconate pyrochlores and understand the mechanisms responsible for the structural transition from the pyrochlore to the (partially) disordered fluorite and weberite phases. Their results suggest that the disordering process is induced mainly by the migration of oxygen ions in the

pyrochlore structure from the 48f to the vacant 8a sites. In this way the eightfold coordinated A^{3+} cations and the sixfold coordinated B^{4+} cations both become sevenfold coordinated. Based on considerations of the projected density of states for the Zr atoms, the authors state that the Zr^{4+} ions intrinsically prefer to be sevenfold coordinated, as in the natural monoclinic state of ZrO_2 . The preference for sevenfold coordination of Zr^{4+} could be one of the driving forces in the disordering transformations of the zirconate pyrochlores.

It was found that the most stable local structure is not the fully disordered fluorite but the semi-disordered weberite, in which half of the cations are ordered on separate sites and the other half are distributed on a single site (see Figure 2.17). The structural model used in this study considers that the sublattice containing both cations could be fully disordered, with a random distribution of cations, or could possess a certain degree of order, which the authors term a quasi-weberite structure. The fact that locally the weberite structure is the most stable for the zirconate and hafnate pyrochlores is in agreement with previous ab-initio studies [228, 229].

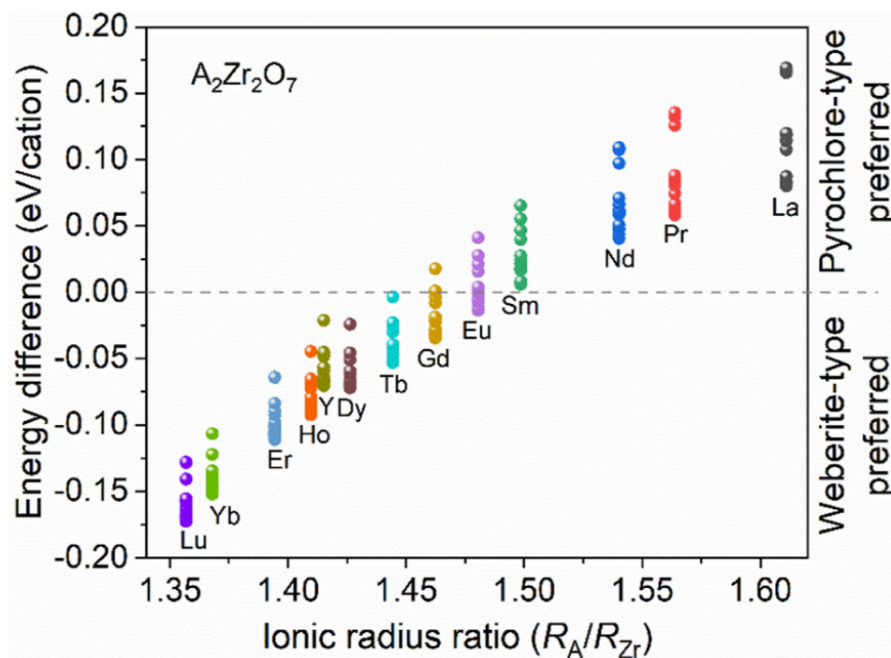


Figure 5.9 Calculated energy difference between the pyrochlore and various partially ordered quasi-weberite structures for the lanthanide zirconates $Ln_2Zr_2O_7$ [227].

Figure 5.9 shows the calculated energy difference between the pyrochlore and various partially ordered quasi-weberite structures for the $Ln_2Zr_2O_7$ lanthanide zirconates. The vertical dots for each of the lanthanides correspond to the weberite structures with varying degrees of order on the sublattice that contains both the Ln^{3+} and Zr^{4+} cations. For the heavier lanthanides $Ln = Tb-Lu$, in particular for Yb, the energy difference is negative, therefore the preferred stable structure is predicted to be a weberite-type phase.

According to [230] the tetrahedra in the pyrochlore structure collectively tilt in a way analogous to the entropically-driven fluxional motions in the silica mineral β -cristobalite, SiO_2 , as illustrated in Figure 5.10. In this study a wide array of experimental techniques, including synchrotron and neutron pair distribution function analysis, nuclear quadrupole resonance and various forms of transmission electron microscopy (SAED, HAADF-STEM, HRSTEM, EELS), were used to study local structural distortions in $Yb_2Ti_2O_7$, $La_2Zr_2O_7$ and $Pr_2Zr_2O_7$.

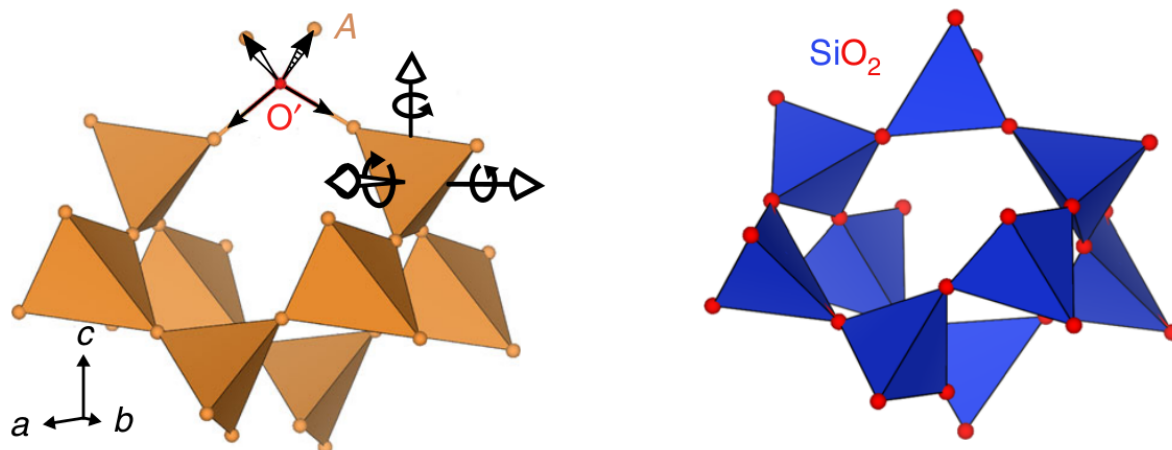


Figure 5.10 Collective tilting of the A_4O_{8b} tetrahedra in the pyrochlore structure (left), analogous to that in β -crystoballite SiO_2 (right) [230].

The authors conclude that all three $A_2B_2O_7$ compounds exhibit small displacements of the A and O ions, on the order of 0.01nm, that cause a slight collective tilting of the A_4O_{8b} tetrahedra. This structural instability occurs even for pristine samples, despite ideal cation ordering, exact stoichiometry, absence of lone pair defects and the nonmagnetic nature of $La_2Zr_2O_7$. If the tetrahedral tilting extends to the long-range structure then the space group is reduced from the pyrochlore $Fd\bar{3}m$ to its subgroup $P4_32_12$.

It is argued that this type of distortion is universal among pyrochlore oxides, driven by the cation size mismatch, rather than defects or electronic effects, and that it explains the absence of ferroelectricity in the pyrochlore compounds. The distortions could be visible as increased intensity at the 442 pyrochlore reflections for high-quality x-ray or neutron data but only if the magnitude of the displacement were greater than about 0.02nm or 0.03nm, while the actual distortions were closer to 0.01nm. Therefore we cannot confirm the presence or absence of this effect using only conventional XRD. Raman spectroscopy (Chapter 6) is more sensitive to the local structure but there also we could not confirm nor rule out this type of distortion due to the coexistence of various forms of disorder leading to somewhat ambiguous results.

This kind of tetrahedral tilting should be distinguished from another type of distortion, where the vertices of the corner-sharing tetrahedra alternately move inwards and outwards, affecting either the A or B sublattice or both of them. If the distortions are long-range ordered, extending to the whole structure, the symmetry is lowered from $Fd\bar{3}m$ to $F\bar{4}3m$. This kind of structure, with alternately large and small tetrahedra, is known as a 'breathing pyrochlore' lattice, illustrated in Figure 5.11, and occurs for some pyrochlore compounds, such as $Pb_2Ru_2O_{6.5}$ and $Pb_2Ir_2O_{6.5}$, but also for spinels and other compounds that contain the corner-sharing tetrahedral 'pyrochlore' lattice [231, 232, 233, 234, 235]. The size ratio between the large and small tetrahedra can vary widely, from close to 1 up to ~ 3 . When the distortion is small, with a size ratio very close to 1, it can be detected through x-ray absorption spectroscopy [236].

Both of the described distortions are not magnetically driven, similar to a static Jahn-Teller distortion, but can alter the magnetic properties of the pyrochlores, since they break the symmetry of the magnetic lattice and thus could affect the extremely sensitive quantum spin ice and spin liquid states.

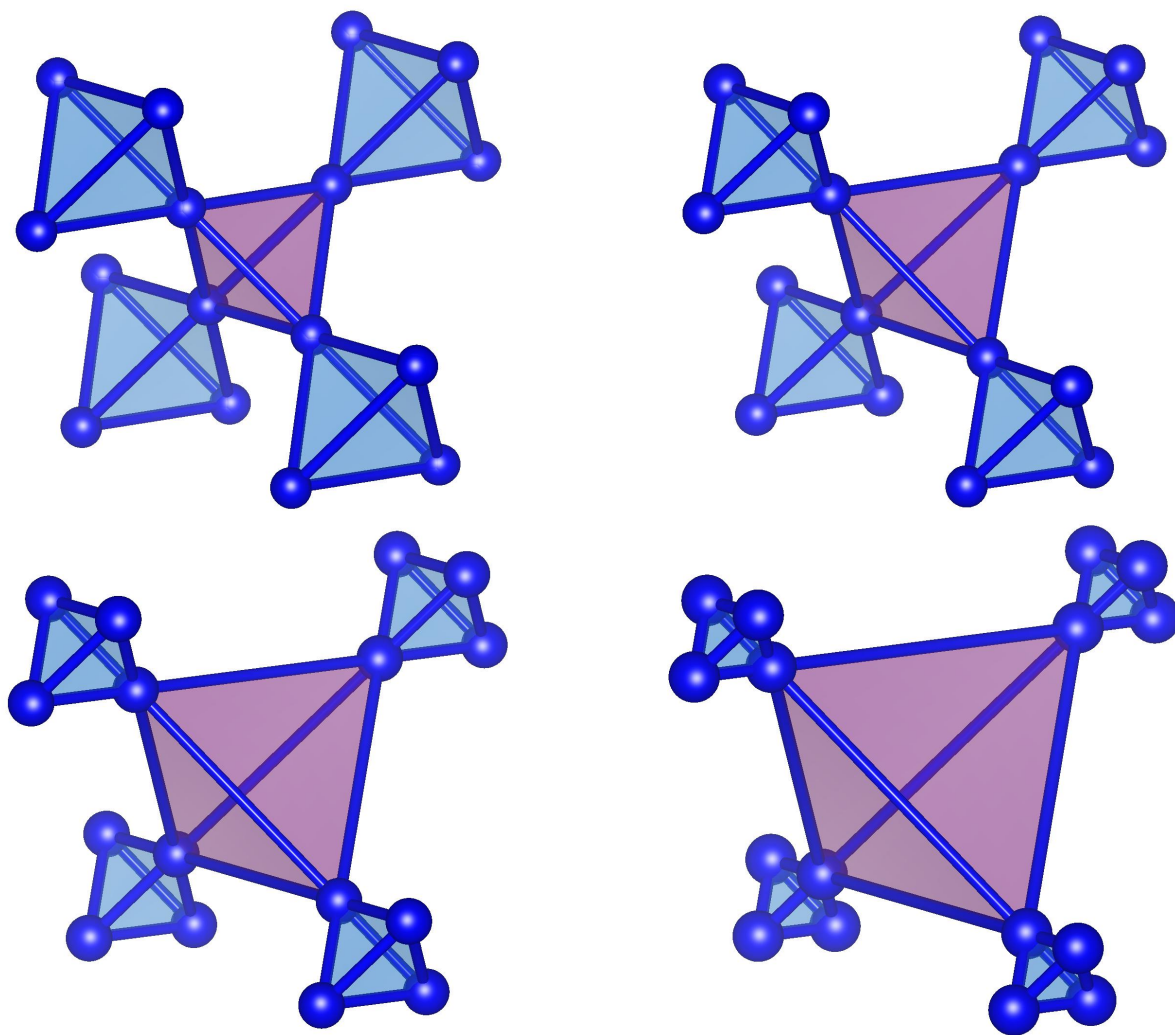


Figure 5.11 Alternating large and small tetrahedra in the breathing pyrochlore lattice, with increasing ratio between the edge lengths of the large and small tetrahedra.

5.3 Qualitative Phase Analysis

Qualitative phase analysis aims to identify the crystalline phases present in a sample by comparing the powder diffractogram with previously measured diffractograms of a large number of phases. It is not quantitative in the sense that the phase fractions can only be determined approximately and a sample might contain phases that cannot be identified.

Phase analysis was performed by the software QualX 2.0 [237] with the POW_COD database, created by using the structural information contained in the Crystallography Open Database (COD) [238, 239]. QualX can also carry out the phase identification by inquiring the PDF-2 commercial database, but we do possess a license for this database. The freely available database comes in two versions: POW_COD, the full database, and POW_COD_INO, containing only inorganic structures. Since this work deals exclusively with inorganic materials we used the considerably smaller inorganic database (POW_COD_INO), thereby significantly speeding up the database lookup during program operation. Figure 5.12 shows the QualX window during the phase analysis of the SS sample $\text{Yb}_2\text{Zr}_2\text{O}_7$.

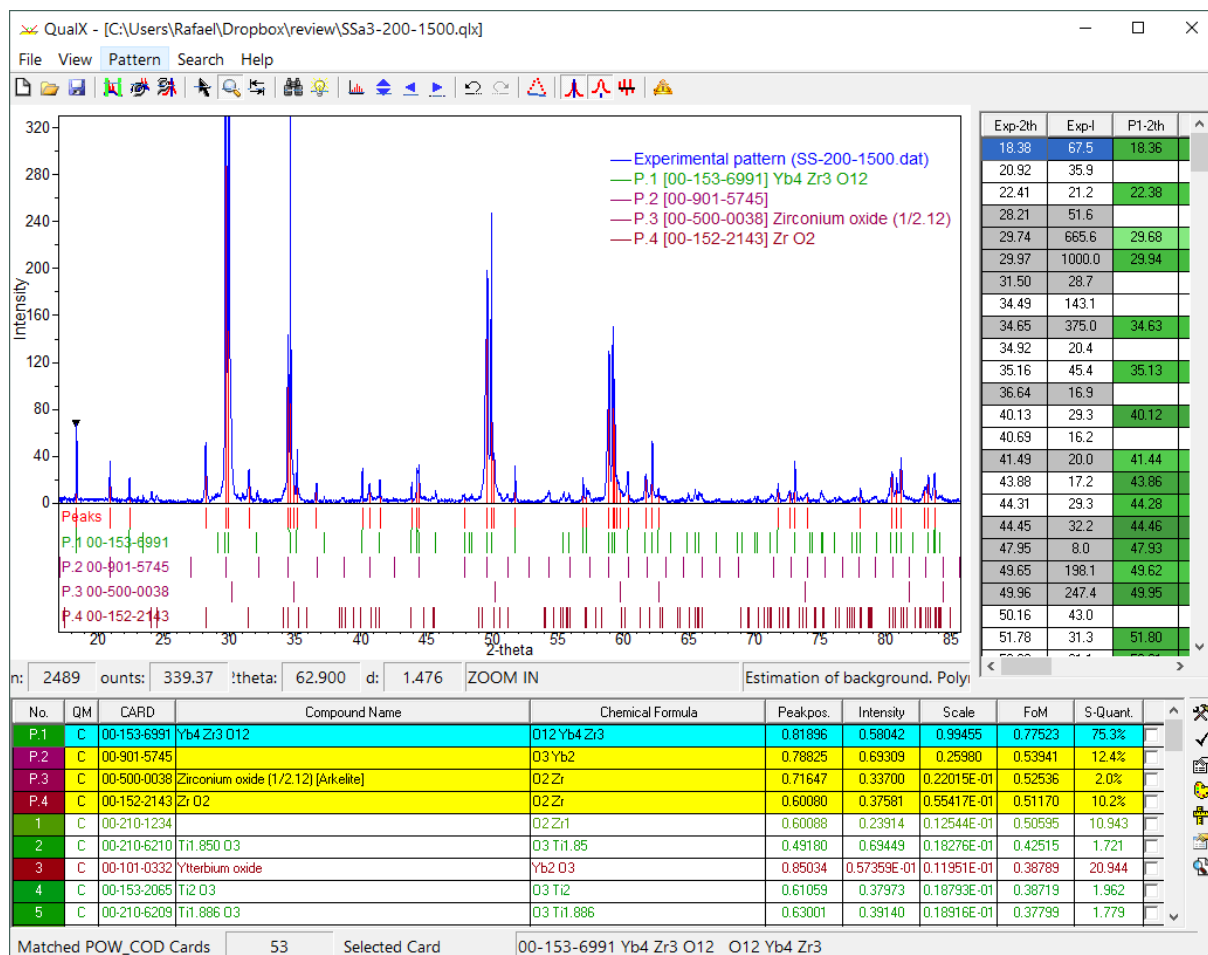


Figure 5.12 QualX window, showing the phase analysis for the SS sample $\text{Yb}_2\text{Zr}_2\text{O}_7$.

After importing the powder diffraction data the program automatically estimates the background contribution, subtracts the background curve from the experimental pattern and locates the diffraction peaks, supplying a set of positions and intensities for each peak. Several controls are available to tune these steps, such as the sensitivity and intensity threshold, but

the default options usually work well. Nevertheless one should verify that most peaks have been identified as such and that small fluctuations above the background noise were not mistakenly recognized as peaks, otherwise the phase identification will be compromised. The set of positions and intensities for each peak is what allows QualX to compare the experimental pattern to the simulated data contained in the structural database. If necessary QualX can also carry out a 2θ zero shift correction, compensating for an instrumental calibration error.

Next we perform $K\alpha_2$ -stripping to remove the splitting of peaks due to the closely spaced $\text{CuK}\alpha_1$ and $\text{CuK}\alpha_2$ wavelengths. This reduces the number of peaks to approximate a powder diffractogram from a truly monochromatic source, thus simplifying the phase identification in the following steps. Before performing the database search for the candidate phases that best match the experimental one it is useful to impose restraints on the allowed results of the search. These restraints can greatly reduce the number of matched phases and should be used if some previous knowledge on structure (e.g. symmetry, cell parameters) or chemical composition of the sample is available. Restraints on the chemical composition can be composed by combinations of chemical elements with the logical operators OR, AND, NOT, ONLY and JUST:

- AND** All elements must be in the resulting phases.
- OR** At least one of the elements must be in the resulting phases.
- NOT** None of the elements can be in the resulting phases.
- ONLY** Only the selected elements must be present simultaneously in the resulting phases (e.g. selecting Cu and Mn only the phases Cu_xMn_y).
- JUST** At least one of selected elements must be in the resulting phases (e.g. selecting Cu and Mn only the phases Cu, Mn, Cu_xMn_y).

Restraints on minimum and/or maximum number of chemical elements in the resulting phase can also be imposed. To determine phase composition in $\text{Yb}_2\text{Zr}_x\text{Ti}_{2-x}\text{O}_7$ the most useful restraints were of the form JUST (Yb AND Zr AND Ti AND O), as shown in Figure 5.13. Sometimes we relaxed these restraints to allow other elements such as the lanthanides (La - Lu), Y, Sc, Hf, Ge, Sn. The reason for this is that the COD database may contain phases that are isomorphous (possessing the same crystal structure) to those in our samples but have not yet been synthesized with the specific combination Yb+Ti+Zr+O, but instead with other rare-earth elements (or Hf, Ge, Sn, etc.).

After imposing restraints on allowable phases we perform the Search-Match step, in which QualX compares the list of peak positions and intensities to the database entries and ranks them according to a figure of merit (FoM). Results with the highest FoM are the most likely to match the sample. The FoM assesses the goodness of the identified phase by taking into account the number of matched peaks and the average difference in peak position/intensity between the observed and database peaks.

Using the toolbar on the right-hand side in Figure 5.14 we can manage the list and accept phases from the results list. When a phase is accepted the program performs a semi-quantitative analysis, based on peak area/intensity, to estimate the weight fraction of the accepted phase in the sample, given as a percentage in the last column (S-Quant) in Fig-

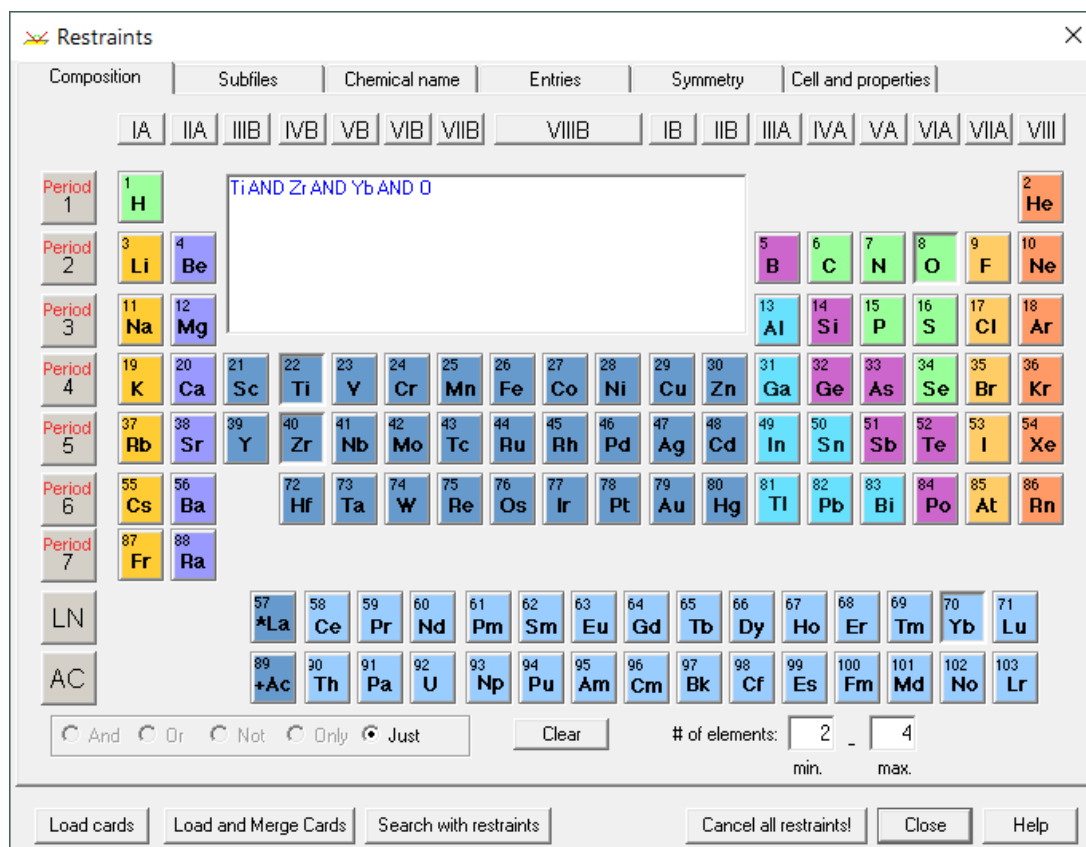


Figure 5.13 Restraints imposed on results of the Search-Match algorithm.

No.	QM	CARD	Compound Name	Chemical Formula	Peakpos.	Intensity	Scale	FoM	S-Quant.
P.1	C	00-153-6991	Yb4 Zr3 O12	O12 Yb4 Zr3	0.81896	0.58042	0.99455	0.77523	75.3%
P.2	C	00-901-5745		O3 Yb2	0.78825	0.69309	0.25980	0.53941	12.4%
P.3	C	00-500-0038	Zirconium oxide (1/2.12) [Arkelite]	O2 Zr	0.71647	0.33700	0.22015E-01	0.52536	2.0%
P.4	C	00-152-2143	Zr O2	O2 Zr	0.60080	0.37581	0.55417E-01	0.51170	10.2%
1	C	00-210-1234		O2 Zr1	0.60088	0.23914	0.12544E-01	0.50595	10.943
2	C	00-210-6210	Ti1.850 O3	O3 Ti1.85	0.49180	0.69449	0.18276E-01	0.42515	1.721
3	C	00-101-0332	Ytterbium oxide	Yb2 O3	0.85034	0.57359E-01	0.11951E-01	0.38789	20.944
4	C	00-153-2065	Ti2 O3	O3 Ti2	0.61059	0.37973	0.18793E-01	0.38719	1.962
5	C	00-210-6209	Ti1.886 O3	O3 Ti1.886	0.63001	0.39140	0.18916E-01	0.37799	1.779
6	C	00-900-7485	[Baddeleyite]	O2 Zr	0.60642	0.10350	0.78013E-02	0.37524	5.317
7	C	00-200-2690	Titanium(II) oxide - HT	Ti O	0.53221	0.19492	0.14120E-01	0.35699	1.427
8	C	00-100-8195	TITANIUM OXIDE (6/11)	Ti6 O11	0.50107	0.14619	0.15886E-01	0.34886	0.941
9	C	00-153-7839	Yb2 O3	O3 Yb2	0.56012	0.91233E-01	0.16823E-01	0.34484	21.442
10	C	00-230-0296	Zirconium Oxide	Zr O2	0.49081	0.94386E-01	0.79148E-02	0.34122	5.393
11	C	00-154-5065	ZrO2 ortho I phase	O2 Zr	0.55597	0.45303	0.30546E-01	0.34099	9.090
12	C	00-900-8082	[Tistarite]	O3 Ti2	0.52952	0.42338	0.98075E-02	0.33826	1.872
13	C	00-100-8196	TITANIUM OXIDE (7/13)	Ti7 O13	0.62569	0.80167E-01	0.83415E-02	0.33336	0.983

Figure 5.14 List of possible phases returned by the Search-Match algorithm. Highlighted phases at the top of the list are accepted phases.

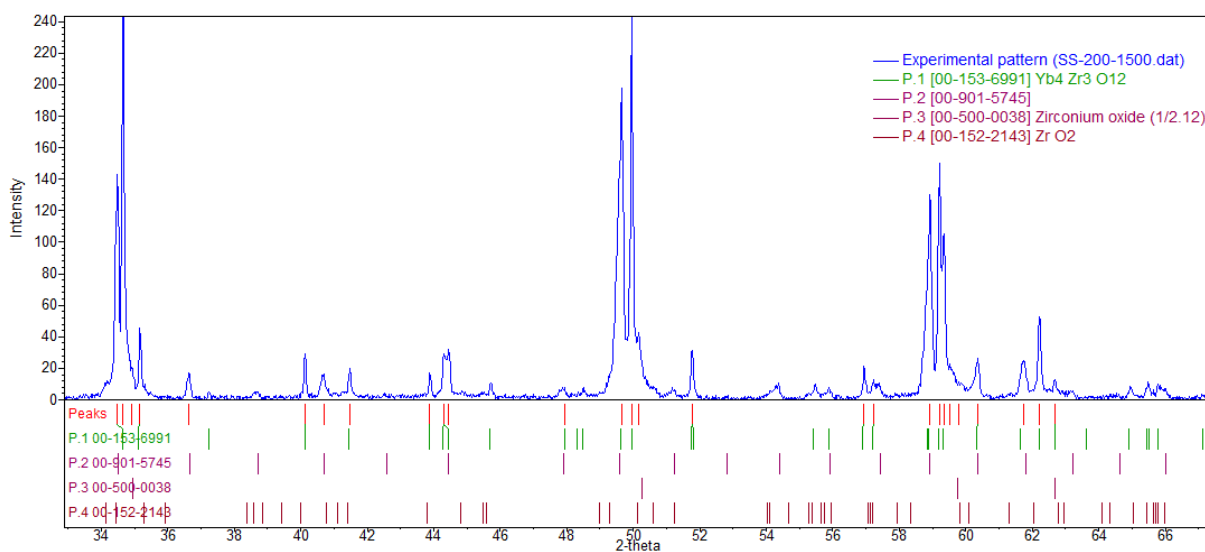


Figure 5.15 Experimental powder diffractogram and tick marks for the accepted phases, indicating peak positions.

Exp-2th	Exp-I	P1-2th	P1-I	P2-2th	P2-I	P3-2th	P3-I	P4-2th	P4-I
18.38	67.5	18.36	41.2						
20.92	35.9			20.93	10.9				
22.41	21.2	22.38	11.2						
28.21	51.6							28.21	55.4
29.74	665.6	29.68	330.5	29.76	259.8				
29.97	1000.0	29.94	994.5			30.15	22.0		
31.50	28.7							31.46	37.5
34.49	143.1			34.50	93.1			34.43	7.7
34.65	375.0	34.63	456.0						
34.92	20.4					34.96	4.6		
35.16	45.4	35.13	29.1					35.30	8.9
36.64	16.9			36.67	16.3				
40.13	29.3	40.12	14.9					40.01	0.1
40.69	16.2			40.70	2.2			40.76	7.6
41.49	20.0	41.44	18.6					41.43	1.4
43.88	17.2	43.86	1.5					43.81	0.0
44.31	29.3	44.28	9.6						
44.45	32.2	44.46	17.2	44.42	18.6				
47.95	8.0	47.93	3.1	47.92	8.2				
49.65	198.1	49.62	279.4	49.59	94.1				
49.96	247.4	49.95	285.3						
50.16	43.0					50.27	12.1	50.14	12.8
51.78	31.3	51.80	3.7						
56.93	21.1	56.91	14.0					57.07	0.0

Figure 5.16 List of peak positions and intensities in experimental data and accepted phases.

ure 5.14. The other columns in the phases list show the FoM and some statistical indicators that quantify the agreement between the experimental pattern and database entries. The phases can be compared by inspecting the frame that contains the diffraction pattern and tick marks representing peak locations for the accepted phases and other phases under consideration (Figure 5.15). Another way of comparing phases is through the list of peak positions and intensities for the experimental data and accepted phases (Figure 5.16).

We can also change the acceptance criteria of the Search-Match algorithm by allowing phases with a lower FoM or change the weight given to the position and/or intensity contributions to the FoM. A detailed description of how the FoM is calculated and of all configurable parameters is available in the QualX manual [240]. In this manner we can expand the phases list if the search has not returned adequate results. Changing the default options might also be necessary when searching for isomorphous phases containing different elements, which can have different lattice parameters, intensity ratios, etc.

5.4 Instrumental Parameters

Rietveld refinements of our XRD data were performed using the software GSAS-II [241]. GSAS-II is an open source Python project for determination of crystal structures by powder and single-crystal diffraction of x-rays or neutrons, providing structure solution and refinement as well as extensive visualization capabilities. GSAS-II supports all stages of data reduction and analysis, including area detector calibration and integration, pattern indexing, LeBail and Pawley intensity extraction and peak fitting. pair distribution function analysis, sequential refinement with subsequent parametric fitting, small-angle scattering, reflectometry fitting, simulation of the effects of stacking faults and magnetic scattering.

In order to perform a Rietveld refinement we need to know the parameters that define the instrumental resolution of the diffractometer. One method for doing this is the so called fundamental parameters approach [242], which requires a complete specification of instrument configuration, including slit widths, beam divergence, distances etc. We tried this approach but the results were not sufficiently good, probably due to incomplete or inaccurate specifications of the internal geometry of the instruments, to which we had no direct access. Therefore we used the empirical approach for determining the instrumental resolution, which consists in measuring a reference material that has been previously characterized by some reliable source. A series of standard reference materials (SRMs) supplied by NIST (the National Institute for Standards and Technology, in the US) are commonly used for this purpose.

The most relevant sample parameters that contribute to diffraction peak broadening are the crystallite size and strain, a measure of internal stresses on the microscopic level. In diffraction studies the strain is usually given as a microstrain value ϵ , which is the fractional deformation of the unit cell $\Delta a/a$, expressed in terms of parts per million,

$$\epsilon = 10^6 \frac{\Delta a}{a} \quad (5.18)$$

Assuming that the reference material has well known crystallite size and microstrain values it is possible to attribute the remaining broadening of the experimental peaks to the instrument, in a process called peak deconvolution. Common reference materials for x-ray diffraction are silicon (Si), aluminum oxide (Al_2O_3) and lanthanum hexaboride (LaB_6). We used aluminum oxide standards for the Bruker D8 Focus and Bruker D8 Discover instruments and a silicon standard for the Rigaku Ultima III (see Table 5.3 for a list of instruments).

Unfortunately we did not have an official NIST SRM, so we simply assumed that the available reference samples have ideal properties that do not lead to any sample-induced broadening. If an SRM were available we could use the values reported in the official certificate to obtain a

more precise instrument calibration by doing an actual refinement of the reference material, not just a peak fit. Another option would be to consider the peak intensities as arbitrary and perform a Le Bail fit to the powder pattern, which does not require information on the atomic structure of the SRM.

The shape of a diffraction peak is influenced by many factors, both due to the diffraction instrument and to the measured sample. Peak shapes in x-ray diffraction are commonly modeled by the Voigt function V , a convolution of a Gaussian and a Lorentzian function,

$$V(x) = \int_{-\infty}^{\infty} G(y)L(x-y)dy = \int_{-\infty}^{\infty} G(x-y)L(y)dy \quad (5.19)$$

where

$$G(x) = \sqrt{\frac{4 \ln 2}{\pi \Gamma_G^2}} \exp\left[-\frac{4 \ln 2}{\pi \Gamma_G^2} x^2\right] \quad (5.20)$$

is a Gaussian function with FWHM Γ_G and

$$L(x) = \frac{2}{\pi \Gamma_L} \frac{1}{1 + \left[\frac{2}{\pi \Gamma_L} x\right]^2} \quad (5.21)$$

is a Lorentzian function with FWHM Γ_L . There is no closed-form analytic expression for the Voigt function, so it has to be computed by numeric integration of (5.19). This is too computationally expensive for applications such as Rietveld refinement, so the Voigt function is usually approximated by the pseudo-Voigt function PV , a linear combination of Gaussian and Lorentzian functions instead of a convolution,

$$PV(x) = \eta G(x) + (1 - \eta) L(x) \quad (5.22)$$

where the mixing parameter η lies between 0 and 1 and controls whether the character of the pseudo-Voigt function is more gaussian or lorentzian in nature. Figure 5.17 shows a Gaussian and the broader, long-tailed Lorentzian function with the same FWHM and total area.

At high 2θ the source emission profile dominates so that the peak profile is mostly lorentzian, therefore η usually decreases with 2θ . Laboratory diffractometer profiles are usually more lorentzian while synchrotron profiles are more gaussian in nature. For the Thompson-Cox-Hastings variant of the pseudo-Voigt function, used by GSAS-II, η is related to the FWHM parameters Γ_G, Γ_L by [243]

$$\eta = 1.36603 \left(\frac{\Gamma_L}{\Gamma}\right) - 0.47719 \left(\frac{\Gamma_L}{\Gamma}\right)^2 + 0.11116 \left(\frac{\Gamma_L}{\Gamma}\right)^3 \quad (5.23)$$

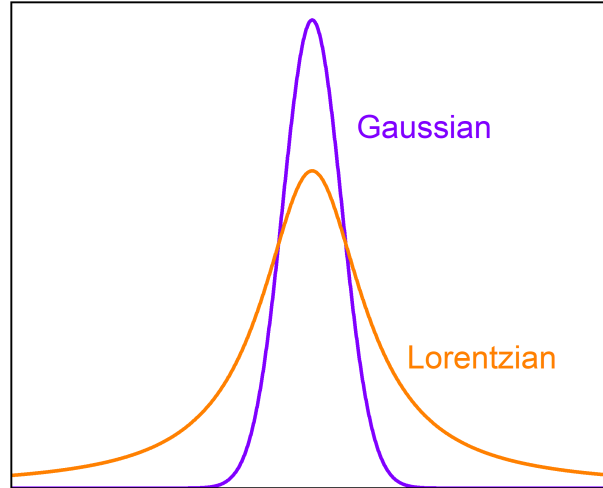


Figure 5.17 Gaussian and Lorentzian functions with the same FWHM and total area.

where

$$\Gamma = \left(\Gamma_G^5 + 2.69269\Gamma_G^4\Gamma_L + 2.42843\Gamma_G^3\Gamma_L^2 + 4.47163\Gamma_G^2\Gamma_L^3 + 0.07842\Gamma_G\Gamma_L^4 + \Gamma_L^5 \right)^{1/5} \quad (5.24)$$

is the approximate FWHM for the combined gaussian and lorentzian contributions. The FWHMs are functions of θ ,

$$\Gamma_G^2 = U \tan^2 \theta + V \tan \theta + W + \frac{P}{\cos^2 \theta} \quad (5.25)$$

for the Gaussian part and

$$\Gamma_L = \frac{X + S_\mu}{\cos \theta} + (Y + S_\epsilon) \tan \theta \quad (5.26)$$

for the Lorentzian part. U, V, W, X, Y are the instrumental contributions to FWHM, while S_μ and S_ϵ are contributions from the sample, due to the crystallite size μ and the microstrain ϵ . S_μ and S_ϵ have the same 2θ dependence as the instrumental parameters X and Y but are refined separately from them. Some refinement software allows both the gaussian and lorentzian sample broadening to be refined, but here we assume that all of the sample-induced broadening is lorentzian. This assumption is valid for common powders, which have a rather wide crystallite size distribution, often modeled by a lognormal distribution [244, 245]. In rare cases, when the crystallite size distribution is very narrow, the gaussian contributions to sample broadening (terms with the same 2θ dependence as U and P) can also be refined. There exist more complex models for Γ_G, Γ_L that take into account anisotropic peak broadening, but our work does not require their use.

There is also a peak position correction,

$$\Delta 2\theta = I_0 + S_d \cos \theta + S_t \sin 2\theta + \frac{I_a(\theta)}{\tan 2\theta} \quad (5.27)$$

where I_0 is a 2θ zero correction to compensate for goniometer misalignment, S_d is the sample displacement, S_t is the sample transparency and $I_a(\theta)$ is an empirical correction to compensate for peak asymmetry.

After determining the instrumental parameters they remain valid for all subsequent measurements as long as the instrument configuration, such as the size of the Soller and divergence slits, are kept fixed. In cases where the instrument parameters are not known, when importing powder diffraction data GSAS-II offers to use default parameter values for some types of instruments. The default values for $\text{CuK}\alpha$ lab data are shown in Listing 5.1.

```
1 #GSAS-II instrument parameter file; do not add/delete items!  
2 Type:PXC  
3 Bank:1.0  
4 Lam1:1.54051  
5 Lam2:1.54433  
6 Zero:0.0  
7 Polariz.:0.7  
8 Azimuth:0.0  
9 I(L2)/I(L1):0.5  
10 U:2.0  
11 V:-2.0  
12 W:5.0  
13 X:0.0  
14 Y:0.0  
15 Z:0.0  
16 SH/L:0.002  
17 Source:CuKa
```

Listing 5.1 Default $\text{CuK}\alpha$ lab instrument parameters provided by GSAS-II.

For conventional diffractometers $U, W > 0$ and $V < 0$ so that the instrument profile curve is convex and positive over the whole 2θ range, with typical values being $U \approx 2$, $V \approx -2$ and $W \approx 5$, the default values provided by GSAS-II. Both the gaussian and lorentzian resolution curves should be non-negative over the whole range. The gaussian profile parabola might be almost flat, making the U, V, W terms hard to refine because of their mutual correlation. In this case it is advised to first refine the lorentzian parameters X, Y and only afterwards the gaussian parameters U, V, W . Z is a constant (independent of 2θ) lorentzian broadening term that is fundamentally not required but occasionally useful when doing precise instrument characterization.

SH/L is a parameter that characterizes the peak asymmetry, especially significant for low angle peaks. To refine this parameter ideally the reference sample should have some low angle peaks. The polarization and azimuth variables are related to the instrument's geometry and were kept fixed at their default values. Once fitted, the zero shift I_0 should be kept fixed as an instrument parameter, so that only the sample displacement parameter S_d is refined for each individual sample.

Some typical instrument parameters are given in [246], both for conventional laboratory and synchrotron sources. Notably the authors argue that for the conventional diffractometers the parameter V is redundant and the gaussian broadening can be accounted for using only the U and W terms in (5.25), i.e. setting $V = 0$.

To determine the instrumental profile we fit individual peaks over the whole 2θ range and refine their peak profile parameters independently. It is recommended to use at least ten well-defined peaks, that have a good signal to noise ratio, in a wide 2θ angular range. Figure 5.18 shows a GSAS-II window with the XRD pattern for Al_2O_3 , one of the reference materials used for instrument calibration. The peaks selected for individual peak fitting are marked with dotted vertical lines. The experimental data is in blue, the background curve in red and the fitted peaks in green. The $K\alpha_1/K\alpha_2$ splitting is apparent at the higher angle peaks and is taken into account by GSAS-II, as evidenced by the pair of wavelengths Lam1 , Lam2 and the intensity ratio $I(\text{L1})/I(\text{L2})$ in Listing 5.1.

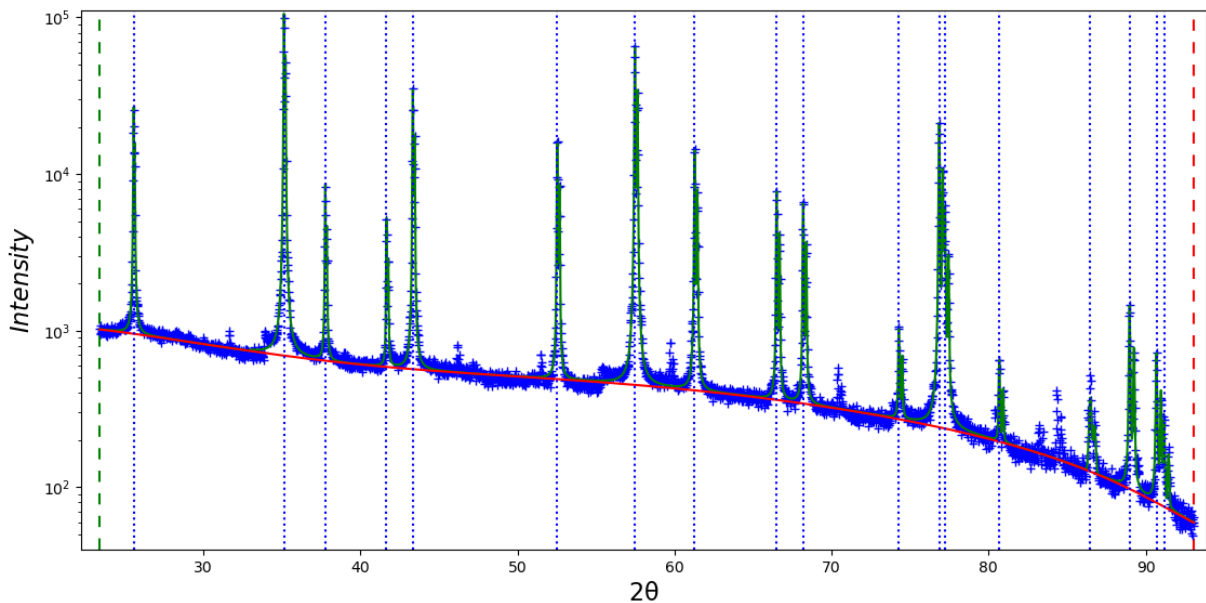


Figure 5.18 Peak fitting of Al_2O_3 reference material in GSAS-II (logarithmic intensity scale).

Figure 5.19 shows the parameters used to fit the individual peaks, including the 2θ position, the intensity and the sigma/gamma values that represent the gaussian and lorentzian contributions to the FWHM ($\sigma^2 = \Gamma_G^2/8 \ln 2$ is the gaussian variance and $\gamma = \Gamma_L$). The peak positions were selected manually and only refined after the intensity, sigma and gamma values had converged. In every step of peak fitting one should verify that the fitted values are reasonable. Sometimes a parameters converges to negative or unreasonably large value. In this case one must try to identify the problem by visual inspection. A common problem is that the peak is split or that another peak is close enough for their tails to overlap and the fitting algorithm tries to include both peaks into a single one.

After peak-fitting the individual peak parameter values are fixed and the instrument profile parameters, that start out with the default values in Listing 5.1, are refined to best adjust to the values obtained from peak-fitting (Figure 5.20). Due to correlation between the peak asymmetry parameter SH/L and X, Y, Z , the lorentzian FWHM might refine to negative values for the first few low angle peaks. This can be addressed by fixing $X = 0$, refining $U, V, W, Y, SH/L$, and only afterwards refining X .

	position	refine	intensity	refine	sigma	refine	gamma	refine
1	25.55779	<input checked="" type="checkbox"/>	171820.5	<input checked="" type="checkbox"/>	2.843	<input type="checkbox"/>	2.626	<input type="checkbox"/>
2	35.13148	<input checked="" type="checkbox"/>	727387.9	<input checked="" type="checkbox"/>	2.738	<input type="checkbox"/>	2.803	<input type="checkbox"/>
3	37.75932	<input checked="" type="checkbox"/>	55475.3	<input checked="" type="checkbox"/>	2.738	<input type="checkbox"/>	2.856	<input type="checkbox"/>
4	41.65992	<input checked="" type="checkbox"/>	34089.8	<input checked="" type="checkbox"/>	2.763	<input type="checkbox"/>	2.938	<input type="checkbox"/>
5	43.33574	<input checked="" type="checkbox"/>	261539.8	<input checked="" type="checkbox"/>	2.783	<input type="checkbox"/>	2.975	<input type="checkbox"/>
6	52.53371	<input checked="" type="checkbox"/>	135890.6	<input checked="" type="checkbox"/>	3.010	<input type="checkbox"/>	3.196	<input type="checkbox"/>
7	57.48119	<input checked="" type="checkbox"/>	549559.3	<input checked="" type="checkbox"/>	3.223	<input type="checkbox"/>	3.329	<input type="checkbox"/>
8	61.28356	<input checked="" type="checkbox"/>	125514.5	<input checked="" type="checkbox"/>	3.438	<input type="checkbox"/>	3.438	<input type="checkbox"/>
9	66.50067	<input checked="" type="checkbox"/>	68517.9	<input checked="" type="checkbox"/>	3.817	<input type="checkbox"/>	3.601	<input type="checkbox"/>
10	68.19198	<input checked="" type="checkbox"/>	61340.6	<input checked="" type="checkbox"/>	3.962	<input type="checkbox"/>	3.657	<input type="checkbox"/>
11	74.28293	<input checked="" type="checkbox"/>	8101.2	<input checked="" type="checkbox"/>	4.596	<input type="checkbox"/>	3.873	<input type="checkbox"/>
12	76.85506	<input checked="" type="checkbox"/>	207298.1	<input checked="" type="checkbox"/>	4.921	<input type="checkbox"/>	3.973	<input type="checkbox"/>
13	77.21695	<input checked="" type="checkbox"/>	58416.5	<input checked="" type="checkbox"/>	4.970	<input type="checkbox"/>	3.987	<input type="checkbox"/>
14	80.67876	<input checked="" type="checkbox"/>	5156.3	<input checked="" type="checkbox"/>	5.479	<input type="checkbox"/>	4.130	<input type="checkbox"/>
15	86.48503	<input checked="" type="checkbox"/>	4440.9	<input checked="" type="checkbox"/>	6.526	<input type="checkbox"/>	4.392	<input type="checkbox"/>
16	88.97662	<input checked="" type="checkbox"/>	15671.8	<input checked="" type="checkbox"/>	7.063	<input type="checkbox"/>	4.515	<input type="checkbox"/>
17	90.68616	<input checked="" type="checkbox"/>	7299.1	<input checked="" type="checkbox"/>	7.466	<input type="checkbox"/>	4.604	<input type="checkbox"/>
18	91.16812	<input checked="" type="checkbox"/>	2389.4	<input checked="" type="checkbox"/>	7.585	<input type="checkbox"/>	4.629	<input type="checkbox"/>

Figure 5.19 List of peak positions, intensities and widths, used in the fitting procedure,

Azimuth: 0.00 Ka1/Ka2: 1.540510/1.544330Å Source type: CuKα

Name (default)	Value	Refine?
I(L2)/I(L1) (0.5000):	0.4859	<input checked="" type="checkbox"/>
Zero (0.0000):	0.0	<input type="checkbox"/>
Polariz. (0.7000):	0.7	<input checked="" type="checkbox"/>
U (2.000):	10.149	<input checked="" type="checkbox"/>
V (-2.000):	-6.686	<input checked="" type="checkbox"/>
W (5.000):	3.837	<input checked="" type="checkbox"/>
X (0.000):	2.257	<input checked="" type="checkbox"/>
Y (0.000):	1.376	<input checked="" type="checkbox"/>
Z (0.000):	0.0	<input type="checkbox"/>
SH/L (0.00200):	0.002	<input type="checkbox"/>

Figure 5.20 Instrumental parameters calculated by GSAS-II to best fit the experimental peak profile.

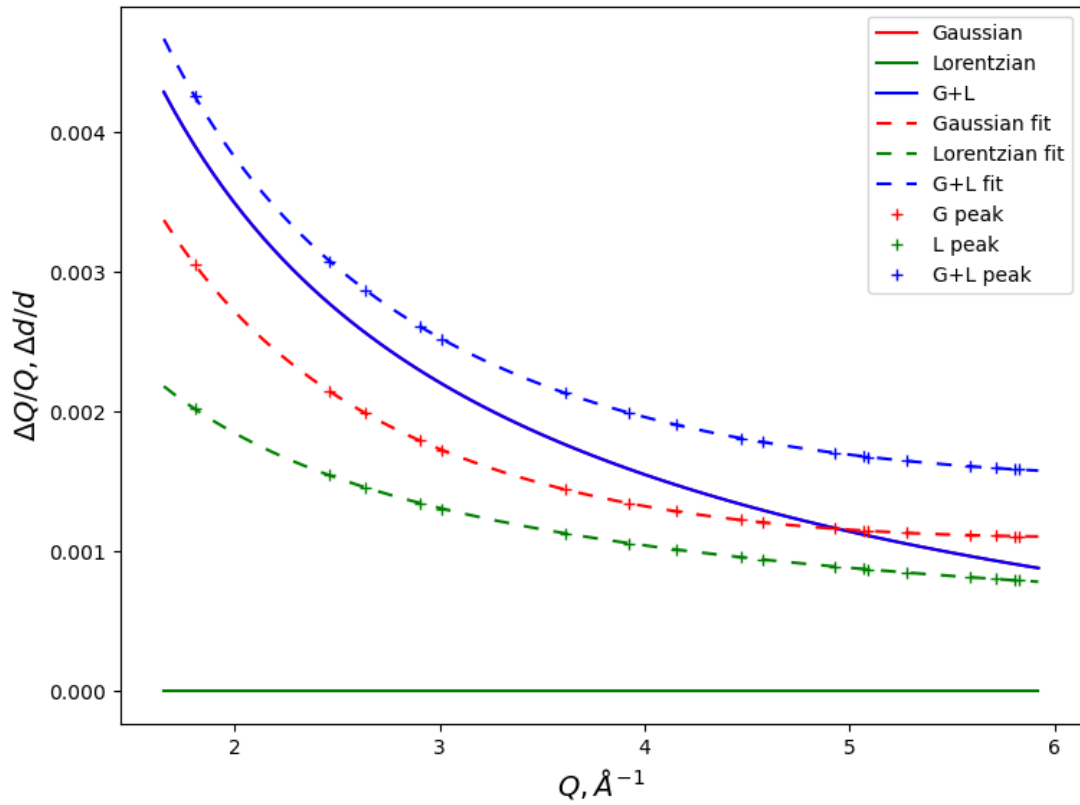


Figure 5.21 Instrumental peak profile curves calculated from the instrumental parameters.

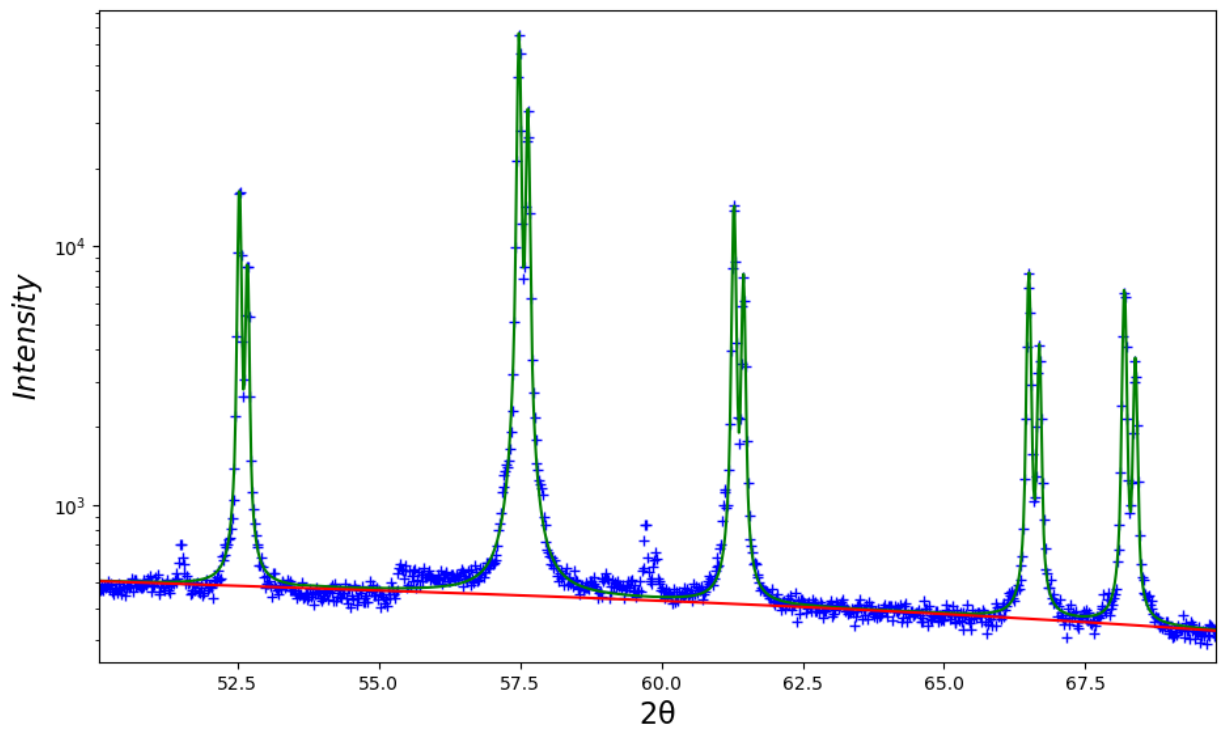


Figure 5.22 Close-up view of fitted peaks in GSAS-II (logarithmic intensity scale).

Figure 5.21 shows the instrumental peak profile curves for the gaussian, lorentzian and combined components, along with the values from the individual peak fits. These curves should be inspected visually to detect problems during refinement of the instrument parameters. The general appearance should be similar to that in Figure 5.21 for most common laboratory diffractometers: decreasing or flat, slightly convex and positive over the whole range. Note that there the horizontal axis is $Q = 2k \sin \theta = 4\pi \sin \theta / \lambda$, the magnitude of the momentum transfer vector in the scattering event, which is proportional to 2θ , and the vertical axis is $\Delta Q/Q = \Delta d/d$, where d is the lattice plane spacing.

Figure 5.22 shows a close-up view of some peaks after the instrument profile fitting was completed. The resulting instrument parameters are shown in Listing 5.2.

```

1 #GSAS-II instrument parameter file; do not add/delete items!
2 Type:PXC
3 Bank:1.0
4 Lam1:1.54051
5 Lam2:1.54433
6 Zero:0.0
7 Polariz.:0.7
8 Azimuth:0.0
9 I(L2)/I(L1):0.4859497613802969
10 U:10.149409576173177
11 V:-6.685905347876194
12 W:3.8372799489407523
13 X:2.256876994518354
14 Y:1.3761022169546244
15 Z:0.0
16 SH/L:0.002
17 Source:CuKa

```

Listing 5.2 Fitted instrument parameters for Al_2O_3 reference material measured by the Bruker D8 Focus diffractometer.

5.5 Rietveld Refinement

To perform a Rietveld refinement in GSAS-II we import the powder diffraction data, usually as a text file with two columns, the 2θ position and measured diffracted intensity at that angle. Then we load the file containing the instrument parameters (Section 5.4) and a CIF (Crystallographic Information Framework) file that contains a description of the phase that will be refined. The CIF is a specification developed by the IUCr (International Union of Crystallography) to standardize the exchange of crystal structure information [247]. Listing 5.3 shows a section of a CIF file for $\text{Yb}_2\text{Ti}_2\text{O}_7$ displaying the relevant information for Rietveld refinement.

```

1 _chemical_formula_sum      '07 Ti2 Yb2'
2 _space_group_IT_number    227
3 _symmetry_space_group_name_H-M 'F d -3 m :2'
4 _cell_angle_alpha         90
5 _cell_angle_beta          90
6 _cell_angle_gamma         90
7 _cell_formula_units_Z     8
8 _cell_length_a            10.034410(4)

```

```

9  _cell_length_b          10.034410(4)
10 _cell_length_c          10.034410(4)
11 _cell_volume            1010.3586(7)
12
13 loop_
14 _atom_site_label
15 _atom_site_type_symbol
16 _atom_site_symmetry_multiplicity
17 _atom_site_Wyckoff_symbol
18 _atom_site_occupancy
19 _atom_site_fract_x
20 _atom_site_fract_y
21 _atom_site_fract_z
22 _atom_site_U_iso_or_equiv
23 Yb Yb3+ 16 d 1.0 0.000000 0.000000 0.000000 0.00782(6)
24 Ti Ti4+ 16 c 1.0 0.500000 0.500000 0.500000 0.00471(14)
25 O1 O2- 8 b 1.0 0.125000 0.125000 0.125000 0.00502(13)
26 O2 O2- 48 f 1.0 0.31898(3) 0.125000 0.125000 0.00658(6)

```

Listing 5.3 Section of a CIF file for Yb₂Ti₂O₇ displaying the relevant information for Rietveld refinement.

General	Data	Atoms	Draw Options	Draw Atoms	RB Models	Map peaks	MC/SA	RMC	ISODISTORT		
Atom parameters list for pyrochlore:											
	Name	Type	refine	x	y	z	frac	site sym	mult	I/A	Uiso
0	Yb	Yb+3	XU	0.00000	0.00000	0.00000	1.0000	-3m(111)	16		0.00782
1	Ti	Ti+4	XU	0.50000	0.50000	0.50000	1.0000	-3m(111)	16		0.00471
2	O1	O-2	XU	0.12500	0.12500	0.12500	1.0000	-43m	8		0.00502
3	O2	O-2	XU	0.31898	0.12500	0.12500	1.0000	mm2(d100)	48		0.00658

Figure 5.23 GSAS-II window displaying the atomic coordinates and other information, imported from the CIF file.

CIF files can be downloaded from online sources such as the [COD \(Crystallography Open Database\)](#) or the [ICSD \(Inorganic Crystal Structure Database\)](#). The information on space group symmetry, lattice parameter and atomic positions can also be entered manually into GSAS-II if a CIF file is not available. Figure 5.23 shows a GSAS-II window displaying the atomic coordinates and other information that were imported from the CIF file.

The software effectively constructs an internal model of the sample that leads to a predicted value for the diffracted intensity as a function of 2θ ,

$$I^{calc}(2\theta) = I^{back}(2\theta) + sA \sum_i L_i P_i M_i |F_i|^2 P V_i (2\theta - 2\theta_i) \quad (5.28)$$

where the sum is over all Bragg peaks i , I^{back} is an arbitrary background function, s is the scale factor, A is the absorption constant, L is the Lorentz polarization factor, P is the preferential orientation factor, M is the multiplicity and F is the structure factor. Detailed descriptions of each term can be found in [197, 200, 201, 202]. The actual models used by current refinement software are even more involved than (5.28), with potentially dozens of terms accounting for effects induced both by the instrument and the sample.

The process of refinement consists in adjusting the parameters of the model (5.28) to achieve a good fit of the calculated intensity $I^{calc}(2\theta)$ to the experimental data $I^{exp}(2\theta)$, essentially a least squares minimization of the error $I^{calc} - I^{exp}$. Since the values of I^{exp} are available at discrete values of 2θ only the values of I^{calc} at the same discrete 2θ values are considered. The quality of the fit can be quantified by a variety of statistical indicators, such as R_{wp} , R_w , R_p , R_{exp} , R_{Bragg} , χ^2 , etc. In our work we used the reduced χ^2 value due to its common usage in the literature, although it might not always be the best goodness of fit indicator [248]. It is defined as

$$\chi^2 = \frac{\sum_i w_i (I_i^{exp} - I_i^{calc})^2}{N - P} = \frac{R_{wp}}{R_{exp}} \quad (5.29)$$

where the sum is over all N data points i , $w_i^{-1} = \sqrt{I^{exp}}$ are weighting factors and P is the number of free variables in the model. χ^2 should approach the value 1 for a perfect fit but in practice this seldom is the case.

The difficulty in Rietveld refinement lies mostly in determining which parameters should be refined and in what order one should do so. The selection of parameters to be refined depends somewhat on the sample and also on the data acquisition procedure. The order in which parameters should be refined is not agreed upon by all researchers, but some general guidelines exist [200, 201, 202, 203]. Here we will describe how the XRD data for the $\text{Yb}_2\text{Zr}_x\text{Ti}_{2-x}\text{O}_7$ samples was refined, so the details of the procedure might not apply to the refinement of other samples.

Usually the variables refined in one step are kept refining in the next step, so that at the end almost all parameters are refined simultaneously. However some combinations of parameters are highly correlated with one another, so their simultaneous refinement can cause problems especially if the fit is not yet very good. Therefore an empirical approach is necessary, where one tries to refine some variables to see if the results are reasonable and returns to the previous step otherwise. We offer some miscellaneous comments and examples of possible problems that might be encountered. These considerations are by no means comprehensive but serve to illustrate some of the challenges in performing a good refinement.

The first parameters to be refined were the histogram scale factor, the lattice parameter (the cubic pyrochlore and fluorite phases have only one lattice parameter a), the sample displacement and some background parameters. Next to every refinable parameter in GSAS-II there is a box that can be checked to toggle the refinement flag on or off. In the atomic parameters table shown in Figure 5.23 the refinement flag is given as a combination of F, X and U, which stand for the fractional site occupancies, atomic coordinates and atomic displacement parameters (ADPs), respectively.

The scale factor is an essentially arbitrary factor that controls the ratio of the calculated and experimental intensities and is always refined. The refinement can diverge if the initial guess for the lattice parameter is too far off from the true value. If a CIF file with a previously determined lattice parameter is not available then it may be necessary to calculate an approximate value from the 2θ position and Miller index of one of the peaks.

The sample displacement S_d (5.27) compensates for the almost inevitable small vertical dis-

placement of the sample's surface from the ideal horizontal diffraction plane and is usually less than about $100\mu\text{m}$ in magnitude for a well-prepared sample. Once refined it should remain at a stable value but may continue to be refined. If the instrument's goniometer radius is set at the wrong value the actual displacement is not the same as the refined value, but if the value is of little concern since the sample displacement is not relevant to the results of the refinement.

The background was modeled by a Chebyshev polynomial, although other options are available in GSAS-II. The background has contributions from both the samples and the instrument and usually increases at low angle. The number of background parameters, which is one less than the order of the polynomial, varied between about 6 and 15. Starting with four terms, the number of parameters was increased in successive refinements until a good fit to the background over the whole 2θ range was observed and adding another term did not significantly improve the quality indicators.

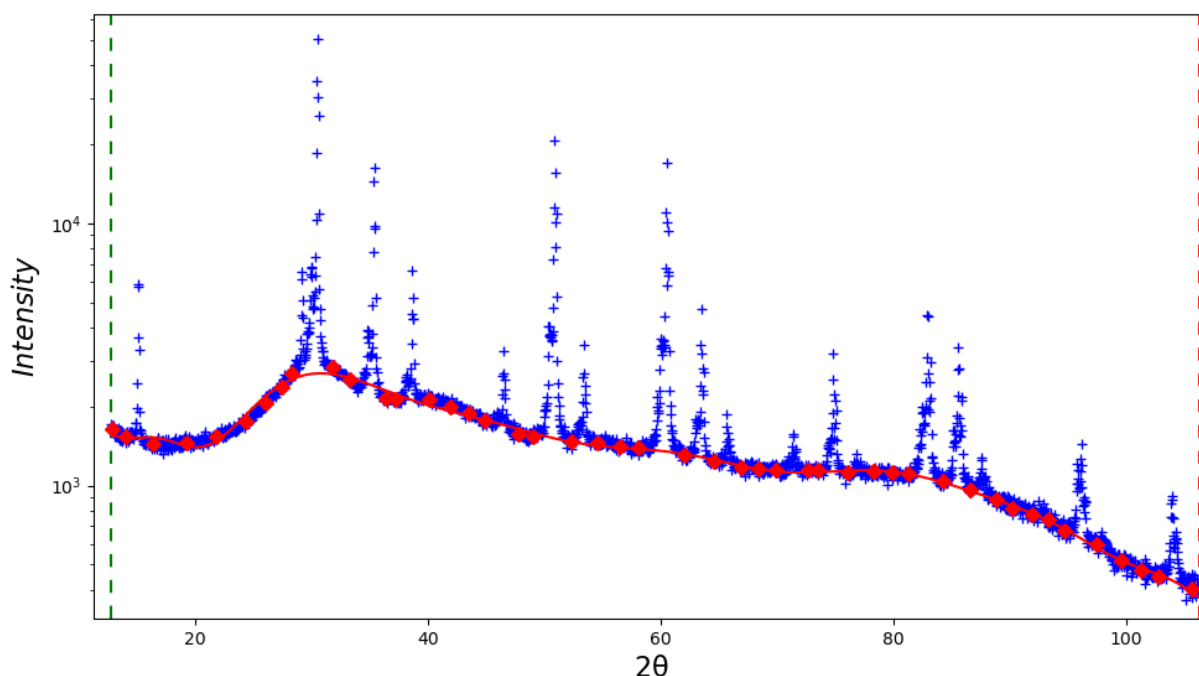


Figure 5.24 Fixed points that were added manually to guide the fitting of the background polynomial (logarithmic intensity scale).

In some cases the background is not very smooth and it may be necessary to guide the fitting of the background polynomial by manually adding fixed points, indicated by the red squares in Figure 5.24. Sometimes it is best to initially fit only the background with up to 30 polynomial terms and then keep the background fixed during subsequent refinement. It is also possible to add Debye-type terms to model the diffuse scattering mostly at low angle. One can change the upper and lower 2θ limits for the data that will be refined (indicated by the dashed vertical lines in Figure 5.24) or add excluded regions in case there is a 2θ interval with no peaks (for instance $2\theta \approx 16^\circ - 28^\circ$ in Figure 5.24).

The statistical indicators are useful to detect if a refinement has improved, but it is important to visually inspect the graph of the powder pattern at most steps of the refinement. In this way one can detect problems with the fit of the calculated curve to the experimental pattern, either by inspecting the peaks directly or by looking at the difference curve. The difference

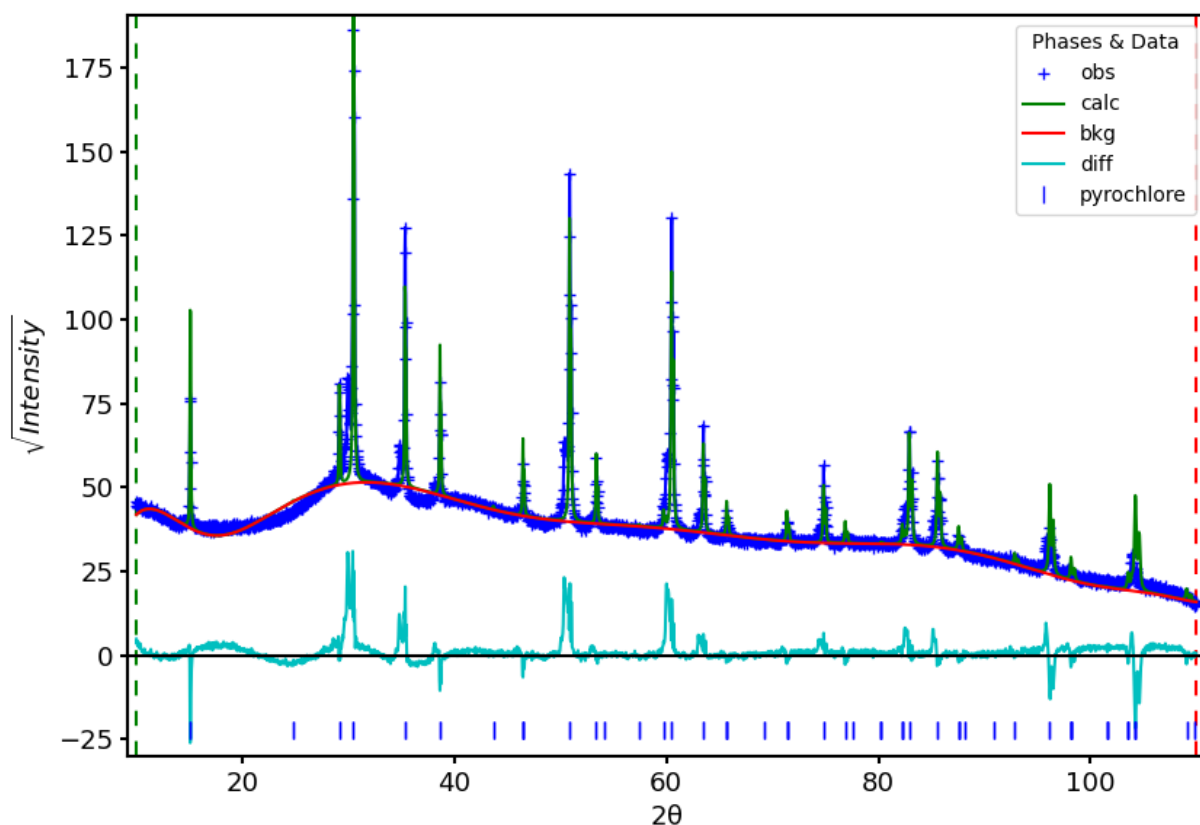


Figure 5.25 Example of the initial steps of a Rietveld refinement. The difference curve clearly shows some problems with the fit.

curve shows $I^{exp} - I^{calc}$ and should be centered around zero with a small amount of random noise. Any systematic deviations from zero indicate a problem with the fit, in particular the noise at the peak positions should be equally distributed on the positive and negative sides.

Figure 5.25 shows an example of the initial steps of a Rietveld refinement. The difference curve clearly shows some problems with the fit, especially with the background and the peaks, which are marked by ticks at every location where a Bragg peak for the refined structure is expected. Note that the y-axis is set to a square root intensity scale, which allows easier visualization of small features with the most intense peaks in a single frame. A logarithmic intensity scale can also be used for the same purpose, although in that case GSAS-II does not display the difference curve and tick marks. Various controls allow the user to zoom in on any particular region of the diffraction pattern to inspect it more closely.

Next we refined the crystallite size and/or the microstrain value. The dominant sample broadening effect for well crystallized powders is often from microstrain, not from crystallite size. The size and microstrain broadening are differentiated by their Q dependence (ΔQ and $\Delta Q/Q$ constant, respectively). To distinguish these possibilities requires high resolution data over a large Q range, which is why usually synchrotron data is necessary to accurately characterize these parameters.

For laboratory diffractometers it is recommended to refine only the microstrain since this effect is easier to detect than crystallite size broadening for lower resolution data. One can try separately refining both terms to see if the fit improves. If the microstrain value gets very small or the crystallite size very large then that term has no effect and can safely be dropped from

the refinement. These variables should not be refined simultaneously (except for high-quality synchrotron data) since they are strongly correlated.

In the next step we refined the atomic coordinates and the isotropic displacement parameters U_{iso} for each atom. The pyrochlore structure has only one free coordinate, the oxygen x_{48f} position, while the fluorite structure has no free coordinates. The coordinates that are fixed by the symmetry of the Wyckoff position are not varied even if the refinement flag is turned on. For structures with more coordinate degrees of freedom it may be prudent to initially refine the coordinates of only one atom or a small set of atoms at a time.

Similarly the ADPs must be handled with care, given that they are rather prone to absorb problems with the other variables that cause them to diverge or become negative. One can try to refine all the ADPs at once to see if the result is reasonable. Often one or more values become negative (indicated in red by GSAS-II), which is not physically sensible. In that case it is best to reset the negative values to a small positive value and try to refine only a subset of the ADPs at a time.

Least Squares Parameters						
View Parameters in Project						
Number of refined variables: 12 + 4 varied via constraints						
Parameter type: Parameter						
<input checked="" type="radio"/> Phase <input type="radio"/> Phase/Histo <input type="radio"/> Histogram <input type="radio"/> Global						
		AUiso		Refinement Status:		
		Phase		<input type="radio"/> All <input checked="" type="radio"/> Refined		
#	Parameter	Ref	Value	Min	Max	Explanation
1	0::AUiso:1	R	0.050077	0.0005	0.50000	Atom Ti1 in pyrochlore: Atomic isotropic displacement parameter
2	0::AUiso:2	R	0.049424	0.0005	0.50000	Atom O1 in pyrochlore: Atomic isotropic displacement parameter
3	0::AUiso:3	R	0.061256	0.0005	0.50000	Atom O2 in pyrochlore: Atomic isotropic displacement parameter
4	0::AUiso:4	C	0.050077	0.0005	0.50000	Atom Zr5 in pyrochlore: Atomic isotropic displacement parameter
"R" indicates a refined variable						
"C" indicates generated from a user entered constraint						

Figure 5.26 Limits imposed on the range of the ADP variables.

One can also impose constraints on the ranges of the variables. Figure 5.26 shows constraints imposed on the ADPs so that they lie in the range $0.0005 \leq U_{iso} \leq 0.5$. It is useful to impose such limits when some variables tend to diverge or converge to a false minimum, however one should be careful not to mask problems with the refinement by using such restraints. For instance, if the one of the ADPs were actually to settle on the value $U_{iso} = 0.0005$, the minimal limit imposed in Figure 5.26, this would not mean that a stable value was reached. Rather, the minimization algorithm would probably have proceeded to lower values, even negative ones, but was impeded from reaching its true minimum by the imposed limit. Therefore if a limit is reached this should indicate a problem with the refinement of that variable or that the imposed limits may be too restrictive.

The ADPs are highly correlated with the site occupancies, since the effect of a positive ADP is to reduce the intensities at high angle (5.13) and a similar effect could be achieved by decreasing the site occupancy of that atom. Therefore a negative ADP could be an indication that the site occupancy is higher than the assumed value. This also means that one should be careful when refining ADPs and occupancies simultaneously.

When the site occupancies are refined they can settle on values greater than 1, which seemingly makes no physical sense. However this is allowable when refining a single phase since we are only interested in the relative scattering power of the different crystalline sites, so that one could divide all of the occupancies by their maximal value among all the sites to normalize them. Thus when refining all the site occupancies one can keep one of these parameters fixed to serve as a reference value for the others. It should be noted that in some refinement software, such as FullProf, the site occupancies are weighted by the multiplicity of the corresponding Wyckoff site. In that case the normalization also would need to account for the relative multiplicity of each site.

Negative ADPs can also be due to incorrect background models, especially at high angles. In that case one can try to slowly increase the number of background parameters while observing the effects on the ADPs and inspecting the fit of the background curve visually. Large ADPs could also indicate some distortion or disordering of the crystal structure, since a static displacement of an atom from its ideal position could be accounted for by the ADP as if the displacement were dynamic, due to thermal motion, thus artificially increasing the ADP from the value it would assume if there were no distortions or disorder.

When two or more atoms inhabit the same crystalline site their ADPs need to be constrained to equal one another. In this case the ADP can no longer be directly interpreted as proportional to the mean square displacement since the masses of the atoms are different. Constraints in GSAS-II can be implemented as equivalences or more complex equations. Under the constraints GSAS-II tree item the "Make atoms equivalent" option automatically sets the coordinates and ADPs of two or more atoms to be equivalent and constrains their site occupancies to add up to one.

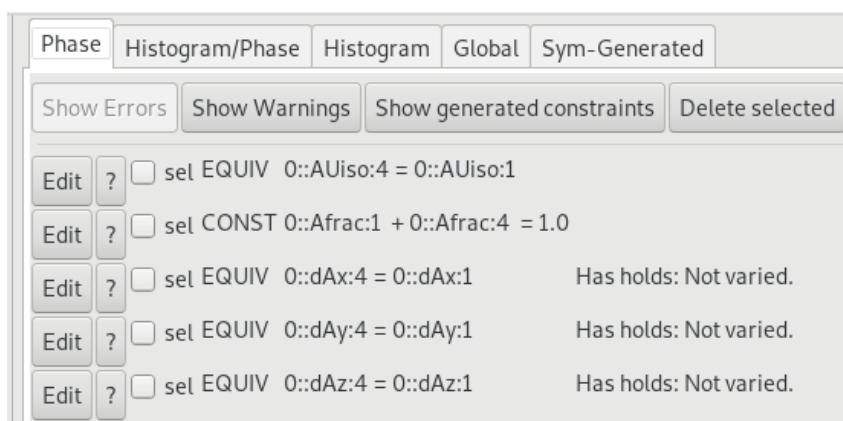


Figure 5.27 Constraints generated by making the Zr and Ti atoms equivalent.

Figure 5.27 shows the constraints generated by making the Zr and Ti atoms equivalent in the pyrochlore structure. For the fluorite structure all three cations are made equivalent (Yb, Zr and Ti). The variables are named as P:H:N, where P is the number of the phase (starting at 0), H is the number of the histogram (the powder pattern, empty if only one pattern is present) and N is the name of the variable, which may contain a number that defines the corresponding atom (also starting at 0). More complex constraints can also be created, for instance for the atoms in the δ -phase we included the site occupancy constraint $f + 6g = 4$ (see Table 2.8).

In general one expects lighter atoms to have higher ADPs, which can be understood by

considering a simple harmonic oscillator model for the displacement of an atom from its equilibrium position. Heavier atoms will have a smaller displacement than lighter ones since their mean thermal energy is the same and a harmonic oscillator's maximal displacement x scales inversely to its mass m , $x \propto m^{-1/2}$. Applying this principle to the pyrochlore oxides, usually the oxygen ADPs should be a few times larger than those of the heavier cations (e.g. $\approx 70/16 = 4.4$ larger than Yb). In reality the ADPs are not that simple and also depend on the crystalline environment of the atoms (how tightly they are bonded to their neighbors, how much empty space surrounds that site, etc).

Since the x-ray scattering power is directly proportional to the atomic mass, the model's parameters that relate to light elements also have less of an effect on the calculated intensity, so that any values related to oxygen should be considered more uncertain and with a larger error bar (i.e. less accurate and less precise) than the same parameters for the cations.

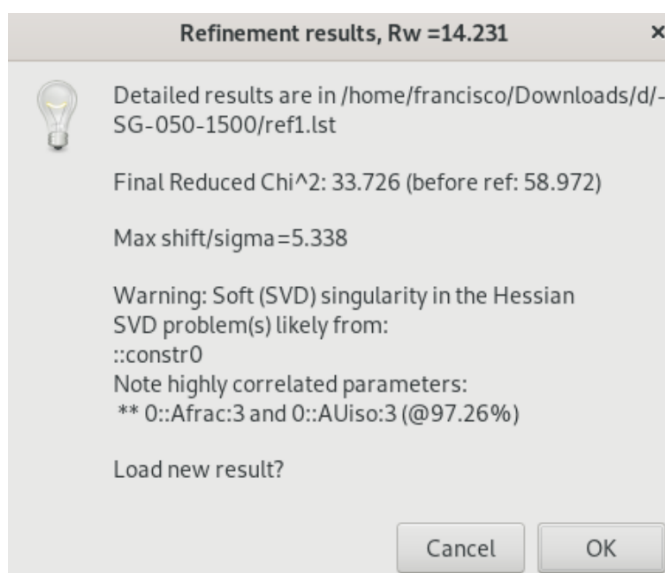


Figure 5.28 Example of a warning dialog in GSAS-II.

If a problem occurs with the refinement there appears an error message or a warning, so that one can refuse the last refinement step if the results are expected to be erroneous or a divergence has occurred. Figure 5.28 shows an example of a warning dialog that appeared when trying to simultaneously refine the ADP and occupancy of an atom. As stated above, these parameters are highly correlated, so their combined refinement lead to a soft singularity in the Hessian, one of the internal matrices used by the least-squares minimization algorithm.

Correlations between variables can be detected by inspecting the variance-covariance matrix, shown in Figure 5.29. In this graphical matrix every row and column represents a refined parameter and the square at the intersection of a row and a column is shaded according to the correlation between the respective parameters, as indicated by the label on the right.

Another useful feature is a graph of the shifts that the refined parameters underwent in the last refinement cycle, normalized by their standard uncertainties (esd). Figure 5.30 shows an example where clearly two of the ADPs (AUiso) have suffered very large shifts, which might indicate a problem with those variables.

If the intensity of a few peaks are wrong, while the errors show no systematic variation with

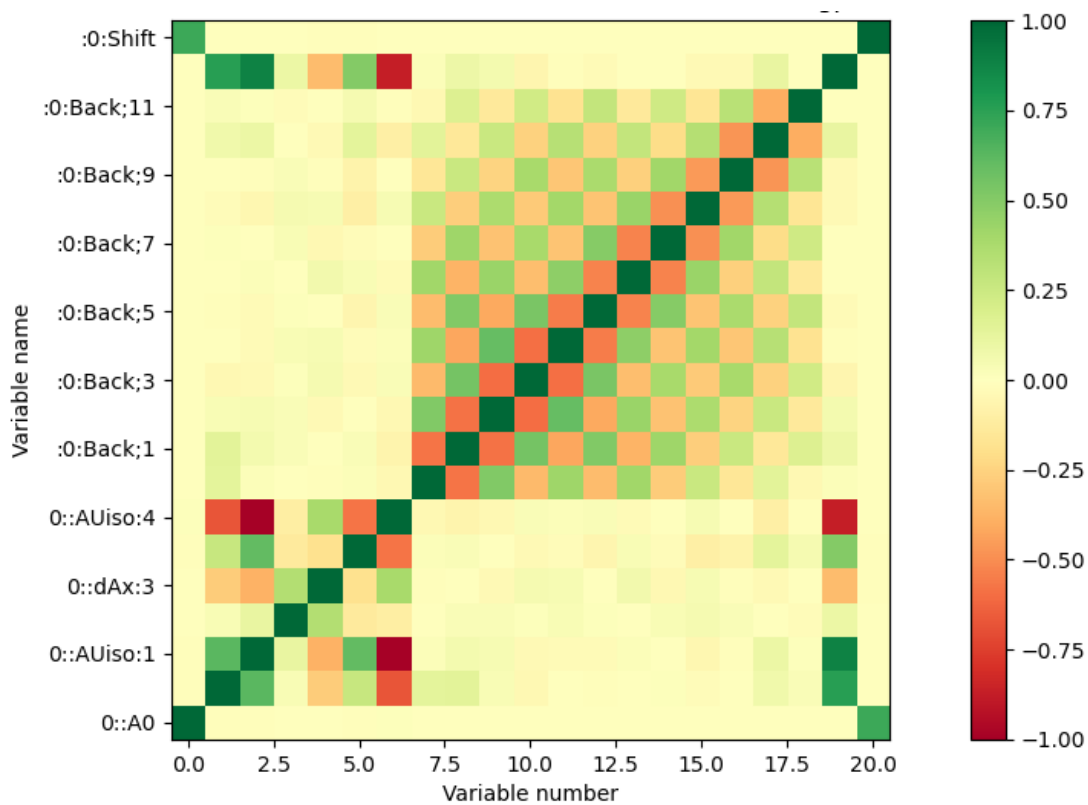


Figure 5.29 The variance-covariance matrix for the refined variables.

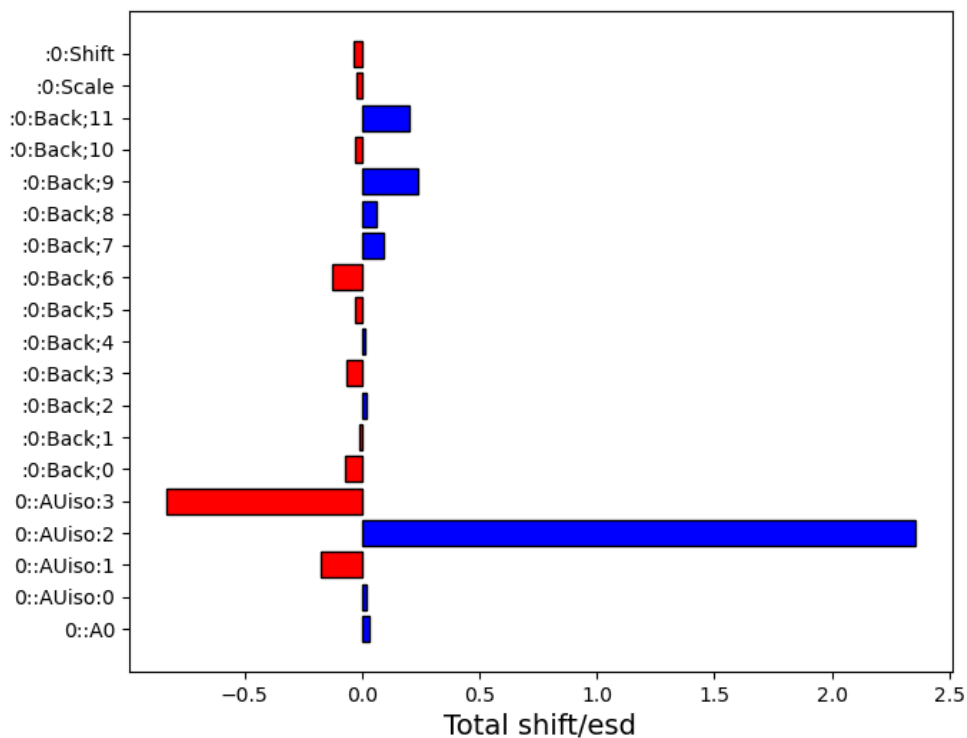


Figure 5.30 Shifts that the refined parameters underwent in the last refinement cycle, normalized by their standard uncertainties (esd).

2θ then preferential orientation effect should be considered. By inspecting the Miller indices of the peaks with abnormal intensities one may be able to identify the crystalline preferential orientation axis for a simple uniaxial model or a starting point for a more complex model.

Anisotropic broadening can be hard to spot visually, so one can try to use a model to account for it and see if the result improves. If an anisotropic model is used for one of the microstrain or crystallite size variables and the other variable changes significantly, that could be a sign of overfitting the data.

The absorption correction is not commonly used for samples measured in the Bragg-Brentano geometry since in that case it affects the whole 2θ range uniformly (i.e. is independent of 2θ). The transparency parameter S_t compensates for finite sample thickness, but is usually not required for inorganic samples, in which the x-ray penetration length is much less than the sample thickness. Nevertheless, sometimes it is useful to refine the transparency parameter since it can model small systematic peak position errors that arise from goniometer inaccuracy. In that case it is best to fix the sample displacement since these parameters are highly correlated.

At the last step of refinement one may refine the instrument parameters to obtain a slightly better fit. This is justified since the instrument parameters were fitted to a reference sample (Section 5.4) and might not be the best possible description of the actual instrumental peak profile, especially if the reference material was not certified to have negligible sample broadening effects, as is the case with the reference materials we used for calibration. Note also that the instrument parameters were inferred from a peak fit, not an actual refinement, which could yield more precise results.

When refining the instrument parameters all sample parameters that affect peak broadening should be fixed, especially the crystallite size and microstrain variables. The lorentzian instrumental profile parameters are especially susceptible to absorb sample broadening effects, so care should be taken to refine them only at the very end of the refinement, when the sample microstrain and crystallite size have converged to stable values. In any case, assuming a good instrument calibration, the instrumental parameters (Figure 5.20) should only change slightly when refined. Significant changes indicate some problem with the refinement and should not be trusted.

The sample displacement S_d should also be fixed while refining the instrument zero shift I_0 (5.27), since these variables are highly correlated. Since the lorentzian peak profile has rather long tails, there can be some interaction between the lorentzian broadening terms (instrumental X , Y , Z and sample μ , ϵ) and the background parameters, which can be identified in the correlation matrix.

In a certain sense a Rietveld refinement is never finished, one just stops at some point when the result is sufficiently good. Additional parameters can always be added but might cause overfitting if there are more parameters than the data supports. There is no generally agreed upon criterion for when to stop a refinement based solely on statistical indicators such as χ^2 . In the end the quality of the fit has to be judged by visual inspection of the fitted curve to the diffraction pattern and by the plausibility of the refined parameters on other grounds, such as previous chemical information on the composition, likely structures etc.

5.6 Results for $\text{Yb}_2\text{Zr}_x\text{Ti}_{2-x}\text{O}_7$

Powder x-ray diffraction measurements were performed using four instruments, listed in Table 5.3. All measurements were performed in the Bragg-Brentano mode (Figure 5.1) with $\text{CuK}\alpha$ radiation. Measurements with the Bruker D8 Focus were performed by Dr. Dimy Nanclares Fernandes Sanches, a researcher at the Federal University of ABC (UFABC).

Instrument	Location
Rigaku Ultima III Bruker D8 Discover	Crystallography Laboratory, Applied Physics Department, Physics Institute, University of São Paulo (FAP - IFUSP).
Bruker D8 Focus	Multiuser Experimental Center, Federal University of ABC (CEM - UFABC)
Rigaku SmartLab SE	Nuclear Research Reactor Center, Nuclear and Energy Research Institute (CRPq - IPEN).

Table 5.3 Instruments used to collect powder diffractograms of samples in this work.

The 2θ angular range of the diffractometers we used was about 5° to 140° , but we did not measure in this entire range since the first peak for the structures under consideration occurs at about 15° and the very high 2θ data is not of sufficient quality to justify the additional measurement time. The angular range was chosen as $2\theta = 10^\circ$ to 70° for initial measurements, to determine the phase evolution with temperature, and $2\theta = 12^\circ$ to 108° for later measurements, to perform Rietveld refinement. The step size in 2θ was chosen as $\Delta(2\theta) = 0.02^\circ$, a good compromise between peak resolution and measuring time.

In all cases the sample was rotated at 10rpm or 15rpm about the vertical axis, to improve the averaging of crystallite orientations. In this way any unevenness in the sample preparation and grain distribution gets smoothed out. Higher rotational speeds (20rpm or more) led to a spreading of the powder, which can reduce acquired data quality due to an uneven sample surface. Preferential orientation of powder grains or small crystallites can skew the relative peak intensities observed in a powder diffraction experiment. By spinning the powder around the axis normal to the sample surface the component of the preferential orientation vector parallel to the surface is averaged out and only the component normal to the surface could remain observable. Since most of the samples used in this work have cubic symmetry the effect of preferential orientation seems to be negligible.

Figures 5.31 to 5.34 show the XRD patterns for the SS $\text{Yb}_2\text{Zr}_x\text{Ti}_{2-x}\text{O}_7$ samples, sintered at 1500°C , and the SG $\text{Yb}_2\text{Zr}_x\text{Ti}_{2-x}\text{O}_7$ samples, sintered at 1500°C , 1200°C and 900°C . The intensities are graphed on a square root scale and the diffraction patterns of each sample are vertically displaced by an arbitrary amount.

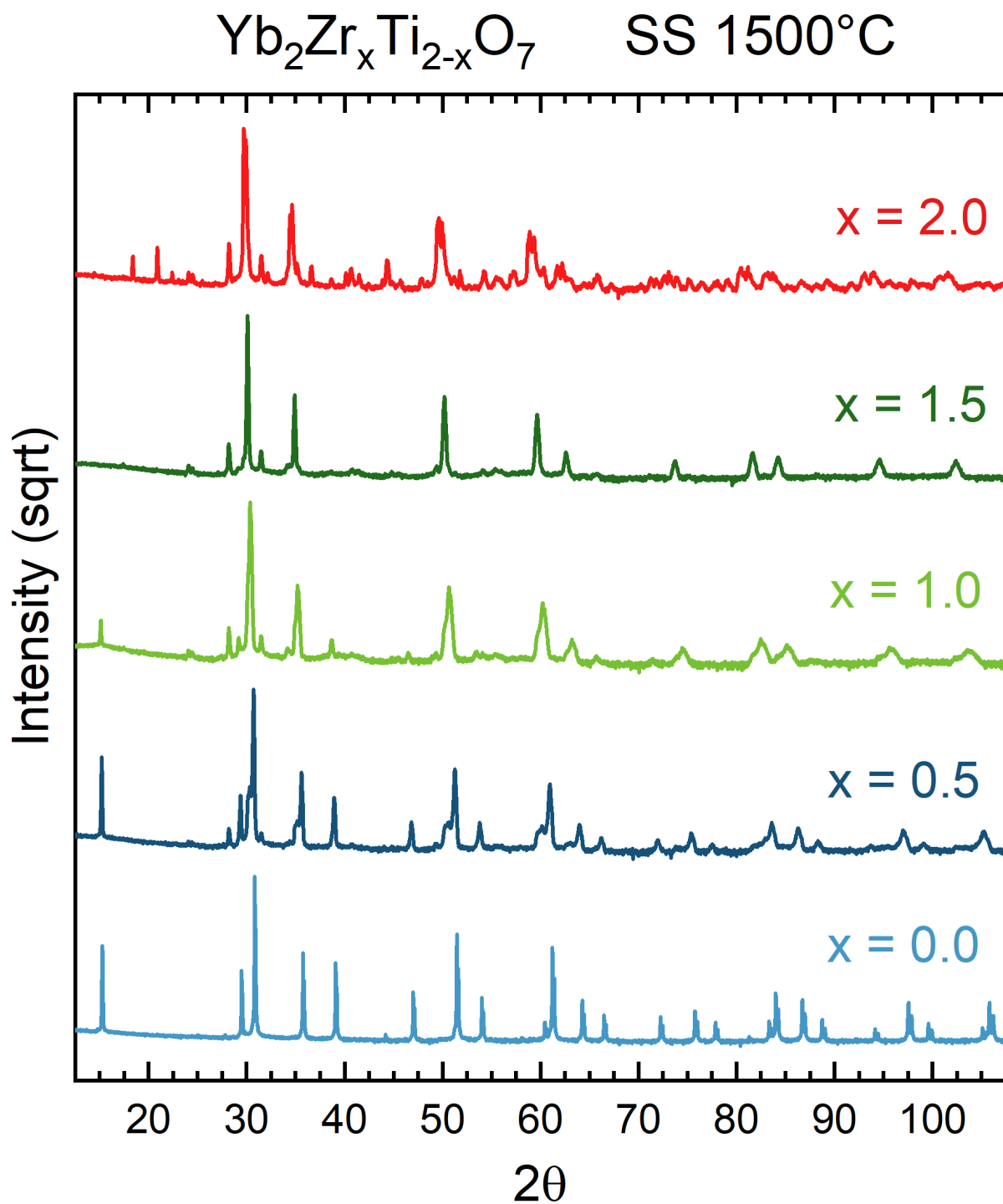


Figure 5.31 XRD patterns for the SS $\text{Yb}_2\text{Zr}_x\text{Ti}_{2-x}\text{O}_7$ samples, sintered at 1500°C (square root intensity scale).

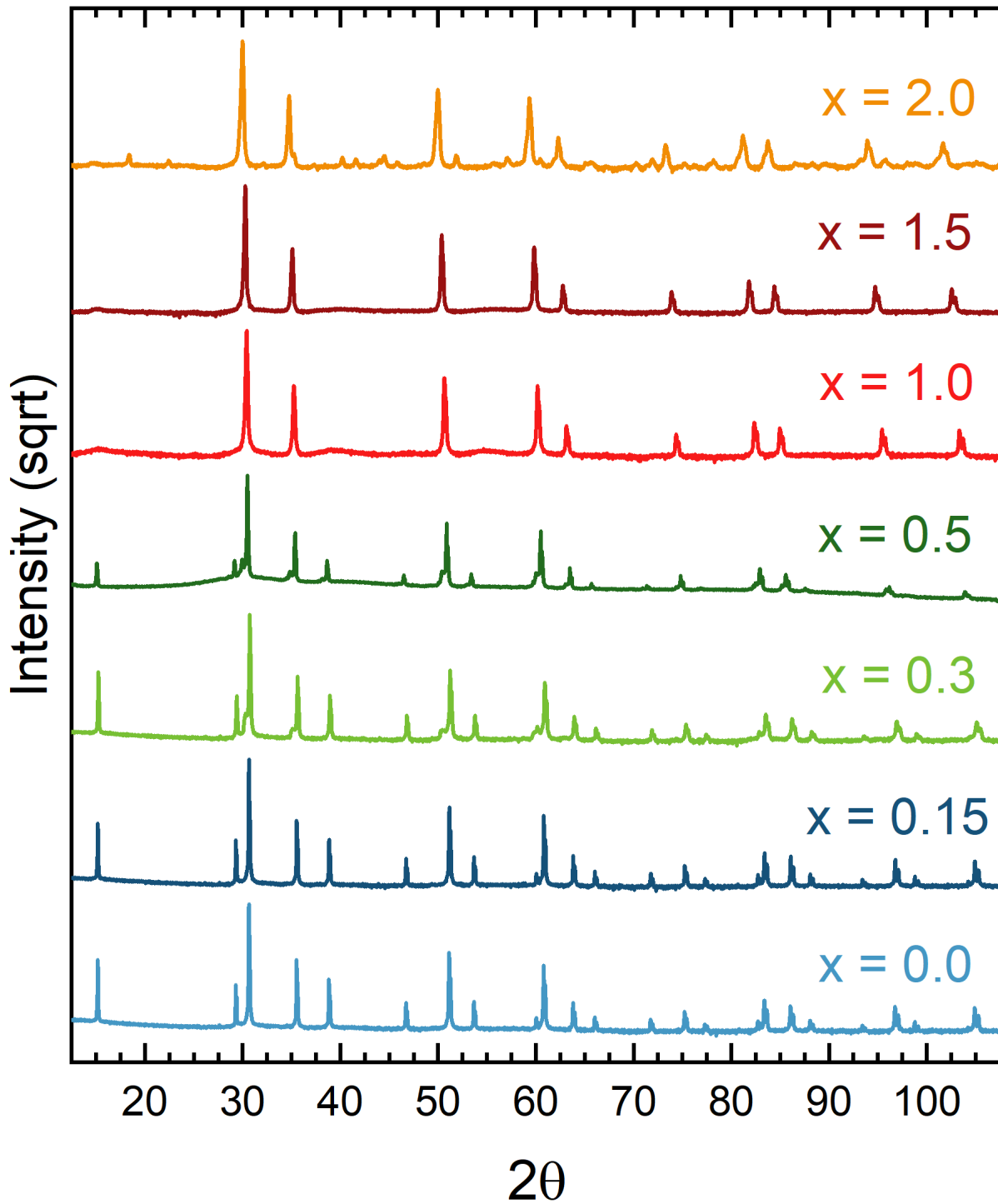
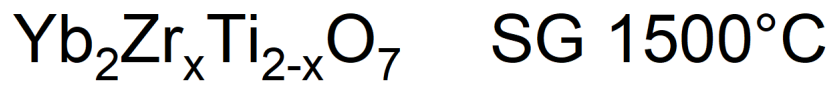


Figure 5.32 XRD patterns for the SG $\text{Yb}_2\text{Zr}_x\text{Ti}_{2-x}\text{O}_7$ samples, sintered at 1500°C (square root intensity scale).

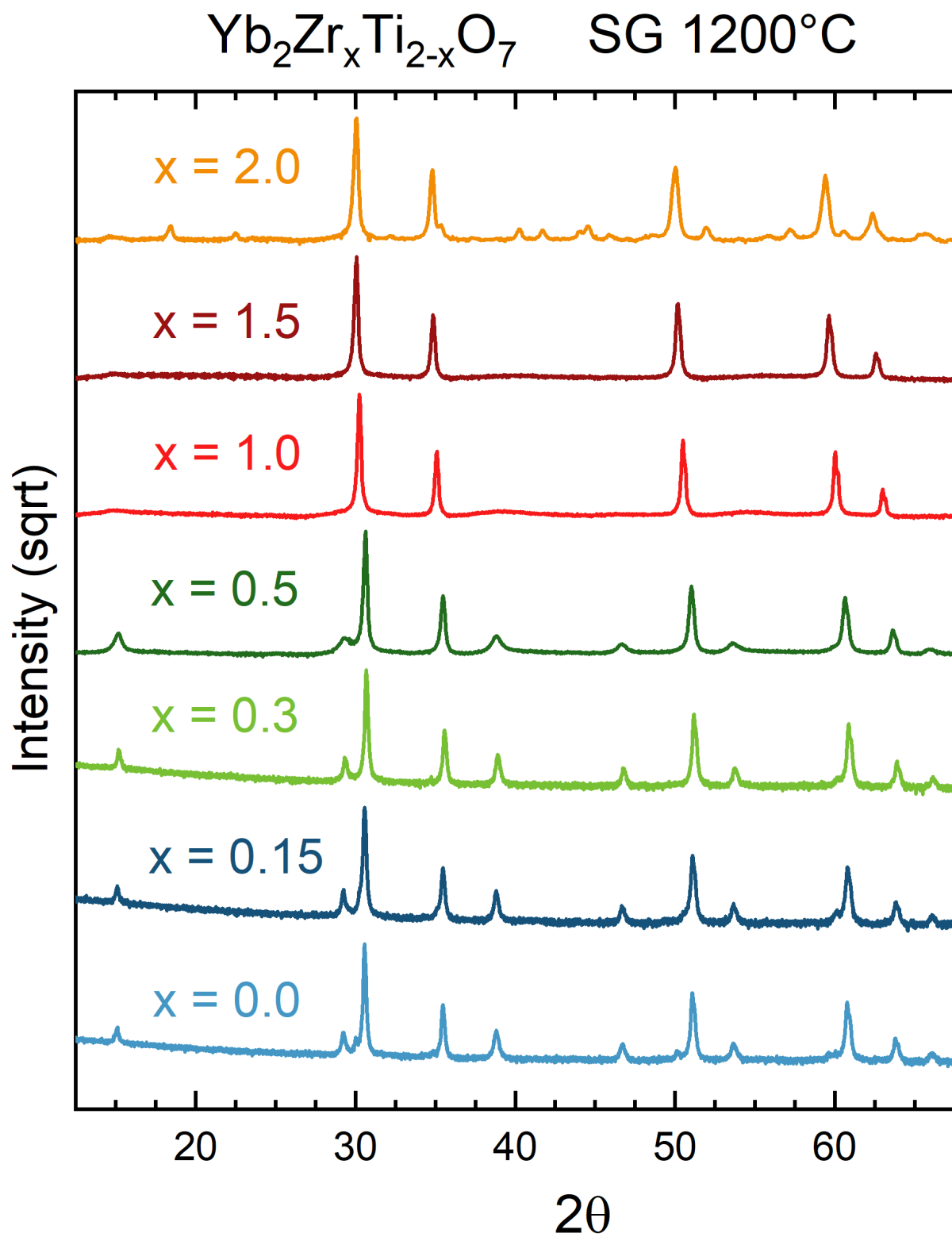


Figure 5.33 XRD patterns for the SG $\text{Yb}_2\text{Zr}_x\text{Ti}_{2-x}\text{O}_7$ samples, sintered at 1200°C (square root intensity scale).

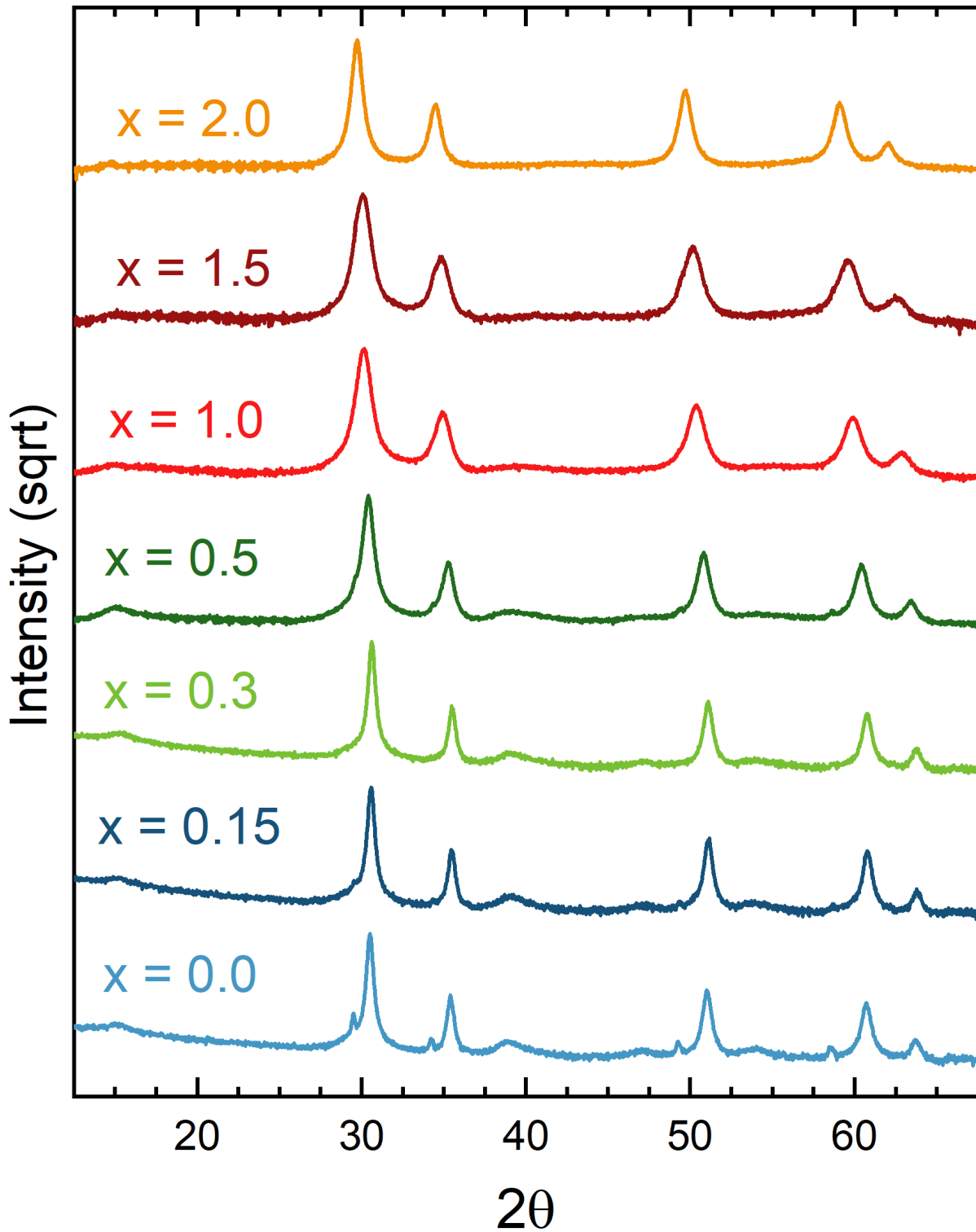
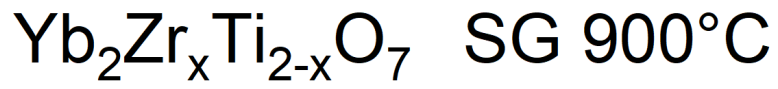


Figure 5.34 XRD patterns for the SG $\text{Yb}_2\text{Zr}_x\text{Ti}_{2-x}\text{O}_7$ samples, sintered at 900°C (square root intensity scale).

5.6.1 Phase Analysis

Using QualX we performed a phase analysis on the $\text{Yb}_2\text{Zr}_x\text{Ti}_{2-x}\text{O}_7$ samples. The SG samples were pure phases, although with a certain degree of structural disorder. On the other hand, the oxide precursors used in the SS synthesis did not coalesce into a pure phase except for $x = 0.0$ ($\text{Yb}_2\text{Ti}_2\text{O}_7$). The SS $\text{Yb}_2\text{Ti}_2\text{O}_7$ sample was confirmed to be a pure phase by Rietveld refinement, after sintering at 1500°C for 50h (10h+40h) with one intermediate grinding. The other SS $\text{Yb}_2\text{Zr}_x\text{Ti}_{2-x}\text{O}_7$ samples ($x = 0.5, 1.0, 1.5, 2.0$) did not form a pure phase even after repeating the sintering+grinding step four times. Ideally we would repeat these steps a few more times until a pure phase is attained, but restricted access to an oven that can reach such high temperatures has hindered progress in the time frame of this thesis.

Yb ₂ Zr ₂ O ₇ Samples			Phase Fraction (weight %)			
Step in SS Synthesis	Sintering Temperature	Sintering Time	Yb ₄ Zr ₃ O ₁₂	Yb ₂ O ₃	ZrO ₂ (monoclinic)	ZrO ₂ (cubic)
0	-	-	-	61.5	38.5	-
1	1500°C	10h	37.0	39.6	23.0	0.4
2	1500°C	40h	61.9	23.3	13.3	1.5
3	1500°C	35h	75.3	12.4	10.2	2.0
4	1200°C	36h	77.1	11.8	8.2	2.9

Table 5.4 Phases present in Yb₂Zr₂O₇ samples after each step in the solid-state synthesis.

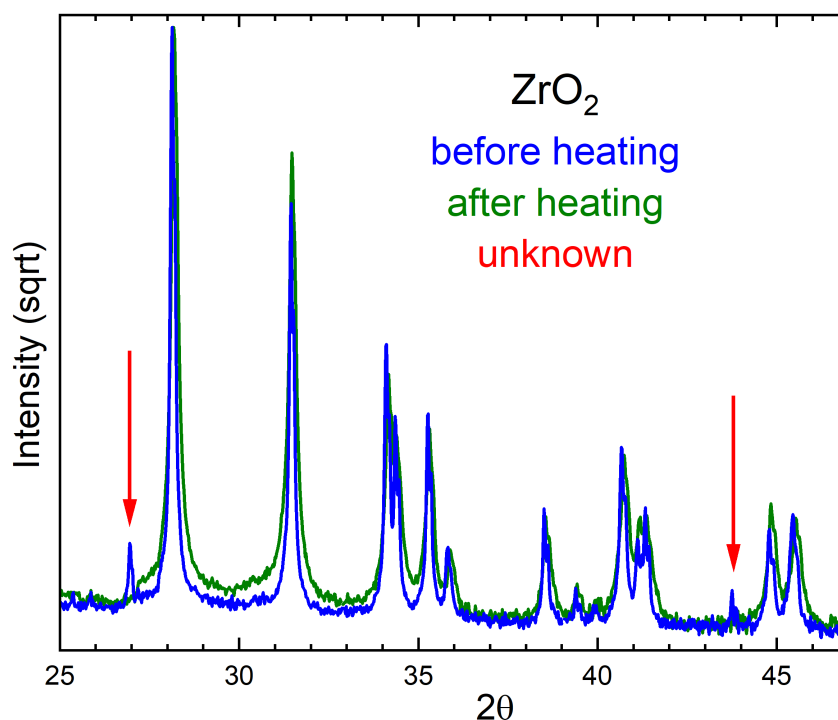


Figure 5.35 Comparison of the XRD pattern of ZrO₂ before and after being heated at 700°C .

As an example, Table 5.4 shows the semi-quantitative phase composition, determined by QualX, for the sample $\text{Yb}_2\text{Zr}_x\text{Ti}_{2-x}\text{O}_7$ with $x = 2.0$ ($\text{Yb}_2\text{Zr}_2\text{O}_7$). We can see that the most stable phase is the $\text{Yb}_4\text{Zr}_3\text{O}_{12}$ δ -phase but there remains a significant amount of unreacted precursor oxides in the sample even after repeating the sintering/grinding step four times. Note that ZrO_2 is present both as a monoclinic phase (space group $\text{P}2_1/\text{c}$, No.14) and cubic phase (space group $\text{Fm}\bar{3}\text{m}$, No. 225). Similar results, indicating a mixture of pyrochlore/fluorite phase with precursor oxides, were obtained for the SS samples $\text{Yb}_2\text{Zr}_x\text{Ti}_{2-x}\text{O}_7$ with $x = 0.5, 1.0, 1.5$.

We measured the XRD patterns of the precursor oxides used in the synthesis to confirm their purity. We also wanted to investigate the change of color that the ZrO_2 underwent when heated at 700°C (Figure 4.3). Figure 5.35 shows that the dark ZrO_2 , before heating, exhibits two additional diffraction peaks when compared to the same sample after being heated. Note that these patterns were measured on different instruments, therefore the peak profiles are slightly different. We could not identify these additional peaks but believe that they indicate reaction products of ZrO_2 with atmospheric gases. The XRD patterns of the ZrO_2 after heating and of the other precursors matched those of reference data in the literature, confirming their purity.

5.6.2 Qualitative Results

In this section we describe some qualitative or semi-quantitative results that do not depend on Rietveld refinement. From now on, unless explicitly mentioned otherwise, we refer to the SG $\text{Yb}_2\text{Zr}_x\text{Ti}_{2-x}\text{O}_7$ samples (synthesized by the sol-gel method) since the SS samples (fabricated by the solid-state reaction) did not form a pure phase, except for $\text{Yb}_2\text{Ti}_2\text{O}_7$. The $\text{Yb}_2\text{Zr}_x\text{Ti}_{2-x}\text{O}_7$ compounds with $x \leq 0.5$ crystallize in the pyrochlore structure, as evidenced by the pyrochlore superstructure peaks, the first one appearing at $2\theta \approx 15^\circ$. The $x = 1.0, 1.5$ compounds are fluorites and do not exhibit the superstructure peaks, although there is very weak diffuse scattering at those positions, as will be discussed further in this section. The $x = 2.0$ compound crystallizes in the non-cubic δ -phase, which is less symmetric than the pyrochlore/fluorite phases, as is evident from the numerous weak peaks in the diffraction pattern.

Vegard's law is an empirical rule that states that the lattice parameter of an alloy or solid solution varies linearly as a function of its constituent elements or compounds. For instance, stated in terms of the lattice parameter of the $\text{Yb}_2\text{Zr}_x\text{Ti}_{2-x}\text{O}_7$ compounds it predicts that

$$a[\text{Yb}_2\text{Zr}_x\text{Ti}_{2-x}\text{O}_7] \approx \left(\frac{x}{2}\right) a[\text{Yb}_2\text{Zr}_2\text{O}_7] + \left(1 - \frac{x}{2}\right) a[\text{Yb}_2\text{Ti}_2\text{O}_7] \quad (5.30)$$

where we take a to signify either the fluorite subcell lattice parameter a_f or the pyrochlore superstructure lattice parameter a_p , so that we can compare the values across the pyrochlore/fluorite transition. We chose a_p for ease of comparison with the predicted values given in Table 2.11. Vegard's law is not a law in the usual sense, but rather a useful heuristic that often predicts values that are close to the experimentally determined ones, although deviations from linear behavior are observed in some cases [249, 250, 251].

The lattice parameter a of $\text{A}_2\text{B}_2\text{O}_7$ is expected to increase with average cation size, $\frac{1}{2}(r_A + r_B)$, which intuitively makes sense considering a rigid-sphere approximation to the ions that compose

the structure. The simplest way to determine the lattice parameter from the diffraction pattern is by applying Bragg's law (5.1) to the position $2\theta_B$ of a strong reflection that is clearly observable across the whole series of compounds.

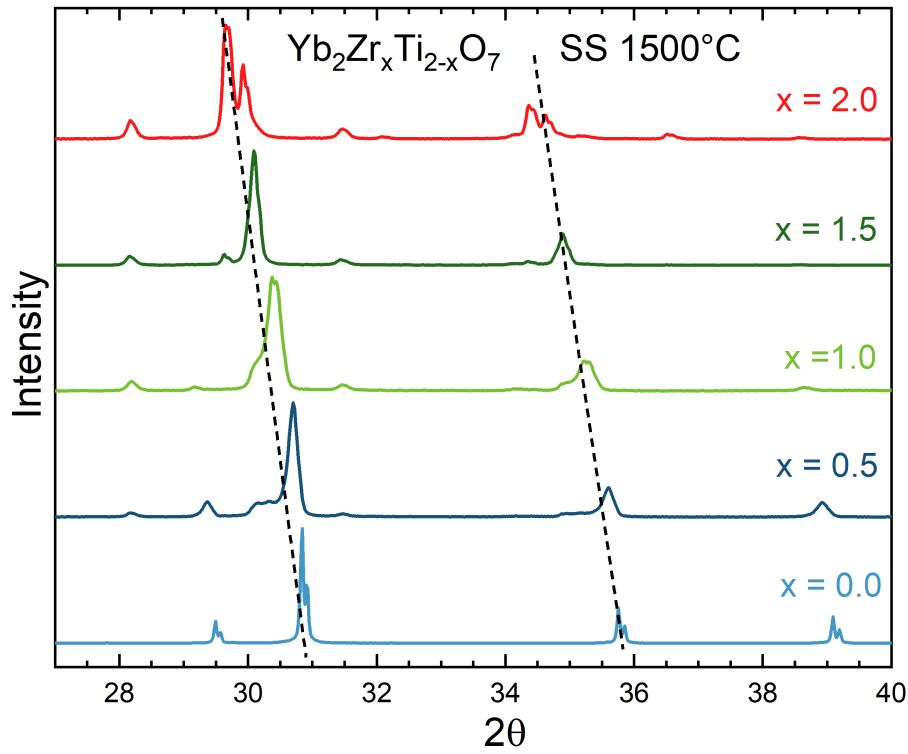


Figure 5.36 The 111 and 200 fluorite peaks show an approximately linear shift in position with increasing x for SS $\text{Yb}_2\text{Zr}_x\text{Ti}_{2-x}\text{O}_7$ samples.

Figure 5.36 shows the 111 and 200 fluorite peaks and the almost linear shift in peak position with increasing x for SS $\text{Yb}_2\text{Zr}_x\text{Ti}_{2-x}\text{O}_7$ samples, due to the approximate linearity of the sine function at low angles ($\theta \approx 15^\circ$ or $\theta \approx 18^\circ$) and Vegard's law (5.30). Note that although the SS samples with $x > 0.0$ did not crystallize into a pure phase, the pyrochlore/fluorite/ δ phases are still the majority phases, so that we can use the strong reflections corresponding to those phases even though other phases are also present.

Table 5.5 lists the 111 fluorite peak positions $2\theta_B$ for SS and SG $\text{Yb}_2\text{Zr}_x\text{Ti}_{2-x}\text{O}_7$ samples and the equivalent pyrochlore lattice parameter a deduced from Bragg's law (5.1) and the relation (5.6) between the lattice parameter and the plane spacing d ,

$$a = \frac{d}{2 \sin \theta} \sqrt{h^2 + k^2 + l^2} = \frac{d}{2 \sin \theta} \sqrt{3} \quad (5.31)$$

for the 111 peak.

Figure 5.37 compares the experimental lattice parameter values for the SG and SS samples, sintered at 1500°C , with the calculated lattice parameters in Table 2.11. All three sets of calculated lattice parameters slightly overestimate the actual ones, although the slope is similar to that of the experimental data. The values calculated by applying Bragg's law to the peak maxima approximately agree with the more precise values obtained from Rietveld refinement (Section 5.6.3), for instance $a = 10.0334\text{\AA} \approx 10.0352\text{\AA}$ for the SS $\text{Yb}_2\text{Ti}_2\text{O}_7$ sample and

x	SS		SG	
	$2\theta_B(^{\circ})$	$a(\text{\AA})$	$2\theta_B(^{\circ})$	$a(\text{\AA})$
0.0	30.8451	10.0334	30.6440	10.09767
0.15			30.651	10.09542
0.3			30.721	10.07296
0.5	30.7019	10.0791	30.4860	10.14875
1.0	30.3745	10.1851	30.4060	10.17482
1.5	30.0881	10.2798	30.2730	10.21847
2.0	29.9244	10.3347	29.9890	10.31299

Table 5.5 Peak maximum positions $2\theta_B$ for SS and SG $\text{Yb}_2\text{Zr}_x\text{Ti}_{2-x}\text{O}_7$ samples and the equivalent pyrochlore lattice parameter a deduced from Bragg's law.

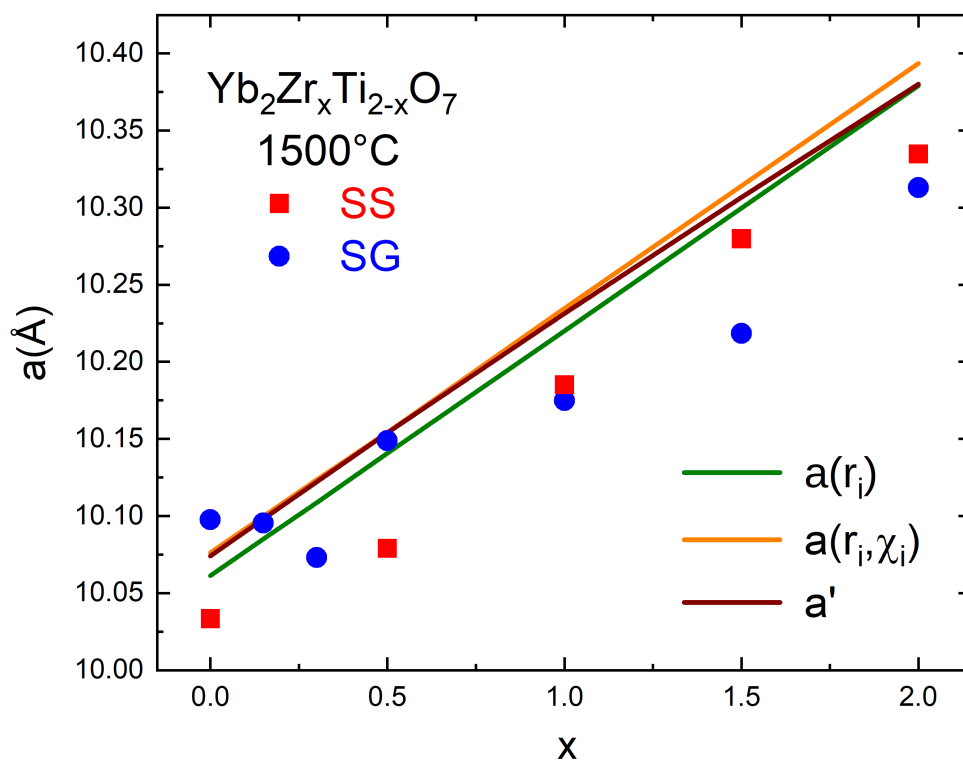


Figure 5.37 Experimental lattice parameter values for both SG and SS samples and calculated lattice parameters from Table 2.11.

$a = 10.09767 \approx 10.09501 \text{ \AA}$ for SG $\text{Yb}_2\text{Ti}_2\text{O}_7$ sample. The slight differences are likely due to peak asymmetry and sample displacement (see Section 5.4 for a discussion of these effects). The Bragg method is still useful to extract approximate values and to compare the lattice parameters of the SG samples with the SS samples, which were not refined due to the admixture of minority phases. More precise values could also be obtained by performing a Le Bail fit which, unlike Rietveld refinement, does not require phase information to deconvolute the XRD pattern [252].

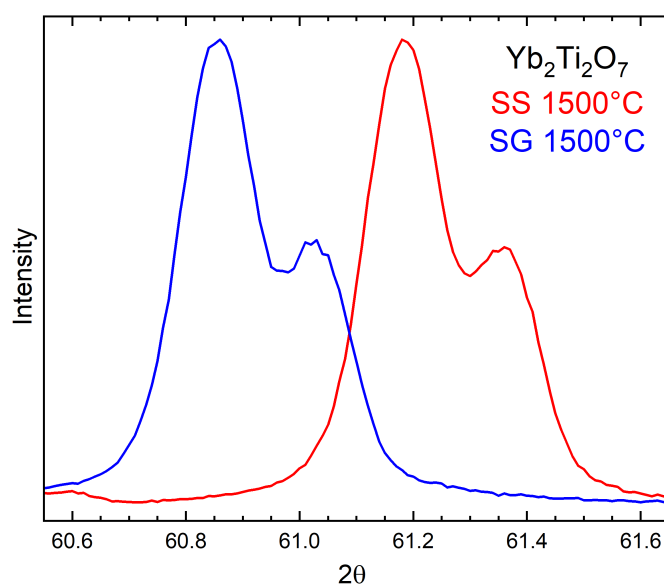


Figure 5.38 The 622 pyrochlore peak for the SG and SS $\text{Yb}_2\text{Ti}_2\text{O}_7$ samples, clearly indicating their distinct lattice parameters.

Both SS and SG $\text{Yb}_2\text{Ti}_2\text{O}_7$ samples were sintered at 1500°C for comparable periods of time and fit well to the pyrochlore structural model (see Section 5.6.3), but the lattice parameter of the SG sample is about 0.6% larger than that of the SS sample. To confirm this discrepancy we measured a few of the most intense peaks for both samples after checking the instrument calibration with a silicon powder standard (PDF#27-1402), whose peak positions have previously been determined to high precision. Figure 5.38 shows that the 622 pyrochlore peak is clearly separated for these samples, and the deduced lattice parameters are consistent with the values listed in Table 5.5 and those obtained from refinement.

Figure 5.39 shows how the 111 fluorite peak evolves with sintering temperature for the $\text{Yb}_2\text{Zr}_x\text{Ti}_{2-x}\text{O}_7$ samples with $x = 0.0, 0.15, 0.3$. The intensities were normalized so that all the peaks have the same height. It is difficult to pinpoint the transition temperature from the lower-temperature fluorite to the higher-temperature pyrochlore structure since the samples with $T < 1200^\circ\text{C}$ exhibit an intermediate kind of order, with local pyrochlore correlations that do not extend to the long-range structure. The 111 fluorite peak widths markedly decrease with rising sintering temperature, indicating the increased crystallinity of the samples sintered at higher temperature.

As described in Section 5.4, the sample-induced broadening of the diffraction peaks arises mostly due to the effects of crystallite size and strain in the crystal structure. Here we assume that the broadening is caused by the size contribution and use Scherrer's equation (5.14) to determine the approximate crystallite size. Table 5.6 lists the crystallite size μ for the SG $\text{Yb}_2\text{Ti}_2\text{O}_7$ samples, determined by the Scherrer method. These values are only approximate

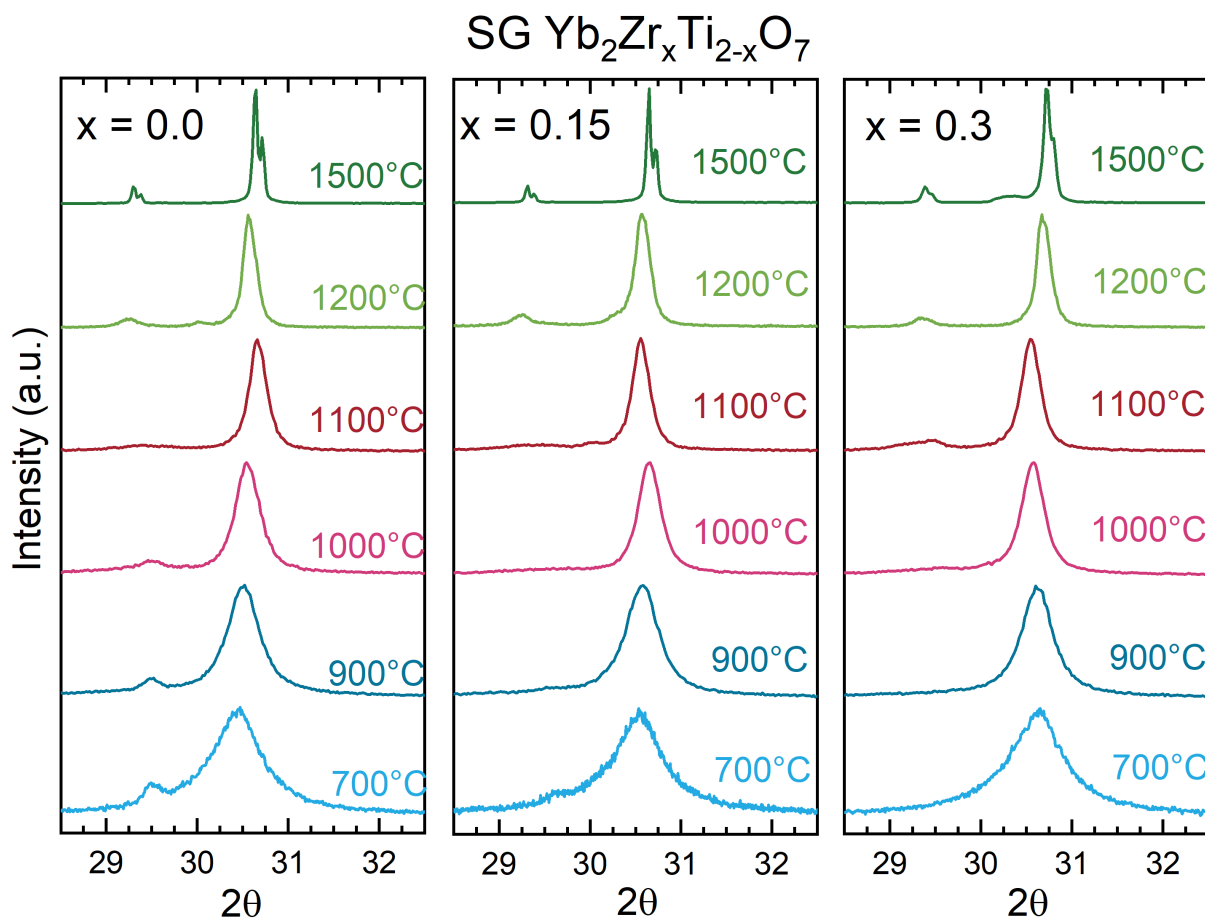


Figure 5.39 The 111 fluorite peak for SG $\text{Yb}_2\text{Zr}_x\text{Ti}_{2-x}\text{O}_7$ samples with $x = 0.0, 0.15, 0.3$, sintered at various temperatures

T (°C)	μ (nm)
700	<10
900	18
1000	28
1100	66
1200	89
1500	>300

Table 5.6 Crystallite size μ for the SG $\text{Yb}_2\text{Ti}_2\text{O}_7$ samples, determined by the Scherrer method.

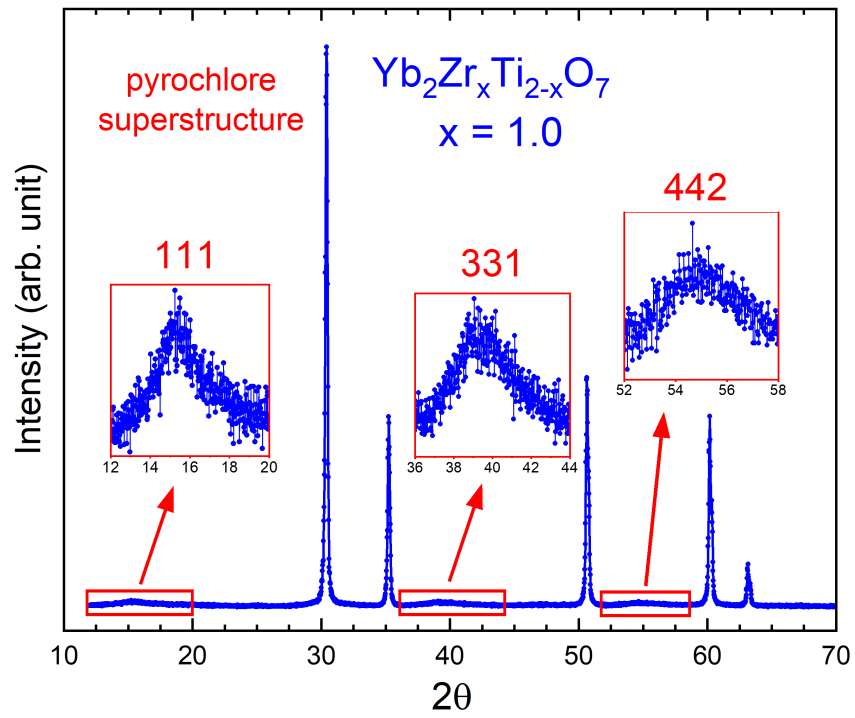


Figure 5.40 Weak pyrochlore superstructure peaks in the XRD pattern of $\text{Yb}_2\text{Zr}_x\text{Ti}_{2-x}\text{O}_7$ with $x = 1.0$.

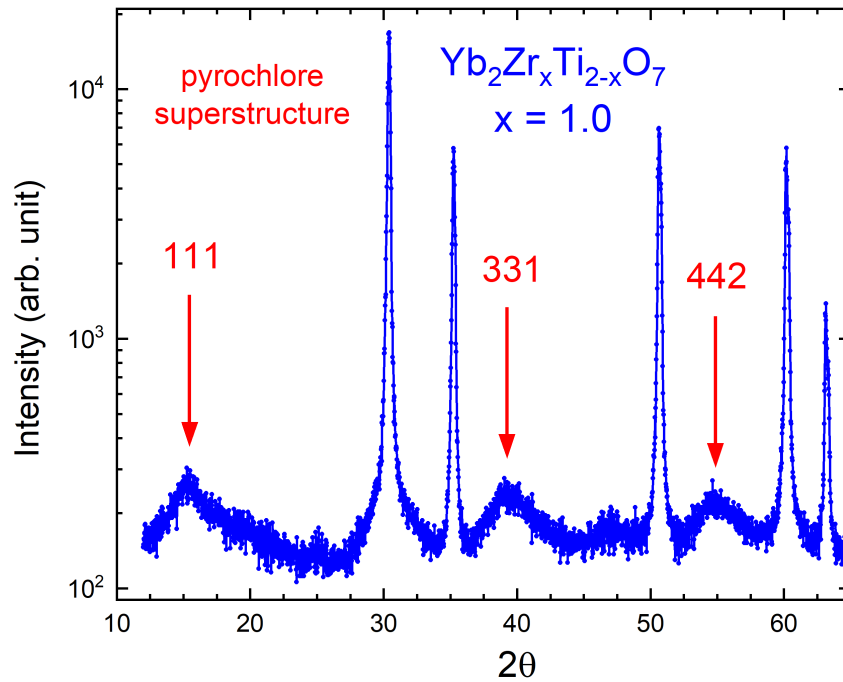


Figure 5.41 Weak pyrochlore superstructure peaks in the XRD pattern of $\text{Yb}_2\text{Zr}_x\text{Ti}_{2-x}\text{O}_7$ with $x = 1.0$, visualized on a logarithmic scale.

since they neglect the strain contribution to peak broadening and only serve to illustrate the increase in crystallinity with higher sintering temperatures.

If the structure is on average a disordered fluorite but possesses some local correlations of the pyrochlore type, we expect to see some diffuse scattering manifest as weak and broad superstructure peaks. Figure 5.40 shows the weak 111, 331 and 442 pyrochlore superstructure peaks (highlighted in the insets) in the XRD pattern of $\text{Yb}_2\text{Zr}_x\text{Ti}_{2-x}\text{O}_7$ with $x = 1.0$, while Figure 5.41 shows the same XRD pattern on a logarithmic intensity scale, allowing us to visualize on a single scale both the strong fluorite peaks and the weak pyrochlore superstructure peaks that are hardly visible on the linear scale.

To quantify the amount of pyrochlore correlations we determined the ratio between the pyrochlore superstructure peak intensities and the fluorite substructure peak intensities. The improved crystallinity at higher temperature shifts some scattered intensity from the background to the fluorite Bragg peaks, greatly increasing their area, an effect not apparent in comparisons such as in Figure 5.39, since the stacked diffractograms have been normalized. For the $x = 1.0$, 1.5 samples the diffuse scattering remains at approximately the same intensity when comparing the samples sintered at 900°C, 1200°C and 1500°C.

We considered the intensity ratio I_{111}/I_{222} of the 111 and 222 pyrochlore peaks, which correspond to the fluorite $\frac{1}{2}\frac{1}{2}\frac{1}{2}$ and 111 Miller indices. The intensity I_{222} depends only on the total scattering power of the A and B cations combined, whether they are separated into two distinct lattices, as in the pyrochlore structure, or randomly distributed on a single lattice, as in the fluorite structure. On the other hand, the I_{111} peak intensity depends on the difference in scattering power between the two lattices, so that if the A/B cations are completely separated on the pyrochlore 16d/16c sites the intensity is maximal, whereas if they are randomly mixed on the single fluorite 4a site the intensity is zero.

Thus I_{111} , normalized by I_{222} , provides a measure of cation ordering, the separation into distinct crystallographic sites, which is proportional to the degree of local pyrochlore correlations. However these intensities (integrated area of the peaks) depend somewhat on the assumed background level and on the function used to fit the peaks. This is particularly problematic for the weak and broad superstructure peaks, since the base of the peak is hard to distinguish from the background of the diffraction pattern. Thus the I_{111}/I_{222} intensity ratio serves as a useful indicator of local superstructure correlations but is of arguable quantitative accuracy. It is inversely correlated with the A/B inversion parameter s introduced in (2.16).

In order to compare the peak intensities we deconvoluted the diffractograms of the mainly fluorite $\text{Yb}_2\text{Zr}_x\text{Ti}_{2-x}\text{O}_7$ samples with $x = 1.0, 1.5$, as a superposition of pseudo-Voigt functions, an example of which is depicted in Figure 5.42. For some of the diffuse peaks the gaussian-lorentzian mixing parameter η in (5.22) refined to a negative value since those peaks are very broad, "super-lorentzian" in character. The negative η is unphysical but the integrated area is very close to the value of a pure lorentzian fitted to the same peak. We tried using a purely lorentzian peak profile for the diffuse peaks but the results were very similar, so to be consistent we kept a pseudo-Voigt profile for all peaks.

Table 5.7 shows the ratio between the 111 and 222 pyrochlore peak intensities, I_{111}/I_{222} , for the $\text{Yb}_2\text{Zr}_x\text{Ti}_{2-x}\text{O}_7$ samples $x = 1.0, 1.5$. Figure 5.43 shows the normalized intensity (area of the peak divided by the total area of all peaks) of the diffuse 111, 331 and 442 pyrochlore

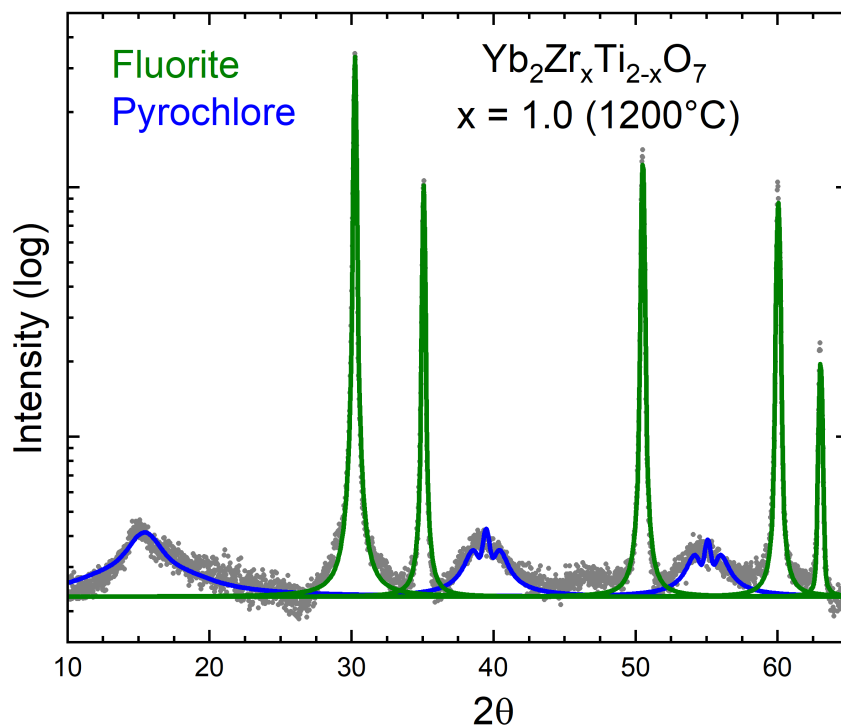


Figure 5.42 Diffractogram of $\text{Yb}_2\text{Zr}_x\text{Ti}_{2-x}\text{O}_7$ with $x = 1.0$ (1200°C), deconvoluted as a superposition of pseudo-Voigt functions.

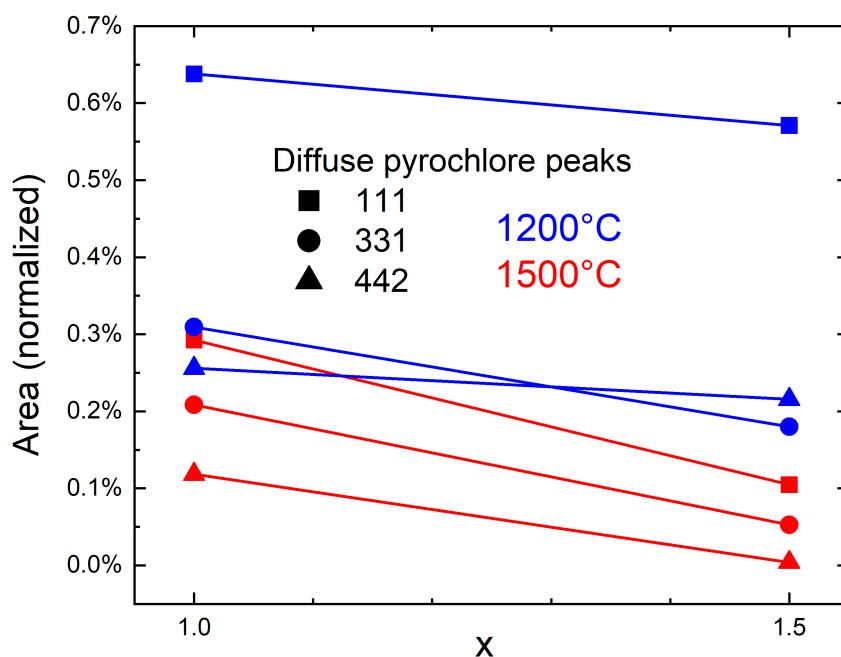


Figure 5.43 Normalized intensity of the diffuse 111, 331 and 442 superstructure peaks for the $x = 1.0, 1.5$ samples.

T (°C)	I_{111}/I_{222} (%)	
	$x = 1.0$	$x = 1.5$
900	1.63	1.12
1200	1.57	1.42
1500	0.68	0.23

Table 5.7 Ratio between the 111 and 222 pyrochlore peak intensities, I_{111}/I_{222} , for the $\text{Yb}_2\text{Zr}_x\text{Ti}_{2-x}\text{O}_7$ samples $x = 1.0, 1.5$.

T (°C)	I_p/I_f (%)	
	$x = 1.0$	$x = 1.5$
900	2.36	2.23
1200	1.20	0.97
1500	0.62	0.16

Table 5.8 Ratio between the combined intensity of the pyrochlore superstructure peaks, I_p , to the combined intensity of the fluorite peaks, I_f .

superstructure peaks for the same samples. The slight decrease from $x = 1.0$ to $x = 1.5$ can be interpreted as a reduction in the drive to local pyrochlore ordering with increasing x .

Another rough measure of the amount of local correlations is the ratio between the combined intensity of the pyrochlore superstructure peaks, I_p , to the combined intensity of the fluorite peaks, I_f . We chose the angular range $2\theta < 70^\circ$, which contains the three most apparent diffuse superstructure peaks and the five most intense Bragg peaks. Table 5.8 lists the ratio I_p/I_f for the $\text{Yb}_2\text{Zr}_x\text{Ti}_{2-x}\text{O}_7$ samples with $x = 1.0, 1.5$, sintered at three temperatures.

The decreasing I_{111}/I_{222} and I_p/I_f ratios indicate that the local pyrochlore correlations become less significant with increasing sintering temperature T . This is consistent with expectations based on the tolerance factors, which predict a morphotropic phase transition at some intermediary value of x , such that for compositions with higher x the disordered fluorite is the more stable phase. Given that the $x = 0.5$ sample still possesses the pyrochlore structure, the experimental value for the pyrochlore/fluorite transition is constrained by $0.5 < x < 1.0$, somewhat lower than the predicted values listed in Table 2.13. The $x = 1.5$ sample is further from the morphotropic phase boundary than the $x = 1.0$ sample, in agreement with the decrease in superstructure peak intensities observed in Figure 5.43.

5.6.3 Refinement Results

We tried to refine the structures of the $\text{Yb}_2\text{Ti}_2\text{O}_7$ SS sample and of all the SG samples, sintered at 900°C , 1200°C and 1500°C . However only a few of those samples (SS $\text{Yb}_2\text{Ti}_2\text{O}_7$ and SG $\text{Yb}_2\text{Zr}_x\text{Ti}_{2-x}\text{O}_7$ with $x = 0.0, 0.15, 2.0$) could be successfully refined. We discuss the results of the successful refinements and some of the issues that prevented a satisfactory structural

refinement of the other samples.

Figure 5.44 shows a refinement of the SS $\text{Yb}_2\text{Ti}_2\text{O}_7$ sample, with $\chi^2 = 3.46$. Figure 5.45 shows the same refinement but using a logarithmic intensity scale, that allows closer inspection of the small features close to the background level and of the less intense peaks at high angle. Table 5.9 lists the structural parameters that resulted from the refinement.

As discussed in Section 5.4, the crystallite size μ and microstrain ϵ parameters should not be considered very reliable, given that their effects on the peak profiles are hard to distinguish using only laboratory XRD data and incorrect instrumental profiles could skew these values. Nevertheless, their order of magnitude indicates that the crystal structure is relatively free of internal stresses and the crystallites are reasonably large.

The parameters associated with the oxygen sublattice (x_{48f} , the site occupancies and U_{iso} values for O_{8b} and O_{48f}), should also be considered somewhat unreliable since XRD is rather insensitive to the oxygen ions. Therefore a site occupancy less than 1 for one of the oxygen sites cannot be considered good evidence of oxygen vacancies. Due to this issue, when refining the site occupancies we decided to constrain the oxygen ion occupancies by imposing a charge neutrality condition, such as

$$16 \text{occ}_{\text{Yb}/16d}(+3) + 16 \text{occ}_{\text{Ti}/16c}(+4) + 48 \text{occ}_{\text{O}/48f}(-2) + 8 \text{occ}_{\text{O}/8b}(-2) = 0 \quad (5.32)$$

where we assume the nominal valencies for all of the ions in the $\text{A}_2\text{B}_2\text{O}_7$ pyrochlore structure, A^{3+} , B^{4+} and O^{2-} . In this way we are effectively determining the amount of oxygen vacancies through the average cation valence, so if there is an excess of Yb as in the stuffed pyrochlore $\text{A}_{2+z}\text{B}_{2-z}\text{O}_{7-z/2}$ with $z > 0$, then there will be an oxygen deficit in the resulting structure and similarly, a Ti excess when $z < 0$ would cause an oxygen excess compared to the ideal stoichiometry. After the refinement has converged we can test its stability by removing the constraint (5.32) to see if the values undergo significant changes.

Initially we refined the site occupancies freely but then fixed the value of the highest-occupancy site (in this case the 16d Yb site) to equal 1. The refined occupancies for the other sites are very close to their ideal values and according to this refinement there is a 1% – 2% excess of Yb compared to Ti. We tried to vary the Ti occupation in small fixed steps to investigate how the quality of the fit depends on this variable. When the difference from the nominal occupancy was larger than $\approx 3\%$ the χ^2 value increased, but there was no clear minimum for smaller deviations ($0.97 \leq \text{occ}_{\text{Ti}/16c} \leq 1.03$).

The U_{iso} values are in the expected range and inversely correlated with the mass of the atoms, also as expected. The U_{iso} value for the O_{8b} ions is less than that for the O_{48f} ions, which makes sense considering that the O_{8b} ions are more tightly bound to the A^{3+} cations.

Visual inspection of Figures 5.44 and 5.45 does not indicate any problems and the refined parameters seem very reasonable, so although the χ^2 is significantly larger than 1 we may consider the structure to be well-refined. It would be interesting to test if additional sintering/grinding steps can improve the crystal structure, possibly allowing a refinement with a lower χ^2 value.

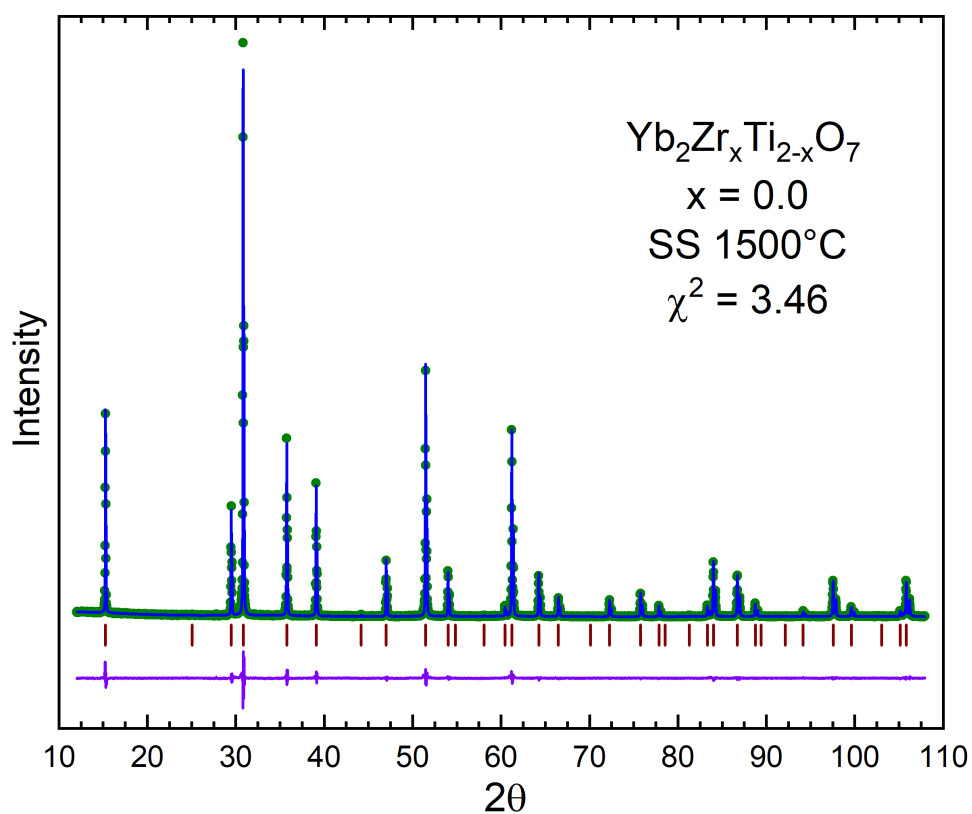


Figure 5.44 A refinement of the SS Yb₂Ti₂O₇ sample (linear intensity scale).

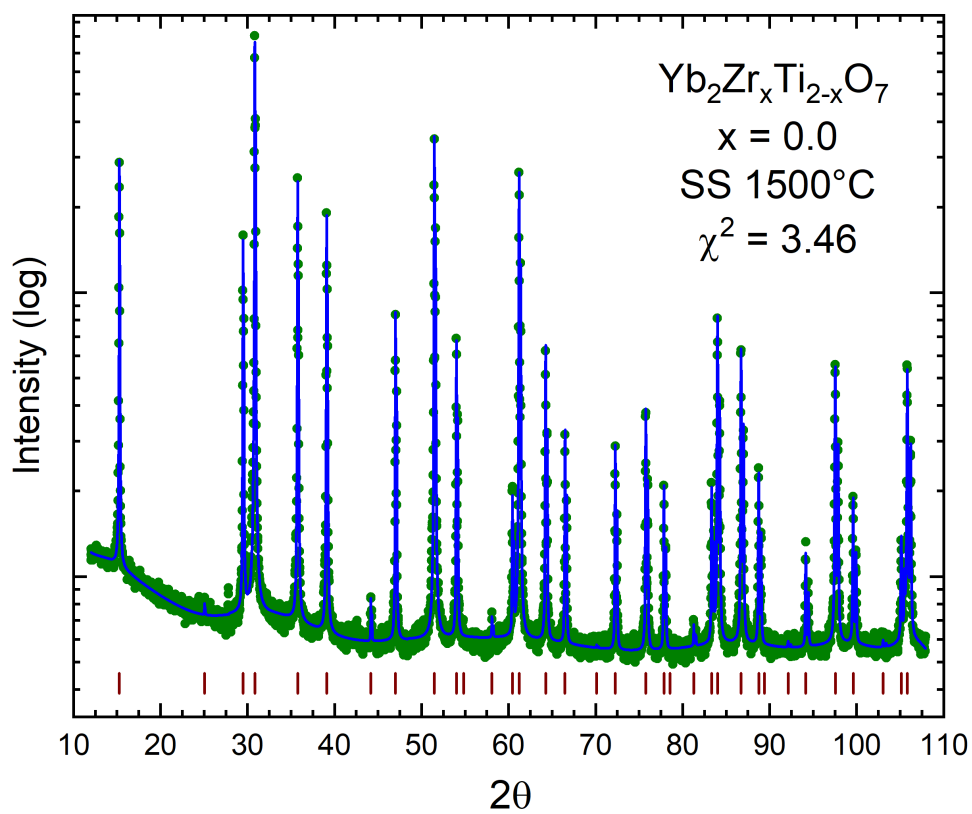


Figure 5.45 A refinement of the SS Yb₂Ti₂O₇ sample (logarithmic intensity scale).

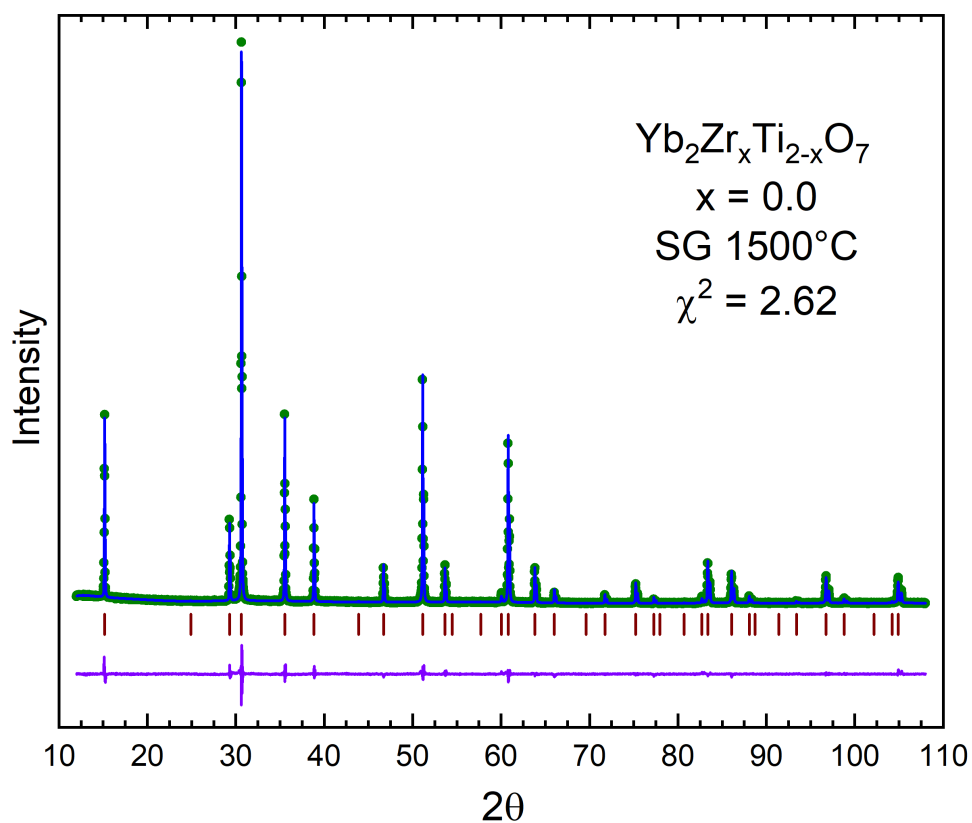


Figure 5.46 A refinement of the SG Yb₂Ti₂O₇ sample (linear intensity scale).

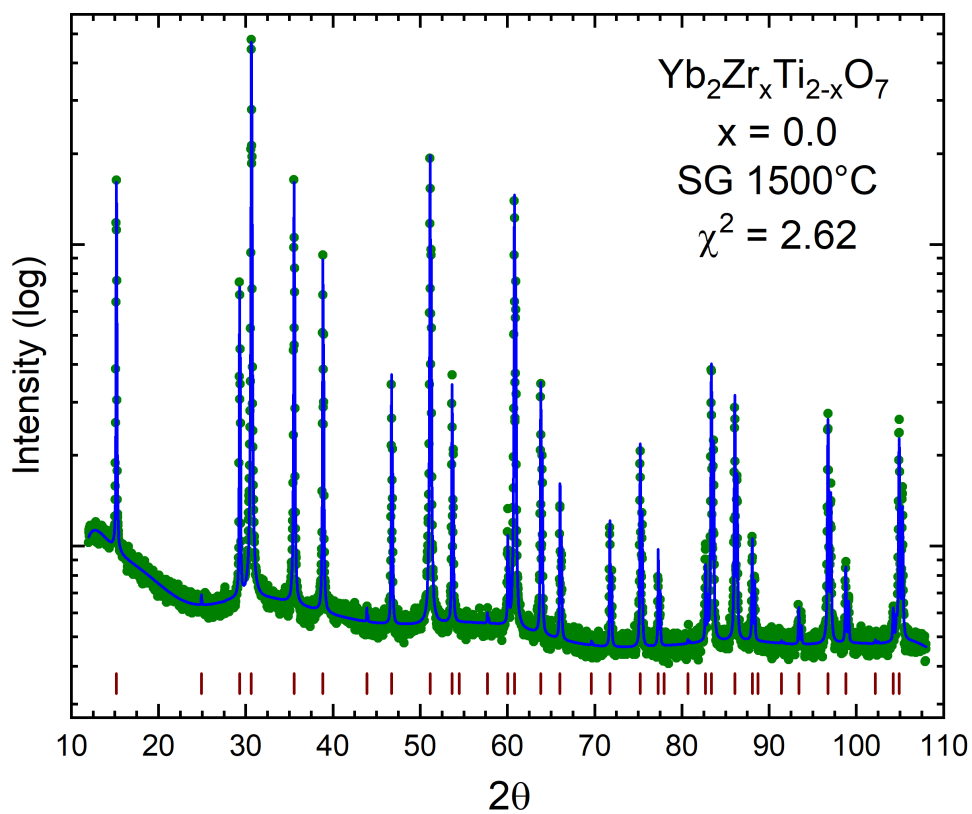


Figure 5.47 A refinement of the SG Yb₂Ti₂O₇ sample (logarithmic intensity scale).

Parameter	Symbol	Refined value	Unit	Occupation
lattice parameter	a	10.03520	Å	
crystallite size	μ	1471	nm	
microstrain	ϵ	389	10^{-6}	
oxygen coordinate	x_{48f}	0.3284		
isotropic	U_{iso} (Yb _{16d})	0.00796		1.000
atomic	U_{iso} (Ti _{16c})	0.00995	Å ²	0.9832
displacement	U_{iso} (O _{8b})	0.01237		0.9883
parameters	U_{iso} (O _{48f})	0.01622		0.9908

Table 5.9 Results of the refinement of SS Yb₂Ti₂O₇, sintered at 1500°C.

Parameter	Symbol	Refined value	Unit	Occupation
lattice parameter	a	10.09501	Å	
crystallite size	μ	1859	nm	
microstrain	ϵ	640	10^{-6}	
oxygen coordinate	x_{48f}	0.3327		
isotropic	U_{iso} (Yb _{16d})	0.02526		0.987
atomic	U_{iso} (Ti _{16c})	0.01517	Å ²	1.012
displacement	U_{iso} (O _{8b})	0.02965		0.962
parameters	U_{iso} (O _{48f})	0.05890		1.008

Table 5.10 Results of the refinement of SG Yb₂Ti₂O₇, sintered at 1500°C.

Figures 5.46 and 5.47 show the refinements for the SG $\text{Yb}_2\text{Ti}_2\text{O}_7$ sample, sintered at 1500°C , while Table 5.10 contains the structural parameters obtained from the refinement. As already discussed in Section 5.6.2, the lattice parameter is about 0.6% larger than that of the SS sample, which likely indicates some amount of structural disorder. Compared to the SS sample, the crystallite size and strain values are both somewhat larger, while the x_{48f} coordinate is only slightly increased.

In this case we constrained the cation occupancies to satisfy $occ_{\text{Yb}/16d} + occ_{\text{Ti}/16c} = 2$ and kept the charge neutrality condition (5.32). The refined values suggest a Yb deficiency of about 2.5% although, as before, these estimates are not very reliable. The U_{iso} values are significantly larger than the corresponding values of the SS sample, which could indicate small static displacements from the ideal atomic positions that would also be consistent with the increased lattice parameter.

We tried to refine the structure with some cation antisite exchange (as in Table 2.12) and oxygen ions occupying the usually vacant 8a sites, but the refinements did not seem to improve significantly and the additional parameters introduced more degrees of freedom, rendering the results less trustworthy. For similar reasons it is not possible to detect variations from the nominal valence of the cations using only conventional XRD.

Figures 5.48 and 5.49 show the refinement of the $\text{Yb}_2\text{Zr}_x\text{Ti}_{2-x}\text{O}_7$ sample with $x = 0.15$, sintered at 1500°C , and Table 5.11 lists the refined parameters.

Parameter	Symbol	Refined value	Unit	Occupation
lattice parameter	a	10.09432	Å	
crystallite size	μ	517	nm	
microstrain	ϵ	298	10^{-6}	
oxygen coordinate	x_{48f}	0.3331		
isotropic atomic displacement parameters	U_{iso} (Yb _{16d})	0.01180		0.991
	U_{iso} (Ti _{16c})	0.01510		0.947
	U_{iso} (Zr _{16c})	0.01510	Å ²	0.053
	U_{iso} (O _{8b})	0.03464		1.025
	U_{iso} (O _{48f})	0.05199		0.9913

Table 5.11 Results of the refinement of $\text{Yb}_2\text{Zr}_x\text{Ti}_{2-x}\text{O}_7$ with $x = 0.15$, sintered at 1500°C .

Since Ti and Zr occupy the same 16c site, their U_{iso} values were constrained to be equal and their occupancies to satisfy $occ_{\text{Ti}} + occ_{\text{Zr}} = 1$. The refined values indicate slightly less Zr than the nominal value, $x = 0.106$ instead of $x = 0.150$, and a 0.6% Yb deficiency. The other parameters are similar to those of the SG $\text{Yb}_2\text{Ti}_2\text{O}_7$ sample, although the lattice parameter is somewhat reduced, even though it would be expected to have slightly increased with the addition of the larger Zr ion. Inspecting the refinement we note that the peak intensities of the experimental data and refined model do not agree very well, some of them being overestimated and others underestimated. This could be due to various effects, such as a nontrivial amount of cation site inversion.

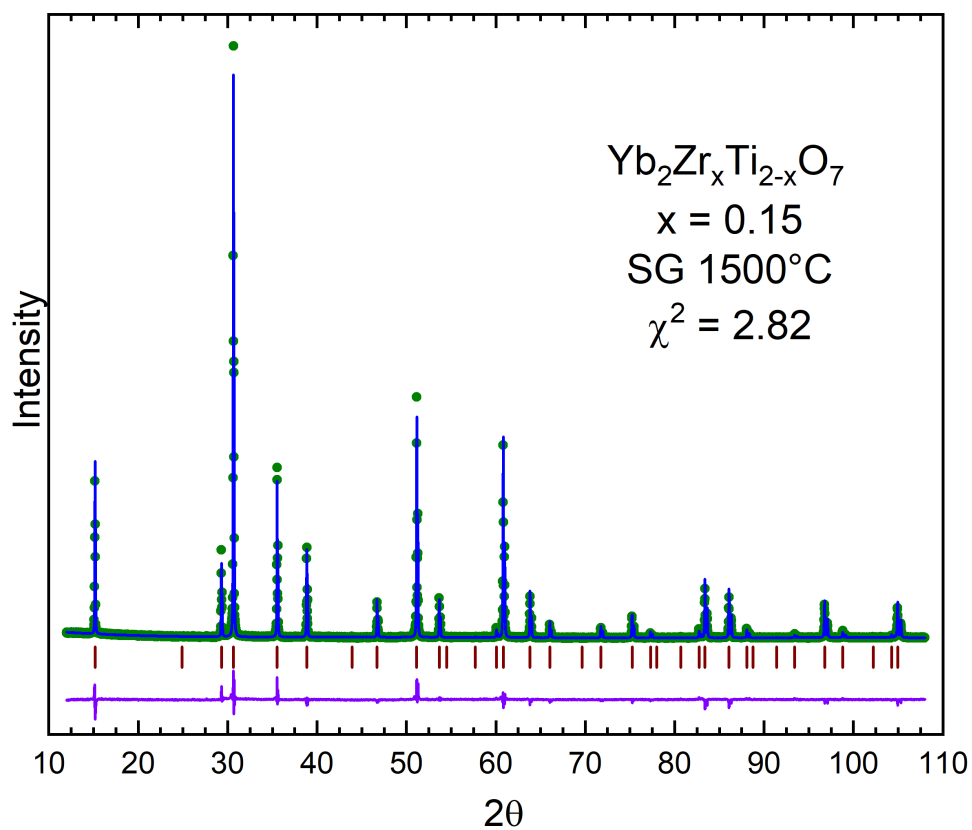


Figure 5.48 A refinement of Yb₂Zr_xTi_{2-x}O₇ with $x = 0.15$, sintered at 1500°C (linear intensity scale).

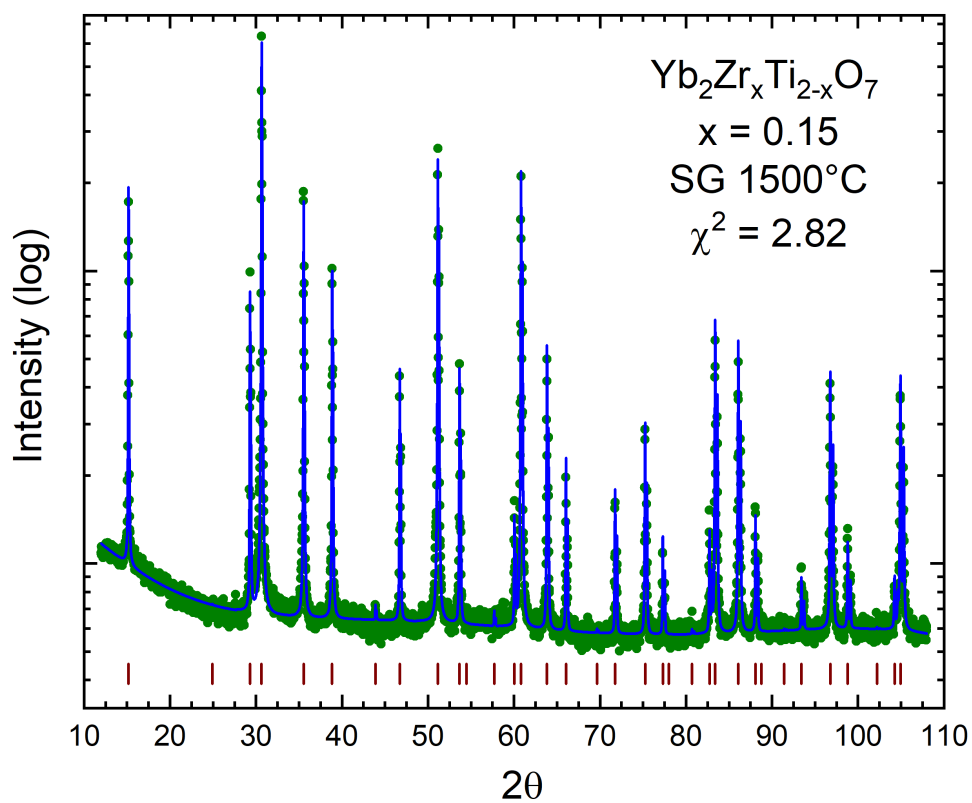


Figure 5.49 A refinement of Yb₂Zr_xTi_{2-x}O₇ with $x = 0.15$, sintered at 1500°C (logarithmic intensity scale).

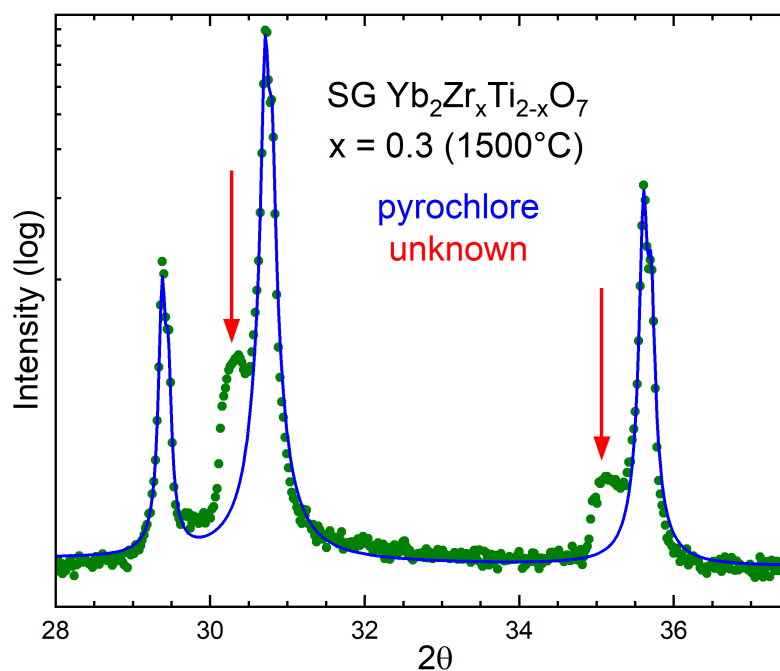


Figure 5.50 Secondary peaks adjacent to the pyrochlore peaks for $\text{Yb}_2\text{Zr}_x\text{Ti}_{2-x}\text{O}_7$ with $x = 0.3$, sintered at 1500°C.

$x = 0.3$			$x = 0.5$		
Index	$2\theta_{main} (^{\circ})$	$2\theta_{sec} (^{\circ})$	Index	$2\theta_{main} (^{\circ})$	$2\theta_{sec} (^{\circ})$
222	30.7	30.3	222	30.5	29.9
400	35.6	35.1	400	35.3	34.8
440	54.2	50.4	331	38.6	38.1
533	60.3	59.9	511	46.4	45.9
622	60.9	60.6	440	50.9	50.3
444	63.9	62.9	531	53.4	53.0

Table 5.12 Miller indices and positions of the main pyrochlore $2\theta_{main}$ and secondary $2\theta_{sec}$ peaks for the $\text{Yb}_2\text{Zr}_x\text{Ti}_{2-x}\text{O}_7$ samples with $x = 0.3, 0.5$, sintered at 1500°C.

The $\text{Yb}_2\text{Zr}_x\text{Ti}_{2-x}\text{O}_7$ samples with $x = 0.3, 0.5$ did crystallize in the pyrochlore phase but exhibited some secondary peaks adjacent to the main pyrochlore peaks. Figure 5.50 shows an example of such secondary peaks for $\text{Yb}_2\text{Zr}_x\text{Ti}_{2-x}\text{O}_7$ with $x = 0.3$, sintered at 1500°C . These peaks do not seem to be associated to an impurity phase, since we could not fit them to any of the phases in the structural database used for qualitative phase analysis.

Table 5.12 lists the Miller indices and positions of the main pyrochlore and unidentified secondary peaks for the $\text{Yb}_2\text{Zr}_x\text{Ti}_{2-x}\text{O}_7$ samples with $x = 0.3, 0.5$, sintered at 1500°C . Note that some of the secondary peaks are adjacent to the pyrochlore-specific peaks (those with odd Miller indices), while some of them are adjacent to the fluorite peaks (those with even indices). The secondary peaks cannot be due to the presence of a secondary pyrochlore phase, with slightly larger lattice parameter, since only some of the peaks are split in this way, whereas if there were another pyrochlore phase then all of the main peaks would have smaller left-side companions.

We believe that these peaks are associated to static structural distortions of the pyrochlore phase. Attempts were made to determine the distortion modes using the ISODISTORT [253] and related programs from the ISOTROPY software suite [254], but the results were inconclusive and no good match to the observed secondary peaks was found. We tried to index the peaks to determine if there could be a reduction of the cubic symmetry to a lesser-symmetry phase (tetragonal, orthorhombic, rhombohedral etc.), but the results also were inconclusive.

For the intermediate $\text{Yb}_2\text{Zr}_x\text{Ti}_{2-x}\text{O}_7$ samples, with $x = 1.0$ and $x = 1.5$, the refinement was not as successful due to the local ordering that manifests as diffuse scattering, discussed in Section 5.2. We may ignore this problem and treat the diffuse scattering as part of the background by manually adding peaks to the background function. This can significantly improve the quality of the fit (lower χ^2 value) but the improvement is artificial since we are disregarding some of the physically relevant structural information. The same considerations apply to all of the $\text{Yb}_2\text{Zr}_x\text{Ti}_{2-x}\text{O}_7$ samples sintered at 900°C , which possess a highly disordered fluorite structure with some incipient local ordering that also could not be adequately refined.

We tried to model the local ordering by including more general, less symmetric sites (Table 2.1) to the ideal pyrochlore coordinates (Table 2.6). In [230] it is noted that in refinements of synchrotron diffraction data for $\text{Yb}_2\text{Ti}_2\text{O}_7$ the Ti ions have a preference for the (x, x, x) 32e sites, while the Yb ions show equal preference for the $(0, y, -y)$ 96h and the (x, x, z) 96g sites. Neutron diffraction indicated that the O_{8b} ions do not move, while the O_{48f} ions tend to relax to the 96g site. These conclusions are almost impossible to reproduce from our laboratory diffraction data due to its limited resolution and statistics when compared to synchrotron and neutron diffraction data.

We tried to refine the structures of the samples with dominant pyrochlore phase using various combinations of the more general positions mentioned above, but the refinements did not systematically improve, often failing to converge or showing almost random increases or decreases of χ^2 when increasing site occupancies in small steps. This is not surprising since the inclusion of more general sites for the atoms in the structure adds more complexity to the model and increases the number of free parameters beyond what can reasonably be fitted using laboratory x-ray data.

Similarly for the samples with dominant fluorite structure, various possibilities were used to try to fit the diffuse scattering at the superstructure positions, all unsuccessful. It seems that a different approach is needed, since the aperiodically modulated local order that originates the diffuse peaks cannot be adequately modeled using a conventional periodically repeating unit cell. Techniques such as the pair distribution function (Section 8.2.2) are better suited to capture the physics of such imperfectly crystalline structures. In summary, the $x = 0.3, 0.5$ pyrochlore samples display structural distortions that could not be unambiguously identified, and the $x = 1.0, 1.5$ fluorite samples display some local ordering that is hard to capture with Rietveld refinement.

The refinement for $\text{Yb}_2\text{Zr}_x\text{Ti}_{2-x}\text{O}_7$ with $x = 2.0$, sintered at 1500°C , is shown in Figures 5.51 and 5.52 and the results listed in Table 5.13. The sample refined well with the $\text{Yb}_4\text{Zr}_3\text{O}_{12}$ δ -phase structure, which has a 4:3 ratio between Yb and Zr, though the nominal proportion is 1:1. It is possible that some Zr was lost during the sol-gel synthesis, given that the Zr precursor tended to precipitate out of solution and stick to the glassware, as described in Chapter 4. However we assume such losses to be at most on the order of a few percent, so we refined the structure as a stuffed δ -phase, assuming equal proportions of Yb and Zr randomly mixed on both the 3a and 18f sites, i.e. the stoichiometry is $(\text{Yb}_{3.5}\text{Zr}_{0.5})\text{Zr}_3\text{O}_{12.25}$, which is equivalent to the $\text{Yb}_2\text{Zr}_2\text{O}_7$ stoichiometry but with a different structure than the $\text{Yb}_2\text{Zr}_2\text{O}_7$ fluorite.

We could relax the $c + 6d = 4$ constraint (see Table 2.8) so that that $\text{A}_4\text{B}_3\text{O}_{12}$ could be anywhere in between $\text{Yb}_4\text{Zr}_3\text{O}_{12}$ and $(\text{Yb}_{3.5}\text{Zr}_{0.5})\text{Zr}_3\text{O}_{12.25}$, but this would likely give unphysical results given the large number of free parameters for the δ -phase structure. Ideally a chemical analysis should be performed on all $\text{Yb}_2\text{Zr}_x\text{Ti}_{2-x}\text{O}_7$ samples to verify what the actual element proportions are, so that we could fix those values in the refinement and focus our attention on other parameters. Constraints were imposed to set the occupations of both cation sites equal to one,

$$\begin{aligned} \text{occ}_{\text{Yb}/3a} + \text{occ}_{\text{Zr}/3a} &= 1 \\ \text{occ}_{\text{Yb}/18f} + \text{occ}_{\text{Zr}/18f} &= 1 \end{aligned} \quad (5.33)$$

for a 1:1 Yb:Zr proportion,

$$3 \text{occ}_{\text{Yb}/3a} + 18 \text{occ}_{\text{Yb}/18f} = \frac{3 + 18}{2} = 10.5 \quad (5.34)$$

and to ensure charge neutrality,

$$\begin{aligned} &3 \left[(+3) \text{occ}_{\text{Yb}/3a} + (+4) \text{occ}_{\text{Zr}/3a} \right] \\ &+ 18 \left[(+3) \text{occ}_{\text{Yb}/18f} + (+4) \text{occ}_{\text{Zr}/18f} \right] \\ &+ 18 \left[(-2) \text{occ}_{\text{O}/18f,1} + (-2) \text{occ}_{\text{O}/18f,2} \right] = 0 \end{aligned} \quad (5.35)$$

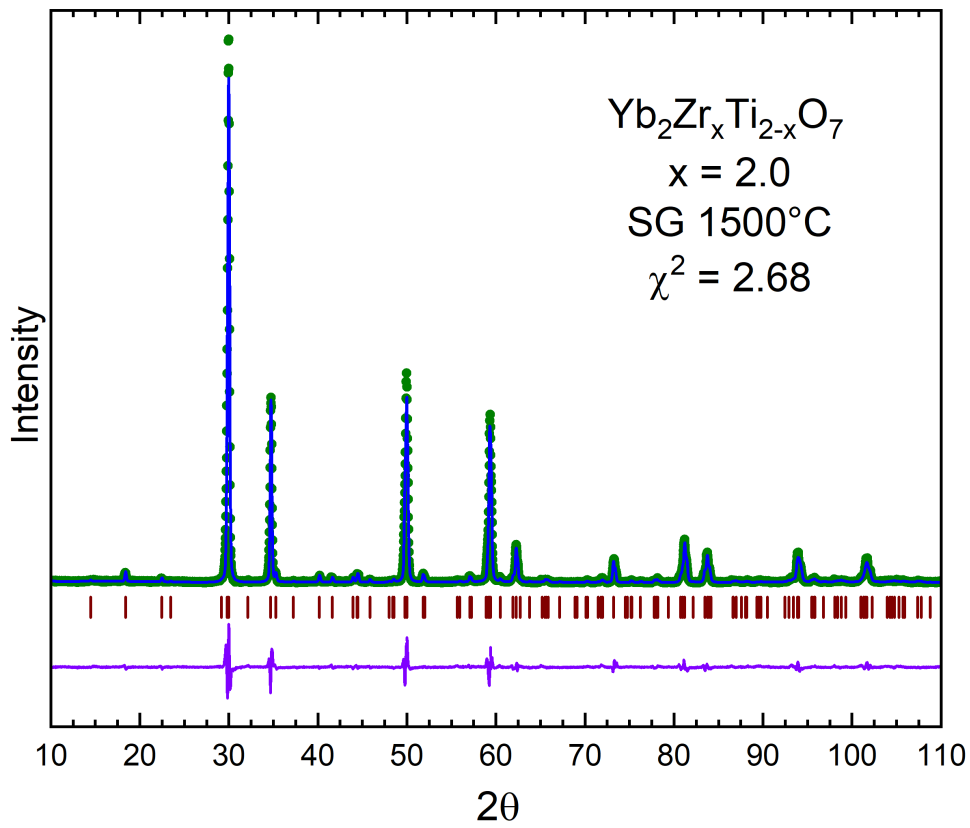


Figure 5.51 A refinement of the SG Yb₂Ti₂O₇ sample (linear intensity scale).

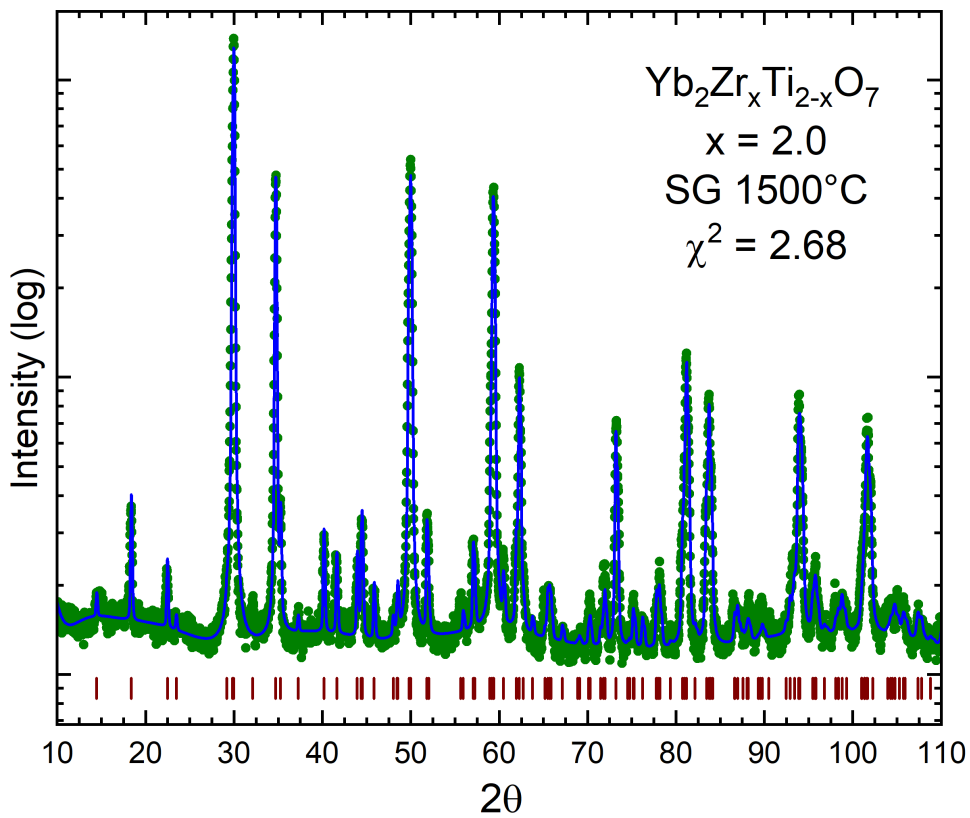


Figure 5.52 A refinement of the SG Yb₂Ti₂O₇ sample (logarithmic intensity scale).

Parameter	Symbol	Refined value	Unit	Occupation
lattice parameters	a	9.65329	Å	
	c	8.98761	Å	
crystallite size	μ	1001	nm	
microstrain	ϵ	194	10^{-6}	
	U_{iso} (Yb _{3a})	0.02080		0.571
isotropic	U_{iso} (Zr _{3a})	0.02080		0.429
atomic	U_{iso} (Yb _{18f})	0.01583	Å ²	0.488
displacement	U_{iso} (Zr _{18f})	0.01583		0.512
parameters	U_{iso} (O _{18f})	0.0315		1.052
	U_{iso} (O _{18f})	0.0315		0.990

Table 5.13 Results of the refinement of $\text{Yb}_2\text{Zr}_x\text{Ti}_{2-x}\text{O}_7$ with $x = 2.0$, sintered at 1500°C .

The oxygen ions at the two inequivalent 18f positions were constrained to have the same U_{iso} displacement parameter, although not required by symmetry. Looking at the refinement in Figures 5.51 and 5.52 we see that the peak heights are somewhat underestimated for the most intense peaks whereas some of the weaker reflections in the lower angular range, $2\theta < 50^\circ$, are slightly overestimated. The intense peaks correspond to the reflections of the parent fluorite structure, of which the δ -phase is a distortion, while the weaker reflections are specific to the non-cubic δ -phase. This led us to believe that there might be a certain amount of a $\text{Yb}_2\text{Zr}_2\text{O}_7$ fluorite phase coexisting with the stuffed $(\text{Yb}_{3.5}\text{Zr}_{0.5})\text{Zr}_3\text{O}_{12}$ δ -phase, or possibly a mixture of the $\text{Yb}_4\text{Zr}_3\text{O}_{12}$ δ -phase with a cubic ZrO_2 fluorite.

Such a mixture of δ and fluorite phases would explain a disproportional increase of the most intense reflections fluorite reflections. However refinements of these proposed two-phase mixtures were not successful. We tried many variants of this scenario but in all cases either the lattice parameter, crystallite size, strain or phase fractions of the fluorite diverged. Another possibility is that the cations are not completely disordered on one or both of the cation sites, but rather that these sublattices may possess some kind of partial order. We did not investigate this possibility since we do not know how to establish a model that is general enough to represent the numerous possibilities for cation ordering, while being sufficiently discriminating to distinguish these options.

5.6.4 $\text{Yb}_2\text{Zr}_x\text{Ti}_{2-x}\text{O}_7$ Phase Diagram

Considering all of the information obtained from the Rietveld refinements and the qualitative results from Section 5.6.2, Figure 5.53 shows an approximate temperature-composition phase diagram for the $\text{Yb}_2\text{Zr}_x\text{Ti}_{2-x}\text{O}_7$ compounds. The vertical axis is the sintering temperature T , while the horizontal axis is the composition x (bottom label), that can also be thought of as the average B^{4+} cation radius in the $\text{A}_2\text{B}_2\text{O}_7$ structure (top label). The black symbols indicate the synthesized samples while the colors represent the structure: blue = pyrochlore, red = fluorite, green = δ -phase.

This phase diagram is not meant to be quantitative or exact but rather intends to illustrate some general conclusions we might draw from the structural information extracted from diffraction data. The first conclusion is that a higher sintering temperature improves the crystallinity of the samples, giving rise to the energetically most stable phase, which makes intuitive sense from a thermodynamics perspective. The most stable high-temperature phase is the pyrochlore for $x \leq 0.5$, the defect fluorite for $x = 1.0, 1.5$, and the δ -phase for $x = 2.0$. The samples sintered at 900°C are not fully equilibrated and are highly disordered.

The second conclusion is that the amount of structural disorder is loosely proportional to the amount of Zr in the composition (proportional to x), although it is arguable if the δ -phase that occurs for $x = 2.0$ is more disordered than the defect fluorite at $x = 1.5$. The effects of sintering temperature T and composition x interact so that, for instance, the transition temperature from fluorite to pyrochlore of the samples with $x \leq 0.5$ increases with x .

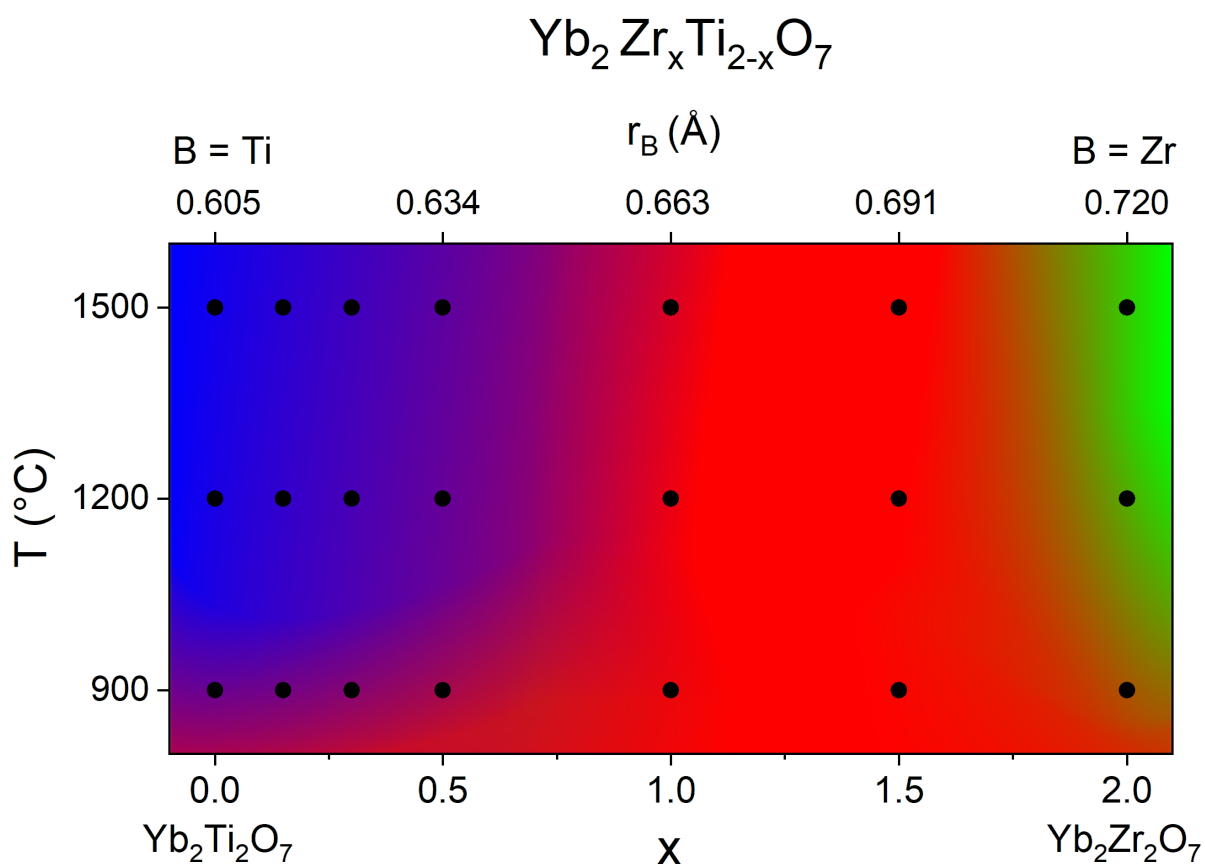


Figure 5.53 Approximate temperature-composition phase diagram for the $\text{Yb}_2\text{Zr}_x\text{Ti}_{2-x}\text{O}_7$ compounds. Colors represent the structure: blue = pyrochlore, red = fluorite, green = δ -phase.

Raman Spectroscopy

In Section 6.1 we introduce Raman spectroscopy and the use of group theory to analyze vibrational modes of solids, and in Section 6.3 we present and discuss the experimental results for the $\text{Yb}_2\text{Zr}_x\text{Ti}_{2-x}\text{O}_7$ samples. The general information on spectroscopy and applications of group theory to materials science were extracted from [255, 256, 257, 258, 259, 260, 261, 262, 263, 264, 265, 266].

6.1 Introduction

Raman spectroscopy is an analytical technique where light shines on a sample and the inelastically scattered light provides information on the vibrational modes of the molecules or crystal structure of the material. It is widely used in chemistry and other fields to analyze chemical composition by "fingerprinting" the molecules present in a sample through their characteristic vibrational modes.

The basic principle is that a monochromatic light beam, generated by a laser, excites a molecule and the light is scattered either elastically or inelastically, as depicted in Figure 6.1. Most of the light is scattered elastically in the process known as Rayleigh scattering, however this strong elastically component of the scattered light carries no chemical or structural information with it. On the other hand, the inelastically scattered light does carry such information, since the energy shift of the scattered photons allows the vibrational modes of the molecule or structure to be inferred.

In order for a photon to be scattered inelastically it needs to interact with some excitation of the sample, gaining or losing energy. After an inelastic scattering event the scattering molecule is in a different vibrational state, so that the photon energy shift allows the determination of the vibrational energies of the molecule. The scattered light with increased wavelength (decreased frequency) is called the Stokes component whereas the light with decreased wavelength (increased frequency) is called the anti-Stokes component. A photon energy gain during the scattering process requires the scattering molecule to be in an excited state, while an energy

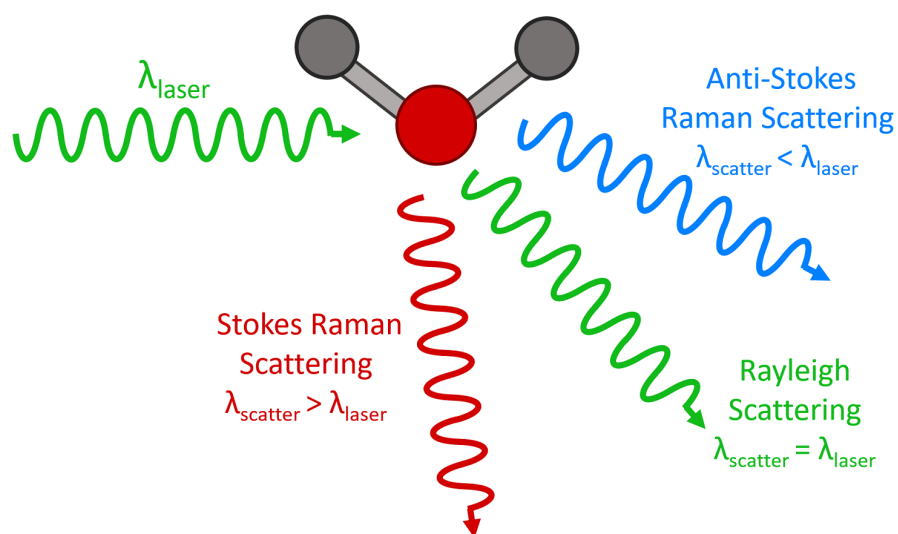


Figure 6.1 Molecule excited by monochromatic light scattering both elastically and inelastically [267].

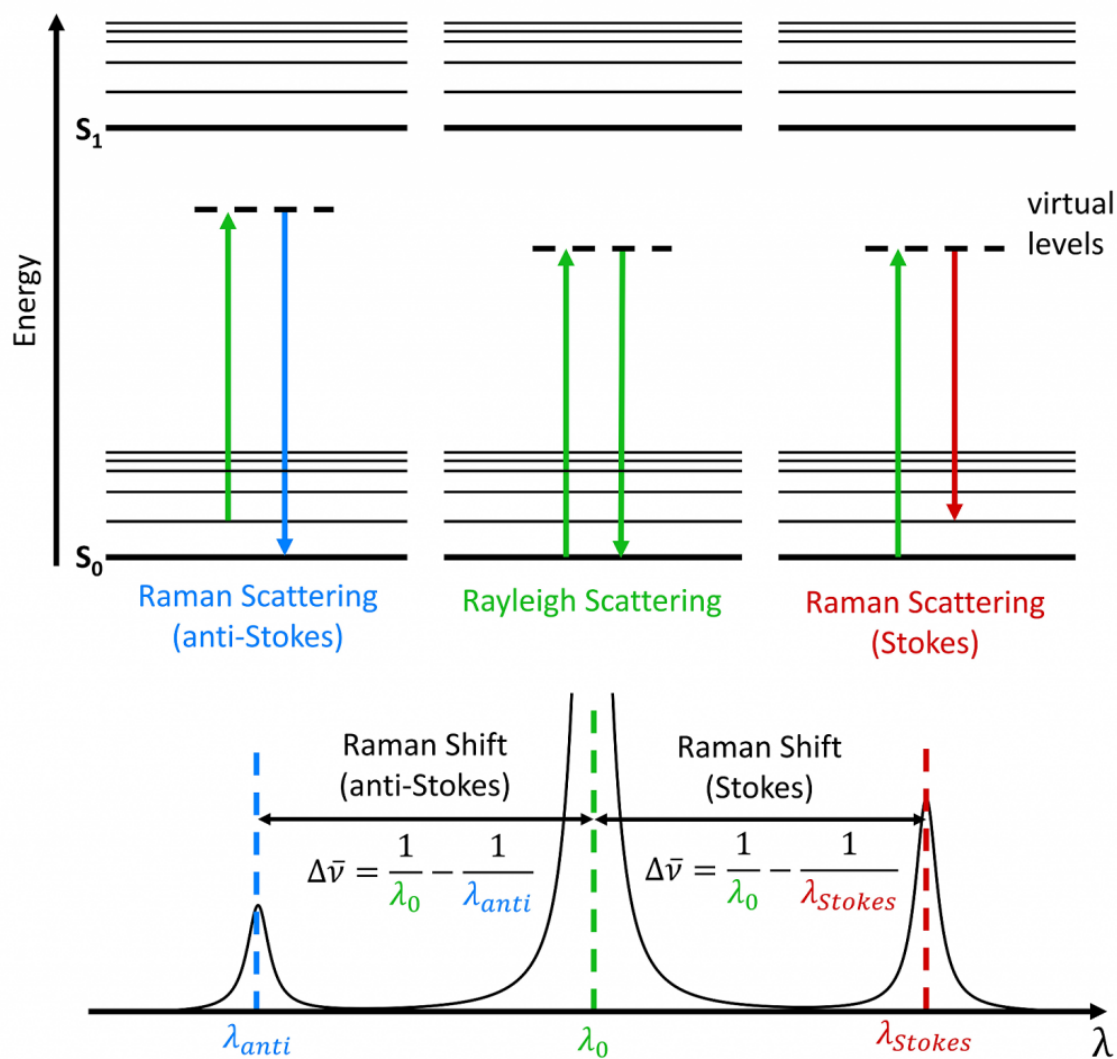


Figure 6.2 Scattering processes visualized on an energy level diagram and the resulting spectrum [267].

loss can always occur, as illustrated in the energy-level diagram in Figure 6.2, where the virtual levels correspond to short-lived excitations of the scattering molecule.

Assuming a typical Boltzmann population of energy states this implies that the anti-Stokes component is weaker than the Stokes component, so usually only the Stokes side of the Rayleigh peak is considered in Raman spectroscopy. Anti-Stokes scattering is also somewhat harder to interpret since it requires considering the population of the higher-energy states, while Stokes scattering more directly probes the available energy levels. At low temperature, due to the thermal depopulation of the higher states, the anti-Stokes component vanishes and Stokes scattering provides a cleaner view of the actual energy level structure than it would at higher temperature.

Raman spectra are commonly given as plots of scattered light intensity as a function of the shift in wavenumber $\tilde{\nu}$ (the inverse wavelength, $\tilde{\nu} = 1/\lambda$), although the wavenumber is often colloquially called a frequency. The energy shift ΔE of a photon is related to the shifts in frequency $\Delta\nu$ and wavenumber $\Delta\tilde{\nu}$ by

$$\Delta E = h \Delta\nu = hc \Delta(1/\lambda) = hc \Delta\tilde{\nu} \quad (6.1)$$

so that a shift in wavenumber has units of cm^{-1} and is proportional to the energy and frequency shifts. In this way the spectrum is independent of the laser wavelength, which would not be the case if the shift in wavelength $\Delta\lambda$ were used as horizontal axis for the spectrum.

Figure 6.3 shows a schematic representation of a Raman spectroscopy setup. A monochromatic light beam is generated by a laser and impinges onto the sample. The laser wavelength can be chosen according to the application to avoid fluorescence and luminescence of the samples, effects that can detrimentally impact the spectroscopic data. The light scattered by the sample is then focused and guided into a spectrometer, where the intense Stokes line is filtered out, a diffraction grating disperses the light into its components and the intensity at each wavelength is measured by a detector.

Infrared (IR) spectroscopy is conceptually similar to Raman spectroscopy but the selection rules for vibrational modes to be Raman- or IR-active differ. In IR spectroscopy the wavelength of the incident radiation, usually in the infrared region of the electromagnetic spectrum, is varied and the absorption by the sample is measured, while in Raman spectroscopy the source wavelength is fixed and only relative energy shifts induced by inelastic scattering are observed. The Raman effect is based on the interaction between the electron cloud of a molecule and the electric field of the incoming light, which can polarize the molecule, inducing a dipole moment, whereas IR absorption depends on the direct interaction of the molecular dipole moment with the electric field of the light.

An electromagnetic field \mathbf{E} can induce an electric dipole moment $\boldsymbol{\mu}_{ind}$ in a molecule and these quantities are linearly related by the polarizability tensor $\boldsymbol{\alpha}$,

$$\boldsymbol{\mu}_{ind} = \boldsymbol{\alpha}\mathbf{E} \quad (6.2)$$

in the weak field limit (this linear approximation is not applicable if the field is very strong).

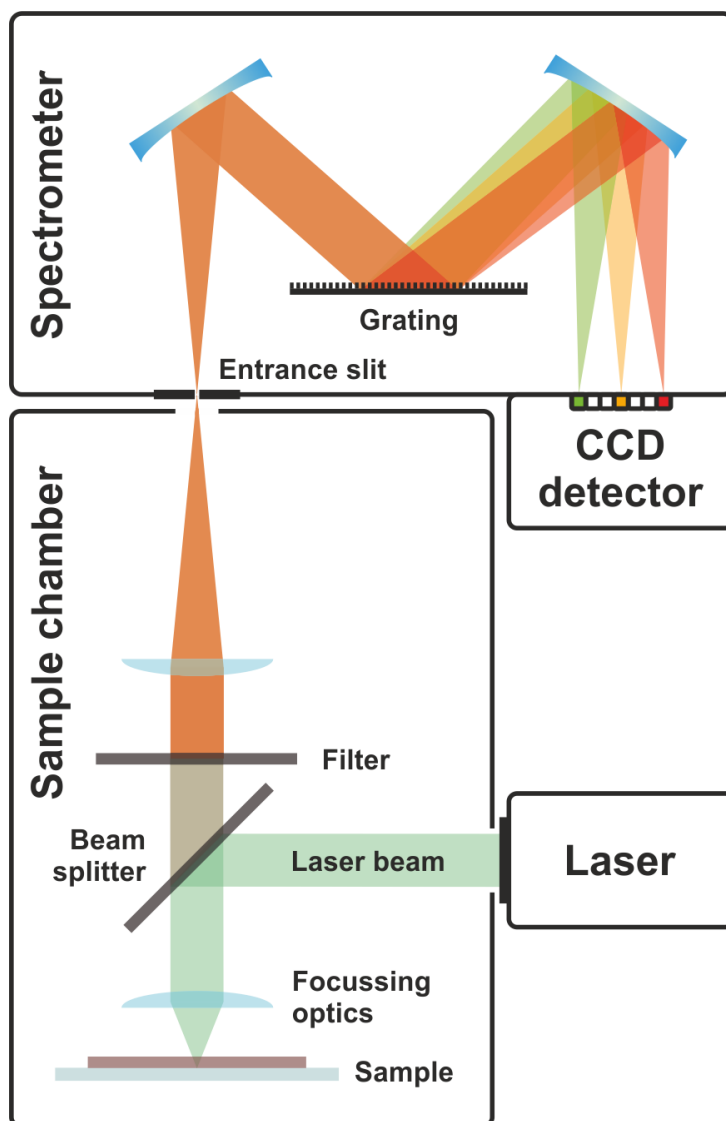


Figure 6.3 Schematic representation of a Raman spectroscopy setup [268].

Letting v stand for a coordinate assigned to a vibrational mode, for instance a bond length or angle between two bonds, the mode will be Raman-active if

$$\frac{\partial \alpha}{\partial v} \neq 0 \quad (6.3)$$

and IR-active if

$$\frac{\partial \mu}{\partial v} \neq 0 \quad (6.4)$$

where μ is the total dipole moment of the molecule. In other words, IR absorption requires a change in the dipole moment of the molecule with the vibrational motion, while Raman scattering requires a change in the polarizability of the molecule when vibrating.

Some vibrational modes can only be detected with one of these techniques and often transitions

that have large Raman intensities have only weak IR intensities and vice versa. A notable example of this is the rule of mutual exclusion, which states that for centrosymmetric molecules (those that possess a center of symmetry) no normal modes can be both IR and Raman active. Therefore these two techniques are often used in combination since they provide information that is highly complementary.

To explain how group theory is used to interpret vibrational motions we use the simple example of a water molecule, H_2O . This molecule possesses four symmetry operations: E , C_2 , σ and σ' , depicted in Figure 6.4. E is the identity operation, C_2 is a rotation by $\pi = 180^\circ$ about the vertical axis, and σ , σ' are two reflections (mirror planes) as indicated in the figure. These four symmetry elements form the group C_{2v} , with the multiplication table given in Table 6.1, where multiplying two symmetries means composing them sequentially to obtain another symmetry.

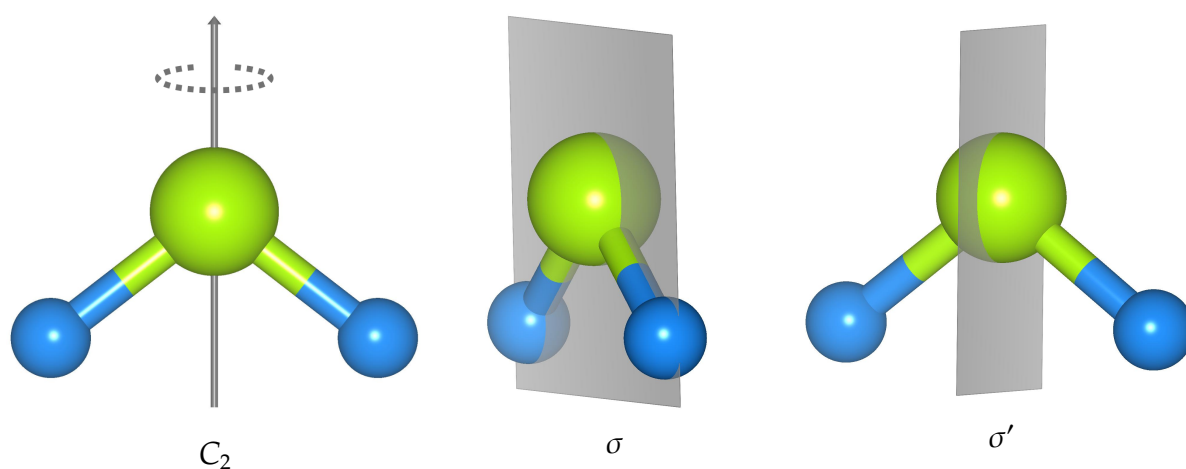


Figure 6.4 Symmetries of H_2O molecule.

\times	E	C_2	σ	σ'
E	E	C_2	σ	σ'
C_2	C_2	E	σ'	σ
σ	σ	σ'	E	C_2
σ'	σ'	σ	C_2	E

Table 6.1 Multiplication table for the group C_{2v} .

For many applications in mathematics and in science it is useful to consider group representations, which are more concrete instantiations of the structure of an abstract group. A representation of a group is a set of square matrices such that a matrix M_g is assigned to every group element g , and the matrix multiplication mirrors the structure of the group, i.e. if f, g, h are three group elements and $fg = h$ then $M_f M_g = M_h$.

The dimension of a representation is defined as the dimension of the matrices that compose it. A group can have representations of arbitrary dimension, but all except a few of these representation are reducible, meaning they can be composed from the fundamental irreducible representations. The character of a group element is defined as the trace of the corresponding matrix. Characters are very useful since they simplify the higher-dimensional matrices down to

one-dimensional numbers while preserving much of the essential information about the group's structure contained in the matrices of a representation.

In the case of the C_{2v} group that describes the symmetries of the H_2O molecule there are four irreducible representations and all of them are one-dimensional, so that the 1×1 matrices are effectively just numbers that are trivially equal to the characters. Table 6.2 shows a character table for the group C_{2v} , a list of characters for each of the four irreducible representations A_1, A_2, B_1, B_2 .

Irrep	E	C_2	σ	σ'
A_1	1	1	1	1
A_2	1	1	-1	-1
B_1	1	-1	1	-1
B_2	1	-1	-1	1

Table 6.2 Character table for the group C_{2v} .

A molecule containing n atoms will in general have $3n$ degrees of freedom, but three of those correspond to translations of the entire molecule and another three correspond to rotations of the whole molecule. These translations and rotations do not change the shape of the molecule, so that there remain $3n - 6$ degrees of freedom that correspond to vibrations (distortions) of the molecule. Thus the H_2O molecule has $3 \times 3 - 6 = 3$ vibrational modes, which can be classified as symmetric stretching, antisymmetric stretching and symmetric bending of the H–O bonds, illustrated in Figure 6.5.

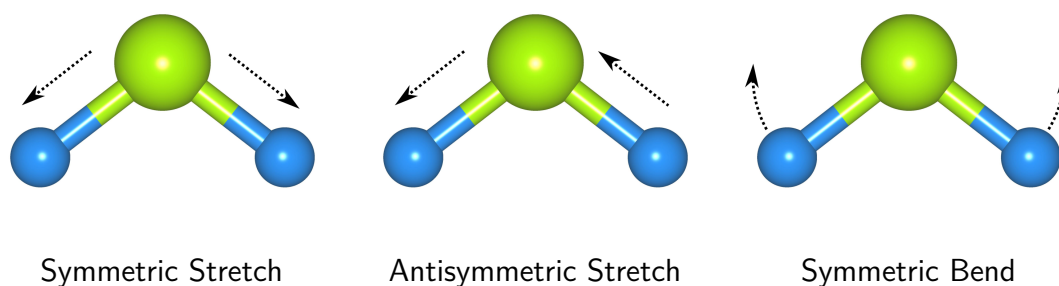


Figure 6.5 Vibrational modes of H_2O molecule.

Vibrational Mode	E	C_2	σ	σ'	Irrep
Symmetric Stretch	1	1	1	1	A_1
Antisymmetric Stretch	1	-1	1	-1	B_1
Bend	1	1	1	1	A_1

Table 6.3 Symmetry properties for each vibrational mode of the H_2O molecule.

Considering how each of these vibrational modes is affected by the C_{2v} symmetry operations we may assign each mode to one of the irreducible representations of the group, as shown in

Table 6.3. The symmetric stretching and bending modes are invariant under all four symmetries, while the antisymmetric stretching mode is transformed into its inverse under the C_2 and σ' operations. Comparing with the character table (Table 6.2) we can assign each mode to an irreducible representation (irrep).

The assignment of an irreducible representation to a vibrational mode is useful since it dictates whether the mode is IR or Raman-active. In a manner analogous to the vibrational modes we may consider how a component of a dipole or quadrupole transforms under the group symmetries. The selection rules for IR and Raman activity are that a mode is IR-active if it transforms as a component of a dipole (x, y, z) and Raman-active if it transforms like the components of a quadrupole ($x^2, y^2, z^2, xy, yz, xz$). This difference originates in the different physical mechanisms for IR absorption and Raman scattering, relating to changes in the dipole moment or in the polarizability tensor, respectively.

In the case of the H_2O molecule, both A_1 and B_1 are IR and Raman-active, so that we expect three coincident bands in the IR and Raman spectra. For more complex molecules it is not as common for modes to be both IR and Raman-active and some modes might not be active at all. Group theory considerations only bring us so far, they cannot predict the intensities or frequencies of the observed bands in experimental spectra, which would require knowledge of additional parameters such as atomic masses, force constants and molecular environment.

6.2 Pyrochlore Raman Modes

Up to now the examples were phrased in terms of molecules for simplicity, but the principles apply equally well to groups of atoms in a solid structure. Raman spectroscopy probes the local bonding in a solid, within a unit cell of the crystal structure. Thus the powder crystallite size has no effect on the peak shape in a Raman spectrum, except for extremely small crystallites such as nanoparticles. This is in contrast to x-ray diffraction, which probes the structure on larger length scales, over many unit cells, and is not very sensitive to the local order. Raman and Infrared spectroscopy are ideal to investigate amorphous or only partially crystalline systems since they do not require a periodic unit cell, as do diffraction experiments. For the pyrochlore compounds they can provide valuable information, especially on the oxygen sublattice.

The laser wavelength λ , on the order of 500nm, is much larger than the typical dimension a of the unit cell of a crystal structure, on the order of 1nm. The photon wavevector k is inversely proportional to its wavelength, $k \propto \lambda^{-1} \ll a^{-1}$, so effectively $k \approx 0$, at the zone center, since the dimensions of the Brillouin zone are proportional to a^{-1} .

Phonons are the quantized version of the elastic vibrations in a solid, analogous to how photons are the quantized particles corresponding to light waves. The relationship $E(p)$ between energy and momentum of a phonon, or equivalently, $\omega(k)$ between frequency and wavevector, is called the dispersion. Phonons can be classified as optical or acoustical according to their behavior at the Brillouin zone center ($k = 0$). Acoustical phonons have a linear dispersion $\omega \propto k$ so that their frequency tends to zero close to the zone center, while the frequency of optical phonons tends to a finite value at the zone center, $\omega \approx cst$. The adjective 'optical' already reveals that it is these phonons that interact with photons, which have a finite energy but lie close to the zone center, $k \approx 0$.

A useful tool for determining the theoretical vibrational modes of a structure is the [Symmetry Adapted Modes calculator](#) [269], available on the website of the [Bilbao Crystallographic Server](#) [270]. Given a CIF file of the crystal structure, the program calculates the irreducible representations to which each vibrational mode belongs.

The symbols used to denote irreducible representations are known as Mulliken Symbols and provide some information on symmetry properties: A or B stand for non-degenerate (one-dimensional) irreps, E for doubly degenerate (two-dimensional) irreps, F or T for triply-degenerate (three-dimensional) ones etc. Subscripts such as g and u signify that the modes have even or odd parity with respect to inversion symmetry, and so on.

Theory predicts 26 vibrational modes for the $Fd\bar{3}m$ (O_h^7) pyrochlore group, 25 of which are optical,

$$\begin{aligned}\Gamma_{acoustic} &= T_{1u} \\ \Gamma_{optical} &= A_{1g} + 3A_{2u} + 3E_u + E_g + 4T_{2u} + 4T_{2g} + 7T_{1u} + 2T_{1g}\end{aligned}\quad (6.5)$$

Of these the Raman (R) and infrared (IR) active modes are

$$\begin{aligned}\Gamma_R &= A_{1g} + E_g + 4T_{2g} \\ \Gamma_{IR} &= 7T_{1u}\end{aligned}\quad (6.6)$$

Similarly for the $Fm\bar{3}m$ (O_h^5) fluorite structure

$$\begin{aligned}\Gamma_{acoustic} &= T_{1u} \\ \Gamma_{optical} &= T_{2g} + 2T_{1u} \\ \Gamma_R &= T_{2g} \\ \Gamma_{IR} &= 2T_{1u}\end{aligned}\quad (6.7)$$

and for the $R\bar{3}$ (C_{3i}^2) δ -phase structure

$$\begin{aligned}\Gamma_{acoustic} &= A_u + {}^1E_u + {}^2E_u \\ \Gamma_{optical} &= 12A_g + 13A_u + 12{}^1E_g + 13{}^1E_u + 12{}^2E_g + 13{}^2E_u \\ \Gamma_R &= 12A_g + 12{}^1E_g + 12{}^2E_g \\ \Gamma_{IR} &= 13A_u + 13{}^1E_u + 13{}^2E_u\end{aligned}\quad (6.8)$$

For a pyrochlore with mixed cations on the B site, $A_2B_xB'_{2-x}O_7$ the representations are

$$\begin{aligned}
 \Gamma_{acoustic} &= T_{1u} \\
 \Gamma_{optical} &= A_{1g} + 4A_{2u} + 4E_u + E_g + 5T_{2u} + 4T_{2g} + 9T_{1u} + 2T_{1g} \\
 \Gamma_R &= A_{1g} + E_g + 4T_{2g} \\
 \Gamma_{IR} &= 9T_{1u}
 \end{aligned} \tag{6.9}$$

so that the Raman-active modes are the same but two additional IR-active modes exist. If structural disorder is included then there may be additional Raman-active modes, so it is difficult to determine the active modes for the disordered fluorite structures that display local distortions from the average structure, as is the case with our $Yb_2Zr_xTi_{2-x}O_7$ samples. In those cases we try to reason from analogy to the vibrational modes of the pyrochlore structure, but further work is required to figure out what is the best approach to deal with such partially disordered structures.

The assignment of vibrational modes to the observed peaks in the Raman spectra of pyrochlore compounds is controversial and not consistent among all publications concerned with the pyrochlore and related fluorite compounds. We considered the reported assignments of vibrational modes in many publications [271, 272, 273, 274, 275, 276, 277, 278, 279, 280, 281, 282, 283, 284, 285, 286, 287, 288, 289, 290, 291, 220, 292, 80, 293, 224, 294, 295, 296, 297, 298] to arrive at the most plausible interpretation, however we cannot guarantee the correctness of all of the information presented here.

In order to assign a frequency to a certain vibrational mode the force constants of a structure are required, but these are difficult to measure directly. Polarized Raman spectroscopy, in which the monochromatic laser beam is polarized and the orientation of the sample is varied, can be used to determine the polarization and orientation dependence of the vibrations and thereby assign frequencies to the normal modes if the crystal structure is known, however this technique requires single crystal samples.

Each of the vibrational modes is generated by a combination of bonds stretching and bending simultaneously, so that we cannot immediately draw conclusions on the nature of the bonds (distances, angles, force constants) solely from the observed frequencies of the modes. For instance, the E_g mode has dominant contributions from A–O stretching and O–B–O bending and smaller contributions from other bonds. To simplify the notation in this chapter, we let O stand for the O_{48f} site and O' for the O_{8b} site in the pyrochlore structure.

In [277] the force constants for the $Yb_2Ti_2O_7$ pyrochlore structure are reported, based on a model with nine force constants, including repulsive O–O, O–O' interactions, attractive Ti–O, Yb–O, Yb–O' interactions and O–Ti–O, O–Yb–O, O–Yb–O' bending force constants. The force constants were adjusted to fit the experimental Raman and IR spectra reported in [294] and the resulting values are listed in Table 6.4. The O–Ti–O bending force constant is dominant and is assigned to the highest frequency T_{2g} Raman and T_{1u} IR modes.

Table 6.5 lists the calculated $\tilde{\nu}_{cal}$ [277] and experimental $\tilde{\nu}_{exp}$ [294] frequencies for the vibrational modes of the $Yb_2Ti_2O_7$ pyrochlore structure. The agreement is reasonably good and the model predicts two bands that were not observed, at 323cm^{-1} and 518cm^{-1} , possibly due

Stretch/Bend	Force Constant (N m ⁻¹)
O'–Yb–O'	3.2
O–Yb–O	8.2
O–Ti–O	25.5
O–Ti–O	43.4
O–O'	21.5
O–O	24.6
Yb–O	8.0
Yb–O'	8.0
Ti–O	41.7

Table 6.4 Force constants for the Yb₂Ti₂O₇ pyrochlore structure [277].

Mode	$\tilde{\nu}_{cal}$ (cm ⁻¹)	$\tilde{\nu}_{exp}$ (cm ⁻¹)
A_{1g}	520	525
E_g	323	-
	611	590
T_{2g}	518	-
	331	320
	220	220
	560	570
	458	450
	394	400
T_{1u}	262	270
	238	235
	136	136
	74	75

Table 6.5 Calculated $\tilde{\nu}_{cal}$ and experimental $\tilde{\nu}_{exp}$ frequencies for the vibrational modes of the Yb₂Ti₂O₇ pyrochlore structure [277].

to a poor signal to noise ratio for the measured spectra. The 39 normal coordinates associated with the zone-center phonons in the model are given in [277]. Some of the modes observed in our Raman spectra occur at frequencies that closely correspond to those of the IR-active modes. Table 6.6 lists the dominant bond stretching or bending motions contributing to each of the T_{1u} IR modes for the $\text{Yb}_2\text{Ti}_2\text{O}_7$ pyrochlore structure, according to [299].

Stretch/Bend	Frequency (cm^{-1})
O'–Yb–O'	119
O–Yb–O	134
Yb–TiO ₆	240
O–Ti–O	290
Yb–O	430
Yb–O'	458
Ti–O	573

Table 6.6 IR modes for the $\text{Yb}_2\text{Ti}_2\text{O}_7$ pyrochlore structure, according to [299].

6.3 Experimental Results

The instrument we used is a Horiba T64000 Raman spectrometer with a 2mW, 532nm green laser and a diffraction grating with 1800 lines/mm, located at the Federal University of ABC (UFABC). The measurements were performed by Dr. Dimy Nanclares Fernandes Sanches, a researcher at UFABC. All of our measurements were performed at room temperature. Initially we measured polycrystalline silicon to check the calibration of the instrument, since silicon has a very well-defined peak, shown in Figure 6.6. The measured value for the peak maximum, at $\tilde{\nu} = 521.1\text{cm}^{-1}$, agrees well with the reference value for stress-free single-crystal silicon, $\tilde{\nu} = 520.9\text{cm}^{-1}$ [300].

We measured Raman spectra of the precursor oxides used in the synthesis and compared them with data from the literature to confirm that the precursors did not exhibit impurities. Figure 6.7 shows a comparison of the Raman spectrum of the precursor oxide Yb_2O_3 with digitized data from [301]. The agreement is good except for a small difference at $\tilde{\nu} \approx 310\text{cm}^{-1}$. The spectra of the other precursor oxides also agreed well with data from the literature.

Raman spectroscopy is useful to determine the phase composition of the samples during the intermediate steps in the synthesis, clearly indicating whether a pure phase was achieved. As discussed in Section 5.6.2, the SS samples (except for $\text{Yb}_2\text{Ti}_2\text{O}_7$) did not form a pure phase. Figure 6.8 shows the Raman spectra of the SS and SG $\text{Yb}_2\text{Zr}_x\text{Ti}_{2-x}\text{O}_7$ samples with $x = 1.5$. Comparing the Raman spectra of these samples it is evident that they did not form the same phase, while the XRD patterns only display much more subtle differences.

In Figure 6.9 the spectra of the SS and SG $\text{Yb}_2\text{Ti}_2\text{O}_7$ samples are compared. It is apparent that the SG sample peaks are slightly broadened and that there are notable peaks at $\tilde{\nu} \approx 120\text{cm}^{-1}$, 600cm^{-1} , 710cm^{-1} that are hardly visible in the SS sample spectrum. A broadening of the peaks in the spectrum can occur if the local crystalline environment suffers slight variations

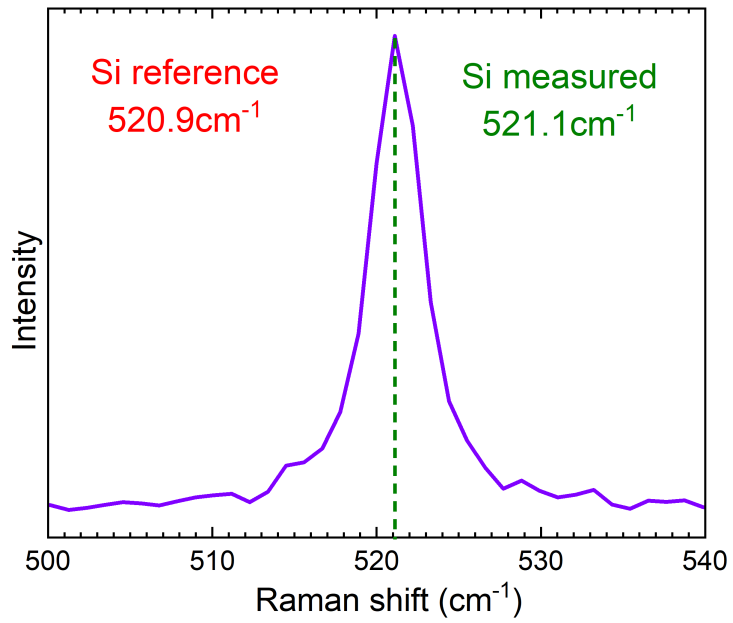


Figure 6.6 Peak in Raman spectrum of polycrystalline silicon.

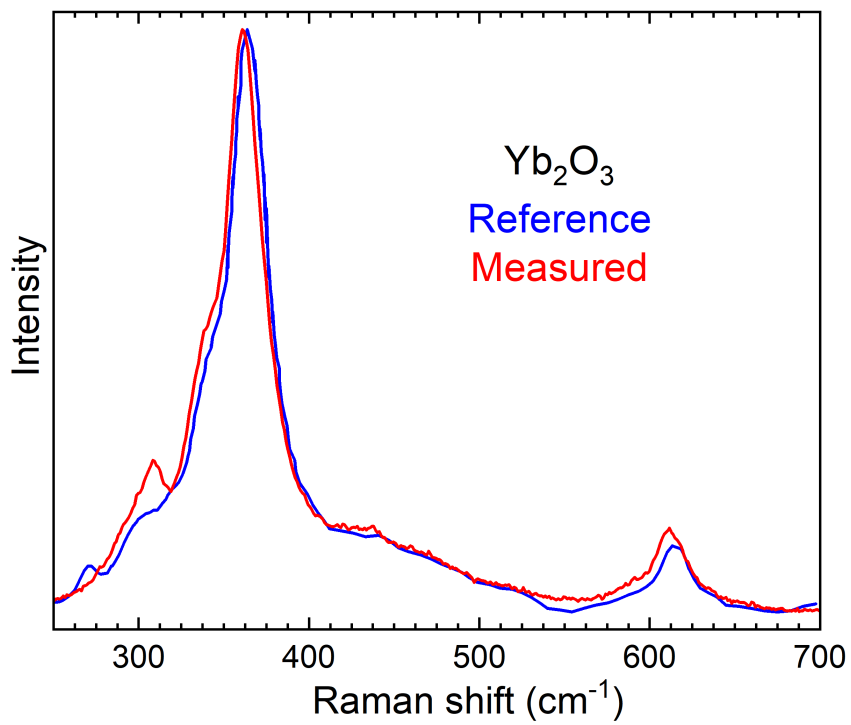


Figure 6.7 Raman spectra of the precursor oxide Yb₂O₃, compared with data from the literature.

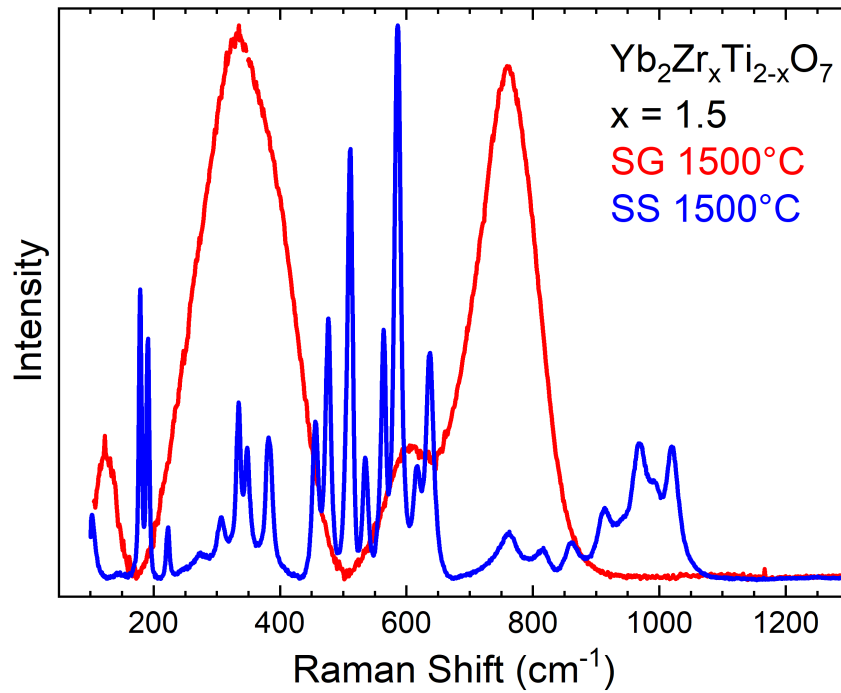


Figure 6.8 Raman spectra of the SS and SG $\text{Yb}_2\text{Zr}_x\text{Ti}_{2-x}\text{O}_7$ samples with $x = 1.5$.

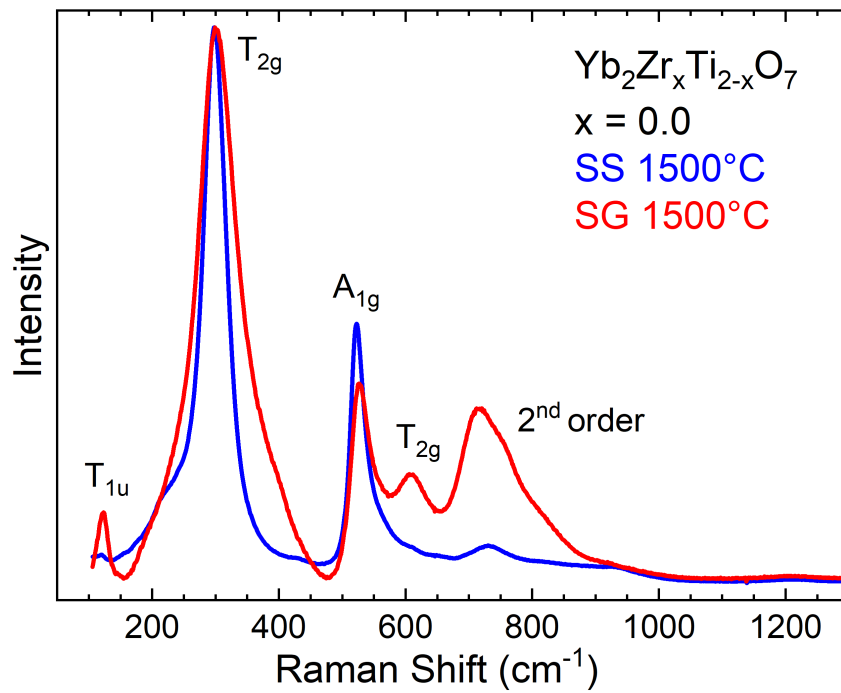


Figure 6.9 Raman spectra of the SS and SG $\text{Yb}_2\text{Ti}_2\text{O}_7$ samples.

over the sample volume excited by the laser. Therefore the observed broadening for the SG $\text{Yb}_2\text{Ti}_2\text{O}_7$ sample is indicative of structural disorder, in agreement with the increased lattice parameter, also argued to be a sign of disorder in Section 5.6.3.

Position (cm^{-1})	Mode	Stretch/Bend
120	T_{1u}	O'–Yb–O'
300	T_{2g}	O–Yb–O
520	A_{1g}	O–Ti–O
600	T_{2g}	O–Ti–O
710	harmonics	Ti–O ₆

Table 6.7 Modes assigned to each of the five clearly visible peaks in the spectrum of the SG $\text{Yb}_2\text{Ti}_2\text{O}_7$ sample, along with the dominant bond stretch or bend contributing to that mode.

Table 6.7 lists the modes assigned to each of the five clearly visible peaks in the spectrum of the SG $\text{Yb}_2\text{Ti}_2\text{O}_7$ sample, along with the dominant bond stretch or bend contributing to that mode. Notably, the peak at $\tilde{\nu} \approx 120\text{cm}^{-1}$ corresponds to an IR-active T_{1u} mode. The T_{1u} modes should not be Raman-active for an ideal pyrochlore structure but we argue that structural disorder breaks the exact site symmetry, altering the selection rules that dictate which vibrational modes should be Raman or IR-active. Small distortions of the BO_6 octahedra or displacements of the A ions could break the symmetry sufficiently to generate significant spectroscopic intensity at excluded positions while still being exceedingly small to detect with x-ray diffraction.

Since the T_{1u} mode at $\tilde{\nu} \approx 120\text{cm}^{-1}$ is related to the O'–Yb–O' bending motion, we believe that a slight displacement of the A^{3+} ion from its ideal position accounts for the Raman activity of this mode. The SS $\text{Yb}_2\text{Ti}_2\text{O}_7$ displays almost no intensity at this position (Figure 6.9) indicating that the A^{3+} ion is very close to its ideal position in the unit cell. These conclusions are consistent with the threefold increase of the refined isotropic atomic displacement parameter for the A^{3+} ion in the SG $\text{Yb}_2\text{Ti}_2\text{O}_7$ sample, when compared to the SS sample (Tables 5.9 and 5.10). As discussed in Section 5.5, the displacement parameters can absorb the effects of static displacements of the atoms, in addition to their dynamical thermal motion.

The peak at $\tilde{\nu} \approx 750\text{cm}^{-1}$ is believed to correspond to harmonic overtones of the other vibrations, mostly associated to the Ti–O₆ octahedron. The broad band from $\tilde{\nu} \approx 700\text{cm}^{-1}$ – 900cm^{-1} has a rather unusual asymmetric shape, probably being a superposition of more than one peak. The interpretation of similar features in the Raman spectra of other pyrochlores is varied and it seems that no one has reliably identified the cause of these higher-frequency bands.

In Figure 6.10 the Raman spectra for the SS and SG $\text{Yb}_2\text{Ti}_2\text{O}_7$ samples are compared with data from the literature [278, 282, 294]. The general agreement is good, although the SG sample clearly shows increased intensity in the 600cm^{-1} – 800cm^{-1} region and the peak at 120cm^{-1} is more pronounced than in the literature sources. There are small differences in the peak positions, although we hesitate to interpret these as physical effects since they could be artifacts of the data digitization procedure. These spectra were normalized by the height of the most intense T_{2g} peak at $\tilde{\nu} \approx 300\text{cm}^{-1}$, but the heights of the background and smaller

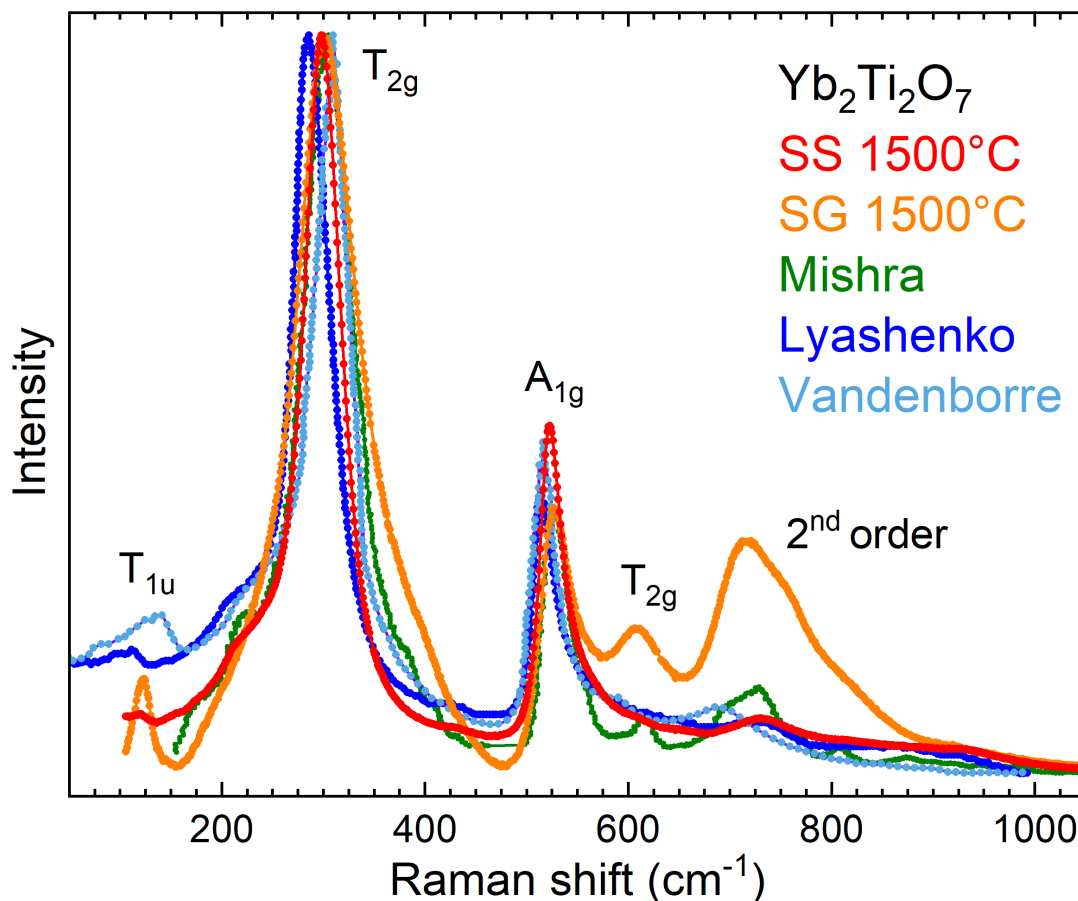


Figure 6.10 Raman spectra for the SS and SG $\text{Yb}_2\text{Ti}_2\text{O}_7$ samples compared with data from the literature [278, 282, 294].

peaks could be affected by a background subtraction that might have been performed by the authors without explicitly mentioning it.

In principle the Raman technique could be used to determine the structural transition from fluorite to pyrochlore but for our $\text{Yb}_2\text{Zr}_x\text{Ti}_{2-x}\text{O}_7$ samples it is rather difficult to differentiate the two phases, given that the local structure of the fluorite samples is closer to that of the pyrochlore phase than of the completely disordered defect fluorite. Figures 6.11 and 6.12 show the spectra of the $\text{Yb}_2\text{Zr}_x\text{Ti}_{2-x}\text{O}_7$ samples with $x = 0.5, 1.5$ sintered at 900°C , 1200°C and 1500°C . According to their Raman spectra all of these samples possess some local pyrochlore-type order, although according to x-ray diffraction the $x = 0.5$ (900°C) and all three $x = 1.5$ samples possess a fluorite structure. The most notable difference is the absence of the A_{1g} peak at $\tilde{\nu} \approx 520\text{cm}^{-1}$ for the fluorite samples. We propose to use the presence or absence of the A_{1g} peak as an indicator of whether the long-range structure is a pyrochlore or fluorite, respectively.

Figure 6.13 shows the spectra of the $\text{Yb}_2\text{Zr}_2\text{O}_7$ sintered at 900°C and 1500°C . XRD indicates that the sample sintered at 900°C possesses a fluorite structure, while the Raman spectrum shows similarities to the δ -phase spectrum of the sample sintered at 1500°C . Therefore it seems likely that the sample sintered at 900°C possesses some local order akin to that of the δ -phase, analogous to the local pyrochlore-type order present in the $x = 1.0, 1.5$ compounds of the $\text{Yb}_2\text{Zr}_x\text{Ti}_{2-x}\text{O}_7$ series. Unfortunately we did not measure the Raman spectrum of the

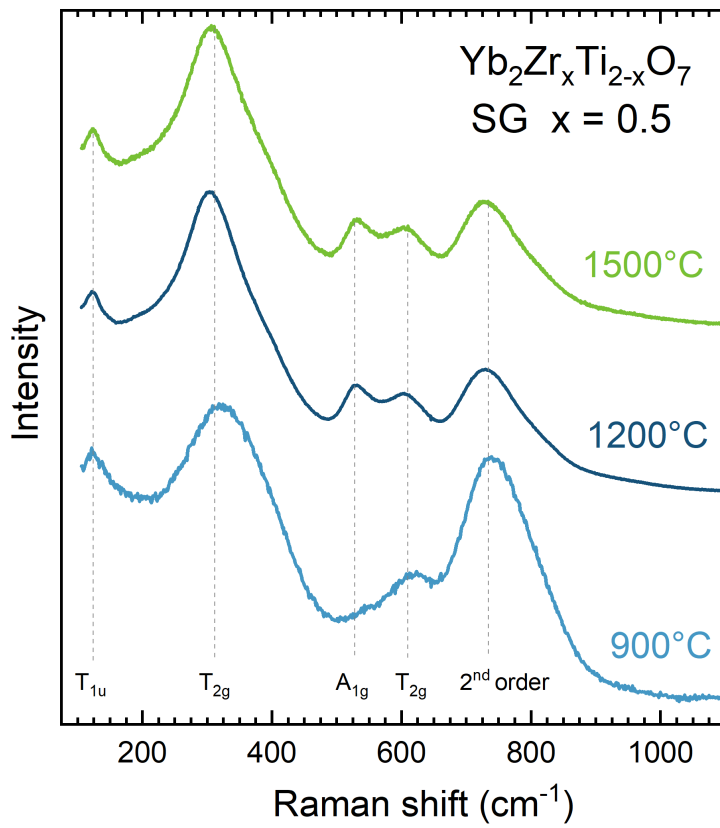


Figure 6.11 Raman spectra of the Yb₂Zr_xTi_{2-x}O₇ samples with x = 0.5.

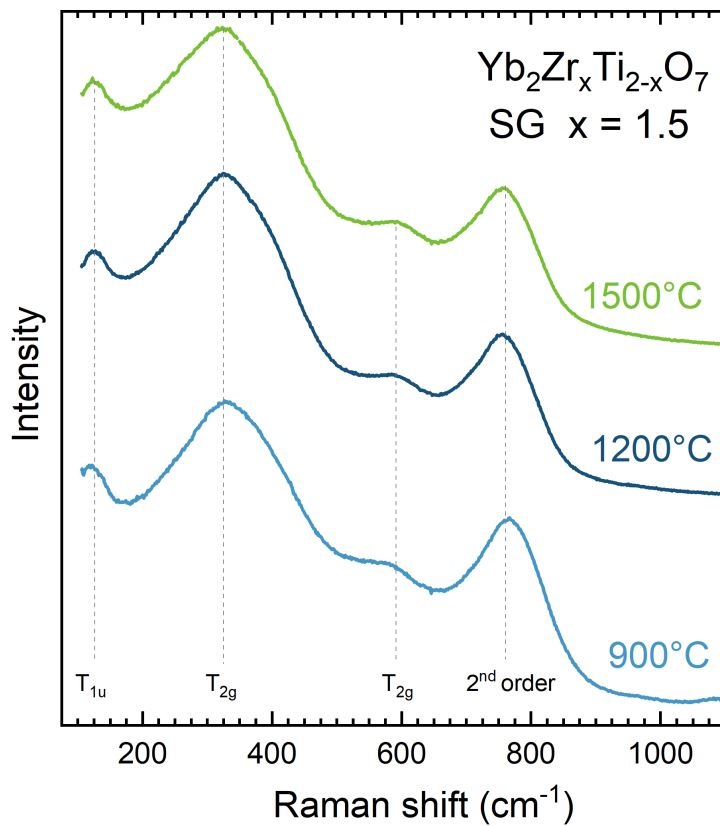


Figure 6.12 Raman spectra of the Yb₂Zr_xTi_{2-x}O₇ samples with x = 1.5.

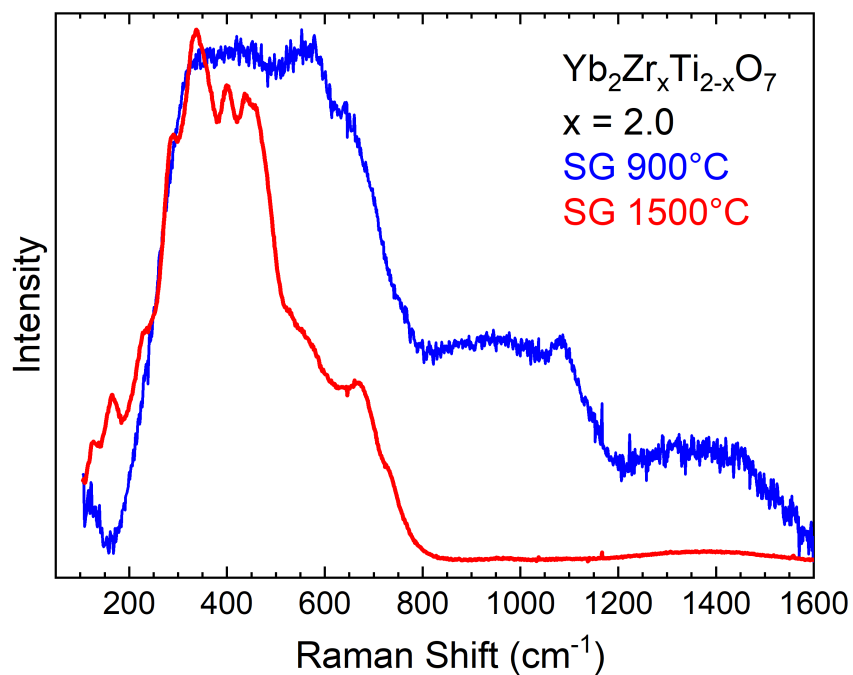


Figure 6.13 Raman spectra of the Yb₂Zr₂O₇ samples, sintered at 900°C and 1500°C.

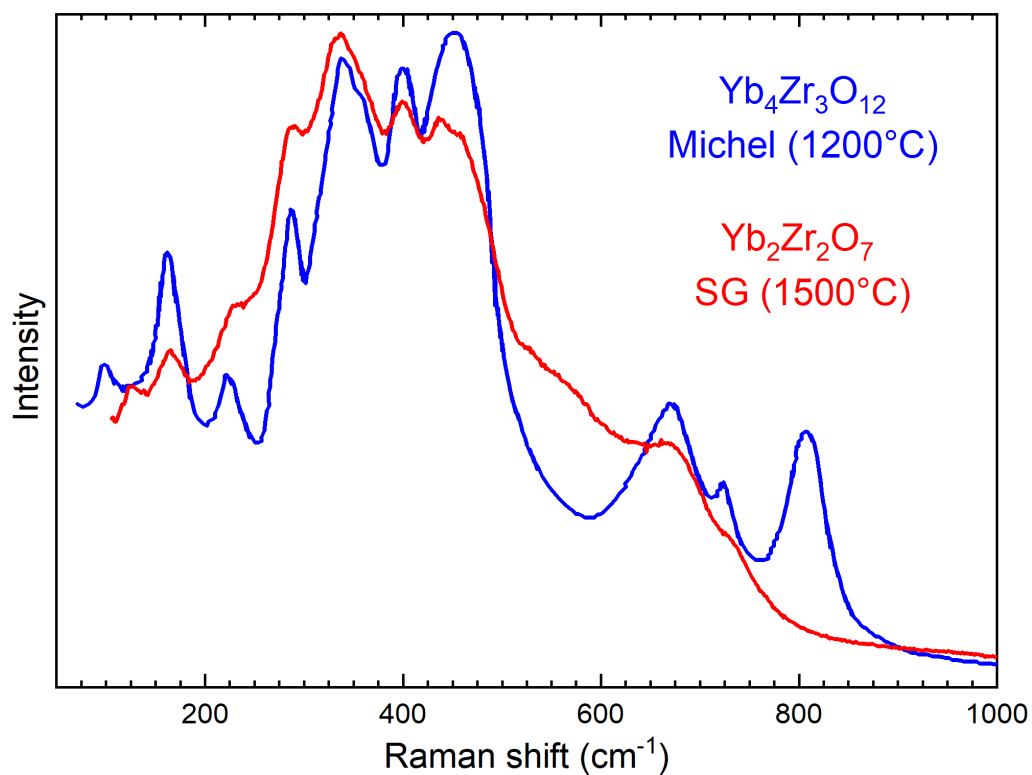


Figure 6.14 Raman spectrum for the Yb₂Zr₂O₇ sample compared with data for Yb₄Zr₃O₁₂ from the literature [281].

$\text{Yb}_2\text{Zr}_2\text{O}_7$ sample that was sintered at 1200°C.

Figure 6.14 shows the Raman spectrum for the $\text{Yb}_2\text{Zr}_2\text{O}_7$ sample compared with data for $\text{Yb}_4\text{Zr}_3\text{O}_{12}$ from the literature [281]. There are clear similarities between these spectra, in particular the peak positions seem to agree well although in the $\text{Yb}_2\text{Zr}_2\text{O}_7$ spectrum the peaks are not as well separated and somewhat broader than those of the $\text{Yb}_4\text{Zr}_3\text{O}_{12}$ spectrum.

The $\text{Yb}_4\text{Zr}_3\text{O}_{12}$ sample was sintered at 1200°C for a whole month, so that the crystal structure was likely better than that of our sample. In our sample the structure is that of a stuffed δ -phase, since the nominal stoichiometry of our sample is $\text{Yb}_2\text{Zr}_2\text{O}_7$ instead of $\text{Yb}_4\text{Zr}_3\text{O}_{12}$, as discussed in Section 5.6.3. It seems that the spectrum of the 900°C $\text{Yb}_2\text{Zr}_2\text{O}_7$ sample could be considered as a superposition of the broad featureless band characteristic of completely disordered fluorites with the sharper peaks corresponding to the δ -phase.

The intrinsic peak profile of a vibration in a solid is represented by a Lorentzian function [302], although this derivation is based on an idealized model of a solid and neglects several factors that can alter the experimental peak shape. In particular, instrumental contributions can often be modeled as Gaussian, so that the convolution of the intrinsic and instrumental profiles is a Voigt function (5.19), which can be approximated by a pseudo-Voigt function (5.22). A range of empirical peak shapes have been proposed for various applications where the peak shapes provide important information on the physical and chemical properties of the system [303, 304].

The area of a Raman peak is proportional to the number of units in the sample that are vibrating, while the height of the peak depends on the number of units vibrating at the median frequency. If the vibrating units in the solid are subjected to slightly different crystalline environments then their frequency distribution will broaden, diminishing the height of the peak while the area remains constant. Therefore the intensity of a mode is more appropriately captured by its area rather than its height. To extract the intensities it is necessary to deconvolute the spectrum into a superposition of individual peaks.

We performed deconvolutions of the Raman spectra with Fityk, an open-source software for nonlinear curve fitting that can be used to analyze data from techniques such as powder diffraction, chromatography, photoluminescence, photoelectron, infrared and Raman spectroscopies [305]. As an example, Figure 6.15 shows a deconvolution of the Raman spectrum for the SG $\text{Yb}_2\text{Ti}_2\text{O}_7$ sample sintered at 1200°C, and Table 6.8 lists the positions, widths and intensities of the fitted Lorentzian peaks.

When comparing peak fits of our Raman data using different fitting functions the peak centers are similar while some differences in the peak intensities arise. Since we do not require accurate values for peak intensities we restricted ourselves to using a Lorentzian profile, which proved to be a good approximation to the experimental peak shape. We tried using a pseudo-Voigt profile but due to the increased number of free parameters (including the Gaussian-Lorentzian mixing parameter) the fitting procedure proved to be very unstable, often diverging.

It is common practice to subtract a smooth background function from the experimental Raman spectra, similar to the background subtraction performed in Rietveld refinement of XRD patterns. The diffuse background of a Raman spectrum is due to instrumental noise and other sample related effects, including fluorescence and luminescence. These contributions are hard

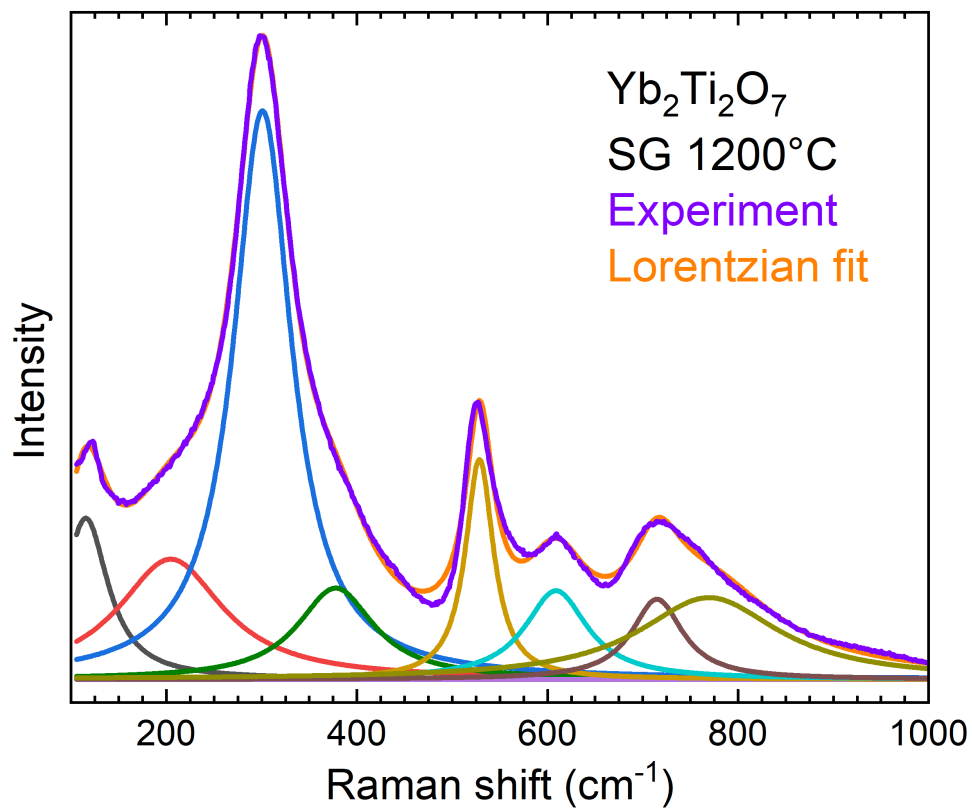


Figure 6.15 Deconvolution of the Raman spectrum for the SG Yb₂Ti₂O₇ sample sintered at 1200°C.

Position (cm ⁻¹)	FWHM (cm ⁻¹)	Area (%)
115	57	8.3
205	134	14.5
301	74	37.9
378	98	8.0
529	36	7.1
609	80	6.4
715	65	4.7
770	179	13.1

Table 6.8 Position, FWHM and percentual area of the Lorentzian peaks fitted to the Raman spectrum of the SG Yb₂Ti₂O₇ sample, sintered at 1200°C.

to estimate, so the subtraction of an arbitrary smooth background function is useful especially when the signal to noise ratio is poor and the relevant information is contained in the peak positions.

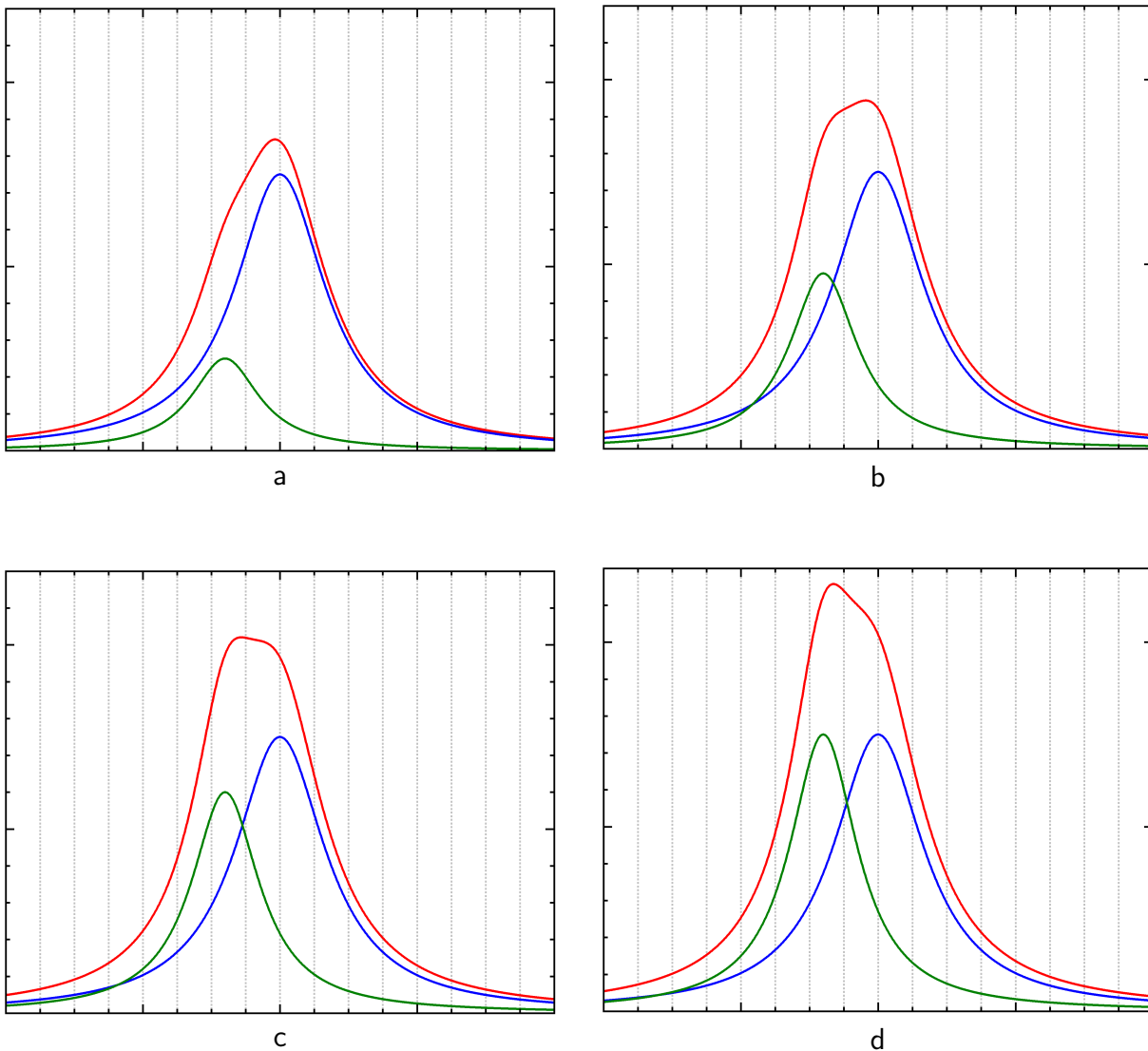


Figure 6.16 Examples of two highly overlapping peaks. The positions and widths of the peaks are fixed while the intensity of the leftmost peak increases from panel a to panel d.

In our work we tried subtracting a background polynomial of degree $\sim 2 - 7$ to facilitate comparison between different samples but this made the peak deconvolution procedure more difficult. Since the background is asymmetric with respect to peak center, the peak baseline is affected by the subtraction of the background curve and the symmetric Lorentzian peak profile cannot account for the asymmetry thus introduced. Due to this issue we only considered the raw spectra, without background subtraction.

Highly overlapping peaks can cause problems if the expected peak locations are not known, as illustrated in Figures 6.16 and 6.17. In Figure 6.16 the positions and widths of the peaks are fixed while the intensity of the leftmost peak increases from panel a to panel d. Since only the additive signal of the two unresolved peaks is observable this could be interpreted as a shift in peak position to lower frequency, even though both peaks have fixed positions and widths. In Figure 6.17 the leftmost peak remains fixed while the width of the large peak increases from

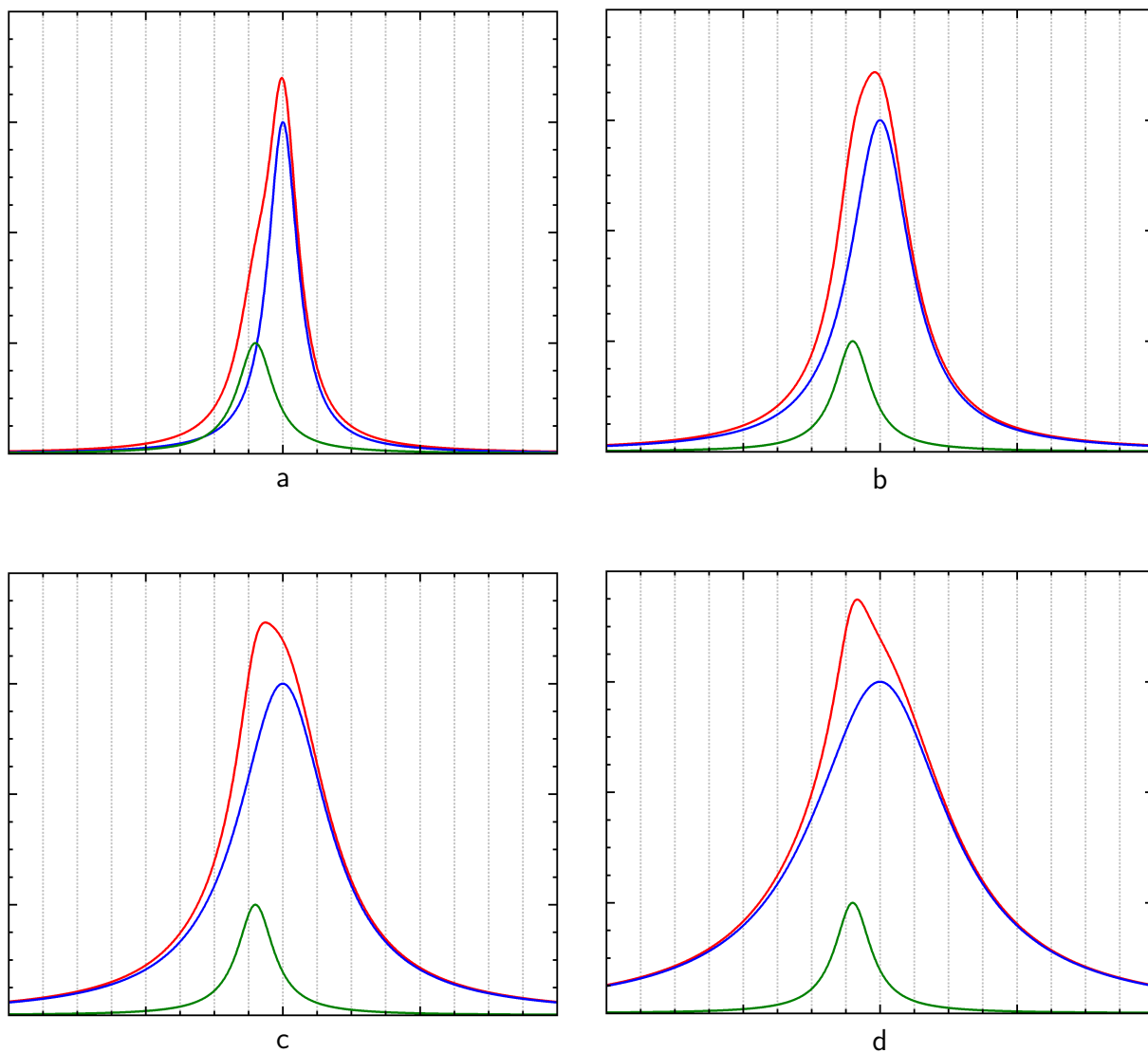


Figure 6.17 Examples of two highly overlapping peaks. The leftmost peak remains fixed while the width of the large peak increases from panel a to panel d.

panel a to panel d. The unintuitive appearance of the superposition could lead to a similar erroneous interpretation.

We performed deconvolutions of the spectra using anywhere from five to eleven peaks and predictably the fit improved with the number of peaks but the results were probably not physically significant. When using eight or more peaks we could obtain different equally good fits by changing the initial parameters (peak centers, intensities and widths), so that the results cannot be considered trustworthy without a consistent physical reason for expecting peaks at specific frequencies.

For instance, the location of the E_g peak, expected at $\tilde{\nu} \approx 330\text{cm}^{-1}$, varied significantly depending on the peak-fitting function and similarly the broad band at $\tilde{\nu} \approx 750\text{cm}^{-1}$ could not be reliably separated into its components since the number and shape of the assumed peaks unpredictably affected the results. Due to these kinds of issues we hesitate to trust the results of deconvolution and decided to use only the most intense, clearly visible peaks. Assuming that the peak asymmetry is low and peaks are not significantly overlapped, we may identify the peak positions with the frequency of the corresponding vibrational modes.

Figures 6.18 and 6.19 show the evolution of the Raman spectra with increasing x along the $\text{Yb}_2\text{Zr}_x\text{Ti}_{2-x}\text{O}_7$ series, for the samples sintered at 1200°C and 1500°C (we only measured the spectra for three of the samples sintered at 900°C , so we could not observe their evolution with x). Note that the A_{1g} peak disappears into the background for the $x = 1.0, 1.5$ samples, sintered at both 1200°C and 1500°C , which we interpret as a sign of long-range fluorite order. However, all of the samples that were classified as fluorites according to x-ray diffraction exhibit spectra that are much more similar to that of a pyrochlore phase than to the spectrum expected of a truly disordered fluorite, with a single very broad band. The local pyrochlore-type order only manifests itself as very weak diffuse scattering in the XRD pattern, as we saw in Section 5.6.2, but is apparent in the Raman spectra of the same samples.

The observed broadening of the pyrochlore Raman bands is likely indicative of defects and the associated stress in the crystal structure, so that the precise frequency of a vibrational mode in the ideal structure is spread out into a range of frequencies on account of the slightly different crystalline environments generated by the internal stresses and structural defects. For the fluorite samples the broadening of the pyrochlore-type bands could also be indicative of nanocrystalline domains, i.e. that the length over which the local pyrochlore correlations extend is very small, on the order 1nm, which is the size of one pyrochlore unit cell.

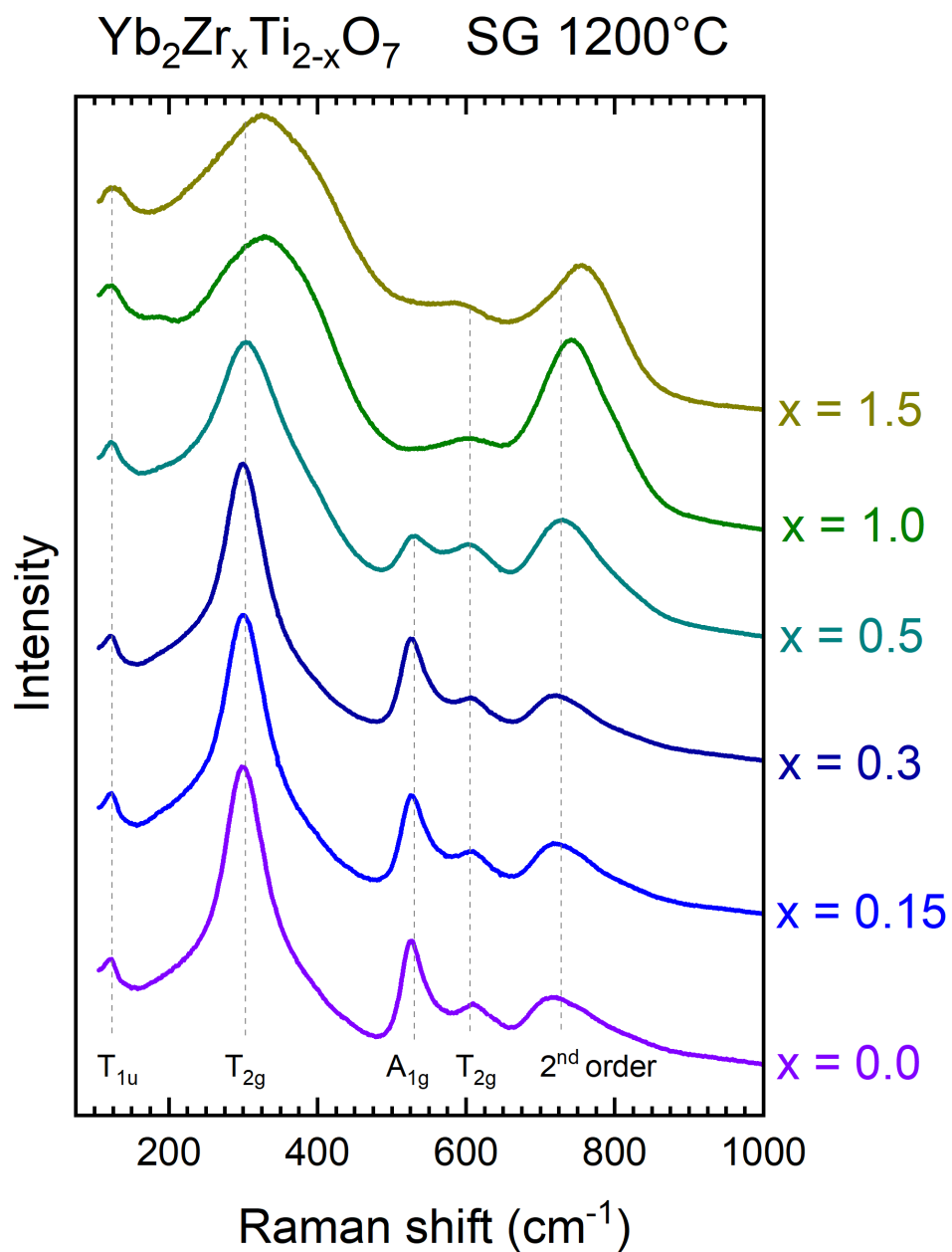


Figure 6.18 Raman spectra of the $\text{Yb}_2\text{Zr}_x\text{Ti}_{2-x}\text{O}_7$ samples sintered at 1200°C.

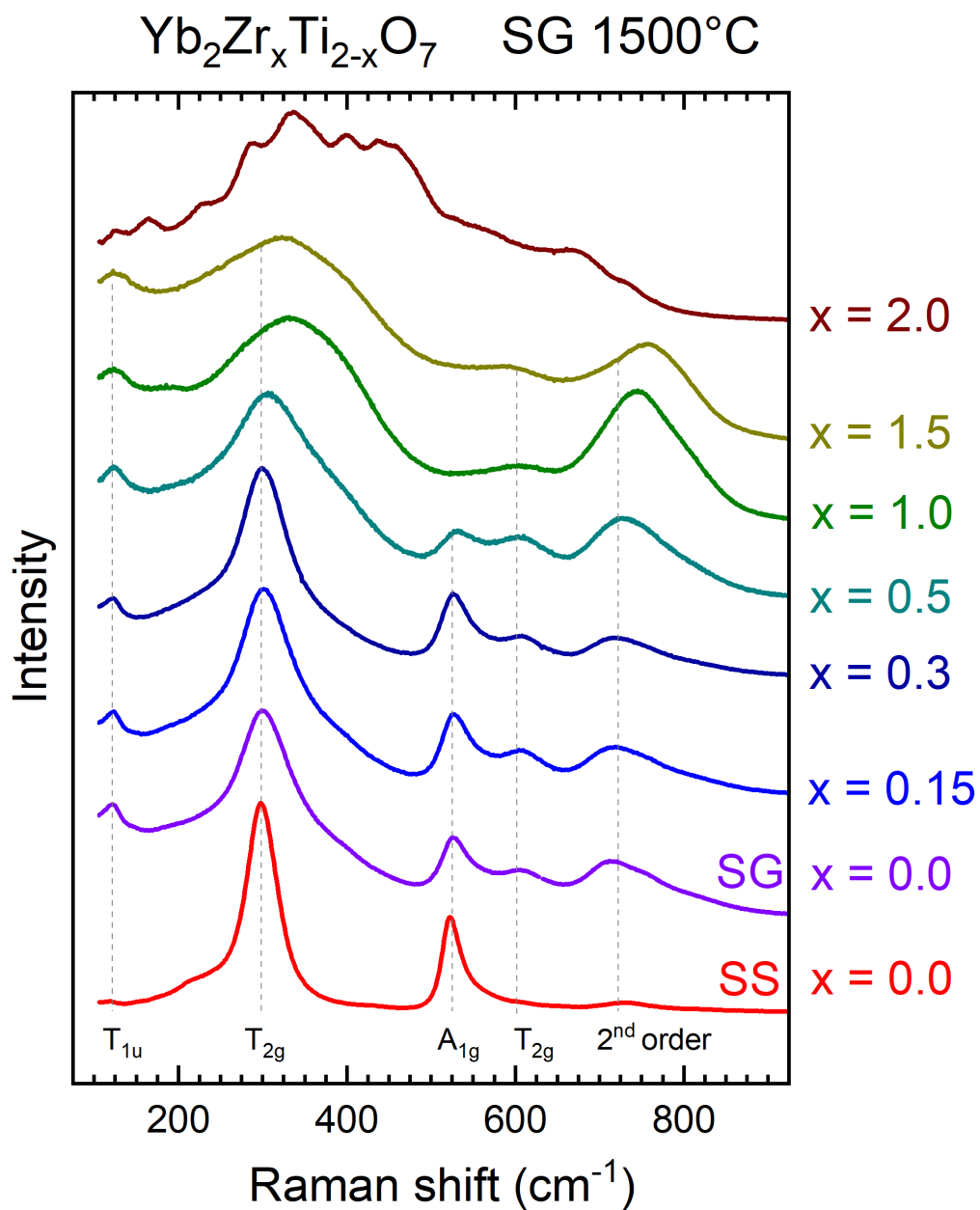


Figure 6.19 Raman spectra of the $\text{Yb}_2\text{Zr}_x\text{Ti}_{2-x}\text{O}_7$ samples and the SS $\text{Yb}_2\text{Ti}_2\text{O}_7$ sample, sintered at 1500°C.

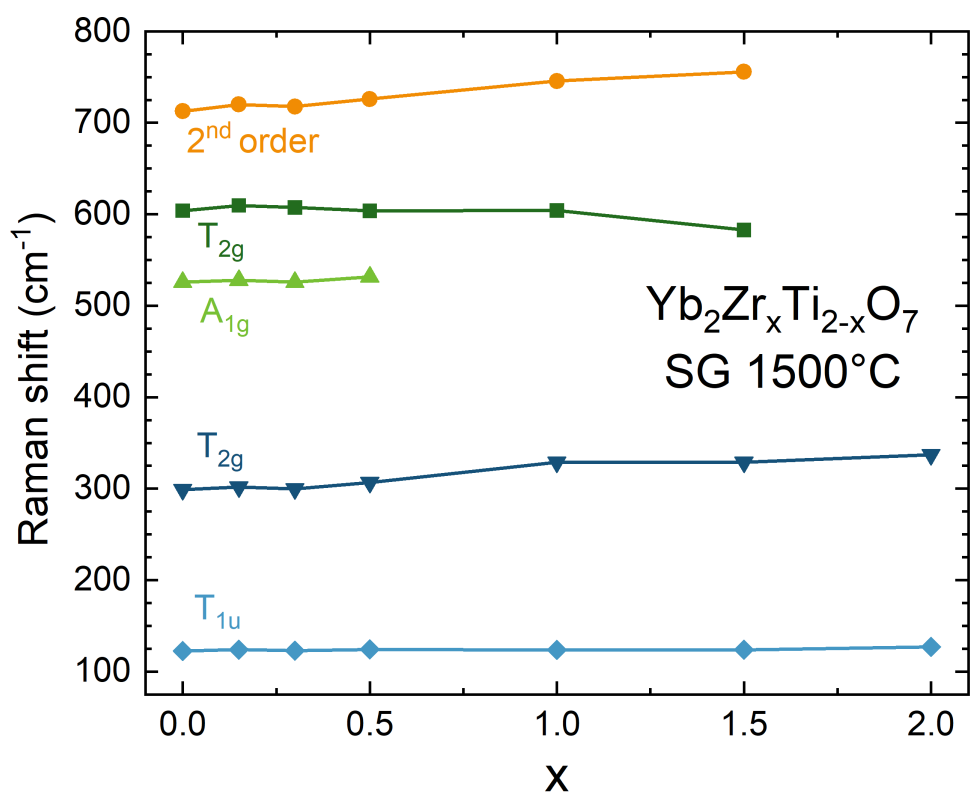


Figure 6.20 Frequencies of the strongest modes as a function of composition x for $\text{Yb}_2\text{Zr}_x\text{Ti}_{2-x}\text{O}_7$ samples, sintered at 1500°C .

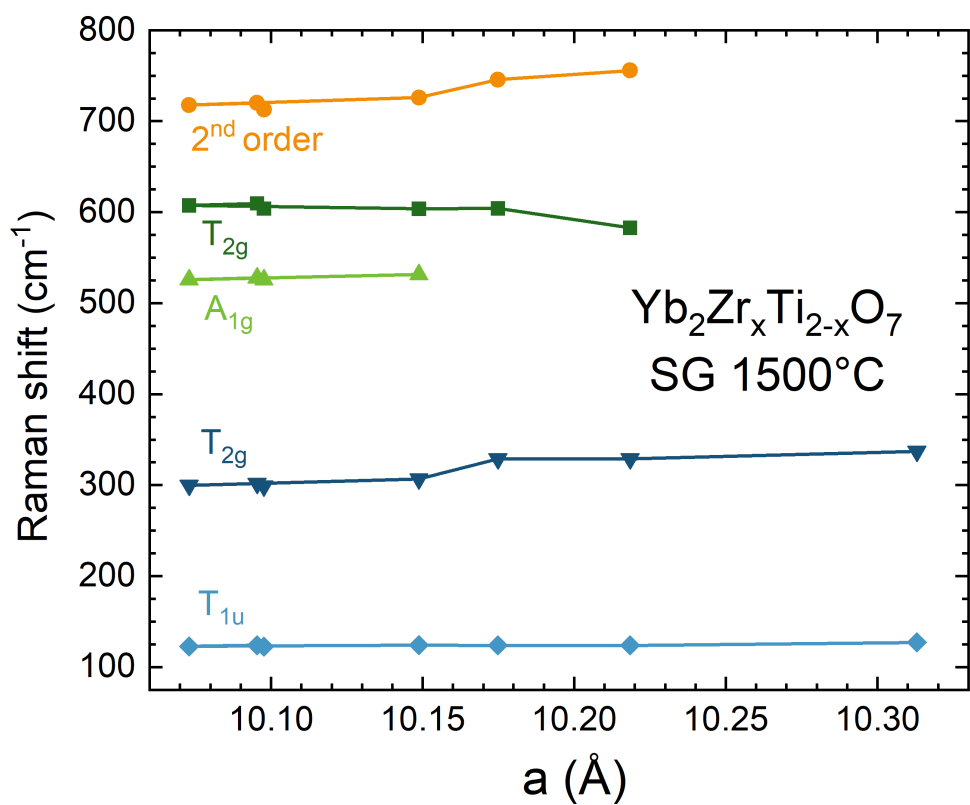


Figure 6.21 Frequencies of the strongest modes as a function of the lattice parameter a for $\text{Yb}_2\text{Zr}_x\text{Ti}_{2-x}\text{O}_7$ samples, sintered at 1500°C .

Figures 6.20 and 6.21 show the evolution of the peak positions with composition x and lattice parameter a . Changes in frequency of the vibrational modes are strongly correlated to changes in lattice parameter. An increase in average cation radius leads to an increase in lattice parameter, which implies larger bond distances and thus weaker bonds that have a lower vibrational frequency.

Comparing the frequencies of the Raman and infrared peaks along series of lanthanide pyrochlores such as the $A_2Ti_2O_7$ titanates, $A_2Sn_2O_7$ stannates, $A_2Zr_2O_7$ zirconates, $A_2Hf_2O_7$ hafnates, $A_2Pt_2O_7$ platinates and $A_2Ru_2O_7$ ruthenates, we can observe how the frequencies evolve with decreasing cation radius r_A , as the A site is occupied by increasingly heavier lanthanides. It is reported that the frequency of some peaks increase almost linearly with decreasing r_A , while those of others remain almost constant along the series [31].

In the $A_2B_2O_7$ pyrochlore structure the B–O bond is on average significantly shorter than the A–O bond, so that the vibrational modes involving the B–O bond have higher frequencies than those involving the A–O bonds. Similarly, the vibrations involving A–O' appear at higher frequency than the corresponding modes involving A–O since the A–O' bonds are shorter than the A–O bonds. The A cations occupy the large vacancies between BO_6 octahedra, so they do not directly contribute to the cohesion of the lattice as much as the B cations.

It is argued that when decreasing r_A the A–O and A–O' bonds are significantly affected while the B–O bonds, which are already relatively short and strong, are less affected. This would imply that the frequencies of the vibrational modes involving the A ion are the ones that show an approximately linear increase while those involving B remain almost constant. In general this seems to be the case but there are some exceptions that cannot be explained by this simple argument, probably due to interactions between the vibrations involving the $AO_6O'_2$ and BO_6 oxygen coordination polyhedra. The evolution of the bending modes involving three ions is more difficult to interpret than the stretching modes involving only two ions, since the bending modes are less rigidly constrained by the local geometry.

In the $Yb_2Zr_xTi_{2-x}O_7$ series the B cation is changing, so that we could compare the peak frequencies with either the average r_B radius or the lattice parameter a . The results should be similar, given that r_B and a are in an approximately linear relationship (see Figure 5.37, recalling that $r_B \propto x$) and indeed Figures 6.20 and 6.21 are very similar. Considering only the increase in average cation radius r_B we should expect a decrease in frequencies of the vibrational modes due to the increase in lattice parameter and average B–O distance, in direct proportion to the amount of Zr.

A more realistic model, considering that there is a disordered mixture of Zr on Ti at a single crystallographic site, predicts that the B cation modes should split into two bands due to the somewhat weaker, more flexible Zr–O bonds when compared to the shorter, more rigid Ti–O bonds. In practice this splitting might be too small to be observable, given that the bands in the experimental spectra are already rather broad so the resolution is very limited.

Table 6.9 lists the bond distances and angles extracted from Rietveld refinement for the SG $Yb_2Ti_2O_7$ sample. Note that the Yb–O' bonds are shorter than the Yb–O bonds, since the $YbO_6O'_2$ cube is compressed along the O'–Yb–O' cube diagonal, as described in Section 2.2.3. The Ti–O bond is even shorter due to the strong hybridization of the Ti 3d orbitals with the O 2p orbitals.

Bond	Distance (Å)	Bond	Angle (°)
Yb–Yb	3.5691	O'–Yb–O'	180.000
Yb–Ti	3.5691	O–Yb–O	116.247
Ti–Ti	3.5691	O–Yb–O'	101.316
Yb–O	2.4569	O–Yb–O'	78.684
Yb–O'	2.1856	O–Yb–O	63.753
Ti–O	1.9703	O–Ti–O	180.000
		O–Ti–O	97.625
		O–Ti–O	82.375
		Ti–O–Ti	129.848
		Yb–O'–Yb	109.471
		Yb–O–Yb	93.162
		Yb–O–Ti	106.936

Table 6.9 Bond distances and angles extracted from Rietveld refinement for the SG Yb₂Ti₂O₇ sample.

Although bond distances and the corresponding force constants are correlated, there is no simple relationship between these values, so that it is not possible to determine how the vibrational frequencies depend on bond distances and angles without considering in detail the interatomic potentials. We should also note that the bond distances and angles obtained from diffraction studies represent the average positions of the atoms, which might not equal the values for the local structure as probed by Raman spectroscopy.

Similar results to those in Table 6.9 were extracted from the Rietveld refinements for the other samples, but we did not discover any clear correlation of bond lengths/angles to the changes in frequency of the Raman modes. Ideally we would consider not only the peak positions, but also their intensities and widths, which can provide additional structural information. However, the non-robustness of the spectral deconvolutions did not allow for such considerations to be made reliably.

Raman spectroscopy is certainly a powerful technique for obtaining information on the local structure of solid materials, but there remain many open questions concerning the interpretation of the spectra we collected, especially for the more disordered structures. Further studies using atomistic simulations seem to be necessary to definitively understand how the local structure of the Yb₂Zr_xTi_{2-x}O₇ compounds is related to their Raman spectra.

In the future, we want to create a model for the local structure of these compounds, based on the results of x-ray diffraction. By adjusting the parameters of the model until a good fit to the experimental spectrum is achieved, we will be able to reliably infer local structural parameters such as bond lengths, angles and force constants. Combining these results with those obtained using other techniques that probe the local order, such as PDF and EXAFS (see Section 8.2), will consolidate our understanding of the partially disordered structures of the Yb₂Zr_xTi_{2-x}O₇ compounds.

Magnetic Properties

We measured the magnetic moment of $\text{Yb}_2\text{Zr}_x\text{Ti}_{2-x}\text{O}_7$ samples in the paramagnetic phase (at 1.2K, magnetic field up to 14.5T) and the zero-field AC susceptibility down to 60mK. In this chapter we describe the experimental setup and results of those measurements. The information on cryogenic techniques and low-temperature physics is based on [306, 307, 308, 309, 310].

7.1 Experimental Setup

7.1.1 Lock-in amplifier

A lock-in amplifier (LIA) can be used to measure small AC signals, even when obscured by noise that is orders of magnitude more intense [311, 312, 313]. It may be necessary to pre-amplify a small signal before entering the LIA, which can introduce additional noise to the experimental signal. The LIA selects a very narrow frequency band, so if the signal has a known frequency it is possible to single out a weak signal from the broad-spectrum noise. The dynamic reserve of a LIA can be up to 100dB, meaning that it is possible to detect a signal flooded by noise that is up to 5 orders of magnitude greater.

To select a unique frequency the LIA requires a reference signal at that frequency, which can be externally supplied or generated by the LIA itself. Typically, an experiment is excited at a fixed frequency and the exciting signal is passed along as reference to the LIA. We describe a simplified workings of a LIA, schematically depicted in Figure 7.1.

Suppose the LIA's input signal is a voltage $V_s \cos(\omega_s t + \phi_s)$ and the reference signal is $V_r \cos(\omega_r t + \phi_r)$. These analog inputs are converted to digital signals by an analog-digital converter (in the past LIAs were analog but most of these have been replaced by digital ones)

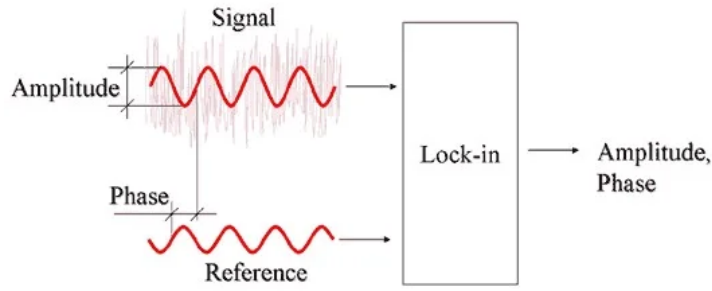


Figure 7.1 Schematic representation of a LIA [314].

and then a mixer multiplies them to get

$$\begin{aligned}
 V_{sr} &= V_s \cos[\omega_s t + \phi_s] \cdot V_r \cos[\omega_r t + \phi_r] \\
 &= \frac{1}{2} V_s V_r \left\{ \cos [(\omega_s - \omega_r)t + (\phi_s - \phi_r)] + \cos [(\omega_s + \omega_r)t + (\phi_s + \phi_r)] \right\} \quad (7.1)
 \end{aligned}$$

The combined signal V_{sr} goes through a low-pass filter, which filters out any AC signal and selects the DC component of V_{sr} . In general $\omega_s \neq \omega_r$ so there is no DC component and the output of the low-pass filter is zero. Only when $\omega_s = \omega_r$ do we get a non-zero output V_{out} :

$$V_{out} = \frac{1}{2} V_s V_r \cos(\phi_s - \phi_r) \quad (7.2)$$

A real low-pass filter has a finite bandwidth and roll-off so that any sufficiently low-frequency component ($\omega_s \approx \omega_r$) can get through the low-pass filter, but usually this is not a significant concern. The extraction of information encoded in a carrier wave with known frequency is essentially the same as in homodyne detection, a wide-spread technique in electrical engineering and other areas of science.

By varying the phase ϕ_r of the reference signal we can modulate the output voltage (7.2). A dual-phase LIA has two reference channels with a quarter-cycle phase difference so that

$$\begin{aligned}
 V_{out,1} &= \frac{1}{2} V_s V_r \cos(\phi_s - \phi_r) \\
 V_{out,2} &= \frac{1}{2} V_s V_r \cos\left(\phi_s - \phi_r - \frac{\pi}{2}\right) \\
 &= \frac{1}{2} V_s V_r \sin(\phi_s - \phi_r) \quad (7.3)
 \end{aligned}$$



Figure 7.2 Front panel of an SR830 LIA.

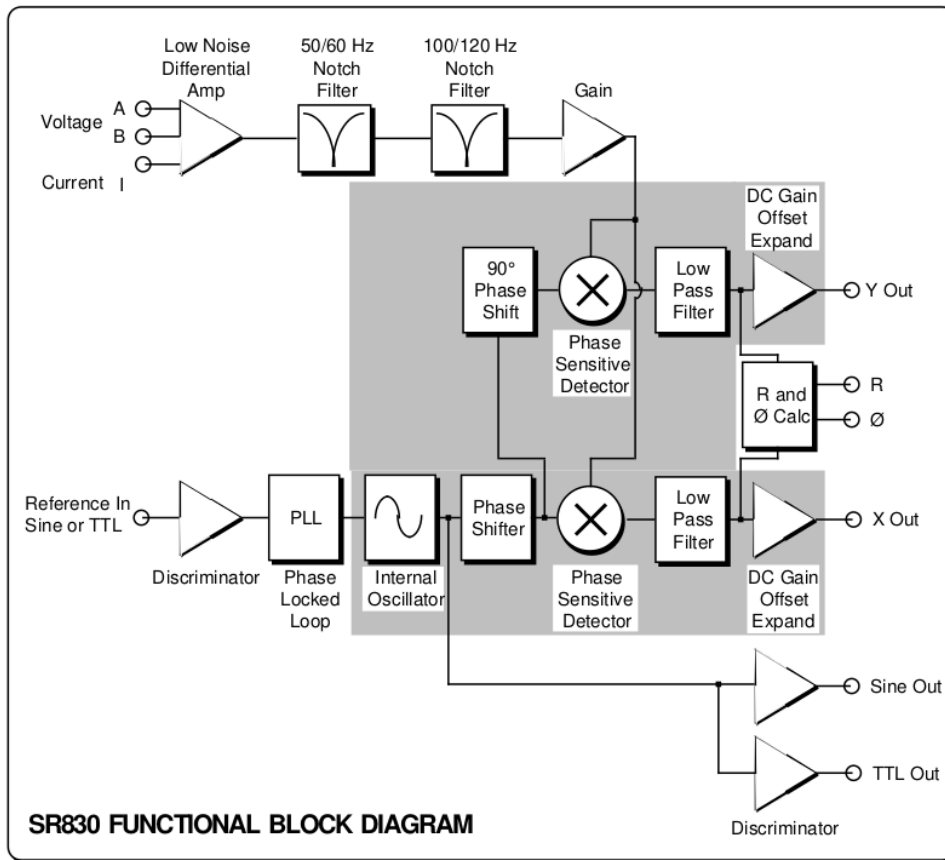


Figure 7.3 Block diagram of the components inside an SR830 LIA [315].

We define a normalized version of $V_{\text{out},1}$ and $V_{\text{out},2}$ as

$$\begin{aligned} V_x &= \frac{V_{\text{out},1}}{\frac{1}{2}V_r} = V_s \cos(\phi_s - \phi_r) \\ V_y &= \frac{V_{\text{out},2}}{\frac{1}{2}V_r} = V_s \sin(\phi_s - \phi_r) \end{aligned} \quad (7.4)$$

so that

$$\begin{aligned} V_s &= \sqrt{V_x^2 + V_y^2} \\ \phi_s &= \arctan\left(\frac{V_y}{V_x}\right) \end{aligned} \quad (7.5)$$

The front panel of a LIA displays V_x , V_y , ϕ_r and allows us to vary the reference phase ϕ_r , as depicted in Figure 7.2. V_x , V_y are rms voltage values and ϕ_r is in degrees. By varying ϕ_r we can shift the signal to the x-channel ($\phi_r = \phi_s$) or to the y-channel ($\phi_r = \phi_s - \frac{\pi}{2}$). Many LIAs have an auto-phase function that automatically adjusts the reference phase shift such that the signal phase is 0. In our measurements we set the phase at the calibration step, using the auto-phase function, and kept it constant throughout the series of measurements, almost all at the same frequency (155Hz). The phase can depend on the signal frequency, and we observed a small but non-zero phase while measuring one of the samples at a higher frequency (2.5kHz instead of 155Hz).

Figure 7.3 shows the more intricate block diagram of the components inside a real SR830 LIA, although the basic functionality is the same as for the simplified model described above.

7.1.2 Susceptometer

The susceptometer that was used to measure the AC magnetic susceptibility is composed of a pair of coils, the outermost primary coil and a pair of inner secondary coils, as shown in Figure 7.4 [316, 317, 318]. During operation an alternating electrical current passes through the primary coil, oscillating sinusoidally with a fixed frequency that can be tuned from $f \approx 10\text{Hz} - 10\text{kHz}$, but in our measurements was set at the fixed value of $f = 155\text{Hz}$. This current generates a magnetic field in the interior of the primary coil, which acts on the set of secondary coils. The oscillating magnetic flux through the secondary coils generates a current, according to Faraday's law of induction [92]. The current in the secondary has the same frequency as the driving current in the primary but is phase delayed by $\frac{\pi}{2}$.

There are two secondary coils, the sample coil that is filled with a sample capsule, and the reference coil that remains empty. Both are identical and positioned symmetrically inside the primary coil, so that the field generated by the primary is the same at both positions. However the secondary coils are wound in opposite directions, so that when the sample coil is empty the inductive signal generated in one coil is exactly canceled by the current generated in the other coil.

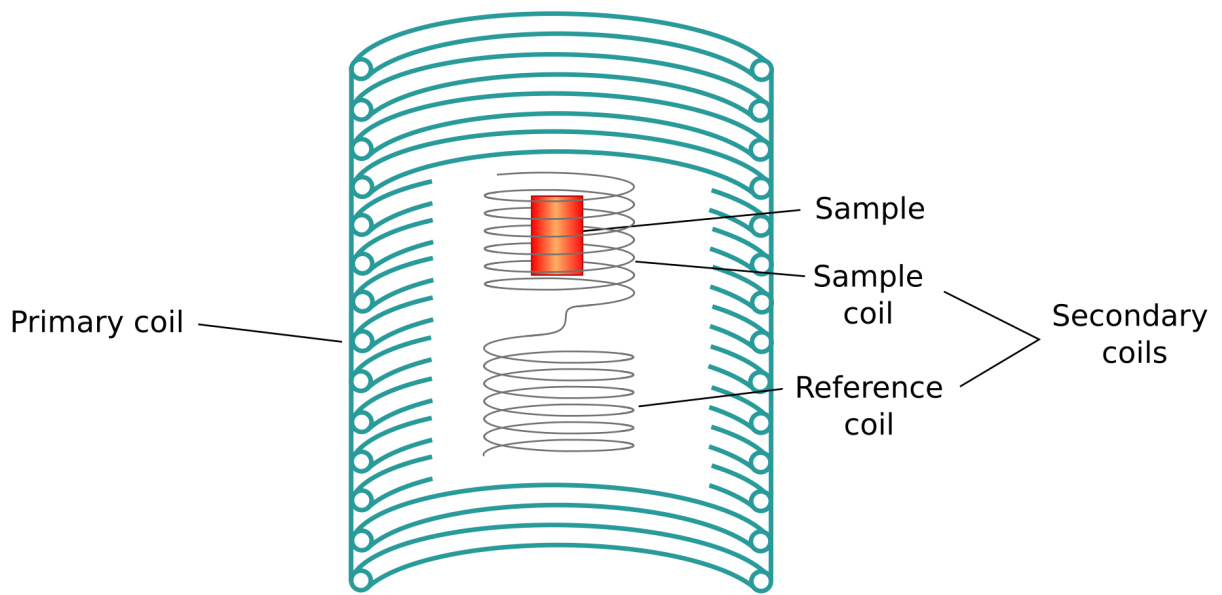


Figure 7.4 Susceptometer, composed of a primary coil and a pair of counterwound secondary coils.



Figure 7.5 Two cryostats in our laboratory, containing the susceptometer (left) and VSM (right).

When a sample is positioned inside the sample coil the magnetic field generated by the current in the primary induces a magnetization of the sample, which thereby generates a magnetic field of its own. The sample's magnetization creates an additional oscillating flux through the sample coil which does not act on the reference coil. In this way the balancing of the flux through the sample and reference coils is broken and the current passing through the secondary coil is directly proportional to the sample's magnetization.

A mutual inductance bridge is a component of many AC susceptometers [319, 320, 321, 322]. A variable inductance compensates the electromotive force (emf) induced in the secondary coil, and its inductance is adjusted until the bridge is balanced. The value of the inductance is proportional to the emf in the secondary, and thus also proportional to the magnetization of the sample.

A small quantity of sample powder was fitted inside a plastic capsule and mounted on the end of an insert that is lowered into a cryostat, shown in Figure 7.5. The cryostat is filled with liquid helium to keep the temperature in the interior at about 4.2K, the liquid's boiling point. Immersed in the liquid helium bath there is a dewar that contains the susceptometer coils described above. This dewar stays in contact with the helium bath until thermal equilibrium sets in and is then sealed off from its surroundings. Then a vacuum pump is connected to the dewar to continually pump the volume above the liquid helium remaining in the dewar. This cools the liquid inside the dewar by removing the more energetic helium atoms that go from the liquid into the gas phase. In this way the temperature of the sample can be reduced to $T \approx 1.1\text{K}$.

When all of the liquid helium (^4He) in the dewar has evaporated it is connected to a container filled with ^3He , the lighter isotope of helium. ^3He is very rare and expensive, so great care must be taken not to lose it or contaminate it with common ^4He . The process is similar to that performed with ^4He : the ^3He is cooled and allowed to condense around the sample, then it is pumped to reduce the temperature, allowing us to reach $T \approx 0.6\text{K}$.

To calibrate the susceptometer we used a crystalline sample of ammonium iron(III) sulfate dodecahydrate, $(\text{NH}_4)\text{Fe}(\text{SO}_4)_2(\text{H}_2\text{O})_{12}$, also known as ferric ammonium sulfate (not to be confused with ferrous ammonium sulfate, or ammonium iron(II) sulfate). This substance is an almost ideal paramagnet since the magnetic Fe^{3+} ions are well separated and thus interact very weakly. After scraping the surface of a piece of crystal to remove any layers of material that could have reacted with the atmosphere, the mass of the sample was measured with high precision.

Knowing the mass of the calibration sample we calculated the expected magnitude of its susceptibility and compared this with the measured inductance value (that equilibrates the inductance bridge) to get a constant calibration factor. When measuring other samples, multiplying the inductance by the previously obtained calibration factor yields the absolute magnetic susceptibility.

The calculated molar Curie constant C_m (3.24) for ferric ammonium sulfate is

$$\begin{aligned} C_m &= \frac{N_A \mu_0 g^2 J(J+1) \mu_B^2}{3k_B} \\ &= 5.502 \cdot 10^{-5} \text{ K m}^3 \text{ mol}^{-1} \\ &= 4.378 \text{ K emu mol}^{-1} \end{aligned} \quad (7.6)$$

so that (3.26) holds,

$$\chi_m = \frac{C_m}{T - \theta_{CW}} \quad (7.7)$$

with $\theta_{CW} \approx 0$, since this substance is an almost ideal paramagnet. The SI unit for susceptibility, $\text{m}^3 \text{ mol}^{-1}$, and the electromagnetic cgs unit of susceptibility, emu mol^{-1} , are related through [90]

$$1 \text{ emu mol}^{-1} = 4\pi \cdot 10^{-6} \text{ m}^3 \text{ mol}^{-1} \quad (7.8)$$

To calibrate the susceptometer we compared the background subtracted output $L - L_0$ of the inductance bridge to (7.7) and extracted a sample-independent constant γ such that

$$\chi = \gamma(L - L_0) \quad (7.9)$$

To this end we fit a line to $(L - L_0)^{-1}$ (Figure 7.6),

$$(L - L_0)^{-1} = \alpha T + \beta \quad (7.10)$$

and use α, β to obtain the calibration constant γ and the Curie-Weiss temperature θ_{CW} ,

$$\begin{aligned} \gamma &= \alpha n_{\text{mol}} C_m \\ \theta_{CW} &= -\beta/\alpha \end{aligned} \quad (7.11)$$

where n_{mol} is the number of moles in our calibration sample. θ_{CW} turns out to be -174mK, confirming that ferric ammonium sulfate is a good approximation of an ideal paramagnet for $T > 1\text{K}$.

We compared the calibration data from the susceptometer with data previously measured by a SQUID susceptometer. The agreement is reasonable, as shown in Figure 7.7.

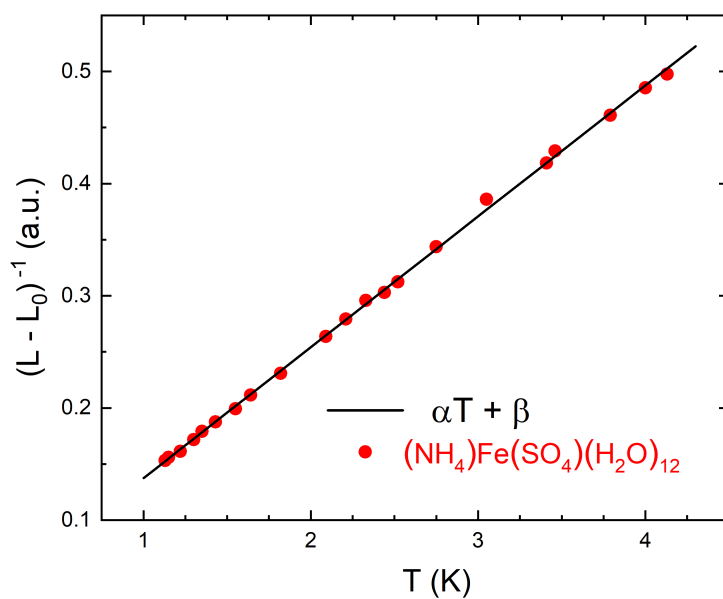


Figure 7.6 Linear fit of the inverse of the susceptometer's background subtracted output signal $(V - V_0)^{-1}$.

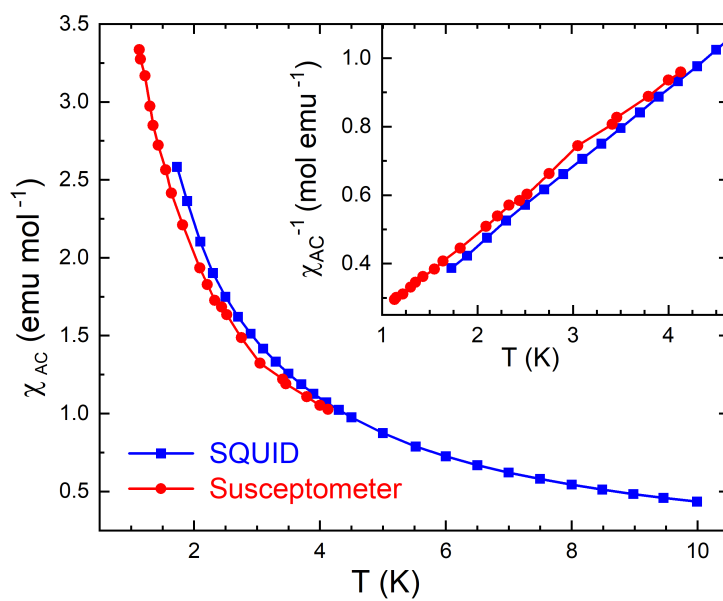


Figure 7.7 Comparison of susceptibility data of ferric ammonium sulfate for the susceptometer and a Quantum Design SQUID.

Fitting the inverse susceptibility of the SQUID data to a line we get

$$\begin{aligned}
 C_m(\text{SQUID}) &= 5.431 \cdot 10^{-5} \text{ K m}^3 \text{ mol}^{-1} \\
 &= 4.322 \text{ K emu mol}^{-1} \\
 \theta_{CW}(\text{SQUID}) &= 52 \text{ mK}
 \end{aligned}
 \tag{7.12}$$

The Curie constant C_m agrees with the calibrated susceptometer's C_m within 1.3%. The Curie-Weiss temperatures do not agree and even differ in sign, but both are acceptably small when considering the susceptibility above 1K. Any calibration errors that lead to a multiplicative factor in C_m will affect the calculated effective moments μ_{eff} but will not change the values of θ_{CW} , since the x-intercept of the inverse susceptibility is not changed by a multiplicative factor in C_m .

7.1.3 Vibrating Sample Magnetometer

The operating principle of the vibrating sample magnetometer (VSM) is also Faraday's law of induction, as for the susceptometer, but instead of a primary coil, the VSM employs a moving sample [323, 324, 325, 326, 327]. If a sample with nonzero magnetization moves through the pickup coil then the variation in magnetic flux produces an emf in the coil. The sample is set in motion by a vibration head similar to an acoustic speaker, driving the sample periodically at a certain frequency, which we set to 157Hz for our measurements. The magnetic field applied to the sample is generated by a large set of superconducting coils that surround the region containing the pick-up coils and sample. In our setup the magnetic field produced by the superconducting coil can reach up to $B \approx 18\text{T}$.

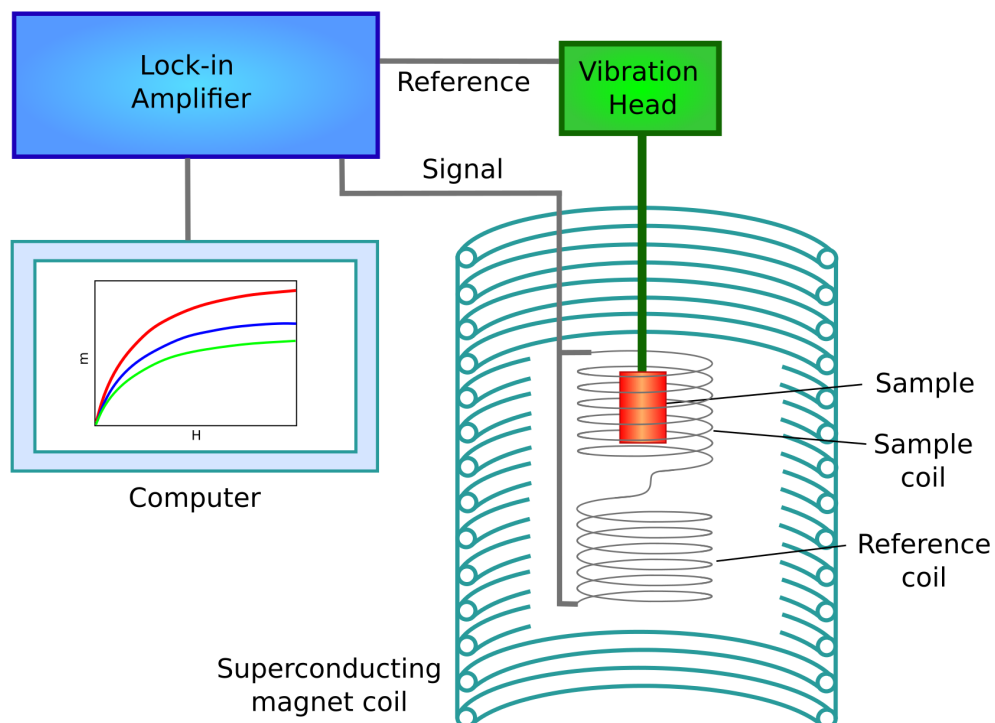


Figure 7.8 Schematics of a vibrating sample magnetometer.

The signal produced in the pickup coil is fed into the LIA and correlated with the driving current that generates the vibration of the sample insert. The amplitude of the synchronous signal is then directly proportional to the magnetization. The schematics of a VSM are represented in Figure 7.8. In our setup the electromagnet is replaced by a superconducting coil, but the operating principle is the same.

To calibrate the VSM we used a the same crystalline sample of ammonium iron sulfate dodecahydrate used to calibrate the susceptometer. We measured the magnetic moment of this sample at 4.14K and magnetic field up to 6T. The phase of the lock-in amplifier was set at 94.78° to maximize the in-phase component of the locked-in signal. Knowing the precise mass of the sample we calculated the expected magnitude of the magnetic moment and compare this with the LIA's output V_{out} to get a constant calibration factor. Multiplying V_{out} (while measuring other samples) by the previously obtained calibration factor yields the absolute magnetic moment.

The magnetic moments in ferric ammonium sulfate are Fe^{3+} ions that have a ground state with $L = 0$, $S = \frac{5}{2}$ and $J = \frac{5}{2}$, according to Hund's rules for a $3d^5$ shell configuration [91]. We performed a non-linear fit of V_{out} to the function

$$V_{\text{out}} = a [6\coth(6bH) - \coth(bH)] \quad (7.13)$$

which is the Brillouin function (3.11) for $J = \frac{5}{2}$ and $g = 2$, as shown in Figure 7.9.

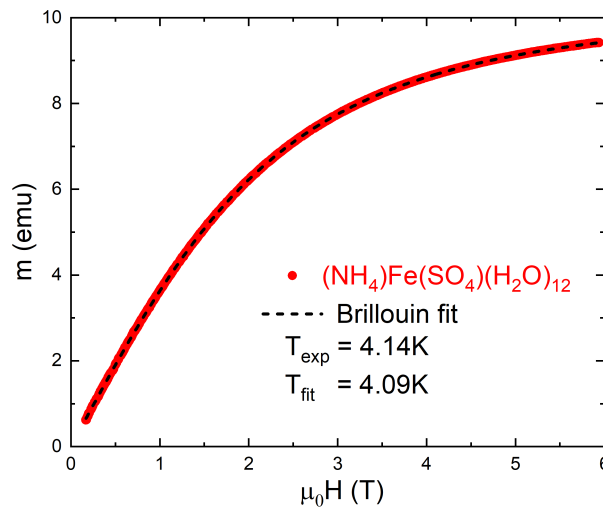


Figure 7.9 Magnetic moment of ferric ammonium sulfate crystal and fitted Brillouin function.

From the fitting constant b we calculate the best-fitting temperature

$$T_{\text{fit}} = \frac{\mu_B}{k_B b} = 4.09\text{K} \quad (7.14)$$

which is very close to the nominal temperature $T_{\text{exp}} = 4.14\text{K}$ measured by the Cernox temperature sensor close to the sample. Comparing the value of the fitting constant a to the expected

magnetic moment calculated from (3.8) we get a sample-independent calibration constant c :

$$c = \frac{n\mu_B}{a} \quad (7.15)$$

where n is the number of magnetic ions in the sample, calculated using the sample mass and molar mass of the compound. Multiplying by c we get the absolute magnetic moment m from the LIA's output signal V_{out} ,

$$m = c V_{\text{out}} \quad (7.16)$$

To confirm the calibration we can plot the magnetic moment per Fe^{3+} ion and check that it saturates at $m_{\text{sat}} = gJ\mu_B = 5\mu_B$, as shown in Figure 7.10.

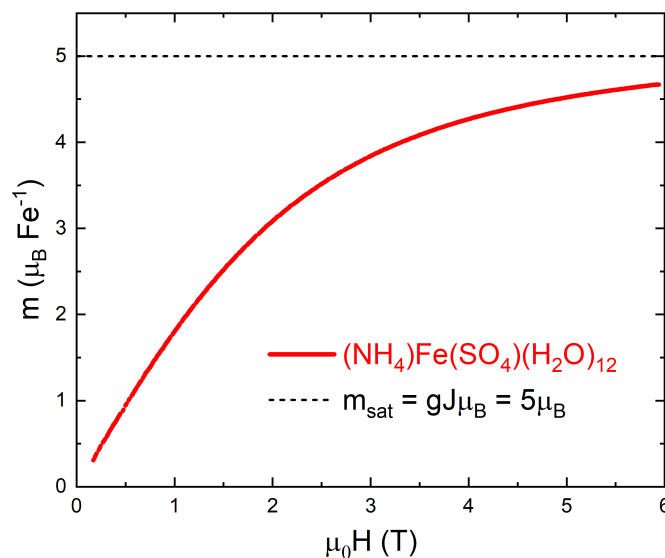


Figure 7.10 Magnetic moment per magnetic ion of ferric ammonium sulfate and the expected saturation level for Fe^{3+} ions.

7.1.4 Adiabatic Demagnetization

An adiabatic demagnetization refrigerator (ADR) uses the magnetocaloric effect to produce cooling [306, 308, 309, 310]. The basic operation of the system is shown in Figure 7.11. It relies on a paramagnetic salt, a substance with magnetic moments so dilute that they barely interact, constituting a good approximation of an ideal paramagnet. The paramagnetic salt is in contact to the sample supposed to be cooled and both are connected to the environment by a heat switch that allows heat conduction only when it is closed.

The cooling cycle works as follows:

1. The switch is closed and the system is in equilibrium with its environment, at a constant temperature.
2. A magnetic field is applied to the paramagnetic salt, generating heat since the entropy of the magnetic moments is reduced when they are all aligned by the applied field.

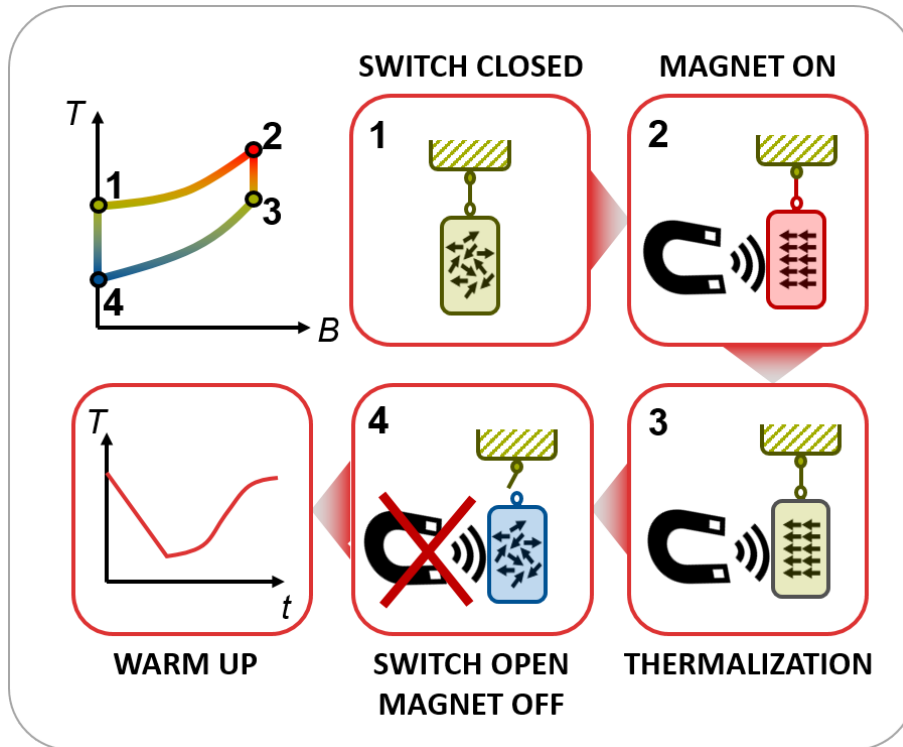


Figure 7.11 Cooling cycle of an adiabatic demagnetization refrigerator [328].

3. While keeping the applied magnetic field constant the excess heat is removed until the system once more reaches equilibrium with its surroundings.
4. The heat switch is opened so that the system is isolated from its surroundings and the magnetic field is slowly reduced to zero. When the magnetic field is removed the magnetic moments in the salt disorder, regaining their orientational entropy. The process is adiabatic, meaning there is no net change in entropy of the system, therefore the entropy related to other degrees of freedom is reduced, i.e. the system is cooled down.

The cooling power can be approximately quantified using a simple thermodynamic model [41]. We assume that the free energy F of a magnetic system is given by

$$dF = -SdT - MdH \quad (7.17)$$

where S , T , M , H are the entropy, temperature, magnetization and magnetic field, respectively. Now the magnetic analog of Maxwell's relations can be derived by asserting that the derivatives commute,

$$\left(\frac{\partial^2 F}{\partial T \partial H} \right) = \left(\frac{\partial^2 F}{\partial H \partial T} \right) \quad (7.18)$$

But

$$\begin{aligned}\left(\frac{\partial^2 F}{\partial T \partial H}\right) &= -\left(\frac{\partial S}{\partial H}\right)_T \\ \left(\frac{\partial^2 F}{\partial H \partial T}\right) &= -\left(\frac{\partial M}{\partial T}\right)_H\end{aligned}\quad (7.19)$$

so that the analogous Maxwell relation is

$$\left(\frac{\partial S}{\partial H}\right)_T = \left(\frac{\partial M}{\partial T}\right)_H \quad (7.20)$$

Multivariate calculus tells us that any system of three variables H, T, S satisfies

$$\left(\frac{\partial T}{\partial H}\right)_S = -\left(\frac{\partial T}{\partial S}\right)_H \left(\frac{\partial S}{\partial H}\right)_T \quad (7.21)$$

For an ideal paramagnet we may assume, due to Curie's Law (3.26), that

$$M \propto \frac{H}{T} \quad (7.22)$$

thus

$$\frac{\partial H}{\partial T} = -\frac{M}{T} \quad (7.23)$$

Combining (7.20), (7.23) and the definition for heat capacity c_H , at constant magnetic field,

$$c_H = T \left(\frac{\partial S}{\partial T}\right)_H \quad (7.24)$$

into (7.21) we get

$$\left(\frac{\partial T}{\partial H}\right)_S = \frac{M}{c_H} \quad (7.25)$$

Therefore an adiabatical (constant entropy S) decrease of the applied magnetic field H causes a drop in temperature proportional to the magnetization M . The effect is particularly significant at low temperature, when c_H is small.

Most pyrochlore oxides have very low thermal conductivity [329], so that thermal equilibration can become a problem at the very low temperature range that the ADR can explore. To improve the heat flow we mixed the sample powders with an ample amount of vacuum grease, which is a good thermal conductor, and the resulting paste was pressed into a transparent polycarbonate capsule. Clear plastics such as polycarbonate, polypropylene, Delrin and PCTFE have low background moments and are cryogenic compatible. However some of the dyes used to color these plastics are magnetic, so it is best to use transparent capsules.

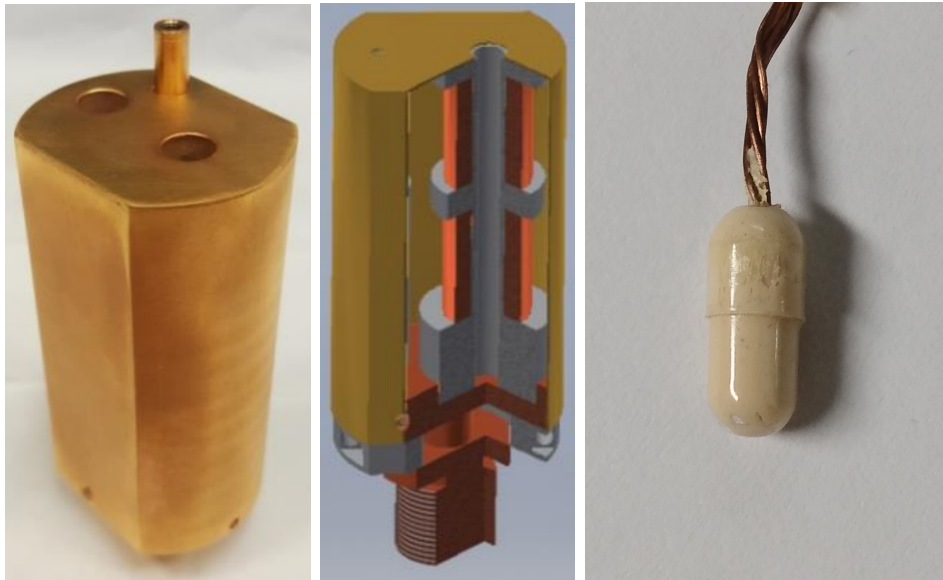


Figure 7.12 Sample holder with heat-sinking post on top (left), cross-sectional view showing the bore hole that contains the susceptometer coils (middle) and capsule containing the sample (right).

A few copper wires were stripped of their insulating coatings using acetone and twisted into a braided cable, with one end remaining splayed. The splayed end of the cable was inserted through a hole in the capsule containing the sample paste, to penetrate as much of the capsule's volume as possible. The other end of the copper cable was tightly threaded around a heat-sinking post on top of the sample holder, shown in Figure 7.12, and covered with a good amount of vacuum varnish to further increase thermal contact.

The sample chamber is sealed off with a piece of indium wire that forms a good vacuum seal when compressed. The whole sample stage, containing the sample, thermometers and the paramagnetic salt are suspended from a few thin strips of kapton tape. After being evacuated the sample chamber is filled with helium gas to act as heat exchanger between the sample stage and the surrounding liquid helium in the cryostat. When thermal equilibrium sets in, at about 4.2K, the exchange gas is removed and some helium inside a small container (the 1K pot) is pumped to reduce the temperature of the sample stage to about 1K. The sorption pump, a piece of activated charcoal, is kept heated to 40K to evaporate all the gases condensed on it. When the heating is turned off the charcoal cools down and absorbs any remaining gas molecules, improving the vacuum.

After magnetizing the paramagnetic salt by an applied field of 4T the heat switch is opened, so that the sample stage floats in the vacuum, only contacting the rest of the apparatus through the thin kapton strips. Then the magnetic field acting on the paramagnetic salt is slowly turned off and the magnetocaloric cooling sets in, absorbing heat from the sample until the temperature is lowered to $\approx 60\text{mK}$. After the minimal temperature has been reached there is

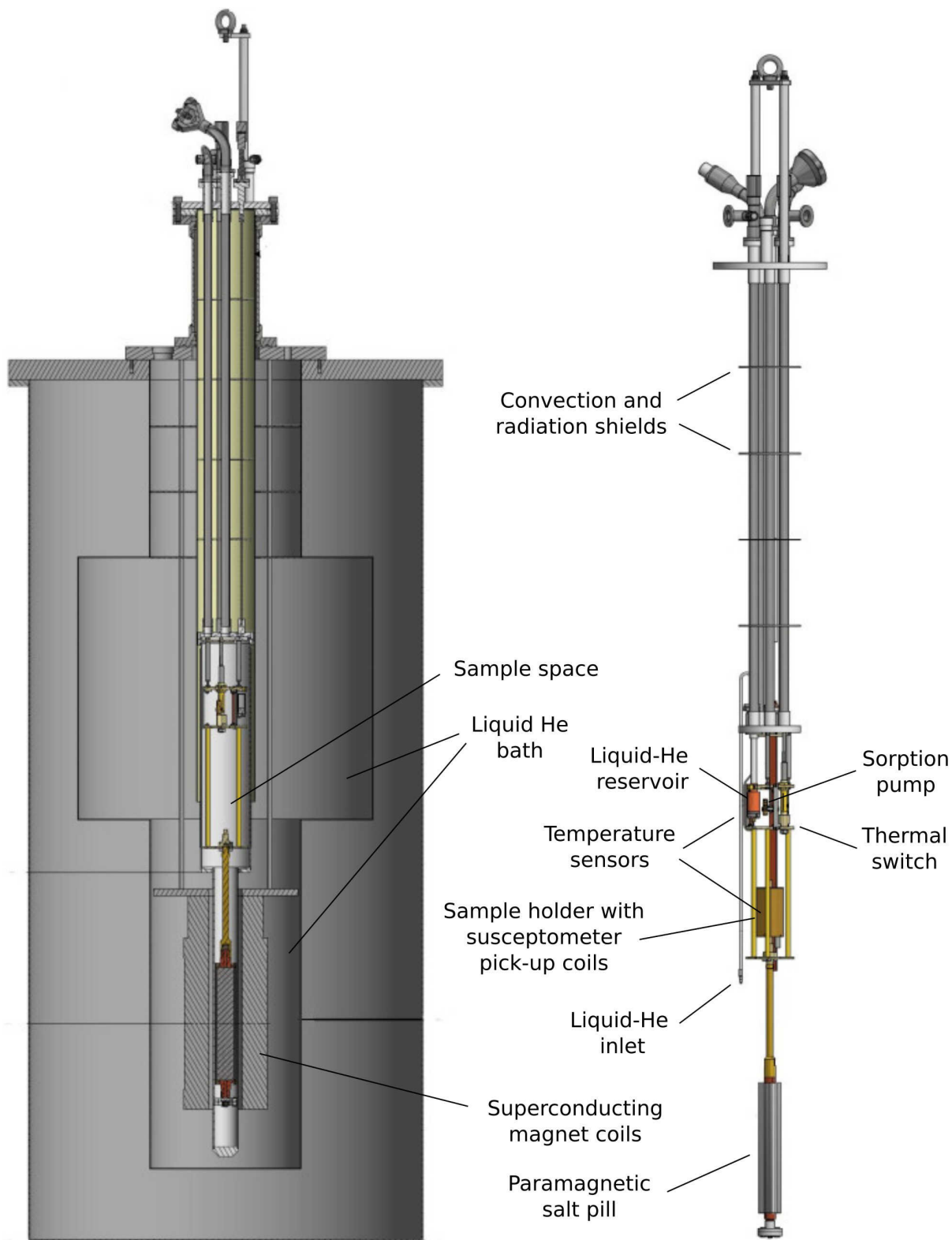


Figure 7.13 Cross-sectional view of the cryostat containing the ADR system (left) and the insert with the sample holder and paramagnetic salt (right). Adapted from [330].

no active heating or cooling mechanism and the system very slowly warms up again, due to the energy leaking in from the environment.

In most measurements a small hysteresis effect (splitting) was observed between the cooling and warming curves close to the minimal temperature our setup can reach, in the 60-80mK range. This is probably due to insufficient thermal coupling between the sample and its surroundings, including the thermometer. Above we described some measures taken to prevent this issue, but the effect is still observable. This leads us to believe that the samples were not completely thermalized when the minimal temperature was reached while cooling down, explaining the hysteresis. Given that the cooling rate is much higher than the heating rate, to avoid spurious temperature readings all data were collected during the slower heating phase of the experiment, in which the sample is assumed to be in thermal equilibrium with the thermometer. The temperature calibration of the thermometer was checked using the gadolinium salt $\text{Gd}_2(\text{SO}_4)_3 \cdot 8\text{H}_2\text{O}$. The measured peak temperature agrees within less than 1mK with the value reported in the literature [331].

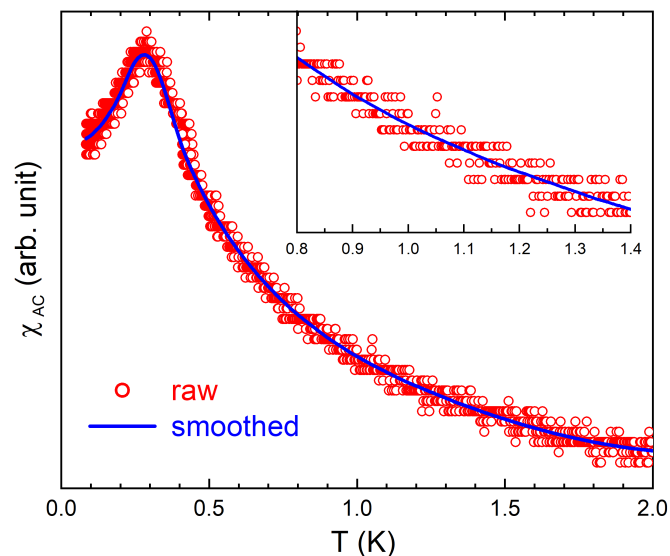


Figure 7.14 Raw susceptibility data for a sample measured with the ADR's susceptometer and a smooth interpolation.

Figure 7.14 shows the raw susceptibility data for a sample measured with the ADR's susceptometer. Due to the noisiness of the raw data we performed an interpolation of the data points to obtain a smooth curve. We do not know the source of the noise in our system, possibly one of the transformers that amplifies the signal before reaching the computer that records the data. The same smoothing operation was applied to the data acquired in all measurements.

We measured the background signal due to the sample holder with an empty polycarbonate capsule, at several frequencies. The background signal is frequency independent and almost temperature independent. It rises slightly at low temperature, but the variation between 80mK and 1K is only 0.06%. Since the variation is so small we simply assume a temperature independent constant to account for the background.

When measuring the $\text{Yb}_2\text{Zr}_x\text{Ti}_{2-x}\text{O}_7$ samples we did not know their mass since the powder was mixed with vacuum grease and an unknown amount of the resulting paste was pressed into the polycarbonate capsule. This means that the results have to be calibrated by fitting

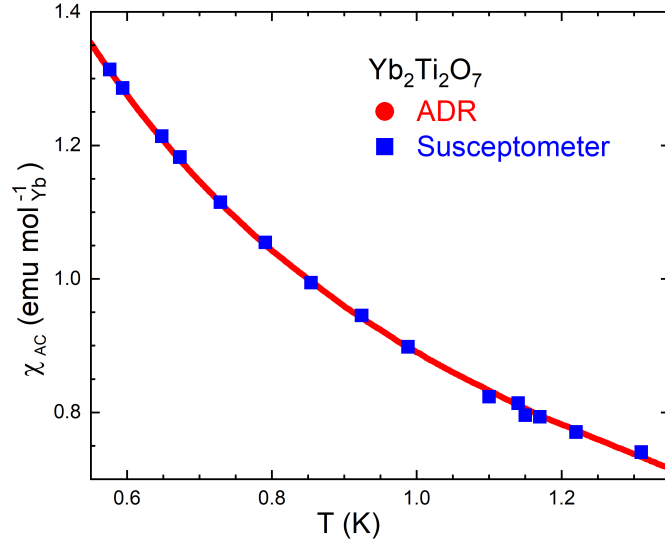


Figure 7.15 Susceptibility data from the ADR’s susceptometer, calibrated to fit the data from the helium bath susceptometer (Section 7.1.2) in the region where these overlap, $\sim 0.6\text{K} - 1.5\text{K}$.

the ADR’s susceptibility data to that of the helium bath susceptometer (Section 7.1.2) in the region where these overlap, $\approx 0.6\text{K} - 1.5\text{K}$, as shown in Figure 7.15.

To explain our method, suppose $f(T)$ represents the smoothed susceptibility data from the ADR’s susceptometer, as a function of temperature T , and $g(T)$ represents the data from the helium bath susceptometer. We pick an arbitrary point T_0 in the overlapping range and define h , the recalibrated version of f , as

$$h(T) = \frac{g'(T_0)}{f'(T_0)} [f(T) - f(T_0)] + g(T_0) \quad (7.26)$$

Letting $T = T_0$ we see that the values and slopes of g and h are equal:

$$\begin{aligned} h(T_0) &= g(T_0) \\ h'(T_0) &= g'(T_0) \end{aligned} \quad (7.27)$$

Rewriting the constants in (7.26) we have

$$h(T) = A(f(T) - B) \quad (7.28)$$

The multiplicative constant A depends on the sample mass, but the additive constant B is approximately independent of the sample because it represents a constant term in susceptibility, mostly due to the empty sample holder and other materials colocated with it, such as the vacuum grease and copper wires used for thermal contact. The calculated values for constants A and B , using (7.26), were adjusted until a good fit was achieved, as in Figure 7.15.

7.2 Magnetization of $\text{Yb}_2\text{Zr}_x\text{Ti}_{2-x}\text{O}_7$

The magnetic moment of the SG $\text{Yb}_2\text{Zr}_x\text{Ti}_{2-x}\text{O}_7$ samples were measured at 1.24K with the vibrating sample magnetometer, as shown in Figure 7.16. At $T = 1.24\text{K}$ these compounds are still well inside the paramagnetic phase, $T \gg T_C$, so the curves resemble the Brillouin function (3.11) that describes the magnetization of a paramagnet. The saturation levels of the magnetic moments were measured at $\mu_0 H = 14.5\text{T}$, although this field might not be sufficient to achieve full saturation. The theoretically predicted saturation moment for a free Yb^{3+} ion is $4\mu_B$ (3.13).

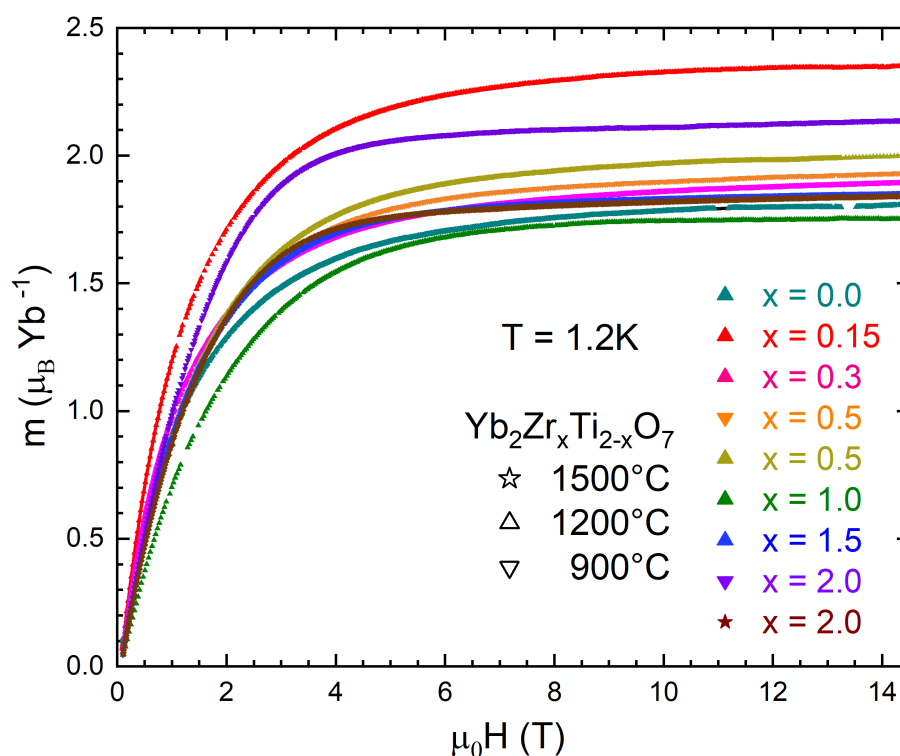


Figure 7.16 Magnetic moment per Yb^{3+} ion in $\text{Yb}_2\text{Zr}_x\text{Ti}_{2-x}\text{O}_7$ for magnetic fields up to 14.5T.

The saturation level m_{sat} varies significantly between samples and shows no distinct ordering with x , although Figure 7.17 shows a possible linear tendency if we consider the different structures separately. However, the $x = 0.15$ sample falls entirely outside of the tentative line, raising questions as to its validity. A small difference is observed between the $x = 0.5$ (900°C) sample, a metastable fluorite, and the $x = 0.5$ (1200°C) sample, a stable pyrochlore phase. The $x = 2.0$ (1500°C) δ -phase has a significantly lower saturation moment than its metastable polymorph, the $x = 2.0$ (900°C) fluorite.

Any error in measuring the mass of the sample powder could lead to wrong values for the magnetization. Another concern is the centering of the capsule containing the samples in the VSM's coil. If the samples were not correctly centered then the absolute value of the magnetization would also be diminished. To investigate if the variation in the saturation levels m_{sat} displayed in Figure 7.17 is a real effect or an experimental artifact, we correlated m_{sat} with the AC susceptibility χ_{AC} measured at the same temperature, $T = 1.24\text{K}$ (see Figure 7.20).

Figure 7.18 shows that there is some correlation, confirming that experimental error is not the sole cause of variation between samples. Points on the dashed line have a constant ratio

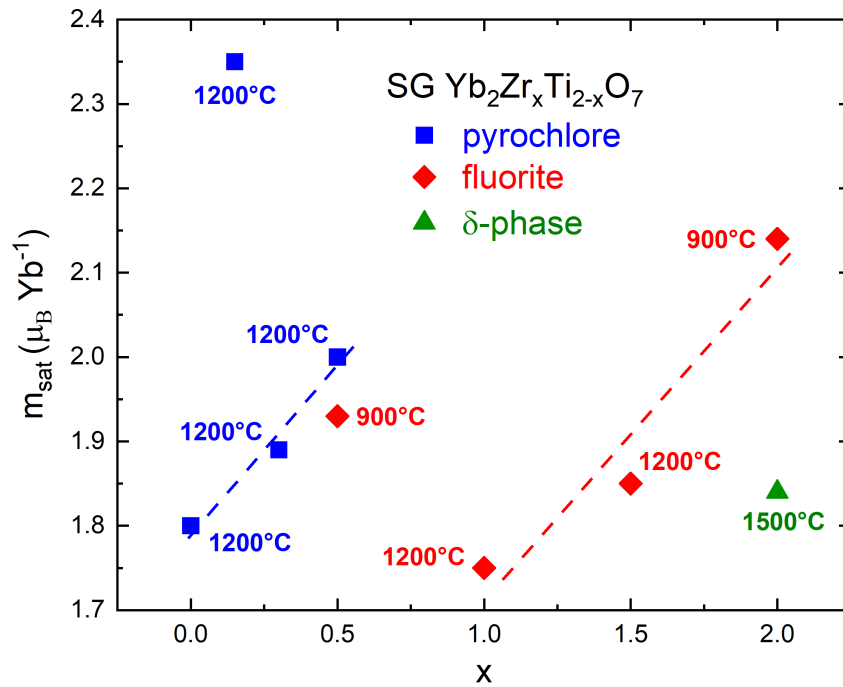


Figure 7.17 Saturation level, measured at $\mu_0 H = 14.5 \text{ T}$, of magnetic moments for $\text{Yb}_2\text{Zr}_x\text{Ti}_{2-x}\text{O}_7$ with varying composition x . Lines are only a guide to the eyes, suggesting a systematic variation.

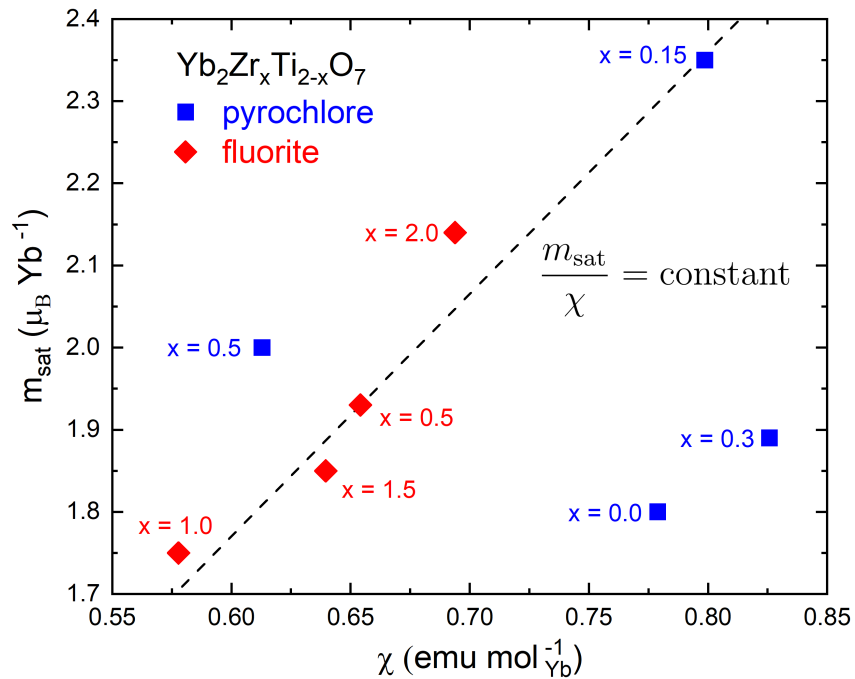


Figure 7.18 Correlation between the saturation moment m_{sat} and susceptibility. Points on the dashed line have a constant ratio $m_{\text{sat}}/\chi_{\text{AC}}$.

m_{sat}/χ_{AC} of the saturation moment to the susceptibility. Notably the $x = 0.15$ sample, which showed a disproportionately large saturation moment in Figure 7.17, seems to fit in better with the higher x fluorite samples than with the isomorphous $x = 0.0$ and $x = 0.3$ pyrochlore samples.

To compare the measured data with that reported in the literature we corrected for the demagnetizing effect to obtain the internal field H_i from the applied field H using

$$H_i = H - \frac{1}{4\pi}NM \quad (\text{cgs units}) \quad (7.29)$$

where N is the demagnetizing factor ($0 \leq N \leq 4\pi$ in cgs units), which was estimated from the susceptibility data. The experimentally measured susceptibility χ_{exp} is related to the real susceptibility χ by

$$\chi_{\text{exp}} = \frac{\chi}{1 + 4\pi N\chi} \quad (7.30)$$

so that when the susceptibility is singular at a phase transition, $\chi \rightarrow \infty$, the experimentally measured susceptibility is $\chi_{\text{exp}} = \frac{1}{4\pi N}$. Therefore the maximal value of χ_{exp} provides an estimate for the demagnetizing factor N .

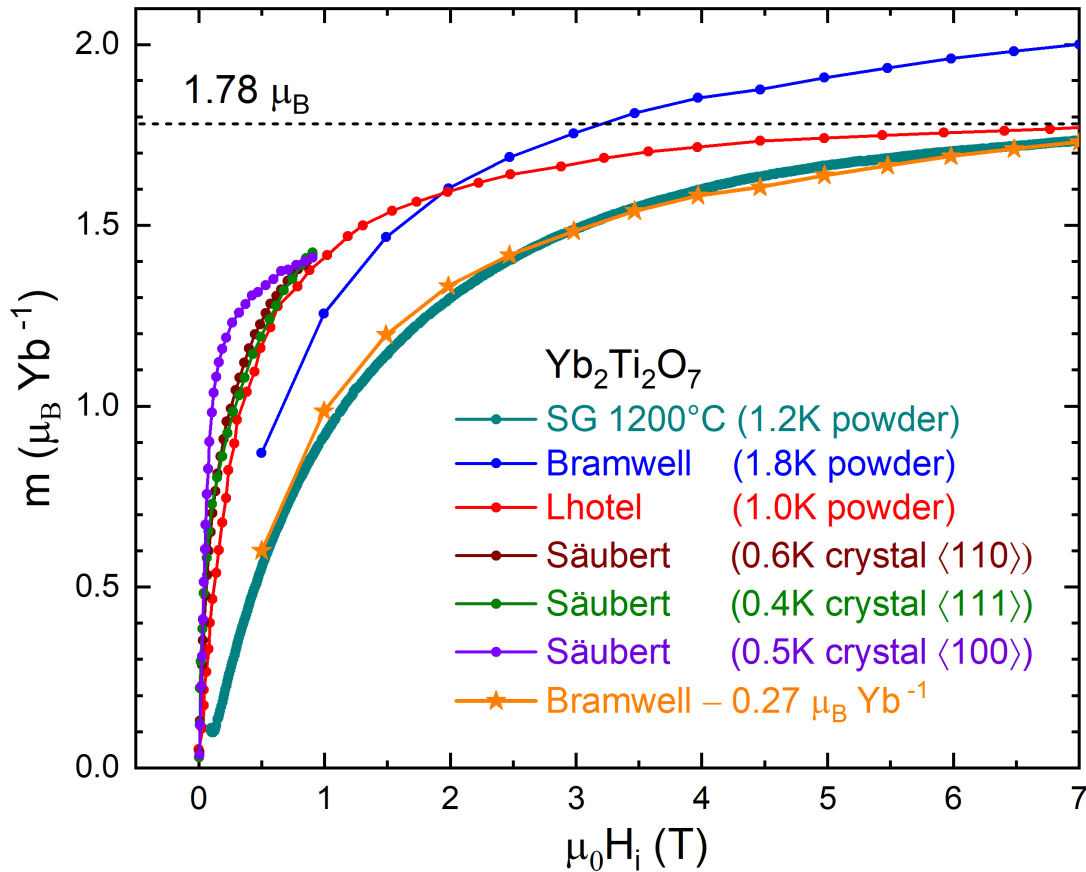


Figure 7.19 Comparison of magnetization for SG $\text{Yb}_2\text{Ti}_2\text{O}_7$ (1200°C) with digitized data from the literature [332, 153, 333].

Figure 7.19 compares the magnetization of the SG $\text{Yb}_2\text{Ti}_2\text{O}_7$ sample, sintered at 1200°C , with digitized data from the literature [332, 153, 333]. The saturation level agrees well with the data from Lhotel et al [153], at $1.78\mu_B \text{ Yb}^{-1}$, but not with the data from Bramwell et al [332]. Curiously, if the constant value $m = 0.27\mu_B \text{ Yb}^{-1}$ is subtracted from Bramwell's data the whole curve agrees quite well with our data. Given that the saturation moment of an Yb^{3+} ion is $\mu = 4\mu_B$ (3.13), it is not clear why the observed saturation moment for an Yb^{3+} ion in $\text{Yb}_2\text{Ti}_2\text{O}_7$ is so small.

We assume that the differences in the shape of the magnetization curve are due to the inferior quality of our samples. It is possible that the SG $\text{Yb}_2\text{Ti}_2\text{O}_7$ sample sintered at 1500°C , or the SS $\text{Yb}_2\text{Ti}_2\text{O}_7$ sample, would yield results closer to those of Lhotel et al. It is reasonable to expect that samples with some structural disorder, as is the case with the SG $\text{Yb}_2\text{Ti}_2\text{O}_7$ sample sintered at 1200°C , exhibit decreased magnetization for relatively small applied field but that eventually full saturation is reached, for a large applied field.

7.3 Susceptibility of $\text{Yb}_2\text{Zr}_x\text{Ti}_{2-x}\text{O}_7$

The molar AC magnetic susceptibilities of the $\text{Yb}_2\text{Zr}_x\text{Ti}_{2-x}\text{O}_7$ compounds were measured with the helium bath susceptometer, described in Section 7.1.2, in the temperature range $T = 4\text{K}$ to $T = 0.5\text{K}$ and with frequency $f = 155\text{Hz}$. It should be noted that when referring to molar susceptibility we always mean the susceptibility per mole of Yb^{3+} ions, not the susceptibility per mole of formula unit $\text{Yb}_2\text{Zr}_x\text{Ti}_{2-x}\text{O}_7$. The latter is twice as large as the former, since one formula unit contains two Yb atoms.

Each sample was measured in two temperature ranges: from $T = 4\text{K}$ to $T = 1.2\text{K}$, while pumping ^4He , and from $T = 1.2\text{K}$ to $T = 0.5\text{K}$, while pumping ^3He . The susceptibilities measured in these two ranges were combined into a single curve, as shown in Figure 7.22.

Figure 7.20 shows the AC susceptibility χ_{AC} for all SG $\text{Yb}_2\text{Zr}_x\text{Ti}_{2-x}\text{O}_7$ samples that were measured, while Figure 7.21 shows the inverse susceptibility χ_{AC}^{-1} for the same samples. We see that for all compounds χ_{AC}^{-1} is to a good approximation a straight line, which is the behavior expected according to the Curie-Weiss Law (3.26). By fitting a line to χ_{AC}^{-1} , as in (3.28), we can extract the values of the Curie-Weiss temperature θ_{CW} and the effective moment μ_{eff} , as explained in Section 3.4.

Figure 7.23 shows a linear fit to the paramagnetic region, from 1.2K to 4K , of the inverse susceptibility for the SG $\text{Yb}_2\text{Ti}_2\text{O}_7$ sample. A small deviation from linear Curie-Weiss behavior becomes apparent below about $T = 1.1\text{K}$, indicating that correlations between the magnetic moments are significant below this temperature. The inverse susceptibility of the other $\text{Yb}_2\text{Zr}_x\text{Ti}_{2-x}\text{O}_7$ samples behaved similarly, being well approximated by a line above $T = 1.2\text{K}$, with deviations appearing below $T \approx 1.2\text{K}$. Table 7.1 lists the Curie-Weiss temperature θ_{CW} , molar Curie constant C_m and effective moment μ_{eff} , extracted from the Curie-Weiss fit, for all of the measured samples.

The Curie-Weiss temperatures θ_{CW} are plotted in Figure 7.24 as a function of composition x . All of the values are negative, which is unexpected, given that $\text{Yb}_2\text{Ti}_2\text{O}_7$ has a ferromagnetic ground state (Section 3.12) and therefore should have $\theta_{CW} > 0$. It is known that θ_{CW} depends on the temperature range to which the Curie-Weiss line is fitted, possibly explaining why all

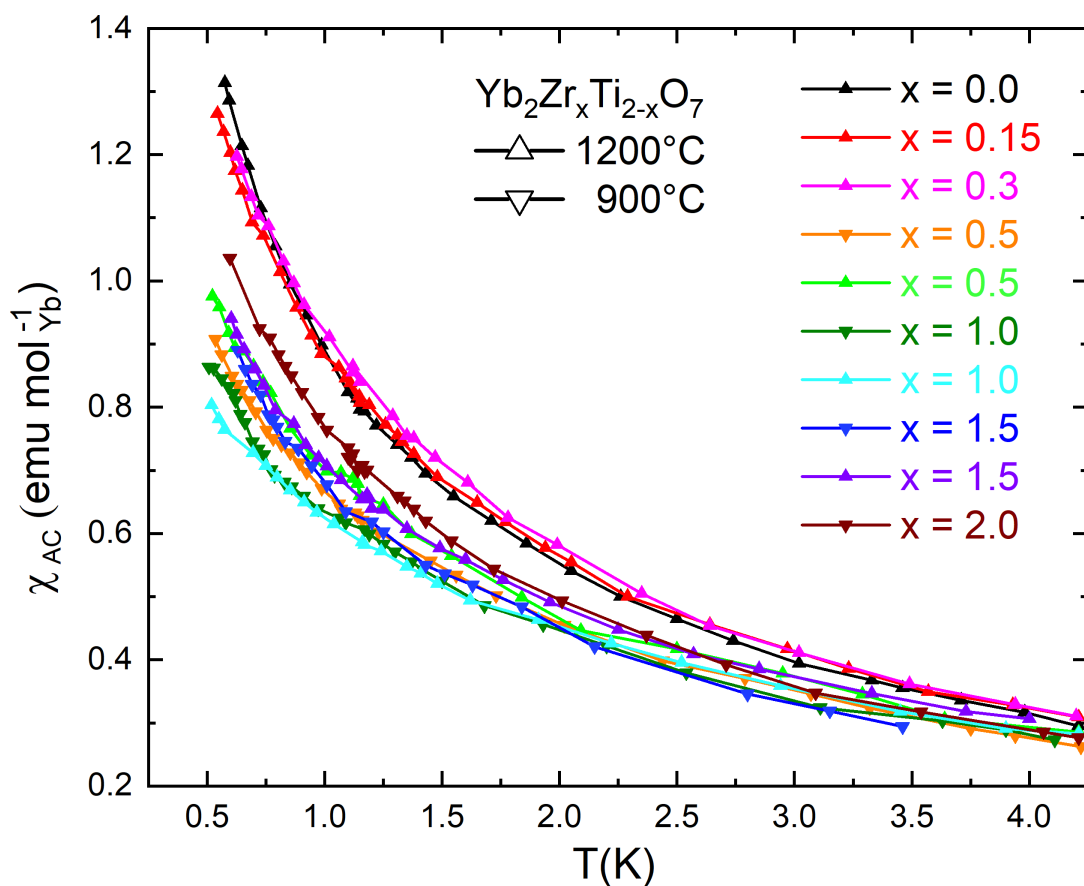


Figure 7.20 Molar susceptibilities of $\text{Yb}_2\text{Zr}_x\text{Ti}_{2-x}\text{O}_7$, in the temperature range $T = 4\text{K}$ to $T = 0.5\text{K}$.

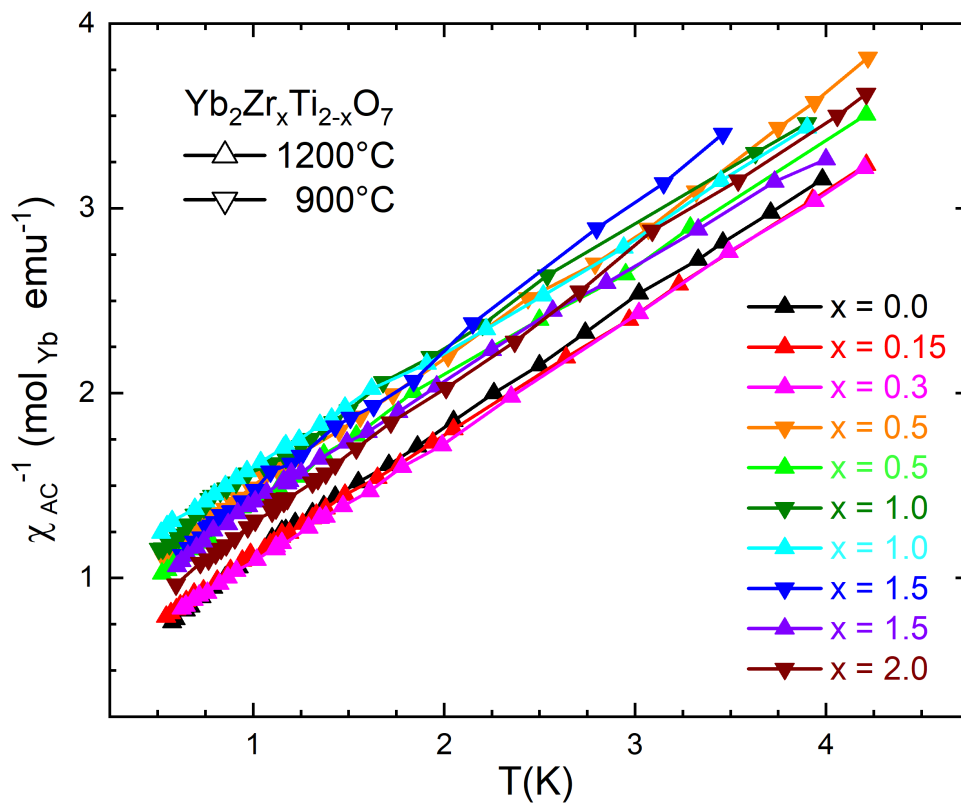


Figure 7.21 Inverse molar susceptibilities of $\text{Yb}_2\text{Zr}_x\text{Ti}_{2-x}\text{O}_7$, in the temperature range $T = 4\text{K}$ to $T = 0.5\text{K}$.

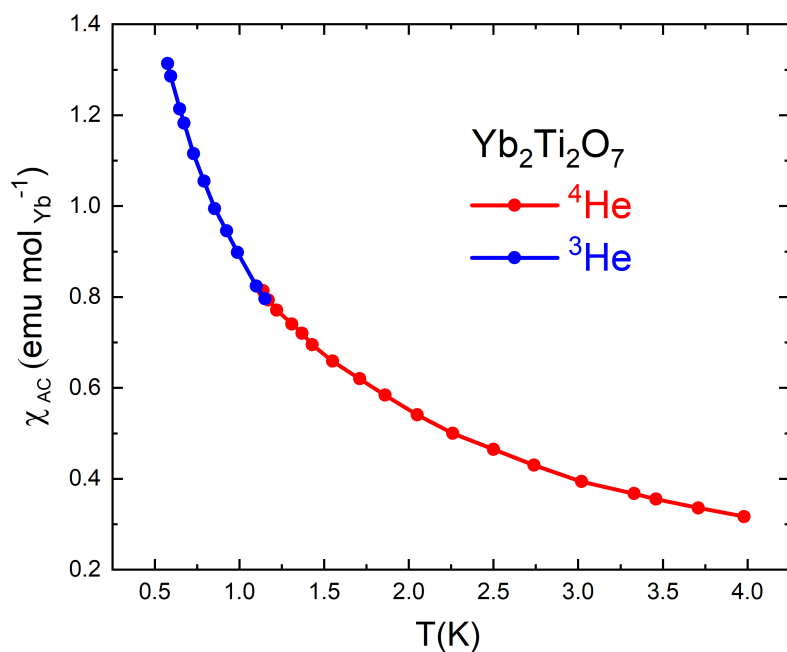


Figure 7.22 Susceptibility of Yb₂Ti₂O₇, measured with the helium bath susceptometer, in two temperature ranges: from $T = 4\text{K}$ to $T = 1.2\text{K}$, while pumping ⁴He, and from $T = 1.2\text{K}$ to $T = 0.5\text{K}$, while pumping ³He.

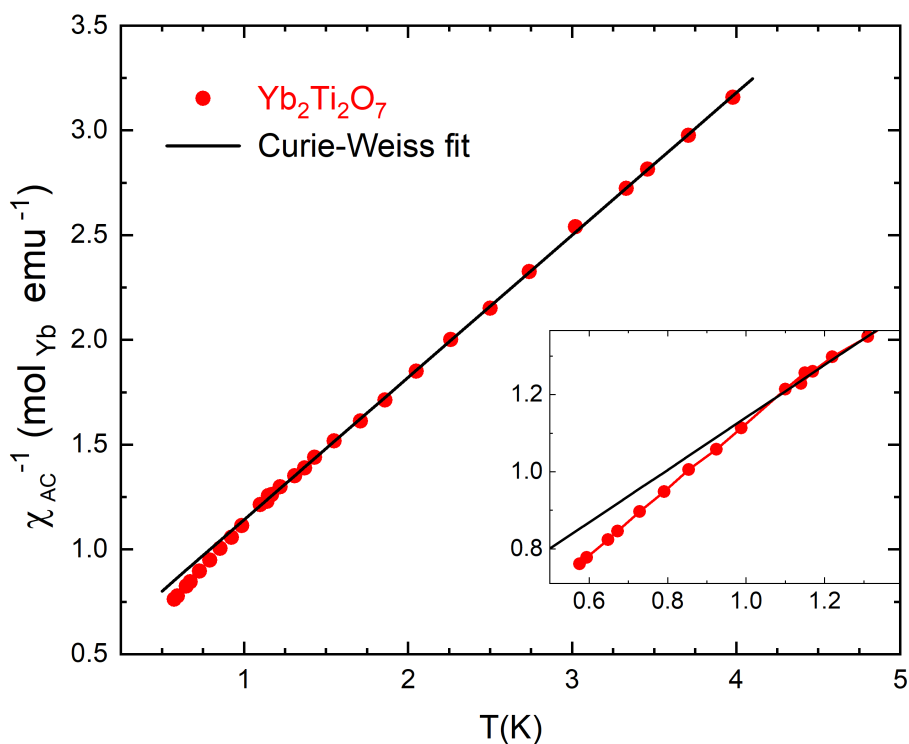


Figure 7.23 Linear fit to the paramagnetic region, from 1.2K to 4K, of the inverse susceptibility of Yb₂Ti₂O₇. The inset shows a magnified view of the deviation from linear Curie-Weiss behavior below $T = 1.1\text{K}$.

x	T (°C)	θ_{CW} (K)	C_m (emu K mol ⁻¹)	μ_{eff} (μ_B)
0.0	1200	-0.68	1.472	3.430
0.15	1200	-0.71	1.524	3.491
0.3	1200	-0.61	1.492	3.455
0.5	900	-1.12	1.421	3.371
0.5	1200	-1.15	1.528	3.496
1.0	900	-1.36	1.506	3.470
1.0	1200	-1.58	1.605	3.582
1.5	900	-0.85	1.269	3.185
1.5	1200	-1.27	1.594	3.570
2.0	900	-0.79	1.375	3.316

Table 7.1 Curie-Weiss temperature θ_{CW} , molar Curie constant C_m and effective moment μ_{eff} , extracted from the Curie-Weiss fit, for the $\text{Yb}_2\text{Zr}_x\text{Ti}_{2-x}\text{O}_7$ samples.

of the values are negative when fitted only up to 4K. Since the absolute values of θ_{CW} are quite small, it could be that a Curie-Weiss fit extended to higher temperature, on the order of 10K or 100K, would yield positive values for these parameters. Unfortunately we were not able to measure the susceptibility up to higher temperature due to technical issues with the instrument usually used for such measurements.

Figure 7.25 shows that the effective moments μ_{eff} are significantly smaller than the value for free Yb^{3+} ions, $\mu_{\text{eff}} = 4.5356 \mu_B$ (3.33). This is to be expected since in $\text{Yb}_2\text{Zr}_x\text{Ti}_{2-x}\text{O}_7$ the Yb^{3+} ions are not free, but rather feel the crystal field environment. The isotropic degeneracy of the ground states predicted by Hund's rule is broken by the crystalline electric field, such that the states are not uniformly populated, as was discussed in Section 3.4. The value of $\mu_{\text{eff}} \approx 3.4\mu_B$ for $\text{Yb}_2\text{Ti}_2\text{O}_7$ is almost double that reported in the recent literature, $\mu_{\text{eff}} \approx 1.3\mu_B$ [176]. The μ_{eff} values also depend on the temperature range over which the Curie-Weiss fit is performed, as for the θ_{CW} values, so a fit extended to higher temperature might yield a smaller μ_{eff} value for $\text{Yb}_2\text{Ti}_2\text{O}_7$, closer to the one reported in the literature.

To measure the susceptibility at a temperature lower than $T = 0.5\text{K}$ the adiabatic demagnetization refrigerator (ADR) was employed. A peak in the magnetic susceptibility is indicative of a magnetic ordering or freezing transition. The temperature at which a peak attains its maximum value is commonly denoted as T_C or T_N , depending on whether the transition is ferromagnetic or antiferromagnetic in nature. To be consistent, here we used the T_C notation for all samples since $\text{Yb}_2\text{Ti}_2\text{O}_7$ is expected to undergo a ferromagnetic transition at $T_C \approx 0.26\text{K}$.

Figure 7.26 shows the susceptibility of the SG and SS $\text{Yb}_2\text{Ti}_2\text{O}_7$ samples compared to digitized data from the literature [334, 153]. In both sources from the literature the peak occurs at $T_C = 243\text{mK}$. The peak corresponding to the SS sample is less sharp than those of the literature samples and its maximum occurs at $T_C = 233\text{mK}$, while the peak corresponding to the SG sample is even broader, with its maximum at $T_C = 280\text{mK}$. The frequencies of the AC signals used to probe the materials are slightly different, but for the $\text{Yb}_2\text{Ti}_2\text{O}_7$ compound

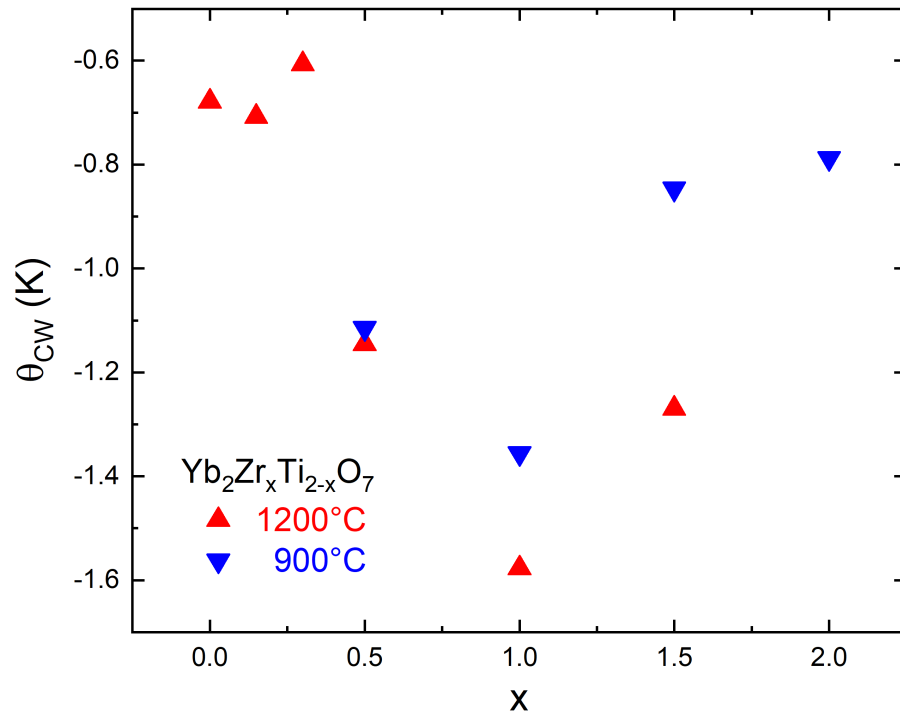


Figure 7.24 Curie-Weiss temperature θ_{CW} for the $\text{Yb}_2\text{Zr}_x\text{Ti}_{2-x}\text{O}_7$ samples, extracted from the Curie-Weiss fit.

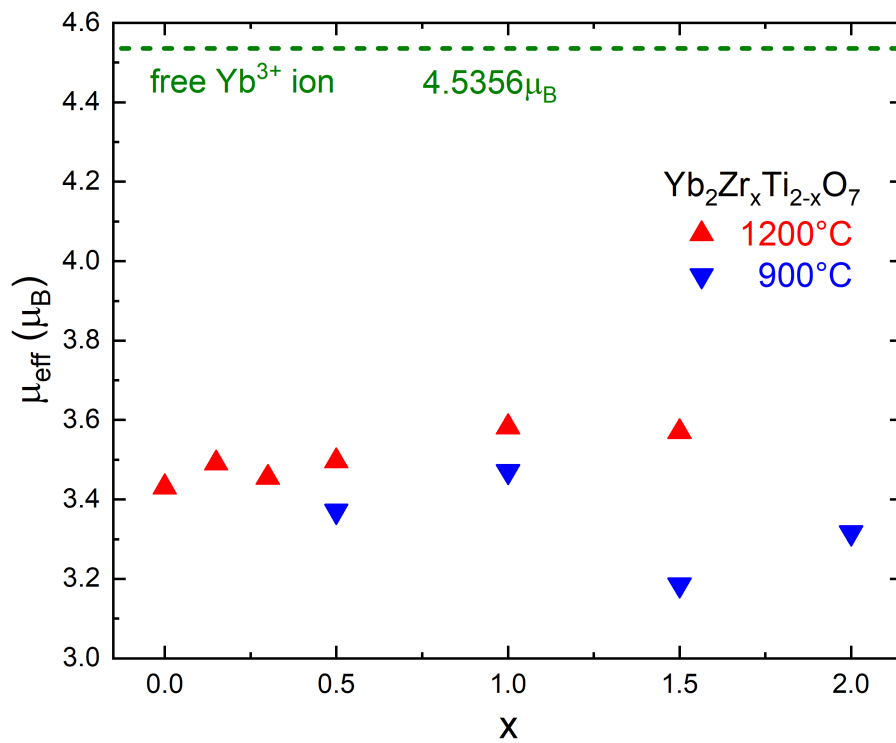


Figure 7.25 Effective moments μ_{eff} for the $\text{Yb}_2\text{Zr}_x\text{Ti}_{2-x}\text{O}_7$ samples, extracted from the Curie-Weiss fit, and for a free Yb^{3+} ion, $\mu_{eff} = 4.5356 \mu_B$.

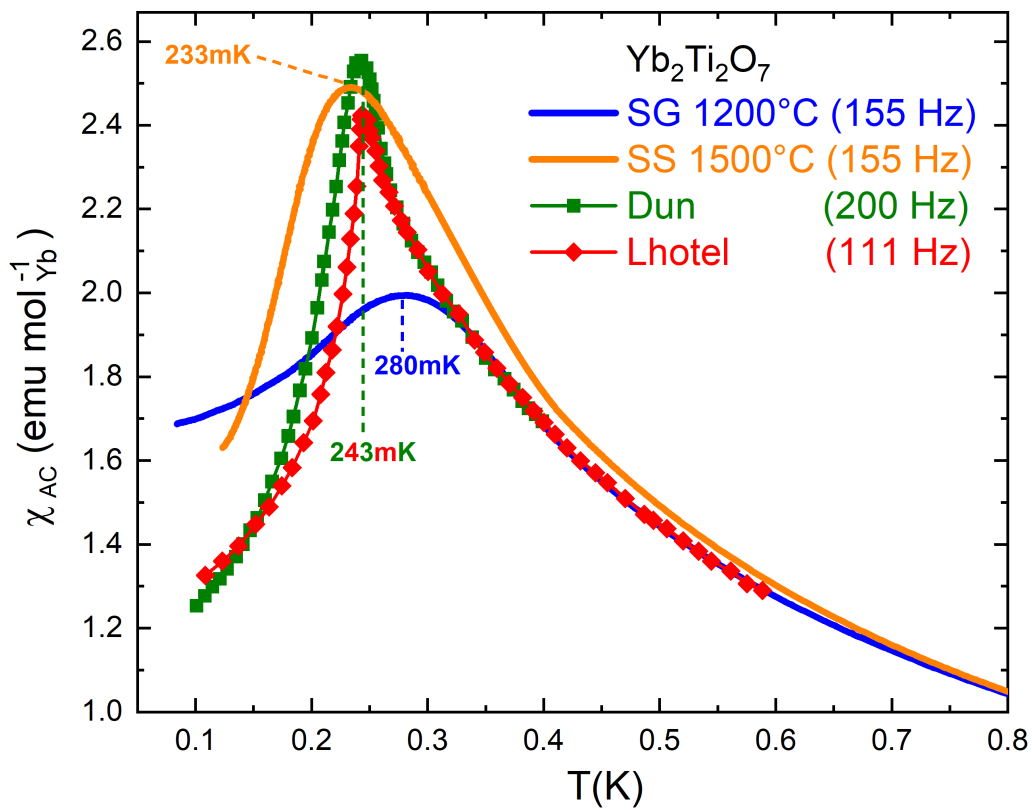


Figure 7.26 AC susceptibility for the SG and SS $\text{Yb}_2\text{Ti}_2\text{O}_7$ samples, compared to digitized data from the literature [334, 153].

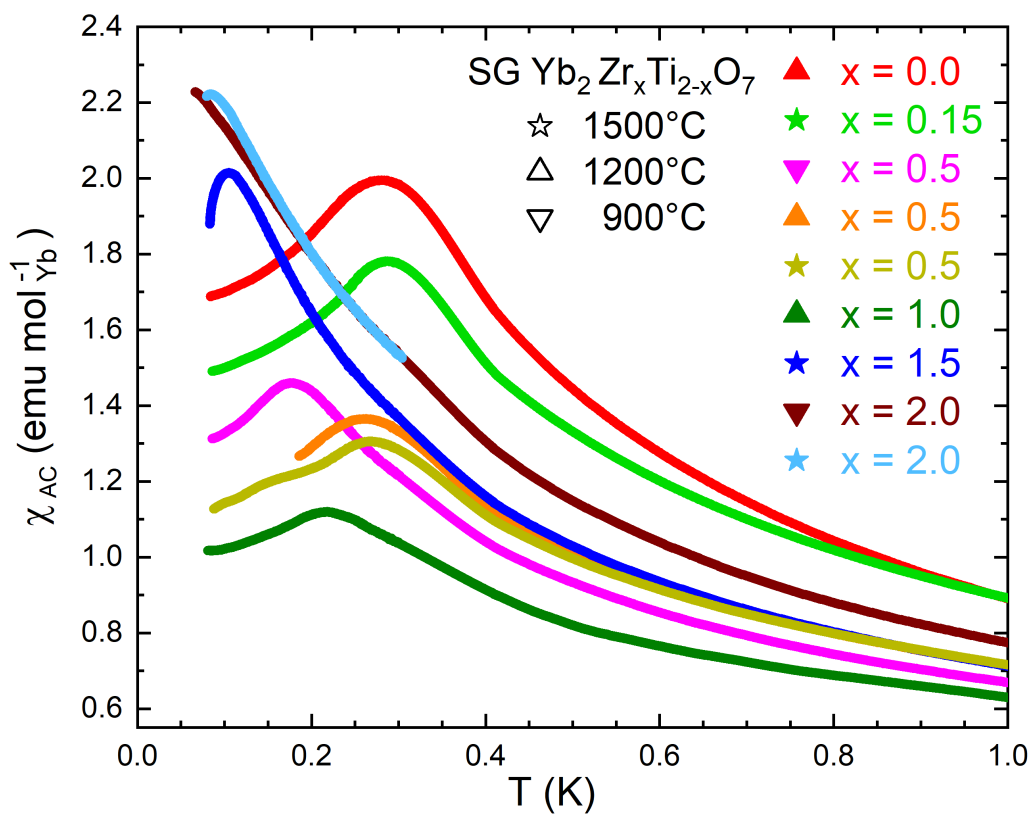


Figure 7.27 AC susceptibility for all of the SG $\text{Yb}_2\text{Zr}_x\text{Ti}_{2-x}\text{O}_7$ samples, measured with the ADR's susceptometer.

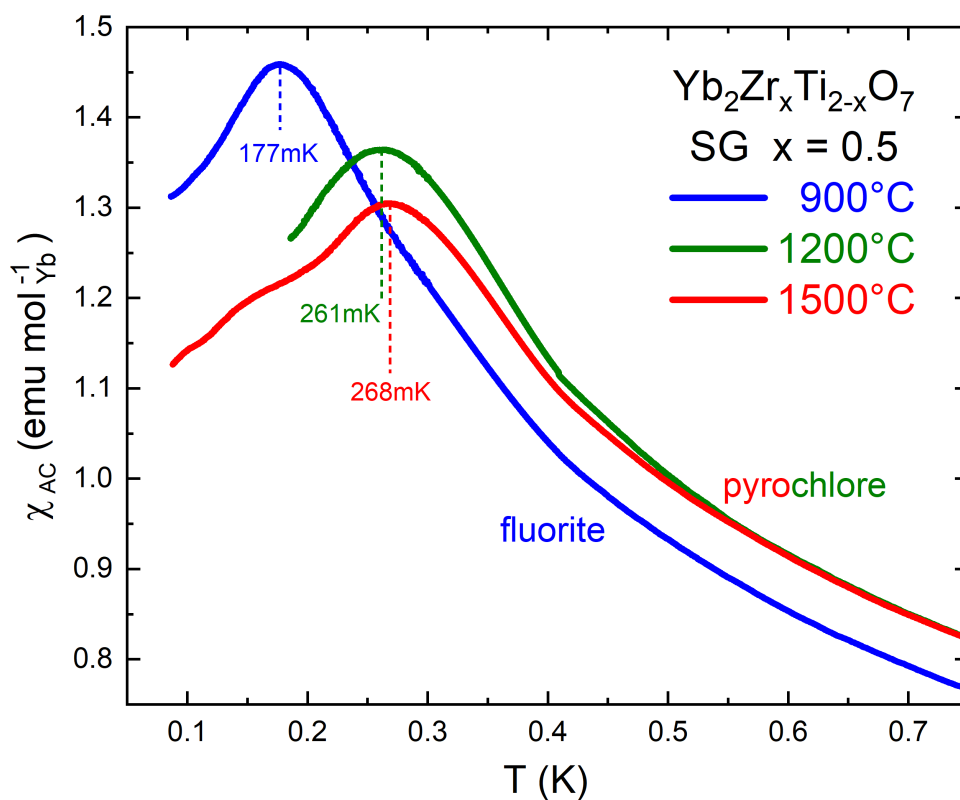


Figure 7.28 AC susceptibility, measured with the ADR's susceptometer, of the $\text{Yb}_2\text{Zr}_x\text{Ti}_{2-x}\text{O}_7$ samples with $x = 0.5$.

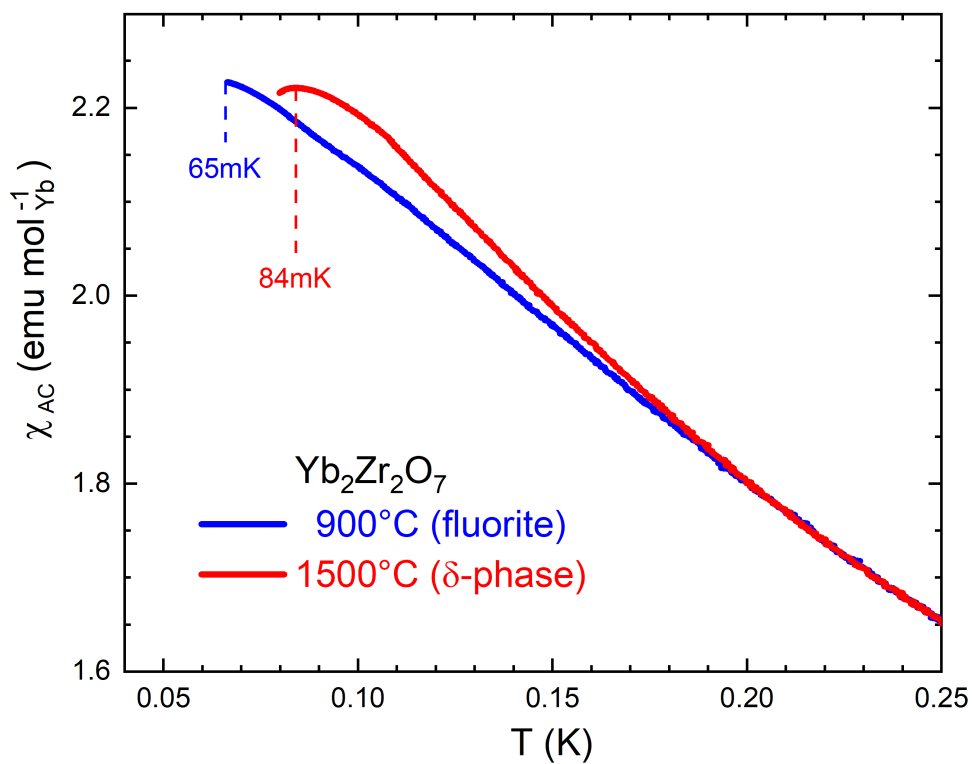


Figure 7.29 AC susceptibility, measured with the ADR's susceptometer, of the $\text{Yb}_2\text{Zr}_2\text{O}_7$ samples.

the peak temperature is to a very good approximation frequency-independent, so the use of different probe frequencies does not invalidate the comparison between these measurements.

As with the literature comparison for the magnetization data in Section 7.2, we believe that the broad peaks are indicative of structural disorder present in our samples, which are probably of lesser quality than those synthesized by the groups from the literature sources. It should be noted that the SS sample underwent only two sintering steps at 1500°C, so it is possible that by repeating this step a few more times the sample's susceptibility could more closely resemble the sharp peaks found in the literature. Note also that the measured SG sample was sintered at 1200°C and XRD data showed a significant increase in crystallinity of this sample after sintering at 1500°C. Therefore it is possible that the SG $\text{Yb}_2\text{Ti}_2\text{O}_7$ sample sintered at 1500°C would also display more well defined transition in the susceptibility. Unfortunately it was not possible to measure this sample due to the limited availability of liquid helium in our laboratory during the months when this thesis was completed.

The AC susceptibility for all SG $\text{Yb}_2\text{Zr}_x\text{Ti}_{2-x}\text{O}_7$ samples measured with the ADR's susceptometer is displayed in Figure 7.27. All of the curves exhibit a broad maximum which, as for the $\text{Yb}_2\text{Ti}_2\text{O}_7$ sample, is likely due to the high degree of imperfections in the crystal structure. The shape of these broad maxima rules out a Schottky-type anomaly and we believe that they indicate a gradual transition to an ordered magnetic state at low temperature.

It is not clear whether the differences in magnitude of the susceptibility are physically significant, and their variation along the $\text{Yb}_2\text{Zr}_x\text{Ti}_{2-x}\text{O}_7$ series seems erratic, not correlated with the composition x . Some of the AC susceptibility measurements were performed at different frequencies but no frequency-dependent shifts of the peak temperature were observed, ruling out spin glass-like dynamics.

Figure 7.28 shows an example of how different structures, resulting from different sintering temperatures, can affect the susceptibility of the $\text{Yb}_2\text{Zr}_x\text{Ti}_{2-x}\text{O}_7$ compound with $x = 0.5$. The disordered fluorite sample, sintered at 900°C, has a lower transition temperature than the more ordered pyrochlore samples, sintered at 1200°C and 1500°C. The magnitude of the susceptibility is also different between the fluorite and pyrochlore samples, although it is not clear how to interpret this difference.

The $\text{Yb}_2\text{Zr}_2\text{O}_7$ samples ($\text{Yb}_2\text{Zr}_x\text{Ti}_{2-x}\text{O}_7$ with $x = 2.0$) show a similar difference in peak temperature, attributed to the structural transformation occurring with increased sintering temperature (Figure 7.29). The more crystalline δ -phase, sintered at 1500°C, has $T_C = 84\text{mK}$, while the less ordered fluorite, sintered at 900°C, has $T_C \leq 65\text{mK}$. The latter sample's susceptibility curve shows a leveling off close to 65mK, the minimal temperature reached during the measurement. It could be that this leveling off consists of the high-temperature side of an actual peak, with its maximum at $\approx 65\text{mK}$. Another possibility is that there is no real peak at that temperature and the leveling off is just an artifact of the measurement, caused by insufficient thermal coupling between the sample and the thermometer, as discussed in Section 7.1.4. Since the interpretation is ambiguous we considered $T_C = 65\text{mK}$ but marked the values corresponding to this sample ($\text{Yb}_2\text{Zr}_x\text{Ti}_{2-x}\text{O}_7$ with $x = 2.0$, sintered at 900°C) with a question mark in the following table and figures.

Table 7.2 lists the susceptibility peak temperature T_C , Curie-Weiss temperature θ_{CW} (the same values as in Table 7.1) and frustration index f (3.40) for all of the measured samples.

	x	T (°C)	T_C (mK)	θ_{CW} (K)	f
SS	0.0	1500	233	-2.30	9.9
SG	0.0	1200	280	-0.68	2.4
	0.15	1500	286	-0.72	2.5
	0.5	900	277	-1.12	4.0
	0.5	1200	261	-1.15	4.4
	0.5	1500	268	-0.68	2.5
	1.0	1200	218	-1.58	7.2
	1.5	1200	105	-1.27	12.1
	2.0	900	≤ 65	-0.79	≥ 12
	2.0	1500	84	-0.79	9.4

Table 7.2 Peak temperature T_C , Curie-Weiss temperature θ_{CW} and frustration index f for $\text{Yb}_2\text{Zr}_x\text{Ti}_{2-x}\text{O}_7$. All samples are SG except for SS $x = 0.0$.

Note that with increasing x in $\text{Yb}_2\text{Zr}_x\text{Ti}_{2-x}\text{O}_7$ the transition temperature of the stable structures, sintered at 1200°C or 1500°C, decreases monotonically from 280mK for $x = 0.0$ to 84mK for $x = 2.0$ (Figure 7.30). This confirms that structural disorder, which is loosely proportional to x , suppresses the magnetic ordering transition. The frustration index is also loosely proportional to x (Figure 7.30), suggesting that the magnetic moments are becoming progressively more frustrated with increasing x .

We should note that in Table 7.2 the Curie-Weiss temperatures for the SS $\text{Yb}_2\text{Ti}_2\text{O}_7$ and for the SG $x = 0.15, 0.5$ (1500°C) samples were obtained from a fit to the susceptibility measured with the susceptometer contained in the ADR, rather than with the helium bath susceptometer of Section 7.1.2. We compared the θ_{CW} values obtained from fits to the susceptibility measured by both susceptometers for a few of the samples, for instance $\theta_{ADR} = -1.4\text{K}$ and $\theta_{He\ bath} = -1.1\text{K}$ for the sample $x = 0.5$ (900°C). Such discrepancies reinforce that the θ_{CW} values we report should not be considered reliable. If more reliable values were available we might be able to draw some conclusions as to how the change in composition affects the competition between ferromagnetism and antiferromagnetism that marks the ground state of $\text{Yb}_2\text{Ti}_2\text{O}_7$.

Unfortunately it is not possible to fully characterize the magnetic ground state of these compounds based solely on bulk measurements such as AC susceptibility and magnetization. A complete picture of the magnetic ground state would require the input of other techniques sensitive to the magnetic lattice's local structure and dynamics, such as neutron scattering.

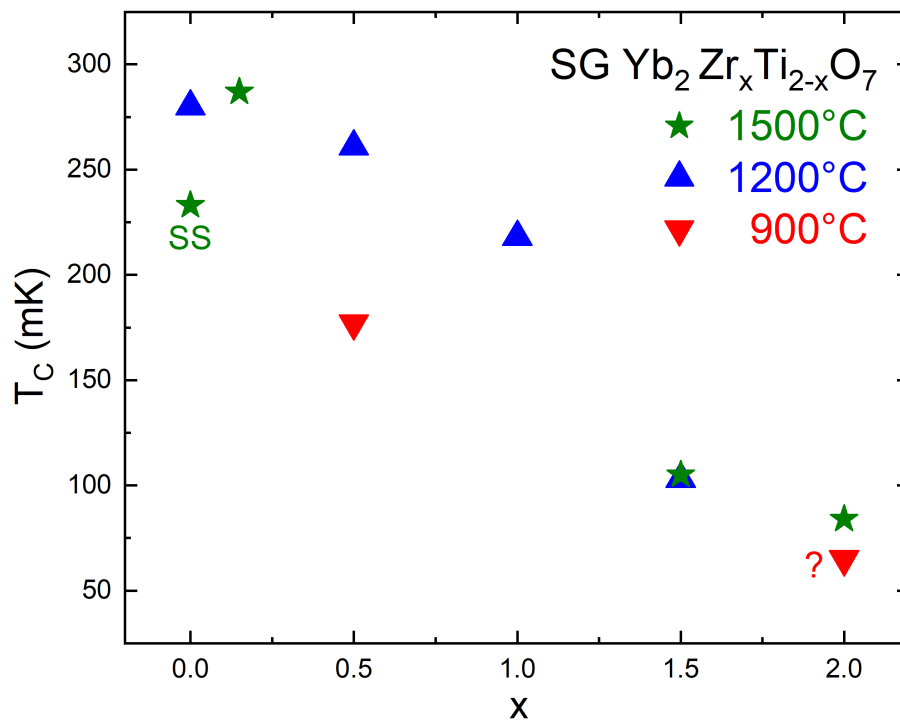


Figure 7.30 Susceptibility peak temperature T_C as a function of composition x in $\text{Yb}_2\text{Zr}_x\text{Ti}_{2-x}\text{O}_7$. All samples are SG except for the one indicated as SS ($x = 0.0$).

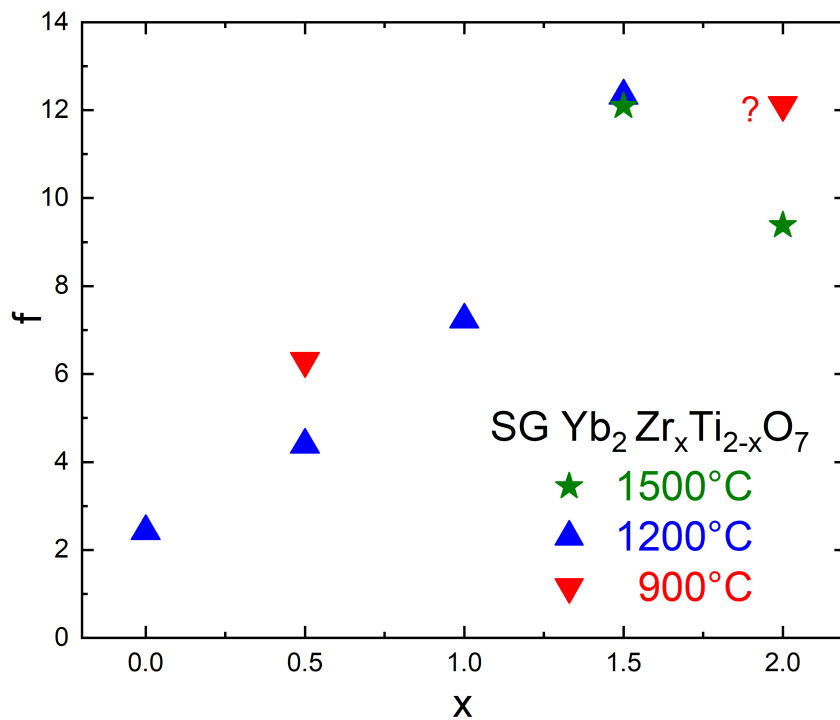


Figure 7.31 Frustration index f as a function of composition x in $\text{Yb}_2\text{Zr}_x\text{Ti}_{2-x}\text{O}_7$.

Conclusion

Section 8.1 summarizes the results of the previous chapters. Section 8.2 mentions some possibilities for extending the current work and explains how different experimental techniques might shed light on some of the unanswered questions raised in this thesis.

8.1 Summary

In Chapter 4 we described the synthesis of the $\text{Yb}_2\text{Zr}_x\text{Ti}_{2-x}\text{O}_7$ samples through the solid-state reaction (SS) and the sol-gel method (SG). Scanning electron microscopy provided some morphological information, though we could not draw any general conclusions since only three samples were imaged. Energy-dispersive spectroscopy confirmed the elemental composition of the samples, but its low accuracy did not allow us to extract any useful information on sample stoichiometry.

In Chapter 5 we described the principles of x-ray diffraction and the process of qualitative phase analysis, instrumental calibration and Rietveld refinement. We also discussed the role of short-range and long-range order, as relating to the pyrochlore and fluorite structures. Phase analysis demonstrated that the SS $\text{Yb}_2\text{Ti}_2\text{O}_7$ sample and the SG samples, sintered at 900°C, 1200°C and 1500°C, did form pure phases, whereas the SS $\text{Yb}_2\text{Zr}_x\text{Ti}_{2-x}\text{O}_7$ samples with $x \geq 0.5$ still contained residual precursor oxide phases, even after multiple sintering and grinding steps. The SG samples sintered at 900°C are disordered fluorite phases, with poor crystallinity, some of them showing signs of incipient pyrochlore ordering.

Considering the $\text{Yb}_2\text{Zr}_x\text{Ti}_{2-x}\text{O}_7$ samples sintered at high temperature (1500°C), the structure ranges from an ordered pyrochlore, for $x \leq 0.5$, to a disordered fluorite, for $x = 1.0, 1.5$, and finally to the rhombohedral δ -phase, for $x = 2.0$. The morphotropic transition from pyrochlore to fluorite occurs in the range $0.5 < x < 1.0$, somewhat less than the value predicted by the structural tolerance factor, $x = 1.21$. The samples sintered at 1200°C possess the same structures as those that were sintered at 1500°C, but with reduced crystallinity and slightly increased disorder.

Rietveld refinement was performed on the SS and SG $\text{Yb}_2\text{Ti}_2\text{O}_7$ samples (sintered at 1500°C), showing that both possess a pyrochlore structure but the SG sample has an increased lattice parameter, likely due to a small amount of structural disorder. The $x = 0.15$ sample was also refined, but the agreement of the experimental and calculated intensities is not ideal, also indicating the presence of some disorder.

The $x = 0.3, 0.5$ samples exhibited a few secondary peaks, adjacent to the main pyrochlore peaks, that could not be identified, but are likely due to distortions of the ideal pyrochlore structure, caused by the substitution of Ti^{4+} by the larger Zr^{4+} ions. The $x = 1.0, 1.5$ samples are disordered defect fluorite phases, but some weak diffuse scattering at the pyrochlore superstructure peak positions indicates that locally the structures possess some pyrochlore-type correlations. The I_{111}/I_{222} and I_p/I_f ratios were used as semi-quantitative measures of the extent to which local pyrochlore order is present.

The $x = 2.0$ sample was successfully refined with the δ -phase structure, despite the nominal stoichiometry of the δ -phase being $\text{A}_4\text{B}_3\text{O}_{12}$ instead of $\text{A}_2\text{B}_2\text{O}_7$. To compensate for this, it is likely that one or both of the cation sites in the δ -phase structure are disproportionately occupied by Zr atoms, but we could not determine how the cations are distributed on these sublattices and whether they are partially ordered or completely disordered.

In summary, the intermediate composition $\text{Yb}_2\text{Zr}_x\text{Ti}_{2-x}\text{O}_7$ samples, close to the morphotropic phase boundary, exhibit either structural distortions or short-range local order that does not extend to the long-range crystal structure. The conclusions from XRD were illustrated in a phase diagram, representing the structure of the samples as a function of composition and sintering temperature.

In Chapter 6 we saw that Raman spectroscopy is a powerful technique to detect local order in solid materials, thus being highly complementary to x-ray diffraction, which probes the long-range order. We also described how principles of group theory, specifically group representations, can be used to classify the vibrational modes of a molecule or solid structure and determine their Raman or infrared activity.

Raman spectra of the SS $\text{Yb}_2\text{Zr}_x\text{Ti}_{2-x}\text{O}_7$ samples clearly indicated that a pure phase was not achieved, which was not as evident in the XRD patterns of those samples. For $\text{Yb}_2\text{Ti}_2\text{O}_7$, the SG sample exhibited significant increases in intensity of some peaks, when compared to the SS sample, despite the fact that the XRD patterns of both are very similar. These differences were interpreted as signs of structural disorder in the SG $\text{Yb}_2\text{Ti}_2\text{O}_7$ sample.

It is notable that many of Raman spectra, including that of SG $\text{Yb}_2\text{Ti}_2\text{O}_7$, clearly displayed a low-frequency T_{1u} peak, which is infrared-active but should not be Raman-active for the ideal pyrochlore structure. The activation of this usually inactive vibrational mode probably stems from structural distortions that displace the A^{3+} ion from its ideal position, so that the inversion symmetry of the pyrochlore 16d site no longer exactly applies.

Despite the fact that the average long-range structure of some samples is a fluorite, there is some incipient local ordering of the pyrochlore-type, which could be seen as very weak diffuse superstructure peaks in the XRD patterns. Raman spectroscopy, given the local nature of the probe, is much better suited to detect such local structural correlations. The local order of all of the fluorite samples resembled those of the pyrochlore samples, except for the absence of the

A_{1g} mode, which could be used as a distinguishing feature for the two long-range structures.

Comparison of the Raman spectrum for the $\text{Yb}_2\text{Zr}_2\text{O}_7$ sample showed remarkable similarities to that reported in the literature for $\text{Yb}_4\text{Zr}_3\text{O}_{12}$, confirming that the $\text{Yb}_2\text{Zr}_2\text{O}_7$ possesses a δ -phase structure, despite having a different stoichiometry than the typical $\text{A}_4\text{B}_3\text{O}_{12}$ δ -phase.

Unfortunately we could not extract much reliable structural information from Raman spectroscopy due to difficulties with deconvoluting the experimental spectra and inconsistencies among the literature reports regarding the interpretation of pyrochlore Raman modes. There remain many open questions concerning the interpretation of the Raman spectra of the $\text{Yb}_2\text{Zr}_x\text{Ti}_{2-x}\text{O}_7$ compounds, which are addressed by some of the suggestions in Section 8.2.

In Chapter 7 we described the instrumentation for low-temperature magnetization and AC magnetic susceptibility measurements, and how the data was analyzed. The magnetization was measured at $T = 1.2\text{K}$, in the paramagnetic region of the $\text{Yb}_2\text{Zr}_x\text{Ti}_{2-x}\text{O}_7$ compounds, applying magnetic fields up to $H = 14.5\text{T}$. The $m(H)$ magnetization curves saturate at quite different levels for the different compositions, ranging from $m \approx 1.75\mu_B/\text{Yb}$ to $m \approx 2.35\mu_B/\text{Yb}$. To investigate if the apparently random variation is due to measurement error, the magnetic moments were correlated with the AC susceptibility measured at the same temperature ($T = 1.2\text{K}$), showing that indeed there is some correlation between these quantities.

A comparison of the magnetization curve $m(H)$ of the SG $\text{Yb}_2\text{Ti}_2\text{O}_7$ sample to that reported in the literature, shows that our sample attains the same saturation level at high field, $H = 14.5\text{T}$, but $m(H)$ grows more slowly with increasing field H , which could be due to structural imperfections pinning magnetic domains, or similar effects arising from structural disorder.

AC magnetic susceptibility measurements were performed in the temperature range $0.06\text{K} \leq T \leq 4\text{K}$, using two different susceptometers, one contained in a pumped helium cryostat and the other in an adiabatic magnetic refrigerator. The AC frequency was kept fixed at $f = 155\text{Hz}$ for most measurements, although a few samples were measured with different frequencies to test for spin glass-like or other frequency-dependent dynamics, which were not observed.

In the temperature range $1\text{K} \leq T \leq 4\text{K}$ the samples exhibited paramagnetic behavior, with approximately linear inverse susceptibility. A Curie-Weiss fit in this range yielded values for the Curie-Weiss temperatures θ_{CW} and effective moments μ_{eff} . The θ_{CW} values are negative for all samples, although their magnitudes are small, on the order of 1K . This is somewhat unexpected, given that $\text{Yb}_2\text{Ti}_2\text{O}_7$ has a ferromagnetic ground state and therefore should have $\theta_{CW} > 0$. The μ_{eff} value for $\text{Yb}_2\text{Ti}_2\text{O}_7$ also is significantly greater than that reported in the literature. We believe that these issues may be due to the restricted temperature range over which the Curie-Weiss fit was performed, so the θ_{CW} and μ_{eff} values should not be considered reliable.

Both the SG and SS $\text{Yb}_2\text{Ti}_2\text{O}_7$ samples exhibit a significantly broadened susceptibility transition, when compared to data in the literature. As with the literature comparison of the magnetization, we believe that the broadening of the transition stems from the inferior quality of our samples, which contain some degree of structural defects. Despite being small, these defects could affect the low-temperature properties of $\text{Yb}_2\text{Ti}_2\text{O}_7$, given the extreme sensitivity of this compound to structural imperfections and non-stoichiometry.

Among the SG $\text{Yb}_2\text{Zr}_x\text{Ti}_{2-x}\text{O}_7$ samples sintered at high temperature, the susceptibility peak

temperature decreases almost linearly from $T_C \approx 280\text{mK}$ for $x = 0.0$ to $T_C \approx 84\text{mK}$ for $x = 2.0$. Therefore the transition to long range magnetic order is suppressed with increasing structural disorder, which is loosely proportional to x in $\text{Yb}_2\text{Zr}_x\text{Ti}_{2-x}\text{O}_7$. This suggests an increase in magnetic frustration with increasing zirconium content, heading towards a ground state with continuously fluctuating spins, for $\text{Yb}_2\text{Zr}_2\text{O}_7$. The transition temperature for the fluorite $\text{Yb}_2\text{Zr}_2\text{O}_7$ sample, sintered at 900°C , is below 65mK , the minimal temperature reachable with our equipment, so it is possible that this highly disordered structure harbors a spin liquid, with no long-range ordered magnetic ground state.

8.2 Future Work

A chemical analysis of the $\text{Yb}_2\text{Zr}_x\text{Ti}_{2-x}\text{O}_7$ samples should be performed to confirm that the proper stoichiometry was achieved. This is especially important for the samples fabricated by the sol-gel method, since it is possible that a small amount of the precursor chemicals adhered to the glassware, thereby altering the proportions of each element. We could not precisely determine the amounts of liquid titanium and zirconium precursors, due to the limited precision of the pipette used to measure the liquid's volume, and the rather uncertain density of these liquids.

Another possibility would be measuring the distribution of chemical elements using some spectroscopic technique that can be applied to nanometric regions of the samples, to detect if the samples are completely uniform or if chemical inhomogeneities exist. Such spectroscopic techniques could possibly provide information on the valence state of the ions contained in the compounds, which we assumed to take their nominal values (A^{3+} , B^{4+} , O^{2-}) throughout this work, an assumption that might not be completely justified.

For certain kinds of measurements single crystals are necessary, so it would be interesting if we could grow crystals of the $\text{Yb}_2\text{Zr}_x\text{Ti}_{2-x}\text{O}_7$ compounds. Crystals of pyrochlore compounds are usually grown from powder samples using the floating zone technique [335, 336, 337, 338]. Since our research group does not possess the equipment nor expertise for such an endeavor, collaboration with other researchers, which do have such resources, would be required.

We want to understand the origins of the structural distortions that occur for the $x = 0.3, 0.5$ $\text{Yb}_2\text{Zr}_x\text{Ti}_{2-x}\text{O}_7$ samples, the local ordering that gives rise to diffuse scattering, for the $x = 1.0, 1.5$ samples, and the cation ordering in the $x = 2.0$ sample. A promising avenue for such investigations would be to compare the experimental diffraction data to simulations, as was done in [80], using the DISCUS software. DISCUS (Diffuse Scattering and Defect Structure Simulations) is a general program to generate disordered atomic structures and compute the corresponding experimental data such as single crystal diffuse scattering or the atomic pair distribution function. Features include symmetry operations, Monte Carlo simulation capabilities, generation of domain structures and nanoparticle simulations [339].

Electron microscopy is widely used to investigate structural properties of pyrochlore and fluorite materials, especially transmission electron microscopy (TEM) [340, 341, 342, 230, 343, 219, 344, 219, 274, 272]. There are many TEM techniques, which can loosely be divided into imaging and diffraction, although these categories overlap. Electron diffraction is in some senses similar to x-ray and neutron diffraction, but complementary in scope to those techniques. TEM would be especially important to shed light on the short and long-range ordering in the

defect fluorites. It could determine whether the local order is more similar to a pyrochlore, weberite, or other structure, and understand how the incommensurate modulation of local units gives rise to a distinct average long-range order.

As we saw in Chapter 6, interpretation of the Raman spectra for the $\text{Yb}_2\text{Zr}_x\text{Ti}_{2-x}\text{O}_7$ compounds was not straightforward, as initially expected. To resolve the somewhat ambiguous vibrational mode assignments and extract useful structural parameters, we propose to computationally simulate the local structure, adjusting the parameters of the model until a good fit to the experimental spectrum is achieved. The same model could be used to calculate thermodynamic quantities, such as the heat capacity, entropy and enthalpy of the system, which are also accessible to experiment and could then be correlated with experimental data to further improve the model, as was done in [284].

It would be interesting to apply infrared spectroscopy to our samples, since infrared and Raman spectroscopy are complementary techniques, as explained in Chapter 6, and the combined information would provide a more complete picture of the local environment of the atoms in the materials. We could improve the information gained from Raman spectroscopy by measuring the samples at cryogenic temperatures (cryo-Raman) and/or using polarized light to aid in identifying the directional dependence of the vibrational modes.

Nuclear magnetic resonance (NMR) has also been used to study the structural properties of pyrochlore compounds [345, 272, 346, 347, 348, 349, 350, 351]. The NMR technique is very sensitive to the local crystalline environment of the active isotope, which could yield valuable information, especially on the structure of the oxygen lattice. This technique requires an NMR-active nucleus, so the sample may need to be enriched with a certain isotope, for instance ^{17}O , which has a natural abundance of only 0.04%. In the case of our samples we could also use ^{47}Ti and ^{49}Ti , whose natural abundance is 7.5% and 5.5%, respectively, although that would preclude measurements on Ti-free samples, such as $\text{Yb}_2\text{Zr}_2\text{O}_7$.

Low temperature specific heat measurements would be an important contribution to understanding the bulk properties of the $\text{Yb}_2\text{Zr}_x\text{Ti}_{2-x}\text{O}_7$ compounds. As was discussed in Section 3.12, the specific heat of $\text{Yb}_2\text{Ti}_2\text{O}_7$ is quite sensitive to structural imperfections and non-stoichiometry, so it would be interesting to see whether our $\text{Yb}_2\text{Ti}_2\text{O}_7$ samples have a specific heat signature that is similar to data in the literature, and how the substitution of Ti by Zr affects the specific heat, both the sharp transition at $T \approx 0.2\text{K}$ and the broad feature at $T \approx 2\text{K}$. The sharp specific heat transition might not be coupled to the magnetic susceptibility transition, given that they occur at slightly different temperatures even for high quality $\text{Yb}_2\text{Ti}_2\text{O}_7$ samples.

By integrating the magnetic contribution to the specific heat we can obtain the entropy associated with the spin configurations, which often yields important insights into low-temperature magnetism. A spin-wave fit to the specific heat in the ordered phase would provide strong evidence regarding the nature of the ground-state magnetic correlations, so that we could determine whether doping with Zr alters the delicate balance between ferromagnetism and antiferromagnetism that gives $\text{Yb}_2\text{Ti}_2\text{O}_7$ its unusual dynamic properties.

Neutron Scattering is an invaluable technique for studying condensed matter systems. Thermal and cold neutrons are uniquely suited to study both the structure and excitations of solid compounds, since they have wavelengths on the order of a few Ångstrom, the lattice plane

spacing of most crystals, and energies on the order 1meV–100meV, the typical energies of many dynamical phenomena in such materials.

Both x-rays and electrons scatter predominantly off the electrons contained in materials, and therefore are less sensitive to light elements. In the case of the magnetic pyrochlores oxides the cations are usually much heavier than the oxygen ions, so the contrast in scattering intensities renders the oxygen ions hardly visible to x-rays. Neutrons do not suffer from this limitation, since the scattering amplitudes of the elements vary somewhat erratically along the periodic table and are not proportional to the atomic mass, as they are for x-rays. Neutron and x-ray diffraction can often elucidate complementary aspects of the structure and combined Rietveld refinements can be performed to yield highly accurate crystal structures.

In addition to the increased light-element sensitivity, neutron scattering is an essential tool to study the structure and dynamics of the magnetic lattices in the pyrochlore compounds [342, 352, 353, 354, 355, 219, 356, 357, 219, 63, 356]. Unlike x-rays, neutrons carry a magnetic dipole moment, that can interact with the magnetic moments in the sample.

Neutron scattering, both elastic and inelastic, would be necessary to determine the structure and dynamics of the magnetic lattice in the $\text{Yb}_2\text{Zr}_x\text{Ti}_{2-x}\text{O}_7$ compounds. For instance, it is not clear how the substitution of Ti by Zr affects the microscopic hamiltonian parameters $J_1 - J_4$ in (3.54), so that the point corresponding to $\text{Yb}_2\text{Ti}_2\text{O}_7$ could move towards the FM/AFM phase boundary or to the intersection where a spin liquid is expected. Such experiments would also provide insight into single-ion effects, such as how the magnetic anisotropy evolves with composition, and two-ion interactions, which are of particular interest considering that increased frustration could dissolve the ordered ground state of $\text{Yb}_2\text{Ti}_2\text{O}_7$.

Another promising avenue for further research would be to investigate how the structural and magnetic properties of the $\text{Yb}_2\text{Zr}_x\text{Ti}_{2-x}\text{O}_7$ compounds evolve with applied pressure. As already noted in Chapter 1, chemical substitution effectively acts as a chemical pressure, so it can have similar effects to physical pressure. Thus applied pressure and chemical substitution both can push a material over boundaries in the structural or magnetic phase diagrams, and may interact in interesting and unpredictable ways.

A few previous studies have investigated how applied pressure changes the structural and magnetic properties of $\text{Yb}_2\text{Ti}_2\text{O}_7$. For instance, in [282] it was found that $\text{Yb}_2\text{Ti}_2\text{O}_7$ undergoes a transition from the cubic pyrochlore phase to a monoclinic phase at $P = 28.6\text{GPa}$, and in [163] it was demonstrated tha pressure stabilizes the SFM ground state, presumably moving the system away from the degenerate FM/AFM boundary. It could be that moderate applied pressure alters the location of the pyrochlore/fluorite and fluorite/ δ -phase transitions along the $\text{Yb}_2\text{Zr}_x\text{Ti}_{2-x}\text{O}_7$ series, and interesting changes in the magnetic properties might be induced as well.

8.2.1 EXAFS Proposal

X-ray absorption spectroscopy (XAS) is a versatile and interdisciplinary technique for the determination of local chemical and physical environment in a wide variety of materials, ranging from crystalline solids to complex structures such as proteins. For crystalline systems it is complementary to x-ray diffraction, which probes the long-range order, but it can also be applied to amorphous and disordered systems, such as glasses and liquids, that do not possess

any long-range order [358].

XAS experiments involve focusing a beam of x-rays onto a sample and measuring the transmission of x-rays in order to determine the absorption by the sample. There are also indirect ways of measuring the absorption, using x-ray fluorescence and Auger electrons, both these methods are less common. An absorption edge occurs when the incident x-ray energy matches the binding energy of an atomic electron within the sample. When the beam energy increases above the edge the absorption increases, causing a drop in the transmitted x-ray intensity. XAS is element-specific, since each absorption edge corresponds to the unique electron binding energy of a chemical element, and is especially sensitive to the oxidation state and coordination chemistry of the atoms.

The absorption spectrum, a plot of the x-ray absorption as a function of incident beam energy, can be loosely divided into two parts, x-ray absorption near edge structure (XANES) and extended x-ray absorption fine structure (EXAFS). XANES refers to the part of the spectrum containing the absorption edge itself and the pre-absorption region (slightly lower in energy), while EXAFS refers to the oscillations that occur in the region immediately above the absorption edge (slightly higher in energy).

When an atom absorbs an x-ray photon, one of its core electrons is ejected, leaving behind a core hole. The atoms surrounding the one that ejected the photoelectron function as point scatterers, changing the phase and amplitude of the photoelectron's wavefunction. Interference between the wavefunctions of the incoming photons and the ejected photoelectrons leads to a modulation of the absorption coefficient, and thereby creates oscillations in the region above the absorption edge. In this way the oscillations carry information on the local environment of the atom, such as distances, coordination number and species of the surrounding atoms [359].

The EXAFS technique has been applied to many pyrochlore compounds, often as a complement to diffraction experiments [286, 360, 361, 362, 363, 364, 352, 354, 355, 365, 356]. Therefore EXAFS would be an ideal method to extend our understanding of the local crystalline structure of the $\text{Yb}_2\text{Zr}_x\text{Ti}_{2-x}\text{O}_7$ compounds.

The EMA (Extreme condition Methods of Analysis) beamline at the LNLS synchrotron (in Campinas, Brazil) is optimized for the study of materials under extreme thermodynamic conditions, within wide ranges of pressure ($P \leq 1000\text{GPa}$), temperature ($0.5\text{K} \leq T \leq 8000\text{K}$) and magnetic fields ($B \leq 11\text{T}$) [366]. Since such conditions require small samples placed in specialized environments, the beamline is designed to have high brilliance, with a flux of up to 10^{14} photons/s and beamsizes down to $0.01\mu\text{m}^2$. This combination of extreme thermodynamic conditions will allow exploration of yet unreached points in $P - T - B$ phase diagrams, in order to tackle complex scientific problems in both applied and fundamental science, using advanced characterization methods such as absorption spectroscopy, diffraction and other scattering techniques.

Appendix A contains the proposal submitted to the regular call for research proposals, from November 8 to December 15 of 2022, of the Sirius Synchrotron, operated by the Brazilian Synchrotron Light Laboratory (LNLS) as a part of the Brazilian Center for Research in Energy and Materials (CNPEM). We proposed measuring the diffraction patterns and XANES/EXAFS for the $\text{Yb}_2\text{Zr}_x\text{Ti}_{2-x}\text{O}_7$ samples at the Yb L3 edge, Ti and Zr K-edges, at selected temperatures in the range $10\text{K} < T < 300\text{K}$. The proposal was rejected, partly due to the high demand at

the EMA beamline, but will be submitted again in the next call for proposals, after revising it to incorporate suggestions made by the LNLS reviewers.

8.2.2 PDF Proposal

The pair distribution function (PDF) is the sine Fourier transform of the total scattering pattern, including both Bragg and diffuse scattering, in a wide range of $Q = \frac{4\pi \sin \theta}{\lambda}$ [367, 368]. In conventional diffraction only sharp Bragg peaks, which arise from long range periodicity, are considered, while diffuse scattering is subtracted along with the background. Local deviations from long-range crystal periodicity give rise to diffuse scattering, which is not strongly localized in Q . In amorphous materials all the scattering is diffuse while in mostly crystalline materials there is both Bragg and diffuse scattering. In a total scattering experiment all the structural information in reciprocal space, contained in both Bragg and diffuse scattering, is used to generate the real space PDF.

The PDF is a radial distribution function of atoms in the sample, thus peaks in the PDF represent pairs of atoms at a certain distance apart from one another. Even in a perfect crystal the peaks are not sharp delta functions because of the thermal motion of the atoms. In addition the peaks can also broaden due to a distribution of pair distances in the material, as occurs with mostly crystalline materials that are to some extent disordered. Therefore the PDF analysis is well suited for both crystalline and amorphous materials and anything in between.

This technique can be applied to diffraction data collected with probes such as x-rays, neutrons and even electrons [369, 370]. The maximal scattering vector Q_{max} , corresponding to the highest 2θ value, is inversely proportional to the real-space resolution, so a high Q_{max} is required to resolve the atomic pairs. In the case of x-ray total scattering this requirement usually implies synchrotron radiation, since laboratory diffractometers have a limited range in reciprocal space. The PDF technique can be applied to data collected with molybdenum and silver laboratory sources ($Q_{max} \approx 17$ and $Q_{max} \approx 22$, respectively) but not with a copper source ($Q_{max} \approx 8$). To obtain reliable diffuse scattering data it is necessary to accurately measure the background noise and diffuse scattering from the sample container and acquire high statistics data, with good signal to noise ratio.

PDF analysis has been widely applied to materials in the pyrochlore family, using both neutrons [226, 371, 372, 340, 373, 230, 223, 374, 375, 231, 63, 376, 377] and synchrotron x-ray probes [340, 360, 361, 230, 376]. As far as synchrotron PDF is concerned, it is similar to EXAFS in the sense that both techniques provide information on the local crystalline structure, but there are some important differences. The PDF technique is better suited to detect short to medium range correlations, on the order of tens of Ångstrom, while EXAFS is practically limited to very short range correlations, on the order of a few Ångstrom.

PDF combines the pair distance information for all elements in the sample, while EXAFS is element-specific, since the energy of the x-ray probe is tuned to the absorption edge of an element. This is advantageous since it is possible to study the local environment surrounding crystalline sites with a specific element, but also requires more measurements (one for each relevant element) than a single total scattering measurement. Also, in some cases there is no appropriate absorption edge for an element, either because the edge energy is too low or the absorption edges of two elements are too closely spaced to detect the EXAFS oscillations.

The Jatobá and Paineira beamlines at the LNLS synchrotron (in Campinas, Brazil) are well suited for total scattering experiments [378]. The Jatobá beamline is currently in its design phase and will be dedicated to the study of a wide range of materials using the total scattering technique. The Paineira beamline, on the other hand, is not designed specifically for the requirements of total scattering but is already in its scientific commissioning phase as of the start of 2023. It is optimized for high-throughput x-ray diffraction of polycrystalline materials in Debye-Scherrer geometry (capillary geometry or transmission mode). Using the highest possible beam energy, 30keV, would allow us to reach $Q_{max} = 29\text{\AA}^{-1}$ in reciprocal space, sufficient for a PDF analysis (Jatobá will be able to reach $Q_{max} = 37\text{\AA}^{-1}$).

Appendix B contains a test proposal submitted as part of the Ricardo Rodrigues Synchrotron Light School (ER2LS), from July 5 to July 16 of 2022, offered by the Brazilian Center for Research in Energy and Materials (CNPEM). The test proposal was intended to give participants the experience of writing a proposal for the Sirius Synchrotron. We proposed measuring powder diffractograms of $\text{Yb}_2\text{Zr}_x\text{Ti}_{2-x}\text{O}_7$ samples at various temperatures, from 300K down to $\sim 100\text{K}$, at the Paineira beamline. This test proposal is currently awaiting unofficial review by researchers at the Brazilian Synchrotron Light Laboratory (LNLS) and, after corrections suggested by them, will (we hope) be submitted as an actual proposal in the next open call, after commissioning of the Paineira beamline.

EXAFS Proposal

This appendix contains the proposal submitted to the regular call for research proposals, from November 8 to December 15 of 2022, of the Sirius Synchrotron, operated by the Brazilian Synchrotron Light Laboratory (LNLS) as a part of the Brazilian Center for Research in Energy and Materials (CNPEM). We proposed measuring the diffraction patterns and XANES/EXAFS for the $\text{Yb}_2\text{Zr}_x\text{Ti}_{2-x}\text{O}_7$ samples at the Yb L3 edge, Ti and Zr K-edges, at selected temperatures in the range $10\text{K} < T < 300\text{K}$. The proposal was rejected, partly due to the high demand at the EMA beamline, but will be submitted again in the next call for proposals, after revising it to incorporate suggestions made by the LNLS reviewers.

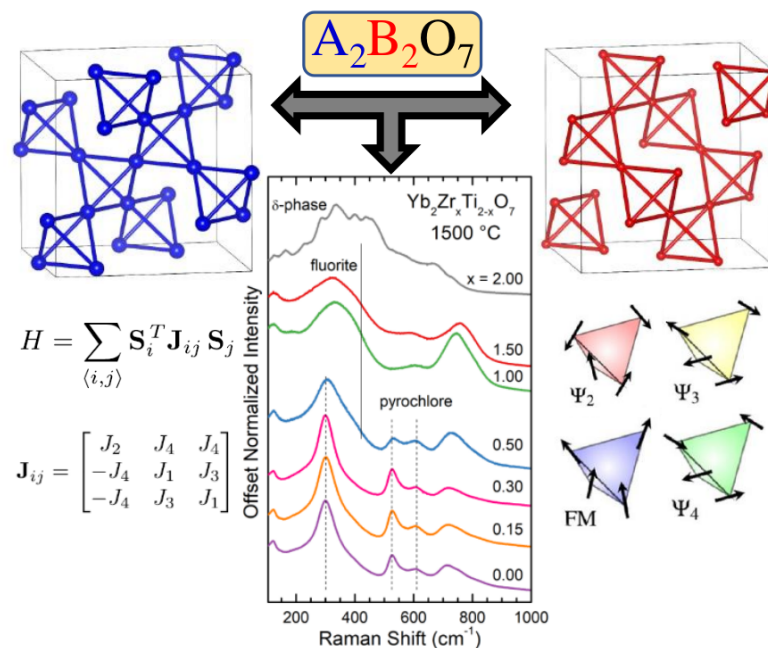


Figure A.1 Graphical abstract submitted as part of the research proposal.

Title

Evolution of local structural disorder in the series of compounds $\text{Yb}_2\text{Zr}_x\text{Ti}_{2-x}\text{O}_7$

Proposers

Main Proposer: Prof. Rafael Sá de Freitas

Principal Investigator (*): Prof. Rafael Sá de Freitas

Co-Proposer: Prof. Fernando Assis Garcia

Experiment Category

Proposal Type: Normal

Research area (*): Physics

Research subarea (*): Materials Physics

Is this proposal related to COVID-19? (*): No

Experiment Requirements

Beamline: EMA

Number of shifts required (*): 12

Support facilities associated with this proposal

LCTE - Laboratory of Extreme Thermodynamic Conditions

Justify the use of this support facility related to the beamline proposal:

Experiment technique

**What is your experience with the technique? Which facilities have you used?
(max 400 characters)**

Our group has ample experience with XANES and EXAFS experiments performed at the LNLS XDS, XAFS2 and EMA beamlines under a range of temperature, pressure and polarization conditions.

Justification for the use of the synchrotron technique

Why does this proposal need Synchrotron Radiation? (max 400 characters)

This proposal is dedicated to the crystal and electronic structures of the series of compounds $\text{Yb}_2\text{Zr}_x\text{Ti}_{2-x}\text{O}_7$. We intend to investigate the Yb, Ti and Zr local electronic and coordination structures by x-ray absorption spectroscopy (XAS) at the Yb L3 edge and Ti and Zr K edges. No conventional source is able to provide high statistics measurements in this energy range.

Involvement with education

Does this proposal involve Msc or Phd students?: Yes

Student 1: Francisco Lieberich

Student 2:

Student 3:

Months for the defense of the thesis: 5

Funding agency

This proposal is associated with scientific project funded by a funding agency?:
Yes

Agency (*): FAPESP

Grant number (*): 2019/25665-1

Abstract of the research proposal

Abstract (max 5 lines):

$\text{Yb}_2\text{Ti}_2\text{O}_7$ undergoes a structural transition from pyrochlore to defect fluorite as Ti is substituted by Zr, resulting in the series of novel compounds $\text{Yb}_2\text{Zr}_x\text{Ti}_{2-x}\text{O}_7$. We propose XRD and XAS experiments to determine the amount of structural disorder and the local electronic and coordination structures of Yb, Zr, Ti, as the composition varies from $x = 0$ to $x = 2$ in $\text{Yb}_2\text{Zr}_x\text{Ti}_{2-x}\text{O}_7$.

Description of the research proposal (max 2500 characters for all fields)

Is this a continuation of a previous proposal?

This is not a continuation proposal.

Scientific background

The pyrochlore family, consisting of over 200 compounds with the structural formula $A_2B_2O_7$, has been explored for a wide range of applications and is one of the most promising experimental models of frustrated magnetism [1]. The extensively studied $Yb_2Ti_2O_7$ pyrochlore is a prominent example of magnetic frustration, displaying a rich magnetic phenomenology, including a puzzling almost-gapless excitation spectrum. Our current understanding [2] of $Yb_2Ti_2O_7$ is that it lives at the very edge of competing ferromagnetic and antiferromagnetic phases, a conclusion already anticipated by the sensitivity to non-stoichiometry at a $< 1\%$ level on bulk magnetic and calorimetric properties [3]. When Ti is gradually substituted by Zr in $Yb_2Ti_2O_7$ the material undergoes a structural transition from an ordered pyrochlore to a disordered defect fluorite, culminating in the even less symmetric δ -phase for $Yb_2Zr_2O_7$. There are no previous studies on magnetic properties of $Yb_2Zr_2O_7$ or on the intermediary compounds $Yb_2Zr_xTi_{2-x}O_7$.

The magnetic properties of materials with localized moments depend on the electronic and coordination structures of the magnetic cation, which is Yb in the case of $Yb_2Ti_2O_7$. Substituting Ti by Zr does not introduce new spins since the magnetism is exclusively associated with Yb ions. Therefore the observed changes in magnetic properties along the series $Yb_2Zr_xTi_{2-x}O_7$ are driven by changes in the electronic properties and coordination of Yb. The possibilities may include an increase in quenched disorder, defects (in particular at the O sites), changes in coordination number/geometry and even changes in the Yb valence, from the predominant 3+ to the less common 2+, thereby directly affecting magnetic properties. Alternatively, the introduction of Zr could change the Ti oxidation state from 4+ to a rare 3+ state, which has spin degrees of freedom.

Whereas x-ray absorption spectroscopy (XAS) provides valuable information on the previously mentioned local properties, synchrotron x-ray diffraction (XRD) can reveal details of the long range crystal structure that cannot be resolved by conventional XRD. We intend to probe these short and long-range properties as the material evolves, through chemical substitution, from an ordered pyrochlore into the disordered fluorite and δ -phase structures. Correlating both datasets will provide crucial information required to understand the magnetic ground state in these compounds.

Expected results

We propose temperature dependent XAS and XRD experiments of selected materials in the series $\text{Yb}_2\text{Zr}_x\text{Ti}_{2-x}\text{O}_7$. The XAS experiments will probe the Yb L3 edge and Ti/Zr K-edges at five temperature points, from about 10K to 300K, including the near edge spectra (XANES, to probe electronic structure) and the extended fine structure (EXAFS, to probe the local structure). The XRD experiments will be performed at 300K and 20K. From the XAS experiments we expect to determine: i) the amount of quenched and dynamic disorder of the Yb-O, Ti-O and Zr-O bonds; ii) the Yb, Ti and Zr coordination structure, in particular the amount of O defects; iii) the Yb, Ti and Zr valences. From the XRD experiments we expect high resolution data to reveal details of the long-range order, especially deviations from the ideal pyrochlore and defect fluorite structures. Low temperature experiments will probe possible structural transitions or distortions that would be of fundamental relevance to low temperature magnetic properties. Results from XRD and XAS will be compared to attain a complete structural characterization of the $\text{Yb}_2\text{Zr}_x\text{Ti}_{2-x}\text{O}_7$ series. This will allow an accurate understanding of how the evolution of magnetic properties along the series $\text{Yb}_2\text{Zr}_x\text{Ti}_{2-x}\text{O}_7$ depends on the structure of the frustrated lattice, with a particular focus on structural disorder.

Previous characterization

Usually pyrochlore compounds are synthesized by the solid-state reaction (SS). As an alternative, in the sol-gel method (SG) precursor chemicals are mixed in liquid form and the resulting gel is dried out to obtain the desired product. We synthesized samples of $\text{Yb}_2\text{Zr}_x\text{Ti}_{2-x}\text{O}_7$, with $x = 0.0, 0.15, 0.3, 0.5, 1.0, 1.5, 2.0$, using both methods, to understand the relative advantages of each synthetic route. Pure phase SS samples could not be obtained, except for $x = 0.0$, even after sintering at 1500°C for many days with multiple intermediate grindings, whereas SG samples are all pure phase. Structural properties were determined by conventional $\text{Cu K}\alpha$ x-ray diffraction (XRD) and Raman spectroscopy (RS), using a 532nm wavelength laser.

With increasing x in $\text{Yb}_2\text{Zr}_x\text{Ti}_{2-x}\text{O}_7$ the structure changes from a pyrochlore to a defect fluorite at $x = 0.5$. In the range $0.5 \leq x < 2.0$ the defect fluorite phase is stable, although XRD and RS spectra display weak pyrochlore superstructure correlations. For $x = 2.0$ the $\text{Yb}_4\text{Zr}_3\text{O}_{12}$ δ -phase structure is stable. RS spectra of SG samples reveal the presence of significant crystallographic site disorder, through broadening of vibrational Raman modes and appearance of IR modes that are Raman-inactive in an ideal, ordered structure (figs. 1 and 2). AC magnetic susceptibility measurements show that with increasing Zr content the transition temperature to the magnetic ground state decreases, consistent with the expectation that structural disorder suppresses magnetic ordering (fig. 3).

Experimental method

High statistics Yb L3, Ti and Zr K-edge XAS spectra will be measured for a total of 5 samples, at selected temperatures in the range $10K < T < 300K$. The temperature variation will allow us to better distinguish the intrinsic and thermal disorder of the Yb-O, Ti-O and Zr-O bonds as well as the degree of O defects (EXAFS) and the Yb, Ti and Zr valences (XANES). A conventional He-flow cryostat will be employed during measurements. The powder samples will be mounted on membranes and measured in transmission mode.

The Yb XANES spectra will be fitted to a lineshape to extract the phenomenological information about the Yb^{3+} and Yb^{2+} components. The Yb-O, Ti-O, Zr-O bond disorder and O defects will be determined by applying multiple scattering theory to the respective EXAFS spectra. Several models for O defects will be tested by creating artificial defects in the cluster scattering potential around each absorbing atom.

Experimental conditions

The temperature dependent measurements require a helium flow cryostat to be used in the temperature interval $10K < T < 300K$. The EMA energy will have to be changed from the Yb L3 edge (8.944 keV), to the Ti K edge (4.966 keV) and then to the Zr K edge (17.998keV). In total, we shall characterize 5 samples, all in polycrystalline form. We require use of the chemistry laboratory to crush and sieve the powder samples for better homogeneity.

Allocated time requested

We request 12 shifts of EMA beamtime, thus organized: 3 shifts dedicated to XRD experiments (5 samples, 2 temperatures) and 9 shifts dedicated to XAS experiments (5 samples x 3 edges x 5 temperatures = 75 spectra). The requested time already takes into account some contingency time.

References

- [1] Jason S. Gardner, Michel J. P. Gingras, and John E. Greedan. “Magnetic pyrochlore oxides”. In: *Rev. Mod. Phys.* 82 (2010), pp. 53–107. DOI: 10.1103/RevModPhys.82.53.
- [2] Allen Scheie et al. “Multiphase magnetism in $Yb_2Ti_2O_7$ ”. In: *Proceedings of the National Academy of Sciences* 117.44 (2020), pp. 27245–27254. DOI: 10.1073/pnas.2008791117.
- [3] K. E. Arpino et al. “Impact of stoichiometry of $Yb_2Ti_2O_7$ on its physical properties”. In: *Phys. Rev. B* 95 (2017), p. 094407. DOI: 10.1103/PhysRevB.95.094407.
- [4] M. L. Sanjuán et al. “Raman and x-ray absorption spectroscopy study of the phase evolution induced by mechanical milling and thermal treatments in $R_2Ti_2O_7$ pyrochlores”. In: *Physical Review B* 84.10 (2011), p. 104207. DOI: 10.1103/PhysRevB.84.104207.

- [5] S.-W. Han, J. S. Gardner, and C. H. Booth. “Structural properties of the geometrically frustrated pyrochlore $\text{Tb}_2\text{Ti}_2\text{O}_7$ ”. In: *Physical Review B* 69.2 (2004), p. 024416. DOI: 10.1103/PhysRevB.69.024416.

Figures PDF

See last pages of this PDF.

Scientific activity (publications) of the proposers

Please list proposer’s publications within the last 3 years.

LNLS related publications (list the most relevant, maximum of 10 publications)

The publications must be registered in the SAU Online database and you may access them from the [List of publications].

- [1] Juliana G. de Abrantes et al. “Vibrational and structural properties of the $R\text{Fe}_4\text{Sb}_{12}$ ($R = \text{Na}, \text{K}, \text{Ca}, \text{Sr}, \text{Ba}$) filled skutterudites”. In: *Phys. Rev. Materials* 6 (2022), p. 085403. DOI: 10.1103/PhysRevMaterials.6.085403.
- [2] M. R. Cantarino et al. “Dynamic magnetism in the disordered hexagonal double perovskite $\text{BaTi}_{1/2}\text{Mn}_{1/2}\text{O}_3$ ”. In: *Phys. Rev. B* 99 (2019), p. 054412. DOI: 10.1103/PhysRevB.99.054412.
- [3] A. G. de Figueiredo et al. “Orbital localization and the role of the Fe and As 4p orbitals in BaFe_2As_2 probed by XANES”. In: *Phys. Rev. B* 105 (2022), p. 045130. DOI: 10.1103/PhysRevB.105.045130.

Other relevant publications to support the proposal (maximum of 5 publications)

Mandatory fields: Title, journal, volume, page and year; OR Title and DOI or link to the publication.

- [1] J. G. A. Ramon et al. “Absence of spin-ice state in the disordered fluorite $\text{Dy}_2\text{Zr}_2\text{O}_7$ ”. In: *Phys. Rev. B* 99 (2019), p. 214442. DOI: 10.1103/PhysRevB.99.214442.
- [2] J.G.A. Ramon et al. “Glassy correlated state induced by disorder in the frustrated antiferromagnet $\text{Tb}_2\text{Zr}_2\text{O}_7$ ”. In: *Journal of Magnetism and Magnetic Materials* 565 (2023), p. 170215. DOI: <https://doi.org/10.1016/j.jmmm.2022.170215>.

- [3] Ivica Zivkovic et al. “Magnetic Field Induced Quantum Spin Liquid in the Two Coupled Trillium Lattices of $\text{K}_2\text{Ni}_2(\text{SO}_4)_3$ ”. In: *Phys. Rev. Lett.* **127** (2021), p. 157204. DOI: [10.1103/PhysRevLett.127.157204](https://doi.org/10.1103/PhysRevLett.127.157204).
- [4] M. Shirai et al. “Doping-induced quantum crossover in $\text{Er}_2\text{Ti}_{2-x}\text{Sn}_x\text{O}_7$ ”. In: *Phys. Rev. B* **96** (2017), p. 180411. DOI: [10.1103/PhysRevB.96.180411](https://doi.org/10.1103/PhysRevB.96.180411).

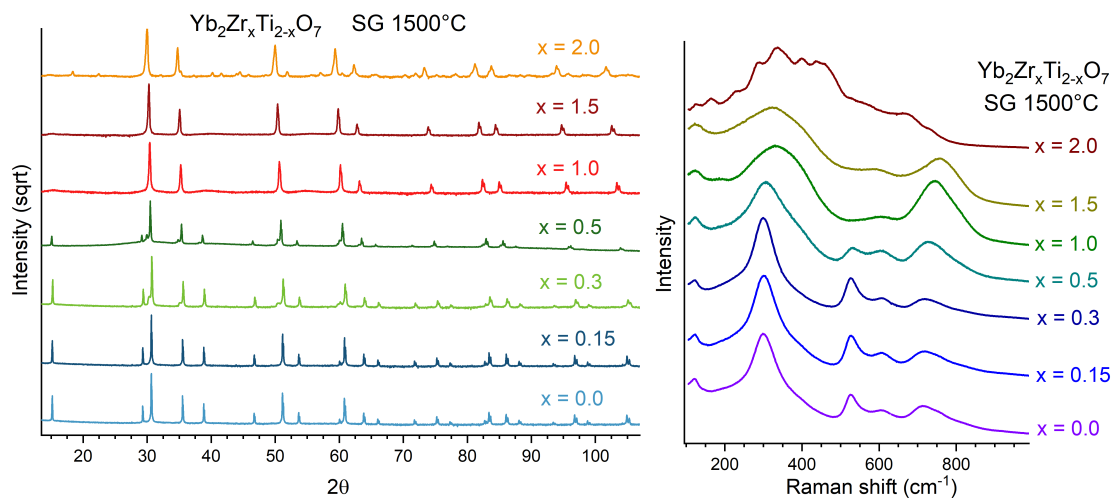


Figure 1: XRD and RS spectra of SG $\text{Yb}_2\text{Zr}_x\text{Ti}_{2-x}\text{O}_7$, sintered at 1500°C .

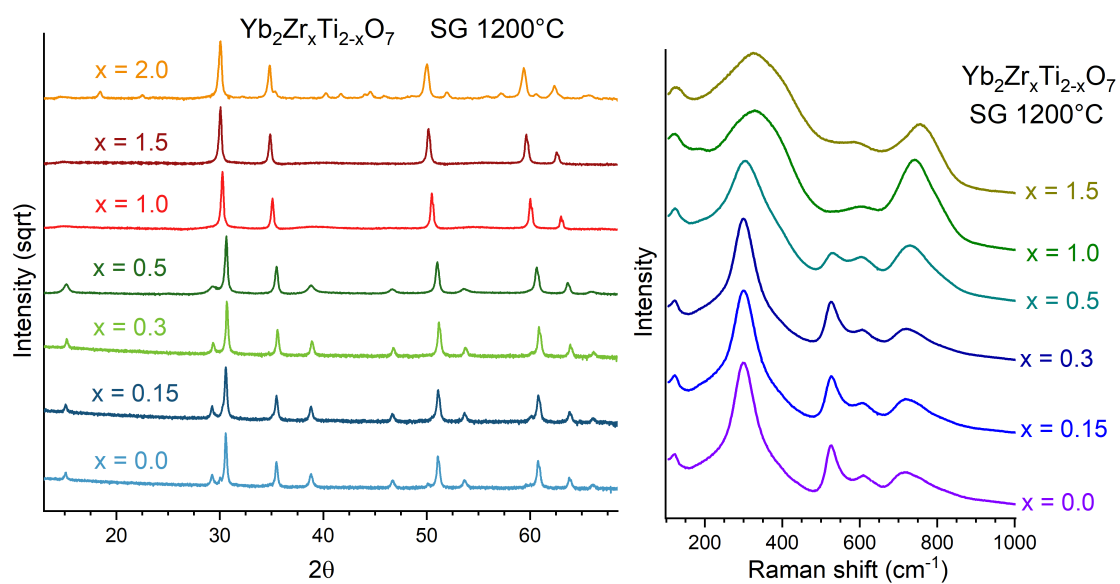


Figure 2: XRD and RS spectra of SG $\text{Yb}_2\text{Zr}_x\text{Ti}_{2-x}\text{O}_7$, sintered at 1200°C .

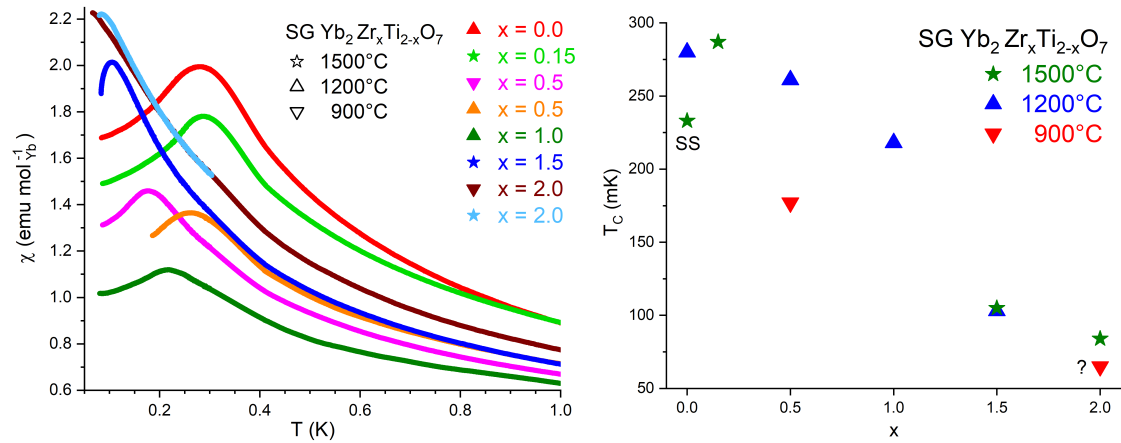


Figure 3: AC magnetic susceptibility χ ($f = 155\text{Hz}$) and transition temperatures T_C of SG $\text{Yb}_2\text{Zr}_x\text{Ti}_{2-x}\text{O}_7$.

PDF Proposal

This appendix contains a test proposal submitted as part of the Ricardo Rodrigues Synchrotron Light School (ER2LS), from July 5 to July 16 of 2022, offered by the Brazilian Center for Research in Energy and Materials (CNPEM). The test proposal was intended to give participants the experience of writing a proposal for the Sirius Synchrotron. We proposed measuring powder diffractograms of $\text{Yb}_2\text{Zr}_x\text{Ti}_{2-x}\text{O}_7$ samples at various temperatures, from 300K down to $\sim 100\text{K}$, at the Paineira beamline. This test proposal is currently awaiting unofficial review by researchers at the Brazilian Synchrotron Light Laboratory (LNLS) and after corrections suggested by them will (we hope) be submitted as an actual proposal in the next open call, after commissioning of the Paineira beamline.

What is your experience with the technique? Which facilities have you used? (max 400 characters)

Our group has ample experience with laboratory x-ray diffraction data collection and analysis. Although we have not had previous opportunity to apply PDF analysis, a member of our group was introduced to the technique at the ER2LS school on synchrotron techniques, offered by CNPEM, and is currently learning more on the topic through reading several books and scientific publications.

Why does this proposal need Synchrotron Radiation? (max 400 characters)

The subtle structural disorder present in pyrochlore and defect fluorite compounds cannot be detected with conventional x-ray sources since it requires high resolution data in a large swath of reciprocal space, with good statistics and accurate background subtraction. These requirements make synchrotron radiation an ideal technique for such investigations.

Abstract (max 400 characters)

$\text{Yb}_2\text{Ti}_2\text{O}_7$ undergoes a structural transition from pyrochlore to defect fluorite as Ti is substituted by Zr, resulting in the series of novel compounds $\text{Yb}_2\text{Zr}_x\text{Ti}_{2-x}\text{O}_7$. We propose a PDF analysis of synchrotron powder diffraction data, to characterize the local structure in these materials. An improved structural knowledge will provide crucial information required to understand the magnetic ground state.

Is this a continuation of a previous proposal? (max 2500 characters)

This is not a continuation proposal.

Scientific background (max 2500 characters)

The pyrochlore family of materials, consisting of over 200 compounds with the structural formula $\text{A}_2\text{B}_2\text{O}_7$, has been explored for many scientific and technological applications and is regarded as one of the most promising experimental models of frustrated magnetism [1]. The extensively studied $\text{Yb}_2\text{Ti}_2\text{O}_7$ pyrochlore is a prominent example of magnetic frustration, displaying a rich magnetic phenomenology, including a puzzling almost-gapless excitation spectrum. Our current understanding [2] of $\text{Yb}_2\text{Ti}_2\text{O}_7$ is that it lives at the very edge of competing ferromagnetic and antiferromagnetic phases, a conclusion already anticipated by the sensitivity to non-stoichiometry at a $< 1\%$ level on bulk magnetic and calorimetric properties [3]. When Ti is gradually substituted by Zr in $\text{Yb}_2\text{Ti}_2\text{O}_7$ (increasing x in $\text{Yb}_2\text{Zr}_x\text{Ti}_{2-x}\text{O}_7$), the material undergoes a structural transition from an ordered pyrochlore to a disordered defect fluorite, culminating in the even less symmetric δ -phase for $\text{Yb}_2\text{Zr}_2\text{O}_7$. The disordering of the pyrochlore structure occurs simultaneously through

oxygen vacancies and cation antisite defects, a somewhat unusual situation when compared to other materials that disorder upon chemical substitution. There are no previous studies on magnetic properties of $\text{Yb}_2\text{Zr}_2\text{O}_7$ or of the intermediary compounds $\text{Yb}_2\text{Zr}_x\text{Ti}_{2-x}\text{O}_7$. Recent studies have shown that pyrochlore and defect fluorite compounds display a subtle interplay of order and disorder on a scale of a few unit cells. One study [4] applied a wide array of experimental techniques, including neutron and synchrotron PDF analysis, to demonstrate a slight lattice distortion in $\text{Yb}_2\text{Ti}_2\text{O}_7$ and $\text{Pr}_2\text{Zr}_2\text{O}_7$, conjectured to be universal among pyrochlores. Another study [5] applied neutron PDF analysis to $\text{Ho}_2\text{Zr}_2\text{O}_7$, suggesting that this material possesses a short range weberite-type structure, which appears as a disordered fluorite when observed at long range. Most commonly the pyrochlore family compounds are synthesized by the traditional solid-state reaction (SS). As an alternative, in the sol-gel method (SG) precursor chemicals are mixed in liquid form and the resulting gel is dried out to obtain the desired product. Our group synthesized samples using both methods, to compare their properties and understand the relative advantages of each synthetic route.

Expected results (max 2500 characters)

We expect to characterize local correlations between atoms in $\text{Yb}_2\text{Zr}_x\text{Ti}_{2-x}\text{O}_7$ samples through a total scattering PDF analysis, complementing the long-range structure deduced from conventional XRD, which neglects diffuse scattering and focuses on Bragg peaks. PDF analysis would be an invaluable aid to understanding the subtle disorder in these structures, since it can determine correlations between atoms on a local scale, as opposed to the global information extracted from Bragg peaks. Most of our fluorite samples show weak pyrochlore superstructure reflections. It is not evident whether these arise from correlations among atoms in the fluorite phase or from spatially localized pyrochlore domains embedded in a fluorite matrix. We also are interested in effects of sintering temperature on structure, given that most samples undergo a phase transition upon heating to about 1000°C , from a metastable phase to a more ordered stable phase. PDF analysis will clarify how order and disorder coexist in the disordered metastable phase and to what degree this disorder persists when heated above 1000°C . For $\text{Yb}_2\text{Zr}_2\text{O}_7$ samples the high temperature stable structure is a δ -phase, which can belong to two distinct space groups, depending on the form of site disorder assumed. PDF analysis will improve our understanding of this rather uncommon structure. Another issue that will benefit from synchrotron data is the poor reliability of refinement results concerning oxygen ion disorder and non-stoichiometry, given the weak scattering of oxygen under conventional x-ray sources. Synchrotron diffraction results will be compared to those obtained using other analytical techniques, such as Raman scattering, which is sensitive to local order through its effect on atomic vibrational modes. Raman scattering is complementary to XRD, in that it is sensitive to deviations from crystalline order and better suited to detect distortions or vacancies in the oxygen lattice. Understanding of low-temperature properties such as magnetic susceptibility and magnetization requires detailed knowledge on the structure of the lattice formed by the

magnetic ions, which can be deduced from diffraction data by the PDF technique. The proposed experiments would provide a solid contribution to understanding the relation between structural and magnetic properties in this class of materials, as the composition evolves through chemical substitution from an ordered to a disordered state.

Previous characterization (max 2500 characters)

Structural properties were determined by conventional Cu K α XRD, indicating that SS (solid-state) samples are more crystalline than SG (sol-gel) samples (fig. 1). Rietveld refinement of this data (fig. 2) reveals increased crystallographic site disorder and strain in SG samples. Raman scattering spectra (fig. 3) confirm the presence of disorder, through broadening of the vibrational modes and appearance of IR modes that are Raman-inactive in an ideal ordered structure. Magnetic susceptibility measurements (fig. 4) show that with increasing Zr content the transition temperature to the magnetic ground state decreases, consistent with the expectation that structural disorder suppresses magnetic ordering. Low-temperature magnetization data (fig. 5) have not yet been adequately modeled since they depend crucially on the local structure of the magnetic lattice.

Experimental method (max 2500 characters)

Powder diffractograms will be collected at the Paineira beamline for a total of 15 samples. Using a beam energy of 30keV ($\lambda = 0.41\text{\AA}$) and angular range $2\theta \leq 145^\circ$ it is possible to reach $Q_{\max} = 29\text{\AA}^{-1}$. Results will be analyzed by Rietveld refinement with GSAS-II, PDF analysis with the DiffPy software suite, and RMC (Reverse Monte Carlo) simulations with RMCProfile.

Experimental conditions (max 2500 characters)

Experiments will be performed at ambient temperature and at the minimum temperature reachable with the cryojet cooler ($\sim 100\text{K}$). Our samples have very high absorption and therefore require very thin capillary tubes (0.3mm or 0.5mm diameter). The beamline energy has to be set at its maximum (30keV for Paineira) to maximize the range in reciprocal space. The detector has to be repositioned to cover the maximal angular range ($3^\circ \leq 2\theta \leq 145^\circ$). We require use of the chemistry laboratory to crush and sieve the powder samples for better homogeneity.

Allocated time requested (max 2500 characters)

We propose to measure powder diffractograms of 15 samples, requiring three 8h shifts at the Paineira beamline. This includes time to change the beamline energy and instrument configurations, cool the samples and empty capillary tubes (necessary for background subtraction), perform the measurements, and some contingency.

References (max 2500 characters)

- [1] Jason S. Gardner, Michel J. P. Gingras, and John E. Greedan. “Magnetic pyrochlore oxides”. In: *Rev. Mod. Phys.* 82 (1 Jan. 2010), pp. 53–107.
- [2] Allen Scheie et al. “Multiphase magnetism in $\text{Yb}_2\text{Ti}_2\text{O}_7$ ”. In: *Proceedings of the National Academy of Sciences* 117.44 (2020), pp. 27245–27254.
- [3] K. E. Arpino et al. “Impact of stoichiometry of $\text{Yb}_2\text{Ti}_2\text{O}_7$ on its physical properties”. In: *Phys. Rev. B* 95 (9 Mar. 2017), p. 094407.
- [4] B. A. Trump et al. “Universal geometric frustration in pyrochlores”. In: *Nature Communications* 9.1 (2018), p. 2619.
- [5] Jacob Shamblin et al. “Probing disorder in isometric pyrochlore and related complex oxides”. In: *Nature Materials* 15.5 (2016), pp. 507–511.

Attached PDF with figures and tables (max 2 pages, 10MB)

see next page

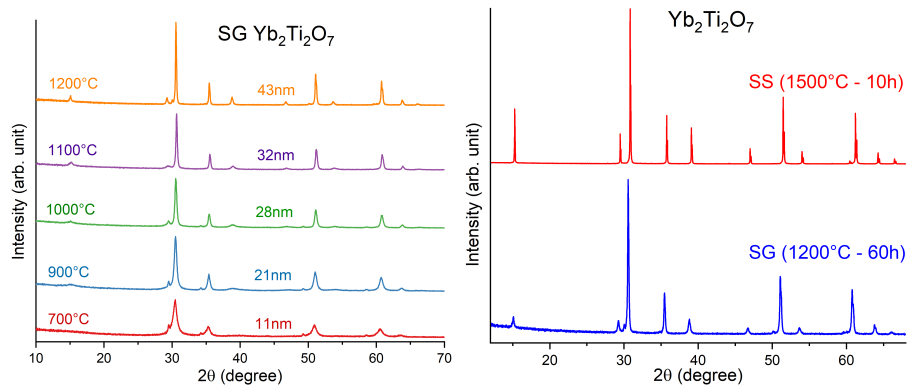


Figure 1: $\text{CuK}\alpha$ x-ray diffractograms of SG and SS $\text{Yb}_2\text{Ti}_2\text{O}_7$, sintered at various temperatures.

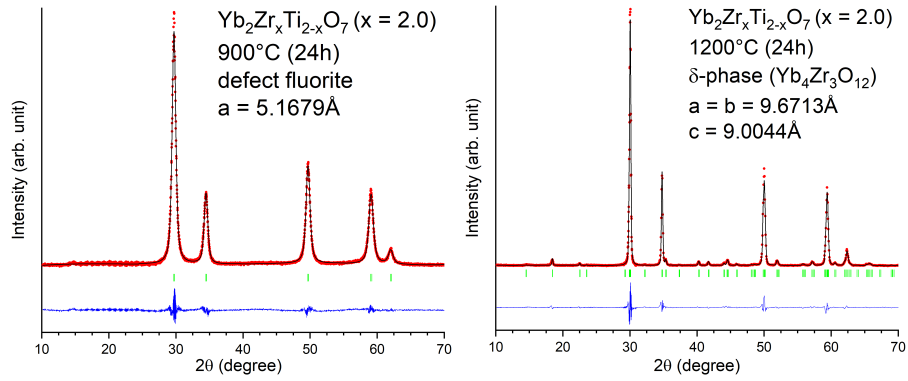


Figure 2: Examples of Rietveld refinement for SG $\text{Yb}_2\text{Zr}_2\text{O}_7$, sintered at 900°C and 1200°C .

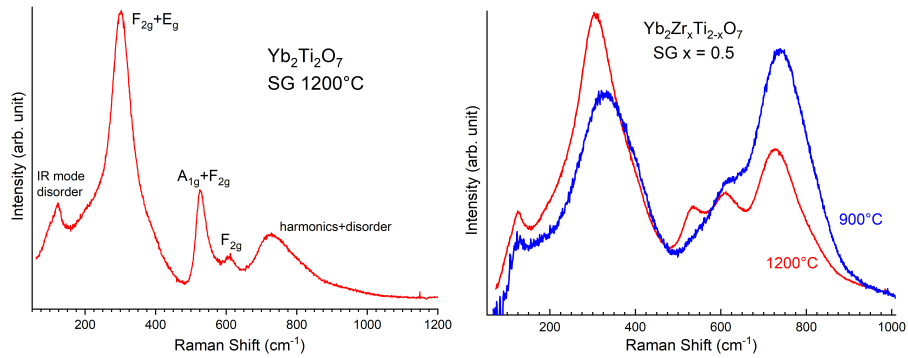


Figure 3: Raman spectra of SG $\text{Yb}_2\text{Zr}_x\text{Ti}_{2-x}\text{O}_7$ with $x = 0.0$ and $x = 0.5$.

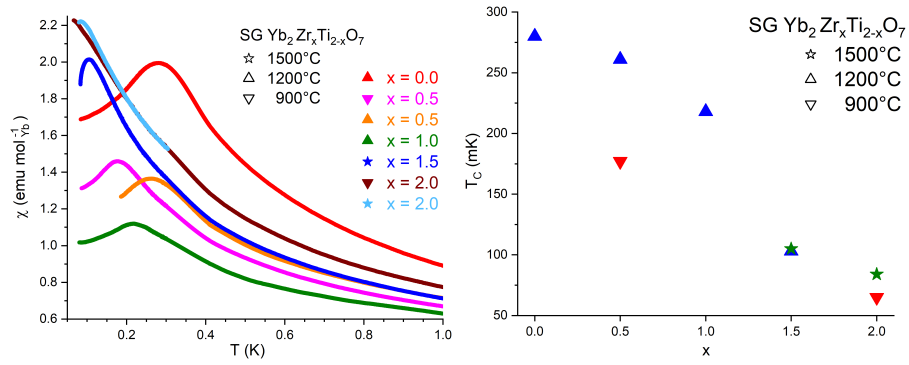


Figure 4: Magnetic susceptibility χ and transition temperatures T_C of SG samples.

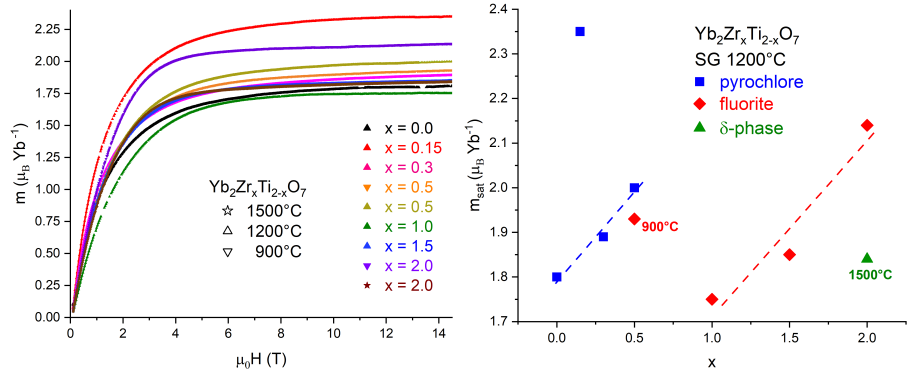


Figure 5: Magnetization m and saturation moments m_{sat} of SG samples, measured at 1.2K.

Bibliography

- [1] [Pyrochlore Mineral Data](#). [Accessed 17-11-2022] (cit. on p. 1).
- [2] Kirti Teja Pasupuleti et al. “Zirconia Based Pyrochlore Thermal Barrier Coatings”. In: *IOP Conference Series: Materials Science and Engineering* 577.1 (2019), p. 012099 (cit. on p. 1).
- [3] E. Jurčišinová and M. Jurčičin. “Adiabatic Cooling Processes in Frustrated Magnetic Systems with Pyrochlore Structure”. In: *Physical Review E* 96.5 (2017), p. 052128 (cit. on p. 1).
- [4] M. A. Frechero et al. “Oxygen Ion Dynamics in Pyrochlore-Type Ionic Conductors: Effects of Structure and Ion-Ion Cooperativity”. In: *Journal of Non-Crystalline Solids*. 7th IDMRCS: Relaxation in Complex Systems 407 (2015), pp. 349–354 (cit. on p. 1).
- [5] Scott A. Speakman et al. “Development of Proton Conductors Using Pyrochlore-Perovskite Phase Boundaries”. In: *Journal of Materials Engineering and Performance* 13.3 (2004), pp. 303–308 (cit. on p. 1).
- [6] Rodney C. Ewing, William J. Weber, and Jie Lian. “Nuclear Waste Disposal—Pyrochlore (A₂B₂O₇): Nuclear Waste Form for the Immobilization of Plutonium and “Minor” Actinides”. In: *Journal of Applied Physics* 95.11 (2004), pp. 5949–5971 (cit. on p. 1).
- [7] Nguyen Duy Cuong et al. “An Extremely High Dielectric Constant in Bismuth-Based Pyrochlore Multilayer Film Capacitors Combined with Percolative Structure”. In: *Applied Physics Letters* 93.21 (2008), p. 212901 (cit. on p. 1).
- [8] Xiaohui Li et al. “Investigation of Pyrochlore-Type A₂Sn₂O₇ (A = La, Nd, Sm, or Gd) Ceramics as Negative Temperature Coefficient Thermistors for High-Temperature Application”. In: *Journal of Physics and Chemistry of Solids* (2022), p. 111205 (cit. on p. 1).
- [9] Sa Li, Zhan-Guo Liu, and Jia-Hu Ouyang. “Hot Corrosion Behaviour of Yb₂Zr₂O₇ Ceramic Coated with V₂O₅ at Temperatures of 600–800°C in Air”. In: *Corrosion Science* 52.10 (2010), pp. 3568–3572 (cit. on pp. 1, 3).
- [10] Artem S. Belousov, Evgeny V. Suleimanov, and Diana G. Fukina. “Pyrochlore Oxides as Visible Light-Responsive Photocatalysts”. In: *New Journal of Chemistry* 45.48 (2021), pp. 22531–22558 (cit. on p. 1).
- [11] Daniel F. Abbott et al. “Design and Synthesis of Ir/Ru Pyrochlore Catalysts for the Oxygen Evolution Reaction Based on Their Bulk Thermodynamic Properties”. In: *ACS Applied Materials & Interfaces* 11.41 (2019), pp. 37748–37760 (cit. on p. 1).

- [12] Sarthak Gaur, Daniel J. Haynes, and James J. Spivey. "Rh, Ni, and Ca Substituted Pyrochlore Catalysts for Dry Reforming of Methane". In: *Applied Catalysis A: General* 403.1 (2011), pp. 142–151 (cit. on p. 1).
- [13] Qi Liu et al. "Controlled Synthesis of Pyrochlore Pr₂Sn₂O₇ Nanospheres with Enhanced Gas Sensing Performance". In: *RSC Advances* 6.26 (2016), pp. 21564–21570 (cit. on p. 1).
- [14] Anjana P. Anantharaman and Hari Prasad Dasari. "Potential of Pyrochlore Structure Materials in Solid Oxide Fuel Cell Applications". In: *Ceramics International* 47.4 (2021), pp. 4367–4388 (cit. on p. 1).
- [15] Lenka Stránská, Petra Šulcová, and Milan Vlček. "Synthesis and Properties of Inorganic Pigments Based on Pyrochlore Compounds with Different Lanthanides". In: *Journal of Thermal Analysis and Calorimetry* 113.1 (2013), pp. 127–135 (cit. on p. 1).
- [16] Jason S. Gardner, Michel J. P. Gingras, and John E. Greedan. "Magnetic Pyrochlore Oxides". In: *Reviews of Modern Physics* 82.1 (2010), pp. 53–107 (cit. on pp. 1, 3).
- [17] S-W. Cheong et al. "Giant Magnetoresistance in Pyrochlore Ti₂-xIn_xMn₂O₇". In: *Solid State Communications* 98.2 (1996), pp. 163–166 (cit. on p. 1).
- [18] K. Ueda et al. "Topological Hall Effect in Pyrochlore Lattice with Varying Density of Spin Chirality". In: *Physical Review Letters* 108.15 (2012), p. 156601 (cit. on p. 1).
- [19] D. Mandrus et al. "Continuous Metal-Insulator Transition in the Pyrochlore Cd₂Os₂O₇". In: *Physical Review B* 63.19 (2001), p. 195104 (cit. on p. 1).
- [20] S. S. Sosin et al. "Magnetocaloric Effect in Pyrochlore Antiferromagnet Gd₂Ti₂O₇". In: *Physical Review B* 71.9 (2005), p. 094413 (cit. on p. 1).
- [21] S. Kamba et al. "Quantum Paraelectric Behavior of Pyrochlore Pb_{1.83}Mg_{0.29}Nb_{1.71}O_{6.39}". In: *Physical Review B* 76.5 (2007), p. 054125 (cit. on p. 1).
- [22] Ritika Dusad et al. "Magnetic Monopole Noise". In: *Nature* 571.7764 (2019), pp. 234–239 (cit. on p. 1).
- [23] L. D. C. Jaubert and P. C. W. Holdsworth. "Signature of Magnetic Monopole and Dirac String Dynamics in Spin Ice". In: *Nature Physics* 5.4 (2009), pp. 258–261 (cit. on p. 1).
- [24] Hironori Sakai et al. "Superconductivity in Pyrochlore Oxide Cd₂Re₂O₇". In: *Physica C: Superconductivity* 378–381 (2002), pp. 43–46 (cit. on p. 1).
- [25] I. A. Sergienko et al. "Metallic "Ferroelectricity" in the Pyrochlore Cd₂Re₂O₇". In: *Physical Review Letters* 92.6 (2004), p. 065501 (cit. on p. 1).
- [26] D. Liu et al. "Multiferroicity in Spin Ice Ho₂Ti₂O₇: An Investigation on Single Crystals". In: *Journal of Applied Physics* 113.17 (2013), p. 17D901 (cit. on p. 1).
- [27] Y. Onose et al. "Observation of the Magnon Hall Effect". In: *Science* 329.5989 (2010), pp. 297–299 (cit. on p. 1).
- [28] T. Fennell et al. "Magnetoelastic Excitations in the Pyrochlore Spin Liquid Tb₂Ti₂O₇". In: *Physical Review Letters* 112.1 (2014), p. 017203 (cit. on p. 1).
- [29] J. N. Reimers, J. E. Greedan, and M. Sato. "The Crystal Structure of the Spin-Glass Pyrochlore, Y₂Mo₂O₇". In: *Journal of Solid State Chemistry* 72.2 (1988), pp. 390–394 (cit. on p. 1).

- [30] Steven T. Bramwell and Michel J. P. Gingras. "Spin Ice State in Frustrated Magnetic Pyrochlore Materials". In: *Science* 294.5546 (2001), pp. 1495–1501 (cit. on p. 1).
- [31] M.A. Subramanian, G. Aravamudan, and G.V. Subba Rao. "Oxide Pyrochlores — A Review". In: *Progress in Solid State Chemistry* 15.2 (1983), pp. 55–143 (cit. on p. 3).
- [32] Dalmau Reig-i-Plessis and Alannah M. Hallas. "Frustrated Magnetism in Fluoride and Chalcogenide Pyrochlore Lattice Materials". In: *Physical Review Materials* 5.3 (2021), p. 030301 (cit. on p. 3).
- [33] Valentina L. Stolyarova et al. "Mass Spectrometric Study of Thermodynamic Properties in the Yb_2O_3 - ZrO_2 System at High Temperatures: Study of the Yb_2O_3 - ZrO_2 System at High Temperatures". In: *Rapid Communications in Mass Spectrometry* 28.1 (2014), pp. 109–114 (cit. on p. 3).
- [34] C. Angeles-Chavez et al. "Structural and Chemical Characterization of Yb_2O_3 - ZrO_2 System by HAADF-STEM and HRTEM". In: *Microscopy and Microanalysis* 15.1 (2009), pp. 46–53 (cit. on p. 3).
- [35] Stephan Stecura. "New ZrO_2 - Yb_2O_3 Plasma-Sprayed Coatings for Thermal Barrier Applications". In: *Thin Solid Films* 150.1 (1987), pp. 15–40 (cit. on p. 3).
- [36] S. Li, Z.-G. Liu, and J.-H. Ouyang. "Study on Hot Corrosion Behavior of $\text{Yb}_2\text{Zr}_2\text{O}_7$ Ceramic against $\text{Na}_2\text{SO}_4 + \text{V}_2\text{O}_5$ Molten Salts at Temperatures of 900-1200 °C in Air: Study on Hot Corrosion Behavior of $\text{Yb}_2\text{Zr}_2\text{O}_7$ Ceramic". In: *Materials and Corrosion* 63.4 (2012), pp. 303–309 (cit. on p. 3).
- [37] Sa Li, Zhan-Guo Liu, and Jia-Hu Ouyang. "Growth of YbVO_4 Crystals Evolved from Hot Corrosion Reactions of $\text{Yb}_2\text{Zr}_2\text{O}_7$ against V_2O_5 and $\text{Na}_2\text{SO}_4 + \text{V}_2\text{O}_5$ ". In: *Applied Surface Science* 276 (2013), pp. 653–659 (cit. on p. 3).
- [38] Jeffrey W. Fergus. "Zirconia and Pyrochlore Oxides for Thermal Barrier Coatings in Gas Turbine Engines". In: *Metallurgical and Materials Transactions E* 1.2 (2014), pp. 118–131 (cit. on p. 3).
- [39] Paweł Pędrak et al. "The Influence of Reactive PS-PVD Process Parameters on the Microstructure and Thermal Properties of $\text{Yb}_2\text{Zr}_2\text{O}_7$ Thermal Barrier Coating". In: *Materials* 15.4 (2022), p. 1594 (cit. on p. 3).
- [40] Meng Zhao et al. "Low Thermal Conductivity of Rare-Earth Zirconate-Stannate Solid Solutions $(\text{Yb}_2\text{Zr}_2\text{O}_7)_{1-x}(\text{Ln}_2\text{Sn}_2\text{O}_7)_x$ ($\text{Ln} = \text{Nd}, \text{Sm}$)". In: *Journal of the American Ceramic Society* 99.1 (2016). Ed. by M. A. White, pp. 293–299 (cit. on p. 3).
- [41] Franz Schwabl. *Statistical Mechanics (Advanced Texts in Physics)*. Springer, 2006, p. 577 (cit. on p. 4).
- [42] Koichi Momma and Fujio Izumi. "VESTA 3 for Three-Dimensional Visualization of Crystal, Volumetric and Morphology Data". In: *Journal of Applied Crystallography* 44.6 (2011), pp. 1272–1276.
- [43] Walter Borchardt-Ott. *Crystallography: An Introduction*. Trans. by Robert O. Gould. 3rd edition. Springer, 2011. 543 pp.
- [44] Christopher Hammond. *The Basics of Crystallography and Diffraction: Fourth Edition*. 4th edition. Oxford: Oxford University Press, 2015. 542 pp.
- [45] Donald E. Sands. *Introduction to Crystallography*. Reprint edition. New York: Dover Publications, 1994. 192 pp.

- [46] Emil Zolotoyabko. *Basic Concepts of Crystallography*. 1st edition. Weinheim, Germany: Wiley-VCH, 2011. 276 pp.
- [47] Zbigniew Dauter and Mariusz Jaskolski. "How to Read (and Understand) Volume A of *International Tables for Crystallography* : An Introduction for Nonspecialists". In: *Journal of Applied Crystallography* 43.5 (2010), pp. 1150–1171.
- [48] David S. Dummit and Richard M. Foote. *Abstract Algebra, 3rd Edition*. 3rd edition. Hoboken, NJ: Wiley, 2003. 944 pp.
- [49] Charles C. Pinter. *A Book of Abstract Algebra: Second Edition*. Second edition. Mineola, N.Y: Dover Publications, 2010. 400 pp.
- [50] *Frucht's Theorem*. In: *Wikipedia*. 2022.
- [51] Gert Sabidussi. "Graphs with given Infinite Group". In: *Monatshefte für Mathematik* 64.1 (1960), pp. 64–67.
- [52] Takanori Tsutaoka et al. "Observation of the Two-Dimensional Reciprocal Lattice by Use of Lattice Grating Sheets and a Laser Pointer". In: *European Journal of Physics* 35.5 (2014), p. 055021.
- [53] Tao Zhang, Ling Li, and Haizhao Yang. *3D Crystal Image Analysis Based on Fast Synchrosqueezed Transforms*. 2018.
- [54] John H. Conway, Heidi Burgiel, and Chaim Goodman-Strauss. *The Symmetries of Things*. 1st edition. Wellesley, Mass: A K Peters/CRC Press, 2008. 444 pp.
- [55] *International Tables for Crystallography, Volume A, 6th Edition, Space-group Symmetry*.
- [56] D. B. Litvin, ed. *Magnetic Group Tables: 1-, 2- and 3-Dimensional Magnetic Subperiodic Groups and Magnetic Space Groups*. Chester, England: International Union of Crystallography, 2013.
- [57] *CIF Dictionaries*.
- [58] Antony R Cleave. "Atomic Scale Simulations for Waste Form Applications".
- [59] C. R. Stanek et al. "Predicted Structure and Stability of A 4 B 3 O 12 δ -Phase Compositions". In: *Physical Review B* 80.17 (2009), p. 174101.
- [60] A.V. Shlyakhtina et al. " δ -Phase to Defect Fluorite (Order–Disorder) Transition in the R2O3–MO2 (R=Sc, Tm, Lu; M=Zr, Hf) Systems". In: *Materials Research Bulletin* 46.4 (2011), pp. 512–517.
- [61] A. Ramanan, J. Gopalakrishnan, and C. N. R. Rao. "Relative Stabilities of Layered Perovskite and Pyrochlore Structures in Transition Metal Oxides Containing Trivalent Bismuth". In: *Journal of Solid State Chemistry* 60.3 (1985), pp. 376–381.
- [62] Lu Cai and Juan C. Nino. "Complex Ceramic Structures. I. Weberites". In: *Acta Crystallographica Section B Structural Science* 65.3 (2009), pp. 269–290.
- [63] Jacob Shamblin et al. "Structural and Magnetic Short-Range Order in Fluorite Yb 2 TiO 5". In: *Physical Review B* 96.17 (2017), p. 174418.
- [64] V. M. Goldschmidt. "Die Gesetze der Krystallochemie". In: *Naturwissenschaften* 14.21 (1926), pp. 477–485.
- [65] Zhen Song and Quanlin Liu. "Tolerance Factor and Phase Stability of the Normal Spinel Structure". In: *Crystal Growth & Design* 20.3 (2020), pp. 2014–2018.

- [66] Zhen Song and Quanlin Liu. "Tolerance Factor, Phase Stability and Order–Disorder of the Pyrochlore Structure". In: *Inorganic Chemistry Frontiers* 7.7 (2020), pp. 1583–1590.
- [67] XiangChun Liu, Rongzi Hong, and Changsheng Tian. "Tolerance Factor and the Stability Discussion of ABO₃-type Ilmenite". In: *Journal of Materials Science: Materials in Electronics* 20.4 (2009), pp. 323–327.
- [68] R. D. Shannon. "Revised Effective Ionic Radii and Systematic Studies of Interatomic Distances in Halides and Chalcogenides". In: *Acta Crystallographica Section A* 32.5 (1976), pp. 751–767.
- [69] VA Isupov and NA Petrov. "Geometric Criteria of Structures of the Pyrochlore Type". In: *Rossiiskaya Akademiya Nauk. Kristallografiya* 3 (1958), pp. 99–100.
- [70] Lu Cai, Alex L. Arias, and Juan C. Nino. "The Tolerance Factors of the Pyrochlore Crystal Structure". In: *Journal of Materials Chemistry* 21.11 (2011), p. 3611.
- [71] Bryan C. Chakoumakos. "Systematics of the Pyrochlore Structure Type, Ideal A₂B₂X₆Y". In: *Journal of Solid State Chemistry* 53.1 (1984), pp. 120–129.
- [72] Mikhail G. Brik and Alok M. Srivastava. "Pyrochlore Structural Chemistry: Predicting the Lattice Constant by the Ionic Radii and Electronegativities of the Constituting Ions". In: *Journal of the American Ceramic Society* 95.4 (2012). Ed. by I. Tanaka, pp. 1454–1460.
- [73] [Home | ICSD](#).
- [74] [Electronegativities of the Elements \(Data Page\)](#). In: *Wikipedia*. 2022.
- [75] R. Mouta, R. X. Silva, and C. W. A. Paschoal. "Tolerance Factor for Pyrochlores and Related Structures". In: *Acta Crystallographica Section B Structural Science Crystal Engineering and Materials* 69.5 (2013), pp. 439–445.
- [76] Antonio F. Fuentes et al. "A Critical Review of Existing Criteria for the Prediction of Pyrochlore Formation and Stability". In: *Inorganic Chemistry* 57.19 (2018), pp. 12093–12105.
- [77] Arthur W. Sleight. "Rare Earth Plumbates with Pyrochlore Structure". In: *Inorganic Chemistry* 8.8 (1969), pp. 1807–1808.
- [78] Kurt E. Sickafus et al. "Radiation-Induced Amorphization Resistance and Radiation Tolerance in Structurally Related Oxides". In: *Nature Materials* 6.3 (2007), pp. 217–223.
- [79] Pardha S. Maram et al. "Probing Disorder in Pyrochlore Oxides Using in Situ Synchrotron Diffraction from Levitated Solids—A Thermodynamic Perspective". In: *Scientific Reports* 8.1 (2018), p. 10658.
- [80] David Simeone et al. "Intricate Disorder in Defect Fluorite/Pyrochlore: A Concord of Chemistry and Crystallography". In: *Scientific Reports* 7.1 (2017), p. 3727.
- [81] Timothy Connor et al. "Pyrochlore Compounds From Atomistic Simulations". In: *Frontiers in Chemistry* 9 (2021), p. 733321.
- [82] M. Ilatovskaia et al. "Experimental Investigation of Phase Relations in the ZrO₂-La₂O₃-Yb₂O₃ System". In: *Journal of Phase Equilibria and Diffusion* 41.4 (2020), pp. 311–328.

- [83] O. Fabrichnaya et al. "New Experimental Investigations of Phase Relations in the Yb₂O₃–Al₂O₃ and ZrO₂–Yb₂O₃–Al₂O₃ Systems and Assessment of Thermodynamic Parameters". In: *Journal of the European Ceramic Society* 35.10 (2015), pp. 2855–2871.
- [84] H. Ondik and H. F. McMurdie. "Phase Diagrams for Zirconium and Zirconia Systems". In: *NIST* ().
- [85] P. Duran and C. Pascual. "Phase Equilibria and Ordering in the System HfO₂–Yb₂O₃". In: *Journal of Materials Science* 19.4 (1984), pp. 1178–1184.
- [86] I. S. Tyshchenko et al. "Isothermal Section of the Al₂O₃–TiO₂–Yb₂O₃ Phase Diagram at 1400°C". In: *Odesa National University Herald. Chemistry* 23 (2018), pp. 50–57.
- [87] R. D. Aughterson et al. "Controlled Disorder for the Yb₂Ti₂–xO₇–2x (x = 0 to 1) Series and Corresponding Radiation Tolerance". In: *Ceramics International* 49.7 (2023), pp. 11149–11157.
- [88] Francine Queyroux. "Sur l'existence d'un composé nouveau Yb₆TiO₁₁ et sur le diagramme d'équilibre Yb₂O₃–TiO₂". In: *Bulletin de Minéralogie* 88.3 (1965), pp. 519–520.
- [89] *Fundamental Physical Constants - Nist.Gov*. [Accessed 17-11-2022].
- [90] Stephen Blundell. *Magnetism in Condensed Matter*. 1st edition. Oxford: Oxford University Press, 2001. 256 pp.
- [91] J. M. D. Coey. *Magnetism and Magnetic Materials*. Illustrated edition. Cambridge: Cambridge University Press, 2010. 625 pp.
- [92] Andrew Zangwill. *Modern Electrodynamics*. Cambridge, England: Cambridge University Press, 2012.
- [93] Sam Mugiraneza and Alannah M. Hallas. "Tutorial: A Beginner's Guide to Interpreting Magnetic Susceptibility Data with the Curie-Weiss Law". In: *Communications Physics* 5.1 (2022), pp. 1–12.
- [94] C V Topping and S J Blundell. "A.C. Susceptibility as a Probe of Low-Frequency Magnetic Dynamics". In: *Journal of Physics: Condensed Matter* 31.1 (2018), p. 013001.
- [95] M. Bałanda. "AC Susceptibility Studies of Phase Transitions and Magnetic Relaxation: Conventional, Molecular and Low-Dimensional Magnets". In: *Acta Physica Polonica A* 124.6 (2013), pp. 964–976.
- [96] Gordon A. Bain and John F. Berry. "Diamagnetic Corrections and Pascal's Constants". In: *Journal of Chemical Education* 85.4 (2008). doi: 10.1021/ed085p532, p. 532.
- [97] John E. Greedan. "Geometrically Frustrated Magnetic Materials". In: *Journal of Materials Chemistry* 11.1 (2001), pp. 37–53.
- [98] C. M. Hurd. "Varieties of Magnetic Order in Solids". In: *Contemporary Physics* 23.5 (1982), pp. 469–493.
- [99] Libor Šmejkal, Jairo Sinova, and Tomas Jungwirth. "Emerging Research Landscape of Altermagnetism". In: *Physical Review X* 12.4 (2022), p. 040501.
- [100] Katie L. Peterson, Kriti Srivastava, and Valérie C. Pierre. "Fluorinated Paramagnetic Complexes: Sensitive and Responsive Probes for Magnetic Resonance Spectroscopy and Imaging". In: *Frontiers in Chemistry* 6 (2018).

- [101] Jun John Sakurai and Jim Napolitano. *Modern Quantum Mechanics*. 3rd ed. Cambridge: Cambridge University Press, 2021.
- [102] P. W. Anderson. "Survey of Theories of Spin Glass". In: *Amorphous Magnetism II*. Ed. by R. A. Levy and R. Hasegawa. Boston, MA: Springer US, 1977, pp. 1–16.
- [103] P.W. Anderson. "The Concept of Frustration in Spin Glasses". In: *Journal of the Less Common Metals* 62 (1978), pp. 291–294.
- [104] J. Vannimenus and G. Toulouse. "Theory of the Frustration Effect. II. Ising Spins on a Square Lattice". In: *Journal of Physics C: Solid State Physics* 10.18 (1977), p. L537.
- [105] Gérard Toulouse. "The Frustration Model". In: *Modern Trends in the Theory of Condensed Matter*. Ed. by Andrzej Pękalski and Jerzy A. Przystawa. Lecture Notes in Physics. Berlin, Heidelberg: Springer, 1980, pp. 195–203.
- [106] Stephen M. Winter et al. "Models and Materials for Generalized Kitaev Magnetism". In: *Journal of Physics: Condensed Matter* 29.49 (2017), p. 493002.
- [107] Jeffrey G. Rau, Eric Kin-Ho Lee, and Hae-Young Kee. "Spin-Orbit Physics Giving Rise to Novel Phases in Correlated Systems: Iridates and Related Materials". In: *Annual Review of Condensed Matter Physics* 7.1 (2016), pp. 195–221.
- [108] Alexei Kitaev. "Anyons in an Exactly Solved Model and Beyond". In: *Annals of Physics*. January Special Issue 321.1 (2006), pp. 2–111.
- [109] A P Ramirez. "Strongly Geometrically Frustrated Magnets". In: *Annual Review of Materials Science* 24.1 (1994), pp. 453–480.
- [110] I. Mirebeau and I. N. Goncharenko. "Tb₂Ti₂O₇: A 'Spin Liquid' Single Crystal Studied under High Pressure and High Magnetic Field". In: *Journal of Physics: Condensed Matter* 17.11 (2005), S771.
- [111] Hiroshi Takatsu et al. "Quantum Spin Fluctuations in the Spin-Liquid State of Tb₂Ti₂O₇". In: *Journal of Physics: Condensed Matter* 24.5 (2012), p. 052201.
- [112] Leon Balents. "Spin Liquids in Frustrated Magnets". In: *Nature* 464.7286 (2010), pp. 199–208.
- [113] C. Broholm et al. "Quantum Spin Liquids". In: *Science* 367.6475 (2020), eaay0668.
- [114] Lucy Clark and Aly H. Abdeldaim. "Quantum Spin Liquids from a Materials Perspective". In: *Annual Review of Materials Research* 51.1 (2021), pp. 495–519.
- [115] J. Knolle and R. Moessner. "A Field Guide to Spin Liquids". In: *Annual Review of Condensed Matter Physics* 10.1 (2019), pp. 451–472.
- [116] J. P. C. Ruff et al. "Structural Fluctuations in the Spin-Liquid State of Tb₂Ti₂O₇". In: *Physical Review Letters* 99.23 (2007), p. 237202.
- [117] Lucile Savary and Leon Balents. "Quantum Spin Liquids: A Review". In: *Reports on Progress in Physics* 80.1 (2017), p. 016502.
- [118] Jinsheng Wen et al. "Experimental Identification of Quantum Spin Liquids". In: *npj Quantum Materials* 4.1 (2019), p. 12.
- [119] Yu Jiang et al. "Order and Disorder in the Local and Long-Range Structure of the Spin-Glass Pyrochlore, Tb₂Mo₂O₇". In: *Journal of Physics: Condensed Matter* 23.16 (2011), p. 164214.
- [120] J. A. Mydosh. *Spin Glasses: An Experimental Introduction*. 1st edition, 2007. 272 pp.

- [121] J A Mydosh. “Spin Glasses: Redux: An Updated Experimental/Materials Survey”. In: *Reports on Progress in Physics* 78.5 (2015), p. 052501.
- [122] P. E. Jönsson et al. “Spin Glasses: A Ghost Story”. In: *Physical Review B* 70.17 (2004). Comment: REVTeX 4 style; 30 pages, 29 figures; revised 2004/07/04, p. 174402. arXiv: [cond-mat/0307640](https://arxiv.org/abs/cond-mat/0307640).
- [123] K. Binder and A. P. Young. “Spin Glasses: Experimental Facts, Theoretical Concepts, and Open Questions”. In: *Reviews of Modern Physics* 58.4 (1986), pp. 801–976.
- [124] Linus Pauling. “The Structure and Entropy of Ice and of Other Crystals with Some Randomness of Atomic Arrangement”. In: *Journal of the American Chemical Society* 57.12 (1935), pp. 2680–2684.
- [125] L Lin et al. “Experimental Observation of Magnetoelectricity in Spin Ice $\text{Dy}_2\text{Ti}_2\text{O}_7$ ”. In: *New Journal of Physics* 17.12 (2015), p. 123018.
- [126] Masafumi Udagawa and Ludovic Jaubert, eds. *Spin Ice*. 1st ed. 2021 edition. Cham, Switzerland: Springer, 2021. 502 pp.
- [127] Steven T Bramwell and Mark J Harris. “The History of Spin Ice”. In: *Journal of Physics: Condensed Matter* 32.37 (2020), p. 374010.
- [128] A. P. Ramirez et al. “Zero-Point Entropy in ‘Spin Ice’”. In: *Nature* 399.6734 (1999), pp. 333–335.
- [129] Antonio Ortiz-Ambriz et al. “Colloquium : Ice Rule and Emergent Frustration in Particle Ice and Beyond”. In: *Reviews of Modern Physics* 91.4 (2019), p. 041003.
- [130] S. T. Bramwell et al. “Measurement of the Charge and Current of Magnetic Monopoles in Spin Ice”. In: *Nature* 461.7266 (2009), pp. 956–959.
- [131] C. Castelnovo, R. Moessner, and S. L. Sondhi. “Magnetic Monopoles in Spin Ice”. In: *Nature* 451.7174 (2008), pp. 42–45.
- [132] C. Paulsen et al. “Far-from-Equilibrium Monopole Dynamics in Spin Ice”. In: *Nature Physics* 10.2 (2014), pp. 135–139.
- [133] Christopher L. Henley. “The ‘Coulomb Phase’ in Frustrated Systems”. In: *Annual Review of Condensed Matter Physics* 1.1 (2010), pp. 179–210.
- [134] C. Castelnovo, R. Moessner, and S.L. Sondhi. “Spin Ice, Fractionalization, and Topological Order”. In: *Annual Review of Condensed Matter Physics* 3.1 (2012), pp. 35–55.
- [135] Jonathan Gustavo Acosta Ramon and Rafael Sá de Freitas. “Vacâncias de oxigênio e diluição de ítrio no pirocloro geometricamente frustrado $\text{Gd}_2\text{Ti}_2\text{O}_7$ ”. 2015.
- [136] R S Freitas and J S Gardner. “The Magnetic Phase Diagram of $\text{Gd}_2\text{Sn}_2\text{O}_7$ ”. In: *Journal of Physics: Condensed Matter* 23.16 (2011), p. 164215.
- [137] Jeffrey G. Rau and Michel J.P. Gingras. “Frustrated Quantum Rare-Earth Pyrochlores”. In: *Annual Review of Condensed Matter Physics* 10.1 (2019), pp. 357–386.
- [138] S. E. Palmer and J. T. Chalker. “Order Induced by Dipolar Interactions in a Geometrically Frustrated Antiferromagnet”. In: *Physical Review B* 62.1 (2000), pp. 488–492.
- [139] Joseph A. M. Paddison et al. “Suppressed-Moment 2-k Order in the Canonical Frustrated Antiferromagnet $\text{Gd}_2\text{Ti}_2\text{O}_7$ ”. In: *npj Quantum Materials* 6.1 (2021), pp. 1–8.

- [140] Han Yan et al. “Theory of Multiple-Phase Competition in Pyrochlore Magnets with Anisotropic Exchange with Application to $\text{Yb}_2\text{Ti}_2\text{O}_7$, $\text{Er}_2\text{Ti}_2\text{O}_7$, and $\text{Er}_2\text{Sn}_2\text{O}_7$ ”. In: *Physical Review B* 95.9 (2017), p. 094422.
- [141] Alannah M. Hallas, Jonathan Gaudet, and Bruce D. Gaulin. “Experimental Insights into Ground-State Selection of Quantum XY Pyrochlores”. In: *Annual Review of Condensed Matter Physics* 9.1 (2018), pp. 105–124.
- [142] Paul A. McClarty, Pawel Stasiak, and Michel J. P. Gingras. “Order-by-Disorder in the X Y Pyrochlore Antiferromagnet”. In: *Physical Review B* 89.2 (2014), p. 024425.
- [143] John McGreevy. “Generalized Symmetries in Condensed Matter”. In: *Annual Review of Condensed Matter Physics* 14.1 (2023), pp. 57–82.
- [144] H. W. J. Blöte, R. F. Wielinga, and W. J. Huiskamp. “Heat-Capacity Measurements on Rare-Earth Double Oxides $\text{R}_2\text{M}_2\text{O}_7$ ”. In: *Physica* 43.4 (1969), pp. 549–568.
- [145] M J P Gingras and P A McClarty. “Quantum Spin Ice: A Search for Gapless Quantum Spin Liquids in Pyrochlore Magnets”. In: *Reports on Progress in Physics* 77.5 (2014), p. 056501.
- [146] J. A. Hodges et al. “First-Order Transition in the Spin Dynamics of Geometrically Frustrated $\text{Yb}_2\text{Ti}_2\text{O}_7$ ”. In: *Physical Review Letters* 88.7 (2002), p. 077204.
- [147] Yukio Yasui et al. “Ferromagnetic Transition of Pyrochlore Compound $\text{Yb}_2\text{Ti}_2\text{O}_7$ ”. In: *Journal of the Physical Society of Japan* 72.11 (2003), pp. 3014–3015.
- [148] Lieh-Jeng Chang et al. “Higgs Transition from a Magnetic Coulomb Liquid to a Ferromagnet in $\text{Yb}_2\text{Ti}_2\text{O}_7$ ”. In: *Nature Communications* 3.1 (2012), p. 992.
- [149] Viviane Peçanha-Antonio et al. “Magnetic Excitations in the Ground State of $\text{Yb}_2\text{Ti}_2\text{O}_7$ ”. In: *Physical Review B* 96.21 (2017), p. 214415.
- [150] J. Gaudet et al. “Gapless Quantum Excitations from an Icelike Splayed Ferromagnetic Ground State in Stoichiometric $\text{Yb}_2\text{Ti}_2\text{O}_7$ ”. In: *Physical Review B* 93.6 (2016), p. 064406.
- [151] A. Scheie et al. “Reentrant Phase Diagram of $\text{Yb}_2\text{Ti}_2\text{O}_7$ in a $\langle 111 \rangle$ Magnetic Field”. In: *Physical Review Letters* 119.12 (2017), p. 127201.
- [152] R. Applegate et al. “Vindication of $\text{Yb}_2\text{Ti}_2\text{O}_7$ as a Model Exchange Quantum Spin Ice”. In: *Physical Review Letters* 109.9 (2012), p. 097205.
- [153] E. Lhotel et al. “First-Order Magnetic Transition in $\text{Yb}_2\text{Ti}_2\text{O}_7$ ”. In: *Physical Review B* 89.22 (2014), p. 224419.
- [154] Lieh-Jeng Chang et al. “Static Magnetic Moments Revealed by Muon Spin Relaxation and Thermodynamic Measurements in the Quantum Spin Ice $\text{Yb}_2\text{Ti}_2\text{O}_7$ ”. In: *Physical Review B* 89.18 (2014), p. 184416.
- [155] K. A. Ross et al. “Two-Dimensional Kagome Correlations and Field Induced Order in the Ferromagnetic X Y Pyrochlore $\text{Yb}_2\text{Ti}_2\text{O}_7$ ”. In: *Physical Review Letters* 103.22 (2009), p. 227202.
- [156] Kate A. Ross et al. “Quantum Excitations in Quantum Spin Ice”. In: *Physical Review X* 1.2 (2011), p. 021002.
- [157] N. R. Hayre et al. “Thermodynamic Properties of $\text{Yb}_2\text{Ti}_2\text{O}_7$ Pyrochlore as a Function of Temperature and Magnetic Field: Validation of a Quantum Spin Ice Exchange Hamiltonian”. In: *Physical Review B* 87.18 (2013), p. 184423.

- [158] A. Yaouanc et al. "Spin Dynamics in Geometrically Frustrated Compounds". In: *Physica B: Condensed Matter* 326.1-4 (2003), pp. 456–459.
- [159] J. S. Gardner et al. "Spin-Spin Correlations in Yb₂Ti₂O₇: A Polarized Neutron Scattering Study". In: *Physical Review B* 70.18 (2004), p. 180404.
- [160] P. Bonville et al. "Transitions and Spin Dynamics at Very Low Temperature in the Pyrochlores Yb₂Ti₂O₇ and Gd₂Sn₂O₇". In: *ICAME 2003*. Ed. by M. E. Elzain et al. Dordrecht: Springer Netherlands, 2004, pp. 103–111.
- [161] Subhro Bhattacharjee et al. "Acoustic Signatures of the Phases and Phase Transitions in Yb₂Ti₂O₇". In: *Physical Review B* 93.14 (2016), p. 144412.
- [162] R. M. D'Ortenzio et al. "Unconventional Magnetic Ground State in Yb₂Ti₂O₇". In: *Physical Review B* 88.13 (2013), p. 134428.
- [163] E. Kermarrec et al. "Ground State Selection under Pressure in the Quantum Pyrochlore Magnet Yb₂Ti₂O₇". In: *Nature Communications* 8.1 (2017), p. 14810.
- [164] K. A. Ross et al. "Dimensional Evolution of Spin Correlations in the Magnetic Pyrochlore Yb₂Ti₂O₇". In: *Physical Review B* 84.17 (2011), p. 174442.
- [165] H. Cao et al. "Ising versus X Y Anisotropy in Frustrated R₂Ti₂O₇ Compounds as "Seen" by Polarized Neutrons". In: *Physical Review Letters* 103.5 (2009), p. 056402.
- [166] Pierre Dalmas de Réotier, Alexander Maisuradze, and Alain Yaouanc. "Recent μ SR Studies of Insulating Rare-Earth Pyrochlore Magnets". In: *Journal of the Physical Society of Japan* 85.9 (2016), p. 091010.
- [167] A. Yaouanc et al. "Single-Crystal versus Polycrystalline Samples of Magnetically Frustrated Yb₂Ti₂O₇ : Specific Heat Results". In: *Physical Review B* 84.17 (2011), p. 172408.
- [168] K. E. Arpino et al. "Impact of Stoichiometry of Yb₂Ti₂O₇ on Its Physical Properties". In: *Physical Review B* 95.9 (2017), p. 094407.
- [169] K. A. Ross et al. "Lightly Stuffed Pyrochlore Structure of Single-Crystalline Yb₂Ti₂O₇ Grown by the Optical Floating Zone Technique". In: *Physical Review B* 86.17 (2012), p. 174424.
- [170] Ali Mostaed et al. "Atomic Structure Study of the Pyrochlore Yb₂Ti₂O₇ and Its Relationship with Low-Temperature Magnetic Order". In: *Physical Review B* 95.9 (2017), p. 094431.
- [171] H Y Xiao et al. "Theoretical Investigation of Structural, Energetic and Electronic Properties of Titanate Pyrochlores". In: *Journal of Physics: Condensed Matter* 19.34 (2007), p. 346203.
- [172] S. M. Koohpayeh, D. Fort, and J. S. Abell. "The Optical Floating Zone Technique: A Review of Experimental Procedures with Special Reference to Oxides". In: *Progress in Crystal Growth and Characterization of Materials* 54.3 (2008), pp. 121–137.
- [173] S. M. Koohpayeh. "Single Crystal Growth by the Traveling Solvent Technique: A Review". In: *Progress in Crystal Growth and Characterization of Materials*. Special Issue: Recent Progress on Fundamentals and Applications of Crystal Growth; Proceedings of the 16th International Summer School on Crystal Growth (ISSCG-16) 62.4 (2016), pp. 22–34.

- [174] D. F. Bowman et al. "Role of Defects in Determining the Magnetic Ground State of Ytterbium Titanate". In: *Nature Communications* 10.1 (2019), p. 637.
- [175] Allen Scheie et al. "Multiphase Magnetism in $\text{Yb}_2\text{Ti}_2\text{O}_7$ ". In: *Proceedings of the National Academy of Sciences* 117.44 (2020), pp. 27245–27254.
- [176] J. D. Thompson et al. "Quasiparticle Breakdown and Spin Hamiltonian of the Frustrated Quantum Pyrochlore $\text{Yb}_2\text{Ti}_2\text{O}_7$ in a Magnetic Field". In: *Physical Review Letters* 119.5 (2017), p. 057203.
- [177] J. Gaudet et al. "Neutron Spectroscopic Study of Crystalline Electric Field Excitations in Stoichiometric and Lightly Stuffed $\text{Yb}_2\text{Ti}_2\text{O}_7$ ". In: *Physical Review B* 92.13 (2015), p. 134420.
- [178] Lucile Savary et al. "Order by Quantum Disorder in $\text{Er}_2\text{Ti}_2\text{O}_7$ ". In: *Physical Review Letters* 109.16 (2012), p. 167201.
- [179] Solene Guitteny et al. "Palmer-Chalker Correlations in the XY Pyrochlore Antiferromagnet $\text{Er}_2\text{Sn}_2\text{O}_7$ ". In: *Physical Review B* 88.13 (2013), p. 134408.
- [180] L. D. C. Jaubert et al. "Are Multiphase Competition and Order by Disorder the Keys to Understanding $\text{Yb}_2\text{Ti}_2\text{O}_7$?" In: *Physical Review Letters* 115.26 (2015), p. 267208.
- [181] A. Scheie et al. "Dynamical Scaling as a Signature of Multiple Phase Competition in $\text{Yb}_2\text{Ti}_2\text{O}_7$ ". In: *Physical Review Letters* 129.21 (2022), p. 217202.
- [182] Junichi Hojo, ed. *Materials Chemistry of Ceramics*. Springer Singapore, 2019.
- [183] Michael E Brown, D Dollimore, and A K Galwey, eds. *Reactions in the Solid State: Volume 22*. Comprehensive Chemical Kinetics. London, England: Elsevier Science, 1980.
- [184] Hermann Schmalzried. *Solid State Reactions*. 2nd ed. Verlag Chemie, 1981.
- [185] Qianqian Zhao et al. "Comparison of $\text{Fe}_2\text{TiO}_5/\text{C}$ Photocatalysts Synthesized via a Nonhydrolytic Sol–Gel Method and Solid-State Reaction Method". In: *RSC Advances* 10.71 (2020), pp. 43762–43772.
- [186] A. F. Fuentes and L. Takacs. "Preparation of Multicomponent Oxides by Mechanochemical Methods". In: *Journal of Materials Science* 48.2 (2013), pp. 598–611.
- [187] Edward L. Dreizin and Mirko Schoenitz. "Mechanochemically Prepared Reactive and Energetic Materials: A Review". In: *Journal of Materials Science* 52.20 (2017), pp. 11789–11809.
- [188] Tomislav Friščić. "New Opportunities for Materials Synthesis Using Mechanochemistry". In: *Journal of Materials Chemistry* 20.36 (2010), pp. 7599–7605.
- [189] William D. Callister Jr and David G. Rethwisch. *Materials Science and Engineering*. 10th edition. Hoboken, NJ: Wiley, 2020. 944 pp.
- [190] A. E. Danks, S. R. Hall, and Z. Schnepf. "The Evolution of 'Sol–Gel' Chemistry as a Technique for Materials Synthesis". In: *Materials Horizons* 3.2 (2016), pp. 91–112.
- [191] George W. Scherer C. Jeffrey Brinker. *Sol-Gel Science*. Elsevier Science Techn., 2013. 912 pp.
- [192] Muili Feyisitan Fakoya and Subhash Nandlal Shah. "Emergence of Nanotechnology in the Oil and Gas Industry: Emphasis on the Application of Silica Nanoparticles". In: *Petroleum* 3.4 (2017), pp. 391–405.

- [193] Chen et al. "Synthesis and Characterization of Pyrochlore-Type Yttrium Titanate Nanoparticles by Modified Sol–Gel Method". In: *Bulletin of Materials Science* 34.3 (2011), pp. 429–434.
- [194] Joseph Goldstein et al. *Scanning Electron Microscopy and X-ray Microanalysis: Third Edition*. Springer US, 2013. 690 pp.
- [195] *Periodic Tables for SEM, TEM, Mass Spec, and NMR | JEOL EDS Perio.*
- [196] Christopher J. Gilmore, James A. Kaduk, and Henk Schenk, eds. *International Tables for Crystallography, Powder Diffraction: Powder Diffraction*. Volume H edition. Chichester: Wiley, 2019. 930 pp.
- [197] R. E. Dinnebier and S. J. L. Billinge, eds. *Powder Diffraction: Theory and Practice*. 1st edition. Cambridge: Royal Society of Chemistry, 2008. 604 pp.
- [198] Vitalij Pecharsky and Peter Zavalij. *Fundamentals of Powder Diffraction and Structural Characterization of Materials, Second Edition*. 2nd edition. Springer, 2008. 768 pp.
- [199] B D Cullity and S R Stock. *Elements of X-ray Diffraction*. 3rd ed. Upper Saddle River, NJ: Pearson, 2001.
- [200] R. A. Young, ed. *The Rietveld Method*. First edition. Chester, England : Oxford ; New York: Oxford University Press, 1993. 312 pp.
- [201] Georg Will. *Powder Diffraction: The Rietveld Method and the Two Stage Method to Determine and Refine Crystal Structures from Powder Diffraction Data*. 2006th edition. Berlin ; New York: Springer, 2005. 233 pp.
- [202] Robert E. Dinnebier, Andreas Leineweber, and John S. O. Evans. *Rietveld Refinement: Practical Powder Diffraction Pattern Analysis Using Topas*. Illustrated edition. Berlin ; Boston: De Gruyter, 2018. 331 pp.
- [203] L. B. McCusker et al. "Rietveld Refinement Guidelines". In: *Journal of Applied Crystallography* 32.1 (1999), pp. 36–50.
- [204] G. Hölzer et al. "K α _{1,2} and K β _{1,3} x-Ray Emission Lines of the 3d Transition Metals". In: *Physical Review A* 56.6 (1997), pp. 4554–4568.
- [205] *D2 PHASER - Dataquality.*
- [206] J. Brentano. "Focussing Method of Crystal Powder Analysis by X-rays". In: *Proceedings of the Physical Society of London* 37.1 (1924), p. 184.
- [207] Wikimedia Commons. *File:Bragg Diffraction 2.Svg — Wikimedia Commons, the Free Media Repository*. [Online; accessed 22-December-2022]. 2020.
- [208] K. N. Trueblood et al. "Atomic Displacement Parameter Nomenclature. Report of a Subcommittee on Atomic Displacement Parameter Nomenclature". In: *Acta Crystallographica Section A: Foundations of Crystallography* 52.5 (1996), pp. 770–781.
- [209] Guangxin Fan et al. "An Insight into the Influence of Crystallite Size on the Performances of Microsized Spherical Li(Ni_{0.5}Co_{0.2}Mn_{0.3})O₂ Cathode Material Composed of Aggregated Nanosized Particles". In: *Journal of Nanoparticle Research* 20.2 (2018), p. 43.
- [210] J. I. Langford and A. J. C. Wilson. "Scherrer after Sixty Years: A Survey and Some New Results in the Determination of Crystallite Size". In: *Journal of Applied Crystallography* 11.2 (1978), pp. 102–113.

- [211] B. E. Warren. *X-Ray Diffraction*. Reprint edition. New York: Dover Publications, 1990. 400 pp.
- [212] P. Scardi, M. Leoni, and R. Delhez. "Line Broadening Analysis Using Integral Breadth Methods: A Critical Review". In: *Journal of Applied Crystallography* 37.3 (2004), pp. 381–390.
- [213] R. Delhez, Th. H. de Keijser, and E. J. Mittemeijer. "Determination of Crystallite Size and Lattice Distortions through X-ray Diffraction Line Profile Analysis: Vorschriften, Methoden Und Bemerkungen". In: *Fresenius' Zeitschrift für analytische Chemie* 312.1 (1982), pp. 1–16.
- [214] Eric J. Mittemeijer and Udo Welzel. "Diffraction Line-Profile Analysis". In: *Modern Diffraction Methods*. John Wiley & Sons, Ltd, 2012, pp. 87–126.
- [215] D. Balzar and S. Popović. "Reliability of the Simplified Integral-Breadth Methods in Diffraction Line-Broadening Analysis". In: *Journal of Applied Crystallography* 29.1 (1996), pp. 16–23.
- [216] F. T. L. Muniz et al. "The Scherrer Equation and the Dynamical Theory of X-ray Diffraction". In: *Acta Crystallographica Section A: Foundations and Advances* 72.3 (2016), pp. 385–390.
- [217] M. a. R. Miranda and J. M. Sasaki. "The Limit of Application of the Scherrer Equation". In: *Acta Crystallographica Section A: Foundations and Advances* 74.1 (2018), pp. 54–65.
- [218] Steven H. Simon. *The Oxford Solid State Basics*. Oxford: Oxford University Press, 2013. 312 pp.
- [219] G. C. Lau et al. "Structural Disorder and Properties of the Stuffed Pyrochlore $\text{Ho}_2\text{Ti}_2\text{O}_7$ ". In: *Physical Review B* 76.5 (2007), p. 054430.
- [220] M. L. Sanjuán et al. "Raman and X-Ray Absorption Spectroscopy Study of the Phase Evolution Induced by Mechanical Milling and Thermal Treatments in $\text{R}_2\text{Ti}_2\text{O}_7$ Pyrochlores". In: *Physical Review B* 84.10 (2011), p. 104207.
- [221] Robert D. Aughterson et al. "Crystal Structures of Orthorhombic, Hexagonal, and Cubic Compounds of the $\text{Sm}(x)\text{Yb}(2-x)\text{TiO}_5$ Series". In: *Journal of Solid State Chemistry* 213 (2014), pp. 182–192.
- [222] G.C. Lau et al. "Long- and Short-Range Order in Stuffed Titanate Pyrochlores". In: *Journal of Solid State Chemistry* 181.1 (2008), pp. 45–50.
- [223] Jacob Shamblin et al. "Probing Disorder in Isometric Pyrochlore and Related Complex Oxides". In: *Nature Materials* 15.5 (2016), pp. 507–511.
- [224] Cameron L. Tracy et al. "Role of Composition, Bond Covalency, and Short-Range Order in the Disordering of Stannate Pyrochlores by Swift Heavy Ion Irradiation". In: *Physical Review B* 94.6 (2016), p. 064102.
- [225] Graham King et al. "Local Structure of the Vacancy Disordered Fluorite Yb_3TaO_7 from Neutron Total Scattering". In: *Journal of Materials Chemistry A* 1.35 (2013), pp. 10487–10494.
- [226] Jacob Shamblin et al. "Similar Local Order in Disordered Fluorite and Aperiodic Pyrochlore Structures". In: *Acta Materialia* 144 (2018), pp. 60–67.

- [227] Fengai Zhao et al. "Probing Local Site Disorder in Zirconate Pyrochlores". In: *Ceramics International* (2023), S0272884223005187.
- [228] Ushio Matsumoto et al. "First-Principles Study on the Stability of Weberite-Type, Pyrochlore, and Defect-Fluorite Structures of $A_2 B_2 O_7$ ($A = Lu^{3+}$, La^{3+} , $B = Zr^{4+}$, Hf^{4+} , Sn^{4+} , and Ti^{4+})". In: *The Journal of Physical Chemistry C* 124.37 (2020), pp. 20555–20562.
- [229] Piotr M. Kowalski. "Formation Enthalpy of Ln₂B₂O₇-type (B=Ti,Sn,Hf,Zr) Compounds". In: *Scripta Materialia* 189 (2020), pp. 7–10.
- [230] B. A. Trump et al. "Universal Geometric Frustration in Pyrochlores". In: *Nature Communications* 9.1 (2018), p. 2619.
- [231] Daniel P. Shoemaker et al. "Reverse Monte Carlo Neutron Scattering Study of the 'Ordered-Ice' Oxide Pyrochlore $Pb_2 Ru_2 O_{6.5}$ ". In: *Journal of Physics: Condensed Matter* 23.31 (2011), p. 315404.
- [232] Mikhail V. Talanov and Valeriy M. Talanov. "Formation of Breathing Pyrochlore Lattices: Structural, Thermodynamic and Crystal Chemical Aspects". In: *CrystEngComm* 22.7 (2020), pp. 1176–1187.
- [233] Jeffrey G. Rau and Michel J. P. Gingras. "Frustration and Anisotropic Exchange in Ytterbium Magnets with Edge-Shared Octahedra". In: *Physical Review B* 98.5 (2018), p. 054408.
- [234] Li Ern Chern, Yong Baek Kim, and Claudio Castelnovo. "Competing Quantum Spin Liquids, Gauge Fluctuations, and Anisotropic Interactions in a Breathing Pyrochlore Lattice". In: *Physical Review B* 106.13 (2022), p. 134402.
- [235] Owen Benton and Nic Shannon. "Ground State Selection and Spin-Liquid Behaviour in the Classical Heisenberg Model on the Breathing Pyrochlore Lattice". In: *Journal of the Physical Society of Japan* 84.10 (2015), p. 104710.
- [236] C. H. Booth et al. "Local Lattice Disorder in the Geometrically Frustrated Spin-Glass Pyrochlore YMo ". In: *Physical Review B* 62.2 (2000), R755–R758.
- [237] Angela Altomare et al. "QUALX2.0: A Qualitative Phase Analysis Software Using the Freely Available Database POW_COD". In: *Journal of Applied Crystallography* 48.2 (2015), pp. 598–603.
- [238] Saulius Gražulis et al. "Crystallography Open Database – an Open-Access Collection of Crystal Structures". In: *Journal of Applied Crystallography* 42.4 (2009), pp. 726–729.
- [239] Saulius Gražulis et al. "Crystallography Open Database (COD): An Open-Access Collection of Crystal Structures and Platform for World-Wide Collaboration". In: *Nucleic Acids Research* 40.D1 (2012), pp. D420–D427.
- [240] *Search Match – Qualx2*.
- [241] Brian H. Toby and Robert B. Von Dreele. "GSAS-II : The Genesis of a Modern Open-Source All Purpose Crystallography Software Package". In: *Journal of Applied Crystallography* 46.2 (2013), pp. 544–549.
- [242] Marcus H. Mendenhall, Katharine Mullen, and James P. Cline. "An Implementation of the Fundamental Parameters Approach for Analysis of X-ray Powder Diffraction Line Profiles". In: *Journal of Research of the National Institute of Standards and Technology* 120 (2015), p. 223.

- [243] P. Thompson, D. E. Cox, and J. B. Hastings. “Rietveld Refinement of Debye–Scherrer Synchrotron X-ray Data from Al₂O₃”. In: *Journal of Applied Crystallography* 20.2 (1987), pp. 79–83.
- [244] Paolo Scardi and Matteo Leoni. “Diffraction Line Profiles from Polydisperse Crystalline Systems”. In: *Acta Crystallographica Section A Foundations of Crystallography* 57.5 (2001), pp. 604–613.
- [245] J. I. Langford, D. Louër, and P. Scardi. “Effect of a Crystallite Size Distribution on X-ray Diffraction Line Profiles and Whole-Powder-Pattern Fitting”. In: *Journal of Applied Crystallography* 33.3 (2000), pp. 964–974.
- [246] James A. Kaduk and Joel Reid. “Typical Values of Rietveld Instrument Profile Coefficients”. In: *Powder Diffraction* 26.1 (2011), pp. 88–93.
- [247] S. R. Hall, F. H. Allen, and I. D. Brown. “The Crystallographic Information File (CIF): A New Standard Archive File for Crystallography”. In: *Acta Crystallographica Section A Foundations of Crystallography* 47.6 (1991), pp. 655–685.
- [248] Brian H. Toby. “R Factors in Rietveld Analysis: How Good Is Good Enough?” In: *Powder Diffraction* 21.1 (2006), pp. 67–70.
- [249] K. T. Jacob, Shubhra Raj, and L. Rannesh. “Vegard’s Law: A Fundamental Relation or an Approximation?” In: *International Journal of Materials Research* 98.9 (2007), pp. 776–779.
- [250] A. R. Denton and N. W. Ashcroft. “Vegard’s Law”. In: *Physical Review A* 43.6 (1991), pp. 3161–3164.
- [251] E-an Zen. “Validity of “Vegard’s Law””. In: *American Mineralogist* 41.5-6 (1956), pp. 523–524.
- [252] Armel Le Bail. “Whole Powder Pattern Decomposition Methods and Applications: A Retrospection”. In: *Powder Diffraction* 20.4 (2005), pp. 316–326.
- [253] Branton J. Campbell et al. “ISODISPLACE : A Web-Based Tool for Exploring Structural Distortions”. In: *Journal of Applied Crystallography* 39.4 (2006), pp. 607–614.
- [254] *ISOTROPY Software Suite*.
- [255] Ewen Smith and Geoffrey Dent. *Modern Raman Spectroscopy: A Practical Approach*. 2nd edition. Hoboken, NJ: Wiley, 2019. 256 pp.
- [256] Peter Larkin. *Infrared and Raman Spectroscopy: Principles and Spectral Interpretation*. 2nd edition. Amsterdam, Netherlands ; Oxford, United Kingdom ; Cambridge, MA, United States: Elsevier, 2017. 286 pp.
- [257] Kannan M. Krishnan. *Principles of Materials Characterization and Metrology*. New York: Oxford University Press, 2021. 880 pp.
- [258] Peter Vandenabeele. *Practical Raman Spectroscopy: An Introduction*. 1st edition. Wiley, 2013. 190 pp.
- [259] Alan Vincent. *Molecular Symmetry and Group Theory : A Programmed Introduction to Chemical Applications, 2nd Edition*. 2nd edition. Chichester ; New York: Wiley, 2001. 202 pp.
- [260] David M. Bishop. *Group Theory and Chemistry*. Revised ed. edition. New York: Dover Publications, 1993. 336 pp.

- [261] Boris S. Tsukerblat. *Group Theory in Chemistry and Spectroscopy: A Simple Guide to Advanced Usage*. Illustrated edition. Mineola, N.Y: Dover Publications, 2006. 464 pp.
- [262] Daniel C. Harris and Michael D. Bertolucci. *Symmetry and Spectroscopy: An Introduction to Vibrational and Electronic Spectroscopy*. New edition. New York: Dover Publications, 1989. 576 pp.
- [263] E. Bright Wilson Jr, J. C. Decius, and Paul C. Cross. *Molecular Vibrations: The Theory of Infrared and Raman Vibrational Spectra*. Revised ed. edition. New York: Dover Publications, 1980. 416 pp.
- [264] Morton Hamermesh. *Group Theory and Its Application to Physical Problems*. Reprint edition. New York: Dover Publications, 1989. 509 pp.
- [265] Michael Tinkham. *Group Theory and Quantum Mechanics*. Illustrated edition. Mineola, N.Y: Dover Publications, 2003. 340 pp.
- [266] Mildred S. Dresselhaus, Gene Dresselhaus, and Ado Jorio. *Group Theory: Application to the Physics of Condensed Matter*. Softcover reprint of hardcover 1st ed. 2008 edition. Berlin Heidelberg: Springer, 2010. 596 pp.
- [267] Granite. *What Is Raman Spectroscopy? | Raman Spectroscopy Principle*.
- [268] *Raman Spectroscopy*. In: *Wikipedia*. 2023.
- [269] E. Kroumova et al. "Bilbao Crystallographic Server : Useful Databases and Tools for Phase-Transition Studies". In: *Phase Transitions* 76.1-2 (2003), pp. 155–170.
- [270] J. Perez-Mato et al. "Crystallography Online: Bilbao Crystallographic Server". In: *Bulgarian Chemical Communications* 43 (2011), pp. 183–197.
- [271] Nayeli M. Cepeda-Sánchez et al. "Cations Size Mismatch versus Bonding Characteristics: Synthesis, Structure and Oxygen Ion Conducting Properties of Pyrochlore-Type Lanthanide Hafnates". In: *Journal of Materials Science* 53.19 (2018), pp. 13513–13529.
- [272] Massey de los Reyes et al. "The Pyrochlore to Defect Fluorite Phase Transition in $\text{Y}_2\text{Sn}_{2-x}\text{Zr}_x\text{O}_7$ ". In: *RSC Advances* 3.15 (2013), p. 5090.
- [273] Wei Fan et al. "Principal Element Design of Pyrochlore-Fluorite Dual-Phase Medium- and High-Entropy Ceramics". In: *Journal of Materials Science & Technology* 107 (2022), pp. 149–154.
- [274] Antonio F. Fuentes et al. "Synthesis of Disordered Pyrochlores, Ti_2O_7 (, Gd and Dy), by Mechanical Milling of Constituent Oxides". In: *Solid State Sciences* 7.4 (2005), pp. 343–353.
- [275] Marianne Glerup, Ole Faurskov Nielsen, and Finn Willy Poulsen. "The Structural Transformation from the Pyrochlore Structure, $\text{A}_2\text{B}_2\text{O}_7$, to the Fluorite Structure, AO_2 , Studied by Raman Spectroscopy and Defect Chemistry Modeling". In: *Journal of Solid State Chemistry* 160.1 (2001), pp. 25–32.
- [276] Lei Guo, Yu Zhang, and Fuxing Ye. "Phase Structure Evolution and Thermo-Physical Properties of Nonstoichiometry $\text{Nd}_{2-x}\text{Zr}_{2+x}\text{O}_{7+x/2}$ Pyrochlore Ceramics". In: *Journal of the American Ceramic Society* 98.3 (2015). Ed. by M. A. White, pp. 1013–1018.
- [277] H. C. Gupta et al. "Lattice Dynamic Investigation of the Zone Center Wavenumbers of the Cubic $\text{A}_2\text{Ti}_2\text{O}_7$ Pyrochlores". In: *Journal of Raman Spectroscopy* 32.1 (2001), pp. 41–44.

- [278] L. P. Lyashenko et al. "Local Structure of Highly Imperfect Fluorite-Derived $R_2Ti_2O_7$ -Based ($R = Yb, Lu$) Solid Solutions". In: *Inorganic Materials* 58.4 (2022), pp. 379–388.
- [279] M. Maczka et al. "Temperature-Dependent Raman Scattering Studies of the Geometrically Frustrated Pyrochlores $Dy_2Ti_2O_7$, $Gd_2Ti_2O_7$ and $Er_2Ti_2O_7$: Raman Scattering Studies of $Dy_2Ti_2O_7$, $Gd_2Ti_2O_7$ and $Er_2Ti_2O_7$ ". In: *Journal of Raman Spectroscopy* 39.4 (2008), pp. 537–544.
- [280] B.P. Mandal et al. "Preparation, XRD and Raman Spectroscopic Studies on New Compounds $RE_2Hf_2O_7$ ($RE=Dy, Ho, Er, Tm, Lu, Y$): Pyrochlores or Defect-Fluorite?". In: *Journal of Solid State Chemistry* 179.7 (2006), pp. 1990–1994.
- [281] D. Michel, M. Perez y Jorba, and R. Collongues. "Study by Raman Spectroscopy of Order-Disorder Phenomena Occurring in Some Binary Oxides with Fluorite-Related Structures". In: *Journal of Raman Spectroscopy* 5.2 (1976), pp. 163–180.
- [282] A. K. Mishra et al. "The Study of Pressure Induced Structural Phase Transition in Spin-Frustrated $Yb_2Ti_2O_7$ Pyrochlore". In: *Journal of Applied Physics* 111.3 (2012), p. 033509.
- [283] Toshihiro Moriga et al. "X-Ray and Raman Study on Coordination States of Fluorite- and Pyrochlore-Type Compounds in the System ZrO_2 - Gd_2O_3 ". In: *Solid State Ionics* 40–41 (1990), pp. 357–361.
- [284] S. Nandi, Y.M. Jana, and H.C. Gupta. "Lattice Dynamical Investigation of the Raman and Infrared Wave Numbers and Heat Capacity Properties of the Pyrochlores $R_2Zr_2O_7$ ($R = La, Nd, Sm, Eu$)". In: *Journal of Physics and Chemistry of Solids* 115 (2018), pp. 347–354.
- [285] Barnita Paul et al. "Structural Properties and the Fluorite–Pyrochlore Phase Transition in $La_2Zr_2O_7$: The Role of Oxygen to Induce Local Disordered States". In: *Journal of Alloys and Compounds* 686 (2016), pp. 130–136.
- [286] V.V. Popov et al. "Formation and Evolution of Crystal and Local Structures in Nanostructured $Ln_2Ti_2O_7$ ($Ln = Gd-Dy$)". In: *Journal of Alloys and Compounds* 746 (2018), pp. 377–390.
- [287] V.V. Popov et al. "Comparative Analysis of Long- and Short-Range Structures Features in Titanates $Ln_2Ti_2O_7$ and Zirconates $Ln_2Zr_2O_7$ ($Ln = Gd, Tb, Dy$) upon the Crystallization Process". In: *Journal of Physics and Chemistry of Solids* 130 (2019), pp. 144–153.
- [288] V.V. Popov et al. "A XAFS Investigation of Amorphous-to-Crystalline and Fluorite-to-Pyrochlore Phase Transitions in $Ln_2M_2O_7$ ($Ln = Gd, Tb, Dy; M = Ti, Zr$)". In: *Radiation Physics and Chemistry* 175 (2020), p. 108469.
- [289] Dylan R. Rittman et al. "Strain Engineered Pyrochlore at High Pressure". In: *Scientific Reports* 7.1 (2017), p. 2236.
- [290] Surajit Saha et al. "High-Pressure Raman and x-Ray Study of the Spin-Frustrated Pyrochlore $Gd_2Ti_2O_7$ ". In: *Physical Review B* 74.6 (2006), p. 064109.
- [291] Surajit Saha et al. "Temperature-Dependent Raman and x-Ray Studies of the Spin-Ice Pyrochlore $Dy_2Ti_2O_7$ and Nonmagnetic Pyrochlore $Lu_2Ti_2O_7$ ". In: *Physical Review B* 78.21 (2008), p. 214102.

- [292] Sheetal and C. S. Yadav. "Evolution of Spin Freezing Transition and Structural, Magnetic Phase Diagram of Dy_{2-x}La_xZr₂O₇". In: *Scientific Reports* 11.1 (2021), p. 19832.
- [293] Surjeet Singh et al. "Manifestation of Geometric Frustration on Magnetic and Thermodynamic Properties of the Pyrochlores Sm₂X₂O₇ (X = Ti, Zr)". In: *Physical Review B* 77.5 (2008), p. 054408.
- [294] M. T. Vandenborre et al. "Rare-Earth Titanates and Stannates of Pyrochlore Structure; Vibrational Spectra and Force Fields". In: *Journal of Raman Spectroscopy* 14.2 (1983), pp. 63–71.
- [295] M. T. Vandenborre, E. Husson, and J. L. Fourquet. "Spectres vibrationnels et champ de force de divers composés de formule A₂B₂O₇ et A₂B₂O₆ de structure pyrochlore". In: *Spectrochimica Acta Part A: Molecular Spectroscopy* 38.9 (1982), pp. 997–1003.
- [296] N. T. Vandenborre, E. Husson, and H. Brusset. "Analyse en coordonnées normales des composés A₂IIIB₂IVO₇ (A = La, Nd; B = Zr, Hf) de structure pyrochlore". In: *Spectrochimica Acta Part A: Molecular Spectroscopy* 37.2 (1981), pp. 113–118.
- [297] P. K. Verma et al. "Experimental and Theoretical Study of Anomalous Temperature Dependence of Phonons in Y₂Ti₂O₇ Pyrochlore". In: *Physical Review B* 106.14 (2022), p. 144303.
- [298] F.X. Zhang and S.K. Saxena. "Structural Changes and Pressure-Induced Amorphization in Rare Earth Titanates RE₂Ti₂O₇ (RE: Gd, Sm) with Pyrochlore Structure". In: *Chemical Physics Letters* 413.1-3 (2005), pp. 248–251.
- [299] John F. McCaffrey, Neil T. McDevitt, and Conrad M. Phillippi. "Infrared Lattice Spectra of Rare-Earth Stannate and Titanate Pyrochlores". In: *JOSA* 61.2 (1971), pp. 209–212.
- [300] V.T. Srikar et al. "Micro-Raman Measurement of Bending Stresses in Micromachined Silicon Flexures". In: *Journal of Microelectromechanical Systems* 12.6 (2003), pp. 779–787.
- [301] Sugandha Dogra Pandey et al. "Anharmonic Behavior and Structural Phase Transition in Yb₂O₃". In: *AIP Advances* 3.12 (2013), p. 122123.
- [302] Wolfgang Demtröder. *Laser Spectroscopy 1: Basic Principles*. 5th ed. 2014 edition. New York: Springer, 2014. 514 pp.
- [303] Xueyin Yuan and Robert A. Mayanovic. "An Empirical Study on Raman Peak Fitting and Its Application to Raman Quantitative Research". In: *Applied Spectroscopy* 71.10 (2017), pp. 2325–2338.
- [304] Vitaly I. Korepanov and Daria M. Sedlovets. "An Asymmetric Fitting Function for Condensed-Phase Raman Spectroscopy". In: *The Analyst* 143.11 (2018), pp. 2674–2679.
- [305] Marcin Wojdyr. "Fityk : A General-Purpose Peak Fitting Program". In: *Journal of Applied Crystallography* 43.5 (2010), pp. 1126–1128.
- [306] Frank Pobell. *Matter and Methods at Low Temperatures*. 3rd, rev. and exp. ed. 2007 edition. Berlin ; New York: Springer, 2007. 480 pp.
- [307] Steven W. Van Sciver. *Helium Cryogenics*. 2nd edition. Springer, 2012. 787 pp.
- [308] Guy K. White and Philip Meeson. *Experimental Techniques in Low-Temperature Physics*. 4th edition. Oxford University Press, 2002. 396 pp.

- [309] Christian Enss and Siegfried Hunklinger. *Low-Temperature Physics*. 2005th edition. Berlin ; New York: Springer, 2005. 587 pp.
- [310] Robert C. Richardson and Eric N. Smith. *Experimental Techniques in Condensed Matter Physics at Low Temperatures*. Revised edition. Boulder, Colo: CRC Press, 1998. 352 pp.
- [311] Richard Burdett. "Amplitude Modulated Signals: The Lock-in Amplifier". In: *Handbook of Measuring System Design*. John Wiley & Sons, Ltd, 2005.
- [312] *Lock-in Amplifier - Application Note*.
- [313] Paul A. Temple. "An Introduction to Phase-sensitive Amplifiers: An Inexpensive Student Instrument". In: *American Journal of Physics* 43.9 (1975), pp. 801–807.
- [314] dkk04747. *Lock-in Amplifier*.
- [315] *Model SR830 DSP Lock-in Amplifier*. Revision 2.5. manual. Stanford Research Systems. 2011.
- [316] Ph. Vanderbemden. "Design of an A.C. Susceptometer Based on a Cryocooler". In: *Cryogenics* 38.8 (1998), pp. 839–842.
- [317] Francisco Almeida. "Development of a Miniature AC Susceptometer for a Cryogenic System". In: 2015.
- [318] C. C. de Faria, A. J. A. de Oliveira, and W. A. Ortiz. "Estudo de Materiais Pela Técnica de Suscetibilidade Magnética AC". In: *Revista Brasileira de Ensino de Física* ().
- [319] M. Prasad, R. R. Rao, and A. K. R. Chaudhuri. "A Versatile AC Mutual Inductance Bridge". In: *Journal of Physics E: Scientific Instruments* 19.12 (1986), p. 1013.
- [320] Michal Lisowski. "Metrological Analysis of the Modified Hartshorn Bridges Used for Susceptibility Measurement at Low Temperatures". In: *Metrology and Measurement Systems* 2 (1995) (2021), pp. 257–275.
- [321] L. J. M. van de Klundert et al. "Induction Methods Used in Low Temperature Physics". In: *Cryogenics* 15.10 (1975), pp. 577–589.
- [322] S. C. Whitmore, S. R. Ryan, and T. M. Sanders. "Mutual Inductance Bridge for Low-temperature Thermometry and Susceptibility Measurements". In: *Review of Scientific Instruments* 49.11 (1978), pp. 1579–1582.
- [323] Wesley Burgei, Michael J. Pechan, and Herbert Jaeger. "A Simple Vibrating Sample Magnetometer for Use in a Materials Physics Course". In: *American Journal of Physics* 71.8 (2003), pp. 825–828.
- [324] N. F. Oliveira and S. Foner. "Operation of Conventional Vibrating Sample Magnetometer at 3He Temperatures and in High Magnetic Fields". In: *Review of Scientific Instruments* 43.1 (1972), pp. 37–39.
- [325] Simon Foner. "Versatile and Sensitive Vibrating-Sample Magnetometer". In: *Review of Scientific Instruments* 30.7 (1959), pp. 548–557.
- [326] S. Foner. "The Vibrating Sample Magnetometer: Experiences of a Volunteer (Invited)". In: *Journal of Applied Physics* 79.8 (1996), pp. 4740–4745.
- [327] V. Lopez-Dominguez et al. "A Simple Vibrating Sample Magnetometer for Macroscopic Samples". In: *Review of Scientific Instruments* 89.3 (2018), p. 034707.
- [328] *Magnetic Refrigeration - Next-Generation Cooling Technology*.

- [329] P. K. Schelling, S. R. Phillpot, and R. W. Grimes. "Optimum Pyrochlore Compositions for Low Thermal Conductivity". In: *Philosophical Magazine Letters* 84.2 (2004), pp. 127–137.
- [330] Cambridge Cryogenics. *mK Magnetic Refrigerator CC51-USP System Information*.
- [331] R. F. Wielinga, J. Lubbers, and W. J. Huiskamp. "Heat Capacity Singularities in Two Gadolinium Salts below 1°K". In: *Physica* 37.3 (1967), pp. 375–392.
- [332] S T Bramwell et al. "Bulk Magnetization of the Heavy Rare Earth Titanate Pyrochlores - a Series of Model Frustrated Magnets". In: *Journal of Physics: Condensed Matter* 12.4 (2000), pp. 483–495.
- [333] S. Säubert et al. "Orientation Dependence of the Magnetic Phase Diagram of $\text{Yb}_2\text{Ti}_2\text{O}_7$ ". In: *Physical Review B* 101.17 (2020), p. 174434.
- [334] Z. L. Dun et al. "Chemical Pressure Effects on Magnetism in the Quantum Spin Liquid Candidates $\text{Yb}_2\text{X}_2\text{O}_7$ ($\text{X} = \text{Sn}, \text{Ti}, \text{Ge}$)". In: *Physical Review B* 89.6 (2014), p. 064401.
- [335] Q.J. Li et al. "Single Crystal Growth of the Pyrochlores $\text{R}_2\text{Ti}_2\text{O}_7$ ($\text{R}=\text{rare Earth}$) by the Optical Floating-Zone Method". In: *Journal of Crystal Growth* 377 (2013), pp. 96–100.
- [336] J.S Gardner, B.D Gaulin, and D.McK Paul. "Single Crystal Growth by the Floating-Zone Method of a Geometrically Frustrated Pyrochlore Antiferromagnet, $\text{Tb}_2\text{Ti}_2\text{O}_7$ ". In: *Journal of Crystal Growth* 191.4 (1998), pp. 740–745.
- [337] G Balakrishnan et al. "Single Crystal Growth of Rare Earth Titanate Pyrochlores". In: *Journal of Physics: Condensed Matter* 10.44 (1998), pp. L723–L725.
- [338] Monica Ciomaga Hatnean et al. "Zirconate Pyrochlore Frustrated Magnets: Crystal Growth by the Floating Zone Technique". In: *Crystals* 6.7 (2016), p. 79.
- [339] *DISCUS Package Home Page*.
- [340] Sarah C. Finkeldei et al. "Insight Into Disorder, Stress and Strain of Radiation Damaged Pyrochlores: A Possible Mechanism for the Appearance of Defect Fluorite". In: *Frontiers in Chemistry* 9 (2021), p. 706736.
- [341] Gregory R. Lumpkin and Robert D. Aughterson. "Perspectives on Pyrochlores, Defect Fluorites, and Related Compounds: Building Blocks for Chemical Diversity and Functionality". In: *Frontiers in Chemistry* 9 (2021), p. 778140.
- [342] Julia L. Payne, Matthew G. Tucker, and Ivana Radosavljević Evans. "From Fluorite to Pyrochlore: Characterisation of Local and Average Structure of Neodymium Zirconate, $\text{Nd}_2\text{Zr}_2\text{O}_7$ ". In: *Journal of Solid State Chemistry* 205 (2013), pp. 29–34.
- [343] Jie Lian et al. "Radiation-Induced Amorphization of Rare-Earth Titanate Pyrochlores". In: *Physical Review B* 68.13 (2003), p. 134107.
- [344] Candice Kinsler-Fedon et al. "Synthesis, Characterization, and Single-Crystal Growth of a High-Entropy Rare-Earth Pyrochlore Oxide". In: *Physical Review Materials* 4.10 (2020), p. 104411.
- [345] Laura Martel et al. "Fingerprint of Local Disorder in Long Range Ordered Isometric Pyrochlores". In: *Scientific Reports* 7.1 (2017), p. 12269.
- [346] R. Sarkar et al. "Spin Freezing in the Disordered Pyrochlore Magnet $\text{NaCaCo}_2\text{F}_7$: NMR Studies and Monte Carlo Simulations". In: *Physical Review B* 96.23 (2017), p. 235117.

- [347] Masahide Nishiyama et al. "NMR Study of Pyrochlore Lattice Antiferromagnet, Melan-thallite Cu_2OCl_2 ". In: *Journal of Physics: Conference Series* 320.1 (2011), p. 012030.
- [348] Simon W. Reader et al. "Cation Disorder in Pyrochlore Ceramics: 89Y MAS NMR and First-Principles Calculations". In: *The Journal of Physical Chemistry C* 113.43 (2009), pp. 18874–18883.
- [349] Hironori Sakai et al. "TI-NMR Study of Pyrochlore Oxide $\text{Ti}_2\text{Ru}_2\text{O}_7$: Observation of Spin-Singlet Formation". In: *Journal of the Physical Society of Japan* 71.2 (2002), pp. 422–424.
- [350] Hironori Sakai et al. "NMR Study of Metallic Pyrochlore Ruthenium Oxides, $\text{Bi}_2\text{Ru}_2\text{O}_7$ and $\text{Pb}_2\text{Ru}_2\text{O}_7$ ". In: *Journal of Physics and Chemistry of Solids*. Proceedings of the 8th ISSP International Symposium 63.6 (2002), pp. 1039–1041.
- [351] O Vyaselev et al. "Cd and Re NMR/NQR in Pyrochlore Compound $\text{Cd}_2\text{Re}_2\text{O}_7$ ". In: *Journal of Physics and Chemistry of Solids*. Proceedings of the 8th ISSP International Symposium 63.6 (2002), pp. 1031–1034.
- [352] Bryce G. Mullens et al. "Average and Local Ordering of $\text{Yb}_2(\text{Ti}_2\text{-Yb})\text{O}_7$ -/2 'Stuffed' Pyrochlores: The Development of a Robust Structural Model". In: *Journal of Solid State Chemistry* 302 (2021), p. 122412.
- [353] G. Sala et al. "Vacancy Defects and Monopole Dynamics in Oxygen-Deficient Pyrochlores". In: *Nature Materials* 13.5 (2014), pp. 488–493.
- [354] S. F. Mayer et al. "A Comprehensive Examination of the Local- and Long-Range Structure of Sb_6O_{13} Pyrochlore Oxide". In: *Scientific Reports* 10.1 (2020), p. 16956.
- [355] S.-W. Han, J. S. Gardner, and C. H. Booth. "Structural Properties of the Geometrically Frustrated Pyrochlore $\text{Tb}_2\text{Ti}_2\text{O}_7$ ". In: *Physical Review B* 69.2 (2004), p. 024416.
- [356] J. van Duijn et al. "Induced Quadrupolar Singlet Ground State of Praseodymium in a Modulated Pyrochlore". In: *Physical Review B* 96.9 (2017), p. 094409.
- [357] I. Mirebeau et al. "Pressure-Induced Crystallization of a Spin Liquid". In: *Nature* 420.6911 (2002), pp. 54–57.
- [358] Andrea Di Cicco. "X-Ray Absorption Spectroscopy Investigations of Disordered Matter". In: *Radiation Physics and Chemistry* 175 (2020), p. 108077.
- [359] Matthew Newville. "Fundamentals of XAFS". In: *Reviews in Mineralogy and Geochemistry* 78.1 (2014), pp. 33–74.
- [360] Peter E.R. Blanchard et al. "Does Local Disorder Occur in the Pyrochlore Zirconates?" In: *Inorganic Chemistry* 51.24 (2012), pp. 13237–13244.
- [361] V.V. Popov et al. "Fluorite-Pyrochlore Phase Transition in Nanostructured $\text{Ln}_2\text{Hf}_2\text{O}_7$ ($\text{Ln} = \text{La-Lu}$)". In: *Journal of Alloys and Compounds* 689 (2016), pp. 669–679.
- [362] P.M. Martin et al. "EXAFS Study of the Structural Phase Transition in the Americium Zirconate Pyrochlore". In: *Journal of Nuclear Materials* 385.1 (2009), pp. 126–130.
- [363] N. J. Hess et al. "Spectroscopic Investigations of the Structural Phase Transition in $\text{Gd}_2(\text{Ti}_{1-y}\text{Zr}_y)_2\text{O}_7$ Pyrochlores". In: *The Journal of Physical Chemistry B* 106.18 (2002), pp. 4663–4677.
- [364] A. V. Kuznetsov et al. "Magnetization of Crystalline and Amorphous Phases of $\text{R}_2\text{Ti}_2\text{O}_7$ and $\text{R}_2\text{Zr}_2\text{O}_7$ ($\text{R} = \text{Gd, Dy, Tb}$)". In: *Journal of Superconductivity and Novel Magnetism* 33.8 (2020), pp. 2395–2404.

- [365] G. Sattonnay et al. "Key Role of the Short-Range Order on the Response of the Titanate Pyrochlore $Y_2Ti_2O_7$ to Irradiation". In: *Physical Review B* 94.22 (2016), p. 224109.
- [366] *Emu – LNLS*.
- [367] Takeshi Egami and S. J. L. Billinge. *Underneath the Bragg Peaks: Structural Analysis of Complex Materials*. Pergamon Materials Series v. 7. Kiddington, Oxford, UK ; Boston: Pergamon, 2003. 404 pp.
- [368] Simon J. L. Billinge. "The Rise of the X-ray Atomic Pair Distribution Function Method: A Series of Fortunate Events". In: *Philosophical Transactions of the Royal Society A: Mathematical, Physical and Engineering Sciences* 377.2147 (2019), p. 20180413.
- [369] Tatiana E. Gorelik et al. "Towards Quantitative Treatment of Electron Pair Distribution Function". In: *Acta Crystallographica Section B Structural Science, Crystal Engineering and Materials* 75.4 (2019), pp. 532–549.
- [370] João Batista Souza Junior et al. "Pair Distribution Function Obtained from Electron Diffraction: An Advanced Real-Space Structural Characterization Tool". In: *Matter* 4.2 (2021), pp. 441–460.
- [371] Devon Lee Drey et al. "Local Ordering in Disordered $Nd_xZr_{1-x}O_{2-0.5x}$ Pyrochlore as Observed Using Neutron Total Scattering". In: *SSRN Electronic Journal* (2021).
- [372] Stefan T. Norberg et al. "Pyrochlore to Fluorite Transition: The $Y_2(Ti_{1-x}Zr_x)_2O_7$ (0.0 - x - 1.0) System". In: *Chemistry of Materials* 24.22 (2012), pp. 4294–4300.
- [373] Eric C. O'Quinn et al. "Advanced Characterization Technique for Mechanochemically Synthesized Materials: Neutron Total Scattering Analysis". In: *Journal of Materials Science* 53.19 (2018), pp. 13400–13410.
- [374] J. E. Greedan et al. "Local and Average Structures of the Spin-Glass Pyrochlore $Y_2Mo_2O_7$ from Neutron Diffraction and Neutron Pair Distribution Function Analysis". In: *Physical Review B* 79.1 (2009), p. 014427.
- [375] Daniel P. Shoemaker et al. "Incoherent Bi Off-Centering in $Bi_2Ti_2O_6O'$ and $Bi_2Ru_2O_6O'$: Insulator versus Metal". In: *Physical Review B* 84.6 (2011), p. 064117.
- [376] Devon L. Drey et al. "Disorder in $Ho_2Ti_{2-x}Zr_xO_7$: Pyrochlore to Defect Fluorite Solid Solution Series". In: *RSC Advances* 10.57 (2020), pp. 34632–34650.
- [377] Bo Jiang et al. "Probing the Local Site Disorder and Distortion in Pyrochlore High-Entropy Oxides". In: *Journal of the American Chemical Society* 143.11 (2021), pp. 4193–4204.
- [378] *Beamlines – LNLS*.